NEURONAL MECHANICS AND TRANSPORT

EDITED BY: Daniel M. Suter and Kyle E. Miller
PUBLISHED IN: Frontiers in Cellular Neuroscience

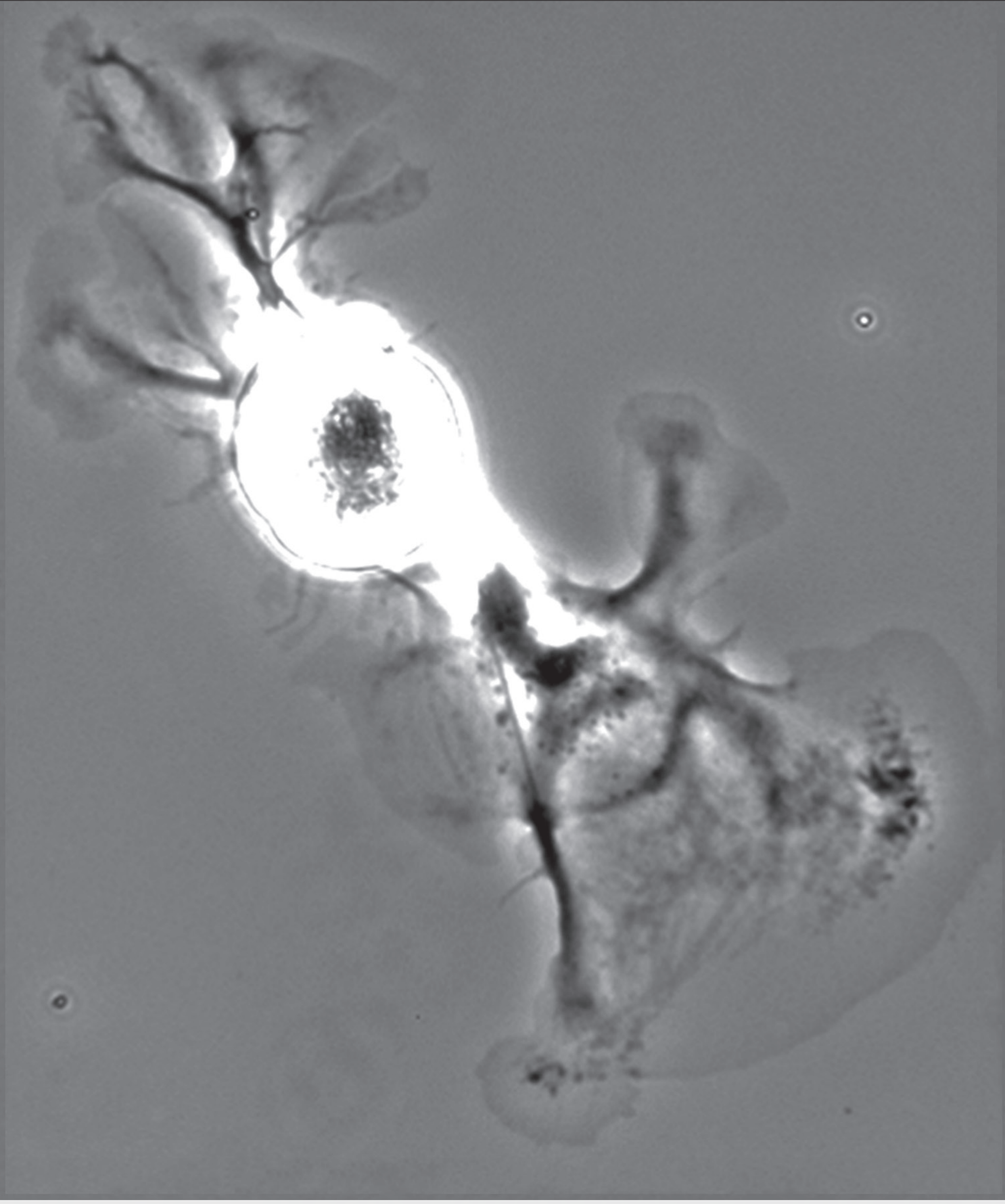

frontiers Research Topics

ISSN 1664-8714
ISBN 978-2-88919-823-8
DOI 10.3389/978-2-88919-823-8

About Frontiers

Frontiers is more than just an open-access publisher of scholarly articles: it is a pioneering approach to the world of academia, radically improving the way scholarly research is managed. The grand vision of Frontiers is a world where all people have an equal opportunity to seek, share and generate knowledge. Frontiers provides immediate and permanent online open access to all its publications, but this alone is not enough to realize our grand goals.

Frontiers Journal Series

The Frontiers Journal Series is a multi-tier and interdisciplinary set of open-access, online journals, promising a paradigm shift from the current review, selection and dissemination processes in academic publishing. All Frontiers journals are driven by researchers for researchers; therefore, they constitute a service to the scholarly community. At the same time, the Frontiers Journal Series operates on a revolutionary invention, the tiered publishing system, initially addressing specific communities of scholars, and gradually climbing up to broader public understanding, thus serving the interests of the lay society, too.

Dedication to Quality

Each Frontiers article is a landmark of the highest quality, thanks to genuinely collaborative interactions between authors and review editors, who include some of the world's best academicians. Research must be certified by peers before entering a stream of knowledge that may eventually reach the public - and shape society; therefore, Frontiers only applies the most rigorous and unbiased reviews.

Frontiers revolutionizes research publishing by freely delivering the most outstanding research, evaluated with no bias from both the academic and social point of view.

By applying the most advanced information technologies, Frontiers is catapulting scholarly publishing into a new generation.

What are Frontiers Research Topics?

Frontiers Research Topics are very popular trademarks of the Frontiers Journals Series: they are collections of at least ten articles, all centered on a particular subject. With their unique mix of varied contributions from Original Research to Review Articles, Frontiers Research Topics unify the most influential researchers, the latest key findings and historical advances in a hot research area! Find out more on how to host your own Frontiers Research Topic or contribute to one as an author by contacting the Frontiers Editorial Office: **researchtopics@frontiersin.org**

NEURONAL MECHANICS AND TRANSPORT

Topic Editors:
Daniel M. Suter, Purdue University, USA
Kyle E. Miller, Michigan State University, USA

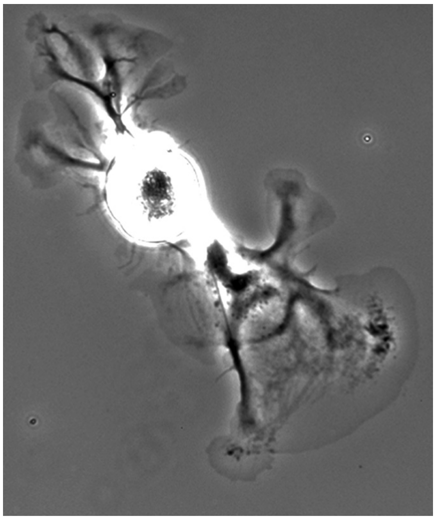

Phase contrast image of Aplysia bag cell neuron cultured on poly-L-lysine-coated glass cover slip. These large neurons provide an excellent model system for cell biological and biophysical analysis of growth cone motility.
Image courtesy of Aih Cheun Lee, Suter Lab

Understanding the underlying mechanisms of how axons and dendrites develop is a fundamental problem in neuroscience and a main goal of research on nervous system development and regeneration. Previous studies have provided a tremendous amount of information on signaling and cytoskeletal proteins regulating axonal and dendritic growth and guidance. However, relatively little is known about the relative contribution and role of cytoskeletal dynamics, transport of organelles and cytoskeletal components, and force generation to axonal elongation. Advancing the knowledge of these biomechanical processes is critical to better understand the development of the nervous system, the pathological progression of neurodegenerative diseases, acute traumatic injury, and for designing novel approaches to promote neuronal regeneration following disease, stroke, or trauma.

Mechanical properties and forces shape the development of the nervous system from the cellular up to the organ level. Recent advances in quantitative live cell imaging, biophysical, and nanotechnological methods such as traction force microscopy, optical tweezers, and atomic force microscopy have enabled researchers to gain better insights into how cytoskeletal dynamics and motor-driven transport, membrane-dynamics, adhesion, and substrate rigidity influence axonal elongation. Given the complexity and mechanical nature of this problem, mathematical modeling contributes significantly to our understanding of neuronal mechanics. Nonetheless, there has been limited direct interaction and discussions between experimentalists and theoreticians in this research area. The purpose of this Frontiers Research Topic is to highlight exciting and important work that is currently developing in the fields of neuronal cell biology, neuronal mechanics, intracellular transport, and mathematical modeling in the form of primary research articles, reviews, perspectives, and commentaries.

Citation: Suter, D. M., Miller, K. E., eds. (2016). Neuronal Mechanics and Transport. Lausanne: Frontiers Media. doi: 10.3389/978-2-88919-823-8

Table of Contents

frontiers in Cellular Neuroscience

EDITORIAL
published: 26 January 2016
doi: 10.3389/fncel.2016.00001

Editorial: Neuronal Mechanics and Transport

Kyle E. Miller[1]* *and Daniel M. Suter*[2]*

[1] *Department of Integrative Biology, Michigan State University, East Lansing, MI, USA,* [2] *Department of Biological Sciences, Bindley Bioscience Center, Purdue University, West Lafayette, IN, USA*

Keywords: neuronal mechanics, force, neuronal development, stiffness, glia, neuronal transport, axonal elongation, neuronal morphology

The Editorial on the Research Topic

Neuronal Mechanics and Transport

Past research on nervous system development was largely centered on the role of molecules and biochemical signaling cascades. However, recent biophysical work has clearly demonstrated the additional importance of forces in shaping neuronal morphology and driving intracellular transport as well as the role of stiffness for cellular behavior. The research topic "Neuronal Mechanics and Transport" brings together related research articles and reviews with the long-term goal of fostering a community of scientists interested in this interdisciplinary topic.

THE SHAPING OF NEURONS, GLIA, AND THE BRAIN

The importance of forces in shaping the morphology of the nervous system spans scales ranging from the whole brain down to individual cells and involves both neurons and glia. Budday et al. focus on cortical folding. They briefly review the developmental biology of the human brain and then discuss modeling and experimental work designed to elucidate the mechanisms underlying cortical folding. They emphasize that local differences in stiffness, growth rate, and cellular force balance during normal development lead to the characteristic pattern of folding and discuss how diseases that impact these underlying processes lead to either increases or decreases in the number of folds. Bollmann et al. investigated durotaxis in microglia using traction force microscopy (Bollmann et al.). Using experimental and theoretical analysis, they make a compelling argument that microglia preferentially migrate toward stiffer regions because they take larger steps in the direction of the stiffer region. In turn Schwann cells are important for myelinating neurons in the peripheral nervous system. Like neurons, they have an extended geometry and locally synthesize proteins in response to local signals and protein demand. Love and Shah monitored ribosomal transport in Schwann cells by expressing a GFP tagged version of the ribosomal L4 subunit and then developed a rate kinetics model of ribosomal transport. They found that initially levels of transport were high, but then declined as Schwann cells began myelination. Together these studies are important because they remind us that glia are as important as neurons when considering the mechanics of nervous system.

Edited and reviewed by:
Christian Hansel,
University of Chicago, USA

Correspondence:
Kyle E. Miller
kmiller@msu.edu;
Daniel M. Suter
dsuter@purdue.edu

Received: *19 December 2015*
Accepted: *04 January 2016*
Published: *26 January 2016*

Citation:
Miller KE and Suter DM (2016) Editorial: Neuronal Mechanics and Transport. Front. Cell. Neurosci. 10:1. doi: 10.3389/fncel.2016.00001

CONTROLLING AXONAL AND DENDRITIC LENGTH, BRANCHING, AND DIAMETER

Controlling local protein production and long distance transport of material is a major engineering challenge for neurons. A recent idea proposes that neurons can sense the length of axons and in turn control the rate of protein production. This leads to the obvious question of how.

Bressloff and Karamched build on the idea, first developed in yeast, that frequency information (i.e., regular variations in the concentration of signaling proteins) is used to regulate the activity of gene networks. They propose that as axons lengthen, the frequency of an encoded signal drops, which in turn alters the rate of material production. This work is important because it points out that as axons lengthen the precision of axonal length measurement may decrease, and it highlights the need for future experimental work. Directly related to the problem of length control is the question of how process branching is regulated. Sholl analysis is an important tool that assesses branching by measuring the number of neuronal processes that pass through concentric circles spaced at fixed internals from the cell body. O'Neill et al. compared Inside-Out, Root-Intermediate-Terminal, and Tips-In Sholl analysis while characterizing the effect of cytosolic PSD-95 interactor (cypin) on the patterning of the dendritic arbors of hippocampal neurons. They found that each approach can detect large changes in branching, but they have regional differences in their sensitivity in detecting subtle variations. They suggest that standard Sholl analysis might be improved by integrating these approaches and by making their use more transparent in software used by biologists. Finally, axons have the remarkable geometrical property of having a relatively uniform diameter over distances that can be as long a meter in humans. How diameter is consistently maintained is especially puzzling as necking (i.e., local thinning) of materials typically occurs in response to large deformations. Two of the founders of the field of neuronal mechanics Heidemann and Bray, propose the novel theory that tension may locally induce breakage and the local compaction of neurofilaments and microtubules. As a result, the transport of cytoskeletal elements along the axon is locally inhibited and material accumulates and allows the axon to return to its original diameter in regions that are locally thin. Together these studies point out the importance of understanding the relationship between neuronal geometry, mechanics, and transport.

BRAIN STRAIN AND ELECTRICAL EXCITABILITY

Most studies on neurons are typically concerned with either mechanical or electrical behavior, yet it has become clear that electrical and mechanical properties in neurons are related to each other. Fan et al. combined an innovative use of flavoprotein auto-fluorescence to track neuronal activity and controlled stretching of mouse brain slices. They demonstrate stretch-induced deformations of neuronal tissue significantly increases electrical excitability of neurons. Drapaca and Drapaca proposes an innovative electromechanical model of neurons that takes into account their viscoelastic and electrical properties as described by a Kelvin-Voigt model and the Hodgkin-Huxley equations. In turn, to test if slow stretch-induced axonal growth leads to changes in electrical activity as seen in rapid deformation, Loverde and Pfister grew rat sensory neurons in axon stretch-growth bioreactors and assessed neuronal activity using whole-cell patch clamp recording, free calcium imaging, and morphological analysis. They found no evidence of large changes in response to slow stretching, which suggests normal axonal lengthening driven by forces is distinct from traumatic axon injury. Together these studies highlight the importance of considering both the mechanical and electrochemical activity in neurons and the need for future studies on this complex problem.

SIGNALING AND MOLECULAR MECHANISMS OF AXONAL ELONGATION

In addition to mechanical forces, biochemical signaling pathways are critical in guiding growth cones correctly to their final destinations. Semaphorin 3A (Sema3A) is an important repulsive guidance cue that modulates the activities of Rac, Cdc42, and RhoA. The spatial and temporal pattern of activation and inactivation of these Rho family GTPases is poorly understood in growth cones. Using FRET microscopy in combination with an innovative method for focally applying Sema3A, Iseppon et al. analyzed how the activities of Cdc42 and RhoA change in response to Sema3A. As expected, they found that Sema3A leads to growth cone collapse, progressive activation of RhoA and overall deactivation of Cdc42. Interestingly, they found waves of Cdc42 activation propagate away from local sites of Sema3A application. An additional level of signaling control in neurons occurs through reactive oxygen species (ROS). While it is undoubted that aberrantly high levels of ROS are damaging, very low levels also disrupt normal neuronal functioning. Wilson and González-Billault review redox balance in neurons with a focus on the complex relationship between high, low, and normal levels of ROS, cellular signaling, cytoskeletal dynamics, vesicle trafficking, axonal elongation, and cognitive function. Of course these signaling pathways must target cytoskeletal elements. Microtubule plus end tracking proteins (+TIPs) bind to the plus ends of microtubules where they regulate assembly, the interaction of microtubules with the actin cytoskeleton and cell signaling. Bearce et al. review recent discoveries of well-established +TIP proteins such as CLASP and EB proteins as well as more newly recognized +TIP proteins XMAP215, TACC3, spectraplakins, and navigators. The review highlights the importance of +TIP proteins in growth cone guidance and the need for more sophisticated tools to study +TIP function including photo-manipulatable proteins and super resolution microscopy. Together, these studies point out the importance for future work that links cellular signaling and neuronal mechanics.

NEURONAL MECHANICS AND FORCES ARE DYNAMIC

An important part of understanding neuronal mechanics is describing force generation in time and space. Over the past years, there has been a surge in the development of technologies that now allow precise control over the physical environment that growth cones navigate, the application of forces to neurons and measurement of the forces they produce. Kerstein et al. provide an excellent overview of the mechanochemical regulation of growth cone motility that covers the generation of traction forces, the molecules important for force sensing, durotaxis, and the interaction between physical and chemical guidance cues. Kilinc et al. expand on this by reviewing newly developed technologies for controlling substrate stiffness, topology, and the chemical extracellular environment in which growth cones navigate. Polackwich et al. specifically investigated the traction forces generated by rat sensory neurons grown in polyacrylamide hydrogels. They showed that growth cones generate force dipoles on the substrate that are similar to those produced by migrating cells, but differ in that the force vectors create a net force that pulls the substrate rearwards and the axon forward. In addition, they noted large fluctuations in force generation that vary with a timescale of tens of seconds. In light of previous studies, they suggest these fluctuations arise as the result of the dynamic formation and disassembly of adhesions to the substrate.

Molecular motors such as kinesin, dynein, and non-muscle myosin II are critical for neuronal force generation. An important new tool for investigating dynein is the novel selective cell permeable dynein inhibitor ciliobrevin. Roossien et al. review its use of in the context of neuronal growth. They provide a brief overview of dynein function, discuss the puzzling question of why disruption of dynein inhibits kinesin (and vice versa) and the need for studies that elucidate the mechanism of action of ciliobrevin. They conclude with a summary figure that suggests dynein contributes to axonal elongation through the well-accepted long-range transport of cytoskeletal elements, organelles, and signaling molecules and in addition through the generation of forces that push the microtubule array forward. Building on the idea that dynein generates extensile forces on the microtubule array along the axon, Jakobs et al. modeled microtubule bundling and the forces associated with microtubule motors in the context of axonal elongation. Their work suggests that unipolar motors generate the forces that drive microtubule bundle expansion and bipolar motors, such as Kinesin-5 oppose this process. This work provides an important bridge between molecular dynamic simulations that focus on the behavior of individual motors and macroscopic analysis that treats the underlying geometry of axons abstractly. Athamneh and Suter first provide a brief overview of neuronal mechanics and then directly tackle the question of why reported values of neuronal forces vary over five orders of magnitude (i.e., from 0.001 to 100 nN). They suggest that a reasonable explanation for this wide degree of variation is that different types of neurons and regions of neurons naturally generate different levels of forces and that the size and mechanical properties of the probe may have an influence on what is and can be measured. In addition, they make the important point that standardized calibration methods are needed to ensure that force measurements are consistent between studies. Altogether, these studies illustrate the importance of bridging molecular, computational, and mechanical analysis for understanding neuronal mechanics.

SUMMARY

Over the past decades there has been an explosion in our knowledge of the molecules that regulate neuronal and glial growth and morphology. At this point, the major molecular players appear to be well-established, and the primary questions center on how they work together to create the physical manifestation of the nervous system. A major technical challenge in the field is to investigate mechanical properties of neurons and relate them to biochemical phenomena. The articles published in this research topic provide an interdisciplinary forum for a new branch of neuroscience dedicated to understanding neuronal mechanics and transport.

AUTHOR CONTRIBUTIONS

All authors listed, have made substantial, direct and intellectual contribution to the work, and approved it for publication.

FUNDING

This work was supported by the following grants: NSF 1146944-IOS (to DS), NSF 0951019-IOS, and NIH 1R01MH094607-01A1 (to KM).

ACKNOWLEDGMENTS

The authors thank Drs. Ahmad Athamneh and Douglas Roossien for their helpful comments on this editorial.

Conflict of Interest Statement: The authors declare that the research was conducted in the absence of any commercial or financial relationships that could be construed as a potential conflict of interest.

frontiers
in Cellular Neuroscience

REVIEW
published: 08 July 2015
doi: 10.3389/fncel.2015.00257

Physical biology of human brain development

Silvia Budday[1], *Paul Steinmann*[1] *and Ellen Kuhl*[2]*

[1] *Chair of Applied Mechanics, Department of Mechanical Engineering, University of Erlangen/Nuremberg, Erlangen, Germany,*
[2] *Department of Mechanical Engineering and Bioengineering, Stanford University, Stanford, CA, USA*

Neurodevelopment is a complex, dynamic process that involves a precisely orchestrated sequence of genetic, environmental, biochemical, and physical events. Developmental biology and genetics have shaped our understanding of the molecular and cellular mechanisms during neurodevelopment. Recent studies suggest that physical forces play a central role in translating these cellular mechanisms into the complex surface morphology of the human brain. However, the precise impact of neuronal differentiation, migration, and connection on the physical forces during cortical folding remains unknown. Here we review the cellular mechanisms of neurodevelopment with a view toward surface morphogenesis, pattern selection, and evolution of shape. We revisit cortical folding as the instability problem of constrained differential growth in a multi-layered system. To identify the contributing factors of differential growth, we map out the timeline of neurodevelopment in humans and highlight the cellular events associated with extreme radial and tangential expansion. We demonstrate how computational modeling of differential growth can bridge the scales–from phenomena on the cellular level toward form and function on the organ level–to make quantitative, personalized predictions. Physics-based models can quantify cortical stresses, identify critical folding conditions, rationalize pattern selection, and predict gyral wavelengths and gyrification indices. We illustrate that physical forces can explain cortical malformations as emergent properties of developmental disorders. Combining biology and physics holds promise to advance our understanding of human brain development and enable early diagnostics of cortical malformations with the ultimate goal to improve treatment of neurodevelopmental disorders including epilepsy, autism spectrum disorders, and schizophrenia.

Keywords: neurodevelopment, connectivity, synaptogenesis, cortical folding, differential growth, lissencephaly, polymicrogyria

Edited by:
Daniel Marcel Suter,
Purdue University, USA

Reviewed by:
Corina Stefania Drapaca,
Pennsylvania State University, USA
Kristian Franze,
University of Cambridge, UK

Correspondence:
Ellen Kuhl,
Department of Mechanical Engineering and Bioengineering,
Stanford University, Bldg. 520,
Stanford, CA 94305, USA
ekuhl@stanford.edu

Received: *28 April 2015*
Accepted: *22 June 2015*
Published: *08 July 2015*

Citation:
Budday S, Steinmann P and Kuhl E (2015) Physical biology of human brain development.
Front. Cell. Neurosci. 9:257.
doi: 10.3389/fncel.2015.00257

1. Introduction

The average adult human brain has a volume of 1350 cm^3, a total surface area of 1820 cm^2, and an average cortical thickness of 2.7 mm (Pakkenberg and Gundersen, 1997). It contains approximately 100 billion neurons, of which 20 billion are located in the cerebral cortex (Herculano-Houzel, 2009). Each cortical neuron has on average 7000 synaptic connections to other neurons, resulting in a total of 0.15 quadrillion synapses and more than 150,000 km of myelinated nerve fibers (Pakkenberg et al., 2003). Gyrification, the folding of the cortical surface, is viewed as a mechanism to maximize the number of cortical neurons and minimize the total fiber length within the limited space inside our skull (Zilles et al., 2013).

In recent years the question what drives cortical folding has engaged researchers across various fields (Richman et al., 1975; VanEssen, 1997). After decades of biological research, physical forces are now increasingly recognized to play a central role in regulating pattern selection and surface morphogenesis (Smith, 2009; Bayly et al., 2013; Franze et al., 2013; Budday et al., 2014b; Ciarletta et al., 2014). While there is a general agreement on the importance of mechanical forces during neurodevelopment (Franze, 2014), to the present day, the physical biology of human brain development remains understudied and poorly understood (Bayly et al., 2014).

From a physical perspective, cortical folding is an instability problem of constrained differential growth in a multi-layered system (Goriely and BenAmar, 2005). From a biological perspective, three distinct phases contribute to differential growth: neuronal division and migration; neuronal connectivity; and synaptogenesis and synaptic pruning (Raybaud et al., 2013). The first phase of brain development spans throughout the first half of gestation and is characterized by the creation of new neurons–at rates of up to 250,000 neurons per minute–and their migration toward the outer brain surface (Blows, 2003). Not surprisingly, neuronal division and migration are associated with a noticeable cortical growth both in thickness and surface area (Sun and Hevner, 2014). However, until mid-gestation, the growth-induced cortical stress is too small to induce cortical folding and the cortical surface remains smooth (Budday et al., 2014b). The second phase spans from mid-gestation throughout 2 years postnatally and is dominated by the formation of neuronal connectivity. The new connections induce an excessive tangential expansion of the outer cortex (Huttenlocher and Dabholkar, 1997), the cortical stress increases, and the cortex begins to fold (Richman et al., 1975). At the same time, myelination reaches its peak and induces extreme white matter growth. The third phase spans throughout the entire lifetime and is associated with mild synaptogenesis, the formation of a few new connections, but mainly with synaptic pruning, the removal of unnecessary neuronal structures (Craik and Bialystok, 2006). Throughout this phase, the human cortex remains plastic, locally adapts its thickness, dynamically adjusts its stress state, and undergoes secondary and tertiary folding (Budday et al., 2015c).

In this review, we summarize biological mechanisms of neuronal division, migration, and connectivity with a view toward the physical phenomena of surface morphogenesis, pattern selection, and evolution of shape. We highlight how physical forces act as regulators in translating these cellular mechanisms into the gyrogenesis of the human brain. We demonstrate how computational modeling of differential growth can predict the classical pathologies of lissencephaly and polymicrogyria, and how the underlying model could be expanded toward other neurodevelopmental disorders including microcephaly and megalencephaly. We conclude with a critical discussion of the role of physics and biology in human brain development and identify future challenges and new frontiers.

2. Neuronal Division and Migration

Neurogenesis involves a precisely orchestrated sequence of cellular events. It begins with the formation of the neocortex at the rostral end of the neural tube, near the outer surface of the embryonic cerebral vesicle (Sidman and Rakic, 1973). In humans, the neural tube closes at embryonic day 30, during the fifth week of gestation (O'Rahilly and Müller, 2006). A primitive ventricular system begins to form and the amniotic fluid is trapped within the central canal. Neural tube closure initiates a rise in intraventricular fluid pressure, which marks the beginning of rapid brain enlargement.

Intracranial pressure is now recognized as an important regulator of normal brain development (Desmond, 1985). In the absence pressure, the brain cavity volume enlarges less rapidly, brain tissue grows at a reduced rate, remains grossly disorganized, and tends to fold inward into the ventricular cavity (Desmond and Jacobson, 1977). In addition to the mechanical regulation through pressure, the cerebrospinal fluid provides biochemical regulation through diffusible extracellular signals, which modulate symmetric and asymmetric progenitor cell division during development and disease (Lehtinen et al., 2011). **Figure 1** illustrates the timeline of early development and neurogenesis including cell division and cell migration.

Early Development is Characterized through Early Proliferation

Between weeks 4 and 5, early development is characterized by interkinetic nuclear migration, an oscillation process during which neuroepithelial cells divide symmetrically at the margin of the ventricle and undergo four phases (Bystron et al., 2008): first, the cell nuclei position themselves at the basal, abventricular locations; then, they move toward the apical ventricular surface; next, they divide symmetrically into two new progenitor cells at the apical surface; and finally, they return toward their basal position. This early proliferation exponentially increases the number of progenitor cells, and ultimately results in both increased surface area and increased thickness of the ventricular zone.

Weeks 4–5 also mark the time period when the first primitive layer of meningeal cells becomes visible (O'Rahilly and Müller, 1986). There is increasing evidence that the fetal meninges play a critical role in brain development. While the mechanical role of the meninges is still not entirely understood, we now know that the dura mater, the arachnoid mater, and the pia mater are far more than protective layers around our brain: By releasing diffusible factors, the meninges form a major signaling center between the cortex and the skull to control the proliferation and migration of neural progenitors and neurons (Siegenthaler and Pleasure, 2011). Not surprisingly, disruption of meningeal function–either globally or locally–can result in complex brain pathologies including cobblestone malformations, lissencephaly, and polymicrogyria (Sun and Hevner, 2014).

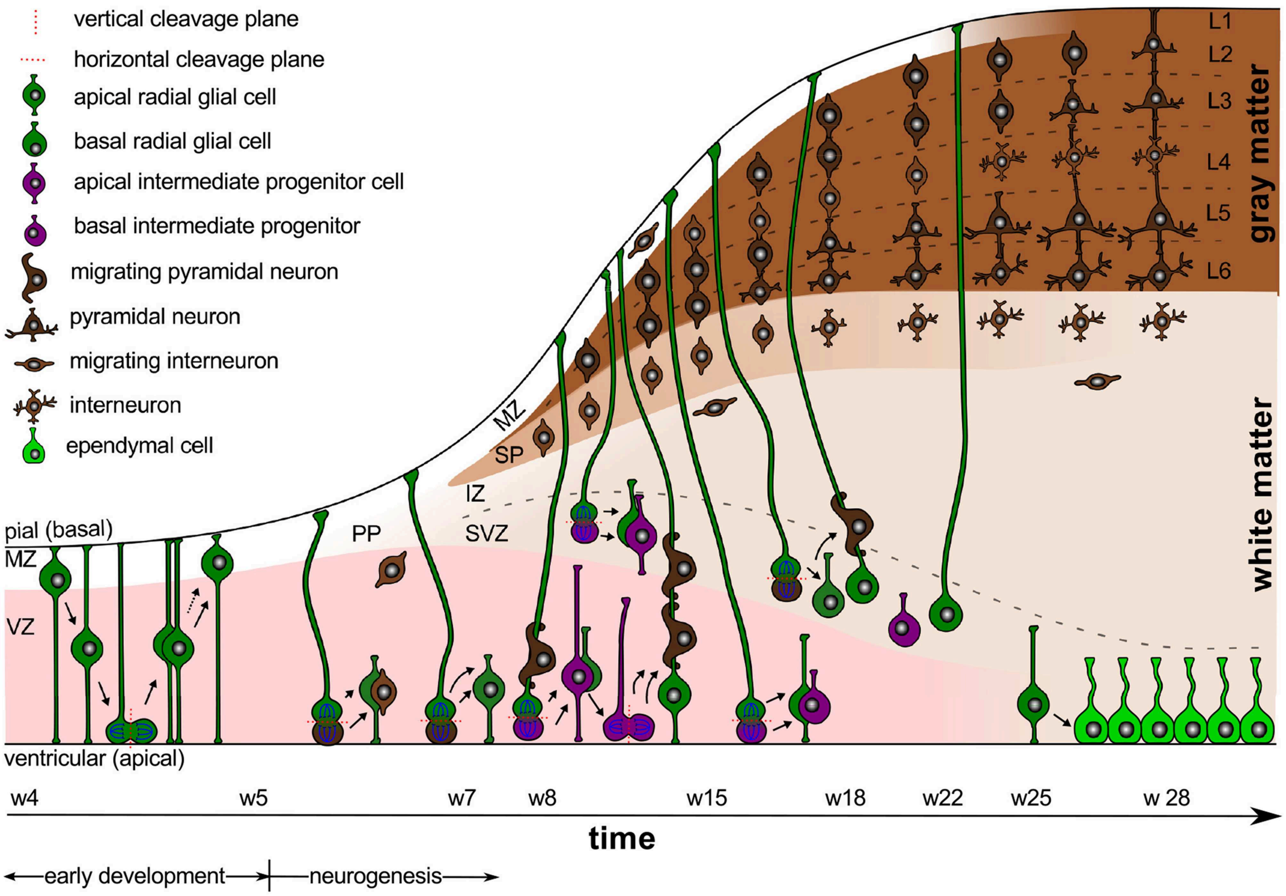

FIGURE 1 | Early development and neurogenesis. Early development is characterized by interkinetic nuclear migration, an oscillatory process during which neuroepithelial cells divide symmetrically at the margin of the ventricle and undergo four phases. Early born neurons are referred to as interneurons and travel tangentially within the marginal and intermediate zones. Neurogenesis begins when progenitor cells switch from symmetric to asymmetric cell division. Apical progenitor cells in the ventricular zone and basal progenitor cells in the subventricular zone accumulate to become the major source of pyramidal neurons.

Gestational Week 5 Marks the Onset of Neurogenesis

Around gestational week 5, the progenitor cells in the ventricular zone, the radial glial cells, begin to switch from symmetric to asymmetric cell division (Iacopetti et al., 1999). **Figure 1** indicates that symmetric cell division is associated with vertical cleavage planes, while asymmetric cell divisions is associated with horizontal cleavage planes (Haydar et al., 2003). During asymmetric division, one daughter cell remains in the ventricular zone as a radial glial cell, the other one becomes either a postmitotic neuron or an intermediate progenitor cell (Pontious et al., 2008). Intermediate progenitor cells eventually undergo terminal symmetric division to create pairs of postmitotic neurons (Noctor et al., 2004).

As **Figure 1** suggests, we can classify radial glial cells and intermediate progenitor cells into two subpopulations, apical and basal: apical radial glial cells and apical intermediate progenitor cells form bipolar radial fibers between the apical and basal surfaces and reside in the ventricular zone (Sun and Hevner, 2014); basal radial glial cells and basal intermediate progenitor cells form a unipolar basal fiber and delaminate from the ventricular zone (Kowalczyk et al., 2009). Both types of basal cells are not attached to the ventricular surface and do not undergo interkinetic nuclear movement (Hansen et al., 2010). Accumulation of basal progenitor cells creates a distinct new compartment above the ventricular zone, the subventricular zone (Haubensak et al., 2004). Its asymmetrically dividing basal radial glial cells become an additional source of intermediate progenitor cells, which are especially important in species with larger brains and longer migration paths (Kriegstein et al., 2006). Asymmetrically dividing basal radial glial cells contribute significantly to cortical growth and folding (Lui et al., 2011).

The ventricular and subventricular zones form an active proliferate zone, the site of origin of pyramidal neurons. Pyramidal neurons eventually migrate outward along the radial glial cells to form the characteristic six-layered cortical structure from inside to outside (Raybaud et al., 2013). Newborn pyramidal neurons pause in the subventricular zone for up to 24 h before they migrate radially. This suggests that the subventricular zone synchronizes the migration of pyramidal neurons and interneurons (Lui et al., 2011).

Before the radial migration of pyramidal neurons begins, early-born cells of various type fill the space near the basal surface to form a dynamic, transient structure, the preplate (Bystron et al., 2008). Cells in the preplate are born before the first radially migrating pyramidal neurons and will either die or migrate tangentially to become inhibitory interneurons, either in the cortex or in the subcortex (DelRío et al., 2000). During early neurogenesis, asymmetric and symmetric cell division provoke a notable radial and tangential expansion of all proliferative zones.

At Gestational Week 7, the Cortical Plate Begins to Develop

Around week 7, radially migrating neurons from the ventricular and subventricular zones initiate the development of the cortical plate. In its early stages, the cortical plate is divided into two layers, a thin superficial marginal zone and an underlying subplate. The marginal zone contains cells that have mostly migrated tangentially; those cells arrest the migration of radially migrating pyramidal neurons to guarantee the inside-out formation of the cortex (Rakic and Zecevic, 2003). The marginal zone will eventually form cortical layer 1 (Raybaud et al., 2013). The underlying subplate contains both, interneurons and postmigratory pyramidal neurons, which transiently connect with incoming axons until the cortex is ready to receive them (Molnár et al., 1998).

Cortical neurons accumulate above the subplate in an inside-out sequence: The earliest-born neurons are destined to become the innermost layer 6, the last-born neurons will become the outer layer 2. Early projection pyramidal neurons of the inner cortical layers originate from apical radial glial cells in the ventricular zone, whereas later neurons in the superficial layers progressively originate from secondary progenitor cells in the subventricular zone (Lui et al., 2011). The development of the whole cortical plate follows a temporal gradient of maturation across the hemisphere: first it forms in the most lateral part of the rostral telencephalic wall; approximately 1 week later, it develops in the dorsocaudal pole (O'Rahilly and Müller, 2006).

The cell-sparse compartment between the proliferative ventricular and subventricular zones and the cortical plate is known as the intermediate zone. It consists of radially and tangentially migrating cells, former preplate cells, and long-range axons (Bystron et al., 2008). The intermediate zone will eventually become white matter tissue. At this point, the proliferative zones still expand radially and tangentially, while the development of the cortical plate initiates a pronounced radial expansion of the cortex.

Until Gestational Week 18, the Cortex Forms Its Six-layered Structure

Between weeks 9 and 12, the human subplate thickens considerably and its cell density decreases (Carney et al., 2007). This phase is accompanied by a gradual thickening of the cortex. The morphology of each cortical neuron that has reached its final position reflects its developmental age (Bayer and Altman, 1991): young cortical neurons have an elongated cell body, a descending axon that connects with a neuron in the subplate, and an apical dendrite (Bystron et al., 2008); following the radial gradient, the age of the neurons increases, their cell bodies become progressively more rounded, and their dendrites elongate perpendicular to the cortical surface (Sidman and Rakic, 1973). This implies that older neurons in the deep cortical layers form connections earlier than younger neurons in the superficial layers.

Between weeks 13 and 15, the ventricular zone becomes progressively thinner as a large percentage of its cells moves outward (Sidman and Rakic, 1973). By this time, the neurons destined for the prospective middle layers of the cortex have arrived. Finally, at gestational week 18, we can clearly distinguish the radial organization of the neocortex with its six distinct layers. However, there is still a striking contrast between the bipolar shaped, immature, superficial cells and the complex shaped, mature, deeper neurons, which already possess elaborately branched dendrites (Sidman and Rakic, 1973). This might explain why in larger brains, which have a greater proportion of late-derived neurons, the outer cortical layers are disproportionately thickened (Hill and Walsh, 2005). At this point, no horizontal intracortical connections have developed yet (Noctor et al., 2001). The formation of the six-layered cortex mainly involves the radial expansion of the cortical plate and subplate, while the proliferative zone begins to attenuate.

After Gestational Week 22, the Cortical Plate Differentiates

The period after week 22 is the most significant time for areal, laminar, and cytological differentiation of the cortical plate. Gyral formation begins around week 24 at the parieto-occipital and central sulci (Takahashi et al., 2012). By week 25–27, the ventricular zone has reduced to a one-cell-thick ependymal layer. The subventricular zone, which is still proliferating, will now become the major source of cortical neurons (Zecevic et al., 2005). The subplate has reached its maximum thickness and begins to attenuate (Kostović et al., 2002); yet, some residual subplate neurons persist throughout life as interstitial neurons in the white matter tissue (Bystron et al., 2008).

By week 28, layer 1 has fully developed. It contains a few neurons and is largely filled with arborizations of apical dendrites and intrinsic tangential axons. The cells that had initially arrested the migration of pyramidal neurons during neuronal migration have now disappeared (Raybaud et al., 2013). Once neuronal migration is complete, the radial glial cells in the subcortical layers disappear or become astrocytes (Misson et al., 1991). Interneurons keep migrating until the last trimester when the migration of pyramidal neurons ceases (Raybaud et al., 2013). They travel tangentially within the marginal and intermediate zones and can enter the cortical plate from either location to form local circuits with cortical pyramidal neurons. Weeks 24–34 mark a critical period for axonal elongation and maturation in the developing white matter (Holland et al., 2015). This period is associated with the beginning of myelination, which transforms the original intermediate zone into white matter tissue. During differentiation, neuronal dendrites elongate perpendicularly and cause a significant tangential expansion of the cortical plate. At the same time, the subplate attenuates and the intermediate zone transforms into white matter tissue. The resulting differential growth between the cortical plate and inner layers of the brain results in an increase in cortical stress and, eventually, in the onset of cortical folding.

Taken together, numerous interacting modes of cell migration shape the developing neocortex. A proper radial and tangential development of the mammalian brain requires different types of progenitor cells, depending on species and stage of development. As a common paradigm, radial glial cells tend to expand the cortex tangentially, whereas intermediate progenitor cells tend to fill the cortical layers radially. In addition to the radial gradient of development, there is a pronounced tangential gradient from primary, via secondary, to highly associative cortices. This tangential gradient results in a similar developmental gradient of connectivity and gyrification, and, after term, in a similar gradient of cortical myelination.

3. Neuronal Connectivity

Figure 2 sketches the final organization of the brain, once all components have fully developed and connected. Besides cell division and cell migration, the formation of connections is a major factor of normal brain development. Before midgestation, there is essentially no direct connection between the cortex and the rest of the central nervous system. At this point, there are only indirect connections between cortical and subcortical structures and the subplate (Haynes et al., 2005). As connectivity develops, axons form and multiply their branches. During the second half of gestation, axons extend branches to numerous cortical and subcortical targets, until each neuron connects with thousands of other neurons (Raybaud et al., 2013). The mechanical forces during this phase of axonal elongation have been extensively studied (Suter and Miller, 2011; O'Toole et al., 2015). They have lead to the popular but controversial hypothesis of surface morphogenesis through axonal tension and compact wiring (Mitchison, 1991). Axonal tension, a mechanisms to bring functionally related units topographically closer together (VanEssen, 1997), can explain folding with realistic stiffness ratios, but disagrees with dissection experiments (Xu et al., 2010). Differential growth, a mechanism to release residual stresses by surface buckling (Ronan et al., 2014), agrees with dissection experiments, but requires unrealistic stiffness ratios (Richman et al., 1975). Combining both mechanisms has motivated theories of stretch- and stress-driven growth, concepts that agree with both realistic stiffness ratios and maximum

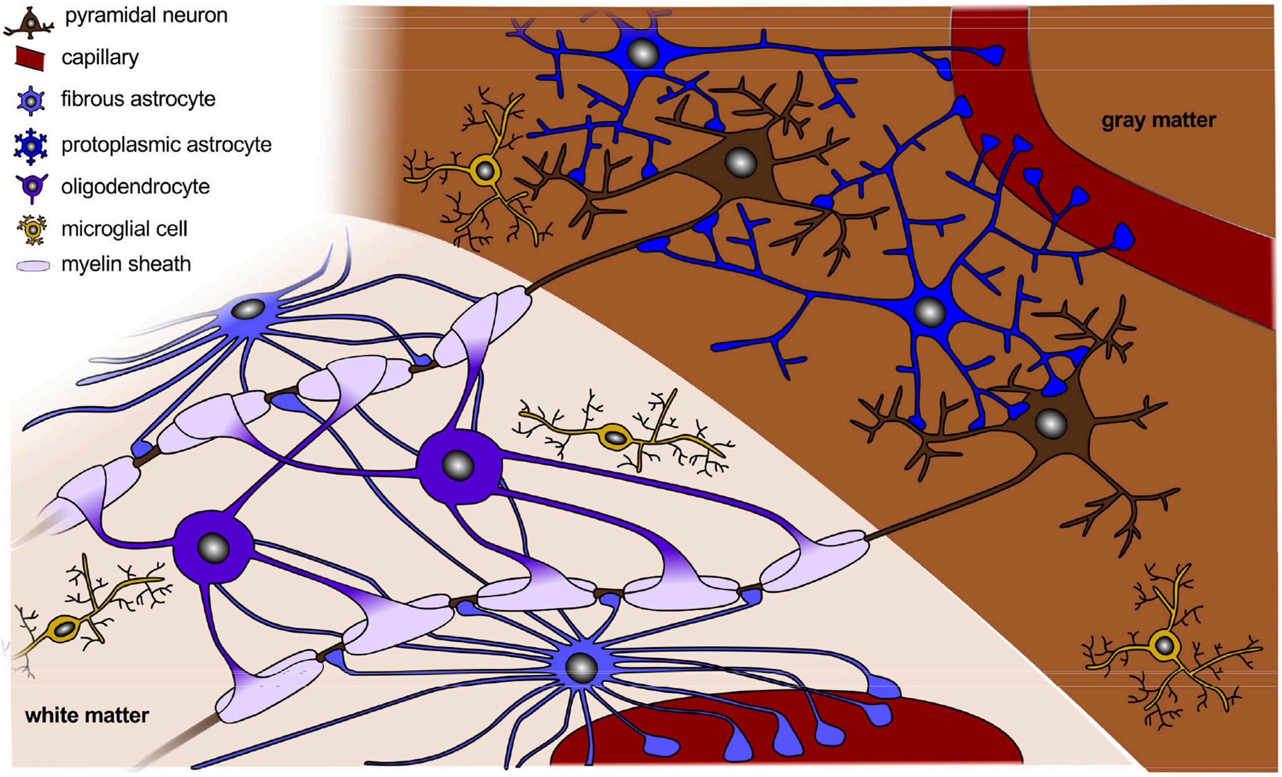

FIGURE 2 | Organization of a fully developed brain. In white matter, myelinated axons allow for rapid nerve impulse conduction; intermediate oligodendrocytes connect and form several myelin sheaths. Fibrous astrocytes ensure supply of nutrients and synaptic processing. In gray matter, neurons form synapses with each other and with protoplasmic astrocytes. In both white and gray matter, microglial cells contribute to clearance of debris and synapse remodeling.

principal stress distributions (Bayly et al., 2013; Budday et al., 2014b).

The most prominent connective structure in the human brain is the corpus callosum, a wide, flat bundle of more than 200 million contralateral axons, which connect the left and right cerebral hemispheres (Luders et al., 2010). The corpus callosum begins to differentiate as a commissural plate around week 8. In the human embryo, the earliest callosal axons appear around week 12, and the adult callosal morphology is achieved around week 20 (Achiron and Achiron, 2001). Agenesis of the corpus callosum, a rare but severe congenital disorder in which the corpus callosum is partially or completely absent, is often associated with profound intellectual disabilities (Palmer and Mowat, 2014).

In the cortex, the formation of connections follows the radial gradient of the inside-out proliferation: First, the early-born deep layer 6 neurons extent branches to the basal gray matter; around week 17, layer 5 neurons form connections with the internal capsule, the brainstem, and the spinal cord; between weeks 22 and 27, layer 4 neurons receive thalamo-cortical connections; last, from week 28 to 32, layer 3 and 2 neurons form intrahemispheric, cortico-cortical association fibers and interhemispheric, commissural connections (Raybaud et al., 2013). Subplate neurons participate in both local and long-distance axonal connections. From week 32 to 47, the development of short horizontal connections in the cortical gray matter and in the subcortical white matter results in a horizontal rather than radial final layering pattern of the neocortex (Marin-Padilla, 1970). The deep layers 6 and 5 project single axons, whereas the superficial layers 4, 3, and 2 and the subplate receive multiple incoming fibers. This implies that connectivity-driven tangential growth mainly affects the superficial layers and the subcortical white matter tissue (Raybaud et al., 2013).

Not only neurons, but also other cellular components such as astrocytes, oligodendrocytes, microglial cells, and capillaries play a crucial role in the proper formation of neuronal connectivity (Barres, 2008). Actually, radial glial cells in the subplate and in the intermediate zone not only produce neurons but also astrocytes and oligodendrocytes (Mizutani et al., 2007). The creation and growth of these additional cells induces an additional volume expansion in the corresponding layers. In the following, we outline the individual development of each cell type.

Astrocytes Guide the Migration of Developing Axons and Neurons

Astrocytes are a sub-type of glial cells in the central nervous system. They play a major role in synaptic transmission and information processing, they guide the migration of developing axons and neurons, and have extensive contacts with blood vessels (Powell and Geller, 1999). Astrocytes develop during the second half of gestation after the mass production of neurons (Freeman, 2010), when the radial glial cells switch from generating exclusively neurons to generating astrocytes (Morrow et al., 2001). The timing of the neuron-astrocyte switch indirectly affects the number of astrocytes in the adult brain (Molofsky et al., 2012). The generation and expansion of astrocytes is largely completed by early postnatal stages, but astrocytes continue to elaborate and refine their branches after birth during the active period of synaptogenesis (Lund and Lund, 1972). Eventually, astrocytes become the most abundant cell type in the human brain (Freeman, 2010).

Morphologically, we can distinguish two types of astrocytes as illustrated in **Figure 2**, protoplasmic and fibrous: protoplasmic astrocytes are primarily located in gray matter tissue and exhibit fine irregular branches in a globoid distribution; fibrous astrocytes are widely spread throughout the white matter tissue and exhibit numerous regular cylindrical fibers (Vaughn and Peters, 1967). Each astrocyte occupies a unique spatial domain and forms discrete borders with its neighbors (Bushong et al., 2002). Human astrocytes are larger, structurally more complex, and more diverse than astrocytes in rodents. The ratio of astrocytes to neurons significantly varies between species: It is 1:6 in worms, 1:3 in rodents, and 1.4:1 in humans (Nedergaard et al., 2003). This suggests that the astrocyte-to-neuron ratio increases with cognitive skills.

Oligodendrocytes Support Neural Migration and Myelinate Axons

Oligodendrocytes are a type of neuroglial cells. They provide structural support and form a myelin sheath around the axon to enable rapid impulse propagation (Freeman, 2010). The first oligodendrocyte progenitor cells form in the ventricular and subventricular zones around week 10, and their formation reaches a peak around week 15 (Jakovcevski et al., 2009). Oligodendrocyte progenitor cells first differentiate into pre-myelinating oligodendrocytes and then transform into mature myelin-forming cells (Pfeiffer et al., 1993). Pre-oligodendrocytes develop in the subplate, in the intermediate zone, and in the cortex by the end of the second trimester. After week 30, mature oligodendrocytes sparsely appear in the intermediate zone, before they increase diffusely after week 40. In humans, significant myelination only occurs after birth supported by a last wave of oligodendrocyte progenitor cells in the postnatal cortex (Kessaris et al., 2006). All oligodendrocytes travel long distances before they arrive at their final destination (Bradl and Lassmann, 2010). Although the vast majority of oligodendrocyte progenitor cells differentiates to myelin-producing oligodendrocytes, some inactive oligodendrocyte progenitor cells persist into late adulthood.

Myelination occurs early during oligodendrocytic differentiation within a narrow window of 12–18 h (Barres, 2008). It is regulated by the electrical activity of neurons: Increasing neuronal firing and axonal signaling enhances myelination (Diemel et al., 1998). Oligodendrocytes selectively wrap axons with diameters larger than $0.2\,\mu$m (Simons and Trajkovic, 2006). At the peak of myelination, oligodendrocytes can create up to three times their weight in membrane per day (McLaurin and Yong, 1995).

Oligodendrocytes and their myelin sheaths are more susceptible to damage than any other cell type in our brain. After demyelination caused by disease, for instance in multiple sclerosis, axons can retrieve new myelin sheaths. During remyelination, inactive adult oligodendrocyte progenitor cells proliferate, switch from their quiescent state to a regenerative phenotype, and generate new oligodendrocytes (Franklin and Ffrench-Constant, 2008). The process of remyelination is similar to myelination during development, except for longer cell cycle times, slower migration rates, and thinner and shorter sheath segments (Ludwin and Maitland, 1984). This suggests that axons with unusually thin myelin sheaths are a pathological hallmark of remyelination.

In rodents, myelination begins already during neurogenesis. In humans, it mainly occurs after birth, when neuronal migration has ceased and primary and partially secondary folds have formed. Myelination in rodents only takes a few weeks, compared to decades in the humans (Yakovlev and Lecours, 1967). Although the absolute number of oligodendrocytes in humans is significantly larger than in rodents, the oligodendrocyte density per white matter volume in humans and rodents is remarkably similar (Bradl and Lassmann, 2010).

Microglial Cells Control Neuronal Proliferation and Differentiation

Microglial cells contribute to neuronal proliferation and differentiation, clear debris, and remodel synapses (Harry, 2013). Unlike all other cell types in our brain, microglial cells are not differentiated from neural stem cells (Yang et al., 2013); they derive from myeloid progenitor cells migrating through the blood vessels (Harry, 2013). By migrating along radial glial cells, white matter tracts, and the vasculature (Rezaie and Male, 1999), microglial cells reach the ventricular zone by week 6, extent into the marginal zone by week 8, and spread into the subventricular zone, the intermediate zone, and the subplate around week 16 (Raybaud et al., 2013). As neurons become established in the brain, the need to clear excess neurons is reduced, and microglial cells undergo a morphological transition from amoeboid to heavily branched (Monier et al., 2006). By week 35, the cells display a fully developed, ramified morphology (Esiri et al., 1991). Microglial cells located in gray matter have a small, dense nucleus with fine branches extending in multiple directions; those in white matter have an elongated cell nucleus and align their fibers with neighboring axons. The majority of microglial cells, about 95%, appears within the first 2 weeks post-natally (Alliot et al., 1999). Eventually, microglial cells comprise approximately 15–20% of the total number of brain cells (Carson et al., 2006). In general, the population of microglial cells correlates with the presence of apoptotic cells and blood vessels (Rezaie and Male, 1999).

Vasculogenesis Ensures Supply With Oxygen and Nutrients

The vasculature of the brain ensures its supply with oxygen and nutrients. The cerebral vesicles begin to form around week 5. During week 6–7, blood channels develop to form a dense capillary bed within the ventricular zone. Since the development of the vascular system closely correlates with cell proliferation and connectivity, it follows the radial gradient from inside to outside and the tangential gradient from primary to secondary and highly associative cortices (Norman and O'Kusky, 1986). During the first half of gestation, the capillary bed is limited to the ventricular and subventricular zones (Allsopp and Gamble, 1979). By week 15, first capillaries appear in the intermediate zone, the subplate, and the deep cortical layers (Marín-Padilla, 2012). From week 22 to 27, the cortical capillary bed progresses from the deep layers toward the surface. Its density increases continuously until week 47. With the attenuation of the proliferate ventricular and subventricular zones, their capillary beds regress (Allsopp and Gamble, 1979). In the white matter, the microvascular density remains low until term (Ballabh et al., 2004).

Synaptogenesis and Synaptic Pruning Shape the Cerebral Cortex

Synaptogenesis, the formation of synapses between the individual neurons, begins before week 27, but occurs mainly after birth, concurrent with the growth of dendrites and axons and with the myelination of axons in the subcortical white matter (Huttenlocher and Dabholkar, 1997). Neurons are not born with the ability to receive synapses, but acquire this ability for instance through contact with astrocytes (Clarke and Barres, 2013). Synaptogenesis consists of three phases: first, immature synapses form between axons and dendrites; then, synapses undergo maturation and convert from a silent to an active state; finally, the synaptic number is reduced to refine the neuronal connections within the circuit (Craige et al., 2006). In humans, synaptic pruning, the process of synapse elimination, starts near the time of birth and is completed by the time of sexual maturation. It is influenced by environmental factors and is widely thought to represent learning (Craik and Bialystok, 2006).

Postnatally, from infancy to adulthood, our brain increases in size by a factor five (Craik and Bialystok, 2006). Throughout this period, the total number of neurons remains virtually unchanged. Postnatal growth is mediated almost exclusively by the myelination of axons and by the growth of synaptic connections. Humans form more synapses than rodents, which contributes to the greater capacity of the human brain to learn and adapt (Preuss et al., 2004).

4. Gyrogenesis

While the early developmental processes are relatively well-characterized on the cellular level, later development of the entire brain with its distinct folded surface morphology remains less well-understood (Ronan et al., 2014). **Figure 3** illustrates the structural changes that take place in our brain after its six cortical layers have formed.

Gyrification Begins around Mid-gestation

Around week 23, the first primary sulci begin to form. Primary gyrification follows the same tangential gradient as proliferation and connectivity, from primary via secondary to high-association cortices. Through term, secondary sulci extend concentrically around the primary sulci. After term, tertiary sulci develop together with short association fibers. Gyrification typically begins slightly earlier in the right hemisphere than in the left (Raybaud et al., 2013).

The expansion of the cortex is an important regulator of brain folding. Several cellular processes correlate with gyral

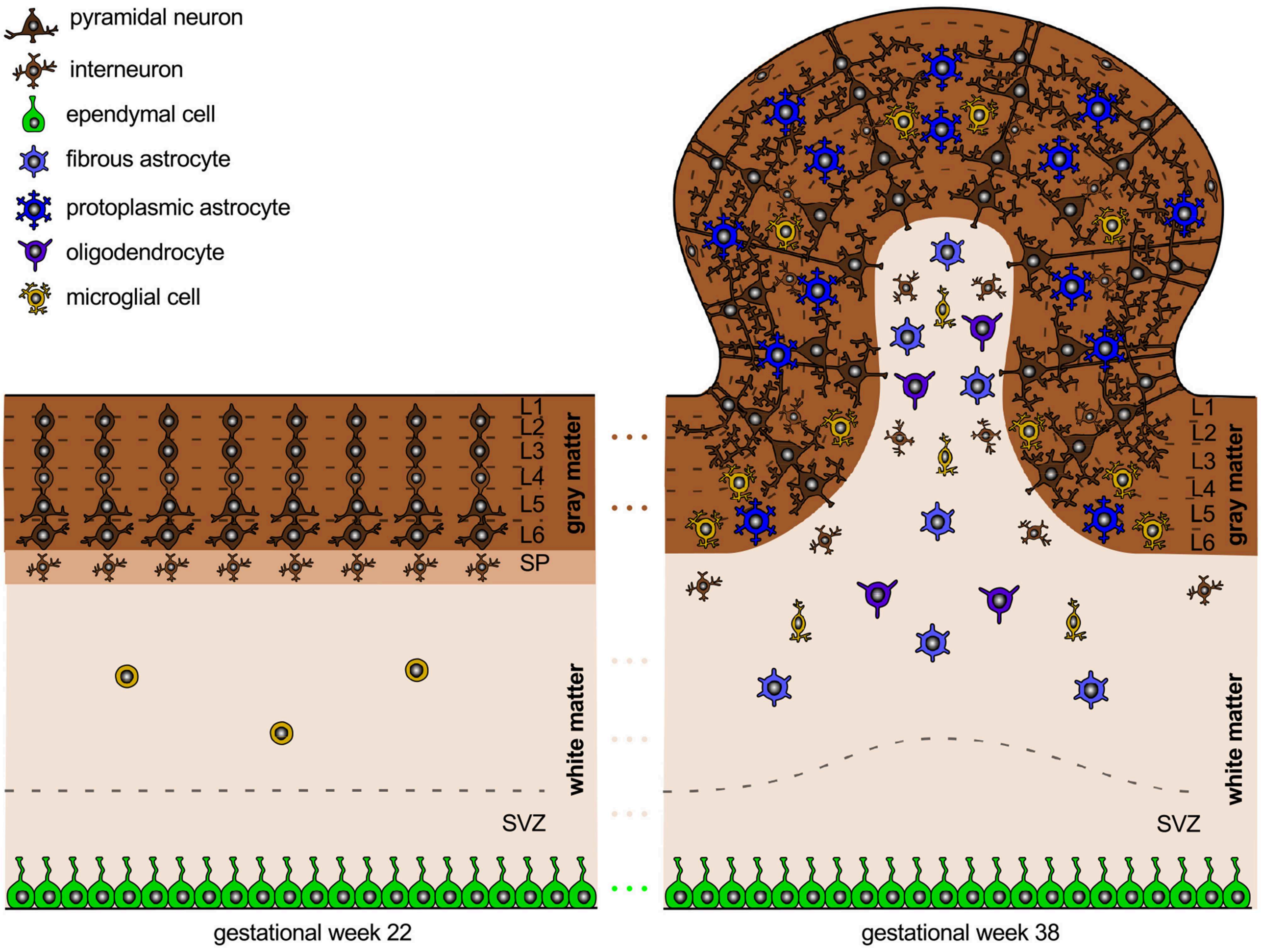

FIGURE 3 | Neural connectivity and gyrification. The connection process follows the radial gradient of the inside-out proliferation. It begins in layer 6 and propagates outward toward layer 2. Connectivity-driven tangential growth mainly affects the superficial layers and triggers the formation of gyri and sulci. The subventricular zone is thicker at sites of growing gyri and thinner beneath developing sulci; both the subplate and the cortex are thicker at the crown of gyri than at the bottom of sulci.

development: cell division in the subventricular zone is most abundant in highly folded regions (Lukaszewicz et al., 2005); the subventricular zone, which hosts basal radial glial cells and intermediate progenitor cells that will eventually differentiate into brain cells, is thicker at sites of growing gyri and thinner beneath developing sulci; both the subplate and the cortex are thicker in the crowns of gyri than underneath sulci (Kostović et al., 2002). Besides cell division, cell survival and cell death can significantly affect brain size and brain morphology. During normal brain development, apoptosis, the programmed death of neurons, cumulatively occurs at sites of developing sulci, while the late migration of superficial neurons is more prominent at the crowns of gyri (Smart and McSherry, 1986). Increased cell death in the exponentially growing early progenitor population can severely reduce the number of neurons and, vice versa, decreased death of progenitor cells exponentially increases the number of neurons. The latter phenomenon can even induce convoluted cortices in otherwise lissencephalic brains (Haydar et al., 1999).

In relation to the timelines of cell division and migration in Section 2 and connectivity in Section 3, gyrification occurs simultaneously with the late migration of superficial neurons and with the formation of neural connectivity as the number of astrocytes, oligodendrocytes, and microglial cells increases.

Cortical Folding is a Mechanical Instability Driven by Differential Growth

A physics-based approach, which has recently gained increased attention, attributes cortical folding to differential growth between the cortex and the subjacent intermediate zone that later transforms into white matter tissue (Richman et al., 1975). The theory assumes that the early radial expansion of the cortical plate is relatively homogeneous across the thickness and does not evoke cortical folding. The later tangential expansion through the formation of horizontal, intracortical connections, however, is limited to the superficial cortical layers 1 through 4, and constrained by the inner layers 5 and 6 and by the underlying white matter. This creates compressive stresses, which may induce surface buckling to release the compression in the superficial layers (Biot, 1937).

The significance of the connectivity-driven tangential expansion of the superficial layers is supported by the fact that by week 18, when the cortex is still smooth, only radial but no tangential intracortical connections have formed (Noctor et al., 2001). Physical models of differential growth–with a morphogenetically growing outer surface on a stretch-driven growing inner core–can provide a mechanistic understanding of various features of brain folding (Bayly et al., 2014; Budday et al., 2014b). These models use the continuum theory of finite growth based on the concept of fictitious configurations (Lee, 1969). They introduce a second order tensor, the growth tensor, as an internal variable to record the history of the growth process (Rodriguez et al., 1994). Within this theory, the overall deformation gradient becomes the product of the elastic tensor, which reflects the reversible mechanical deformation, and the growth tensor, which reflects the biological process of growth (Ambrosi et al., 2011). Key to this theory is the fact that only the elastic part of the deformation generates stress. Once the stress in the cortical layer has reached a critical value, it is energetically more efficient for the cortex to bend rather than to be compressed (Cai et al., 2011). At this critical instability point, around week 23 in the healthy human brain, the cortex begins to fold (Moulton and Goriely, 2011). We can predict this folding analytically using simplified bi-layered models (Cao and Hutchinson, 2012), or computationally using elliptical or ellipsoidal models within a finite element analysis. While analytical models provide valuable insight into the critical conditions at the onset of folding, they fail to predict the interaction of gyri and sulci beyond the instability point (Balbi et al., 2015). Computational modeling can predict advanced surface morphologies and ultimately help correlate neurodevelopmental disruptions on the cellular level with structural malformations on the organ level (Budday et al., 2014a).

Although cortical folding does not occur before neuronal migration has ceased and all cortical layers have been established, cellular processes during neurogenesis play a major role in pattern selection (Raybaud et al., 2013). Increased asymmetric cell division in early brain development, for example, results in a reduced number of progenitor cells and neurons; fewer neurons migrate toward the cortical plate and will later expand tangentially (Sun and Hevner, 2014). A reduced number of progenitor cells not only reduces the number of migrating neurons, but may also reduce the number of radial migration paths; fewer neurons distribute over fewer radial glial cell fibers. This suggests that altered progenitor proliferation affects both the radial and the tangential organization of the cortical plate.

Increasing the Cortical Thickness Increases the Gyral Wavelength

Physics-based models predict that the gyral wavelength increases with increasing cortical thickness (Allen, 1969; Bayly et al., 2013), which is mostly determined by the radial organization of the cortical plate at the onset of folding. These models were initially developed to explain geological folding (Biot, 1937) and have recently been adopted for cortical folding (Bayly et al., 2014; Budday et al., 2014b). **Figure 4** illustrates how changes in cortical thickness can modulate surface morphogenesis: the

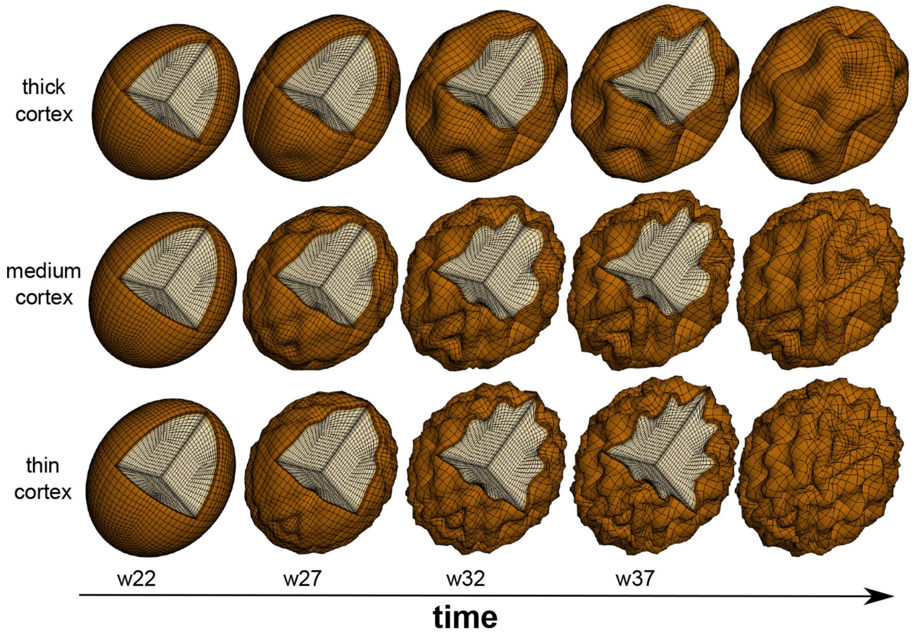

FIGURE 4 | Physics-based modeling of differential growth. The surface morphology varies significantly with cortical thickness and gestational time. Decreasing the cortical thickness, from top to bottom, increases the number of folds and decreases the gyral wavelength. After the onset of folding around mid-gestation, the formation of new connections causes an excessive tangential expansion of the cortex, which increases the folding amplitude and surface complexity, from left to right.

thinner the cortex, the shorter the gyral wavelength (Goriely et al., 2015). Growth-induced instabilities are initiated at the mechanically weakest spot (BenAmar and Goriely, 2005; Goriely and BenAmar, 2005). During neurogenesis, regional differences in the thickness of the subventricular zone could result in a heterogeneous cortical thickness, and folding would first occur in regions where the cortex is thinnest (Le Gros Clark, 1945). During early neuronal migration, thickness variations of the subventricular zone could serve as early markers of the developing folding pattern (Ciarletta et al., 2014). Taken together, it seems likely that small regional thickness variations in the newly established six-layered cortex largely shape primary folding. Other factors including local differences in synaptogenesis and synaptic pruning, and changes in mechanical properties due to myelination, rather gain significance during the later secondary and tertiary phases of cortical folding (Budday et al., 2015c).

Figure 5 demonstrates that not only the cortical thickness itself, but also the ratio of cortical thickness to total brain volume plays an essential role in pattern selection (Le Gros Clark, 1990). The mammalian brain varies significantly in size, shape, and convolutional complexity, but only marginally in cortical thickness (Welker et al., 2015). Physical models and computational simulations of growing brains with varying volume and constant thickness predict that the surface complexity increases with absolute brain size (Budday et al., submitted). A comparative simulation of squirrel, capybara, lion, and chimpanzee brains with volumes on the order of 10, 60, 180, and 400 cm^3 predicts the emergence of 22, 48, 76, and 92 major folds. If both total volume and cortical thickness were to increase proportionally, brains morphology would scale isometrically and similar folding patterns would emerge (Zilles et al., 2013). In agreement with geometric scaling studies of brain morphology, the computational model explains why increased brain volume at constant cortical thickness enhances folding (Hofman, 1989). The simulations are consistent with the observation that an increased thickness of the subventricular zone and an increased proliferation of progenitor cells increase the cortical thickness, cortical surface area, and brain size, but do not affect cortical folding (Sun and Hevner, 2014). In addition to the organization of the cortical layers at the onset of folding, the connectivity of the individual layers plays a crucial role throughout the folding process: radially forming connections primarily increase the cortical thickness, whereas horizontally forming connections induce tangential expansion, which will eventually enhance cortical folding (Moulton and Goriely, 2011).

Increasing the Cortical Stiffness Increases the Gyral Wavelength

Physics-based models predict that the gyral wavelength increases with the third root of the stiffness contrast between cortex and subcortex (Bayly et al., 2013). From an analytical point of view, growth-induced surface buckling requires that the stiffness of the gray matter layer is equal or larger than the stiffness of the white matter core (Cao and Hutchinson, 2011; Budday et al., 2015a). Motivated by these analytical considerations, the simulations in **Figures 4**, **5** use a stiffness contrast of three (Budday et al., 2014a). Throughout the past decade, numerous series of mechanical tests have been performed to characterize the stiffness contrast between gray and white matter tissue (Bilston, 2011; Miller, 2011). Testing brain remains challenging because of its extreme softness, its remarkable time dependence, and its microstructural architecture. On the small scale, scanning force microscopy revealed that gray matter was about twice as stiff as white matter, on the order of 100 vs. 50 Pa for ultra thin mouse spinal cord slices (Koser et al., 2015) and 500 vs. 250 Pa for rat cerebellum slices (Christ et al., 2010). On a larger scale, mechanical indentation tests found the opposite with gray matter about one third softer than gray matter, 1.8 vs. 1.2 kPa (Kaster et al., 2011) and 2 vs. 3 kPa (van Dommelen et al., 2010) for porcine brain and 1.9 vs.

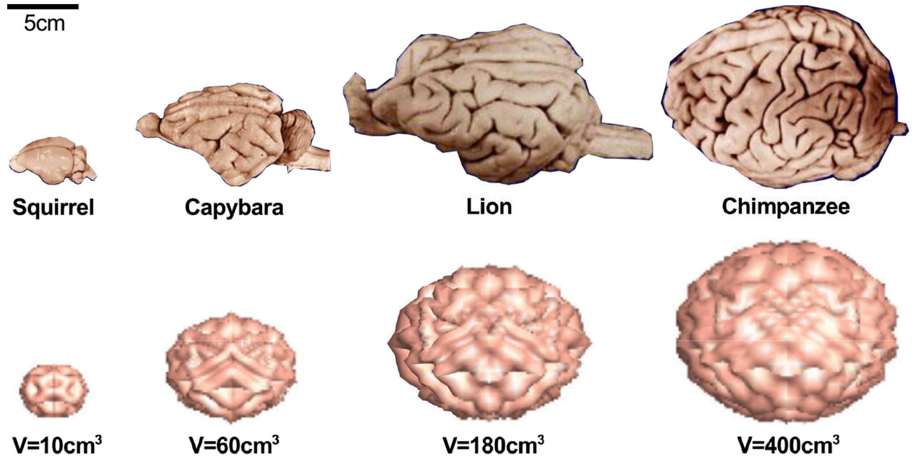

FIGURE 5 | The mammalian brain varies significantly in size, shape, and convolutional complexity, but only marginally in cortical thickness (Welker et al., 2015) (top). Physical models and computational simulations of growing brains with varying volume and constant thickness predict that the surface complexity increases with absolute size (Budday et al., submitted) (bottom). Our model predicts 22 major folds for the squirrel brain, 48 major folds for the capybara brain, 76 major folds for the lion brain, and 92-folds for the chimpanzee brain.

1.4 kPa for bovine brain (Budday et al., 2015b). Discrepancies in these measurements not only reflect the extreme strain rate sensitivity of brain tissue, but also its non-linear behavior and its compression stiffening (Mihai et al., submitted). *In vivo*, magnetic resonance elastography suggests that mature gray and white matter are rather indistinguishable with shear stiffnesses on the order of 3 kPa in ferrets (Feng et al., 2013), and 3.1 vs. 2.7 kPa in humans (Green et al., 2008).

The microstructure of brain tissue–and with it the mechanical properties–change drastically during early brain development: While gray matter remodels from a radial to a tangential organization and intercellular cross-linking increases significantly during the third trimester, the degree of cross-linking in white matter remains low until term (Raybaud et al., 2013). This suggests that, during gyrification, between weeks 22 and 38, white matter is softer than gray matter, but then stiffens after term when myelination and the formation of astrocytic branches give rise to a highly cross-linked microstructure. White matter stiffening during brain development could not only explain the observed discrepancies in stiffness contrast (Budday et al., 2015b; Koser et al., 2015), but also the folding at low stiffness contrasts in agreement with the Biot condition (Biot, 1963).

The realistic prediction of cortical folding with the help of physics-based models requires the clarification of the mechanical properties of gray and white matter tissue–not only in the mature, but more importantly in the developing brain. Ultimately, this could unravel an important point of criticism against the hypothesis of differential growth, the fact that instabilities would manifest themselves in the form of creases rather than folds if gray matter was softer than white matter at the onset of the instability (Hutchinson, 2013). Since myelination already starts during neurogenesis in rodents (Rockland and DeFelipe, 2011), an increase in white matter stiffness with increased myelination could also explain why rodent brains are less folded than mammalian brains.

5. Malformations of Cortical Development

Malformations–as a result of interrupted cortical development–are common causes of mental disorders including developmental delay and epilepsy (Barkovich et al., 2012). However, the clinical features are quite ambiguous: similar structural abnormalities can cause diverse symptoms. For example, the same brain regions are affected by gray matter loss in patients with different psychiatric conditions such as schizophrenia, major depression, and addiction (Goodkind et al., 2015). The severity of cognitive abnormalities scales with the degree of cortical dysplasia. This suggests that brain function is closely correlated to brain structure and that it is essential to understand how and why structural abnormalities form. In addition to the pathologies that originate from disrupted neurodevelopment, several diseases are caused by dysfunction of mature brain cells. A typical example is oligodendrocyte loss associated with demyelination in multiple sclerosis. In the following, we focus on pathologies associated with neurodevelopment and illuminate the underlying mechanisms of four malformations, which originate during the early stages of neurogenesis.

Lissencephaly Is a Migration Disorder Associated with a Smooth Brain

Lissencephaly literally means smooth brain and is associated with abnormal neuronal migration (Barkovich et al., 2005). As a result, migrating neurons fail to split the preplate into marginal zone and subplate; instead they form layers below the preplate with a reverse outside-in pattern (Sheppard and Pearlman, 1997). Large numbers of neurons do not even reach the cortical plate and diffusely deposit anywhere between the ventricular and pial surfaces (Friede, 1989); others overmigrate in the marginal zone and in the meninges. This implies that cortical lamination is completely disrupted.

The cortex of the lissencephalic human brain is significantly thickened–10 to 20 mm compared to 2–4 mm in normal brains–and typically consists of only four layers: an outer marginal layer 1, a superficial cellular layer 2 with numerous large and disorganized pyramidal neurons, a variable cell sparse layer 3, and a thick deep cellular layer 4 composed of medium and small neurons (Golden and Harding, 2004). The critical time window for the initiation of lissencephalic aberrations precedes gyrification, between weeks 11 and 13 (Aronica et al., 2012). Macroscopically, the classical hallmark of the disease becomes apparent only after week 22, when cortical folds fail to form: The connectivity-driven expansion is distributed over a significantly thicker cortex, which reduces the amount of compressive stresses and suppresses cortical folding. This suggests that the disease originates from disruptions during early brain development and neurogenesis, not from disruptions of the folding process itself.

Figure 6 illustrates the abnormal neuronal migration during lissencephaly. Instead of forming six organized cortical layers as illustrated in **Figure 1**, the lissencephalic brain typically only forms four disorganized, thickened layers. Consistent with the pathology of lissencephaly (Budday et al., 2014a), the computational simulation of differential growth (Budday et al., 2014b) predicts that a considerably thickened cortex fails to fold since its growth-induced compressive stresses are too small to induce buckling.

Polymicrogyria is an Organization Disorder Associated with Many Small Folds

Polymicrogyria is a developmental malformation of the human brain characterized by an excessive number of small folds. It evolves from abnormal development or loss of neurons in the deep cortical layers after completion of neuronal migration (Friede, 1989). Typically, layer 5 is damaged and the superficial layers overfold and fuse during gyrogenesis (Judkins et al., 2011). Deep layer neurons might retain a radial distribution without any laminar organization (Ferrer, 1984). This suggests that connectivity-driven growth after week 22 is mainly limited to the superficial layers, whereas the deep layers do not grow at all. The thinning of the cortex is magnified by the fact that the damaged deep cortical layers impede perfusion between week 20 and 24 and prohibit migration of astrocytes and oligodendrocytes (Ferrer and Catalá, 1991). This causes an undersupply of the superficial layers and cumulative cell death. Ultimately, polymicrogyric brains exhibit very thin cortices with an excessive number of small irregular folds (Guerrini et al.,

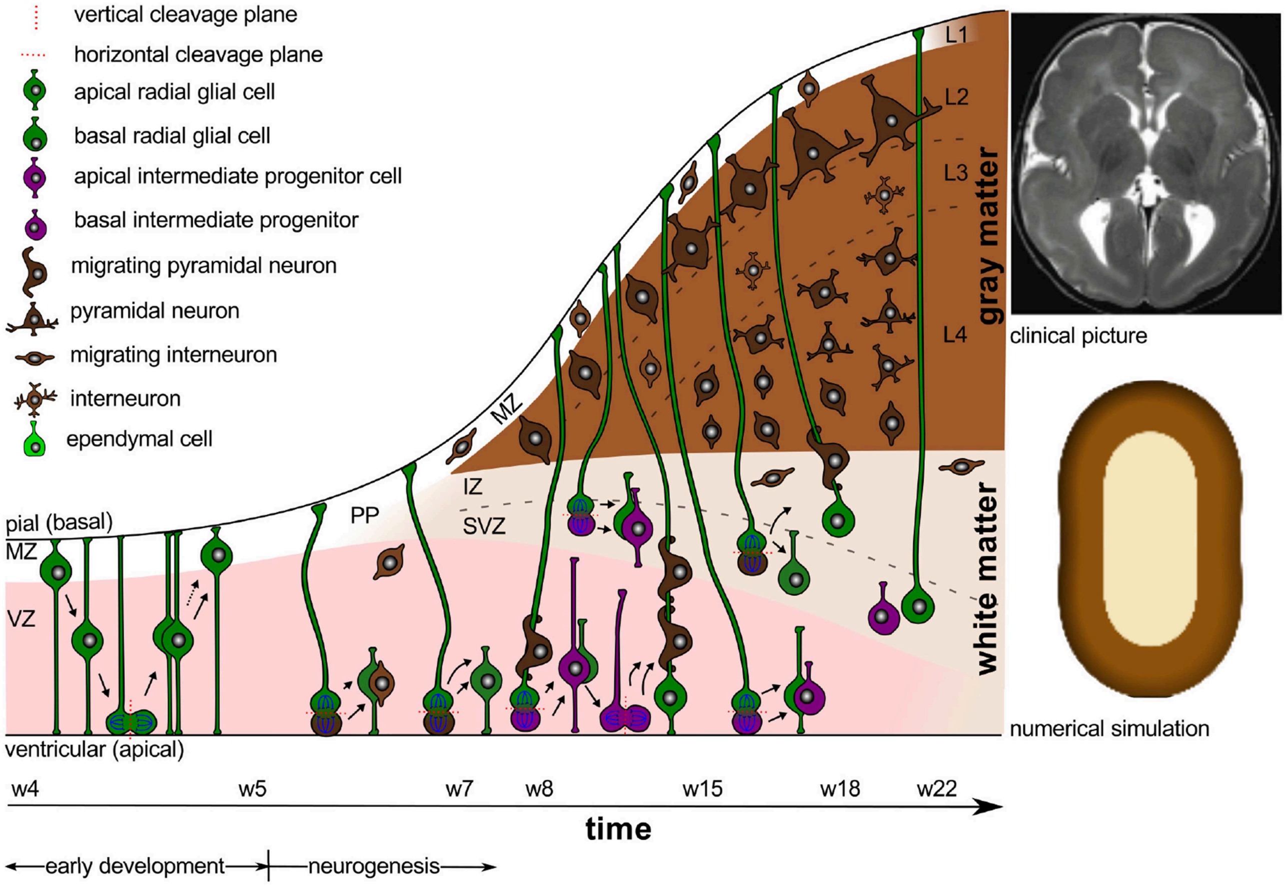

FIGURE 6 | Lissencephaly. Cortical malformations result from abnormal neuronal migration during the early stages of neurogenesis. The extensively thickened cortex typically only consists of four disorganized layers. Consistent with the clinical picture of lissencephaly (Budday et al., 2014a) (top right), the numerical simulation (Budday et al., 2014b) (bottom right) predicts the absence of folds for extensively thickened cortices.

2008). We can distinguish between layered polymicrogyria and unlayered polymicrogyria.

Figure 7 illustrates a layered polymicrogyric cortex. In comparison to the healthy human cortex in **Figure 3**, the polymicrogyric cortex consists of only four layers: an outer molecular layer corresponding to the healthy layer 1, a second cellular layer resulting from the fusion of the healthy layers 2 through 4, a third layer devoid of neurons representing the damaged layer 5, and a deep cellular layer similar to the healthy layer 6 (Gilbert-Barness and Debich-Spicer, 2008). Consistent with the pathology of polymicrogyria (Budday et al., 2014a), the computational simulation of differential growth (Budday et al., 2014b) predicts the emergence of small superficial folds as a result of cortical thinning and reduced growth in the subjacent layers.

Microcephaly is a Neurodevelopmental Disorder Associated with a Small Brain

Microcephaly is a rare developmental disorder associated with an abnormally small brain. In microcephalic brains, an altered cleavage plane during progenitor cell division reduces vertical, symmetric cell division and promotes horizontal, asymmetric cell division. This reduces the overall number of progenitor cells and neurons and decreases the cortical volume. In mild cases, the decrease in the total number of neurons is not accompanied by a commensurate loss of cortical folding (Bond et al., 2002). In more severe cases, however, an additional increase of apoptosis results in thinned cortices and abnormally small convolutions (Barkovich et al., 2005). These observations are consistent with the computational model of differential growth, which predicts that a thinner cortex in a proportionally smaller brain does not affect the folding pattern, whereas a markedly thin cortex in a normal brain evokes abnormally small convolutions.

Megalencephaly is a Neurodevelopmental Disorder Associated with an Enlarged Brain

Megalencephaly is a rare developmental disorder associated with an abnormally large brain. In megalencephalic brains, during early brain development, shortened cell cycles and increased cell cycle reentry increase the number of progenitor cells and neurons (Sun and Hevner, 2014). In mild cases, megalencephalic brains are enlarged but otherwise normal. In severe cases, the larger brain size is accompanied by enhanced folding, potentially

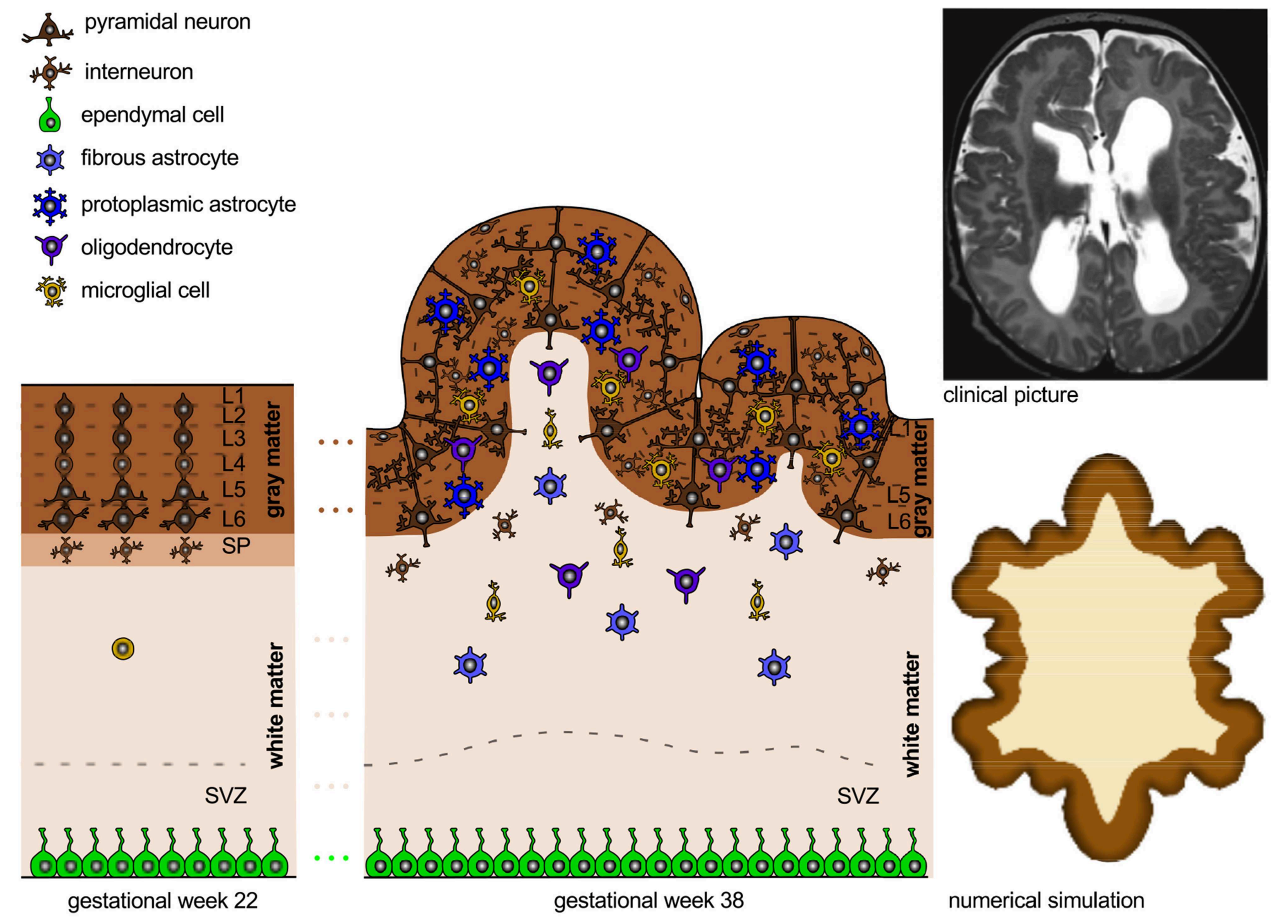

FIGURE 7 | Polymicrogyria. Cortical malformations resulting from abnormal neuronal organization. Increased cellular necrosis and disturbed neuronal connectivity result in a thinned cortex with an excessive number of small irregular folds. Consistent with the clinical picture of polymicrogyria (Budday et al., 2014a) (top right), the numerical simulation (Budday et al., 2014b) (bottom right) predicts the emergence of many, small irregular folds for thin cortices and reduced growth of inner layers.

brought about by decreased apoptosis (Barkovich et al., 2005). The increased number of progenitor cells and neurons leads to a proportional increase of brain volume and cortical thickness, which evokes normal folding patterns corresponding to the physical model of differential growth. Decreased apoptosis could initiate a faster tangential expansion of the cortex, which we could model by increasing the cortical growth rate. This would mimic neurons that normally undergo apoptosis, but now still form cortico-cortical connections. Consistent with the pathology of severe megalencephaly, an increase of the growth ratio between the superficial layers, which form horizontal cortico-cortical connections, and the subcortical layers, which are less involved in horizontal connectivity, induces folding patterns similar to those in simulations of polymicrogyric brains (Budday et al., 2014a).

6. Discussion

Neurodevelopment involves a highly orchestrated sequence of events, which is tightly regulated by the complex interplay of various cell types both in space and time. The objective of this review was to summarize the timeline of human brain development and to correlate events on the cellular level to pattern selection and surface morphogenesis on the organ level. To bridge these biological scales, we have adopted a popular physical model for brain folding: the mechanism of differential growth.

Neurodevelopment begins with cell division and cell migration, which ultimately result in the formation of the characteristic six-layered cortex. Throughout this process, intermediate progenitor cells tend to fill the cortical layers radially, while radial glial cells tend to expand the cortex tangentially. From a mechanical point of view, unconstrained radial growth causes a thickening of the cortex, whereas constrained tangential expansion generates compressive stress, which may eventually induce cortical folding. When neuronal migration is mostly completed, cortical neurons begin to form connections with other neurons. Neuronal connectivity involves the growth of neuronal dendrites and axons, the generation and expansion of astrocytes, oligodendrocytes and microglial cells, the formation of synapses, and the development of the vasculature system. These phenomena collectively result in an excessive tangential expansion of the outer cortex, an increase in cortical stress, and a folding of the cortical layer. Postnatally, synaptogenesis, synaptic pruning, and myelination mediate further cortical and subcortical growth, alter the cortical stress state, and reshape the cerebral cortex. Disruption of any of these events can result in severe cortical malformations, which are associated with neurological disorders including developmental delay and epilepsy. Although gyrification occurs in synchrony with neuronal connectivity–after all neurons have reached their final position in the developing cortex–early neuronal migration has a significant influence on cortical folding. Neuronal migration sets the stage for the folding process; disturbed initial conditions trigger disrupted neuronal connectivity and cortical malformations.

Lissencephaly, for instance, originates from disrupted early migration, although its classical hallmark–the absence of folds–does not make an appearance until the neuronal connectivity initiates folding. The absence of folding in the lissencephalic brain can be explained by a fairly simple physics-based model for growth-induced mechanical instabilities: the compressive forces induced by neuronal connectivity are distributed over an extensively thickened cortex; the resulting tangential stress within the cortex, the force divided by the thickness, is therefore significantly smaller than in healthy brains and fails to initiate folding. Even if the connectivity process itself is entirely normal, the smooth cortex precludes the formation of short association fibers and normal functioning of the brain. Polymicrogyria, in contrast, is a true organization disorder. At the end of neural migration, the cortex exhibits regular initial conditions, but the connectivity process itself is disturbed. Increased cell death and damage of deeper cortical layers result in a cortex with small superficial folds. Although the origin of this pathology is entirely different from lissencephaly, the same physics-based model can explain its malformations: a locally thinned cortex and reduced tangential expansion in the deeper layers reduce the critical wavelength, and induce an increased number of small folds.

Advances in the physical modeling and computational simulation of living systems can give insights into the underlying mechanisms of cortical folding that complement our current knowledge of neurodevelopment. They allow us to bridge cellular phenomena and whole organ form and function. Naturally, computational models of brain development have to simplify the complex biological problem. The challenge is to capture the critical processes without oversimplifying the biological system. In this review, we have shown that a fairly simple physical model can predict how the mammalian cortex evolves under physiological and pathological conditions. This model explains cortical malformations as emergent properties of cellular disruptions, either during early cellular division and migration or during later cellular organization and connectivity.

7. Conclusion

Neurodevelopment is a complex, dynamic process that involves several contributing genetic, environmental, biochemical, and physical factors; it is unlikely to be deciphered by a single discipline alone. Researchers of various fields are beginning to come together to elucidate normal and abnormal brain development through close multidisciplinary collaborations. A traditional biological approach, for example, can identify cells and genes that regulate malformations of cortical development; yet, it fails to substantiate the classical hallmark of the disease, the malformed cortex. A physical approach cannot explain the genetic origin of cortical malformations; yet, it can explain growth-induced instabilities, quantify cortical stress, identify the critical stress necessary to induce folding, rationalize emergent folding patterns, and predict gyral wavelengths and gyrification indices. If calibrated and validated appropriately, physics-based models allow us to bridge the scales–from phenomena on the cellular level toward form and function on the organ level–and make quantitative predictions. Recent advances in neuroimaging would allow us to create high precision, personalized models for cortical folding. Combining biology and physics can help us advance our understanding of human neurodevelopment, identify early markers of cortical malformations, and, ultimately, improve treatment of developmental disorders including epilepsy, autism spectrum disorders, and schizophrenia.

Author Contributions

SB has performed the simulations, designed all figures, and written the manuscript. PS has discussed the outline and overseen the writing process. EK has implemented the initial computational method, discussed the outline, and mentored the writing process.

Acknowledgments

This study was supported by the German National Science Foundation grant STE 544/50-1 to SB and PS and by the Bio-X IIP seed grant "Understanding gyrification dynamics in the human brain" to EK.

References

Achiron, R., and Achiron, A. (2001). Development of the human fetal corpus callosum: a high resolution, cross-sectional sonographic study. *Ultrasound Obstet. Gynecol.* 18, 343–347. doi: 10.1046/j.0960-7692.2001.00512.x

Allen, H. G. (1969). *Analysis and Design of Structural Sandwich Panels*. Oxford: Pergamon Press.

Alliot, F., Godin, I., and Pressac, B. (1999). MicroGlia derive from progenitors, originating from the yolk sac, and which proliferate in the brain. *Dev. Brain Res.* 117, 145–152.

Allsopp, G., and Gamble, H. J. (1979). Light and electron microscopic observations on the development of the blood vascular system of the human brain. *J. Anat.* 128, 461–477.

Ambrosi, D., Ateshian, G. A., Arruda, E. M., Cowin, S. C., Dumais, J., Goriely, A., et al. (2011). Perspectives on biological growth and remodeling. *J. Mech. Phys. Solids* 59, 863–883. doi: 10.1016/j.jmps.2010.12.011

Aronica, E., Becker, A. J., and Spreafico, R. (2012). Malformations of cortical development. *Brain Pathol.* 22, 380–401. doi: 10.1111/j.1750-3639.2012.00581.x

Balbi, V., Kuhl, E., and Ciarletta, P. (2015). Morphoelastic control of gastro-intestinal organogenesis: theoretical predictions and numerical insights. *J. Mech. Phys. Solids* 78, 493–510. doi: 10.1016/j.jmps.2015.02.016

Ballabh, P., Braun, A., and Nedergaard, M. (2004). Anatomic analysis of blood vessels in germinal matrix, cerebral cortex, and white matter in developing infants. *Pediatr. Res.* 56, 117–124. doi: 10.1203/01.PDR.0000130472.30874.FF

Barkovich, A. J., Kuzniecky, R. I., Jackson, G. D., Guerrini, R., and Dobyns, W. B. (2005). A developmental and genetic classification for malformations of cortical development. *Neurology* 65, 1873–1887. doi: 10.1212/01.wnl.0000183747.05269.2d

Barkovich, A. J., Guerrini, R., Kuzniecky, R. I., Jackson, G. D., and Dobyns, W. B. (2012). A developmental and genetic classification for malformations of cortical development: update 2012. *Brain* 135, 1348–1369. doi: 10.1093/brain/aws019

Barres, B. A. (2008). The mystery and magic of Glia: a perspective on their roles in health and disease. *Neuron* 60, 430–440. doi: 10.1016/j.neuron.2008.10.013

Bayer, S. A., and Altman, J. (1991). *Neocortical Development*. New York, NY: Raven Press.

Bayly, P. V., Okamoto, R. J., Xu, G., Shi, Y., and Taber, L. A. (2013). A cortical folding model incorporating stress-dependent growth explains gyral wavelengths and stress patterns in the developing brain. *Phys. Biol.* 10:016005. doi: 10.1088/1478-3975/10/1/016005

Bayly, P. V., Taber, L. A., and Kroenke, C. D. (2014). Mechanical forces in cerebral cortical folding: a review of measurements and models. *J. Mech. Behav. Biomed. Mater.* 29, 568–581. doi: 10.1016/j.jmbbm.2013.02.018

BenAmar, M., and Goriely, A. (2005). Growth and instability in soft tissues. *J. Mech. Phys. Solids* 53, 2284–2319. doi: 10.1016/j.jmps.2005.04.008

Bilston, L. E. (2011). *Neural Tissue Biomechanics*. Heidelberg: Springer.

Biot, M. A. (1937). Bending of an infinite beam on an elastic foundation. *J. Appl. Mech.* 59, A1–A7.

Biot, M. A. (1963). Surface instability of rubber in compression. *Appl. Sci. Res.* 12, 168–182.

Blows, W. T. (2003). Child brain development. *Nurs. Times* 99, 28–31.

Bond, J., Roberts, E., Mochida, G. H., Hampshire, D. J., Scott, S., Askham, J. M., et al. (2002). Aspm is a major determinant of cerebral cortical size. *Nat. Genet.* 32, 316–320. doi: 10.1038/ng995

Bradl, M., and Lassmann, H. (2010). Oligodendrocytes: biology and pathology. *Acta Neuropathol.* 119, 37–53. doi: 10.1007/s00401-009-0601-5

Budday, S., Raybaud, C., and Kuhl, E. (2014a). A mechanical model predicts morphological abnormalities in the developing human brain. *Sci. Rep.* 4:5644. doi: 10.1038/srep05644

Budday, S., Steinmann, P., and Kuhl, E. (2014b). The role of mechanics during brain development. *J. Mech. Phys. Solids* 72, 75–92. doi: 10.1016/j.jmps.2014.07.010

Budday, S., Kuhl, E., and Hutchinson, J. W. (2015a). Period-doubling and period-tripling in growing bilayered systems. *Philos. Mag.* doi: 10.1080/14786435.2015.1014443. (in press).

Budday, S., Nay, R., de Rooij, R., Steinmann, P., Wyrobek, T., Ovaert, T. C., et al. (2015b). Mechanical properties of gray and white matter brain tissue by indentation. *J. Mech. Behav. Biomed. Mater.* 46, 318–330. doi: 10.1016/j.jmbbm.2015.02.024

Budday, S., Steinmann, P., and Kuhl, E. (2015c). Secondary instabilities modulate cortical complexity in the mammalian brain. *Philos. Mag.* doi: 10.1080/14786435.2015.1024184. (in press).

Bushong, E. A., Martone, M. E., Jones, Y. Z., and Ellisman, M. H. (2002). Protoplasmic astrocytes in ca1 stratum radiatum occupy separate anatomical domains. *J. Neurosci.* 22, 183–192.

Bystron, I., Blakemore, C., and Rakic, P. (2008). Development of the human cerebral cortex: boulder committee revisited. *Nat. Rev. Neurosci.* 9, 110–122. doi: 10.1038/nrn2252

Cai, S., Breid, D., Crosby, A. J., Suo, Z., and Hutchinson, J. W. (2011). Periodic patterns and energy states of buckled thin films on compliant substrates. *J. Mech. Phys. Solids* 59, 1094–1114. doi: 10.1016/j.jmps.2011.02.001

Cao, Y., and Hutchinson, J. W. (2011). From wrinkles to creases in elastomers: the instability and imperfection-sensitivity of wrinkling. *Proc. R. Soc. A Math. Phys. Eng. Sci.* 20110384. doi: 10.1098/rspa.2011.0384

Cao, Y., and Hutchinson, J. W. (2012). Wrinkling phenomena in neo-hookean film/substrate bilayers. *J. Appl. Mech.* 79, 031019. doi: 10.1115/1.4005960

Carney, R. S., Bystron, I., López-Bendito, G., and Molnár, Z. (2007). Comparative analysis of extra-ventricular mitoses at early stages of cortical development in rat and human. *Brain Structure Funct.* 212, 37–54. doi: 10.1007/s00429-007-0142-4

Carson, M. J., Doose, J. M., Melchior, B., Schmid, C. D., and Ploix, C. C. (2006). Cns immune privilege: hiding in plain sight. *Immunol. Rev.* 213, 48–65. doi: 10.1111/j.1600-065X.2006.00441.x

Christ, A. F., Franze, K., Gautier, H., Moshayedi, P., Fawcett, J., Franklin, R. J. M., et al. (2010). Mechanical differences between white and gray matter in the rat cerebellum measured by scanning force microscopy. *J. Biomech.* 43, 2986–2992. doi: 10.1016/j.jbiomech.2010.07.002

Ciarletta, P., Balbi, V., and Kuhl, E. (2014). Pattern selection in growing tubular tissues. *Phys. Rev. Lett.* 113:248101. doi: 10.1103/PhysRevLett.113.248101

Clarke, L. E., and Barres, B. A. (2013). Emerging roles of astrocytes in neural circuit development. *Nat. Rev. Neurosci.* 14, 311–321. doi: 10.1038/nrn3484

Craige, A. M., Graf, E. R., and Linhoff, M. W. (2006). How to build a central synapse: clues from Cell culture. *Trends Neurosci.* 29, 8–20. doi: 10.1016/j.tins.2005.11.002

Craik, F. I. M., and Bialystok, E. (2006). Cognition through the lifespan: mechanisms of change. *Trends Cogn. Sci.* 10, 131–138. doi: 10.1016/j.tics.2006.01.007

DelRío, J. A., Martínez, A., Auladell, C., and Soriano, E. (2000). Developmental history of the subplate and developing white matter in the murine neocortex. Neuronal organization and relationship with the main afferent systems at embryonic and perinatal stages. *Cereb. Cortex* 10, 784–801. doi: 10.1093/cercor/10.8.784

Desmond, M. E., and Jacobson, A. G. (1977). Embryonic brain enlargement requires cerebrospinal fluid pressure. *Dev. Biol.* 57, 188–198.

Desmond, M. E. (1985). Reduced number of brain Cells in so-called neural overgrowth. *Anat. Rec.* 212, 195–198.

Diemel, L. T., Copelman, C. A., and Cuzner, M. L. (1998). Macrophages in cns remyelination: friend or foe? *Neurochem. Res.* 23, 341–347.

Esiri, M. M., al Izzi, M. S., and Reading, M. C. (1991). Macrophages, microGlial cells, and hla-dr antigens in fetal and infant brain. *J. Clin. Pathol.* 44, 102–106.

Feng, Y., Clayton, E. H., Chang, Y., Okamoto, R. J., and Bayly, P. V. (2013). Viscoelastic properties of the ferret brain measured *in vivo* at multiple frequencies by magnetic resonance elastography. *J. Biomech.* 46, 863–870. doi: 10.1016/j.jbiomech.2012.12.024

Ferrer, I., and Catalá, I. (1991). Unlayered polymicrogyria: structural and developmental aspects. *Anat. Embryol.* 184, 517–528.

Ferrer, I. (1984). A Golgi analysis of unlayered polymicrogyria. *Acta Neuropathol.* 65, 69–76.

Franklin, R. J., and Ffrench-Constant, C. (2008). Remyelination in the cns: from biology to therapy. *Nat. Rev. Neurosci.* 9, 839–855. doi: 10.1038/nrn2480

Franze, K., Janmey, P. A., and Guck, J. (2013). Mechanics in neuronal development and repair. *Annu. Rev. Biomed. Eng.* 15, 227–251. doi: 10.1146/annurev-bioeng-071811-150045

Franze, K. (2014). The mechanical control of nervous system development. *Development* 140, 3069–3077. doi: 10.1242/dev.079145

Freeman, M. R. (2010). Specification and morphogenesis of astrocytes. *Science* 330, 774–778. doi: 10.1126/science.1190928

Friede, R. L. (1989). *Developmental Neuropathology*. Berlin; Heidelberg: Springer.

Gilbert-Barness, E., and Debich-Spicer, D. E. (2008). *Handbook of Pediatric Autopsy Pathology*. New Jersey, NJ: Humana Press.

Golden, J. A., and Harding, B. N. (2004). *Pathology & Genetics: Developmental Neuropathology*. Los Angeles, CA: ISN Neuropathology Press.

Goodkind, M., Eickhoff, S. B., Oathes, D. J., Jiang, Y., Chang, A., Jones-Hagata, L. B., et al. (2015). Identification of a common neurobiological substrate for mental illness. *JAMA Psychiatry* 72, 305–315. doi: 10.1001/jamapsychiatry.2014.2206

Goriely, A., and BenAmar, M. (2005). Differential growth and instability in elastic shells. *Phys. Rev. Lett.* 94:198103. doi: 10.1103/PhysRevLett.94.198103

Goriely, A., Geers, M. G. D., Holzapfel, G. A., Jayamohan, J., Jerusalem, A., Sivaloganathan, S., et al. (2015). Mechanics of the brain: perspectives, challenges, and opportunities. *Biomech. Model. Mechanobiol.* doi: 10.1007/s10237–015–0662–4. [Epub ahead of print].

Green, M. A., Bilston, L. E., and Sinkus, R. (2008). *In vivo* brain viscoelastic properties measured by magnetic resonance elastography. *NMR Biomed.* 21, 755–764. doi: 10.1002/nbm.1254

Guerrini, R., Dobyns, W. B., and Barkovich, A. J. (2008). Abnormal development of the human cerebral cortex: genetics, functional consequences and treatment options. *Trends Neurosci.* 31, 154–162. doi: 10.1016/j.tins.2007.12.004

Hansen, D. V., Lui, J. H., Parker, P. R., and Kriegstein, A. R. (2010). Neurogenic radial Glia in the outer subventricular zone of human neocortex. *Nature* 464, 554–561. doi: 10.1038/nature08845

Harry, G. J. (2013). MicroGlia during development and aging. *Pharmacol. Ther.* 139, 313–326. doi: 10.1016/j.pharmthera.2013.04.013

Haubensak, W., Attardo, A., Denk, W., and Huttner, W. B. (2004). Neurons arise in the basal neuroepithelium of the early mammalian telencephalon: a major site of neurogenesis. *Proc. Natl. Acad. Sci. U.S.A.* 101, 3196–3201. doi: 10.1073/pnas.0308600100

Haydar, T. F., Kuan, C.-Y., Flavell, R. A., and Rakic, P. (1999). The role of cell death in regulating the size and shape of the mammalian forebrain. *Cereb. Cortex* 9, 621–626. doi: 10.1093/cercor/9.6.621

Haydar, T. F., Ang, E., and Rakic, P. (2003). Mitotic spindle rotation and mode of cell division in the developing telencephalon. *Proc. Natl. Acad. Sci. U.S.A.* 100, 2890–2895. doi: 10.1073/pnas.0437969100

Haynes, R. L., Borenstein, N. S., Desilva, T. M., Folkerth, R. D., Liu, L. G., Volpe, J. J., et al. (2005). Axonal development in the cerebral white matter of the human fetus and infant. *J. Compar. Neurol.* 484, 156–167. doi: 10.1002/cne.20453

Herculano-Houzel, S. (2009). The human brain in numbers: a linearly scaled-up primate brain. *Front. Hum. Neurosci.* 3:31.3–31.11. doi: 10.3389/neuro.09.031.2009

Hill, R. S., and Walsh, C. A. (2005). Molecular insights into human brain evolution. *Nature* 437, 64–67. doi: 10.1038/nature04103

Hofman, M. A. (1989). On the evolution and geometry of the brain in mammals. *Prog. Neurobiol.* 32, 137–158.

Holland, M. A., Miller, K. E., and Kuhl, E. (2015). Emerging brain morphologies from axonal elongation. *Ann. Biomed. Eng.* doi: 10.1007/s10439–015–1312–9. [Epub ahead of print].

Hutchinson, J. W. (2013). The role of nonlinear substrate elasticity in the wrinkling of thin films. *Philos. Trans. R. Soc. Lond. A* 371:20120422. doi: 10.1098/rsta.2012.0422

Huttenlocher, P. R., and Dabholkar, A. S. (1997). Regional differences in synaptogenesis in human cerebral cortex. *J. Compar. Neurol.* 387, 167–178.

Iacopetti, P., Michelini, M., Stuckmann, I., Oback, B., Aaku-Saraste, E., and Huttner, W. B. (1999). Expression of the antiproliferative gene tis21 at the onset of neurogenesis identifies single neuroepithelial cells that switch from proliferative to neuron-generating division. *Proc. Natl. Acad. Sci. U.S.A.* 96, 4639–4644.

Jakovcevski, I., Filipovic, R., Mo, Z., Rakic, S., and Zecevic, N. (2009). Oligodendrocyte development and the onset of myelination in the human fetal brain. *Front. Neuroanat.* 3:5. doi: 10.3389/neuro.05.005.2009

Judkins, A. R., Martinez, D., Ferreira, P., Dobyns, W. B., and Golden, J. A. (2011). Polymicrogyria includes fusion of the molecular layer and decreased neuronal populations, but normal cortical laminar organization. *J. Neuropathol. Exp. Neurol.* 70, 438–443. doi: 10.1097/NEN.0b013e31821ccf1c

Kaster, T., Sack, I., and Samani, A. (2011). Measurement of the hyperelastic properties of *ex vivo* brain tissue slices. *J. Biomech.* 44, 1158–1163. doi: 10.1016/j.jbiomech.2011.01.019

Kessaris, N., Fogarty, M., Iannarelli, P., Grist, M., Wegner, M., and Richardson, W. D. (2006). Competing waves of oligodendrocytes in the forebrain and postnatal elimination of an embryonic lineage. *Nat. Neurosci.* 9, 173–179. doi: 10.1038/nn1620

Koser, D. E., Moeendarbary, E., Hanne, J., Kuerten, S., and Franze, K. (2015). Cns Cell distribution and axon orientation determine local spinal cord mechanical properties. *Biophys. J.* 108, 2137–2147. doi: 10.1016/j.bpj.2015.03.039

Kostović, I., Judaš, M., Radoš, M., and Hrabač, P. (2002). Laminar organization of the human fetal cerebrum revealed by histochemical markers and magnetic resonance imaging. *Cereb. Cortex* 12, 536–544. doi: 10.1093/cercor/12.5.536

Kowalczyk, T., Pontious, A., Englund, C., Daza, R. A., Bedogni, F., Hodge, R., et al. (2009). Intermediate neuronal progenitors (basal progenitors) produce pyramidal–projection Neurons for all layers of cerebral cortex. *Cereb. Cortex* 19, 2439–2450. doi: 10.1093/cercor/bhn260

Kriegstein, A. R., Noctor, S., and Martínez-Cerdeño, V. (2006). Patterns of neural stem and progenitor Cell division may underlie evolutionary cortical expansion. *Nat. Rev. Neurosci.* 7, 883–890. doi: 10.1038/nrn2008

Le Gros Clark, W. E. (1945). "Deformation patterns in the cerebral cortex," in *Essays on Growth and Form*, eds W. E. Le Gross Clark and P. B. Medawar (London: Oxford University Press), 1–22.

Le Gros Clark, W. E. (1990). "Why does cerebral cortex fissure and fold? A review of determinants of gyri and sulci," in *Cerebral Cortex,* Vol. 8B, eds E. G. Jones and A. Peters (New York, NY: Springer Science+Business Media), 3–136.

Lee, E. H. (1969). Elastic-plastic deformation at finite strains. *J. Appl. Mech.* 36, 1–6.

Lehtinen, M. K., Zappaterra, M. W., Chen, X., Yang, Y. J., Hill, A. D., Lun, M., et al. (2011). The cerebrospinal fluid provides a proliferative niche for neural progenitor cells. *Neuron* 69, 893–905. doi: 10.1016/j.neuron.2011.01.023

Luders, E., Thompson, P. M., and Toga, A. W. (2010). The development of the corpus callosum in the healthy human brain. *J. Neurosci.* 30, 10985–10990. doi: 10.1523/JNEUROSCI.5122-09.2010

Ludwin, S. K., and Maitland, M. (1984). Long-term remyelination fails to reconstitute normal thickness of central myelin sheaths. *J. Neurol. Sci.* 64, 193–198. doi: 10.1016/0022-510X(84)90037-6

Lui, J. H., Hansen, D. V., and Kriegstein, A. R. (2011). Development and evolution of the human neocortex. *Cell* 146, 18–36. doi: 10.1016/j.cell.2011.06.030

Lukaszewicz, A., Savatier, P., Cortay, V., Giroud, P., Huissoud, C., Berland, M., et al. (2005). G1 phase regulation, area-specific Cell cycle control, and cytoarchitectonics in the primate cortex. *Neuron* 47, 353–364. doi: 10.1016/j.neuron.2005.06.032

Lund, R. D., and Lund, J. S. (1972). Development of synaptic patterns in the superior colliculus of the rat. *Brain Res.* 42, 1–20.

Marín-Padilla, M. (2012). The human brain intracerebral microvascular system: development and structure. *Front. Neuroanat.* 6:38. doi: 10.3389/fnana.2012.00038

Marin-Padilla, M. (1970). Prenatal and early postnatal ontogenesis of the human motor cortex: a golgi study. I. the sequential development of the cortical layers. *Brain Res.* 23, 167–183.

McLaurin, J. A., and Yong, V. W. (1995). Oligodendrocytes and myelin. *Neurol. Clin.* 13, 23–49.

Miller, K. (2011). *Biomechanics of the Brain*. New York, NY: Springer.

Misson, J. P., Takahashi, T., and Caviness, V. S. (1991). Ontogeny of radial and other astroGlial Cells in murine cerebral cortex. *Glia* 4, 138–148.

Mitchison, G. (1991). Neuronal branching patterns and the economy of cortical wiring. *Proc. R. Soc. Lond. B Biol. Sci.* 245, 151–158.

Mizutani, K., Yoon, K., Dang, L., Tokunaga, A., and Gaiano, N. (2007). Differential notch signalling distinguishes neural stem Cells from intermediate progenitors. *Nature* 449, 351–355. doi: 10.1038/nature06090

Molnár, Z., Adams, R., and Blakemore, C. (1998). Mechanisms underlying the early establishment of thalamocortical connections in the rat. *J. Neurosci.* 18, 5723–5745.

Molofsky, A. V., Krenick, R., Ullian, E., hsin Tsai, H., Deneen, B., Richardson, W. D., et al. (2012). Astrocytes and disease: a neurodevelopmental perspective. *Genes Dev.* 26, 891–907. doi: 10.1101/gad.188326.112

Monier, A., Evrard, P., Gressens, P., and Verney, C. (2006). Distribution and differentiation of microGlia in the human encephalon during the first two trimesters of gestation. *J. Compar. Neurol.* 499, 565–582. doi: 10.1002/cne.21123

Morrow, T., Song, M.-R., and Ghosh, A. (2001). Sequential specification of neurons and Glia by developmentally regulated extracellular factors. *Development* 128, 3585–3594.

Moulton, D. E., and Goriely, A. (2011). Circumferential buckling instability of a growing cylindrical tube. *J. Mech. Phys. Solids* 59, 525–537. doi: 10.1016/j.jmps.2011.01.005

Nedergaard, M., Ransom, B., and Goldman, S. A. (2003). New roles for astrocytes: redefining the functional architecture of the brain. *Trends Neurosci.* 26, 523–530. doi: 10.1016/j.tins.2003.08.008

Noctor, S. C., Flint, A. C., Weissman, T. A., Dammerman, R. S., and Kriegstein, A. R. (2001). Neurons derived from radial Glial cells establish radial units in neocortex. *Nature* 409, 714–720. doi: 10.1038/35055553

Noctor, S. C., Martínez-Cerdeño, V., Ivic, L., and Kriegstein, A. R. (2004). Cortical neurons arise in symmetric and asymmetric division zones and migrate through specific phases. *Nat. Neurosci.* 7, 136–144. doi: 10.1038/nn1172

Norman, M. G., and O'Kusky, J. R. (1986). The growth and development of microvasculature in human cerebral cortex. *J. Neuropathol. Exp. Neurol.* 45, 222–232.

O'Rahilly, R., and Müller, F. (1986). The meninges in human development. *J. Neuropathol. Exp. Neurol.* 45, 588–608.

O'Rahilly, R. R., and Müller, F. (2006). *The Embryonic Human Brain: An Atlas of Developmental Stages*. New York, NY: John Wiley & Sons.

O'Toole, M., Lamoureux, P., and Miller, K. E. (2015). Measurement of subCellular force generation in neurons. *Biophys. J.* 108, 1027–1037. doi: 10.1016/j.bpj.2015.01.021

Pakkenberg, B., and Gundersen, J. G. (1997). Neocortial neuron number in humans: effect of sex and age. *J. Compar. Neurol.* 384, 312–320.

Pakkenberg, B., Pelvig, D., Marner, L., Bundgaard, M. J., Gundersen, H. J. G., Nyengaard, J. R., et al. (2003). Aging and the human neocortex. *Exp. Gerontol.* 38, 95–99. doi: 10.1016/S0531-5565(02)00151-1

Palmer, E. E., and Mowat, D. (2014). Agenesis of the corpus callosum: a clinical approach to diagnosis. *Am. J. Med. Genet.* 166, 184–197. doi: 10.1002/ajmg.c.31405

Pfeiffer, S. E., Warrington, A. E., and Bansal, R. (1993). The oligodendrocyte and its many Cellular processes. *Trends Cell Biol.* 3, 191–197.

Pontious, A., Kowalczyk, T., Englund, C., and Hevner, R. F. (2008). Role of intermediate progenitor cells in cerebral cortex development. *Dev. Neurosci.* 30, 24–32. doi: 10.1159/000109848

Powell, E. M., and Geller, H. M. (1999). Dissection of astrocyte-mediated cues in neuronal guidance and process extension. *Glia* 26, 73–83.

Preuss, T. M., Cáceres, M., Oldham, M. C., and Geschwind, D. H. (2004). Human brain evolution: insights from microarrays. *Nat. Rev. Genet.* 5, 850–860. doi: 10.1038/nrg1469

Rakic, S., and Zecevic, N. (2003). Emerging complexity of layer i in human cerebral cortex. *Cereb. Cortex* 13, 1072–1083. doi: 10.1093/cercor/13.10.1072

Raybaud, C., Ahmad, T., Rastegar, N., Shroff, M., and Nassar, A. M. (2013). The premature brain: developmental and lesional anatomy. *Neuroradiology* 55, 23–40. doi: 10.1007/s00234-013-1231-0

Rezaie, P., and Male, D. (1999). Colonisation of the developing human brain and spinal cord by microGlia: a review. *Microsc. Res. Tech.* 45, 359–382.

Richman, D. P., Stewart, R. M., Hutchinson, J. W., and Caviness, V. S. (1975). Mechanical mode of brain convolutional development. *Science* 189, 18–21.

Rockland, K. S., and DeFelipe, J. (2011). Cortical white matter: beyond the pale. *Front. Neuroanat.* 5:67. doi: 10.3389/fnana.2011.00067

Rodriguez, E. K., Hoger, A., and McCulloch, A. D. (1994). Stress-dependent finite growth in soft elastic tissues. *J. Biomech* 27, 455–467.

Ronan, L., Voets, N., Rua, C., Alexander-Bloch, A., Hough, M., Mackay, C., et al. (2014). Differential tangential expansion as a mechanism for cortical gyrification. *Cereb. Cortex* 24, 2219–2228. doi: 10.1093/cercor/bht082

Sheppard, A. M., and Pearlman, A. L. (1997). Abnormal reorganization of preplate neurons and their associated extracellular matrix: an early manifestation of altered neocortical development in the reeler mutant mouse. *J. Compar. Neurol.* 378, 173–179.

Sidman, R. L., and Rakic, P. (1973). Neuronal migration, with special reference to developing human brain: a review. *Brain Res.* 62, 1–35.

Siegenthaler, J. A., and Pleasure, S. J. (2011). We have got you 'covered': how the meninges control brain development. *Curr. Opin. Genet. Dev.* 21, 151–158. doi: 10.1016/j.gde.2010.12.005

Simons, M., and Trajkovic, K. (2006). Neuron-Glia communication in the control of oligodendrocyte function and myelin biogenesis. *J. Cell. Sci.* 119, 4381–4389. doi: 10.1242/jcs.03242

Smart, I. H., and McSherry, G. M. (1986). Gyrus formation in the cerebral cortex of the ferret. II. description of the internal histological changes. *J. Anat.* 147, 27–43.

Smith, D. H. (2009). Stretch growth of integrated axon tracts: extremes and extrapolations. *Prog. Neurobiol.* 89, 231–239. doi: 10.1016/j.pneurobio.2009.07.006

Sun, T., and Hevner, R. F. (2014). Growth and folding of the mammalian cerebral cortex: from molecules to malformations. *Nat. Rev. Neurosci.* 15, 217–232. doi: 10.1038/nrn3707

Suter, D. M., and Miller, K. E. (2011). The emerging role of forces in axonal elongation. *Prog. Neurobiol.* 94, 91–101. doi: 10.1016/j.pneurobio.2011.04.002

Takahashi, E., Folkerth, R. D., Galaburda, A. M., and Grant, P. E. (2012). Emerging cerebral connectivity in the human fetal brain: an mr tractography study. *Cereb. Cortex* 22, 455–464. doi: 10.1093/cercor/bhr126

van Dommelen, J. A. W., van der Sande, T. P. J., Hrapko, M., and Peters, G. W. M. (2010). Mechanical properties of brain tissue by indentation: interregional variation. *J. Mech. Behav. Biomed. Mater.* 3, 158–166. doi: 10.1016/j.jmbbm.2009.09.001

VanEssen, D. C. (1997). A tension-based theory of morphogenesis and compact wiring in the central nervous system. *Nature* 385, 313–318.

Vaughn, J. E., and Peters, A. (1967). Electron microscopy of the early postnatal development of fibrous astrocytes. *Am. J. Anat.* 121, 131–151.

Welker, W., Johnson, I. J., and Noe, A. (2015). *Comparative Mammalian Brain Collections.* Available online at: http://brainmuseum.org

Xu, G., Knutsen, A. K., Dikranian, K., Kroenke, C. D., Bayly, P. V., and Taber, L. A. (2010). Axons pull on the brain, but tension does not drive cortical folding. *J. Biomech. Eng.* 132, 071013. doi: 10.1115/1.4001683

Yakovlev, P. I., and Lecours, A. R. (1967). "The myelogenetic cycles of regional maturation of the brain," in *Regional Development of the Brain in Early Life,* ed A. Minkowsky (Oxford: Blackwell Science), 3–70.

Yang, Y., Higashimori, H., and Morel, L. (2013). Developmental maturation of astrocytes and pathogenesis of neurodevelopmental disorders. *J. Neurodev. Disord.* 5, 1–8. doi: 10.1186/1866-1955-5-22

Zecevic, N., Chen, Y., and Filipovic, R. (2005). Contributions of cortical subventricular zone to the development of the human cerebral cortex. *J. Compar. Neurol.* 491, 109–122. doi: 10.1002/cne.20714

Zilles, K., Palomero-Gallagher, N., and Amunts, K. (2013). Development and cortical folding during evolution and ontogeny. *Trends Neurosci.* 36, 275–284. doi: 10.1016/j.tins.2013.01.006

Conflict of Interest Statement: The authors declare that the research was conducted in the absence of any commercial or financial relationships that could be construed as a potential conflict of interest.

frontiers
in Cellular Neuroscience

ORIGINAL RESEARCH
published: 23 September 2015
doi: 10.3389/fncel.2015.00363

Microglia mechanics: immune activation alters traction forces and durotaxis

Lars Bollmann[1,2‡], *David E. Koser*[1,3†‡], *Rajesh Shahapure*[1], *Hélène O. B. Gautier*[1], *Gerhard A. Holzapfel*[2], *Giuliano Scarcelli*[4], *Malte C. Gather*[5], *Elke Ulbricht*[1†] and *Kristian Franze*[1*]

[1] Department of Physiology, Development and Neuroscience, University of Cambridge, Cambridge, UK, [2] Faculty of Computer Science and Biomedical Engineering, Institute of Biomechanics, Graz University of Technology, Graz, Austria, [3] Department of Physics, Institute for Theoretical Physics, University of Cologne, Cologne, Germany, [4] Fischell Department of Bioengineering, University of Maryland, College Park, MD, USA, [5] Scottish Universities Physics Alliance (SUPA), School of Physics and Astronomy, University of St Andrews, St Andrews, UK

Edited by:
Daniel Marcel Suter,
Purdue University, USA

Reviewed by:
Jeffrey Urbach,
Georgetown University, USA
Gil Lee,
University College Dublin, Ireland

***Correspondence:**
Kristian Franze,
Department of Physiology,
Development and Neuroscience,
University of Cambridge, Downing
Street, Cambridge CB2 3DY, UK
kf284@cam.ac.uk

†Present Address:
David E. Koser,
Department of Clinical Neurobiology,
Medical Faculty of Heidelberg
University and DKFZ Heidelberg,
Heidelberg, Germany;
Elke Ulbricht,
Biotechnology Center, Technische
Universität Dresden, Dresden,
Germany

‡These authors have contributed equally to this work.

Received: 22 June 2015
Accepted: 31 August 2015
Published: 23 September 2015

Citation:
Bollmann L, Koser DE, Shahapure R, Gautier HOB, Holzapfel GA, Scarcelli G, Gather MC, Ulbricht E and Franze K (2015) Microglia mechanics: immune activation alters traction forces and durotaxis. Front. Cell. Neurosci. 9:363. doi: 10.3389/fncel.2015.00363

Microglial cells are key players in the primary immune response of the central nervous system. They are highly active and motile cells that chemically and mechanically interact with their environment. While the impact of chemical signaling on microglia function has been studied in much detail, the current understanding of mechanical signaling is very limited. When cultured on compliant substrates, primary microglial cells adapted their spread area, morphology, and actin cytoskeleton to the stiffness of their environment. Traction force microscopy revealed that forces exerted by microglia increase with substrate stiffness until reaching a plateau at a shear modulus of ∼5 kPa. When cultured on substrates incorporating stiffness gradients, microglia preferentially migrated toward stiffer regions, a process termed durotaxis. Lipopolysaccharide-induced immune-activation of microglia led to changes in traction forces, increased migration velocities and an amplification of durotaxis. We finally developed a mathematical model connecting traction forces with the durotactic behavior of migrating microglial cells. Our results demonstrate that microglia are susceptible to mechanical signals, which could be important during central nervous system development and pathologies. Stiffness gradients in tissue surrounding neural implants such as electrodes, for example, could mechanically attract microglial cells, thus facilitating foreign body reactions detrimental to electrode functioning.

Keywords: migration, mechanotaxis, foreign body reaction, random walk, LPS, CNS, gliosis, biased random walk

Introduction

The central nervous system (CNS) is separated from the systemic immune system by the blood–brain barrier, which protects the tissue from most infections. When pathogens cross the blood-brain-barrier, after brain lesions, or in any other CNS dysfunction, microglial cells form the first line of immune defense. After detection of a pathological signal, microglia become activated and migrate toward the stimulus, where they release a large number of signaling molecules, proliferate, and phagocytose cells and debris (Kettenmann et al., 2011).

Chemical interactions of microglial cells with their environment have been extensively studied in the past. However, in order to migrate, microglia need to exert forces on their environment. While they exert forces on the surrounding tissue, they probe its mechanical properties (Franze et al., 2013). Yet, forces exerted by microglial cells have not been measured, and their mechanical interactions with their environment are currently poorly understood.

Glial cells respond to the stiffness of their environment in different ways. Astrocytes, for example, increase their spread area, overall morphological complexity, and F-actin organization on stiffer growth substrates (Georges et al., 2006; Moshayedi et al., 2010). Similarly, oligodendrocyte progenitor cells increase their area and complexity on stiffer substrates, but show an optimum in survival and proliferation at intermediate values of CNS tissue stiffness (Jagielska et al., 2012). Morphologies of microglial cells also become more complex on stiffer substrates, and similarly to astrocytes, they upregulate inflammatory mediators when exposed to an environment with increased stiffness (Moshayedi et al., 2014).

Stiff neural implants, for example, were shown to activate and attract microglia and astrocytes, while soft implants that were mechanically matched to the surrounding CNS tissue diminished this foreign body reaction *in vivo* (Moshayedi et al., 2014). It was suggested that the large stiffness of a common neural implant, such as an electrode, triggers microglia migration toward that foreign body (Franze et al., 2013), in a similar fashion as some cell types migrate from softer to stiffer matrices in a process termed durotaxis (Lo et al., 2000). However, while substrate stiffness was shown to regulate glial cell migration (Mori et al., 2013; Kim et al., 2014), direct experimental proof for an impact of the mechanical properties of the surrounding on microglia migration is currently missing.

CNS tissue is mechanically heterogeneous at a length scale relevant to individual cells (Elkin et al., 2007; Christ et al., 2010; Franze et al., 2011; Iwashita et al., 2014; Koser et al., 2015). Furthermore, its mechanical properties may alter with age (Sack et al., 2011; Arani et al., 2015) and in pathological conditions (Murphy et al., 2011; Riek et al., 2012; Schregel et al., 2012; Streitberger et al., 2012; Chauvet et al., 2015). Thus, microglia are exposed to varying mechanical signals on their way to sites of damage. To test if these signals may impact the interactions of microglial cells with their environment, we measured traction forces exerted by microglia as a function of substrate stiffness. We furthermore investigated their migratory behavior on substrates with stiffness gradients, and developed a model to predict microglia migration based on their traction forces.

Materials and Methods

All chemicals were purchased from Sigma-Aldrich (Sigma-Aldrich Company Ltd., Gillingham, UK), unless otherwise stated.

Polyacrylamide Substrates

To obtain deformable cell culture substrates of varying stiffness or incorporated stiffness gradients, modified protocols of Grevesse et al. (2013) and Moshayedi et al. (2010) were used. Substrates were made of polyacrylamide (PAA), which is a transparent, homogeneous, isotropic, and linearly elastic material. PAA gels were polymerized on imaging dishes (μ-Dish, Ibidi, Germany) for traction force microscopy and on coverslips otherwise. Surfaces of the imaging dishes or coverslips were cleaned with 70% ethanol and made hydrophilic with 0.1% sodium hydroxide (NaOH). (3-Aminopropyl) trimethoxysilane (APTMS) was applied for a duration of 3 min to the NAOH-treated surface. Subsequently, it was washed and covered with 0.5% glutaraldehyde for 30 min. PAA stock solutions for homogeneous substrates were made of 500 μl 40% acrylamide (AA), 65 μl 100% hydroxy-acrylamide (OH-AA) and 250 μl 2% bis-acrylamide (Bis-AA, Fisher scientific, UK). PAA premixes for gradient substrates were made according to Moshayedi et al. (2010).

Preparation of PAA Substrates for Traction Force Microscopy

Fluorescent nanoparticles (FluoSpheres carboxylate, 0.2 μm, crimson, Life Technologies, UK) were added to the PAA premixes, which were then placed in an ultrasonic bath for 30 s to separate the beads. Subsequently, premixes were degassed for 10 min. Adding 1.5 μL N,N,N′,N′-tetramethyl-ethylenediamine (TEMED) and 5 μL of a 10% ammonium persulfate solution (APS) initiated the cross-linking of the gels. Immediately thereafter, 8 μl of the solution were pipetted on the imaging dish. A coverslip that had been cleaned and made hydrophobic with RainX (Kraco Car Care International Ltd., UK) was lowered onto the drop to create a gel layer of even thickness. The imaging dish was then inverted to ensure that beads settled close to the gel surface. Once the gel had polymerized, the surface was covered with PBS and the coverslip was removed. The gels were subsequently washed and sterilized under UV light for ∼15 min. To promote cell adhesion, gel surfaces were treated with 100 μg/ml poly-D-lysine (PDL) for 2 h.

Preparation of Stiffness Gradient Substrates

Two Parafilm-covered microscope slides were used to enclose a glutaraldehyde-treated $22 \times 22\ \text{mm}^2$ coverslip and a $22 \times 40\ \text{mm}^2$ coverslip cleaned and made hydrophobic with RainX. The treated sides were facing each other and separated by a U-shaped spacer made of Parafilm. Bulldog clips were used to hold the chamber together (Koser et al., under review).

PAA premixes for substrates with shear moduli of $G' \sim 100$ Pa and $G' \sim 10$ kPa were prepared as described in Moshayedi et al. (2010). In the 10 kPa premix, 5 μl of PBS were substituted by 5 μL of 1% (w/v) fluorescein O,O′-dimethacrylate diluted in DMSO. The premix solutions were vortexed and then desiccated for 10 min. Polymerization was initiated as described above. The bottom half of the chamber was then filled with the premix of the stiff substrate ($G' \sim 10$ kPa), the upper half subsequently with the premix for the soft substrate ($G' \sim 100$ Pa). Diffusion led to overlapping linear gradients in stiffness and fluorescence intensity (Supplementary Figure 1 and Koser et al., under review). Therefore, the fluorescence intensity could be used as readout for the local substrate stiffness. Once the gel had polymerized, the chamber was submerged in PBS and the coverslips separated. The gel was sterilized under a UV lamp for 1 h and washed three times in filter-sterilized PBS. The gel was then incubated over night at room temperature in a 1:99 Cell-Tak™ (BD Biosciences)—PBS solution (Koch et al., 2012), and subsequently treated with a 1:10 poly-L-lysine (PLL)–PBS solution for 2 h.

Microglial Cell Cultures

All animal experiments of this study were conducted in accordance with the UK Animals (Scientific Procedures) Act (1986). Neonatal P0-P2 Sprague Dawley rats (for TFM, actin morphology and cell size experiments) or P0–P5 mice (C57BL/6; for migration assays) were decapitated and their cortices dissected from the exposed brains, or whole brains used, respectively. Microglia were obtained following Giulian and Baker (1986) and Mccarthy and De Vellis (1980). The rat cortices were cut into small pieces, minced and incubated in a cell dissociation solution containing papaya proteinase 1 (Papain) at 37°C for 1 h. To stop papain digestion, an Ovomuccoid (Trypsin inhibitor) solution was added. Mice brains were minced mechanically and filtered through cell strainers. The cell suspension was centrifuged at 1000 rpm for 8 min. The resulting pellet of cells was suspended in glia medium [DMEM (Gibco, Life Technologies Ltd., UK) + 3.8 mM L-Glutamine + 10% fetal bovine serum (FBS) (Gibco) + 1% Penicillin Streptomycin (PenStrep) (Gibco); as described by (Moshayedi et al., 2010)] and incubated in PDL or PLL-coated T-75 flasks. The mixed glial cultures were kept at 37°C in a 5% CO_2–incubator and the medium was changed after 12 h and thereafter every 2–3 days and. After reaching confluence, flasks were shaken overnight at about 200 rpm using an orbital shaker to promote the detachment of microglia and oligodendrocyte precursor cells (OPCs). The supernatant was then removed, leaving T-75 flasks with predominantly astrocytes. Separation of microglia and OPCs was achieved by pouring the suspension into an untreated plastic dish and incubating it for 30 min at 37°C. Microglia attached to plastic quickly and the medium containing OPCs was removed and replaced by fresh culturing medium. To shake off the microglial cells, either the plastic dish was placed on ice and shaken at 400 rpm on an orbital shaker for about 30 min, or the culture medium was replaced by 10 mL of a 9:1 HBSS:trypsin solution and incubated for 5 min. 10 mL of FBS were added to stop the trypsin activation. In both cases cell suspension was then transferred to a 15 ml tube and centrifuged at 500–1000 rpm for 1–7 min. Subsequent to removing the supernatant, the cell pellet was resuspended using glia medium or Leibovitz medium (PAA, Hamshire, UK) containing 2.05 mM L-Glutamine. The fraction of microglial cells in the final cell culture was found to be $\geq$95%.

Cell Staining and Fluorescence Imaging

Microglial cells were cultured on single stiffness PAA substrates and glass for 12 h and fixed. Before culturing, the glass was cleaned with 70% ethanol and treated with 100 μg/ml poly-D-lysine (PDL) for 2 h. In order to label F-actin, cells were washed with PBS and then fixed with 4% PFA in PBS for 10 min, permeabilized in 0.1% Triton PBS for 5 min, and then washed with PBS four times for 15 min. Cells were incubated with Alexa Fluor488 phalloidin (Life Technologies, UK) at 2 units in 300 μl per gel for 1 h. Nuclei were stained using 1 μg/mL DAPI followed by three washes in PBS for 15 min. Cover slips with gels and stained cells were then mounted onto imaging slides using Fluoromount G (SouthernBiotech, USA). For fluorescence imaging, an upright microscope (Eclipse Ni, Nikon, Japan) with a precentered fiber illuminator (intensilight C-HGFI, Nikon, Japan) was used. Images were acquired using a high sensitivity camera (iXON3, Andor Technology Ltd, UK), a 60X water immersion objective ($NA = 1$, Nikon, Japan) and NIS-Elements software (Nikon, Japan). A subset of images was recorded using an inverted Leica DMI3000 microscope (63X oil immersion objective, $NA = 1.4$) with a CCD camera (dfc 340fx).

Time Lapse Imaging for TFM

The cell suspensions were seeded onto the PAA gels and kept in a 5% CO_2- incubator for 10 min to allow for cell adhesion. An additional 2 ml of glia medium per imaging dish was then carefully added to ensure cell survival. The cells were kept at 37°C until imaging.

The imaging setup consisted of an inverted microscope (Axio Observer.A1, Carl Zeiss Ltd., UK), an EMCCD camera (iXON3, Andor Technology Ltd, UK), a HXP 200C illuminator (Zeiss, Germany) and 40X water immersion objective ($NA = 1.1$, Zeiss, Germany). A petri dish heater was used to keep the sample at ∼37°C (JPK Instruments AG, Germany). Images were acquired using ANDOR Solis software. Fluorescence images of beads were taken every 30 s. After 10 min, lipopolysaccharide was added to the medium (LPS, Gibco) resulting in a final concentration of 1–2 μg/ml. After 5 min incubation time, imaging was continued for another 10 min. After the acquisition of images, Trypsin (Gibco) was added to the culture medium to detach cells from the gel. Reference images of fluorescent beads at the "relaxed" state were taken ∼10 min thereafter. We performed two independent traction force experiments on four substrates of varying stiffness ($G' = 100$ Pa, 300 Pa, 1 kPa, 10 kPa; **Table 1**).

Time Lapse Measurements for Cell Tracking

To avoid drifting of the coverslip during the experiment, the coverslip with the stiffness gradient substrate was glued to the bottom of a petri dish. Approximately 50,000 cells in 2 ml Leibovitz medium were seeded on the gel. The petri dish was placed inside a petri dish heater (JPK Instruments AG, Germany) set to 37°C on an inverted microscope (Axio Observer.A1, Carl Zeiss Ltd., UK) using a 10x objective (EC Plan-Neofluar 10x/0.30 Ph1, Carl Zeiss Ltd., UK) and a CCD camera (1/3″ CCD fire wire color camera, The Imaging Source, UK). Images were acquired using SPM 4.0 Software (JPK Instruments AG, Germany). As

TABLE 1 | Components of PAA substrates for traction force microscopy.

G' (Pa)	100% PBS (μL)	PAA stock solution (μL)	Beads (μL)
∼100	437	53	10
∼300	432	58	10
∼1000	415	75	10
∼10000	340	150	10

the fluorescence intensity correlated linearly with the substrate stiffness (Supplementary Figure 1 and Koser et al., under review), fluorescence intensity was employed as a readout for the local substrate stiffness. Therefore, after the cells had settled, the region of interest was selected based on the fluorescence signal of the gradient and a sufficient number of cells. Pictures of the gradient gel's fluorescence were taken to calculate the absolute stiffness and the steepness of the stiffness gradient of the gel. Subsequently, time-lapse sequences of microglial cells were recorded at 1 image per minute for at least 3 h. 4 independent experiments were performed in this way. In 2 of these experiments, LPS was added in a concentration of (1–2) μg/mL after 1–4 h, and time-lapse data were acquired separately.

Data Analysis

Traction Stresses

For the calculation of traction stresses, a modified version of the code by Koch et al. (2012) was used in MATLAB (MathWorks Inc., MA, USA). The code is based on the method of Sabass et al. (2008) and Betz et al. (2011). In order to observe traction stresses of single cells, a region of interest (ROI) was identified for each cell. To calculate the discrete deformation field for the ROI with respect to the reference image, a 2D cross-correlation algorithm was applied. The continuous deformation field was obtained by applying Gauss interpolation to the resulting discrete deformation field of the ROI. The inverse Boussinesq Green function was used in the Fourier space to calculate the traction stresses on the substrate surface from the continuous deformation field. The peak traction stress is defined by the largest value of the resulting traction stress map. The average stress is computed as the mean of all stresses that are greater than a threshold value. The threshold value was defined as 30% of the present peak traction stress value (Koch et al., 2012). Hence, one peak and one average stress value was obtained for each cell at each time step. The medians of the average and peak stresses recorded over 10 min (corresponding to 20 data points per cell) were statistically compared in case of control cells, and the median stresses recorded over 5 min (corresponding to 10 data points per cell) were compared for treated cells after incubation in LPS for 10 min.

To feed stress distributions underneath the cells in our model, we discretized the traction stress map using a spatial resolution of ∼3 μm. Contours of cells were obtained from phase contrast images. Stress distributions were calculated for the first time step.

Cell Tracking

To track cells we used an automatic custom-written tracking software based on the software of Graham Milne (PhD Thesis, University of St. Andrews, 2007). In total, 267 cells in standard medium and 128 cells in a medium with LPS were tracked. The starting position of each cell was set to the origin of the coordinate system, and the y-axis of the coordinate system was aligned with the direction of the gradient (with the positive y-direction pointing toward the stiffer side of the gradient). The mean stiffness of the gradient substrate at which the cells were tracked was ∼5 kPa, the mean steepness of the stiffness gradient ∼8.35 Pa/μm.

Selection process of actively moving cells

Cells that are not actively migrating include two subpopulations: adhered, non-motile cells and non-adhered, diffusing cells. Mean squared displacements (MSDs) of both subpopulations will be smaller or equal the MSD of a freely diffusing particle of comparable size, while we expect the MSD of actively moving cells to be larger. We thus calculated the MSD of each tracked cell and used the following inequality as a selection criterion for actively moving cells:

$$MSD > \frac{k_B T}{3\pi \eta r} t, \tag{1}$$

where k_B is the Boltzmann constant, $T = 310$ K the absolute temperature, η the viscosity of the medium, r the radius of the particle and t the time. We obtained the average radius of the cells by measuring the diameter of 10 randomly selected cells ($r \approx 8\,\mu$m). Furthermore, we assumed the viscosity of the medium to be $\eta \approx 1$ mPa s. The used cutoff in Equation (1) is about that of the Brownian motion of a freely diffusing particle of the same size. Due to this criterion, the majority of cells (∼83%) was rejected; thus, the results shown represent only a subpopulation of microglia (38 cells in the control condition and 22 LPS-treated cells).

Directness

The directness D (also known as the straightness index or the net to gross displacement ratio) is defined by

$$D = \left\langle \frac{d_e}{d_t} \right\rangle, \tag{2}$$

with the Euclidean distance (the shortest linear distance between the start and endpoints of a path, also called the net displacement) d_e and the total travel distance (or contour length) d_t of each cell (Codling et al., 2008), while ⟨⟩ represents the mean.

Contour and Euclidean velocity

The contour velocity v_c is defined by

$$v_c = \frac{\sum_{i=2}^{N} \left| \vec{p}_i - \vec{p}_{i-1} \right|}{t}, \tag{3}$$

with the position $\vec{p}_i$ of the cell on the ith frame, the total frame number N and the imaging time t. The Euclidean velocity vector $\vec{v}_e$ and its components $v_{e,x}$ and $v_{e,y}$ were calculated by

$$\vec{v}_e = \begin{pmatrix} v_{e,x} \\ v_{e,y} \end{pmatrix} = \frac{1}{t}\left(\vec{p}_s - \vec{p}_e\right), \tag{4}$$

with the start position $\vec{p}_s$ and end position $\vec{p}_e$ of the cell.

Turning and direction angles

The turning angle φ is defined for the third component of the vector product $\left(\vec{p}_i - \vec{p}_{i-1}\right) \times \left(\vec{p}_{i-1} - \vec{p}_{i-2}\right)$ being ≥ 0 by

$$\varphi = \cos^{-1} \frac{\left(\vec{p}_i - \vec{p}_{i-1}\right) \cdot \left(\vec{p}_{i-1} - \vec{p}_{i-2}\right)}{\left|\vec{p}_i - \vec{p}_{i-1}\right| \left|\vec{p}_{i-1} - \vec{p}_{i-2}\right|}, \tag{5a}$$

and for the third component of $\left(\vec{p}_i - \vec{p}_{i-1}\right) \times \left(\vec{p}_{i-1} - \vec{p}_{i-2}\right)$ being < 0 by

$$\varphi = 2\pi - \cos^{-1} \frac{\left(\vec{p}_i - \vec{p}_{i-1}\right) \cdot \left(\vec{p}_{i-1} - \vec{p}_{i-2}\right)}{\left|\vec{p}_i - \vec{p}_{i-1}\right| \left|\vec{p}_{i-1} - \vec{p}_{i-2}\right|}, \tag{5b}$$

with the position $\vec{p}_i$ of the cell on the *i*th frame. The direction angle θ is defined for the third component of $\left(\vec{p}_i - \vec{p}_{i-1}\right) \times \vec{d}$ being ≥ 0 by

$$\theta = \cos^{-1} \frac{\left(\vec{p}_i - \vec{p}_{i-1}\right) \cdot \vec{d}}{\left|\vec{p}_i - \vec{p}_{i-1}\right| \left|\vec{d}\right|}, \tag{6a}$$

and for the third component of $\left(\vec{p}_i - \vec{p}_{i-1}\right) \times \vec{d}$ being < 0 by

$$\theta = 2\pi - \cos^{-1} \frac{\left(\vec{p}_i - \vec{p}_{i-1}\right) \cdot \vec{d}}{\left|\vec{p}_i - \vec{p}_{i-1}\right| \left|\vec{d}\right|}, \tag{6b}$$

where $\vec{d}$ is the direction vector of the gradient (pointing along the gradient and toward the stiffer side of the gradient).

We used the turning angle φ to calculate the probability of a cell to move forward, backwards, left, and right, and the direction angle θ for the probability of a cell to move along the gradient, perpendicular to it, to the stiff side, and to the soft side. A cell was defined as moving forward if φ was between −45° (315°) and 45° (backwards: 135° and 225°; left: 45°and 135°; right: 225° and 315°). A cell was defined to move along the gradient, if θ was between −45° and 45° or between 135° and 255° (perpendicular to the gradient: 45°and 135° or 225° and 315°; to the stiff side: −45° and 45°; to the soft side: 135° and 255°).

Correlation index of movement

The correlation index of movement (*CI*) is defined by (Codling et al., 2008)

$$CI = \sqrt{\left(\int_{-\pi}^{\pi} \cos\varphi p(\varphi) d\varphi\right)^2 + \left(\int_{-\pi}^{\pi} \sin\varphi p(\varphi) d\varphi\right)^2}, \tag{7a}$$

where φ is the angle between two movement steps (i.e., the turning angle) and *p(θ)* is its probability density function. For our analysis we discretize the probability density function *p*(φ)* by binning the data into $\pi/9$ wide parts φ^*. Therefore, *CI* is calculated by

$$CI = \sqrt{\left(\sum_{\varphi \in \varphi^*} \cos\varphi p^*(\varphi)\right)^2 + \left(\sum_{\varphi \in \varphi^*} \sin\varphi p^*(\varphi)\right)^2}, \tag{7b}$$

where $CI \in [0,1]$. A value close to 0 suggests an uncorrelated movement and a value close to 1 a highly correlated movement.

Bias index of movement

The bias index of movement (*BI*) is mathematically similar to the *CI*. Instead of the turning angle φ, the direction of cells relative to the stiffness gradient θ is taken into account. The *BI* can be calculated by

$$BI = \sqrt{\left(\sum_{\theta \in \theta^*} \cos\theta p^*(\theta)\right)^2 + \left(\sum_{\theta \in \theta^*} \sin\theta p^*(\theta)\right)^2}, \tag{8}$$

where $BI \in [0,1]$. A value close to 0 suggests an unbiased movement and a value close to 1 a highly biased movement. It has to be noted that a high *BI* can be caused by a correlated random walk; in this case *CI* would be high as well.

Statistical Tests

Data were tested for normal distribution by the Kolmogorov-Smirnov or Lilliefors tests. When two groups were compared, significance was tested either with Student's *t*-test (in case of normal distribution) or the Mann-Whitney *U*-test (in case of non-normal distribution). If more than two groups were compared either a One-Way or Two-Way ANOVA was used in case all groups were normally distributed, or a Kruskal-Wallis ANOVA otherwise. Two-tailed tests were used throughout the analysis. In the text we mention either the mean ± SEM or the median.

Results

Cell Morphology Changes with Substrate Stiffness

To investigate how microglia mechanically interact with their environment, we first investigated how their morphology changes with substrate stiffness. Primary microglial cells were cultured on soft, elastic substrates made of polyacrylamide with shear moduli G' of 100, 300, and 1000 Pa, spanning the range of reported neural tissue stiffness (Franze et al., 2013). The spread area of primary microglial cells significantly increased with substrate stiffness ($p < 0.05$, Kruskal-Wallis ANOVA) (**Figure 1**). The median cell spread area increased from 112 μm^2 on soft substrates ($G' \sim 100$ Pa), to 163 μm^2 on stiff substrates ($G' \sim 1000$ Pa) ($p < 0.01$, Mann-Whitney *U*-test).

After 12 h *in vitro*, microglia cultured on 100 Pa substrates showed many actin-rich filopodia-like processes (44 ± 3, average ± SEM, $n = 14$) (**Figure 2A**). Microglial cells on

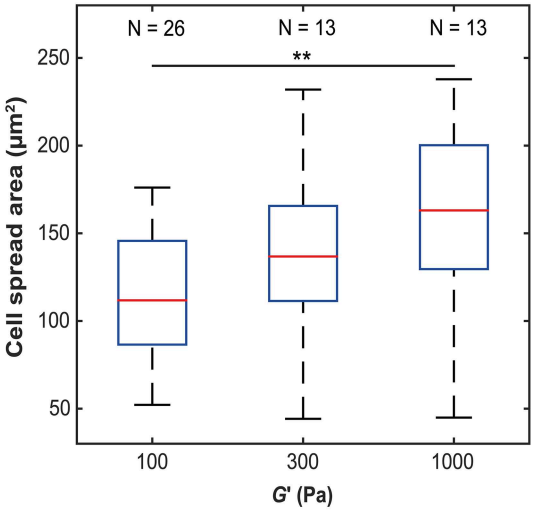

FIGURE 1 | Microglia spread area as a function of substrate stiffness. The spread area of microglial cells significantly increased with substrate stiffness ($p < 0.05$, Kruskal-Wallis ANOVA; for $G' \sim 100$ Pa vs. 1 kPa, $p < 0.01$, Mann-Whitney U-test). $^{**}p < 0.01$.

substrates of $G' \sim 300$ Pa appeared in a more round or amoeboid shape (**Figure 2B**), with fewer processes than on softer substrates (24 ± 6, $n = 5$; $p < 0.05$, Mann-Whitney U-test). Furthermore, F-actin was distributed more homogeneously throughout the cells. The shape of microglia changed drastically when cultured on 1 kPa substrates or on glass (**Figures 2C,D**). Cells possessed more complex morphologies with long, distinct processes and lamellipodia-like structures at their tips.

Microglia Traction Stresses Increase with Substrate Stiffness

Changes in cell spread area and in the F-actin cytoskeleton are often accompanied by changes in cellular forces (Tolic-Norrelykke and Wang, 2005; Califano and Reinhart-King, 2010; Fournier et al., 2010; Stricker et al., 2010). To measure microglial traction forces, we embedded fluorescent nanoparticles in compliant substrates, which allowed tracking substrate deformations due to forces exerted by cells (**Figure 3**).

Peak substrate deformations changed with substrate stiffness ($p < 10^{-6}$, Kruskal-Wallis ANOVA). While maximum deformations were significantly smaller on substrates of $G' \sim 100$ Pa compared to those of 300 Pa ($p < 0.05$, Mann-Whitney U-test), there was no notable difference between 300 Pa and 1000 Pa substrates. A significant decline in peak substrate deformations was observed for 10 kPa substrates if compared to 1000 Pa substrates ($p < 10^{-3}$) (**Figure 3**).

The traction stress (force per unit area) exerted by individual microglial cells, which is responsible for the observed substrate deformations, showed fluctuations over time (**Figure 4A**), indicating that force generation is a dynamic process. We did not find any distinct traction stress patterns as a function of substrate stiffness (Supplementary Figure 2). Peak as well as average traction stresses exerted by microglial cells changed significantly with substrate stiffness ($p < 10^{-12}$, Kruskal-Wallis ANOVA and $p < 10^{-14}$, One-Way ANOVA, respectively). Within the investigated range, traction forces increased with substrate stiffness ($p < 0.01$ for all comparisons, Mann-Whitney U-test) (**Figures 4B,C**).

Influence of LPS on Traction Stresses

In numerous pathological processes in the CNS, microglial cells become activated and migrate toward the stimulus. Lipopolysaccharide (LPS), as part of the outer membrane of gram-negative bacteria, elicits a strong immune reaction, which is in the CNS initiated by microglia (abd-el-Basset and Fedoroff, 1995; Nakamura, 2002). In order to observe the influence of microglia activation on the forces exerted by the cells, we performed traction force experiments on microglia treated with 1–2 µg/ml LPS.

After incubation in LPS-containing medium for ~5 min, we found a trend for traction forces to decrease within 10 min on stiffer substrates (1000 Pa and 300 Pa) and to increase slightly on 100 Pa gels (**Figure 5**). Testing if the slopes of the peak traction stresses over time significantly differed from 0 yielded a p-value of 0.06 at 1 kPa (one sample t-test); for all other conditions $p > 0.06$. Investigating the dependence of peak and average traction stresses on substrate stiffness *and* 10–15 min LPS treatment revealed interaction p-values of 0.002 and 0.004 (Two-Way ANOVA), respectively, indicating that the substrate stiffness-dependent traction forces significantly changed when microglia were activated by LPS.

Durotaxis of Microglia

CNS tissue is mechanically heterogeneous (Elkin et al., 2007; Christ et al., 2010; Franze et al., 2011; Iwashita et al., 2014; Koser et al., 2015). When microglial cells migrate through CNS tissue, they will thus encounter regions with different mechanical properties. To test if local changes in the stiffness of the environment impact microglia migration, we cultured microglial cells on compliant substrates incorporating stiffness gradients of ~8.35 Pa/µm and tracked the trajectories of actively migrating cells using time lapse microscopy (see Materials and Methods and Equation 1).

Cells cultured on these compliant substrates migrated comparatively straight; the median directness D (Equation 2), which is the ratio between the shortest linear distance between the start and endpoints of a path and the total travel distance, was 0.73. Furthermore, microglia stopped frequently, with a median stopping rate of 41% (i.e., no movement between 41% of consecutive frames, see Materials and Methods), and traveled with a median contour velocity v_c (based on the contour length of the migration path; Equation 3) of 1.48 µm/min, and a median Euclidean velocity v_e (based on a straight line between start and end position; Equation 4 and **Figure 6C**) of 0.82 µm/min (**Figure 6**). Endpoints of the migration paths showed a non-uniform circular distribution ($p < 0.01$, Rayleigh test) and were strongly biased toward the stiffer side of the gradient (**Figure 6A**), indicating that microglial cells showed durotaxis.

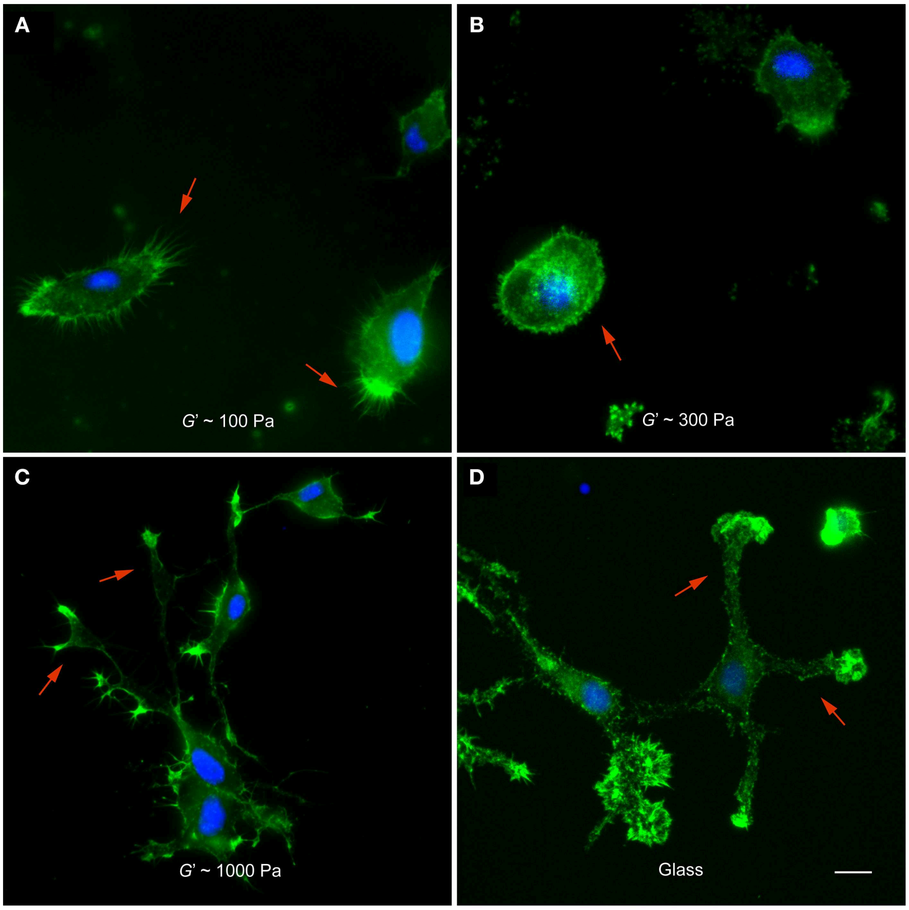

FIGURE 2 | Microglia morphology depends on substrate stiffness. (A–D) Representative fluorescence images of microglial cells on substrates of different stiffness. F-actin appears in green, nuclei in blue. **(A)** On substrates of $G' \sim 100$ Pa, microglial cells showed many filopodia-like processes (red arrows). **(B)** On stiffer substrates ($G' \sim 300$ Pa), they showed amoeboid morphologies (red arrow) with significantly fewer processes ($p < 0.05$, Mann-Whitney *U*-test). **(C,D)** On 1000 Pa substrates and on glass, microglial cells had complex morphologies with lamellipodia-like structures at the tips of long processes (red arrows). Scale bar: 10 µm.

LPS Treatment Changes Microglia Migration Behavior

To test if the activation of microglia changed their tendency to migrate toward stiffer substrates, we then applied LPS to cells seeded on gels with stiffness gradients.

The directness of LPS-treated cells $D_{LPS} = 0.70$ was similar to that of control cells ($p > 0.7$, Mann-Whitney *U*-test). However, cells sped up by ∼60% compared to untreated cells (median contour velocity of 2.36 µm/min compared to 1.48 µm/min; $p < 0.05$, Mann-Whitney *U*-test), which can be attributed to a significant decrease in median stall phases (0% and 41% for LPS-treated and control cells, respectively; $p < 10^{-4}$, Mann-Whitney *U*-test). The median Euclidean velocity of LPS-treated cells was significantly higher as well (1.35 µm/min; $p < 0.05$, Mann-Whitney *U*-test) (**Figures 6D–G**).

Endpoints of migration were even stronger biased toward the stiffer side of the gradient (**Figure 6B**) with a highly non-uniform circular distribution (Rayleigh test of uniformity for endpoints; $p < 0.001$). When splitting the Euclidean velocity into its components parallel ($v_{e,\,x}$) and perpendicular ($v_{e,y}$) to the stiffness gradient, the velocity perpendicular to the gradient was similar in control and LPS-treated microglia ($v_{e,x\ control} = 0.42\,\mu\text{m/min}$, $v_{e,x\ LPS} = 0.52\,\mu\text{m/min}$; p > 0.2, Mann-Whitney *U*-test). However, the velocity toward the stiffer side of the gradient was significantly higher in LPS-treated cells ($v_{e,y\ control} = 0.45\,\mu\text{m/min}$, $v_{e,y\ LPS} = 0.73\,\mu\text{m/min}$; $p < 0.05$, Mann-Whitney *U*-test) (**Figures 6H,I**).

Relating Traction Forces to Durotactic Behavior

Mathematical Description of Substrate Stiffness-dependent Traction Forces

The distributions of average stresses we found on all substrates (except substrates of 10 kPa, which were excluded because most deformations were below our optical resolution limit) can be well described by a Burr type XII distribution (**Figures 7A–C**). The probability density function p of the three-parameter Burr distribution is

$$p\left(\sigma; \alpha, c, k\right) = \frac{kc\left(\frac{\sigma}{\alpha}\right)^{c-1}}{\alpha\left[1+\left(\frac{\sigma}{\alpha}\right)^{c}\right]^{k+1}}, \qquad (9)$$

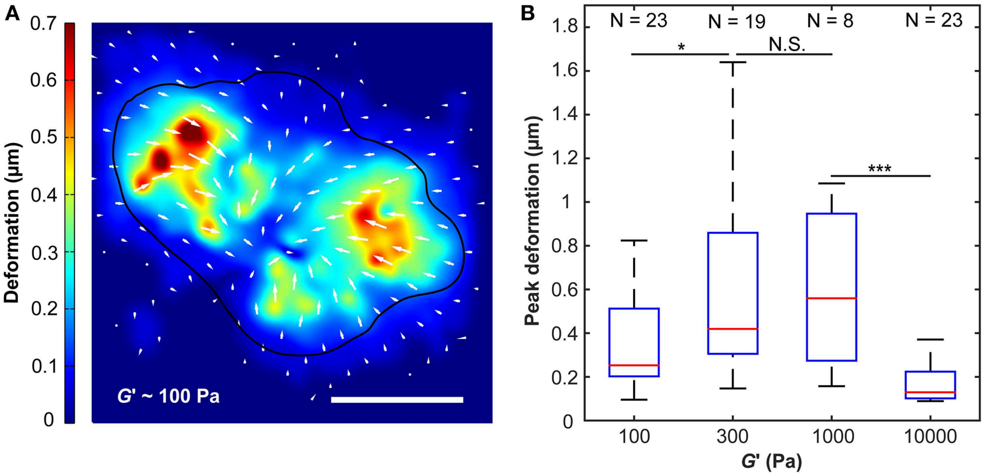

FIGURE 3 | Substrate deformations as a function of substrate stiffness. (A) Substrate deformation field of one representative cell grown on a ∼100 Pa substrate (cell outline in black). Deformation directions are indicated by white arrows, absolute deformations are shown by false colors. Scale bar: 10 μm. **(B)** Peak deformations reached a maximum on substrates of around $G' \sim 300$–1000 Pa. N, number of analyzed cells. $^*p < 0.05$; $^{***}p < 0.001$.

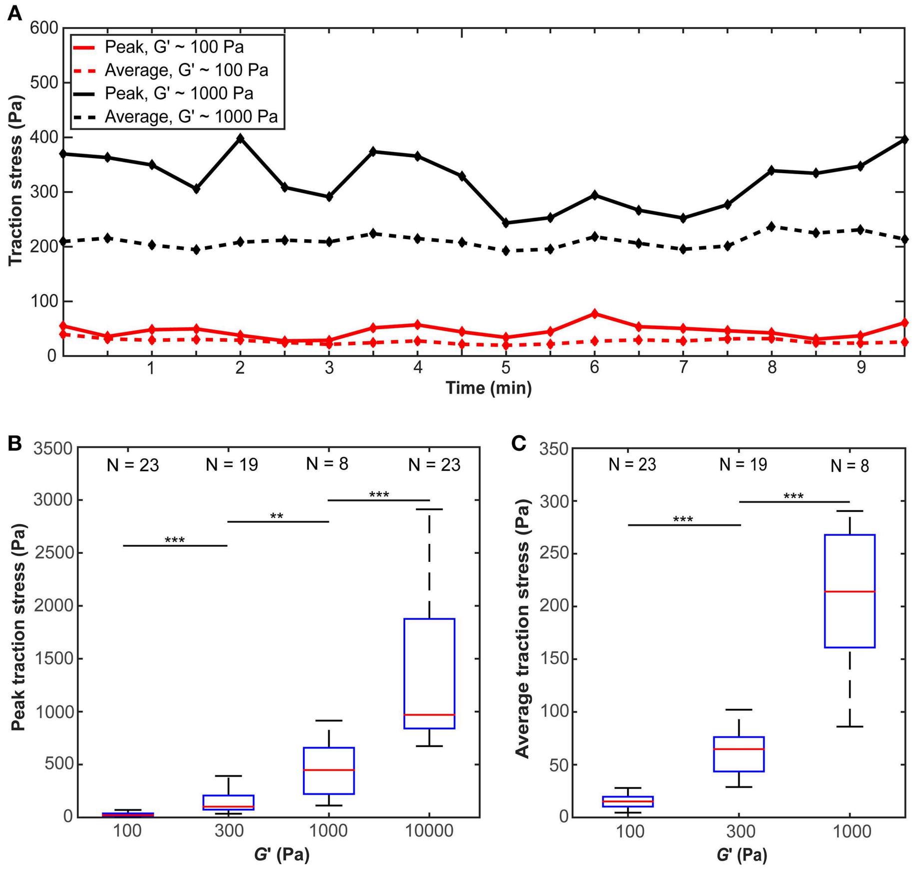

FIGURE 4 | Microglial cells exert larger forces on stiffer substrates. (A) Average and peak traction stress as a function of time for two representative cells on gels of $G' \sim 100$ Pa and ∼1000 Pa. Traction stresses fluctuate over time. **(B)** Peak traction stress and **(C)** average traction stress as a function of substrate stiffness G'. Average traction stress values for a substrate stiffness of $G' \sim 10$ kPa were excluded because most deformations were below our optical resolution limit. N: number of analyzed cells. $^{**}p < 0.01$; $^{***}p < 0.001$.

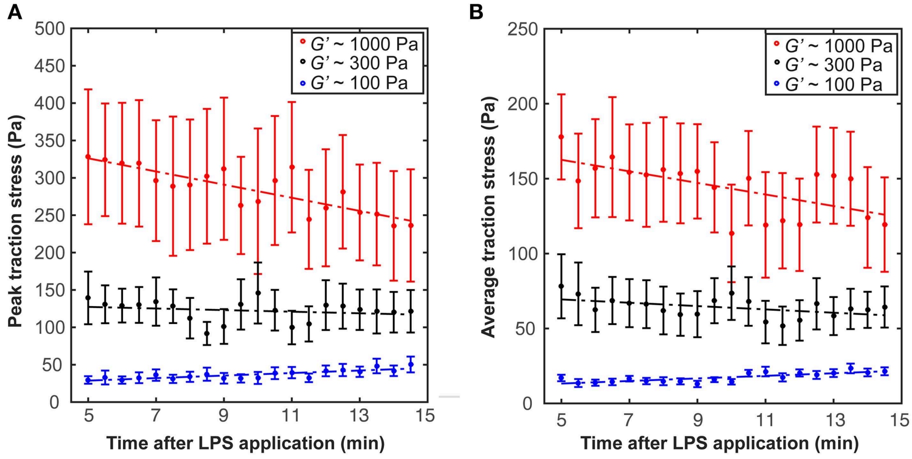

FIGURE 5 | Microglia activation through LPS changes traction stresses. After 5 min incubation in LPS, **(A)** peak traction stresses and **(B)** average traction stresses decreased on stiffer substrates ($G' \sim 300$ or 1000 Pa) but slightly increased on soft gels of $G' \sim 100$ Pa (shown is the mean ± SEM).

with the positive scale parameter α and the two positive shape parameters c and k. When the stress distributions were normalized by their standard deviations, they were statistically similar ($p > 0.25$, Kruskal-Wallis ANOVA) and fell on one master curve (**Figure 7D**). Therefore, only the scale parameter α but not the shape parameters c and k depended on the substrate stiffness.

The ratio between peak stress and standard deviation of the stress distribution was similar for the different substrates ($\sigma_{\max}/\mathrm{SD}(\sigma) = 4.48 \pm 0.01$; $p > 0.1$, One-Way ANOVA), suggesting that the peak stress alone is sufficient to predict the distribution of microglial traction stresses on compliant substrates of arbitrary stiffness.

Using these results, we can make a prediction on the dependency of the scaling parameter α on the shear modulus G' of the substrate microglial cells grow on (**Figure 8A**). This dependency can be described by

$$\alpha\left(G'\right) = -ae^{-bG'} + a, \tag{10a}$$

with the fitting parameters $a = 77.28$ and $b = 0.00086$/Pa. The adjusted R^2–value of this fit is 0.99. In the same way, the dependency of the median traction stress on the shear modulus can be described by

$$\sigma\left(G'\right) = -ae^{-bG'} + a, \tag{10b}$$

with the fitting parameters $a = 53.2$ Pa and $b = 0.00083$/Pa (**Figure 8B**). The adjusted R^2–value of this fit is 0.99.

A Random Walk-based Description of Microglia Durotaxis

To investigate why microglial cells preferentially migrated toward stiffer substrates, we first tested if there was a dependency of the movement direction of a cell on its previous direction (governed by the turning angle φ; Equations 5a,b). There was no difference in the likelihood of moving forward (0.22 ± 0.04), backward (0.23 ± 0.03), left (0.25 ± 0.04) or right (0.30 ± 0.04; $p > 0.4$, Kruskal-Wallis ANOVA). A similar trend was observed after exposing microglia to LPS ($p > 0.95$). The correlation index $CI \in [0,1]$ (Equation 7b), which is a measure of the correlation between the angle of two consecutive steps, was 0.04 in both conditions, indicating that turning angles were not correlated, and that the observed durotaxis cannot be explained by a persistency in motion with non-uniform starting conditions.

Next, we investigated the dependence of a cell's motion on the gradient direction (governed by the direction angle θ; Equations 6a,b). The likelihood of a cell to move along the gradient (0.50 ± 0.04; 0.48 ± 0.05 for LPS-treated cells) was the same as perpendicular to it (0.50 ± 0.04; 0.52 ± 0.05 for LPS-treated cells) ($p > 0.5$ for both conditions). However, cells preferentially moved toward the stiffer side of the gradient (0.31 ± 0.04; 0.32 ± 0.05 for LPS- treated cells) compared to the softer side (0.19 ± 0.02; 0.16 ± 0.03 for LPS-treated cells) ($p < 0.01$ in both conditions). The bias index $BI \in [0,1]$ (Equation 8), which is a measure of the correlation between the step direction (i.e., angle) and the stiffness gradient, was 0.15 in control cells and 0.16 in LPS-treated cells, indicating that cell migration was biased along the mechanical gradient. Microglia activation through LPS-treatment did not alter the impact of the stiffness gradient on the migration direction ($p > 0.5$, Mann-Whitney U-test).

As not only the likelihood to move in a certain direction can influence the direction bias of cells but also a dependence of the step-length (and thus velocity) on directionality, we studied step-length distributions of microglia migrating on stiffness gradients. While step-lengths (measured every minute) were independent of the average gradient direction ($d_{\|G} \approx d_{\perp G} = 1.35\,\mu$m; $1.27\,\mu$m for LPS-treated cells; $p > 0.4$ for both conditions, Mann-Whitney U-test), they did depend on the direction of the previous step. Lengths of steps parallel to the previous movement direction $d_{\|M} = 1.41\,\mu$m ($1.30\,\mu$m for LPS-treated cells) were larger than step lengths perpendicular to it $d_{\perp M} = 1.30\,\mu$m ($0.84\,\mu$m for LPS-treated cells) ($p < 0.05$, $p_{LPS} = 0.078$, Mann

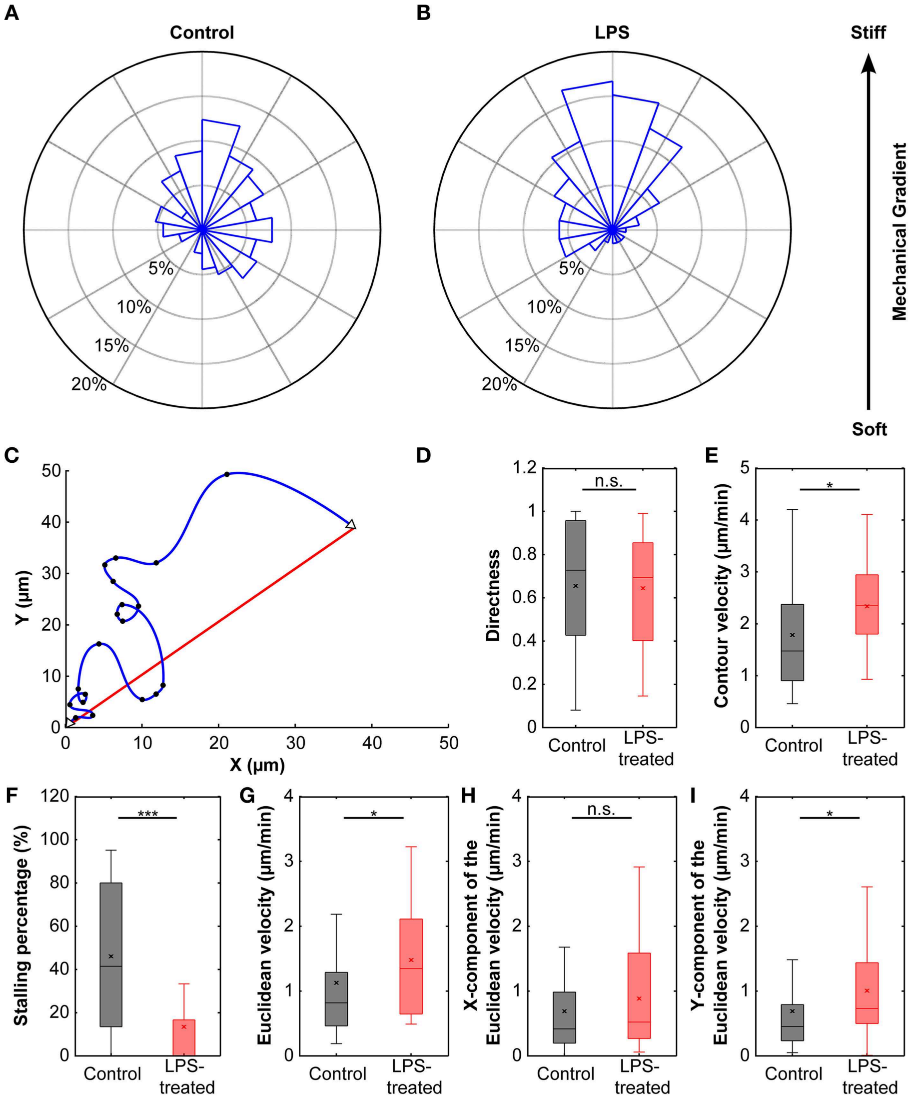

FIGURE 6 | Durotaxis of microglial cells. (A) Distribution of microglial cell positions at the end of an experiment. Cells were cultured on compliant substrates (∼5 kPa) incorporating a stiffness gradient of ∼8 Pa/μm and preferentially migrated toward the stiffer side of the substrate ($N = 38$). **(B)** After activation with LPS, microglia durotaxis was significantly enhanced ($N = 22$). Rose plots were obtained from binned endpoints (bin size: of 60°, with 20° overlap). **(C)** Schematic plot of microglia migration. Start and end positions are marked with open triangles; black dots indicate cell positions recorded during time-lapse imaging. The blue curve shows the actual migration path ("contour"), the red line indicates the Euclidean distance between start and end position. **(D)** The directness D was similar for control and LPS-treated cells ($p > 0.7$, Mann-Whitney *U*-test). **(E,G)** Contour velocity v_C and Euclidean velocity v_E significantly increased after application of LPS ($p < 0.05$, Mann-Whitney *U*-test). **(F)** Stalling phases were highly reduced after LPS treatment ($p < 10^{-4}$, Mann-Whitney *U*-test). **(H,I)** While the component of the Euclidean velocity perpendicular to the mechanical gradient (x-component) was similar for control and LPS-treated cells ($p > 0.2$, Mann-Whitney *U*-test), the component toward the stiffer side of the gradient (y-component) was significantly increased after application of LPS ($p < 0.05$, Mann-Whitney *U*-test). $^*p < 0.05$; $^{***}p < 0.001$.

Whitney *U*-test). Furthermore, we found a tendency of the step length to be higher parallel $d_{\|M1} = 1.76\,\mu\text{m}$ ($1.47\,\mu\text{m}$ for LPS-treated cells) than antiparallel $d_{\|M2} = 1.32\,\mu\text{m}$ ($1.27\,\mu\text{m}$ for LPS-treated cells) to the previous movement direction ($p = 0.089$, $p_{\text{LPS}} = 0.068$, Mann Whitney *U*-test). These results combined indicated that cells migrated faster if they did not change their direction.

Step-length probability distributions, which depended on the direction of the previous step, were well-approximated by the Burr distribution (**Figure 9**; Equation 9). When step-length distributions were normalized by their standard deviations, they were statistically similar ($p > 0.20$, Kruskal-Wallis ANOVA) and fell again on one master curve (**Figure 9D**). Therefore, only the scale parameter α but not the shape parameters c and k depended on the turning angle φ.

Next, we tested if we can predict the directional bias of microglia migrating on stiffness gradients (e.g., endpoints position, direction angle distribution of endpoints, directness, and the velocity) using a 2D biased random walk model with step-length distributions dependent on the turning angle φ. The

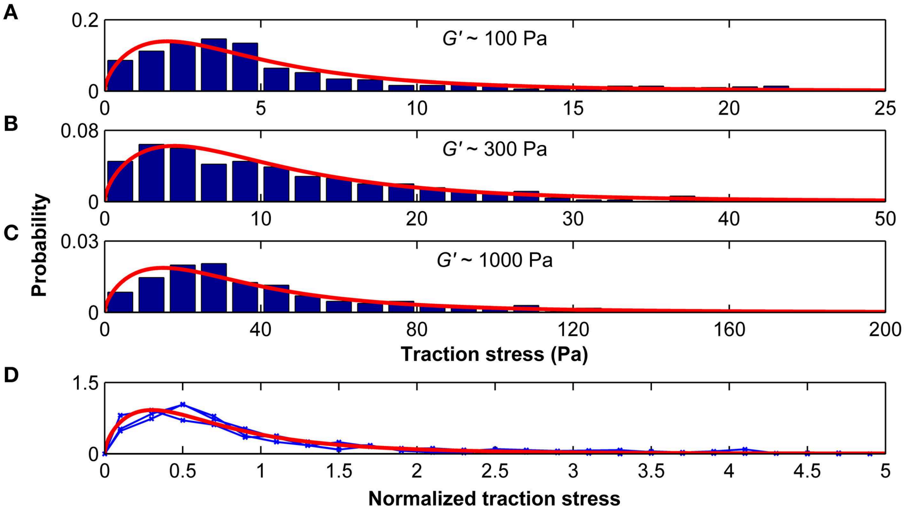

FIGURE 7 | Traction stresses are distributed according to a Burr distribution. Stress distributions for microglia growing on substrates of $G' \sim 100$, ~ 300, and ~ 1000 Pa are shown in **(A–C)**, respectively. Red curves represent the best three-parameter Burr distribution fits. **(D)** The stress distributions were normalized by their standard deviation. Blue curves show the normalized stress distributions for $G' \sim 100$, ~ 300, and ~ 1000 Pa, which were statistically similar ($p > 0.25$, Kruskal-Wallis ANOVA). The red curve shows the Burr distribution fit for all data combined.

walk was modeled by moving 228 cells (6 times as many as in the experiments) at each time step (corresponding to 1 min) by a length l in a direction angle θ at a time distribution matching that of the experimental data. The bias was imposed on the system by setting the direction angle distribution of θ to be a circular normal (or von Mises) distribution of the form

$$p\left(\theta;\kappa\right) = \frac{e^{\kappa \cos\theta}}{2\pi I_0(\kappa)}, \tag{11}$$

where $I_0(\kappa)$ is the modified Bessel function of order 0. The parameter κ was set to 0.30, accounting for the ~31% likelihood to move to the stiffer side of the gradient, the ~19% likelihood to move to the softer side of the gradient, and the ~50% likelihood to move perpendicular to the gradient, as found in our experiments. The step-length l was set to 0 µm with a 41% chance to account for stall phases. Otherwise, the step-length l was randomly selected from a Burr distribution (see Equation 9); a random number $R \in [0,1]$ was transformed by the inverse cumulative distribution function of the Burr distribution

$$l\left(R;\alpha,c,k\right) = \alpha\left[\frac{1}{(1-R)^{1/k}} - 1\right]^{1/c}. \tag{12}$$

To account for the dependence of the step length on the turning angle φ, we applied the φ-dependent fitting parameters of the Burr distributions used in **Figure 9**. The results of our simulation closely matched our experimental findings. Endpoints were strongly biased toward the stiffer side of the gradient (**Figure 10**), with a non-uniform circular distribution ($p < 10^{-12}$, Rayleigh test). Furthermore, both the angular distribution of endpoints ($p > 0.1$, Kuiper's test) and their coordinates were similar to our experimental data ($p > 0.05$ and $p > 0.85$ for the coordinates perpendicular and along the gradient, respectively, Mann Whitney U-test). While the contour velocity was similar (1.30 µm/min, $p > 0.10$), the directness D was lower compared to the experimental data (0.44; $p < 10^{-3}$). Accordingly, also the Euclidean velocity was significantly reduced (0.47 µm/min, $p < 10^{-3}$). However, when we adapted the number of simulated cells to that of the experiments ($N = 38$) and matched the stalling percentage distributions, the directness was similar (0.55; $p > 0.25$). Hence, a biased random walk model approximates our experimental findings very well.

Next, we simulated the long time behavior of microglia (1000 cells for 1000 min). As expected, endpoint positions of simulated cells were biased even stronger toward the stiffer side of the gradient ($p < 0.001$ for the comparison with our experimental data, Kuiper's test) (**Figure 10B**) with a clearer non-uniform circular distribution ($p \approx 0$, Rayleigh test of uniformity for endpoints). Furthermore, the median contour velocity did not change compared to our experimental data (1.40 µm/min vs. 1.48 µm/min in the experiments; $p > 0.50$, Mann-Whitney U-test). The component of the Euclidean velocity toward the stiffer side of the mechanical gradient, which is an expression for the migration velocity along the gradient for long time periods, was 0.215 ± 0.002 µm/min (compared to 0.45 µm/min in the experiments), while the component perpendicular to the gradient was close to 0 µm/min. The median directness D was highly reduced (0.16; $p < 10^{-18}$).

Connecting Traction Forces and Durotaxis Through a Stress Fluctuation Model

We finally used a simple numerical simulation to test if the observed bias of migrating microglia toward the stiffer side of their substrate may be caused by the interplay between the traction stresses transmitted to the substrate, the local substrate

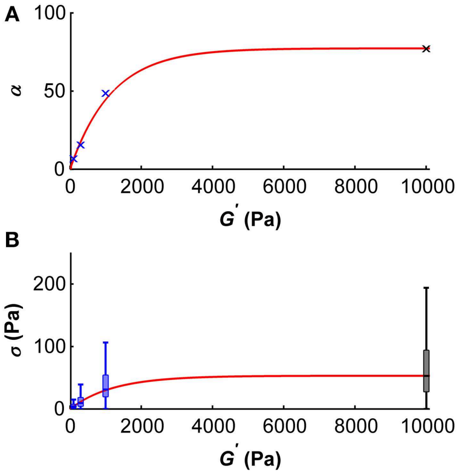

FIGURE 8 | Dependency of the scale parameter α (A) and the traction stress σ (B) on the gel's shear modulus *G*′. (A) Blue crosses represent α values determined for *G*′ ~100, ~300, and ~1000 Pa, the black cross represents an α value approximated for *G*′ ~ 10 kPa using the master curve and the constant peak stress to standard deviation ratio. An initial regime of fast increase of α (which scales proportionally with the median traction stress) was observed for shear moduli below ~2 kPa. The red curve represents the best fit with an adjusted R^2-value of 0.99. **(B)** Boxplots of the traction stresses σ for *G*′ ~100, ~300, and ~1000 Pa are shown in blue. Black boxplot shows the estimated traction stress σ for *G*′ ~10 kPa. An initial regime of fast increase of σ was observed for shear moduli below ~2 kPa. The red curve represents the best fit through the median traction stresses with an adjusted R^2 value of 0.99.

stiffness underneath the cell, and the steepness of the stiffness gradient. For this purpose, we idealized the cell's interface with the hydrogel to be a perfect circle, which we discretized into pixels of $0.3 \times 0.3\,\mu\text{m}^2$. We made the following assumptions: (i) The cell is directly tethered to the substrate in each pixel, and it exerts shear stresses on each pixel which are distributed according to the master curve of the stress distributions (**Figure 7D**). (ii) All stresses are radially and inwardly orientated. (iii) At each pixel, the substrate can move individually and has a constant shear storage modulus G'. (iv) Cells move by attaching to the surface, contracting and reattaching at the new position.

The directional bias of cell movement on substrates with changing mechanical properties can be illustrated by simplifying the problem to a one-dimensional cell consisting of two sides (or one-dimensional "pixels") exerting forces on a linearly elastic half-space. Let's assume that the one-dimensional shear stress on one side is τ_1 and on the second side $\tau_2 = -\tau_1$. The shear strain γ on each side of the cell is then calculated by

$$\gamma = \frac{\tau}{G'}, \tag{13a}$$

where G' is the shear storage modulus of the substrate underneath that pixel. The shear strain γ is linked to the surface displacement Δl by

$$\gamma \approx \frac{\Delta l}{L}, \tag{13b}$$

where L is the effective thickness of the gel (up to which the substrate is deformed), which we assume to be constant. Thus, the one-dimensional deformation underneath both cell sides is

$$\Delta l \approx L\frac{\tau}{G'}. \tag{13c}$$

A stiffness gradient in the substrate will thus impose a migratory bias on the cell, leading to a directed migration of length ΔL, calculated by

$$\Delta L = -\frac{\Delta l_1 + \Delta l_2}{2} \approx -\frac{L}{2}\left(\frac{\tau_1}{G_1'} + \frac{\tau_2}{G_2'}\right), \tag{13d}$$

where $\Delta L \neq 0\,\mu\text{m}$ only if $G_1' \neq G_2'$. Hence, it is the difference in shear modulus of the substrate underneath the cells that causes the bias in microglia migration. This argumentation can be easily extended to three dimensions according to

$$\vec{\Delta L} \approx -\varepsilon \sum_{i=1}^{N} \frac{1}{G_i'} \vec{\tau_i}, \tag{14}$$

where N is the number of pixels underneath the cell, and $\varepsilon = L/N$. For the simulation, we used a gradient steepness of 8.35 Pa/μm, and positioned the middle of the cell at a shear modulus of $G' \sim$ 5 kPa.

Simulating, 100 cells moving 50 steps each led to a von Mises distribution of the direction angle θ with $k = 0.29$, which is very close to what we assumed in our random walk model (see Equation 11). We found no difference in the likelihood of moving forward (0.24 ± 0.01), backward (0.26 ± 0.01), left (0.25 ± 0.01) or right (0.25 ± 0.01) relative to the previous movement direction ($p > 0.60$, Kruskal-Wallis ANOVA). However, the probability of moving toward the stiffer side of the gradient was significantly higher (0.31 ± 0.01) than to the softer side (0.20 ± 0.01) ($p < 10^{-21}$, Mann-Whitney U-test). These results were very similar to our experimental data ($p > 0.3$, Mann-Whitney U-tests). Furthermore, the simulated step lengths were distributed according to a Burr distribution, as in our experiments and as used in our random walk model. Thus, our stress fluctuation model nicely captures the main features of the movement bias of microglia along mechanical gradients.

Discussion

In this study, we found that microglial cells adapt their morphology and cytoskeleton to the stiffness of their environment. Their spread area increased on stiffer substrates, similarly as that of astrocytes (Georges et al., 2006; Moshayedi et al., 2010) (**Figure 1**). Furthermore, their morphology increased in complexity, in agreement with a previous report (Moshayedi et al., 2014): microglia morphologies changed from round and weakly polarized with numerous filopodia-like protrusions on soft to a lamellipodia-dominated, strongly polarized phenotype with many large cell processes on stiffer substrates (**Figure 2**) (Bergert et al., 2012; Liu et al., 2015). Actin was found mostly in the periphery on soft substrates, while it was distributed

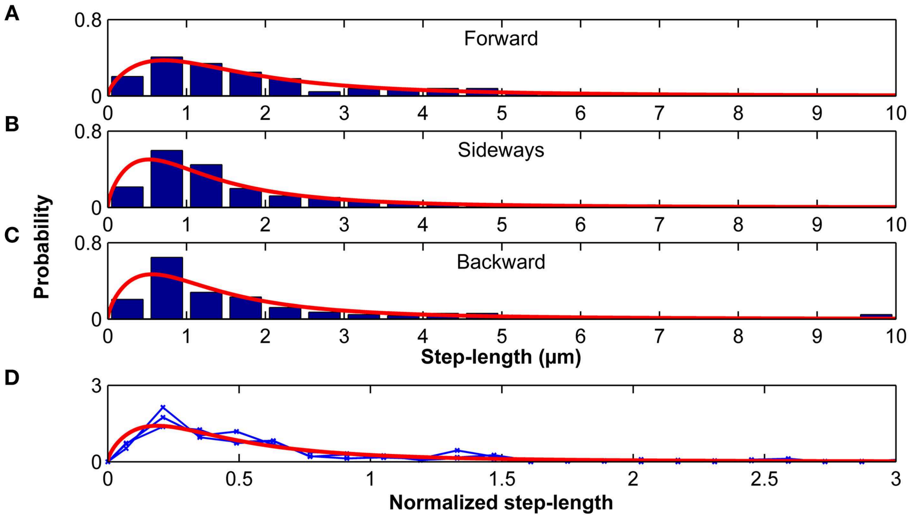

FIGURE 9 | Step lengths are distributed according to a Burr distribution. Step-length distributions for the forward **(A)**, sideways **(B)** and backward movements **(C)** of microglia relative to their previous step direction. Red curves represent the best Burr distribution fits. **(D)** Step-length distributions were normalized by their standard deviation. Blue curves show the normalized stress distributions for the forward, sideways, and backward movements, which were statistically similar ($p > 0.20$, Kruskal-Wallis ANOVA). The red curve shows the Burr distribution fit for all data combined.

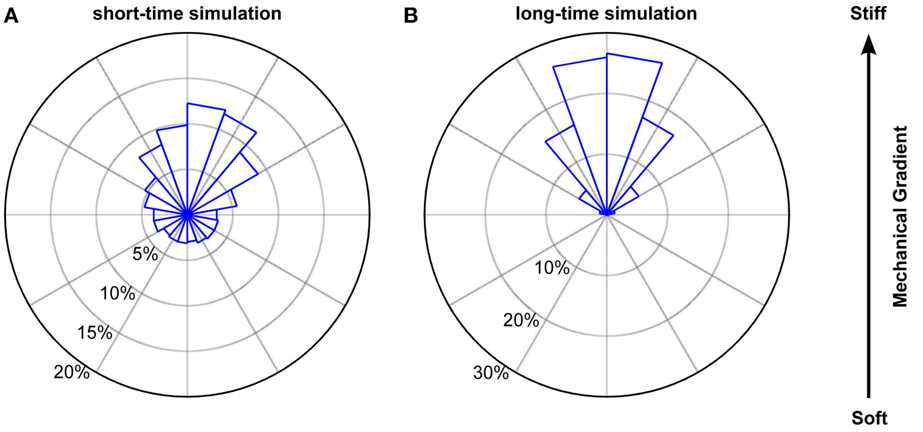

FIGURE 10 | Simulated biased random walk of microglial cells migrating on a mechanical gradient. (A) Simulation for 228 cells (6 times as many as in our experiments) with a migration time distribution matching that of the experiments. Microglia were similarly biased toward the stiffer side of the substrate as found in the experiments ($p > 0.1$, Kuiper's test). **(B)** Simulation for 1000 cells migrating 1000 min. On longer time scales, cells showed a robust migration toward the stiffer side of the gradient ($p < 0.01$, Kuiper's test).

throughout the cells on stiffer substrates. These differences in cytoskeletal arrangements could have substantial impact on microglia, as the dynamic state of the actin cytoskeleton profoundly affects their behavior and function (Uhlemann et al., 2015).

Traction forces exerted by microglia initially increased with substrate stiffness and saturated around a shear modulus of ∼5 kPa (**Figures 4**, **8B**). Similar trends have been described for other cell types (Ghibaudo et al., 2008; Califano and Reinhart-King, 2010; Han et al., 2012; Koch et al., 2012; Trichet et al., 2012) and were predicted using active matter theory (Marcq et al., 2011), suggesting this to be a general tissue cell behavior. However, the specific substrate stiffness at which traction stresses saturate is cell type-specific (Ghibaudo et al., 2008; Califano and Reinhart-King, 2010; Han et al., 2012; Koch et al., 2012; Trichet et al., 2012).

Stress distributions of microglia are well-described by a Burr distribution (**Figure 7**). The shape parameters c and k are independent of the surrounding stiffness, while the scale parameter α depends on the shear modulus of the substrate. At substrates of $G' \sim 5$ kPa, α reaches a plateau, and estimated median microglial traction forces saturate (**Figure 8**).

Microglial cells were most sensitive to substrate rigidity in a range of G' between 0 and ∼2000 Pa (**Figure 8**), which matches the range of CNS tissue stiffness (Franze et al., 2013). Thus, microglia seem to be mechanically tuned to their natural environment. Furthermore, they are significantly stronger than their neighboring CNS neurons; the mean traction stresses exerted by hippocampal neurons are an order of magnitude lower than microglial traction stresses measured in this study (Koch et al., 2012).

Most microglia grown on compliant cell culture substrates were not migratory, as usually found for microglia grown on glass or tissue culture plastics (abd-el-Basset and Fedoroff, 1995; Lively and Schlichter, 2013). Nevertheless, when exposed to stiffness gradients in the substrate, a subset of microglial cells migrated—preferentially toward the stiffer side in a process called durotaxis (Lo et al., 2000; Isenberg et al., 2009; Kuo et al., 2012; Plotnikov et al., 2012; Raab et al., 2012; Vincent et al., 2013) (**Figure 6**). The migratory bias imposed by the mechanical gradient was similarly strong as seen in chemotaxis of leucocytes toward LTB4 (Foxman et al., 1999), suggesting a similar importance of mechanical signaling in immune cell attraction as chemical signaling.

Microglia migration on stiffness gradients was more likely to be in the direction of increased stiffness. Furthermore, step lengths were larger when moving parallel than perpendicular to the previous step, effectively amplifying migration toward stiff (as the likelihood of a step toward the stiffer side was higher). Microglia durotaxis was well-approximated using a 2D biased random walk model with changing step-lengths (distributed according to a Burr distribution, **Figure 9**) depending on the turning angle φ.

Differences in the local stiffness of the substrate underneath the cells were sufficient to explain durotaxis by a purely physical mechanism as previously discussed (Bischofs and Schwarz, 2003; Lazopoulos and Stamenovic, 2008), and as predicted by our stress fluctuation model (**Figure 10**). Thus, microglia showed durotaxis even when they were migrating on substrates whose stiffness was beyond their sensitive range, i.e., $G' > 2$ kPa. On these substrates, cellular traction forces can be considered rather constant across an individual cell, indicating that durotaxis does not require an intracellular traction force gradient.

Instead, a cell pulling on the substrate underneath will deform softer substrates more than stiffer ones, and a stiffer substrate will provide more traction. If a cell pulls on a substrate incorporating a stiffness gradient, it will thus pull itself toward the stiffer side. On softer substrates below $G' \sim 2$ kPa, microglia will pull significantly stronger on the stiffer side (**Figures 4**, **8**), modulating the durotactic effect. However, even if the local stresses on both sides of the cell are similar (i.e., on substrates with $G' > \sim 5$ kPa as in our experiments), cells will show the same durotactic bias as long as the ratio of the steepness of the gradient to the absolute substrate stiffness remains constant. This finding adds to previous work showing that the gradient strength is important for cellular durotaxis (Isenberg et al., 2009; Vincent et al., 2013), and it fits to the idea that a cell can only measure the stiffness of the surrounding relative to its own stiffness (Schwarz et al., 2006; Trichet et al., 2012).

In addition to this physical mechanism, cell type-specific mechanotransduction signaling pathways (Franze et al., 2009; Plotnikov et al., 2012; Raab et al., 2012), and stiffness-dependent local changes in cell morphology, such as stress fiber formation (Trichet et al., 2012), cell polarization (Isenberg et al., 2009; Raab et al., 2012), focal adhesion formation (Plotnikov et al., 2012), or a local change in their contact angle at the substrate surface (Style et al., 2013), could contribute to the observed durotactic behavior. Furthermore, microglia also respond to chemical guidance molecules. If exposed to mechanical and chemical cues, cells will integrate both types of signals and respond accordingly. Chemotaxis can be implemented in our stress fluctuation model in the future by adding an appropriate term.

Nowadays, neural implants (e.g., electrodes) are routinely used to treat patients suffering from Parkinson's disease and clinical depression. A major problem with long-term implants is their encapsulation by local immune cells in a process termed foreign body reaction (He and Bellamkonda, 2008; Tresco and Winslow, 2011). In the brain, microglial cells are activated by an implant and migrate toward it, which significantly contributes to the progression of foreign body reactions. Our stress fluctuation model provides a useful starting point to understand why and how microglia migrate toward stiff implants in the CNS.

At least three factors are likely to contribute to a stiffening of the tissue surrounding neural implants, and thus to establishing a local stiffness gradient. (i) Contact of microglial cells with stiff materials leads to their activation (Moshayedi et al., 2014). Glial cell activation, on the other hand, which is correlated with an increased expression of intermediate filaments, leads to a stiffening of the cells (Lu et al., 2011). (ii) The increase in traction forces we observed on stiffer substrates (**Figure 4**) is likely to lead to an increase in cytoskeletal tension, contributing to a stiffening of cells on stiffer substrates (Engler et al., 2004; Solon et al., 2007; Zemel et al., 2010). (iii) Both microglia migration toward the implant and their proliferation at the implant lead to a local increase in cell density, which again contributes to a local stiffening of the tissue (Koser et al., 2015). Thus, tissue surrounding neural implants is likely to be stiffer than healthy tissue further away. For the same reasons, microglia in contact with this stiffer tissue probably also stiffen to some degree. Thus, the three-dimensional arrangement of microglia around neural implants should effectively lead to a stiffness gradient in the tissue, attracting further glial cells to the implant in a durotactic fashion, and thus facilitating foreign body reactions.

Immuno-activation by LPS-treatment significantly changed microglial traction stresses. Forces exerted by cells grown on stiffer substrates ($G' \sim 300$ or 1000 Pa) decreased after LPS-activation, while forces slightly increased when cells were cultured on soft substrates of $G' \sim 100$ Pa (**Figure 5**). At the same time, LPS-application led to a significant increase in migration velocity and a decrease in stalling phases (**Figure 6**). Faster migration (and lower traction forces) are often a consequence of decreased adhesion (Fournier et al., 2010). LPS treatment furthermore focused microglia migration toward the stiffer side of the substrate, likely because of the strong decrease in stalling phases, which should lead to an enhancement of the durotactic bias. The activation-dependent tuning of the mechanical interactions between microglia and their environment might thus be an important mechanism controlling microglia morphology and function *in vivo*.

Ultimately, durotaxis of microglia might be required during normal CNS functioning and to react to a multitude of CNS disorders. Stiffness gradients in neural tissue at the cellular scale exist throughout life (Elkin et al., 2007; Christ et al., 2010; Franze et al., 2011; Iwashita et al., 2014; Koser et al., 2015). Furthermore, many CNS pathologies are accompanied by changes in neural tissue stiffness (Murphy et al., 2011; Riek et al., 2012; Schregel et al., 2012; Streitberger et al., 2012; Chauvet et al., 2015), which are potentially sensed by microglia. Local gradients in tissue stiffness might provide an important signal contributing to microglia activation and migration toward the pathological stimulus. On the other hand, microglia durotaxis might also contribute to the pathogenesis of CNS disorders, and to facilitating foreign body reactions to neural implants (Moshayedi et al., 2014). Future, studies will shed more light on how cell mechanics is involved in physiological and pathological processes in the CNS.

Author Contributions

KF conceived the project; LB, DK, GS, MG and KF designed the research; LB, DK, HG, RS, and EU performed research; LB, DK, and KF analyzed data; LB, DK, and KF wrote the paper, with contributions from all co-authors.

Acknowledgments

The authors thank Daniel Koch for providing software for traction force microscopy analysis, Kimberley Evans, Ragnhildur Thora Karadottir, and James Fawcett for help with microglial cells, Berenike Maier, Ulrich Schwarz, Timo Betz, Ivana Cvijovic, and Emad Moeendarbary for helpful discussions and technical support. This work was supported by the Austrian Agency for International Cooperation in Education and Research (Scholarship to LB), Faculty of Computer Science and Biomedical Engineering at Graz University of Technology (Scholarship to LB), German National Academic Foundation (Scholarship to DK), Wellcome Trust/University of Cambridge Institutional Strategic Support Fund (Research Grant to KF), Isaac Newton Trust (Research Grant 14.07 (m) to KF), Leverhulme Trust (Research Project Grant RPG-2014-217 to KF), UK Medical Research Council (Career Development Award to KF), and the Human Frontier Science Program (Young Investigator Grant RGY0074/2013 to GS, MG, and KF).

Supplementary Material

The Supplementary Material for this article can be found online at: http://journal.frontiersin.org/article/10.3389/fncel.2015.00363

References

abd-el-Basset, E., and Fedoroff, S. (1995). Effect of bacterial wall lipopolysaccharide (LPS) on morphology, motility, and cytoskeletal organization of microglia in cultures. *J. Neurosci. Res.* 41, 222–237. doi: 10.1002/jnr.490410210

Arani, A., Murphy, M. C., Glaser, K. J., Manduca, A., Lake, D. S., Kruse, S. A., et al. (2015). Measuring the effects of aging and sex on regional brain stiffness with MR elastography in healthy older adults. *Neuroimage* 111, 59–64. doi: 10.1016/j.neuroimage.2015.02.016

Bergert, M., Chandradoss, S. D., Desai, R. A., and Paluch, E. (2012). Cell mechanics control rapid transitions between blebs and lamellipodia during migration. *Proc. Natl. Acad. Sci. U.S.A.* 109, 14434–14439. doi: 10.1073/pnas.1207968109

Betz, T., Koch, D., Lu, Y. B., Franze, K., and Käs, J. A. (2011). Growth cones as soft and weak force generators. *Proc. Natl. Acad. Sci. U.S.A.* 108, 13420–13425. doi: 10.1073/pnas.1106145108

Bischofs, I. B., and Schwarz, U. S. (2003). Cell organization in soft media due to active mechanosensing. *Proc. Natl. Acad. Sci. U.S.A.* 100, 9274–9279. doi: 10.1073/pnas.1233544100

Califano, J. P., and Reinhart-King, C. A. (2010). Substrate stiffness and cell area predict cellular traction stresses in single cells and cells in contact. *Cell Mol. Bioeng.* 3, 68–75. doi: 10.1007/s12195-010-0102-6

Chauvet, D., Imbault, M., Capelle, L., Demene, C., Mossad, M., Karachi, C., et al. (2015). In *v*ivo measurement of Brain Tumor elasticity using intraoperative shear wave elastography. *Ultraschall Med.* doi: 10.1055/s-0034-1399152. [Epub ahead of print].

Christ, A. F., Franze, K., Gautier, H., Moshayedi, P., Fawcett, J., Franklin, R. J., et al. (2010). Mechanical difference between white and gray matter in the rat cerebellum measured by scanning force microscopy. *J. Biomech.* 43, 2986–2992. doi: 10.1016/j.jbiomech.2010.07.002

Codling, E. A., Plank, M. J., and Benhamou, S. (2008). Random walk models in biology. *J. R. Soc. Interface* 5, 813–834. doi: 10.1098/rsif.2008.0014

Elkin, B. S., Azeloglu, E. U., Costa, K. D., and Morrison, B. III. (2007). Mechanical heterogeneity of the rat hippocampus measured by atomic force microscope indentation. *J. Neurotrauma* 24, 812–822. doi: 10.1089/neu.2006.0169

Engler, A. J., Griffin, M. A., Sen, S., Bönnemann, C. G., Sweeney, H. L., and Discher, D. E. (2004). Myotubes differentiate optimally on substrates with tissue-like stiffness: pathological implications for soft or stiff microenvironments. *J. Cell Biol.* 166, 877–887. doi: 10.1083/jcb.200405004

Fournier, M. F., Sauser, R., Ambrosi, D., Meister, J. J., and Verkhovsky, A. B. (2010). Force transmission in migrating cells. *J. Cell Biol.* 188, 287–297. doi: 10.1083/jcb.200906139

Foxman, E. F., Kunkel, E. J., and Butcher, E. C. (1999). Integrating conflicting chemotactic signals. The role of memory in leukocyte navigation. *J. Cell Biol.* 147, 577–588. doi: 10.1083/jcb.147.3.577

Franze, K., Francke, M., Günter, K., Christ, A. F., Körber, N., Reichenbach, A., et al. (2011). Spatial mapping of the mechanical properties of the living retina using scanning force microscopy. *Soft. Matter* 7, 3147–3154. doi: 10.1039/c0sm01017k

Franze, K., Gerdelmann, J., Weick, M., Betz, T., Pawlizak, S., Lakadamyali, M., et al. (2009). Neurite branch retraction is caused by a threshold-dependent mechanical impact. *Biophys. J.* 97, 1883–1890. doi: 10.1016/j.bpj.2009.07.033

Franze, K., Janmey, P. A., and Guck, J. (2013). Mechanics in neuronal development and repair. *Annu. Rev. Biomed. Eng.* 15, 227–251. doi: 10.1146/annurev-bioeng-071811-150045

Georges, P. C., Miller, W. J., Meaney, D. F., Sawyer, E. S., and Janmey, P. A. (2006). Matrices with compliance comparable to that of brain tissue select neuronal over glial growth in mixed cortical cultures. *Biophys. J.* 90, 3012–3018. doi: 10.1529/biophysj.105.073114

Ghibaudo, M., Saez, A., Trichet, L., Xayaphoummine, A., Browaeys, J., Silberzan, P., et al. (2008). Traction forces and rigidity sensing regulate cell functions. *Soft Matter* 4, 1836–1843. doi: 10.1039/b804103b

Giulian, D., and Baker, T. J. (1986). Characterization of ameboid microglia isolated from developing mammalian brain. *J. Neurosci.* 6, 2163–2178.

Grevesse, T., Versaevel, M., Circelli, G., Desprez, S., and Gabriele, S. (2013). A simple route to functionalize polyacrylamide hydrogels for the independent tuning of mechanotransduction cues. *Lab. Chip.* 13, 777–780. doi: 10.1039/c2lc41168g

Han, S. J., Bielawski, K. S., Ting, L. H., Rodriguez, M. L., and Sniadecki, N. J. (2012). Decoupling substrate stiffness, spread area, and micropost density: a close spatial relationship between traction forces and focal adhesions. *Biophys. J.* 103, 640–648. doi: 10.1016/j.bpj.2012.07.023

He, W., and Bellamkonda, R. V. (2008). "A molecular perspective on understanding and modulating the performance of chronic central nervous system (CNS) recording electrodes," in *Indwelling Neural Implants: Strategies for Contending with the In Vivo Environment,* ed W. M. Reichert (Boca Raton, FL: CRC Press), 151–176.

Isenberg, B. C., Dimilla, P. A., Walker, M., Kim, S., and Wong, J. Y. (2009). Vascular smooth muscle cell durotaxis depends on substrate stiffness gradient strength. *Biophys. J.* 97, 1313–1322. doi: 10.1016/j.bpj.2009.06.021

Iwashita, M., Kataoka, N., Toida, K., and Kosodo, Y. (2014). Systematic profiling of spatiotemporal tissue and cellular stiffness in the developing brain. *Development* 141, 3793–3798. doi: 10.1242/dev.109637

Jagielska, A., Norman, A. L., Whyte, G., Vliet, K. J., Guck, J., and Franklin, R. J. (2012). Mechanical environment modulates biological properties of oligodendrocyte progenitor cells. *Stem Cells Dev.* 21, 2905–2914. doi: 10.1089/scd.2012.0189

Kettenmann, H., Hanisch, U. K., Noda, M., and Verkhratsky, A. (2011). Physiology of microglia. *Physiol. Rev.* 91, 461–553. doi: 10.1152/physrev.00011.2010

Kim, S. N., Jeibmann, A., Halama, K., Witte, H. T., Wölte, M., Matzat, T., et al. (2014). ECM stiffness regulates glial migration in Drosophila and mammalian glioma models. *Development* 141, 3233–3242. doi: 10.1242/dev.106039

Koch, D., Rosoff, W. J., Jiang, J., Geller, H. M., and Urbach, J. S. (2012). Strength in the periphery: growth cone biomechanics and substrate rigidity response in peripheral and central nervous system neurons. *Biophys. J.* 102, 452–460. doi: 10.1016/j.bpj.2011.12.025

Koser, D. E., Moeendarbary, E., Hanne, J., Kuerten, S., and Franze, K. (2015). CNS cell distribution and axon orientation determine local spinal cord mechanical properties. *Biophys. J.* 108, 2137–2147. doi: 10.1016/j.bpj.2015.03.039

Kuo, C. H., Xian, J., Brenton, J. D., Franze, K., and Sivaniah, E. (2012). Complex stiffness gradient substrates for studying mechanotactic cell migration. *Adv. Mater.* 24, 6059–6064. doi: 10.1002/adma.201202520

Lazopoulos, K. A., and Stamenovic, D. (2008). Durotaxis as an elastic stability phenomenon. *J. Biomech.* 41, 1289–1294. doi: 10.1016/j.jbiomech.2008.01.008

Liu, Y. J., Le Berre, M., Lautenschlaeger, F., Maiuri, P., Callan-Jones, A., Heuzé, M., et al. (2015). Confinement and low adhesion induce fast amoeboid migration of slow mesenchymal cells. *Cell* 160, 659–672. doi: 10.1016/j.cell.2015.01.007

Lively, S., and Schlichter, L. C. (2013). The microglial activation state regulates migration and roles of matrix-dissolving enzymes for invasion. *J. Neuroinflammation* 10, 75. doi: 10.1186/1742-2094-10-75

Lo, C. M., Wang, H. B., Dembo, M., and Wang, Y. L. (2000). Cell movement is guided by the rigidity of the substrate. *Biophys. J.* 79, 144–152. doi: 10.1016/S0006-3495(00)76279-5

Lu, Y. B., Iandiev, I., Hollborn, M., Körber, N., Ulbricht, E., Hirrlinger, P. G., et al. (2011). Reactive glial cells: increased stiffness correlates with increased intermediate filament expression. *FASEB J.* 25, 624–631. doi: 10.1096/fj.10-163790

Marcq, P., Yoshinaga, N., and Prost, J. (2011). Rigidity sensing explained by active matter theory. *Biophys. J.* 101, L33–35. doi: 10.1016/j.bpj.2011.08.023

Mccarthy, K. D., and de Vellis, J. (1980). Preparation of separate astroglial and oligodendroglial cell cultures from rat cerebral tissue. *J. Cell Biol.* 85, 890–902. doi: 10.1083/jcb.85.3.890

Mori, H., Takahashi, A., Horimoto, A., and Hara, M. (2013). Migration of glial cells differentiated from neurosphere-forming neural stem/progenitor cells depends on the stiffness of the chemically cross-linked collagen gel substrate. *Neurosci. Lett.* 555, 1–6. doi: 10.1016/j.neulet.2013.09.012

Moshayedi, P., Costa, L. D., Christ, A., Lacour, S. P., Fawcett, J., Guck, J., et al. (2010). Mechanosensitivity of astrocytes on optimized polyacrylamide gels analyzed by quantitative morphometry. *J. Phys. Condens. Matter* 22:194114. doi: 10.1088/0953-8984/1022/1019/194114

Moshayedi, P., Ng, G., Kwok, J. C., Yeo, G. S., Bryant, C. E., Fawcett, J. W., et al. (2014). The relationship between glial cell mechanosensitivity and foreign body reactions in the central nervous system. *Biomaterials* 35, 3919–3925. doi: 10.1016/j.biomaterials.2014.01.038

Murphy, M. C., Huston, J. III., Jack, C. R. Jr., Glaser, K. J., Manduca, A., Felmlee, J. P., et al. (2011). Decreased brain stiffness in Alzheimer's disease determined by magnetic resonance elastography. *J. Magn. Reson. Imaging* 34, 494–498. doi: 10.1002/jmri.22707

Nakamura, Y. (2002). Regulating factors for microglial activation. *Biol. Pharm. Bull.* 25, 945–953. doi: 10.1248/bpb.25.945

Plotnikov, S. V., Pasapera, A. M., Sabass, B., and Waterman, C. M. (2012). Force fluctuations within focal adhesions mediate ECM-rigidity sensing to guide directed cell migration. *Cell* 151, 1513–1527. doi: 10.1016/j.cell.2012.11.034

Raab, M., Swift, J., Dingal, P. C., Shah, P., Shin, J. W., and Discher, D. E. (2012). Crawling from soft to stiff matrix polarizes the cytoskeleton and phosphoregulates myosin-II heavy chain. *J. Cell Biol.* 199, 669–683. doi: 10.1083/jcb.201205056

Riek, K., Millward, J. M., Hamann, I., Mueller, S., Pfueller, C. F., Paul, F., et al. (2012). Magnetic resonance elastography reveals altered brain viscoelasticity in experimental autoimmune encephalomyelitis. *NeuroImage Clin.* 1, 81–90. doi: 10.1016/j.nicl.2012.09.003

Sabass, B., Gardel, M. L., Waterman, C. M., and Schwarz, U. S. (2008). High resolution traction force microscopy based on experimental and computational advances. *Biophys. J.* 94, 207–220. doi: 10.1529/biophysj.107.113670

Sack, I., Streitberger, K. J., Krefting, D., Paul, F., and Braun, J. (2011). The influence of physiological aging and atrophy on brain viscoelastic properties in humans. *PLoS ONE* 6:e23451. doi: 10.1371/journal.pone.0023451

Schregel, K., Wuerfel, E., Garteiser, P., Gemeinhardt, I., Prozorovski, T., Aktas, O., et al. (2012). Demyelination reduces brain parenchymal stiffness quantified *in vivo* by magnetic resonance elastography. *Proc. Natl. Acad. Sci. U.S.A.* 109, 6650–6655. doi: 10.1073/pnas.1200151109

Schwarz, U. S., Erdmann, T., and Bischofs, I. B. (2006). Focal adhesions as mechanosensors: the two-spring model. *Biosystems* 83, 225–232. doi: 10.1016/j.biosystems.2005.05.019

Solon, J., Levental, I., Sengupta, K., Georges, P. C., and Janmey, P. A. (2007). Fibroblast adaptation and stiffness matching to soft elastic substrates. *Biophys. J.* 93, 4453–4461. doi: 10.1529/biophysj.106.101386

Streitberger, K. J., Sack, I., Krefting, D., Pfüller, C., Braun, J., Paul, F., et al. (2012). Brain viscoelasticity alteration in chronic-progressive multiple sclerosis. *PLoS ONE* 7:e29888. doi: 10.1371/journal.pone.0029888

Stricker, J., Falzone, T., and Gardel, M. L. (2010). Mechanics of the F-actin cytoskeleton. *J. Biomech.* 43, 9–14. doi: 10.1016/j.jbiomech.2009.09.003

Style, R. W., Che, Y., Park, S. J., Weon, B. M., Je, J. H., Hyland, C., et al. (2013). Patterning droplets with durotaxis. *Proc. Natl. Acad. Sci. U.S.A.* 110, 12541–12544. doi: 10.1073/pnas.1307122110

Tolic-Norrelykke, I. M., and Wang, N. (2005). Traction in smooth muscle cells varies with cell spreading. *J. Biomech.* 38, 1405–1412. doi: 10.1016/j.jbiomech.2004.06.027

Tresco, P. A., and Winslow, B. D. (2011). The challenge of integrating devices into the central nervous system. *Crit. Rev. Biomed. Eng.* 39, 29–44. doi: 10.1615/CritRevBiomedEng.v39.i1.30

Trichet, L., Le Digabel, J., Hawkins, R. J., Vedula, S. R., Gupta, M., Ribrault, C., et al. (2012). Evidence of a large-scale mechanosensing mechanism for cellular adaptation to substrate stiffness. *Proc. Natl. Acad. Sci. U.S.A.* 109, 6933–6938. doi: 10.1073/pnas.1117810109

Uhlemann, R., Gertz, K., Boehmerle, W., Schwarz, T., Nolte, C., Freyer, D., et al. (2015). Actin dynamics shape microglia effector functions. *Brain Struct. Funct.* doi: 10.1007/s00429-015-1067-y. [Epub ahead of print].

Vincent, L. G., Choi, Y. S., Alonso-Latorre, B., del álamo, J. C., and Engler, A. J. (2013). Mesenchymal stem cell durotaxis depends on substrate stiffness gradient strength. *Biotechnol. J.* 8, 472–484. doi: 10.1002/biot.201200205

Zemel, A., Rehfeldt, F., Brown, A. E., Discher, D. E., and Safran, S. A. (2010). Optimal matrix rigidity for stress-fibre polarization in stem cells. *Nat. Phys.* 6, 468–473. doi: 10.1038/nphys1613

Conflict of Interest Statement: The authors declare that the research was conducted in the absence of any commercial or financial relationships that could be construed as a potential conflict of interest.

frontiers in Cellular Neuroscience

ORIGINAL RESEARCH
published: 19 August 2015
doi: 10.3389/fncel.2015.00306

Ribosomal trafficking is reduced in Schwann cells following induction of myelination

James M. Love[1] *and Sameer B. Shah*[1, 2]*

[1] *Fischell Department of Bioengineering, University of Maryland, College Park, MD, USA,* [2] *Departments of Orthopaedic Surgery and Bioengineering, University of California, San Diego, La Jolla, CA, USA*

Local synthesis of proteins within the Schwann cell periphery is extremely important for efficient process extension and myelination, when cells undergo dramatic changes in polarity and geometry. Still, it is unclear how ribosomal distributions are developed and maintained within Schwann cell projections to sustain local translation. In this multi-disciplinary study, we expressed a plasmid encoding a fluorescently labeled ribosomal subunit (L4-GFP) in cultured primary rat Schwann cells. This enabled the generation of high-resolution, quantitative data on ribosomal distributions and trafficking dynamics within Schwann cells during early stages of myelination, induced by ascorbic acid treatment. Ribosomes were distributed throughout Schwann cell projections, with ∼2-3 bright clusters along each projection. Clusters emerged within 1 day of culture and were maintained throughout early stages of myelination. Three days after induction of myelination, net ribosomal movement remained anterograde (directed away from the Schwann cell body), but ribosomal velocity decreased to about half the levels of the untreated group. Statistical and modeling analysis provided additional insight into key factors underlying ribosomal trafficking. Multiple regression analysis indicated that net transport at early time points was dependent on anterograde velocity, but shifted to dependence on anterograde duration at later time points. A simple, data-driven rate kinetics model suggested that the observed decrease in net ribosomal movement was primarily dictated by an increased conversion of anterograde particles to stationary particles, rather than changes in other directional parameters. These results reveal the strength of a combined experimental and theoretical approach in examining protein localization and transport, and provide evidence of an early establishment of ribosomal populations within Schwann cell projections with a reduction in trafficking following initiation of myelination.

Keywords: ribosome, transport, Schwann cell, neuron, myelination, live imaging, modeling

OPEN ACCESS

Edited by:
Kyle Miller,
Michigan State University, USA

Reviewed by:
Paul C. Bressloff,
University of Utah, USA
Tomas Luis Falzone,
National Scientific and Technical Research Council, Argentina

Correspondence:
Sameer B. Shah,
Department of Orthopaedic Surgery,
University of California, San Diego,
9500 Gilman Drive, MC 0863,
La Jolla, CA 92093, USA
sbshah@ucsd.edu

Received: *21 May 2015*
Accepted: *27 July 2015*
Published: *19 August 2015*

Citation:
Love JM and Shah SB (2015) Ribosomal trafficking is reduced in Schwann cells following induction of myelination.
Front. Cell. Neurosci. 9:306.
doi: 10.3389/fncel.2015.00306

Introduction

Schwann cells (SCs), a major cell type of the peripheral nervous system, are tasked with supporting neurons in numerous ways, from enhancing electrical conduction (Waxman and Bennett, 1972) to providing trophic factors for axonal growth and regeneration (Son and Thompson, 1995; Bryan et al., 2000). In this capacity, they possess a distinctive bipolar architecture; internode distances of up to 500 μm require distances between the Schwann cell body and distal processes to reach over 200 μm (Jacobs and Cavanagh, 1969). As in neurons, another polarized cell of unusual geometry (Twiss and van Minnen, 2006), myelinating and unmyelinating SCs appear to synthesize particular proteins at the site of demand within projections, rather than in the cell body (Gould and Mattingly, 1990).

In contrast to ER-bound ribosomes, which are mainly tasked with the production of membrane-associated or secreted proteins (Caro and Palade, 1964; Jamieson and Palade, 1967; Leader, 1979), cytosolic protein synthesis occurs on free ribosomes and is typically responsible for producing many proteins locally, including intracellular signaling molecules, transcription factors, and cytoskeletal elements (Ganoza and Williams, 1969). Evidence of local protein synthesis in myelinating cells remains mostly indirect, based on the presence of mRNA in isolated polysomes and granules within both unmyelinating and myelinating glial cells (Brophy et al., 1993). Additionally, myelin basic protein (MBP) mRNA has been observed to be distributed throughout SC and oligodendrocyte projections (Trapp et al., 1987, 1988; Griffiths et al., 1989; Gould and Mattingly, 1990), and radiolabeled MBP (2 min) appears early compared to the cell body-synthesized protein PLP (30 min) in the myelin fraction of oligodendrocytes, providing additional evidence for translation of MBP within the myelin fraction (Colman et al., 1982).

Lacking from our current understanding is how these free ribosomal populations are distributed in Schwann cells during development and how ribosomal distribution is influenced by Schwann cell interactions with neurons. Developing a better understanding of these mechanisms may provide better insight into protein synthetic dynamics as well as the stability of observed ribosomal structures, in preparation for translation of Schwann cell proteins as well as, intriguingly, those potentially transmitted to neurons (Court et al., 2008, 2011). We used quantitative biological and theoretical approaches to probe the hypothesis that the induction of myelination would increase trafficking of ribosomes, to account for the required increase in production of myelin associated proteins. Expression of fluorescently labeled ribosomal subunits in primary Schwann cells allowed us to track ribosomal transport in real time, and quantify changes in patterns of ribosomal localization and transport during both their initial interactions with neurons in culture and in early phases of myelination. Multiple regression analysis and the development of a data-driven rate kinetic model enabled us to develop further insight into these changes. Our data suggest that stable ribosome-enriched foci appear early during Schwann cell projection extension and are maintained during early stages of myelination. However, transport of new ribosomes into projections slows upon induction of myelination, primarily due to increased conversion of anterograde (outward) moving particles to a stationary pool.

Materials and Methods

Animal Usage and Euthanasia

Animal usage was in accordance with protocols approved by the UCSD Institutional Animal Care and Use Committee (IACUC). Pregnant female rats were euthanized by asphyxiation with CO_2 followed by confirmation via secondary means (removal of major organs). P2 neonates were incapacitated with CO_2 followed by euthanization via decapitation.

DRG Collection and Culture

DRG culture methods were adapted from previously published methods (Lee et al., 1995). Dorsal root ganglia (DRGs) were removed from E15 Sprague-Dawley rats in HBSS. DRGs were dissociated in trypsin for 30 min at 37°C. Following trypsinization, samples were washed 3x in fresh pre-warmed media. DRGs (~30,000 per plate) were plated on laminin-coated glass coverslips placed within 24-well plates supplemented with 500 μl of prewarmed DRG media consisting of MEM with 10% FBS, 2% B27, 1 ng/ml NGF, and 1% Penicillin/Streptomycin. One day post-plating, culture media was supplemented with 1 ug/ml FdU to eliminate contaminating fibroblasts and Schwann cells. Media was alternated every 2–3 days between FdU application and fresh media for a period of 2 weeks to obtain a mostly purified neuronal culture (**Figure 1A**).

Schwann Cell Isolation

Schwann cells were isolated and cultured per previously published methods (Lee et al., 1995). Primary Schwann cells were obtained from the sciatic nerves of ~10 P2 Sprague-Dawley rat pups (20 nerves). Nerves were dissected into 14 ml of L15 media then spun down at 3000 rpm for 2 min. Media was aspirated off and nerves were resuspended in 2 ml L-15 and 1 ml 10 mg/ml collagenase type P and incubated at 37°C for 45 min, mixing every 10 min. Tissue was spun down for 2 min at 1000 × g, media aspirated off and pre-warmed digestion solution added (3 ml 0.25% trypsin and 1 ml DNase [1.2 mg/ml]) Sample was incubated for 15 min at 37°C. Following incubation, the reaction was halted by supplementing sample with 5 mL DMEM and 10% FBS. Sample was centrifuged for 2 min at 1000 × g followed by two washes with 10 ml of ice cold L15 media followed by 1000 × g centrifugations. Samples were supplemented with 5 ml of media and triturated. Cells were spun down at 1000 × g and media removed for transfection.

Transfection

Nucleofection was performed according to manufacturer's instructions (4D-Nucleofector™ System, Lonza AG, Switzerland) using P3 primary cell solution and program setting DC-100 to transfect. Either 3 μg of L4-GFP plasmid (a generous gift of Dr. Tim Krüger (Krüger et al., 2007) or control GFP plasmid (Lonza AG, Switzerland) were used.

Expression persisted for up to 2 weeks in culture. However, the percentage of cells expressing the plasmid decreased over time, as has been previously reported (Pedraza and Colman, 2000). Thus, our experimental time course was conservatively chosen to span early phases of myelination, and includes cells from 1 day post-transfection (Day 1) to cells 1 week post-transfection (Day 7) (**Figure 1A**).

Induction of Myelination

Myelination was induced with ascorbic acid per published protocols (Eldridge et al., 1987). On the fourth day of

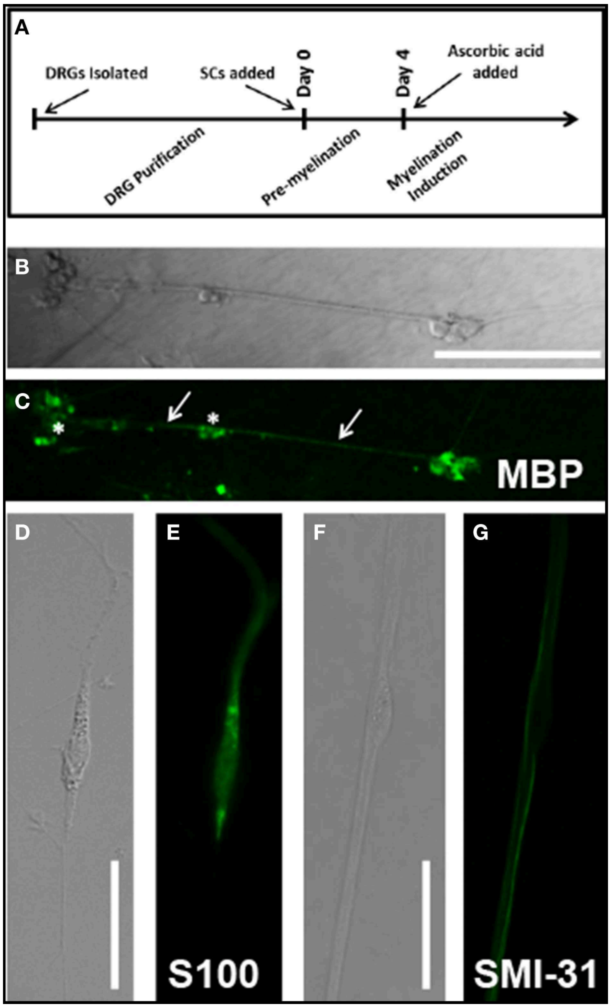

FIGURE 1 | (A) Cell culture timeline. All experimental days reference days since Schwann cell addition to neuronal culture; Confirmation of myelination protocols and cell culture techniques was observed through immunolabeling: **(B)** DIC image of Day 14AA culture indicates several clusters of Schwann cells and neurons (stars) as well as fascicles of myelinated DRG axons (arrows); **(C)** MBP immunostain of Day 14AA culture shows low levels of MBP expression, indicative of early myelination; **(D)** DIC image of cultured Schwann cells at Day 1 **(E)** S100 immunostain identifies cultured Schwann cells; **(F)** DIC image of a single Schwann cell (star) abutting neuronal processes; **(G)** SMI-31 (phosphorylated neurofilament) immunostain identifies location of neuronal processes relative to Schwann cell body (star); Scale bar B/C: 200 μm, D/E/F/G: 50 μm.

co-culture with neurons, Schwann cell media was supplemented with 50 μg/ml ascorbic acid to initiate the process of myelination. Cells treated with ascorbic acid and observed were designated (Day 7AA) in contrast with untreated cells (Day 7 No AA). Myelination was confirmed using immunocytochemistry at day 14 (see **Figures 1B,C**). Schwann cells in culture were identifiable by immunostaining against S100 (see **Figures 1D,E**) while neurons were identified by immunostaining against SMI-31 phosphorylated neurofilament (see **Figures 1F,G**).

Immunocytochemistry

Immunocytochemistry was performed at various developmental time points, using published protocols (Love et al., 2012). Samples were labeled with one or a combination of the following primary antibodies: mouse anti-S100 (Sigma-Aldrich S2532), mouse anti-SMI31 (abcam ab24573), mouse anti-MBP, human anti-Ribo-P (Immunovision HPO-0100), mouse anti-RPL4 (Sigma-Aldrich WH0006124M1), mouse anti-tubulin (Sigma-Aldrich T9026). Appropriate species specific fluorescently-labeled secondary antibodies were used to visualize primary antibody localization. Secondary antibodies used included: Alexa Fluor 488-goat anti-mouse (Invitrogen A-11001), Alexa Fluor 594-goat anti-mouse (Invitrogen A-11032), Alexa Fluor 594-goat anti-rabbit (Invitrogen A-11037), and Alexa Fluor 594-goat anti-human (Jackson Immunoresearch 109-585-003). Desired samples were incubated for 30 min prior to mounting in Alexa Fluor 594-phalloidin (Invitrogen A-12381) to visualize actin.

Analysis for co-localization was performed using ImageJ plugin JACoP (Bolte and Cordelières, 2006). Images were analyzed for overlapping expression using the Manders coefficient, which incorporates both position and fluorescence intensity into assessment of co-localization (Manders et al., 1992).

Imaging

Cells were imaged using a Leica SP5 system within an environmental chamber (Tokai Hit, Japan) that, for live-imaging experiments, enabled maintenance of the environment at 37°C and 5% CO_2. Standard lasers and filters were used. An argon laser enabled excitation at 488 nm with HeNe lasers for 594 nm. Emission was captured between 500 and 550 nm (GFP, Alexa-Fluor 488) and 600–650 (Alexa-Fluor 594). Laser power and gains were adjusted to provide best images for each sample. Images were obtained using a 63x glycerol (80% glycerol/20% water) immersion objective with a pinhole of 1 airy (102.9 μm). Time-lapse images were taken at a resolution of 512 × 512 pixels with 3x line averaging. Stand-alone images were captured with a resolution of 1024 × 1024 pixels with 3x line averaging.

Time course images of transfected cells were captured at 5 s intervals for a period of 5 min. The capture rate and imaging period were chosen based upon several factors including anticipated transport rates, desired resolution, and minimization of photobleaching and phototoxicity.

Image Processing and Analysis

Custom Matlab (Mathworks, Inc.) programs were modified from previous studies (Chetta and Shah, 2011; Love et al., 2012) to convert time course images into a kymograph. Kymographs allow for visualization of changes in an intensity profile of a 1-dimensional trace over time with the time variable displayed along the y-axis and cellular position along the x-axis. Kymograph traces in our analysis were made along the long axis of the SC projection allowing visualization of transport throughout the projection with a thickness of three pixels. The trace was suppressed to a single pixel thickness by choosing the maximum intensity value of the three. Kymographs were analyzed for both ribosomal distributions along the projection as well as transport characteristics of mobile ribosomal populations.

For characterization of ribosomal distributions, kymographs were averaged along the y-axis providing an average projection profile for the 5 min imaging duration. The profile was manually segmented to separate the cell body from the projection for characterization. Stable populations of ribosomes were noted within the projections through identification of peaks in the average intensity above background fluorescence levels (>3x). Peaks within 5 pixels ($\sim$2.5 μm) were counted as a single peak to minimize double counting. Average fluorescence levels were identified for both the cell body and projection regions. Peak distance values were determined from identified peak locations and specified projection start.

Transport parameters were computed based upon manual identification of mobile ribosomal particles with a continuous trajectory from frame to frame and an intensity of at least 3x above background. In addition to direction of movement in previous frames, intensity and line-width of a trajectory were also factored into particle tracking. Additionally, kymographs were blinded for experimental group. We used a conservative inclusion criteria in analyzing traces that potentially merged or split. Trajectories that appeared to merge were not double-analyzed in areas of potential overlap (i.e., one of the two trajectories was truncated at the merge site (or initiated at the split site). Thus, tracks were not incorrectly lengthened, but may have been prematurely truncated. Such track shortening was assumed to have minimal impact on results and their interpretation due to the following rationale: (i) average velocities, which are measured from directional runs would be unaffected; (ii) net velocities, which are weighted by track duration (shorter tracks contribute less) would be minimally affected; (iii) increases in directional populations for a given direction would inversely correlate with run duration (e.g., an increase in anterograde particles would correspond with a decrease in anterograde run duration). This was not observed. In no case did a significant increase or decrease in particle number correspond to a corresponding reduction or increase, respectively, in run duration. Mean particle parameters were computed and presented as average values. Net velocity was computed based on the aggregate distance traveled by all particles in a given sample divided by the time window of observation (Pathak et al., 2013). This provides a reasonable surrogate for the collective level of transport conducted by a cell throughout the duration of the 5-min imaging window.

Multiple Regression Analysis

Multiple regression analysis was performed on the z-scored data of all individual traces within an experimental group. The dependent variable (net velocity) was regressed against the independent variables average velocity, total duration, anterograde velocity, anterograde duration, stationary velocity, stationary duration, retrograde velocity, and retrograde duration. Higher β-weights indicate a stronger contribution to the regression model.

Modeling

A ribosomal transport model was implemented using a rate kinetics model to evaluate transitions from stationary, retrograde, and anterograde ribosomal populations. The model, modified slightly from its original form (Zadeh and Shah, 2010), used a system of coupled differential equations for each population:

$$\frac{d[Ant]}{dt} = k_{+1}[Stat] - k_{-1}[Ant] \tag{1}$$

$$\frac{d[Ret]}{dt} = k_{+2}[Stat] - k_{-2}[Ret] \tag{2}$$

The stationary population was set as an infinite source and sink with a value of 1 particle (**Table 1**). The model schematic can be seen in **Figure 7**. Particle quantities while modeled as concentrations within the equations refer to instantaneous particle counts. Initial values of anterograde and retrograde particles were calculated by dividing the average number of particles per experiment by the experimental duration (**Table 1**). The model was implemented in MATLAB (MathWorks, Natick, MA) using the differential equation solver ode45 which implements a Runge-Kutta method with a variable step size. In order to find a unique best solution, rates were varied between 0.001 and 1.001 in 0.02 steps for each rate constant (**Table 2**). Sensitivity analysis for each model parameter was performed by varying each parameter over its allowed range, and plotting model outputs. Best fit was determined by minimizing the mean square error (MSE) between modeled parameters and experimental data for net velocity and the number of particles in each state (**Table 3**). A maximum MSE of 0.02 for the net velocity fit was chosen such that the model fit within the range of standard errors observed experimentally. Initial model fit was made using the time points untreated with ascorbic acid (Days 1, 3, and 7). A fit was then made between the Day 4 time point of

TABLE 1 | Model initial particle counts.

	Initial values
Anterograde particles	0.4034
Retrograde particles	0.0782
Stationary particles	1

Initial particle counts used to seed the model simulation.

TABLE 2 | Model constants and rate variations.

	Model parameters
Anterograde velocity (μm/s)	0.650782634
Retrograde velocity (μm/s)	−0.439211217
Velocity scaling factor	0.925432705
Minimum tested K-value (K_{+1}, K_{-1}, K_{+2}, K_{-2})	0.001
Maximum tested K-value (K_{+1}, K_{-1}, K_{+2}, K_{-2})	1.001
K-value iteration	0.02

Directional velocities used to determine net velocities within the model, as well as, range over which rate constants were iterated during model fitting.

TABLE 3 | Model results.

	Data	Model	Percent error
NET VELOCITY			
Day 3	0.1981	0.2308	16.51
Day 7—No AA	0.7285	0.3027	10.50
Day 7—AA	0.1292	0.1314	1.70
ANTEROGRADE PARTICLES			
Day 3	0.3509	0.4671	33.11
Day 7—No AA	0.7285	0.5868	19.45
Day 7—AA	0.5096	0.4682	8.12
RETROGRADE PARTICLES			
Day 3	0.0808	0.1670	106.68
Day 7—No AA	0.3642	0.1806	50.41
Day 7—AA	0.3796	0.3949	4.03

Model outputs and percent error for net velocity, anterograde particle count, and retrograde particle count.

the untreated fit (time point at which ascorbic acid was added) and the Day 7 treated group. Within the model, net velocity was calculated by multiplying the instantaneous particle populations of each state by the instantaneous velocity of the population for a given time step and summing the two populations. Due to the lack of significant difference between anterograde and retrograde velocities, the average velocities across the four experimental time points was used as a constant throughout the model (**Table 2**). A velocity scaling factor (**Table 2**) was applied to allow for the starting net velocity of the model to match the experimental.

Statistical Analysis

In all cases a One-Way ANOVA was performed across all experimental groups (Day 1, Day 3, Day 7 No AA, Day 7 AA). Additionally, Tukey's HSD was performed *post-hoc* to determine significant differences between individual groups of interest while accounting for multiple comparisons. Differences were considered significant for $p < 0.05$. A minimum sample size of 7 was used for each group, corresponding to a statistical power of 0.91 and effect size capable of being detected of 0.96.

Results

L4-GFP Transfection and Ribosomal Expression in Schwann Cells

We confirmed and characterized transfection of SCs with the L4-GFP plasmid (**Figure 2A**). Only ∼15% of cells were successfully transfected; however, comparison of localization patterns of L4-GFP in transfected cells with localization patterns observed in cells immuno-labeled for ribosomal protein L4 showed strong agreement (**Figure 2B**). Of particular note were the characteristic punctate expression within the nucleolus, which has been observed previously for L4-GFP as well as several other ribosomal subunits (Krüger et al., 2007), and higher relative fluorescence within the cell body compared to the projection of the SC. Immunolabeled L4 also co-localized with Ribo-P, a marker for phosphorylated ribosomes, both inside and outside of the nucleus (**Figure 2C**; Nucleus: Manders M1 = 0.61; M2 = 0.79; Extranuclear: M1 = 0.58; M2 = 0.89). The expression profile of L4-GFP also differed greatly from that of GFP expression (**Figure 2D**), which was evenly distributed in low levels throughout the entirety of the SC.

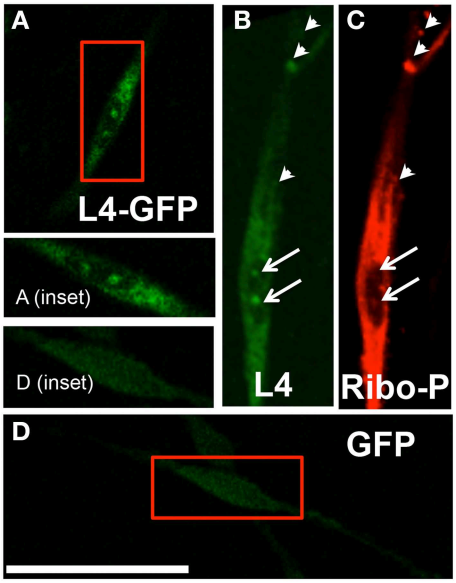

FIGURE 2 | (A) Typical pattern of a transfected Schwann cell expressing L4-GFP (magnified in inset); **(B)** A separate schwann cell immunostained with anti-L4; **(C)** Schwann cell immunostained with anti-Ribo-P shows co-localization with L4 expression, based on Manders co-localization analysis (arrows indicate nucleolar labeling; arrowheads indicate prominent co-localizing puncta); **(D)** Transfected Schwann cell expressing GFP (magnified in inset) shows continuous low-level expression throughout cell, including the nuclear compartment, and differs from the L4-GFP labeling pattern; Scale bar: 50 μm.

Ribosomal Expression Characteristics within Schwann Cell Projections

Following successful transfection, SCs associated with neurons were identified based on the position of cell bodies and projections of each cell type. We investigated these cells to determine the development of ribosomal distributions within SC projections over time and following myelination induction (**Figure 1A**). We compared early (Days 1 and 3) and late (Day 7 No AA) time points for untreated cells, and for the late time point, also cells treated with ascorbic acid at day 4 to induce myelination (Day 7AA).

The ratio of cell body fluorescence to projection fluorescence (average cell body pixel value/average projection pixel value) was used to determine any difference in bulk localization of ribosomes. This ratio was calculated for sub-saturation fluorescence, and was independent of any cell to cell differences in fluorescence expression. The ratios at each time point were consistent, falling between 0.406 and 0.429 ($p = 0.486$; One-Way ANOVA, **Figure 3A**), suggesting no net increase or decrease in projection expression levels among all experimental groups.

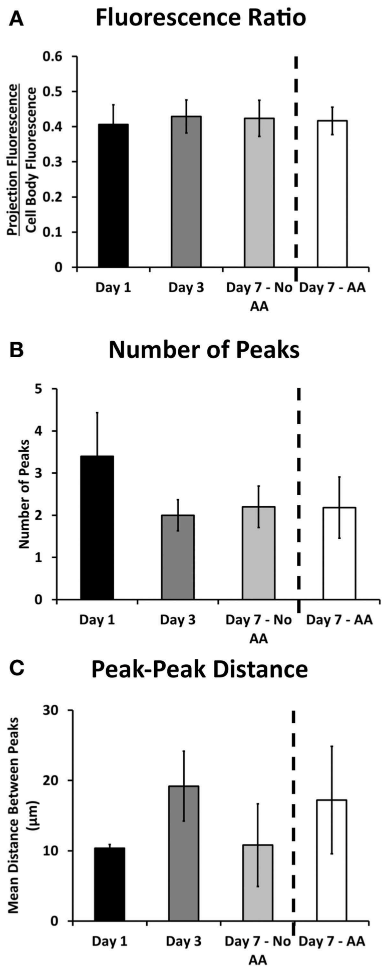

FIGURE 3 | Ribosomal expression in the projections of Schwann cells remained relatively consistent throughout the experimental proceedings according to a number of metrics. (A) The ratio of fluorescence in the projection compared to the cell body remained consistent throughout the experimental groups; **(B)** The number of observed ribosomal peaks (or puncta) did not vary significantly throughout the experimental groups; **(C)** The distance between peaks varied albeit not significantly throughout the experiment (Means ± SEM). *Statistics: 1-way ANOVA.*

Bright, stationary ribosomal patches dotting the Schwann cellular projection were consistently observed at each time point. The peaks were characterized by a minimum 3x increase in fluorescence over the average projection expression level. The number of these peaks did not change amongst the experimental groups (between 2.2 and 3.4; $p = 0.77$; One-Way ANOVA, **Figure 3B**). Additionally the peak to peak distance did not vary ($p = 0.605$ One-Way ANOVA, **Figure 3C**). Several additional morphological and fluorescence parameters of interest, including projection length, total fluorescence, and distances of peaks from cell bodies were also calculated (**Table 4**). These also yielded no significant differences. This evidence points to an early establishment and inherent stability of the ribosomal clusters following SC alignment with neurons, independent of time or early myelination.

Cytoskeletal Characteristics of Ribosomal Clusters in Schwann Cells

Based on observations of apparently stable ribosomal clusters, we tested whether any particular cytoskeletal components were associated with local ribosomal clusters. In neurons, previous reports indicated high densities of F-actin subjacent to ribosome-enriched periaxoplamic ribosomal plaques (PARPs) (Koenig and Martin, 1996). We therefore tested whether a similar phenomenon also occurred in SCs, by examining co-localization of immunolabeled L4 and phalloidin-labeled F-actin. We did observe bright regions of actin along the SC projection, interspersed with dim regions, enabling analysis of co-localization with ribosomal clusters. However, L4 clusters in SC projections showed no specific co-localization or apparent proximity to F-actin in SCs alone (Manders = 0.179 ± 0.082), in the presence of neurons without induction of myelination (Day 1; Manders = 0.341 ± 0.288) and in the presence of neurons following induction of myelination (Day 7AA; Manders = 0.197 ± 0.113) (**Figures 4A–C**). The apparent offset of phalloidin and L4 is likely resultant from cortical localization of actin and central cytoplasmic localization of L4. We also examined localization of ribosomes relative to microtubules, based on co-localization of Ribo-P with tubulin. However, fluorescent intensity of tubulin was uniformly consistent along the projection and thus precluded quantitative analysis of co-localization (data not shown).

Ribosomal Transport Characteristics within Schwann Cell Projections

Though densities were apparently stable, movies of L4-GFP dynamics, captured using time-lapse fluorescence microscopy, revealed movement of less intense L4-GFP puncta between densities. Thus, to examine whether ribosomal transport contributed to the maintenance of densities, we next quantitatively characterized the movement of L4-GFP using kymograph analysis, which allowed the observation of moving L4-GFP particles, and the characterization of puncta directionality, velocity, and duration of movement (**Figure 5**). Individual puncta were treated as single particles, independent of fluorescence intensity.

The summation of net velocity for each individual L4-GFP particle within a given movie offers a summary of directionality and extent of movement within a cell during our imaging period. Normalization of this displacement to the imaging duration yields net velocity, which enables comparison with bulk transport rates captured over a longer time frame (Love et al., 2012; Pathak et al., 2013). There are significant differences in net velocity of ribosomes over the course of Schwann cell development ($p = 0.0038$, One-Way ANOVA, **Figure 6A**). In particular, though ribosomal transport is anterograde (away from the Schwann cell body) at all-time points, ribosomal transport at Day 7 increases in the absence of ascorbic acid, but is suppressed in the presence of ascorbic acid. (Mean ± SEM; No AA: 0.388 ± 0.074; AA: 0.129 ± 0.025, $p = 0.00189$, Tukey's HSD).

We further examined individual transport parameters to determine their contribution to net velocity in each experimental group. The comprehensive data set, including statistical analysis,

TABLE 4 | Projection data.

	Day 1	Day 3	Day 7—No AA	Day 7 AA	*P*-value (ANOVA)
Projection length (μm)	62.33 ± 9.08	80.19 ± 10.423	71.58 ± 9.52	93.15 ± 24.45	0.486
Cell body Avg. intensity	12.94 ± 2.4	12.65 ± 2.1491	13.28 ± 1.58	13.89 ± 1.29	0.496
Projection Avg. intensity	4.68 ± 0.46	4.63 ± 0.69534	5.22 ± 0.41	5.63 ± 0.72	0.77
Projection/Cell body ratio	0.41 ± 0.06	0.43 ± 0.046995	0.42 ± 0.05	0.42 ± 0.04	0.605
Number of peaks	3.4 ± 1.03	2 ± 0.36927	2.2 ± 0.49	2.18 ± 0.72	0.663
Avg. distance peak to cell body (μm)	24.78 ± 6.28	35.04 ± 10.52	30.75 ± 12.83	41.62 ± 17.79	0.525
Avg. distance peak to peak (μm)	10.38 ± 0.51	19.19 ± 4.9773	10.8 ± 5.88	17.22 ± 7.65	0.713

Additional values from projection analysis show little variability between experimental groups, p-values based on 1-ANOVA of experimental group.

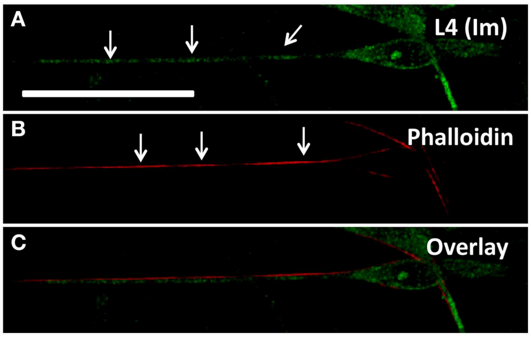

FIGURE 4 | (A) Schwann cell immunostained for L4 shows expression throughout the projection with specifically punctate regions (arrows) corresponding to ribosomal rich regions; **(B)** Phalloidin staining highlights cortical regions rich in actin (arrows) but not necessarily corresponding with ribosomal rich regions **(C)**. Scale bar: 50 μm.

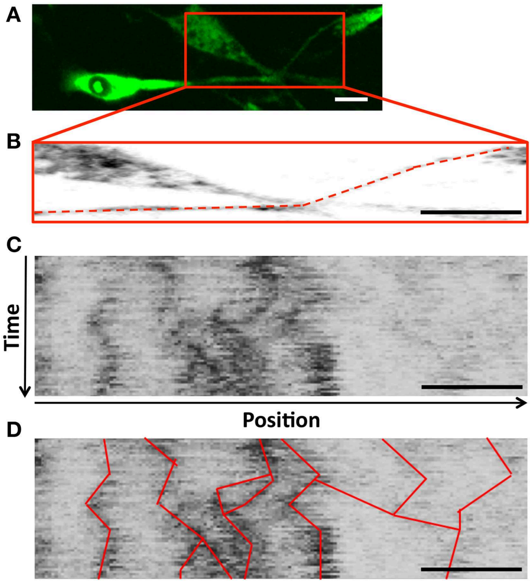

FIGURE 5 | (A) Schwann cell projections were cropped and traced to develop **(B)** Sample trace (dashed line) used to develop a kymograph **(C)** a kymograph (y-axis: time, increasing downward; x-axis: position along the projection, with anterograde to the right); **(D)** Trajectories for puncta observed in consecutive frames were traced on the kymograph to identify ribosomal movement throughout the projection, and allow for quantification of transport parameters during the course of the experiment; Scale bar: 20 μm, duration 5 min.

is summarized in **Table 5**. For clarity, we discuss key findings below.

The average ribosomal velocity was also dependent upon the developmental state of the Schwann cell ($p = 0.0025$ One-Way ANOVA, **Figure 6B**). Most notably, there was a significant reduction in average velocity from Day 3 (0.56 μm/s) to Day 7 (No AA: 0.25 μm/s; AA: 0.22 μm/s) irrespective of ascorbic acid treatment (Day 3–Day 7 No AA: $p = 0.041$; Day 3–Day 7 AA: $p = 0.004$, Tukey's HSD). While the reduction in average velocity might be expected in the case of Day 7AA, where net velocity is also reduced, this was unexpected in the case of the untreated Day 7 group, where net velocity in fact increases. This apparent paradox indicates that other phenomena are integral in determining the net velocity.

Average particle run durations varied between 18 and 27 s in the anterograde direction and 12 and 24 s in the retrograde direction (**Figure 6C**). There was a trend toward increasing durations in both the anterograde and retrograde directions. Significance differences were observed in both directions between early time points and Day 7AA (Anterograde: Day 1–Day 7 AA: $p = 0.016$; Day 3–Day 7 AA: $p = 0.038$; Retrograde: Day 1–Day 7AA: $p = 0.0018$; Day 1–Day 7 AA: 0.0070). Additionally a difference was observed between Day 7 in the absence of ascorbic acid and Day 1 in the retrograde direction ($p = 0.011$).

A final component of net velocity is the number and proportion of particles being transported in each direction. There were significant differences in both particle populations (Anterograde: $p = 0.006$; Retrograde: $p = 0.000006$, One-Way ANOVA, **Figure 6D**). Of note in the case of the anterograde particles is the significant increase in anterograde particles from Day 3 (5.125 particles) to Day 7 (No AA: 8.25 particles) in the absence of ascorbic acid ($p = 0.005$, Tukey's HSD), but not the presence of ascorbic acid (AA: 5.6 particles; $p = 0.918$, Tukey's HSD). This increase in particle number thus may be a key factor contributing to the observed increase in net velocity.

Multiple Regression

We performed multiple regression analysis on a particle by particle basis to determine the individual contributions of

TABLE 5 | Transport data.

	Day 1	Day 3	Day 7—No AA	Day 7 AA	*P*-Value(ANOVA)
Net velocity (μm/s)	0.233 ± 0.046	0.198 ± 0.02	0.338 ± 0.074	0.129 ± 0.025†	0.0038
Avg. velocity (μm/s)	0.496 ± 0.064	0.558 ± 0.062	0.246 ± 0.039$^{\wedge}$	0.216 ± 0.09	0.00258
Avg. Ant. Vel. (μm/s)	0.765 ± 0.055	0.802 ± 0.065	0.624 ± 0.086	0.621 ± 0.075	0.178
Avg. Ret. Vel. (μm/s)	−0.52 ±0.234	−0.38 ± 0.122	−0.525 ± 0.148	−0.474 ± 0.08	0.848
Tot. Ant. Part	6.86 ± 0.67	5.13 ± 0.46	8.25 ± 0.8$^{\wedge}$	5.6 ± 0.58†	0.00628
Tot. Ret. Part.	1.71 ± 0.52	1.56 ± 0.26	4.63 ± 0.53$^{*\wedge}$	4.67 ± 0.61	0.00000615
Ant. Duration (s)	17.65 ± 2.01	20.55 ± 1.37	26.49 ± 2.18*	27.32 ± 2.21$^{*\wedge}$	0.00525
Ret. Duration (s)	11.79 ± 1.95	15.51 ± 1.58	23.62 ± 2.3	24.41 ± 2.28$^{*\wedge}$	0.000326

Values from transport analysis showing variability among velocities and particle distributions between groups, p-values passed on 1-ANOVA (Tukey HSD, $p < 0.05$ compared to *Day 1, $^{\wedge}$Day 3, †Day 7—No AA)

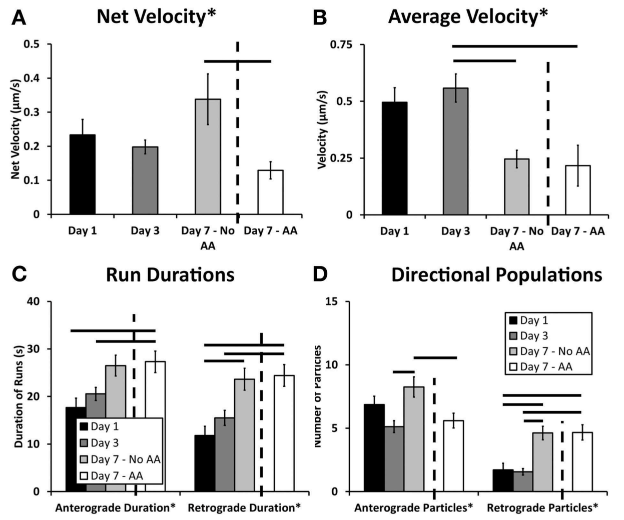

FIGURE 6 | Kymograph analysis provided a clear picture of the dynamics of ribosomal transport. (A) Net velocity, a measurement that provides a relative comparison of the bulk transport occurring in the cell, showed increased levels after 7 days. These levels were decreased when the cultures were treated with ascorbic acid indicating an effect of this treatment and early myelination on ribosomal transport; **(B)** In both day 7 treatment groups, the average velocity was decreased compared to day 3; **(C)** Anterograde and retrograde durations varied over the course of the experiment showing significant differences between early and late time points; **(D)** The number of anterograde particles increased after 7 days in the absence of ascorbic acid compared to both the day 3 and day 7 ascorbic acid treated groups. Additionally, there was an increase in retrograde particles in both the day 7 groups compared to the earlier time points, likely influencing the observed changes in net velocity (Means ± SEM) *Statistics: 1-way ANOVA (* $p < 0.05$); Tukey HSD* (**–** $p < 0.05$).

TABLE 6 | Multiple regression.

	Day 1	Day 3	Day 7 No AA	Day 7 AA
Avg. Vel.	0.021	0.022	0.480	0.525
Tot. Time	0.537	0.003	−0.352	−0.250
Avg. Ant. Vel.	0.413	0.474	−0.041	−0.041
Time Ant.	0.000	0.474	0.952	0.630
Avg Ret. Vel.	0.028	0.042	−0.060	−0.081
Time Ret.	−0.595	−0.244	0.295	−0.028

β-weights for multiple regression of z-scored data for independent variables regressed against the dependent variable net velocity show a shift from anterograde velocity dependence at early time points (Days 1 and 3) to anterograde time dependence at later time points (Day 7).

each component measurement (independent variables) to the resultant net velocity (dependent variable). A complete summary of regression results is found in **Table 6**. At early time points, anterograde velocity had a strong influence on net velocity (Day 1: 0.431; Day 3: 0.474), with additional contributions from directional durations (Day 1 total duration: 0.537; Day 1 retrograde duration: -0.595; Day 3 anterograde duration: 0.474). At later stages, irrespective of ascorbic acid treatment, directional (anterograde) duration continued to contribute most strongly to net velocity (Day 7 AA: 0.630; Day 7 no AA: 0.925). Though the effect of anterograde velocity was sharply diminished, average velocity also contributed strongly to the model (AA: 0.525; No AA: 0.480). Thus, under the assumption that each parameter is modulated, at least partially, by a different set of biological influences, these results suggest that regulation of ribosomal transport in Schwann cells evolves temporally, but is not influenced by early myelination.

Ribosomal Transport Model

A limitation of the narrow temporal window during which transport was assessed as well as a finer understanding of factors underlying outcomes from multiple regression analysis was an inability to examine directional transitions in particle movement. Thus, we developed a simple yet informative kinetic model, driven and validated by our experimental data, which was captured over a time frame of minutes, on net transport, which was measured over a time frame of days (**Figure 7**). The model determined a set of rate constants that best fit experimental parameters for net velocity and the number of anterograde and retrograde particles, based on computed mean squared error (**Table 3**). Numerical solution of the system of differential equations was stable. Model fits were extremely strong (No AA: MSE = 0.4037; AA: MSE = 0.0042), and were unique within the wide range of allowed parameter values. Sensitivity analysis was also performed for each rate constant over this range of values

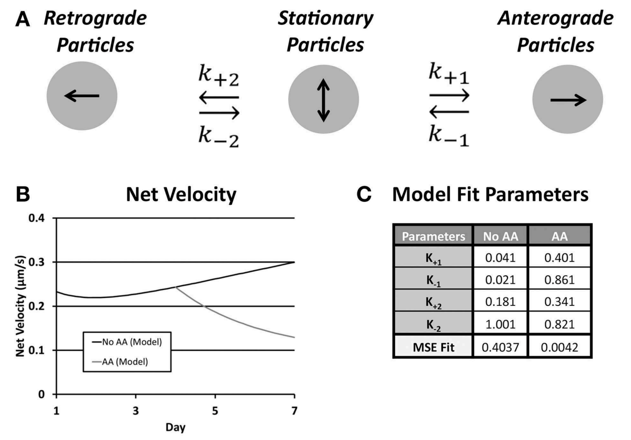

Parameters	No AA	AA
K_{+1}	0.041	0.401
K_{-1}	0.021	0.861
K_{+2}	0.181	0.341
K_{-2}	1.001	0.821
MSE Fit	0.4037	0.0042

FIGURE 7 | (A) Schematic of the rate kinetic model shows possible particle states and transition rate constants between the three states; **(B)** Plot of net velocity from optimized model output; **(C)** Following ascorbic acid treatment the rate of conversion from anterograde to stationary (k_{-1}) as did the conversion rate from stationary to both anterograde (k_{+1}) and retrograde (k_{+2}) increased resulting in an overall reduction in net velocity. MSE fit agreement was strong in both treatment groups.

(**Supplemental Figure 1**), and revealed that the model was most sensitive to changes in k_{+1} followed by k_{+2}.

The transition of rate constants upon addition of ascorbic acid provided information about the shift in ribosomal transport during onset of myelination. In both cases the rate of conversion from stationary to anterograde particles increased (k_{+1}, No AA: 0.041; AA: 0.181). This was accompanied by an even greater increase in the rate of conversion of anterograde particles to stationary (k_{-1}, No AA: 0.021; AA: 0.861). This caused an inversion of the ratio of the rate constants shifting the preference of particles in this state toward the stationary population. Similarly, there was an increase in the rate of particles converting from stationary to retrograde (k_{+2}, No AA: 0.181; AA: 0.341). Combined with the decrease in the rate of conversion form stationary (k_{-2}, No AA: 1.001; AA: 0.821) increased the favorability of the retrograde position following ascorbic acid treatment. This led to a decrease in anterograde particles and an increase in retrograde particles resulting in a decreased net velocity observed within the model. Cumulatively, these results suggest that the increases in k_{-1} and k_{+2} are the likely drivers of decreased anterograde and increased retrograde particle number, as well as, decreased net velocity following induction of myelination.

Discussion

The localization, dynamics, and activity of protein synthetic machinery have received increased attention in neurons (Gould and Mattingly, 1990; DiStefano et al., 1992; Morris and Hollenbeck, 1995; Twiss and van Minnen, 2006; Pathak et al., 2013), motivated in large part by the demands imposed by neuronal polarity and geometry. Local protein synthesis has been less extensively studied in Schwann cells, though they also extend long projections, and thus also face similar metabolic, structural, and biochemical demands (Jacobs and Cavanagh, 1969; Colman et al., 1982; Gould and Mattingly, 1990). Additionally, recent evidence has suggested that Schwann cells are a source of mRNA and ribosomes for neurons recovering from injury, providing additional rationale for localizing protein synthetic machinery to SC projections (Court et al., 2008, 2011).

This study used a combined experimental and theoretical approach to examine the localization and movement of ribosomes within the projections of Schwann cells at high resolution. While several important studies have documented the presence of mRNA and ribosomes in SC projections (Colman et al., 1982; Trapp et al., 1987, 1988; Griffiths et al., 1989; Gould and Mattingly, 1990), the development and plasticity of ribosomal populations locally remain unknown. Our overall hypothesis was that local populations would be developed early during projection extension to enable projection outgrowth. However, such populations would then require supplementation, both for maintenance, given the ∼40 h half-life of ribosomes (Weber, 1972), as well as to sustain increased interactions with neurons, which may be stably myelinated for years (Elson et al., 2004). Our results support our original hypothesis of anterograde transport of ribosomes developing ribosomal populations in the projections of Schwann cells during initial projection elongation. In early phases of myelination, ribosome trafficking decreases slightly as expected, in line with a shift toward a maintenance regime.

Stable Ribosomal Populations

Localization patterns of L4-GFP in projections of transfected Schwann cells showed strong agreement with the localization patterns of immunolabeled L4. Two characteristics, seen both in transfected cells and immuno-labeled cells, are of particular note. First, similar to MBP mRNA distributions described previously (Trapp et al., 1987, 1988; Gould and Mattingly, 1990), there was a level of punctate ribosomal expression throughout the projection. It is possible that these ribosomes are associated with RNA granules of varying size and function, as suggested for oligodendrocytes (Thomas et al., 2005). Second, there were 2–3 stable peaks of high fluorescence intensity within each Schwann cell projection, likely pointing to locations of ribosomal clustering. These peaks were apparent upon initial projection extension on day 1 and persist throughout the 7 days of observation both in the presence and absence of ascorbic acid. This pattern too is similar to MBP mRNA densities within SC projections (Gould and Mattingly, 1990). Future studies will reveal whether ribosomal densities synthesize proteins for stages of myelination or participate in ribosomal transfer to neurons (Gould and Mattingly, 1990; Court et al., 2008) at structures yet to be formed. For instance, Schmidt-Lanterman incisures have been suggested as the region of ribosomal transfer following injury and occur at similarly spaced intervals (∼25–30 µm) (Buchthal et al., 1987) as the observed ribosomal clusters (Buchthal et al., 1987; Court et al., 2008). Interestingly, while protein synthesis does not appear to extend into the Schmidt-Lanterman incisures there does seem to be significant ribosomal localization to the surface network in the region adjacent the incisures (Gould and Mattingly, 1990).

To probe a possible structural basis for observed ribosomal densities, cells were co-labeled for RPL4 and cytoskeletal components. In neurons, ribosomal clusters (periaxoplasmic ribosomal plaques) are observed within axons and cluster around regions enriched in F-actin (Koenig and Martin, 1996). Similarly, Schmidt-Lanterman incisures are enriched in F-actin (Trapp et al., 1989; Court et al., 2008, 2011) However, co-labeling of ribosomal subunits with F-actin and tubulin failed to display any obvious co-localization with ribosomal clusters (**Figure 4**). On the other hand, it is possible that a specific set of actin- or tubulin-associated proteins rather than the filaments themselves may play a role in docking or sequestering ribosomes (Wilhelm and Vale, 1993).

Ribosomal Movement

By Day 1 after neuronal contact, newly synthesized ribosomes containing L4-GFP were already distributed throughout Schwann cell projections. Additionally, distributions revealed minimal changes between Day 1 and Day 7, in the presence or absence of ascorbic acid. Though it was somewhat surprising that ribosomal densities were stabilized so rapidly, also of interest was the activity of more dynamic populations of directionally moving ribosomes observed using time-lapse microscopy. Kymograph analysis, which captured ribosomal transport characteristics at each experimental time point at high resolution, enabled us to quantify and compare transport parameters in greater detail.

Individual transport parameters were integrated into an estimate of net movement (net velocity) of ribosomal populations, which served as a rough surrogate for ribosomal demand at a given stage of growth or myelination. The nucleus was the source of newly synthesized fluorescent ribosomal subunits, and as such explains the net anterograde velocities for each experimental group. Bulk rates were ∼0.1–0.3 μm/s (∼8–25 mm/day), which corresponds to an intermediate rate of transport in a neuron (Brown, 2000). Interestingly, at early time points, the net velocity remained quite stable, but diverged at Day 7, dependent upon ascorbic acid treatment; ascorbic acid treatment led to an overall reduction in net anterograde velocity, whereas the absence of ascorbic acid led to an increase.

The cellular processes driving reduced net velocity in the presence of ascorbic acid are mostly unexplored. Reduced ribosomal demand may simply represent a more focused diversion of translational machinery to the myelination process (Lemke and Chao, 1988). On the other hand, several Schwann cell activities appear to be coupled to early stages of SC-neuron contact and myelination. Structurally, neuronal contact alters the nucleation, polarity, and distribution of microtubules within myelinating Schwann cells (Kidd et al., 1994). In addition, consistent with reduced cellular extension and crawling during neuronal interactions, mobility of Schwann cell membranes and their associated cytoskeleton is reduced and adhesion is enhanced (Feltri et al., 1994; Nobes and Hall, 1999; Love et al., 2012). Alternatively, cell morphological changes may reflect a redistribution or change in the stability of microtubules, which may result from Schwann cell differentiation and maturation. It is not inconceivable that such structural changes during early stages of Schwann cell differentiation and myelination could influence the directionality, duration, and overall levels of ribosomal transport. Indeed, initiation of myelination in regenerating nerves results in altered expression and distribution of several genes and proteins in Schwann cells, including neurofilaments (Fabrizi et al., 1997), TGF-beta (Scherer et al., 1993), P0 glycoprotein (LeBlanc et al., 1992), and ion channels (Chiu et al., 1994).

While there are drastic changes in net velocity with the initiation of myelination, the average anterograde and retrograde velocities did not change, suggesting that the regulation of molecular motor activity is changed, not the responsible motors themselves. While it is unclear which motors are responsible for ribosomal transport in Schwann cells, in other cellular systems the distribution of ribosomes depends on early endosome trafficking of both kinesin-3 and dynein (Higuchi et al., 2014; Palacios, 2014). Parameters that might change include binding affinities, number of available motor proteins, and initiation of transport all of which would affect net velocity but not the individual components of velocity (Lipowsky et al., 2010). The observed decrease in net ribosomal trafficking is attributable to increased levels of retrograde moving particles as well as a reduction in anterograde particles. The increase in retrograde particles at Day 7, for both ascorbic acid-treated and untreated cells, are perhaps due to ribosomal recycling (Lafontaine, 2010). The reduction in anterograde transport may reflect increased demand for protein synthesis, which we speculate occurs in stationary ribosomes docked on structures such as those discussed above. Despite this reduction in anterograde movement, the fact that the net velocity remains positive at these times suggests that ribosomes are required in the periphery on an ongoing basis, perhaps to maintain and replenish the stable ribosomal pools.

Theoretical Modeling of Ribosomal Transport

To further understand differences in transport, we used our high-resolution assessment of transport to develop and validate a simple, yet powerful, data-driven rate kinetic model of ribosomal transport. This model was particularly effective at describing the transfer of particles from one movement state (stationary, anterograde, or retrograde) to another, providing insight into underlying transport dynamics not amenable to other types of analyses.

For example, population analysis indicated that both anterograde and retrograde populations decreased, and as a consequence, the magnitude of net velocity was also reduced. Our model enabled us to assess whether these reductions in anterograde and retrograde populations resulted from increased transition from moving to stationary particles, decreased transition from stationary to moving particles, or both. For our case, the model revealed an increased rate of conversion from anterograde to stationary (higher k_{-1}), an increased rate of conversion from stationary to retrograde (higher k_{+2}), and a slightly lower rate of conversion from retrograde to stationary (lower k_{-2}) upon addition of ascorbic acid. These three changes thus drove the observed reduction in anterograde movement and net velocity.

The model also raises hypotheses about different mechanisms for the decrease in both anterograde and retrograde populations. The increased conversion of anterograde particles to stationary may be resultant of myelin compaction and other restrictions on transport within the projection compartment. The increased recruitment of retrograde particles may result from a decreased demand for local ribosomes due to their very specialized functions in the myelination process. Such possibilities may be considered and tested in future experiments.

Despite the unique solution provided by the model the simplicity of the model possesses some limitations based on experimental observations and procedures. This includes the lack of time points for the model fit for ascorbic acid due to the differential fit of these cultures at earlier time points when ascorbic acid was lacking. Additionally, omitted from the model was the ability of particles to transfer directly from anterograde to retrograde. This was done because in the time scale of the imaging (5 s) we did not observe any particles that directly transitioned. Rather they would become stationary for a short period of at least 15 s before transitioning between states. Finally, it is worth comparing our modeling approach to a number of other excellent theoretical models of intracellular transport. Such models differ in a variety of features, including the identity of cargoes modeled (e.g., a single generic cargo vs. populations of specific cargoes), motor configurations on a given cargo, details on mechanisms by which cargoes move, stop, or change their direction, and the modeling strategy itself (Badoual et al., 2002; O'Toole et al., 2008; Lipowsky et al., 2010; Bressloff and Newby, 2013; Gumy et al., 2014). These models also span a variety of temporal and spatial scales. Our model, based on the original rate kinetics framework of Smith and Simmons (Smith and Simmons, 2001; Kuznetsov, 2010; Zadeh and Shah, 2010), exploited experimental measurements in single cargoes to answer questions related to the transition of directional bulk cargo populations. In this context, there were minimal effects of spatial gradients and diffusion on ribosomal distribution within our time scale of interest. Experimentally, visible fluorescent puncta did not move in a manner consistent with diffusion [i.e., runs were directional for >15 s, and thus attributed to motor-driven movement (convection)]. Also, background fluorescence, likely representing soluble ribosomal subunits, remained evenly distributed through the imaged regions of the axon during imaging. Thus, in light of the absence of any experimental evidence, diffusion did not contribute appreciably to the model, and was ignored. Similarly, no gradients in any transport parameter were detectable along the length of the projection (possibly due to the low number of moving particles along each projection), and thus were also not factored into our final model.

Conclusions and Future Directions

This study provides a first quantitative look into the establishment of ribosomal populations within Schwann cells following neuronal contact and myelination, and transport changes associated with a hypothesized change in demand for a local protein synthesis source. While others have shown that proteins are synthesized locally in Schwann cell projections and are required for myelination, we are the first to observe, quantify, and model the process dynamics during early development and myelination. The observed ribosomal transport decrease into the Schwann cell projection is likely tied to a decrease in demand for protein synthesis. However, many questions remain to be answered about how and why such dynamics occur, including which motor proteins are at work, the effect of early and late myelination on local protein synthesis, and the role, if any, early ribosomal localization may have on the proposed process of transcytosis(Court et al., 2008). Our initial findings open the possibility for a number of future studies that might be integral in developing translational clinical solutions for nervous system disease and injury.

Acknowledgments

We gratefully acknowledge funding support from the Alzheimer's Association (NIRG09133270) and National Science Foundation (CBET-0932590). We also acknowledge helpful conversations with members of the Neuromuscular Bioengineering Laboratory.

Supplementary Material

The Supplementary Material for this article can be found online at: http://journal.frontiersin.org/article/10.3389/fncel.2015.00306

Supplemental Figure 1 | Model traces for varying rate constants show degree of sensitivity for the unique solution. No AA groups were highly sensitive to forward rate constants, k_{+1} **(A)** and k_{+2} **(C)**, yet slightly less sensitive to variations in reverse rate constants, k_{-1} **(B)** and k_{-2} **(D)**. Similar results held for parameter variations in the AA treated model with higher sensitivity to changes in both forward rate constants, k_{+1} **(E)** and k_{+2} **(G)**, and lower sensitivity to the changes in the reverse rates, k_{-1} **(F)** and k_{-2} **(H).**

References

Badoual, M., Jülicher, F., and Prost, J. (2002). Bidirectional cooperative motion of molecular motors. *Proc. Natl. Acad. Sci. U.S.A.* 99, 6696–6701. doi: 10.1073/pnas.102692399

Bolte, S., and Cordèlieres, F. P. (2006). A guided tour into subcellular colocalization analysis in light microscopy. *J. Microsc.* 224(Pt 3), 213–232. doi: 10.1111/j.1365-2818.2006.01706.x

Bressloff, P. C., and Newby, J. M. (2013). Stochastic models of intracellular transport. *Rev. Mod. Phys.* 85, 135–196. doi: 10.1103/RevModPhys.85.135

Brophy, P. J., Boccaccio, G. L., and Colman, D. R. (1993). The distribution of myelin basic protein mRNAs within myelinating oligodendrocytes. *Trends Neurosci.* 16, 515–521. doi: 10.1016/0166-2236(93)90196-S

Brown, A. (2000). Slow axonal transport: stop and go traffic in the axon. *Nat. Rev. Mol. Cell Biol.* 1, 153–156. doi: 10.1038/35040102

Bryan, D. J., Holway, A. H., Wang, K. K., Silva, A. E., Trantolo, D. J., Wise, D., et al. (2000). Influence of glial growth factor and Schwann cells in a bioresorbable guidance channel on peripheral nerve regeneration. *Tissue Eng.* 6, 129–138. doi: 10.1089/107632700320757

Buchthal, F., Carlsen, F., and Behse, F. (1987). Schmidt-Lanterman clefts: a morphometric study in human sural nerve. *Am. J. Anat.* 180, 156–160. doi: 10.1002/aja.1001800205

Caro, L. G., and Palade, G. E. (1964). Protein synthesis, storage, and discharge in the pancreatic exocrine cell. An autoradiographic study. *J. Cell Biol.* 20, 473–495. doi: 10.1083/jcb.20.3.473

Chetta, J., and Shah, S. B. (2011). A novel algorithm to generate kymographs from dynamic axons for the quantitative analysis of axonal transport. *J. Neurosci. Methods* 199, 230–240. doi: 10.1016/j.jneumeth.2011.05.013

Chiu, S. Y., Scherer, S. S., Blonski, M., Kang, S. S., and Messing, A. (1994). Axons regulate the expression of Shaker-like potassium channel genes in Schwann cells in peripheral nerve. *Glia* 12, 1–11. doi: 10.1002/glia.440120102

Colman, D. R., Kreibich, G., Frey, A. B., and Sabatini, D. D. (1982). Synthesis and incorporation of myelin polypeptides into CNS myelin. *J. Cell Biol.* 95(2 Pt 1), 598–608. doi: 10.1083/jcb.95.2.598

Court, F. A., Hendriks, W. T., MacGillavry, H. D., Alvarez, J., and van Minnen, J. (2008). Schwann cell to axon transfer of ribosomes: toward a novel understanding of the role of glia in the nervous system. *J. Neurosci.* 28, 11024–11029. doi: 10.1523/JNEUROSCI.2429-08.2008

Court, F. A., Midha, R., Cisterna, B. A., Grochmal, J., Shakhbazau, A., Hendriks, W. T., et al. (2011). Morphological evidence for a transport of ribosomes from Schwann cells to regenerating axons. *Glia* 59, 1529–1539. doi: 10.1002/glia.21196

DiStefano, P. S., Friedman, B., Radziejewski, C., Alexander, C., Boland, P., Schick, C. M., et al. (1992). The neurotrophins BDNF, NT-3, and NGF display distinct patterns of retrograde axonal transport in peripheral and central neurons. *Neuron* 8, 983–993. doi: 10.1016/0896-6273(92)90213-W

Eldridge, C. F., Bunge, M. B., Bunge, R. P., and Wood, P. M. (1987). Differentiation of axon-related Schwann cells *in vitro*. I. Ascorbic acid regulates basal lamina assembly and myelin formation. *J. Cell Biol.* 105, 1023–1034. doi: 10.1083/jcb.105.2.1023

Elson, K., Ribeiro, R. M., Perelson, A. S., Simmons, A., and Speck, P. (2004). The life span of ganglionic glia in murine sensory ganglia estimated by uptake of bromodeoxyuridine. *Exp. Neurol.* 186, 99–103. doi: 10.1016/j.expneurol.2003.10.017

Fabrizi, C., Kelly, B. M., Gillespie, C. S., Schlaepfer, W. W., Scherer, S. S., and Brophy, P. J. (1997). Transient expression of the neurofilament proteins NF-L and NF-M by Schwann cells is regulated by axonal contact. *J. Neurosci. Res.* 50, 291–299.

Feltri, M. L., Scherer, S. S., Nemni, R., Kamholz, J., Vogelbacker, H., Scott, M. O., et al. (1994). Beta 4 integrin expression in myelinating Schwann cells is polarized, developmentally regulated and axonally dependent. *Development* 120, 1287–1301.

Ganoza, M. C., and Williams, C. A. (1969). *In vitro* synthesis of different categories of specific protein by membrane-bound and free ribosomes. *Proc. Natl. Acad. Sci. U.S.A.* 63, 1370–1376. doi: 10.1073/pnas.63.4.1370

Gould, R. M., and Mattingly, G. (1990). Regional localization of RNA and protein metabolism in Schwann cells *in vivo*. *J. Neurocytol.* 19, 285–301. doi: 10.1007/BF01188399

Griffiths, I. R., Mitchell, L. S., McPhilemy, K., Morrison, S., Kyriakides, E., and Barrie, J. A. (1989). Expression of myelin protein genes in Schwann cells. *J. Neurocytol.* 18, 345–352. doi: 10.1007/BF01190837

Gumy, L. F., Katrukha, E. A., Kapitein, L. C., and Hoogenraad, C. C. (2014). New insights into mRNA trafficking in axons. *Dev. Neurobiol.* 74, 233–244. doi: 10.1002/dneu.22121

Higuchi, Y., Ashwin, P., Roger, Y., and Steinberg, G. (2014). Early endosome motility spatially organizes polysome distribution. *J. Cell Biol.* 204, 343–357. doi: 10.1083/jcb.201307164

Jacobs, J. M., and Cavanagh, J. B. (1969). Species differences in internode formation following two types of peripheral nerve injury. *J. Anat.* 105(Pt 2), 295–306.

Jamieson, J. D., and Palade, G. E. (1967). Intracellular transport of secretory proteins in the pancreatic exocrine cell. II. Transport to condensing vacuoles and zymogen granules. *J. Cell Biol.* 34, 597–615. doi: 10.1083/jcb.34.2.597

Kidd, G. J., Andrews, S. B., and Trapp, B. D. (1994). Organization of microtubules in myelinating Schwann cells. *J. Neurocytol.* 23, 801–810. doi: 10.1007/BF01268092

Koenig, E., and Martin, R. (1996). Cortical plaque-like structures identify ribosome-containing domains in the Mauthner cell axon. *J. Neurosci.* 16, 1400–1411.

Krüger, T., Zentgraf, H., and Scheer, U. (2007). Intranucleolar sites of ribosome biogenesis defined by the localization of early binding ribosomal proteins. *J. Cell Biol.* 177, 573–578. doi: 10.1083/jcb.200612048

Kuznetsov, A. V. (2010). Comparison of active transport in neuronal axons and dendrites. *Math. Biosci.* 228, 195–202. doi: 10.1016/j.mbs.2010.10.003

Lafontaine, D. L. (2010). A 'garbage can' for ribosomes: how eukaryotes degrade their ribosomes. *Trends Biochem. Sci.* 35, 267–277. doi: 10.1016/j.tibs.2009.12.006

Leader, D. P. (1979). Protein-biosynthesis on membrane-bound ribosomes. *Trends Biochem. Sci.* 4, 205–208. doi: 10.1016/0968-0004(79)90081-1

LeBlanc, A. C., Windebank, A. J., and Poduslo, J. F. (1992). P0 gene expression in Schwann cells is modulated by an increase of cAMP which is dependent on the presence of axons. *Brain Res. Mol. Brain Res.* 12, 31–38. doi: 10.1016/0169-328X(92)90065-J

Lee, D. A., Zurawel, R. H., and Windebank, A. J. (1995). Ciliary neurotrophic factor expression in schwann-cells is induced by axonal contact. *J. Neurochem.* 65, 564–568. doi: 10.1046/j.1471-4159.1995.65020564.x

Lemke, G., and Chao, M. (1988). Axons regulate schwann-cell expression of the major myelin and Ngf receptor genes. *Development* 102, 499–504.

Lipowsky, R., Beeg, J., Dimova, R., Klumpp, S., and Muller, M. J. I. (2010). Cooperative behavior of molecular motors: Cargo transport and traffic phenomena. *Physica E* 42, 649–661. doi: 10.1016/j.physe.2009.08.010

Love, J. M., Pathak, G. K., Chetta, J., and Shah, S. B. (2012). Variability in membrane continuity between schwann cells and neurons. *Cell. Mol. Bioeng.* 5, 450–462. doi: 10.1007/s12195-012-0250-y

Manders, E. M., Stap, J., Brakenhoff, G. J., van Driel, R., and Aten, J. A. (1992). Dynamics of three-dimensional replication patterns during the S-phase, analysed by double labelling of DNA and confocal microscopy. *J. Cell Sci.*103(Pt 3), 857–862.

Morris, R. L., and Hollenbeck, P. J. (1995). Axonal transport of mitochondria along microtubules and F-actin in living vertebrate neurons. *J. Cell Biol.* 131, 1315–1326. doi: 10.1083/jcb.131.5.1315

Nobes, C. D., and Hall, A. (1999). Rho GTPases control polarity, protrusion, and adhesion during cell movement. *J. Cell Biol.* 144, 1235–1244. doi: 10.1083/jcb.144.6.1235

O'Toole, M., Latham, R., Baqri, R. M., and Miller, K. E. (2008). Modeling mitochondrial dynamics during *in vivo* axonal elongation. *J. Theor. Biol.* 255, 369–377. doi: 10.1016/j.jtbi.2008.09.009

Palacios, I. M. (2014). Hop-on hop-off: polysomes take a tour of the cell on endosomes. *J. Cell Biol.* 204, 287–289. doi: 10.1083/jcb.201401019

Pathak, G. K., Love, J. M., Chetta, J., and Shah, S. B. (2013). A comparative quantitative assessment of axonal and dendritic mRNA transport in maturing hippocampal neurons. *PLoS ONE* 8:e65917. doi: 10.1371/journal.pone.0065917

Pedraza, L., and Colman, D. R. (2000). Fluorescent myelin proteins provide new tools to study the myelination process. *J. Neurosci. Res.* 60, 697–703. doi: 10.1002/1097-4547(20000615)60:6<697::AID-JNR1>3.0.CO;2-U

Scherer, S. S., Kamholz, J., and Jakowlew, S. B. (1993). Axons modulate the expression of transforming growth factor-betas in Schwann cells. *Glia* 8, 265–276. doi: 10.1002/glia.440080407

Smith, D. A., and Simmons, R. M. (2001). Models of motor-assisted transport of intracellular particles. *Biophys. J.* 80, 45–68. doi: 10.1016/S0006-3495(01)75994-2

Son, Y. J., and Thompson, W. J. (1995). Schwann cell processes guide regeneration of peripheral axons. *Neuron* 14, 125–132. doi: 10.1016/0896-6273(95)90246-5

Thomas, M. G., Tosar, L. J. M., Loschi, M., Pasquini, J. M., Correale, J., Kindler, S., et al. (2005). Staufen recruitment into stress granules does not affect early mRNA transport in oligodendrocytes. *Mol. Biol. Cell* 16, 405–420. doi: 10.1091/mbc.E04-06-0516

Trapp, B. D., Andrews, S. B., Wong, A., O'Connell, M., and Griffin, J. W. (1989). Co-localization of the myelin-associated glycoprotein and the microfilament components, F-actin and spectrin, in Schwann cells of myelinated nerve fibres. *J. Neurocytol.* 18, 47–60. doi: 10.1007/BF01188423

Trapp, B. D., Hauer, P., and Lemke, G. (1988). Axonal regulation of myelin protein mRNA levels in actively myelinating Schwann cells. *J. Neurosci.* 8, 3515–3521.

Trapp, B. D., Moench, T., Pulley, M., Barbosa, E., Tennekoon, G., and Griffin, J. (1987). Spatial segregation of mRNA encoding myelin-specific proteins. *Proc. Natl. Acad. Sci. U.S.A.* 84, 7773–7777. doi: 10.1073/pnas.84.21.7773

Twiss, J. L., and van Minnen, J. (2006). New insights into neuronal regeneration: the role of axonal protein synthesis in pathfinding and axonal extension. *J. Neurotrauma* 23, 295–308. doi: 10.1089/neu.2006.23.295

Waxman, S. G., and Bennett, M. V. (1972). Relative conduction velocities of small myelinated and non-myelinated fibres in the central nervous system. *Nat. New Biol.* 238, 217–219. doi: 10.1038/newbio238217a0

Weber, M. J. (1972). Ribosomal RNA turnover in contact inhibited cells. *Nat. New Biol.* 235, 58–61. doi: 10.1038/newbio235058a0

Wilhelm, J. E., and Vale, R. D. (1993). RNA on the move: the mRNA localization pathway. *J. Cell Biol.* 123, 269–274. doi: 10.1083/jcb.123.2.269

Zadeh, K. S., and Shah, S. B. (2010). Mathematical modeling and parameter estimation of axonal cargo transport. *J. Comput. Neurosci.* 28, 495–507. doi: 10.1007/s10827-010-0232-9

Conflict of Interest Statement: The authors declare that the research was conducted in the absence of any commercial or financial relationships that could be construed as a potential conflict of interest.

frontiers
in Cellular Neuroscience

ORIGINAL RESEARCH
published: 21 July 2015
doi: 10.3389/fncel.2015.00281

A frequency-dependent decoding mechanism for axonal length sensing

Paul C. Bressloff* **and Bhargav R. Karamched**

Department of Mathematics, University of Utah, Salt Lake City, UT, USA

We have recently developed a mathematical model of axonal length sensing in which a system of delay differential equations describe a chemical signaling network. We showed that chemical oscillations emerge due to delayed negative feedback via a Hopf bifurcation, resulting in a frequency that is a monotonically decreasing function of axonal length. In this paper, we explore how frequency-encoding of axonal length can be decoded by a frequency-modulated gene network. If the protein output were thresholded, then this could provide a mechanism for axonal length control. We analyze the robustness of such a mechanism in the presence of intrinsic noise due to finite copy numbers within the gene network.

Keywords: axonal length control, biochemical oscillations, frequency decoding, gene network, protein thresholds, intrinsic noise

Edited by:
Kyle Miller,
Michigan State University, USA

Reviewed by:
Bruce Graham,
University of Stirling, UK
Matthew Ryan O'Toole,
Kettering University, USA

***Correspondence:**
Paul C. Bressloff,
Department of Mathematics,
University of Utah, 155 South 1400
East, Salt Lake City, UT 84112, USA
bressloff@math.utah.edu

Received: *29 April 2015*
Accepted: *10 July 2015*
Published: *21 July 2015*

Citation:
Bressloff PC and Karamched BR (2015) A frequency-dependent decoding mechanism for axonal length sensing.
Front. Cell. Neurosci. 9:281.
doi: 10.3389/fncel.2015.00281

1. Introduction

Size homeostasis is fundamental to cell biology. The ability of a cell to assess its own size or length allows for proper regulation of biochemical processes to meet physiological requirements. Several mechanisms by which cells determine the sizes of subcellular structures have been identified. Some examples include molecular rulers, quantal synthesis, and dynamic balance (Marshall, 2004). The roles that such mechanisms play for relatively small cells in sensing size have been delineated, but it is largely unclear how large cells are able to accomplish this. The problem is particularly acute for neurons, which, in addition to being large cells, exhibit the most variety in cellular size, ranging from a micron to a meter in length in humans.

It is likely that different growth mechanisms act as the underlying length sensors for axons at different stages of development. The initial growth rate of an axon is determined by pre-programmed transcription factor levels (Lallemend and Ernfors, 2012), whereas the interstitial growth rates of axons that have connected to their targets are driven by by the stretching of the organism (Smith, 2009). A central question is whether or not there exists an intrinsic length sensing mechanism in axons that can coordinate between the output of transcriptional and metabolic processes controlled by the nucleus and the differential growth and maintenance needs of axons of different sizes. Theoretical analysis and *in vitro* experimental studies of axonal growth in a variety of neuronal types support the existence of intrinsic length sensors (Goslin and Banker, 1989; Samsonovich and Ascoli, 2006; Brown et al., 2008; O'Toole et al., 2008; Kam et al., 2009), but the underlying mechanisms are largely unknown. Initially, it was hypothesized that molecular diffusion was the fundamental mechanism for sensing length, but given the lengths involved, it is unlikely that diffusion is the underlying mechanism. A more tenable early hypothesis for a length sensor in axons involved the use of molecular rulers. This idea certainly solves the problem of a mechanism accounting for large amounts of growth in relatively small amounts of time; however, the sheer variability in the lengths of axons renders a molecular ruler based length sensing mechanism unfeasible.

Recently, a mechanism for axonal length sensing based on bidirectional motor transport was proposed by Rishal et al. (2012), which is distinct from the aforementioned mechanisms. A schematic illustration of the motor-based model is shown in **Figure 1**. A signal is produced at the cell body and is subsequently carried by kinesin motors to the tip of the growing axon, where it activates the production of another chemical signal. The latter is transported by dynein motors back to the cell body, where it inhibits the production of the original chemical signal via negative feedback. Once the axon grows past some critical length, the amount of inhibitory chemical signal located at the cell body begins to oscillate with a frequency that decreases as axonal length increases. If axonal growth is correlated with this frequency, then spatial information regarding length of the axon can be communicated to the cell body, where frequency-dependent activation of transcription factors could regulate axonal growth (Cai et al., 2008). Computer simulations of this mechanism provided results that are consistent with what was proposed in Rishal et al. (2012). An important prediction of these simulations is that reducing either anterograde or retrograde signals by partial knockdown of kinesin or dynein motor activity should increase axonal length. This prediction has been confirmed experimentally in peripheral sensory neurons (Rishal et al., 2012). Note that a previous model of Kam et al. (2009) is inconsistent with the experimental data. The earlier model assumes that the unidirectional transport of a retrograde signal by dynein motors maintains axonal growth until the signal at the cell body becomes too weak due to a constant rate of signal loss en route. In this case, the partial knockdown of motor activity would lead to shorter axons. Hence the experimental results provide circumstantial evidence for frequency-encoded axonal length.

Such cellular behavior has been shown to exist in the context of protein production in response to the gonadotropic releasing hormone (GnRH), which pulses at various frequencies over time (Krakauer et al., 2002). Distinct frequencies have been observed to induce the production of disparate proteins. This phenomenon was mathematically analyzed in Krakauer et al. (2002). The results suggest that cellular decoding of frequency-encoded information is possible due to the difference in time scales for gene activity and protein lifetime. Even more interestingly, it has been shown that cells are able to keep protein levels with less variability in response to a pulsatile signal as opposed to a constant signal (Tostevin et al., 2012).

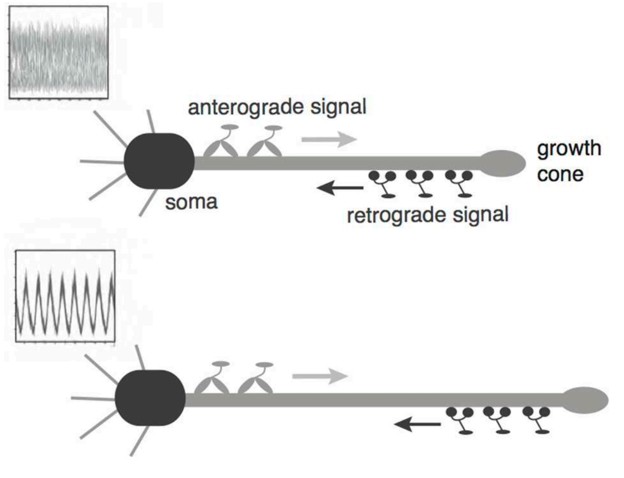

FIGURE 1 | Schematic diagram of the bidirectional motor-transport mechanism for axonal length sensing hypothesized by Rishal et al. (2012). A kinesin-based anterograde signal activates a dynein-based retrograde signal that itself represses the anterograde signal via negative feedback. The frequency of the resulting oscillatory retrograde signal decreases with axonal growth.

We have recently developed a mathematical version of the computational model given by Rishal et al. (2012), which provides analytical insights into the proposed dynamical mechanism underlying the frequency-encoding of axonal length (Karamched and Bressloff, 2015). The simplest version of the model consists of a pair of delay-differential equations that keeps track of the chemical signals at the somatic and distal ends of the axon. The dynamics of kinesin and dynein motors are not modeled explicitly; instead, their active transport is assumed to introduce a discrete delay that varies linearly with axonal length. We showed how oscillations arise at a critical axonal length via a Hopf bifurcation, and obtained a length-dependent frequency consistent with the previous computational model. In this paper we explore another major aspect of the proposed axonal length-sensing mechanism, namely, how the frequency-based information about axonal length could be decoded at the cell body. As briefly suggested by Rishal et al. (2012), one possibility is that that the frequency-dependent signal could modulate the nuclear import of a transcription factor and thus coordinate the regulation of gene expression. Although the frequency-dependent modulation of gene expression has been observed in yeast (Cai et al., 2008), for example, the role of such a mechanism in axonal length-sensing is currently unknown. Indeed, there is only indirect evidence for the frequency-encoding mechanism itself (Rishal et al., 2012). However, this is precisely a situation where mathematical modeling can play a role, namely, in exploring the consequences of a hypothesized model. Indeed, in our previous work we showed that when the stochastic nature of motor transport is taken into account, there may be a deterioration in the accuracy of the length-encoding mechanism in the case of long axons. In this paper we show that an analogous problem may occur for the length-decoding mechanism when the intrinsic noise of a gene network is included.

In order to develop the basic theory, we feed the oscillating retrograde signal from the delayed feedback model into a simple feedforward gene network. Following along similar lines to Krakauer et al. (2002), we show how even a simple gene network can convert a frequency code to an amplitude code, resulting in a mean protein output that is a monotonically decreasing function of axonal length. If the protein output were thresholded, then this could provide a mechanism for axonal length control, under the assumption that when the protein output falls below threshold, this activates or inactivates another gene circuit that plays a crucial role in axonal growth. Analogous thresholding mechanisms have been investigated within the context of intracellular protein concentration gradients, which are used to determine spatial position within a cell so that, for example, cell division occurs at the appropriate time and location (Tostevin et al., 2007; Tostevin, 2011). Similarly, developmental morphogen gradients control patterns of gene expression so that each stage of cell differentiation occurs at the correct spatial location within an embryo. For biological effectiveness, these gradient-based mechanisms must be robust to intrinsic and extrinsic cellular noise (Tostevin, 2011; Howard, 2012). The main aim of our paper is to demonstrate how the issue of robustness to noise carries over to the proposed frequency decoding mechanism and, hence, that it can be analyzed along similar lines to protein concentration gradients. The structure of the paper is as follows. In Section 2 we briefly review our previous delayed-feedback model for the frequency-based encoding of axonal length and then show how the frequency can be decoded by a simple feedforward gene network. In Section 3 we consider a stochastic version of the gene network and estimate the variance in the protein output concentration along the lines of Tostevin et al. (2012). For completeness, we fill in the details of the calculations whose results were quoted in Tostevin et al. (2012). It should also be noted that these authors focused on comparing the variance in protein output when the input signal is oscillatory with the corresponding variance for constant inputs, establishing that the former is smaller. Here we are interested in the effects of intrinsic noise on frequency decoding itself.

2. Model

2.1. Delayed Feedback Model of Frequency Encoding

We begin by briefly reviewing the delayed feedback model presented in Karamched and Bressloff (2015). Consider an axon of length L with $x = 0$ corresponding to the proximal end (adjacent to the cell body or soma) and $x = L$ corresponding to the distal end (axonal tip). Let $u_E(t)$ represent the anterograde chemical signal at $x = L$ at time t. This is the excitatory chemical from the mechanism proposed by Rishal et al. (2012), which is produced at the proximal end and carried by kinesin motors to the distal end. Similarly, let $u_I(t)$ represent the retrograde signal at $x = 0$ at time t, which is transported from the distal end by dynein motors. We assume the simplest possible model of active transport, where both types of motors travel at a constant speed v along the axon. (Elsewhere we explicitly model the stochastic dynamics of molecular motor transport using a system of advection-diffusion equations, see Karamched and Bressloff, 2015). This assumption means that for a given axonal length L, there is a delay $\tau \equiv L/v$ between the production of a chemical signal at one end and its arrival at the opposite end. Finally, exploiting the fact that axonal growth occurs on a much slower time scale than that of motor transport, we treat L as fixed and investigate the occurrence of chemical oscillations for a given delay. This then determines a relationship between the frequency of the retrograde signal's oscillation and axonal length. More explicitly, the delayed feedback model takes the form Karamched and Bressloff (2015).

$$\frac{du_E}{dt} = I_0 - \gamma u_E - W_I f[u_I(t-\tau)], \tag{1}$$

$$\frac{du_I}{dt} = -\gamma u_I + W_E f[u_E(t-\tau)], \tag{2}$$

with γ decay rate. For simplicity, we take γ to be equal for both chemical signals. The weights W_E and W_I represent the strengths of the positive and negative feedback terms, respectively, based on some form of Michaelis-Menten kinetics. The function f can therefore be any monotonically increasing function that saturates to some finite value at infinity. For concreteness, we take f to be a Hill function

$$f[u] = \frac{u^n}{K^n + u^n}, \tag{3}$$

with dissociation constant K and Hill coefficient n. The input I_0 represents the constant rate at which the proximal chemical signal is produced in the absence of any negative feedback ($W_I = 0$). In Karamched and Bressloff (2015) we took $n = 4$ and fixed the scale of the weights W_E, W_I and input I_0 by setting $K = 2$. In order to coincide with the results of Rishal et al. (2012) we also set $\gamma^{-1} = 100$ sec. Since motor velocities are of order 1 μm/s, it follows that setting $\tau\gamma = 1$ corresponds to an axonal length of 100 μm. (In the following we fix the units of time by setting $\gamma = 1$).

In Karamched and Bressloff (2015) we carried out a linear stability analysis of Equations (1) and (2) and derived the following Hopf bifurcation conditions (Karamched and Bressloff, 2015):

$$\omega = \cot(\omega\tau), \qquad \sqrt{\alpha_E\alpha_I}\sin(\omega\tau) = 1, \tag{4}$$

where ω denotes the frequency of the periodic solution and $\alpha_P \equiv W_P f'[u_P^*]$ for $P = E, I$ and u_P^* the steady state of the corresponding chemical signal. We immediately notice two facts from Equation (4). First, if $\tau = 0$, then the bifurcation conditions cannot be satisfied, suggesting that there exists a critical delay τ_c past which Equations (1) and (2) have periodic solutions. This corresponds with the existence of some critical axonal length L_c past which signals will oscillate. Second, the bifurcation conditions can only be satisfied if $\sqrt{\alpha_E\alpha_I} > 1$. It follows that the feedback strengths W_P must be sufficiently large and/or the Hill function must be sufficiently steep. The latter implies that oscillations are facilitated if the chemical signal interactions are cooperative in nature, as reflected by the value of n in the delayed feedback model. The existence of the Hopf bifurcation point does not in itself guarantee the onset of stable limit cycles for $\tau > \tau_c$. However, this can be verified numerically, and one finds that the frequency of the oscillation beyond the bifurcation point is a monotonically decreasing function of L, see **Figure 2**.

In conclusion, the above delayed feedback model makes explicit the role of negative feedback in the frequency encoding mechanism for axonal length sensing. (The same basic mechanism also holds for our more detailed advection-diffusion model, Karamched and Bressloff, 2015). We now turn to a possible mechanism for decoding the frequency of the oscillatory retrograde signal, and thus recovering the axonal length. To that end, we will feed the retrograde signal from our model into a

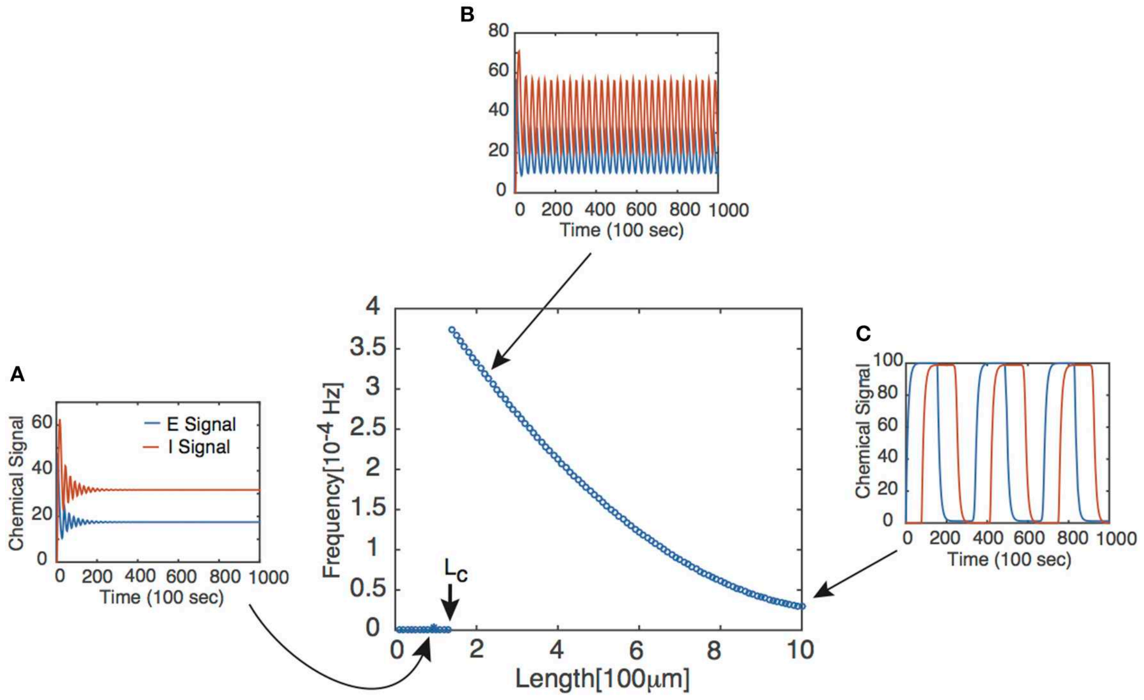

FIGURE 2 | Frequency of periodic solutions plotted against axonal length. [Plot was obtained by looking at the power spectrum of the retrograde signal and taking the frequency of the signal to be where the sharp peak of the spectrum occurred.] Insets show time series plots at specific values of the delay generated using the dde23 program in MATLAB: **(A)** $\tau = 1$, **(B)** $\tau = 2$, **(C)** $\tau = 10$. Other parameter values are $n = 4$, $I_0 = 10$, $W_E = W_I = 9.5$ such that $\tau_C \approx 1.5$.

simple gene network with a feedforward network topology. Note that from this perspective, the details of the particular mechanism for generating the oscillatory signal are not important, so we will focus on the simple delayed feedback model given by Equations (1) and (2).

2.2. Frequency Decoding by a Feedforward Gene Network

Suppose that the oscillating retrograde signal from the delayed feedback model triggers a signaling cascade via the action of certain kinases that ultimately leads to the translocation of a transcription factor into the nucleus of a given neuron and causes the rapid activation of some gene and subsequent production of some protein C

$$\begin{aligned} u_I(t) &\rightarrow \text{phosphorylation and translocation} \\ &\xrightarrow{fast} \text{Active Gene} \xrightarrow{fast} C \xrightarrow{\lambda} \emptyset \end{aligned}$$

with λ decay rate. This motivates the following model for the dynamics of protein C (Krakauer et al., 2002):

$$\frac{dc}{dt} = h[u_I(t)] - \lambda c, \tag{5}$$

where c denotes the concentration of protein C and $h[u]$ is a monotonically increasing function satisfying $h \to h^* \in (0, \infty)$ as $u \to \infty$. This is introduced to reflect the fact that the retrograde signal does not directly activate the gene. Define $g(t) \equiv h[u(t)]$. Then g is T-periodic, where T is the period of $u_I(t)$. Following Krakauer et al. (2002), we obtain the time-dependent solution for $c(t)$ and show that this simple feedforward network can act as a frequency decoder. Introduce the integrating factor $e^{\lambda t}$. Then,

$$\begin{aligned} \frac{d}{dt}(e^{\lambda t}c(t)) &= g(t)e^{\lambda t} \\ \Rightarrow c(t) &= c(t_0)e^{-\lambda(t-t_0)} + \int_{t_0}^{t} g(s)e^{-\lambda(t-s)}ds. \end{aligned}$$

We integrate over a period of $u_I(t)$ so that, for $m \in \mathbb{N}$,

$$\begin{aligned} c((m+1)T) &= c(mT)e^{-\lambda T} + \int_{mT}^{(m+1)T} g(s)e^{-\lambda((m+1)T-s)}ds \\ &= c(mT)e^{-\lambda T} + e^{-\lambda T}\int_0^T g(s)e^{\lambda s}ds. \end{aligned} \tag{6}$$

Equation (6) gives a recursive finite difference equation for c at integer multiples of the period of $u_I(t)$. For large m, we thus have

$$c(mT) = \frac{e^{-\lambda T}}{1 - e^{-\lambda T}}\int_0^T g(s)e^{\lambda s}ds. \tag{7}$$

Hence, $c(t)$ converges to a T-periodic solution following any transient dynamics, as shown in **Figure 3**. More significantly, there is now a strong DC component to the signal so that the relative amplitude of the oscillatory part has been suppressed. Indeed it is possible to find parameter values for which $c(t) \approx \bar{c}$, where $\bar{c}$ is the time-averaged protein output (Krakauer et al., 2002). Therefore, in order to characterize the protein output in terms of the frequency ω of $u_I(t)$, we find the time average of $c(t)$ post transience. This can be done by simply integrating Equation (5) over a period of $u_I(t)$:

$$\bar{c} = \frac{1}{\lambda T}\int_0^T g(s)ds \equiv \frac{\bar{g}}{\lambda}. \tag{8}$$

Equation (8) is an intuitive result. It says that the average protein output from the feedforward serial network is equal to the ratio of the average protein activation rate to the protein decay rate.

To make the relationship between $\bar{c}$ and T more explicit, we perform the following. Assume that in the post-transient time regime, the maximum value of $u_I(t)$ is given by U_M and that the minimum value is given by U_m, and that the u_I transitions from U_M to U_m occur very quickly compared to other temporal dynamics. Further assume that $h[u]$ is a Hill function with a large Hill coefficient, so that $h[U_M] = A$ and that $h[U_m] \approx 0$. Let $\eta < T$ denote the amount of time for which $u_I(t)$ is at its maximum value in a given period, $\eta = \kappa T$ for $0 < \kappa < 1$. Then, $\bar{g} \approx A\eta/T$ and

$$\bar{c} \approx \frac{A\eta}{\lambda T}. \tag{9}$$

Note that the assumptions made regarding $u_I(t)$ are consistent with the behavior of the retrograde signal for sufficiently long delays (see **Figure 2**).

Equation (9) suggests that if the protein decay rate λ, the rate of protein activation A, and the pulse-width η are constant, then the mean protein output $\bar{c}$ is a monotonically decreasing function of the period T of the pulsatile retrograde signal. In the context of the delayed feedback model, this means that $\bar{c}$ is a monotonically decreasing function of axonal length L. Although the analytical representation of $\bar{c}$ was obtained by making assumptions that simplified the analysis of Equation (5), and the pulse-width η is not fixed (see **Figure 2**), one still finds numerically that $\bar{c}$ decreases monotonically with L, see **Figure 4**. (As shown by Krakauer et al. (2002), it is also possible to modify the simple gene network so that the protein output becomes independent of pulse width). Note that if U_M is sufficiently large, then $A \approx h^*$ due to the saturating nature of h. What is more, changing the value of U_M will not alter $\bar{c}$ significantly unless it is reduced by a considerable amount. Thus, the mean protein output of the system is relatively insensitive to the amplitude of the input signal and responds only to the frequency of the input signal, making the feed forward serial network a plausible means by which a neuron can decode the oscillating retrograde signal from the delayed feedback model.

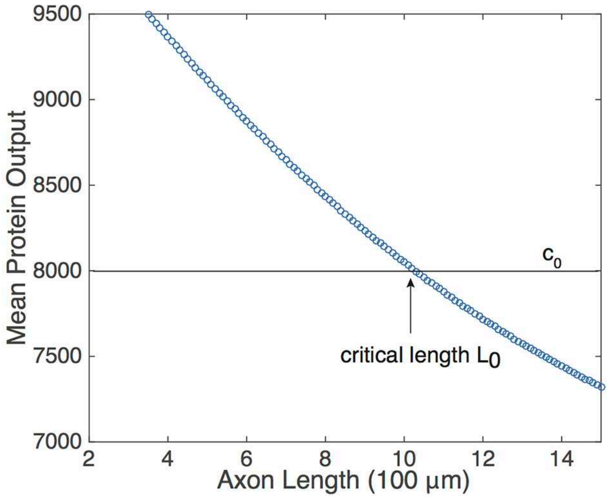

FIGURE 4 | Relationship of the mean protein output $\bar{c}$ and axonal length L, obtained by time averaging the solution to Equation (5) for several values of τ. Function definitions and parameter values are as in **Figures 2**, **4**. The existence of a threshold protein output c_0 could provide a mechanism for determining a critical length L_0.

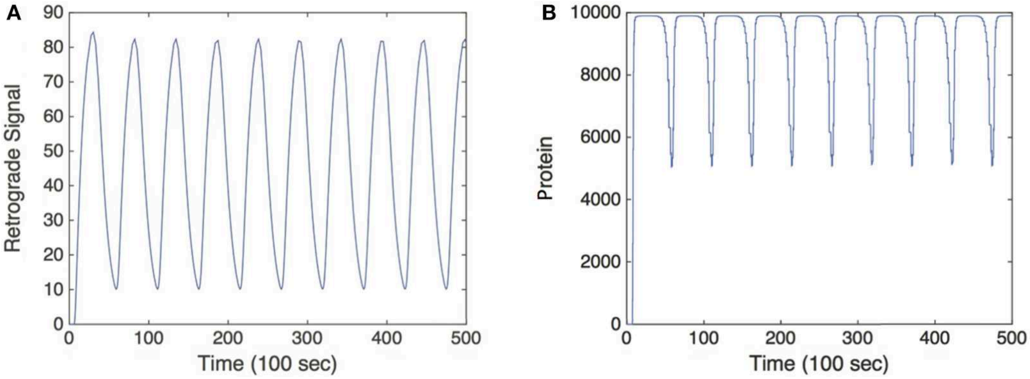

FIGURE 3 | Simulation of the feed forward serial network Equation (5) in response to a retrograde signal from Equation (2). (A) Retrograde signal being fed into gene network, $\tau = 5$. **(B)** Convergence of the solutions of Equation (5) to a T-periodic solution post transience. $h[u]$ is taken to be the same function as $f[u]$ defined in Equation (3) multiplied by a factor of 1000, and we set $\lambda = 0.01$. Other parameter values are as in **Figure 2**.

The monotonic relationship between $\bar{c}$ and L suggests that the underlying intrinsic axonal length sensor could be based on a threshold protein value. That is, suppose that a given neuron is pre-programmed to grow until the mean protein output reaches some threshold value, c_0, see **Figure 4**. Based on the mean protein output, the neuron would be able to sense its critical length L_0 and stop growing, for example. Analogous thresholding mechanisms have been investigated within the context of intracellular protein concentration gradients, which are used to determine spatial position within a cell so that, for example, cell division occurs at the appropriate time and location (Tostevin et al., 2007; Tostevin, 2011). Similarly, developmental morphogen gradients control patterns of gene expression so that each stage of cell differentiation occurs at the correct spatial location within an embryo. For biological effectiveness, these gradient-based mechanisms must be robust to intrinsic and extrinsic cellular noise (Tostevin, 2011; Howard, 2012). The issue of robustness to noise carries over to the proposed axonal-length sensing mechanism, and can be analyzed along similar lines to protein concentration gradients. Therefore, we now investigate the impact of intrinsic noise in a gene network arising from finite copy numbers on the shape of the deterministic $\bar{c}$ vs. L curve.

3. Effects of Intrinsic Noise on Axonal Length Sensing

3.1. Stochastic Gene Network

In order to investigate the effects of intrinsic noise, we consider an extended version of the network analyzed in Section 2.2 in which we explicitly include the dynamics of gene activation. Suppose that a gene promoter has two states: an inactive state Q and an active state Q^*. In the active state, the gene produces the protein C at a rate of μ, and the protein subsequently decays at a rate λ. The promoter is activated in response to the pulsatile retrograde signal $u_I(t)$ and deactivates at a constant rate of β, see **Figure 5**:

$$Q \underset{\beta}{\overset{u_I(t)}{\rightleftharpoons}} Q^* \overset{\mu}{\rightarrow} C \overset{\lambda}{\rightarrow} \emptyset. \tag{10}$$

Suppose there are N total gene promoters, each of which can exist in an active state or an inactive state. If N is sufficiently large, then the effects of intrinsic noise are negligible and one can represent the deterministic dynamics using kinetic equations. Let $x(t)$ and $c(t)$ denote, respectively, the fraction of active genes and the concentration of proteins (number of proteins per gene) at time t. Then

$$\frac{dx}{dt} = s(t)(1-x) - \beta x, \quad \frac{dc}{dt} = \mu x(t) - \lambda c(t), \tag{11}$$

where $s(t)$ is the input to the gene network, which is taken to be the concentration of promoters. The latter is itself controlled by the oscillatory retrograde signal $u_I(t)$ coming from the delayed feedback model. As in the previous model, we will take $s(t) = h[u_I(t)]$. Assume without loss of generality that $x(0) = 0$, so that the solution for $x(t)$ takes the form

$$x(t) = \int_0^t s(z)\exp\Big(\beta(z-t) + \int_t^z s(\xi)d\xi\Big)dz. \tag{12}$$

We would like to calculate the time-averaged level of active genes in the large-time limit. In order to simplify our calculations, we proceed as in Section 2.2 and take the oscillatory signal $s(t)$ to consist of square pulses of unit height, width η and period T. Setting $t = MT$, positive integer M, we can break up the integrals on the right-hand side of Equation (12) into a sum of integrals evaluated over a single period:

$$\begin{aligned} x(MT) &= \sum_{n=0}^{M-1} \int_{nT}^{(n+1)T} s(z)\exp\Big(\beta(z-MT) + \int_{MT}^{z} s(\xi)d\xi\Big)dz \\ &= \frac{1}{\beta+1}\Big[\exp\Big((\beta+1)\eta\Big) - 1\Big]\Big(\frac{\exp(-\beta MT - M\eta) - 1)}{1-\exp(\beta T+\eta)}\Big). \end{aligned}$$

The second line comes from evaluating the various integrals and summing the resulting geometric series. Taking the limit $M \to \infty$ shows that $x(MT) \to \Gamma$ with

$$\Gamma \equiv \frac{1}{\beta+1}\Big[1 - \exp\Big((\beta+1)\eta\Big)\Big]\frac{1}{1-\exp(\beta T+\eta)}.$$

For $t \in [0, \eta]$, we have $x(t) = x_0(t)$ with

$$\frac{dx_0}{dt} = 1-(1+\beta)x_0 \Rightarrow x_0(t) = \frac{1}{1+\beta}\Big(1-e^{-(\beta+1)t}\Big) + \Gamma e^{-(\beta+1)t},$$

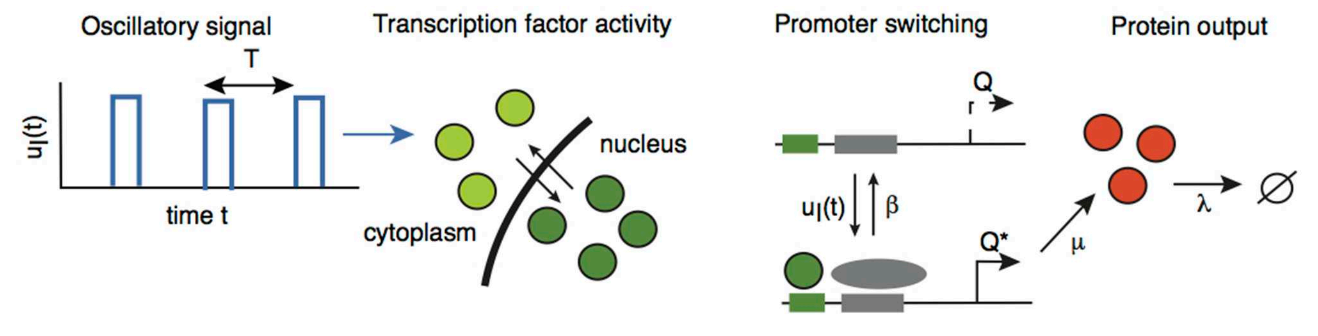

FIGURE 5 | A gene promoter driven by the oscillatory retrograde signal $u_I(t)$. Adapted and redrawn from Tostevin et al. (2012).

whereas for $t \in (\eta, T]$, we have $x(t) = x_1(t)$ with

$$\frac{dx_1}{dt} = -\beta x_1 \Rightarrow x_1(t) = x_0(\eta)e^{-\beta(t-\eta)}.$$

We have imposed continuity of the solution at $t = \eta$. Finally, $\bar{x}$ is obtained by averaging the resulting periodic function over $[0, T]$.

$$\begin{aligned}\bar{x} &= \frac{1}{T}\Big[\int_0^\eta x_0 dt + \int_\eta^T x_1 dt\Big] \\ &= \frac{1}{\beta+1}\Big[\frac{\eta}{T} + \frac{1}{T\beta(\beta+1)}\frac{1-e^{\beta(T-\eta)}}{1-e^{\beta T+\eta}}(e^{\eta(\beta+1)}-1)\Big]. \quad (13)\end{aligned}$$

The formula for $\bar{x}$ given above can be intuited in the following way. The fraction η/T corresponds to the fraction of time that $s(t)$ is "on". The latter term in the bracketed sum is a correction for the alterations in the time-scale of the gene promoter reaction to $s(t)$. When $s(t) = 1$, the time-scale of the gene promoter response is given by $(\beta + 1)^{-1}$, whereas when $s(t) = 0$, the time-scale is given by β^{-1}. Finally, the time-averaged protein output is

$$\bar{c} = \frac{\mu}{\lambda}\bar{x}.$$

As in the simpler gene network of Section 2.2, we find that the time-averaged protein output is a monotonically decreasing function of T even though the pulse-width η also changes with T as in **Figure 2**.

Now suppose that N is sufficiently small so that fluctuations due to low copy numbers cannot be ignored. In order to calculate the size of fluctuations, we have to consider the chemical master equation of the reaction scheme (Equation 10). Let n_1 denote the total number of activated genes and let n_2 denote the number of proteins that are present. Let $P \equiv P(n_1, n_2, t)$ denote the probability that at a given time t there are n_1 active genes and n_2 proteins available. The master equation is then given by

$$\begin{aligned}\frac{dP}{dt} &= s(t)(N - n_1 + 1)P(n_1 - 1, n_2, t) \\ &\quad + \beta(n_1 + 1)P(n_1 + 1, n_2, t) \\ &\quad + \mu n_1 P(n_1, n_2 - 1, t) + \lambda(n_2 + 1)P(n_1, n_2 + 1, t) \\ &\quad - (s(t)(N - n_1) + \beta n_1 + \mu n_1 + \lambda n_2)P(n_1, n_2, t). \quad (14)\end{aligned}$$

The first two terms correspond to the activation or the deactivation of a gene that results in having n_1 active genes and n_2 proteins. The second two terms correspond to the production or the degradation of a protein that results in having n_1 active genes and n_2 proteins. The last terms correspond to the ways that the system can leave the state of having n_1 active genes and n_2 proteins. It is difficult to solve the master equation explicitly, so we carry out a system size expansion with respect to N. That is, set $n_1 = Nx$, $n_2 = Nc$ and rewrite Equation (14) as

$$\begin{aligned}\frac{dP}{dt} &= N[s(t)\left(1 - x + \frac{1}{N}\right)P(n_1 - 1, n_2, t) \\ &\quad + \beta\left(x + \frac{1}{N}\right)P(n_1 + 1, n_2, t) \\ &\quad + \mu x P(n_1, n_2 - 1, t) + \lambda\left(c + \frac{1}{N}\right)P(n_1, n_2 + 1, t) \\ &\quad - (s(t)(1 - x) + \beta x + \mu c + \lambda c)P(n_1, n_2, t)].\end{aligned}$$

The master equation is now just a sum of terms of the form $f(\mathbf{n}/N)P(\mathbf{n}, t)$, where $\mathbf{n} \equiv (n_1, n_2)$ and f is the corresponding propensity function. Performing the change of variables $f(\mathbf{n}/N)P(\mathbf{n}, t) = f(\mathbf{x})p(\mathbf{x}, t)$, where $\mathbf{x} \equiv (x, c)$, and Taylor expanding in powers of N^{-1} to second order leads to the Fokker-Planck equation

$$\begin{aligned}\frac{dp}{dt} &= -\frac{\partial}{\partial x}\Big([s(t)(1 - x) - \beta x]p\Big) - \frac{\partial}{\partial c}\Big([\mu x - \lambda c]p\Big) \\ &\quad + \frac{1}{2N}\frac{\partial^2}{\partial x^2}\Big([s(t)(1 - x) + \beta x]p\Big) + \frac{1}{2N}\frac{\partial^2}{\partial c^2}\Big([\mu x + \lambda c]p\Big).\end{aligned}$$

In the case of a constant input $s(t) = \alpha$, the deterministic kinetic Equation (11) have the unique fixed point solution

$$x^* = \frac{\alpha}{\alpha + \beta}, \quad c^* = \frac{\mu}{\lambda}x^*.$$

In this case, neglecting transients, the Fokker-Planck equation describes a stochastic process characterized by Gaussian fluctuation about the fixed point (x^*, c^*). It is then relatively straightforward to calculate the stationary variance Δc of the protein output, given the mean $\langle c\rangle = c^*$:

$$\begin{aligned}\Delta c &= \frac{1}{\gamma}\Big[\frac{\mu^2\alpha\beta}{(\alpha + \beta + \lambda)(\alpha + \beta)^2} + \frac{\alpha\mu}{\alpha + \beta}\Big] \\ &= \frac{\mu}{\lambda}\frac{\alpha}{\alpha + \beta}\Big[1 + \frac{\mu\beta}{(\alpha + \beta + \lambda)(\alpha + \beta)}\Big] \\ &= \langle c\rangle\Big[1 + \frac{\mu\beta}{(\alpha + \beta + \lambda)(\alpha + \beta)}\Big].\end{aligned}$$

The expression for the variance in the case of constant input consists of an intrinsic Poissonian term due to random protein production and an extrinsic term due to fluctuations in the gene promoters themselves. The calculation of the variance in the case of an oscillatory input $s(t)$ is considerably more involved, even when it takes the form of square pulses. However, stochastic simulations show that the protein variance in response to an oscillatory signal is less than the protein variance in response to a constant input, assuming that time-averaged means are the same (Tostevin et al., 2012). Let α_{eff} be the effective constant input for which the time-averaged and noise-averaged protein output $\langle\bar{c}\rangle$ can be written as

$$\langle\bar{c}\rangle = \frac{\mu}{\lambda}\frac{\alpha_{\text{eff}}}{\alpha_{\text{eff}} + \beta}. \quad (15)$$

It follows that for an oscillatory input

$$\Delta\bar{c} \le \langle\bar{c}\rangle\Big[1 + \frac{\mu\beta}{(\alpha_{\text{eff}} + \beta + \lambda)(\alpha_{\text{eff}} + \beta)}\Big], \quad (16)$$

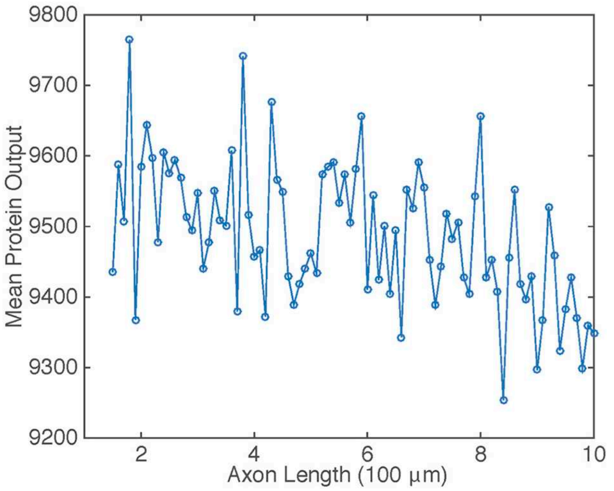

FIGURE 6 | Plot of mean protein output $\bar{c}$ vs. axonal length L. Results are based on simulations of the chemical master Equation (14) using the Gillespie algorithm with input $s(t) = h[u_l(t)]$. Parameter values used to generate retrograde signal $u_l(t)$ are the same as in **Figure 2**. Other parameter values are $\beta = 1$, $\mu = 0.1$, $\lambda = 0.01$, and $N = 1000$.

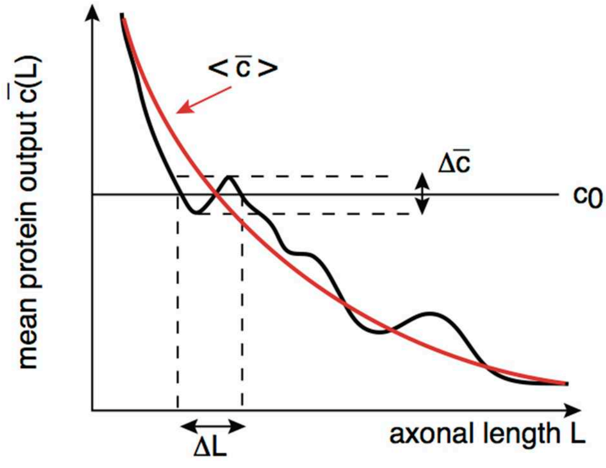

FIGURE 7 | Schematic diagram illustrating how the presence of noise in the protein output leads to an uncertainty ΔL in the critical axonal length L_0 at which the threshold is crossed. An analogous result applies to decoding of protein concentration gradients.

where

$$\Delta\bar{c}(L) = \langle[\bar{c}(L) - \langle\bar{c}(L)\rangle]^2\rangle.$$

The dependence of $\bar{c}$ on axonal length L in the presence of intrinsic noise is shown in **Figure 6**. The general inverse relationship is still prevalent in this situation, but fluctuates due to the stochasticity in the gene switching.

3.2. Errors in Axonal Length-Sensing

By analogy with the effects of intrinsic noise in protein concentration gradients (Howard, 2012), the presence of noise in the protein output leads to an uncertainty ΔL in the critical axonal length L_0 at which the threshold c_0 is crossed. This is illustrated schematically in **Figure 7**. Although the time-averaged protein output $\bar{c}$ is still approximately a monotonically decreasing function of axonal length L on large length-scales, fluctuations due to intrinsic noise mean that it is non-monotonic on smaller length scales. It follows that the protein output can cross threshold several times over small changes in L resulting in an uncertainty ΔL with regards to the critical axonal length. The uncertainty ΔL can be estimated as follows: Suppose that in the absence of noise $\bar{c}(L_0) = c_0$. Denoting the variance in the concentration due to intrinsic noise by $\Delta\bar{c}(L_0)$, we then have the approximation

$$c_0 = \bar{c}(L_0 + \Delta L/2) + \frac{1}{2}\sqrt{\Delta\bar{c}(L_0)} \approx \bar{c}(L_0) - \frac{\Delta L}{2}|\bar{c}'(L_0)| + \frac{1}{2}\sqrt{\Delta\bar{c}(L_0)},$$

which yields the result

$$\Delta L|\langle\bar{c}'(L_0)\rangle| = \sqrt{\Delta\bar{c}(L_0)}). \tag{17}$$

If we ignore the correction factor in Equation (16) and approximate the stochastic process by a Poisson process, then $\Delta\bar{c} \approx \bar{c}$ and

$$\Delta L \sim \frac{\sqrt{\langle\bar{c}(L_0)\rangle}}{|\langle\bar{c}'(L_0)\rangle|}.$$

As a further approximation, suppose that $\langle\bar{c}(L)\rangle \sim 1/T$, where T is the period of oscillations produced by an axon of length L, so that $|\langle\bar{c}'(L)\rangle| \sim 1/(L'(T)T^2)$ (using the fact that L increases monotonically with T and $L(T)$ is the inverse of the function $T(L)$). It follows that

$$\frac{\Delta L}{L_0} \sim \frac{T_0^{3/2}L'(T_0)}{L(T_0)},$$

with T_0 the oscillation period at the critical length L_0, i.e., $L(T_0) = L_0$. Assuming that the length L increases at least linearly with T, we see that the relative error grows with the critical oscillation period T_0 and, hence, the critical axonal length L_0. Although this is a crude estimate, we find that the same qualitative behavior is observed in numerical simulations of the full stochastic model. This is shown in **Figure 8**, where we plot the relative error $\Delta L/L_0$ vs. axonal length. Our analysis suggests that the frequency-encoded protein threshold mechanism could break down for long axons. An analogous result was shown to hold in Karamched and Bressloff (2015), where the robustness of the encoding of axonal length in the frequency of a pulsatile signal was investigated. There we found that the encoding of axonal length into frequency became less reliable at long axon lengths due to accumulation of white noise signified by a high coefficient of variation in the frequency of the retrograde signal. In this work, the retrograde signal is deterministic, and the error in protein output is accounted for strictly by the random variations in the activities of independent gene promoters. Hence the error in

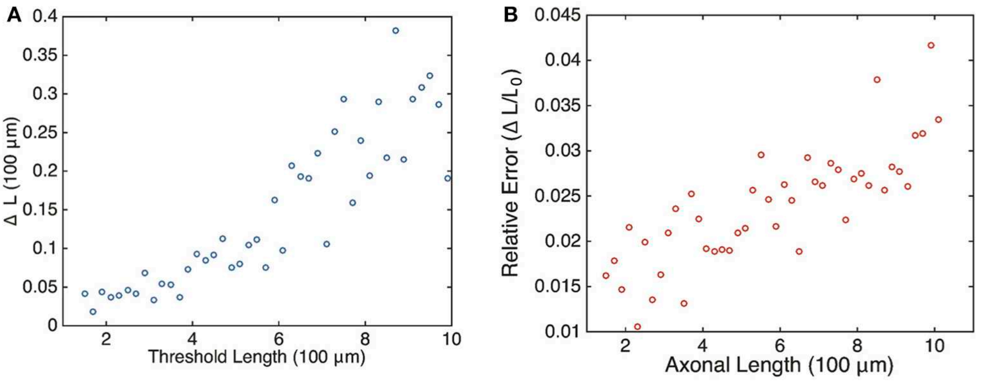

FIGURE 8 | Plot of estimated errors in axonal length based on 100 simulations of the chemical master Equation (14) using the Gillespie algorithm with input $s(t) = h[u_l(t)]$. (A) Plot of uncertainty in axonal length ΔL vs. threshold axonal lengths L_0. **(B)** Relative error ($\Delta L/L_0$) vs. axonal length. Same parameters as **Figure 6**. L_0 was found by averaging over the mean protein outputs and determining what length that protein value corresponded to according to the curve shown in **Figure 4**. ΔL was determined by looking at what axonal length each individual mean protein output realization corresponded to according to Equation (4) and then finding the variance in this set of values.

length sensing could be more devastating in real life situations, since noise would impact both the encoding and the decoding processes. Thus, wherever the sources of noise may be, their impact on this frequency-dependent mechanism is clear: large neurons would have a more difficult time sensing their own length when compared with smaller neurons.

4. Discussion

In this paper we extended the recent delayed-feedback model of axonal length-sensing based on the frequency of an oscillating retrograde signal (Rishal et al., 2012; Karamched and Bressloff, 2015) in order to investigate the issue of frequency decoding. In particular, we showed that the mean protein output of a simple feedforward gene network responding to the pulsatile retrograde signal of the delayed feedback model varies inversely with axonal length. Specifically, we derived approximate analytical results which make explicit the inverse relationship, and introduced the notion that frequency decoding could be done based on a protein threshold mechanism. We then investigated the reliability of such a mechanism subject to intrinsic noise stemming from finite copy numbers within a gene network by analyzing a chemical master equation, which describes the random switching of genes and production of protein. The results of these simulations suggest that the accuracy in the information the neuron receives regarding axonal length declines as axonal length itself grows. The latter could have serious implications for the utility of this mechanism in the context of axonal injury, where accurate information regarding the locality of an affliction is necessary for a neuron to set a regenerative process in motion. Of course, the noise sensitivity could be a consequence of using a simple feedforward gene network. Our work shows that there needs to be some additional processing to increase the robustness to noise, perhaps by including some form of feedback. Indeed, one can view our simple gene network as the first stage in a more complex network that carries out the thresholding of the protein output. For example, one could consider a mutual repressor model, which consists of two repressor proteins whose transcription is mutually regulated, that is, the protein product of one gene binds to the promoter of the other gene and represses its output (Gardner et al., 2000). Such a network can act as a bistable switch. If one of the genes were also driven by the retrograde signal as outlined in Section 3, then the switch could be activated or inactivated below a critical frequency. We hope to explore the effects of noise in this more complex network elsewhere—here we wanted to separate out the frequency decoding mechanism from the thresholding mechanism.

There are several other issues we hope to explore in the future. First, we would like to feed the retrograde signal arising from a model that more accurately describes motor dynamics into the feedforward serial gene network. For example, an advection-diffusion equation could be used to model motor dynamics (Karamched and Bressloff, 2015), and the aforementioned chemical signal network could be coupled to these dynamics to generate a pulsatile retrograde signal. It would be interesting to take this idea to a higher level and perform a fully stochastic simulation of motor dynamics, where we allow for binding and unbinding of motors to microtubular tracks. Such a simulation would allow us to characterize noise in the system better, and provide more accurate representations of errors inherent in the axon length sensing mechanism. Finally, Equation (9) indicates that mean protein output is sensitive to the frequency of the incoming pulse signal, but that it is also sensitive to the fraction of time for which the incoming signal is at its peak value. Hence the feedforward serial network does not generate a frequency filter in the strictest sense. We would be interested in seeing the result of feeding the retrograde signal into a network that allows for more acute frequency sensitivity.

Finally, we note that an alternative axonal length-sensing mechanism has been proposed by Roossien et al. (2013). These authors studied axonal growth in Drosophila neurons. In particular, they tracked the movement of docked mitochondria in order to establish that the physical mechanism of growth cone advance in Drosophila is similar to vertebrate neurons. That is, the bulk forward translocation of microtubules along the axon underlies the advance of the growth cone C-domain. They also compared the length of axons grown on two different substrates, either poly-ornithine or Drosophila ExtraCellular Matrix (DECM). They found that axons grown on the faster substrate DECM ended up being longer than the other substrate. The authors suggested that if a length sensor were the sole regulator of the cessation of elongation, then neurons grown on poly-ornithine would be expected to sustain elongation for a longer time than neurons grown on DECM so that they end up having similar lengths. Since this was not observed, it suggests that there may be some internal clock that is independent of axonal length and terminates elongation after a set period of growth.

Author Contributions

PB designed the research; PB and BK developed the analysis; BK performed the numerical simulations; PB and BK wrote the paper.

Acknowledgments

PCB was supported by NSF grant DMS-1120327.

References

Brown, K. M., Gillette, T. A., and Ascoli, G. A. (2008). Quantifying neuronal size: summing up trees and splitting the branch difference. *Semin. Cell Dev. Biol.* 19, 485–493. doi: 10.1016/j.semcdb.2008.08.005

Cai, L., Dalal, C. K., and Elowitz, M. B. (2008). Frequency-modulated nuclear localization bursts coordinate gene regulation. *Nature* 45, 485–491. doi: 10.1038/nature07292

Gardner, T. S., Cantor, C. R., and Collins, J. J. (2000). Construction of a genetic toggle switch in *e. coli. Nature* 403, 339–342. doi: 10.1038/35002131

Goslin, K., and Banker, G. (1989). Experimental observations on the development of polarity by hippocampal neurons in culture. *J. Cell Biol.* 108, 1507–1516. doi: 10.1083/jcb.108.4.1507

Howard, M. (2012). How to build a robust intracellular concentration gradient. *Trends Cell Biol.* 22, 311–317. doi: 10.1016/j.tcb.2012.03.002

Kam, N., Pilpel, Y., and Fainzilber, M. (2009). Can molecular motors drive distance measurements in injured neurons? *PLoS Comput. Biol.* 5:e1000477. doi: 10.1371/journal.pcbi.1000477

Karamched, B., and Bressloff, P. C. (2015). Delayed feedback model of axonal length sensing. *Biophys. J.* 108, 2408–2419. doi: 10.1016/j.bpj.2015.03.055

Krakauer, D. C., Page, K. M., and Sealfon, S. (2002). Module dynamics of the gnrh transduction network. *J. Theor. Biol.* 218, 457–470. doi: 10.1016/S0022-5193(02)93092-4

Lallemend, F., and Ernfors, P. (2012). Molecular interactions underlying the specification of sensory neurons. *Trends Neurosci.* 35, 373–381. doi: 10.1016/j.tins.2012.03.006

Marshall, W. J. (2004). Cellular length control. *Ann. Rev. Cell Dev. Biol.* 20, 677–693. doi: 10.1146/annurev.cellbio.20.012103.094437

O'Toole, M., Latham, R., Baqri, R. M., and Miller, K. E. (2008). Modeling mitochondrial dynamics during *in vivo* elongation. *J Theor. Biol.* 255, 369–377. doi: 10.1016/j.jtbi.2008.09.009

Rishal, I., Kam, N., Perry, R. B., Shinder, V., Fisher, E. M. C., Giampietro, S., et al. (2012). A motor-driven mechanism for cell-length sensing. *Cell Rep.* 1, 608–616. doi: 10.1016/j.celrep.2012.05.013

Roossien, D. H., Lamoureux, P., Vactor, D. V., and Miller, K. E. (2013). Drosophila growth cones advance by forward translocation of the neuronal cytoskeletal meshwork *in vivo*. *PLoS ONE* 8:e80136. doi: 10.1371/journal.pone.0080136

Samsonovich, A. V., and Ascoli, G. A. (2006). Morphological homeostasis in cortical dendrites. *Proc. Natl. Acad. Sci. U.S.A.* 103, 1569–1574. doi: 10.1073/pnas.0510057103

Smith, D. H. (2009). Stretch growth of integrated axon tracts: extremes and exploitations. *Prog. Neurobiol.* 89, 231–239. doi: 10.1016/j.pneurobio.2009.07.006

Tostevin, F. (2011). Precision of sensing cell length via concentration gradients. *Biophys. J.* 100, 294–303. doi: 10.1016/j.bpj.2010.11.046

Tostevin, F., de Ronde, W., and ten Wolde, P. R. (2012). Reliability of frequency and amplitude decoding in gene regulation. *Phys. Rev. Lett.* 108:108104. doi: 10.1103/PhysRevLett.108.108104

Tostevin, F., ten Wolde, P. R., and Howard, M. (2007). Fundamental limits to position determination by concentration gradients. *PLoS Comput. Biol.* 3:e78. doi: 10.1371/journal.pcbi.0030078

Conflict of Interest Statement: The authors declare that the research was conducted in the absence of any commercial or financial relationships that could be construed as a potential conflict of interest.

frontiers
in Cellular Neuroscience

ORIGINAL RESEARCH
published: 30 July 2015
doi: 10.3389/fncel.2015.00285

Assessing effects on dendritic arborization using novel Sholl analyses

Kate M. O'Neill[1,2], Barbara F. Akum[1], Survandita T. Dhawan[1], Munjin Kwon[1], Christopher G. Langhammer[1] and Bonnie L. Firestein[1]*

[1] Department of Cell Biology and Neuroscience, Rutgers University, Piscataway, NJ, USA, [2] Graduate Program in Biomedical Engineering, Rutgers University, Piscataway, NJ, USA

Determining the shape of cell-specific dendritic arbors is a tightly regulated process that occurs during development. When this regulation is aberrant, which occurs during disease or injury, alterations in dendritic shape result in changes to neural circuitry. There has been significant progress on characterizing extracellular and intrinsic factors that regulate dendrite number by our laboratory and others. Generally, changes to the dendritic arbor are assessed by Sholl analysis or simple dendrite counting. However, we have found that this general method often overlooks local changes to the arbor. Previously, we developed a program (titled Bonfire) to facilitate digitization of neurite morphology and subsequent Sholl analysis and to assess changes to root, intermediate, and terminal neurites. Here, we apply these different Sholl analyses, and a novel Sholl analysis, to uncover previously unknown changes to the dendritic arbor when we overexpress an important regulator of dendrite branching, cytosolic PSD-95 interactor (cypin), at two developmental time points. Our results suggest that standard Sholl analysis and simple dendrite counting are not sufficient for uncovering local changes to the dendritic arbor.

Keywords: neuron, dendrite, Sholl, morphology, tracing, image analysis

Edited by:
Kyle Miller,
Michigan State University, USA

Reviewed by:
Ruth M. Empson,
University of Otago, New Zealand
Jyothi Arikkath,
University of Nebraska Medical Center, USA

***Correspondence:**
Bonnie L. Firestein,
Nelson Biological Laboratories,
Department of Cell Biology and Neuroscience, Rutgers University,
Room D413, 604 Allison Road,
Piscataway, NJ 08854-8082, USA
firestein@biology.rutgers.edu

Received: *28 May 2015*
Accepted: *13 July 2015*
Published: *30 July 2015*

Citation:
O'Neill KM, Akum BF, Dhawan ST, Kwon M, Langhammer CG and Firestein BL (2015) Assessing effects on dendritic arborization using novel Sholl analyses.
Front. Cell. Neurosci. 9:285.
doi: 10.3389/fncel.2015.00285

Introduction

Neurons are polarized cells that send information through a main axon and receive information through highly branched dendrites. The development and patterning of dendrites is a tightly regulated process that is essential for proper functioning of the central nervous system. The overall shape of the dendritic arbor determines the inputs that neurons receive and how inputs are processed, thus affecting synaptic output (Miller and Jacobs, 1984; Eilers and Konnerth, 1997; Hausser et al., 2000; Vetter et al., 2001; Schaefer et al., 2003; Elston and Fujita, 2014). The arbor is shaped by intrinsic and extrinsic factors (Landgraf and Evers, 2005; Libersat, 2005; Santiago and Bashaw, 2014; Dong et al., 2015; Sainath and Gallo, 2015) and can also be influenced by trauma or disease (reviewed in Kulkarni and Firestein, 2012). Disorders in which neuronal morphology is disturbed highlight the importance of proper dendritic shape to the overall functioning of neuronal networks (Zoghbi, 2003; Kulkarni and Firestein, 2012).

A number of metrics may be used to identify dendritic arbor morphology (Uylings and Van Pelt, 2002). Sholl analysis (Sholl, 1953) has been an instrumental tool in revealing changes to the dendritic arbor as a whole. Sholl analysis includes counting the number of dendritic intersections that occur at fixed distances from the soma in concentric circles. This analysis reveals the number of branches, branch geometry, and overall branching patterns of neurons (Caserta et al., 1995). Performing this process by hand is time-consuming and introduces inherent variability due to inconsistency and experimenter bias. Our laboratory developed a semi-automated Sholl analysis program, called Bonfire, that not only performs analysis on the entire arbor but also analyzes subsets of dendrites (primary/secondary/tertiary, root/intermediate/terminal) within the arbor (Kutzing et al., 2010; Langhammer et al., 2010). This detailed reporting of the data allows for morphological analysis to occur on a much smaller scale.

A major focus of our work is to understand how changes to the dendritic arbor are mediated by various intrinsic and extrinsic factors. We identified a protein termed cypin (*cy*tosolic *P*SD-95 *in*teractor) as a core regulator of dendritic arborization (Akum et al., 2004; Fernandez et al., 2008). Cypin promotes local microtubule assembly in the dendrite by binding tubulin heterodimers, resulting in increased primary and secondary dendrite numbers (Akum et al., 2004). We have found that cypin is a core regulator of dendritogenesis, and two well-studied regulators of dendrite number, brain-derived neurotrophic factor (BDNF) and the small GTPase RhoA, act via cypin-dependent pathways (Chen and Firestein, 2007; Kwon et al., 2011). Recently, we developed new Sholl analyses to determine how BDNF acts at subregions of the arbor and found novel action of BDNF at terminal regions of the arbor (Langhammer et al., 2010). Since cypin promotes local microtubule assembly (Akum et al., 2004), and our previous studies have only assessed the effects of overexpression and knockdown of cypin by either counting primary and secondary dendrites (Akum et al., 2004; Charych et al., 2006; Fernandez et al., 2008) or by using conventional Sholl analysis (Chen and Firestein, 2007; Kwon et al., 2011), it is not yet known whether cypin has region-specific effects on the dendritic arbor. Here, we alter cypin protein levels in cultured rat hippocampal neurons by overexpression from day *in vitro* (DIV) 6–10 and from DIV 10–12, and we apply several types of Sholl analyses on specific regions of the dendritic arbor. Our data show that cypin promotes proximal branching at both time points and that these increases are order-specific. These results suggest that that traditional Sholl analysis and dendrite number counts are not sufficient to describe cypin-promoted changes to the dendritic arbor.

Materials and Methods

Primary Culture and Transfection of Hippocampal Neurons

This study was carried out in accordance with the recommendations of the National Institute of Health's Guide for the Care and Use of Laboratory Animals (DHHS Publication No. [NIH] 85-23 and all subsequent revisions thereof) and to the Public Health Service Policy on Humane Care and Use of Laboratory Animals followed by Rutgers Institutional Animal Care and Use Committee. The protocol was approved by the Rutgers Institutional Animal Care and Use Committee.

Hippocampal neurons were isolated from embryonic rats at day 18 of gestation (E18) as we have previously described (Firestein et al., 1999). After isolation, the hippocampi were dissociated via manual trituration and plated at a density of 2×10^5/well on 12-mm glass coverslips (Fisher) in 24-well plates (Corning). Coverslips were coated with 0.5 mg/mL poly-D-lysine (PDL; Sigma) for at least 1 h at 37°C prior to plating cells. Cultures were maintained in Neurobasal medium supplemented with B27, GlutaMAX, and penicillin/streptomycin (all from Life Technologies) in a humidified 37°C incubator with 5% CO_2. Cells were grown for 6 days *in vitro* (DIV) or 10 DIV prior to transfection.

A subset of neurons were transfected at DIV 6 with pEGFP-C1 or pEGFP-C1-cypin and pmRFP using Lipofectamine LTX and Plus reagent according to the manufacturer's instructions (Kwon et al., 2011) and fixed with 4% paraformaldehyde in phosphate-buffered saline (PBS), pH 7.4, at DIV 10. Additional neurons were transfected at DIV 10 with pEGFP-C1 or pEGFP-C1-cypin using Lipofectamine 2000 according to the manufacturer's instructions and fixed at DIV 12 for imaging and analysis.

Immunostaining and Imaging

At the appropriate DIV, neurons were fixed with 4% paraformaldehyde in PBS for 15 min and incubated in blocking buffer (PBS containing 0.1% Triton X-100, 2% normal goat serum, and 0.02% sodium azide) for 1 h. All antibodies were diluted in blocking buffer. Cells were incubated with primary antibody for 2 h at room temperature. Primary antibodies were used at a concentration of 1:500 and included mouse anti-MAP2 (BD Pharmigen), chicken anti-GFP (Rockland), and rabbit anti-cypin (Chen and Firestein, 2007). After primary antibody incubation, coverslips were washed three times with PBS and incubated with secondary antibody for 1 h at room temperature. Secondary antibodies were used at a concentration of 1:250 and included Alexa Fluor 488 donkey anti-chicken, Alexa Fluor 555 donkey anti-rabbit, and Alexa Fluor 647 donkey anti-mouse (all from Life Technologies). After secondary antibody incubation, coverslips were washed twice with PBS and incubated with Hoechst dye for 5 min at room temperature to stain nuclei. Coverslips were washed one final time with PBS and mounted onto glass microscope slides with Fluoromount G (Southern Biotechnology). Transfected cells were visualized by immunofluorescence on an Olympus Optical IX 50 microscope (Tokyo, Japan) with a Cooke SensiCam charge-coupled device (CCD) cooled camera fluorescence imaging system and Image Pro software (Media Cybernetics).

Assessment of Dendrite Number Using Semi-automated Sholl Analysis and Statistics

Semi-automated Sholl analysis was used as previously described (Kutzing et al., 2010; Langhammer et al., 2010). Briefly, 8-bit images of hippocampal neurons were traced using the NeuronJ plugin (Meijering et al., 2004) for ImageJ (NIH, Bethesda, MD), and tracing files (∗.ndf files) were generated. The data were organized and converted to SWC files (Cannon et al., 1998) using MATLAB (Mathworks), and the connectivity of the tracings was checked in NeuronStudio (Rodriguez et al., 2006). Once the tracings were finalized in NeuronStudio, the data were exported to Excel using MATLAB. Prism (Graphpad) was used for all statistical analyses. For analysis of Sholl curves, two-way ANOVA was used followed by Bonferroni Multiple Comparisons test. For analysis of dendrite numbers, Student *t*-tests were used, and Welch's correction was included when appropriate. All tracings and analyses were performed with the experimenter blinded to the condition. A subset of neurons for this study were retraced from images analyzed in Kwon et al. (2011). All analyses of the retraced images presented here are new, and data generated from non-conventional Sholl analyses (RIT and Tips-In) are novel and were not included in Kwon et al. (2011). Neurons were counted only when at least two authors agreed that they were viable without access to condition information. All dendrites are defined as not branching or resulting in bifurcation (Van Pelt and Verwer, 1985, 1986; Verwer and Van Pelt, 1990).

Labeling Schemes Used for Analysis

We use three labeling schemes to analyze cypin-promoted changes to the dendritic arbor (**Figure 1**). It is important to note that Sholl data are always reported at distance from the cell body in μm, regardless of the labeling scheme. Inside-Out Sholl analysis is conventional Sholl analysis (Langhammer et al., 2010). Dendrites that extend from the cell body are defined as primary dendrites, and those that emanate from primary dendrites are secondary dendrites. Dendrites that emanate from secondary dendrites are tertiary dendrites, and so on. In this labeling scheme, dendrites classified as tertiary and higher are grouped together. In the Root-Intermediate-Terminal (RIT) scheme (Langhammer et al., 2010), root dendrites emerge from the cell body, and terminal dendrites are those dendrites that do not branch further. All other dendrites are labeled as intermediate dendrites. Tips-In analysis (Rodriguez, 2007) is the opposite of Inside-Out analysis. This scheme defines the outermost, terminal dendrites as primary dendrites. Secondary dendrites are dendrites that are one order in from the outermost dendrite; they can be the penultimate dendrite or a root dendrite with only one branch, as shown in the right panel of **Figure 1**. Tertiary and higher order dendrites are one order closer to the soma after the penultimate (secondary) dendrite. These dendrites correspond to primary dendrites in the Inside-Out labeling scheme that branch at least twice.

Results

Sholl Analysis for Neurons Overexpressing Cypin from DIV 6–10

As illustrated in the representative images in **Figure 2A**, overexpression of cypin from DIV 6–10 promotes dendrite branching in hippocampal neurons, in agreement with our previous work (Akum et al., 2004; Chen and Firestein, 2007; Fernandez et al., 2008; Kwon et al., 2011). Sholl analysis performed with all branch orders grouped (Total Sholl, **Figure 2B**), as is standard in the field, is the same analysis regardless of whether we perform Inside-Out, Root-Intermediate-Terminal (RIT), or Tips-In analysis. Total Sholl analysis shows that cypin significantly increases proximal branches at 0–42 μm from the soma when overexpressed from DIV 6–10. The causes for this change can be parsed out

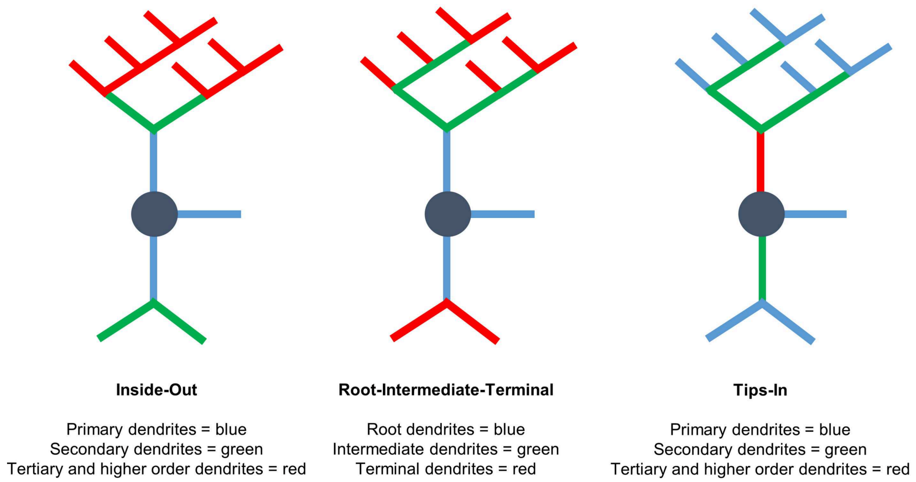

FIGURE 1 | Three different Sholl analyses used to assess the effects of cypin overexpression on the dendritic arbor. (Left) Inside-Out Sholl analysis is conventional Sholl analysis (Langhammer et al., 2010). Dendrites that extend from the cell body are defined as primary dendrites, those that emanate from primary dendrites are secondary dendrites, those that emanate from secondary dendrites are tertiary dendrites, and so on. Dendrites classified as tertiary and higher are grouped together. **(Middle)** In the Root-Intermediate-Terminal (RIT) scheme (Langhammer et al., 2010), root dendrites emerge from the cell body, and terminal dendrites are those dendrites that do not branch further. All other dendrites are considered intermediate dendrites. **(Right)** Tips-In analysis (Rodriguez, 2007) defines terminal dendrites as primary dendrites. Secondary dendrites are dendrites that are one order in from the outermost dendrite and can be the penultimate dendrite or a root dendrite with only one branch, as shown in the figure. Tertiary and higher order dendrites are one order closer to the soma after the penultimate (secondary) dendrite. These dendrites correspond to primary dendrites in the Inside-Out labeling scheme that branch at least twice. This is a novel analysis, presented within this paper.

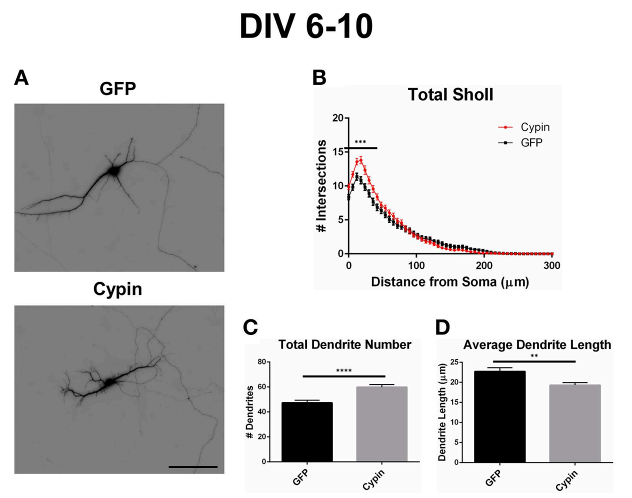

FIGURE 2 | Overexpression of cypin from DIV 6–10 increases proximal branching and total dendrite number but decreases average dendrite length. (A) Representative images of hippocampal neurons overexpressing GFP or GFP-cypin (cypin) from DIV 6–10. Scale bar = 100 μm. **(B)** Sholl analysis of all orders of branches (Total Sholl) shows that overexpression of cypin significantly increases dendrite branching at 0–42 μm from the cell body (***$p < 0.001$). Statistics were calculated using Two-Way ANOVA followed by Bonferroni multiple comparisons test. **(C)** Overexpression of cypin results in a significant increase in the total number of dendrites (****$p < 0.0001$). Total number of dendrites represents sum of all dendrites, regardless to what category they belong. Statistics were calculated by unpaired, two-tailed Student's *t*-test. **(D)** Overexpression of cypin results in a significant decrease in the average length of dendrites (**$p < 0.001$). Average length is the mean length of all dendrites, regardless to what category they belong. Statistics were calculated by unpaired, two-tailed Student's *t*-test with Welch's correction. Error bars indicate SEM. $n = 50$ neurons for GFP, and $n = 55$ neurons for cypin.

when examining Sholl curves for different branch categories and comparing these differences among the three methods of analysis.

When analyzing the dendritic arbor using the Inside-Out method, cypin overexpression promotes the greatest increase in primary branches, branches that emerge from the soma, and higher order branches (tertiary and above). Primary branches significantly increase at 0–18 μm from the soma when cypin is overexpressed (**Figure 3A**). Secondary branches, which emerge from primary dendrites, significantly increase at 6–12 μm from the soma (**Figure 3B**). Higher order dendrites significantly increase at 18–42 μm and at 54–60 μm from the soma in neurons overexpressing cypin (**Figure 3C**). These results indicate that, at DIV 6–10, when dendritic branches extend from primary and secondary branches and very little pruning has yet to occur (i.e., stage 4) (Dotti et al., 1988; Akum et al., 2004), cypin exerts the greatest effects on primary and higher order branches (tertiary and above) but not on secondary branches.

When analyzing the dendritic arbor using the RIT method, cypin overexpression significantly changes all categories of dendrites. Like the Inside-Out method, significant changes occur in proximal dendrites less than 100 μm from the soma. Because primary dendrites in the Inside-Out method and root dendrites in the RIT method are defined as the same, changes observed in root dendrites are the changes observed in primary dendrites: cypin overexpression significantly increases root dendrites at 0–42 μm from the soma (**Figure 3D**). This method of Sholl analysis shows a difference from that of Inside-Out Sholl analysis when comparing secondary dendrites and intermediate dendrites (**Figure 3E**). Intermediate dendrites include all dendrites that are not root dendrites or terminal dendrites. Significant increases in dendrites of neurons overexpressing cypin are observed at 6–12 μm from the soma, similar to changes seen in secondary dendrites analyzed by the Inside-Out method. Additionally, an increase in intermediate dendrites at 30 μm from the soma is also observed. These results indicate that the significant increases observed at 6 and 12 μm are due to increased secondary dendrites but that the increase at 30 μm is due to increased higher order, intermediate branches. The Sholl curves for terminal dendrites show similar increases to those seen in tertiary and higher order dendrites: neurons overexpressing cypin have significantly increased dendrite branching at 18–42 μm from the soma (**Figure 3F**). Interestingly, the increases observed at 54 and 60 μm from the soma that are observed for tertiary and higher order dendrites are not observed for terminal dendrites, indicating that terminal dendrites closer to the cell body (within 50 μm) are most affected by cypin overexpression.

When analyzing the dendritic arbor using the Tips-In method, cypin overexpression from DIV 6–10 exerts the greatest effect on primary dendrites and on tertiary and higher order dendrites. In this labeling scheme, primary dendrites are the outermost (terminal) dendrites. The resulting curve from this analysis is distinct from the terminal Sholl curve resulting from the RIT method, likely because primary dendrites in this case are a combination of terminal dendrites as well as root dendrites that do not branch (see **Figure 1**, right panel). For primary dendrites in the Tips-In scheme, significant increases are observed at 0–42 μm from the soma (**Figure 3G**), which are the same distances observed for increased dendrites resulting from Total Sholl analysis (**Figure 2B**). Secondary dendrites in this scheme are dendrites that are one order in from the outermost dendrite, either the penultimate dendrite or a root dendrite with only one branch (**Figure 1**, right panel). This curve is distinct from the intermediate Sholl curve from the RIT method and the secondary Sholl curve from the Inside-Out method. Significant increases are only observed at 6 μm from the soma (**Figure 3H**), indicating that the penultimate dendrite is only affected by cypin overexpression at distances very close to the soma. Finally, dendrites labeled as tertiary and higher order are one order closer to the soma after the penultimate (secondary) dendrite; they are the antepenultimate (third to last) dendrite. These dendrites correspond to primary dendrites in the Inside-Out labeling scheme that branch at least twice (**Figure 1**, right panel). For tertiary and higher order dendrites, significant increases are observed at 0–24 μm away from the soma (**Figure 3I**).

Dendrite Number for Neurons Overexpressing Cypin from DIV 6–10

Cypin overexpression from DIV 6–10 affects the total number of dendrites and dendrites of specific orders, depending on the

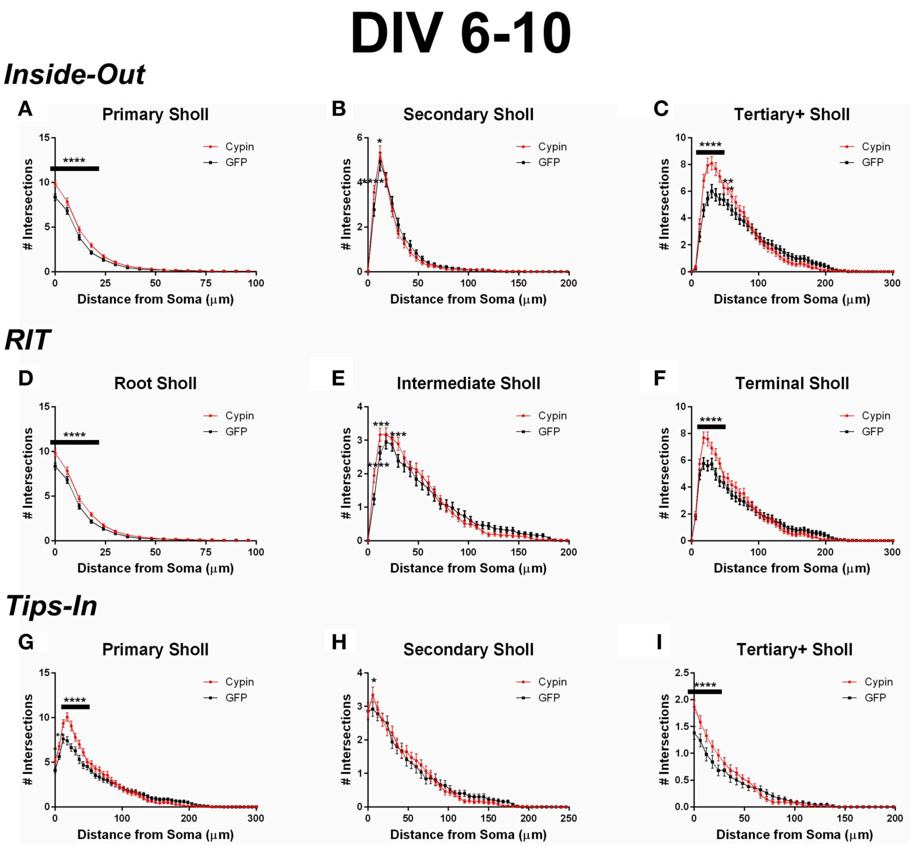

FIGURE 3 | Sholl analysis using three different labeling methods for neurons overexpressing cypin from DIV 6–10. (A–C) Sholl analysis using Inside-Out (conventional) labeling method. **(A)** Sholl analysis of primary dendrites (Primary Sholl) shows that overexpression of cypin significantly increases branching at 0–18 μm (****$p < 0.0001$). **(B)** Sholl analysis of secondary dendrites (Secondary Sholl) shows that overexpression of cypin significantly increases dendrites at 6 and 12 μm from the soma (****$p < 0.0001$ and *$p < 0.05$, respectively). **(C)** Sholl analysis of tertiary and higher order dendrites (Tertiary+ Sholl) shows that overexpression of cypin significantly increases dendrites at 18–42 μm from the soma (****$p < 0.0001$) and at 54 μm (**$p < 0.01$) and 60 μm (*$p < 0.05$) from the soma. **(D–F)** Sholl analysis using RIT labeling method. (**D**) Sholl analysis of root dendrites (Root Sholl) shows that overexpression of cypin significantly increases branching at 0–18 μm from the cell body (****$p < 0.0001$). **(E)** Sholl analysis of intermediate dendrites (Intermediate Sholl) shows that overexpression of cypin significantly increases dendrites at 6 μm (****$p < 0.0001$) from the soma and at 12 and 30 μm from the soma (both ***$p < 0.001$). **(F)** Sholl analysis of terminal dendrites (Terminal Sholl) shows that overexpression of cypin significantly increases dendrites at 18–42 μm from the soma (****$p < 0.0001$). **(G–I)** Sholl analysis using Tips-In labeling method. **(G)** Sholl analysis of primary dendrites shows that overexpression of cypin significantly increases branching at 0 μm (*$p < 0.05$), 6 μm (**$p < 0.01$), and 12–42 μm from the soma (****$p < 0.0001$). **(H)** Sholl analysis of secondary dendrites shows that overexpression of cypin significantly increases branching at 6 μm from the soma (*$p < 0.05$). **(I)** Sholl analysis of tertiary and higher order dendrites shows that overexpression of cypin significantly increases dendrite branching at 0–24 μm from the soma (****$p < 0.0001$). Statistics were calculated using Two-Way ANOVA followed by Bonferroni multiple comparisons test. Error bars indicate SEM. $n = 50$ neurons for GFP, and $n = 55$ neurons for cypin.

labeling scheme. For all labeling schemes, the total dendrite count is identical by definition ($p > 0.9999$ as determined by One-Way ANOVA), and cypin overexpression from DIV 6–10 significantly increases dendrites (**Figure 2C**). The different labeling schemes indicate unique regulation of dendrite number by cypin.

For the Inside-Out labeling scheme, cypin overexpression significantly increases primary dendrites (**Figure 4A**) as well as tertiary and higher order dendrites (**Figure 4C**), with no significant effect on secondary dendrites (**Figure 4B**). This labeling scheme points to cypin-promoted increases in primary and higher order (>secondary) dendrite number.

For the RIT labeling scheme, overexpression of cypin significantly increases all dendrite types; root, intermediate, and terminal dendrite numbers are significantly increased (**Figures 4D–F**). When comparing these graphs to the Inside-Out graphs, it becomes clear that different labeling schemes demonstrate cypin-promoted effects on dendrite number differently. As with the Sholl curves, the difference in root dendrites is identical for that of primary dendrites because the two types of dendrites are identical (**Figure 4D**). While there is no significant difference observed for secondary dendrites for the Inside-Out method, there is a significant increase in intermediate dendrites when cypin is overexpressed (**Figure 4E**). This is also reflected in the Sholl curves, with an additional significant difference at 30 μm from the soma for intermediate dendrites (**Figure 3E**) when compared to secondary dendrites (**Figure 3B**).

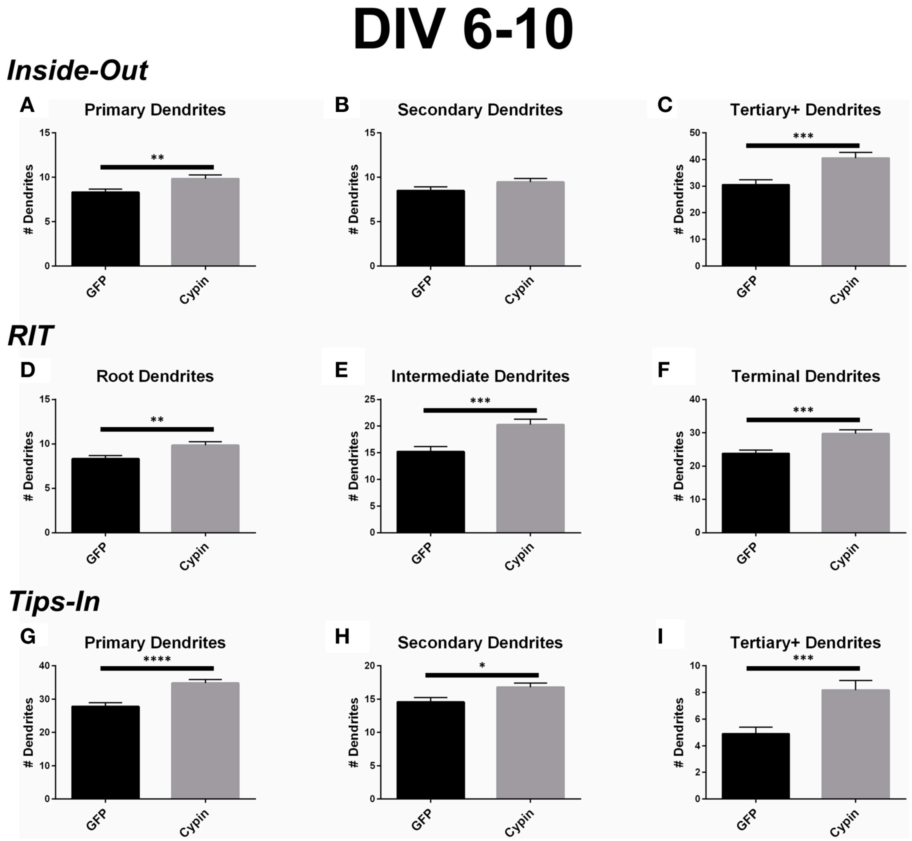

FIGURE 4 | Cypin increases the number of dendrites by specifically targeting certain categories of dendrites when overexpressed in neurons from DIV 6–10. (A–C) Dendrite numbers divided into categories using Inside-Out (conventional) labeling method. **(A)** Overexpression of cypin significantly increases the number of primary dendrites (**$p < 0.01$). **(B)** Overexpression of cypin does not significantly increase the number of secondary dendrites. **(C)** Overexpression of cypin significantly increases the number of tertiary and higher order dendrites (***$p < 0.001$). **(D–F)** Dendrite numbers divided into categories using RIT labeling method. **(D)** Overexpression of cypin significantly increases the number of root dendrites (**$p < 0.01$). **(E)** Overexpression of cypin significantly increases the number of intermediate dendrites (***$p < 0.001$). **(F)** Overexpression of cypin significantly increases the number of terminal dendrites (***$p < 0.001$). **(G–I)** Dendrite numbers divided into categories using Tips-In labeling method. **(G)** Overexpression of cypin significantly increases the number of primary dendrites (****$p < 0.0001$). **(H)** Overexpression of cypin significantly increases the number of secondary dendrites (*$p < 0.05$). **(I)** Overexpression of cypin significantly increases the number of tertiary and higher order dendrites (***$p < 0.001$). Statistics calculated by unpaired, two-tailed Student's *t*-test. Error bars indicate SEM. $n = 50$ neurons for GFP, and $n = 55$ neurons for cypin.

Additionally, terminal dendrites significantly increase due to cypin overexpression, indicating that increased branching is due to increased intermediate branches (**Figure 4F**).

Interestingly, unlike the Inside-Out method, the Tips-In method shows significantly increased numbers of dendrites for all categories (**Figures 4G–I**). As with Sholl analysis for this method, the primary dendrites are terminal dendrites or root dendrites that do not branch, and these types of dendrites are significantly increased for neurons overexpressing cypin from DIV 6–10 (**Figure 4G**). Secondary dendrites, defined under this labeling scheme, are either the penultimate dendrite or a root dendrite with only one branch. In this case, they significantly increase with cypin overexpression (**Figure 4H**). Finally, tertiary and higher order dendrites are primary dendrites with two or more branches. We also observe a significant increase in these branches as a result of cypin overexpression (**Figure 4I**).

Dendrite Length for Neurons Overexpressing Cypin from DIV 6–10

In addition to the effects of cypin overexpression from DIV 6–10 on dendrite number and spatial arrangement, cypin overexpression affects the lengths of dendrites. As shown in **Figure 2C**, overexpression of cypin significantly increases the total number dendrites, but as shown in **Figure 2D**, it also significantly decreases the average dendritic length, perhaps due to the exhaustion of a limiting reagent required for dendrite growth (Charych et al., 2006).

When analyzed according to the Inside-Out labeling method, overexpression of cypin significantly decreases the length of tertiary and higher order dendrites (**Figure 5C**). Interestingly, the length of primary dendrites is not affected (**Figure 5A**) although their numbers are increased (as shown in **Figure 4A**). Secondary dendrite length is not affected by cypin overexpression

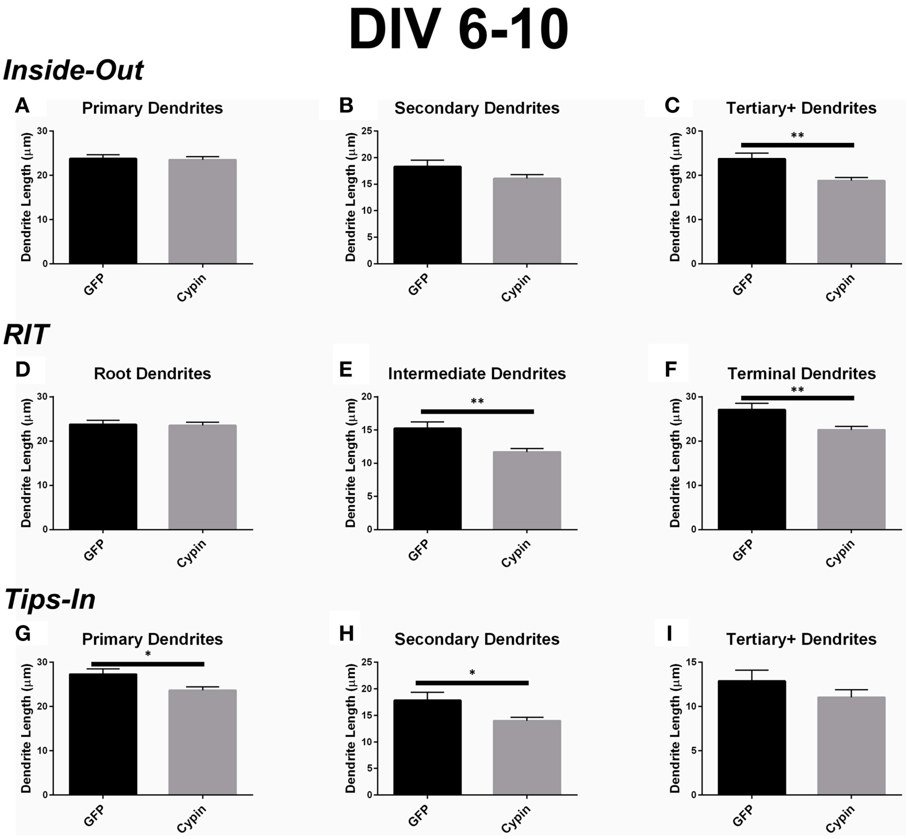

FIGURE 5 | Cypin decreases the length of dendrites by specifically targeting certain categories of dendrites when overexpressed in neurons from DIV 6-10. (A–C) Average dendrite length divided into categories using Inside-Out (conventional) labeling method. **(A)** Cypin overexpression does not significantly change the length of primary dendrites. **(B)** Cypin overexpression does not significantly decrease the length of secondary dendrites. **(C)** Cypin overexpression significantly decreases the length of tertiary and higher order dendrites ($^{**}p < 0.001$). For **(A,B)** statistics were calculated by unpaired, two-tailed Student's *t*-tests, and for **(C)**, statistics were calculated by unpaired, two-tailed Student's *t*-tests with Welch's correction. **(D–F)** Average dendrite length divided into categories using RIT labeling method. **(D)** Cypin overexpression does not significantly change the length of root dendrites. **(E)** Cypin overexpression significantly decreases the length of intermediate dendrites ($^{**}p < 0.001$). **(F)** Cypin overexpression significantly decreases the length of terminal dendrites ($^{**}p < 0.001$). For **(D)**, statistics were calculated by unpaired, two-tailed Student's *t*-tests, and for **(E,F)**, statistics were calculated by unpaired, two-tailed Student's *t*-tests with Welch's correction. **(G–I)** Average dendrite length divided into categories using Tips-In labeling method. **(G)** Cypin overexpression significantly decreases the length of primary dendrites ($^{*}p < 0.05$). **(H)** Cypin overexpression significantly decreases the length of secondary dendrites ($^{*}p < 0.05$). **(I)** Cypin overexpression does not significantly decrease the length of tertiary and higher order dendrites. For **(G–I)**, statistics were calculated by unpaired, two-tailed Student's *t*-tests with Welch's correction. Error bars indicate SEM. $n = 50$ neurons for GFP, and $n = 55$ neurons for cypin.

(**Figure 5B**). These data indicate that overexpression of cypin specifically changes the length of higher order dendrites.

The dendrite length data from the RIT method complement the data gathered using the Inside-Out method. While cypin overexpression does not affect the length of root dendrites (**Figure 5D**), it significantly decreases the lengths of intermediate and terminal dendrites (**Figure 5E** and **Figure 5F**, respectively). Only tertiary and higher order dendrite numbers significantly decrease with cypin overexpression when analyzed using the Inside-Out method, indicating that analysis of two different classes (intermediate and terminal) are combined, thus eliminating information. Additionally, while no significant difference in length is observed for secondary dendrites (**Figure 5B**), a significant decrease in intermediate dendrite length results from cypin overexpression (**Figure 5E**). Based on these data, cypin overexpression affects the length of intermediate branches, most likely higher order (>secondary) dendrite branches, and terminal branches.

Finally, the data for the Tips-In method indicate that overexpression of cypin significantly decreases the length of primary and secondary dendrites (**Figures 5G,H**). Primary dendrites are terminal dendrites or root dendrites that have not branched, and secondary dendrites are the penultimate branch or a root dendrite that has branched once (**Figure 1**, right panel). While these are two very different categories of branches, cypin overexpression significantly decreases the lengths of both of these types of branches. Cypin overexpression does not result in a change in length of tertiary and higher order dendrites (**Figure 5I**).

Sholl Analysis for Neurons Overexpressing Cypin from DIV 10–12

As we previously reported (Akum et al., 2004; Chen and Firestein, 2007; Fernandez et al., 2008; Kwon et al., 2011), overexpression of cypin from DIV 10–12 also promotes dendrite branching in hippocampal neurons as demonstrated in the representative images in **Figure 6A**. Sholl analysis performed with all branch orders grouped (Total Sholl, **Figure 6B**) is the same analysis regardless of which labeling method is used. Total Sholl analysis shows that overexpression of cypin significantly increases proximal branches at 18–30 μm from the soma when it is overexpressed from DIV 10–12. As with our analysis of neurons overexpressing cypin from DIV 6–10, we can identify the mechanism by which this change occurs by examining Sholl curves for different branch categories and comparing these differences among the three analysis methods.

When analyzing the dendritic arbor using the Inside-Out method, cypin overexpression from DIV 10–12 promotes proximal branching in all branch types. Primary branches significantly increase at 0–6 μm from the soma when cypin is overexpressed (**Figure 7A**). Secondary dendrites, which emerge from primary dendrites, significantly increase at 12 μm from the soma (**Figure 7B**). Higher order dendrites significantly increase at 18–36 μm from the soma in neurons overexpressing cypin (**Figure 7C**). These results indicate that during DIV 10–12, at the end of the active dendrite branching period in our cultured neurons (i.e., stage 4) (Dotti et al., 1988; Akum et al., 2004), cypin overexpression promotes increases in all branch types at specific distances from the soma.

Cypin overexpression also promotes increases in all categories of dendrites when analyzed by the RIT labeling method. As with the Inside-Out method, significant changes occur in proximal dendrites less than 50 μm from the soma. Primary dendrites identified by the Inside-Out method and root dendrites identified by the RIT method are identical, and thus, the changes observed in these dendrite categories are the same: a significant increase in root dendrites at 0–6 μm from the soma (**Figure 7D**). There is a difference, however, when comparing secondary dendrites from the Inside-Out method and intermediate dendrites from the RIT method because intermediate dendrites include all dendrites that are not root or terminal dendrites. For neurons overexpressing cypin, significant increases in intermediate dendrites are observed at 12–18 μm from the soma using the RIT method (**Figure 7E**), whereas there is a sole significant increase at 12 μm from the soma for secondary dendrites when using the Inside-Out method (**Figure 7B**). This difference indicates that the significant increase at 12 μm is due to increased secondary dendrites, whereas the increase at 18 μm is due to increases in higher order dendrites. The Sholl curves for terminal dendrites analyzed using the RIT method show similar increases to those identified as tertiary and higher order using the Inside-Out method. Neurons overexpressing cypin show significantly increased branching 18–36 μm from the soma (**Figure 7F**). These results reveal that cypin-promoted increases in higher order dendrites at these distances are specifically due to increased terminal dendrite branching.

When analyzing the dendritic arbor using the Tips-In method, cypin overexpression results in increased dendrites of all categories. Primary branches are the outermost, or terminal, dendrites in this labeling scheme. The Sholl curve for these branches is similar to that of the terminal branches for RIT but has some important differences. For the Tips-In labeling scheme, primary dendrites include terminal dendrites and root dendrites that do not branch (**Figure 1**, right panel). Primary dendrites significantly increase in neurons overexpressing cypin at 18–30 μm from the soma (**Figure 7G**), which are the same distances observed for increased dendrites identified by Total Sholl analysis (**Figure 6B**). These data indicate that the outermost dendrites and root dendrites that do not branch are responsible for the overall increases observed. Secondary dendrites in this scheme are dendrites that are one order in from the outermost dendrite, either the penultimate dendrite or a root dendrite with only one branch (**Figure 1**, right panel). The Sholl curve resulting from analysis of secondary dendrites from the Tips-In method is distinct from the intermediate Sholl curve from the RIT method and the secondary Sholl curve from the Inside-Out method. For the Tips-In method, significant increases in branching occur at 6–18 μm from the soma for neurons overexpressing cypin (**Figure 7H**). In contrast, intermediate dendrites identified by the RIT method significantly increase at 12–18 μm from the soma

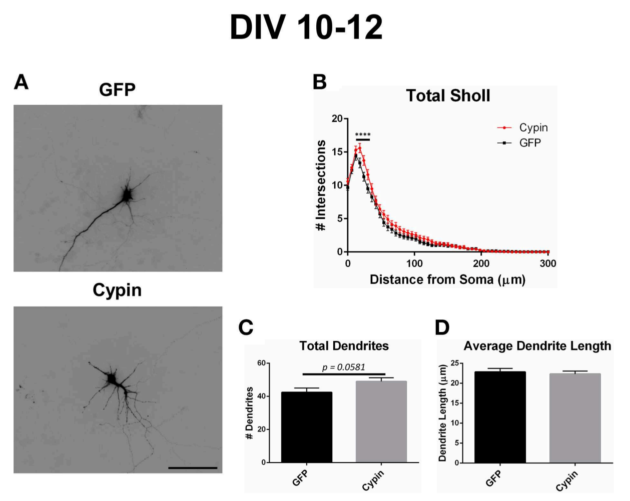

FIGURE 6 | Cypin overexpression from DIV 10–12 increases proximal branching with no significant effect on total dendrite number or average dendrite length. (A) Representative images of hippocampal neurons overexpressing GFP or GFP-cypin (cypin) from DIV 10–12. Scale bar = 100 μm. **(B)** Sholl analysis for all orders of branches (Total Sholl) shows that overexpression of cypin significantly increases dendrite branching at 18–30 μm from the soma (****$p < 0.0001$). Statistics were calculated using Two-Way ANOVA followed by Bonferroni multiple comparisons test. **(C)** Cypin overexpression results in an increase that approaches significance in the number of total dendrites ($p = 0.0581$). Total number of dendrites represents sum of all dendrites, regardless to what category they belong. **(D)** Cypin overexpression does not significantly change average dendrite length. Average length is the mean length of all dendrites, regardless to what category they belong. For **(C,D)**, statistics were calculated by unpaired, two-tailed Student's *t*-test. Error bars indicate SEM. $n = 35$ neurons for GFP, and $n = 51$ neurons for cypin.

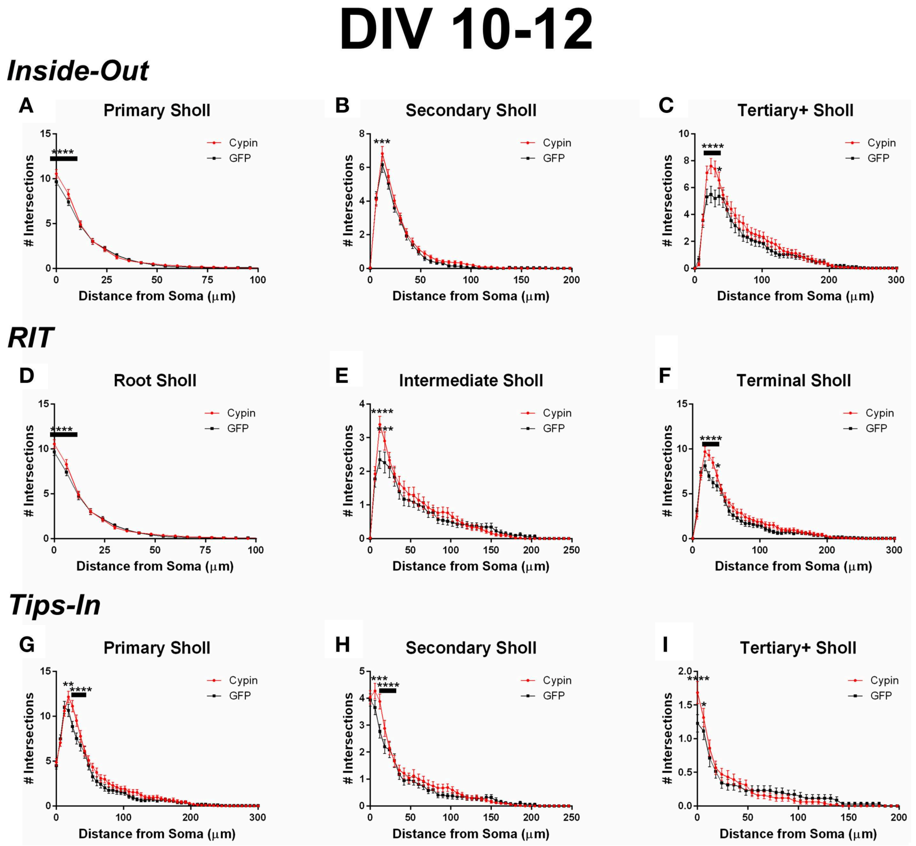

FIGURE 7 | Sholl analysis using three different labeling methods for neurons overexpressing cypin from DIV 10–12. (A–C) Sholl analysis using Inside-Out (conventional) labeling method. **(A)** Sholl analysis of primary dendrites (Primary Sholl) shows that overexpression of cypin significantly increases branching at 0–6 μm from the soma (****$p < 0.0001$). **(B)** Sholl analysis of secondary dendrites (Secondary Sholl) shows that overexpression of cypin significantly increases branching at 12 μm from the soma (***$p < 0.01$). **(C)** Sholl analysis of tertiary and higher order dendrites (Tertiary + Sholl) shows that overexpression of cypin significantly increases branching at 18–30 μm from the soma (****$p < 0.0001$) and at 36 μm from the soma (*$p < 0.05$). **(D–F)** Sholl analysis using RIT labeling method. **(D)** Sholl analysis of root dendrites (Root Sholl) shows that overexpression of cypin significantly increases branching at 0–6 μm from the soma (****$p < 0.0001$). **(E)** Sholl analysis of intermediate dendrites (Intermediate Sholl) shows that overexpression of cypin significantly increases dendrite branching at 12 μm (****$p < 0.0001$) and at 18 μm (***$p < 0.001$) from the soma. **(F)** Sholl analysis of terminal dendrites (Terminal Sholl) shows that overexpression of cypin significantly increases dendrite branching at 18–30 μm from the soma (****$p < 0.0001$) and at 36 μm from the soma (*$p < 0.05$). **(G–I)** Sholl analysis using Tips-In labeling method. **(G)** Sholl analysis of primary dendrites shows that overexpression of cypin increases branching at 18 μm from the soma (**$p < 0.01$) and at 24–30 μm from the soma (****$p < 0.0001$). **(H)** Sholl analysis of secondary dendrites shows that overexpression of cypin increases dendrite branching at 6 μm from the soma (***$p < 0.001$) and at 12–18 μm from the soma (****$p < 0.0001$). **(I)** Sholl analysis of tertiary and higher order dendrites shows that overexpression of cypin significantly increases branching at the soma (0 μm, ****$p < 0.0001$) and at 6 μm from the soma (*$p < 0.05$). Statistics were calculated using Two-Way ANOVA followed by Bonferroni multiple comparisons test. Error bars indicate SEM. $n = 35$ neurons for GFP, and $n = 51$ neurons for cypin.

(**Figure 7E**). These differences can be explained by how dendrites are grouped. Secondary dendrites, as defined by the Tips-In scheme, include intermediate dendrites and root dendrites with only one branch. Thus, the additional significant increase at 6 μm could be due to an increase in root dendrites with only one branch. Finally, dendrites labeled as tertiary and higher order are the antepenultimate (third to last) dendrite. These dendrites correspond to root dendrites that branch twice or more. For tertiary and higher order dendrites of the Tips-In scheme, significant increases occur at 0–6 μm from the soma (**Figure 7I**). These increases correspond to those observed for primary dendrites identified by the Inside-Out scheme and root dendrites identified by the RIT scheme.

Dendrite Number for Neurons Overexpressing Cypin from DIV 10–12

Cypin overexpression from DIV 10–12 affects dendrites of specific orders, depending on the labeling scheme. For all labeling schemes, the total dendrite count is identical by definition ($p > 0.9999$ as determined by One-Way ANOVA), and cypin overexpression from DIV 10–12 results in an increase in dendrite number that approaches significance ($p = 0.0581$; **Figure 6C**). The Inside-Out labeling scheme shows that cypin overexpression does not increase primary, secondary, or tertiary and higher order dendrite number (**Figures 8A–C**). Similarly, the RIT labeling scheme suggests that cypin overexpression does not increase root or intermediate dendrite number

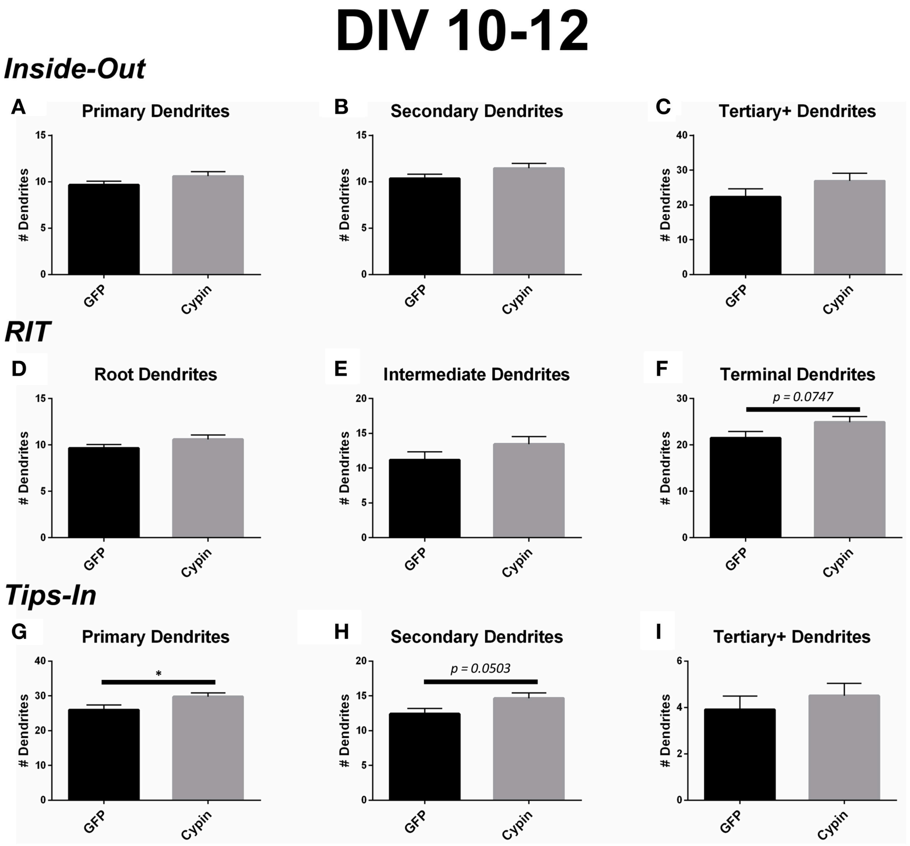

FIGURE 8 | Cypin increases outermost dendrites when overexpressed in neurons from DIV 10–12. **(A–C)** Dendrite numbers divided into categories using Inside-Out (conventional) labeling method. **(A)** Cypin overexpression does not increase the number of primary dendrites. **(B)** Cypin overexpression does not increase the number of secondary dendrites. **(C)** Cypin overexpression does not increase the number of tertiary and higher order dendrites. For **(A,B)**, statistics were calculated by unpaired, two-tailed Student's *t*-tests with Welch's correction, and for **(C)**, statistics were calculated by unpaired, two-tailed Student's *t*-tests. **(D–F)** Dendrite numbers divided into categories using RIT labeling method. **(D)** Cypin overexpression does not increase the number of root dendrites. **(E)** Cypin does not increase the number of intermediate dendrites. **(F)** Cypin overexpression causes an increase in the number of terminal dendrites that approaches significance ($p = 0.0747$). For **(D,E)**, statistics were calculated by unpaired, two-tailed Student's *t*-tests with Welch's correction, and for **(F)**, statistics were calculated by unpaired, two-tailed Student's *t*-tests. **(G–I)** Dendrite numbers divided into categories using Tips-In labeling method. **(G)** Cypin overexpression significantly increases the number of primary dendrites ($^*p < 0.05$). **(H)** Cypin overexpression results in an increase that approaches significance in the number of secondary dendrites ($p = 0.0503$). **(I)** Cypin overexpression does not significantly change the number of tertiary and high order dendrites. For **(G–I)**, statistics were calculated by unpaired, two-tailed Student's *t*-test. Error bars indicate SEM. $n = 35$ neurons for GFP, and $n = 51$ neurons for cypin.

(**Figure 8D** and **Figure 8E**, respectively). However, cypin overexpression causes an increase in terminal dendrite number that approaches significance ($p = 0.0747$; **Figure 8F**). Complementing these results, the Tips-In labeling scheme shows that cypin overexpression results in a significant increase in primary dendrites (**Figure 8G**), which are terminal dendrites or dendrites with no branches (**Figure 1**, right panel). This significant increase was masked in the previous labeling schemes due to how the dendrites are grouped. Additionally, cypin overexpression causes an increase that approaches significance ($p = 0.0503$) in secondary branches (**Figure 8H**), which are the penultimate intermediate branch or root dendrites that have branched once (**Figure 1**, right panel). Using this method, no increases in tertiary and higher order dendrites are detected (**Figure 8I**).

Dendrite Length for Neurons Overexpressing Cypin from DIV 10–12

Cypin overexpression from DIV 10–12 results in changes to the length of specific orders of dendrites, depending on the labeling scheme. For all labeling schemes, the total dendrite count is identical, and cypin overexpression from DIV 10–12 does not affect overall dendrite length (**Figure 6D**). The Inside-Out labeling scheme suggests that cypin overexpression does not affect dendrite length according to this labeling method (**Figures 9A–C**). Similarly, the RIT labeling scheme suggests that cypin overexpression has no effect on dendrite length (**Figures 9D–F**). In contrast, the Tips-In labeling scheme suggests that cypin overexpression results in a significant decrease in the length of tertiary and higher order dendrites (**Figure 9I**) without any effect on primary or secondary dendrite length (**Figure 9G**

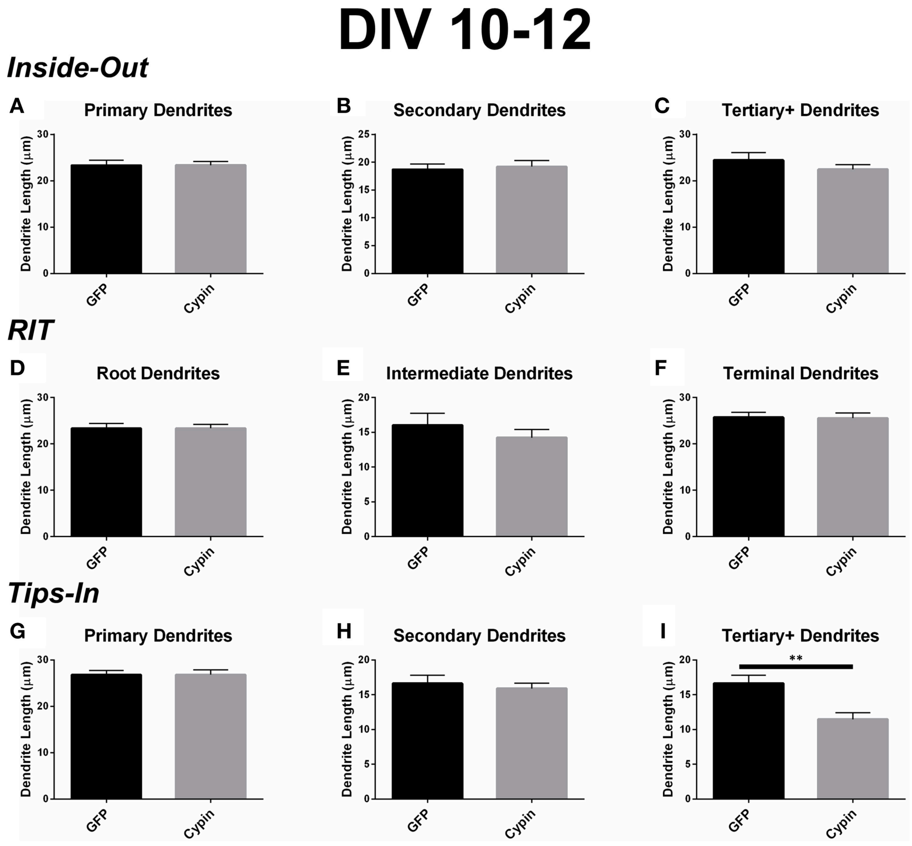

FIGURE 9 | Cypin decreases the length of innermost dendrites when overexpressed in neurons from DIV 10–12. (A–C) Average dendrite length divided into categories using Inside-Out (conventional) labeling method. **(A)** Cypin overexpression does not significantly change the length of primary dendrites. **(B)** Cypin overexpression does not significantly change the length of secondary dendrites. **(C)** Cypin overexpression does not significantly change the length of tertiary and higher order dendrites. For **(A)**, statistics were calculated by unpaired, two-tailed Student's *t*-tests, and for **(B,C)**, statistics were calculated by unpaired, two-tailed Student's *t*-tests with Welch's correction. **(D–F)** Average dendrite length divided into categories using RIT labeling method. **(D)** Cypin overexpression does not significantly change the length of root dendrites. **(E)** Cypin overexpression does not significantly change the length of intermediate dendrites. **(F)** Cypin overexpression does not significantly change the length of terminal dendrites. For **(D)**, statistics were calculated by unpaired, two-tailed Student's *t*-tests, and for **(E,F)**, statistics were calculated by unpaired, two-tailed Student's *t*-tests with Welch's correction. **(G–I)** Average dendrite length divided into categories using Tips-In labeling method. **(G)** Cypin overexpression does not significantly change the length of primary dendrites. **(H)** Cypin overexpression does not significantly change the length of secondary dendrites. **(I)** Cypin overexpression significantly decreases the length of tertiary and higher order dendrites ($^{**}p < 0.01$). For **(G,H)**, statistics were calculated by unpaired, two-tailed Student's *t*-tests with Welch's correction, and **(I)**, statistics were calculated by unpaired, two-tailed Student's *t*-tests. Error bars indicate SEM. $n = 35$ neurons for GFP, and $n = 51$ neurons for cypin.

and **Figure 9H**, respectively). Taken together, these data suggest that overexpression of cypin specifically affects the lengths of root dendrites with two or more branches. Moreover, we would not have detected this subtle change without using the Tips-In labeling method.

Discussion

Developmental Effects of Cypin Overexpression Is Revealed By Three Types of Sholl Analysis

Our laboratory has published a number of studies reporting an important role for the protein cypin in the regulation of dendrite branching and arborization (Akum et al., 2004; Charych et al., 2006; Chen and Firestein, 2007; Fernandez et al., 2008; Kwon et al., 2011). Until now, our data have been presented as changes in primary and secondary dendrite number and analyzed by conventional Sholl analysis. In the present study, we ask whether the combination of different types of Sholl analysis can uncover local changes to the dendritic arbor promoted by cypin overexpression. This work employs our semi-automated Sholl analysis program ("Bonfire") (Langhammer et al., 2010) and includes three different labeling schemes (Inside-Out, RIT, and Tips-In) to identify previously unreported changes to the dendritic arbor.

To elucidate whether cypin mediates distinct effects on the arbor at different developmental timepoints, we overexpressed cypin from DIV 6–10 and from DIV 10–12, corresponding to periods of active proximal and distal branching (Dotti et al., 1988). When overexpressed from DIV 6–10, cypin increases dendritic branching at 0–42 μm from the soma (**Figure 2B**), but when overexpressed from DIV 10–12, cypin increases dendritic branching at 18–30 μm from the soma (**Figure 6B**). Thus, the increase in dendrite branching caused by cypin occurs farther out from the soma at the later developmental time point, suggesting that cypin has specific effects. This may be due to the fact that cypin promotes local microtubule assembly (Akum et al., 2004), and the location of this assembly during distinct times in development, possibly dependent on to where cypin is targeted, may affect specific regions of the arbor.

In terms of dendrite number, cypin significantly increases total dendrite number (**Figure 2C**) when overexpressed from DIV 6–10 with decreased overall dendrite length (**Figure 2D**). An increase that approaches significance ($p = 0.0581$) in total dendrite number is observed when cypin is overexpressed from DIV 10–12 (**Figure 6C**) with no change in average length (**Figure 6D**). Taken together, these data suggest that cypin alters the dendritic arbor uniquely depending on when in development it is overexpressed. The observed differences in the effect on total dendrite number and average dendrite length could be caused by overexpression of cypin for 96 h versus 48 h. While 48 h (DIV 10–12) was sufficiently long enough to change the dendritic arbor as seen in Total Sholl analysis (**Figure 6B**), it may not have been long enough to significantly change overall dendrite number in the experiments used for this study.

The Effects of Cypin Overexpression on the Dendritic Arbor: Analysis by Labeling Scheme

Several tools (Sholl, 1953; Van Pelt and Verwer, 1985, 1986; Verwer and Van Pelt, 1990; Caserta et al., 1995; Cannon et al., 1998; Uylings and Van Pelt, 2002; Meijering et al., 2004; Rodriguez et al., 2006) have been developed to assist in Sholl analysis, but to our knowledge, Bonfire is the first to offer multiple labeling schemes and generate individual Sholl graphs of different dendrite categories. We have shown that when using these different labeling schemes—Inside-Out, RIT, and Tips-In—the Sholl curves produced can lead to different interpretations of the effects of cypin overexpression on the process of dendrite branching. Inclusion of all of three of the labeling schemes in analysis provides the most complete picture of changes occurring to the arbor.

While Inside-Out is the traditional method for labeling dendrites, information is lost by grouping tertiary and higher order dendrites together. Depending on how the neuron has developed, there may be many tertiary dendrites proximal to the cell body, and they may be several orders away from the terminal branch that is quite far from the cell body. These two types of dendrites would be grouped together in the Inside-Out labeling scheme. The Root-Intermediate-Terminal (RIT) labeling scheme is better suited for uncovering differences in intermediate and terminal dendrites, as they are in separate categories. The RIT scheme suggests that during DIV 6-10, cypin-promoted increases in intermediate dendrites (**Figure 3E**) are due to increased secondary dendrites at 6–12 μm from the soma (**Figure 3B**) and to increased tertiary and higher order dendrites at 30 μm (**Figure 3C**). Additionally, increased terminal branching (**Figure 3F**) appears to result in increased tertiary and higher order dendrites due to the corresponding distances at which significant increases occur. However, terminal branching is not responsible for the increases seen at 54–60 μm from the soma for tertiary and higher order dendrites (**Figure 3C**). For DIV 10–12, the differences in the RIT scheme compared with the Inside-Out scheme indicate that cypin-promoted increases in tertiary and higher order dendrites (**Figure 7C**) are due to an increase in terminal branches (**Figure 7F**) at the corresponding distances, which was the same broad similarity observed for DIV 6–10 overexpression. For intermediate dendrites (**Figure 7E**), it is likely that increased secondary dendrites account for the increased dendrites at 12 μm (**Figure 7B**), whereas tertiary and higher order dendrites are likely responsible for increased dendrites at 18 μm from the soma (**Figure 7C**).

The Tips-In labeling scheme reveals subtle differences that are not uncovered by the other two labeling schemes, even when used in combination. Sholl analysis of primary dendrites using the Tips-In method (**Figure 3G**) suggests that during DIV 6–10, increased proximal dendrites are root dendrites that do not branch, and increased dendrites further from the cell body are higher order terminal branches. For DIV 6–10 overexpression, significant increases are observed at 0–24 μm from the soma for tertiary and higher order dendrites (**Figure 3I**). The increases at 12 μm and closer to the soma are likely due to primary/root dendrites (**Figure 3D**), whereas increases further than 12 μm from the soma are likely due to a combination of intermediate dendrites (**Figure 3E**). For DIV 10–12, increases in Tips-In primary dendrites are observed at 18–30 μm (**Figure 7G**) due to increased terminal branching (**Figure 7F**). Unlike changes detected when cypin is overexpressed at DIV 6–10, there are no increases observed at distances that correspond to the root Sholl analysis using the RIT method, indicating that the increases observed in **Figure 7G** are due to increased terminal branching only and not due to root dendrites. For Tips-In secondary dendrites, increases are observed at 6–18 μm from the soma (**Figure 7H**). The increase at 6 μm is likely due to primary/root dendrites (**Figure 7A**), the increase at 12 μm due to secondary dendrites (**Figure 7B**), and the increase at 18 μm due to tertiary and higher order dendrites (**Figure 7C**). For tertiary and higher order dendrites (**Figure 7I**), increases seen within 6 μm from the soma are likely due to root/primary dendrites that have branched twice since no corresponding increases are observed in other dendrite categories.

Overexpression of Cypin Promotes Shorter Higher Order Dendrites

Regardless of the type of Sholl analysis used, our results strongly suggest that cypin promotes shorter dendrites that are of second order or above. Why would cypin promote increased branching but decreased length? One possibility is that cypin-promoted increases in total dendrites may exhaust a limiting reagent, possibly tubulin or membrane components. A second possibility is that cypin acts via the protein PSD-95. Cypin promotes decreased clustering of PSD-95 (Firestein et al., 1999), which dramatically increases dendrite number but decreases dendrite length (Charych et al., 2006; Sweet et al., 2011a). The de-clustering of PSD-95 may allow correct polarity of microtubules, increasing branching closer to the cell body (Sweet et al.,

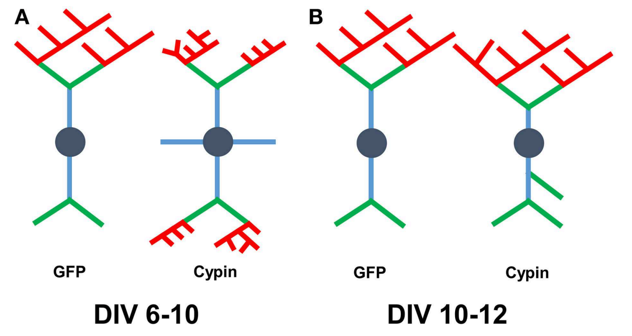

FIGURE 10 | Schematic of results when combining analysis using all three labeling schemes. (A) Changes that occur to the arbor as a result of cypin overexpression from DIV 6–10. Overexpression of cypin increases primary dendrite numbers (blue) and tertiary and higher order dendrite numbers (red). Overexpression of cypin also increases intermediate dendrite numbers (green and red) and terminal dendrite numbers (green and red) but not secondary dendrite numbers (green). Overexpression of cypin decreases tertiary and higher order dendrite length, intermediate dendrite length, and terminal dendrite length but does not affect primary or secondary dendrite length. **(B)** Changes that occur to the arbor as a result of cypin overexpression from DIV 10–12. Overexpression of cypin increases primary dendrites as labeled by Tips-In (terminal dendrites, green and red) and secondary dendrites as labeled by Tips-In (intermediate or root dendrites, green, and blue). Overexpression of cypin significantly decreases tertiary and higher order dendrite length as labeled by Tips-In (root dendrites that branch twice or more). For schematics shown in **(A,B)**, dendrites are labeled according to the Inside-Out (conventional) method.

2011a,b). It is interesting that all labeling schemes yield this result, although the particular orders of dendrites differ. Combining all three Sholl analyses allows us to detect changes to dendrite number and length at subdivisions of the dendritic arbor.

How could cypin-promoted increases in higher order dendrites affect the development of neural networks? Increased number of dendrite branches may allow for increased number of synaptic connections. This may result in increased network activity or, potentially, increased synchronization. Importantly, since these new branches are shorter, local neural circuitry may be affected more than long-range circuitry.

It has been shown by our group that signaling pathways that regulate local changes to the dendritic arbor also act via a cypin-dependent mechanism. For example, brain-derived neurotrophic factor (BDNF) increases cypin protein levels to increase proximal dendritic branching (Kwon et al., 2011). BDNF transcripts may be targeted to the cell body or both the cell body and the dendrites (An et al., 2008), and these distinct trafficking events of BDNF may affect the arbor differently. In addition, RhoA, which itself is locally translated (Wu et al., 2005), regulates the translation of cypin (Chen and Firestein, 2007), which in turn results in increased dendrites. The use of conventional Sholl analysis and dendrite counting may miss the specific effects of local events, and thus, the application of our multiple Sholl analyses will allow for determination of how BDNF and RhoA act to regulate the arbor at specific sites in our future studies.

Conclusions

Overall, we find that cypin overexpression affects Sholl curves, dendrites numbers, and dendrite lengths differently depending on the developmental timepoint and length of time cypin is overexpressed. Combining our Bonfire program (Langhammer et al., 2010) and these different labeling schemes allows us to better understand how factors, such as cypin, act to regulate neuronal morphology, and hence, function. A schematic summarizing the changes that cypin overexpression exerts on the dendritic arbor is included in **Figure 10A** for overexpression at DIV 6–10 and in **Figure 10B** for overexpression at DIV 10–12. Future studies will include collaborations with mathematicians to construct ways to integrate the Inside-Out, RIT, and Tips-In schemes to describe arbors without having to perform the analyses separately. In addition, we would like to use these analyses to devise a system by which we can describe different arbor types (i.e., pyramidal, stellate). Ultimately, we hope that our analyses can be combined with data stored in other neuronal morphology databases (Ascoli et al., 2007). Our ultimate goal is to construct an analysis method that is easy to use, clearly understood, and can serve as a base for comparison between neuron types, different treatments, and experiments performed by different laboratories.

Acknowledgments

This work is funded in part by National Science Foundation grants IBN-0919747 and IBN-1353724 and New Jersey Commission on Brain Injury Research grant #CBIR14IRG019 (to BF). KO is supported by the National Institutes of Health under the Ruth L. Kirschstein National Research Service Award T32 GM8339 from the NIGMS and a Predoctoral Fellowship from the New Jersey Commission on Brain Injury Research #CBIR13FEL002.

References

Akum, B. F., Chen, M., Gunderson, S. I., Riefler, G. M., Scerri-Hansen, M. M., and Firestein, B. L. (2004). Cypin regulates dendrite patterning in hippocampal neurons by promoting microtubule assembly. *Nat. Neurosci.* 7, 145–152. doi: 10.1038/nn1179

An, J. J., Gharami, K., Liao, G. Y., Woo, N. H., Lau, A. G., Vanevski, F., et al. (2008). Distinct role of long 3′ UTR BDNF mRNA in spine morphology and synaptic plasticity in hippocampal neurons. *Cell* 134, 175–187. doi: 10.1016/j.cell.2008.05.045

Ascoli, G. A., Donohue, D. E., and Halavi, M. (2007). NeuroMorpho.Org: a central resource for neuronal morphologies. *J. Neurosci.* 27, 9247–9251. doi: 10.1523/JNEUROSCI.2055-07.2007

Cannon, R. C., Turner, D. A., Pyapali, G. K., and Wheal, H. V. (1998). An on-line archive of reconstructed hippocampal neurons. *J. Neurosci. Methods* 84, 49–54. doi: 10.1016/S0165-0270(98)00091-0

Caserta, F., Eldred, W. D., Fernandez, E., Hausman, R. E., Stanford, L. R., Bulderev, S. V., et al. (1995). Determination of fractal dimension of physiologically characterized neurons in two and three dimensions. *J. Neurosci. Methods* 56, 133–144. doi: 10.1016/0165-0270(94)00115-W

Charych, E. I., Akum, B. F., Goldberg, J. S., Jornsten, R. J., Rongo, C., Zheng, J. Q., et al. (2006). Activity-independent regulation of dendrite patterning by postsynaptic density protein PSD-95. *J. Neurosci.* 26, 10164–10176. doi: 10.1523/JNEUROSCI.2379-06.2006

Chen, H., and Firestein, B. L. (2007). RhoA regulates dendrite branching in hippocampal neurons by decreasing cypin protein levels. *J. Neurosci.* 27, 8378–8386. doi: 10.1523/JNEUROSCI.0872-07.2007

Dong, X., Shen, K., and Bülow, H. E. (2015). Intrinsic and extrinsic mechanisms of dendritic morphogenesis. *Annu. Rev. Physiol.* 77, 271–300. doi: 10.1146/annurev-physiol-021014-071746

Dotti, C. G., Sullivan, C. A., and Banker, G. A. (1988). The establishment of polarity by hippocampal neurons in culture. *J. Neurosci.* 8, 1454–1468.

Eilers, J., and Konnerth, A. (1997). Dendritic signal integration. *Curr. Opin. Neurobiol.* 7, 385–390. doi: 10.1016/S0959-4388(97)80067-0

Elston, G. N., and Fujita, I. (2014). Pyramidal cell development: postnatal spinogenesis, dendritic growth, axon growth, and electrophysiology. *Front. Neuroanat.* 8:78. doi: 10.3389/fnana.2014.00078

Fernández, J. R., Welsh, W. J., and Firestein, B. L. (2008). Structural characterization of the zinc binding domain in cytosolic PSD-95 interactor (cypin): role of zinc binding in guanine deamination and dendrite branching. *Proteins* 70, 873–881. doi: 10.1002/prot.21683

Firestein, B. L., Brenman, J. E., Aoki, C., Sanchez-Perez, A. M., El-Husseini, A. E., et al. (1999). Cypin: a cytosolic regulator of PSD-95 postsynaptic targeting. *Neuron* 24, 659–672. doi: 10.1016/S0896-6273(00)81120-4

Häusser, M., Spruston, N., and Stuart, G. J. (2000). Diversity and dynamics of dendritic signaling. *Science* 290, 739–744. doi: 10.1126/science.290.5492.739

Kulkarni, V. A., and Firestein, B. L. (2012). The dendritic tree and brain disorders. *Mol. Cell. Neurosci.* 50, 10–20. doi: 10.1016/j.mcn.2012.03.005

Kutzing, M. K., Langhammer, C. G., Luo, V., Lakdawala, H., and Firestein, B. L. (2010). Automated Sholl analysis of digitized neuronal morphology at multiple scales. *J. Visual. Exp*. 45:2354. doi: 10.3791/2354

Kwon, M., Fernández, J. R., Zegarek, G. F., Lo, S. B., and Firestein, B. L. (2011). BDNF-promoted increases in proximal dendrites occur via CREB-dependent transcriptional regulation of cypin. *J. Neurosci.* 31, 9735–9745. doi: 10.1523/JNEUROSCI.6785-10.2011

Landgraf, M., and Evers, J. F. (2005). Control of dendritic diversity. *Curr. Opin. Cell Biol.* 17, 690–696. doi: 10.1016/j.ceb.2005.09.005

Langhammer, C. G., Previtera, M. L., Sweet, E. S., Sran, S. S., Chen, M., and Firestein, B. L. (2010). Automated Sholl analysis of digitized neuronal morphology at multiple scales: whole cell Sholl analysis versus Sholl analysis of arbor subregions. *Cytometry Part A* 77A, 1160–1168. doi: 10.1002/cyto.a.20954

Libersat, F. (2005). Maturation of dendritic architecture: lessons from insect identified neurons. *J. Neurobiol.* 64, 11–23. doi: 10.1002/neu.20142

Meijering, E., Jacob, M., Sarria, J. C., Steiner, P., Hirling, H., and Unser, M. (2004). Design and validation of a tool for neurite tracing and analysis in fluorescence microscopy images. *Cytometry Part A* 58A, 167–176. doi: 10.1002/cyto.a.20022

Miller, J. P., and Jacobs, G. A. (1984). Relationships between neuronal structure and function. *J. Exp. Biol.* 112, 129–145.

Rodriguez, A. (2007). *NeuronStudio Documentation.* Available online at: http://research.mssm.edu/cnic/help/ns/labeledges.html

Rodriguez, A., Ehlenberger, D. B., Hof, P. R., and Wearne, S. L. (2006). Rayburst sampling, an algorithm for automated three-dimensional shape analysis from laser scanning microscopy images. *Nat. Protoc.* 1, 2152–2161. doi: 10.1038/nprot.2006.313

Sainath, R., and Gallo, G. (2015). Cytoskeletal and signaling mechanisms of neurite formation. *Cell Tissue Res.* 359, 267–278. doi: 10.1007/s00441-014-1955-0

Santiago, C., and Bashaw, G. J. (2014). Transcription factors and effectors that regulate neuronal morphology. *Development* 141, 4667–4680. doi: 10.1242/dev.110817

Schaefer, A. T., Larkum, M. E., Sakmann, B., and Roth, A. (2003). Coincidence detection in pyramidal neurons is tuned by their dendritic branching pattern. *J. Neurophysiol.* 89, 3143–3154. doi: 10.1152/jn.00046.2003

Sholl, D. A. (1953). Dendritic organization in the neurons of the visual and motor cortices of the cat. *J. Anat.* 87, 387–406.

Sweet, E. S., Previtera, M. L., Fernández, J. R., Charych, E. I., Tseng, C. Y., Kwon, M., et al. (2011a). PSD-95 alters microtubule dynamics via an association with EB3. *J. Neurosci.* 31, 1038–1047. doi: 10.1523/JNEUROSCI.1205-10.2011

Sweet, E. S., Tseng, C. Y., and Firestein, B. L. (2011b). To branch or not to branch: how PSD-95 regulates dendrites and spines. *Bioarchitecture* 1, 69–73. doi: 10.4161/bioa.1.2.15469

Uylings, H. B., and Van Pelt, J. (2002). Measures for quantifying dendritic arborizations. *Network* 13, 397–414. doi: 10.1088/0954-898X/13/3/309

Van Pelt, J., and Verwer, R. W. (1985). Growth models (including terminal and segmental branching) for topological binary trees. *Bull. Math. Biol.* 47, 323–336. doi: 10.1007/BF02459919

Van Pelt, J., and Verwer, R. W. (1986). Topological properties of binary trees grown with order-dependent branching probabilities. *Bull. Math. Biol.* 48, 197–211. doi: 10.1007/BF02460023

Verwer, R. W., and Van Pelt, J. (1990). Analysis of binary trees when occasional multifurcations can be considered as aggregates of bifurcations. *Bull. Math. Biol.* 52, 629–641. doi: 10.1007/BF02462102

Vetter, P., Roth, A., and Hausser, M. (2001). Propagation of action potentials in dendrites depends on dendritic morphology. *J. Neurophysiol.* 85, 926–937.

Wu, K. Y., Hengst, U., Cox, L. J., Macosko, E. Z., Jeromin, A., Urquhart, E. R., et al. (2005). Local translation of RhoA regulates growth cone collapse. *Nature* 436, 1020–1024. doi: 10.1038/nature03885

Zoghbi, H. Y. (2003). Postnatal neurodevelopmental disorders: meeting at the synapse? *Science* 302, 826–830. doi: 10.1126/science.1089071

Conflict of Interest Statement: Drs. Bonnie L. Firestein reports patent US US7338769 B2 titled "Methods for identifying agonists of cypin" and patent US 7790843 B2 titled "Cypin polypeptide and fragments thereof."

frontiers in Cellular Neuroscience

OPINION
published: 12 August 2015
doi: 10.3389/fncel.2015.00316

Tension-driven axon assembly: a possible mechanism

Steven R. Heidemann[1]* **and Dennis Bray**[2]

[1] Department of Physiology, Michigan State University, East Lansing, MI, USA, [2] Department of Physiology, Development and Neuroscience, University of Cambridge, Cambridge, UK

Keywords: axonal elongation, biomechanics, cytoskeleton dynamics, neural development, mechanotransduction, cellular

As the contents of this issue of "Frontiers" attest, the study of the mechanical aspects of neuronal development has come a long way since the 1970's and 80's when we became interested in the topic. The vast majority of cells in multicellular organisms are continually pushed and pulled, compressed, and stretched throughout their life and a diversity of mechanisms have evolved to protect against and harness these forces. Nerve cells are no exception, and several excellent reviews in recent years have examined ways in which mechanical inputs influence their development and function (Smith, 2009; Suter and Miller, 2011; Franze, 2013). However, it seems to us that certain aspects of this response have not been given the attention they deserve. In particular tension-driven axon assembly seems to be in a class of its own and quite distinct from other effects of tension such as modifications of cell migration, perturbation of division cycles, or changes in synthetic activity. Axon growth under these conditions is an exaggerated transformation of a nerve cell manifest by the prolonged accretion of new cellular material. Under the right circumstances, the rate and extent of this mass addition is remarkably large, to the degree that it implies an unusual, possibly unique mechanism. A pulled axon grows as though the nerve cell contained telescopic machinery prefabricated for elongation. But the identity of this nascent structure (if it exists), where it is stored, and how it is triggered to self-assemble into axon, remain to be discovered.

Mature axons have been known to be under tension since the early days of neuroanatomy. Harrison described the second phase of growth in which axons, having reached their target tissue while the axon is very short, increase their length coordinate with surrounding tissues—referring to it as "passive stretching" (Harrison, 1935). Weiss (1941) explicitly postulated that growth following synaptogenesis was due to mechanical tension. He described the "towing" of the axon as a result of the migration of the post-synaptic cell, as in the lateral line organ of zebrafish (Gilmour et al., 2004). Much later it became evident that mechanical tension has an essential role in the other, first phase of growth. Growth cones from individual sympathetic neurons growing in culture were recorded migrating away from the cell soma, pulling out neurites as they went (Bray, 1979). Vectorial analysis of the outgrowths produced in this way confirmed that they were tension-generated networks anchored at their free ends.

Incidentally, the curious observation was made in this early work that growth cones could be redirected by displacing their neurites with a fine microneedle. Pulling the neurite in a southwesterly direction, for example, caused the growth cone to head northeast, and so on. Growth was always along the vector of maximum tension and, even more dramatically, removal of the tension on a neurite caused the growth cone to bifurcate to produce a branch. This effect is as yet unexplained but seems to imply that tension within the body of the growth cone can direct the assembly of cytoskeletal structures such as microtubules and filopodia.

A series of experiments performed in the 1980s showed that, under appropriate conditions, mechanical tension is the determining stimulus leading to formation and elongation of an axon. Growth cones, or more precisely the terminal segment of neurites, were lifted from the culture surface by means of an electrode and then pulled under carefully controlled conditions. The axons

Edited by:
Daniel Marcel Suter,
Purdue University, USA

Reviewed by:
Jeffrey Urbach,
Georgetown University, USA
Bryan Pfister,
NJ Institute of Technology, USA

***Correspondence:**
Steven R. Heidemann,
heideman@msu.edu

Received: 28 May 2015
Accepted: 29 July 2015
Published: 12 August 2015

Citation:
Heidemann SR and Bray D (2015) Tension-driven axon assembly: a possible mechanism.
Front. Cell. Neurosci. 9:316.
doi: 10.3389/fncel.2015.00316

formed in these experiments had a normal diameter, contained a typical cytoskeletal array, and were capable of subsequent elongation via a growth cone. Growth cones and axons could also be initiated *de novo* from embryonic chick sensory and forebrain neurons (Bray, 1984; Chada et al., 1997). In embryonic rat hippocampal neurons, applied tension was shown to specify which of several initial neurites take on a differentiated axonal fate. In a neuron typically extending only one axon, tension could stimulate formation of multiple axons (Lamoureux et al., 2002).

This approach has shown that all tested axonal types grow in response to applied tension and, particularly significant, the rate of elongation is directly proportional to the magnitude of applied tension. This robust linear function ($r > 0.9$ in 97% of trials) has been demonstrated for embryonic chick sensory (Zheng et al., 1991) and forebrain neurons (Chada et al., 1997) as well as embryonic rat hippocampal neurons (Lamoureux et al., 2002), and rat retinal ganglion neurons (Steketee et al., 2014). Such simple proportionality between tensions and elongation rates is the defining characteristic of an ideal (Newtonian) fluid-mechanical element, a dashpot. That is, the experimenter (or growth cone) produces a pulling force that the axon accommodates in a fluid-like manner, dissipating the force by elongating more axon. This is a strong physical argument for an immediate and direct relationship between tension and the axonal assembly process (O'Toole et al., 2008).

Experimentally applied mechanical tension can cause far more robust axonal growth than is observed "physiologically," either *in vitro* or *in situ*. The most extreme example is the work of Smith and Pfister (Pfister et al., 2004; Smith, 2009). Embryonic (E15) rat dorsal root ganglia were explanted onto two overlapping membranes that were then gradually separated by a stepper motor, i.e., placed under continuous mechanical tension, such that the axons were elongating in the space between the membranes. This experimental system supported axonal elongation rates of ∼400 μm/h, ∼10-fold greater than the typical advance rate of growth cones! As for mass addition, this protocol permitted axonal tracts some 10 cm in length after 2 weeks of towing with axonal diameters 30% greater than cultures grown out solely by growth cone activity. The axons elongated by experimental tension were shown to have a normal cytoskeletal array and were electrically active (Pfister et al., 2006, see also Loverde and Pfister, 2015, this issue).

The data are persuasive therefore that tension can be the proximate cause for axonal elongation. By "proximate" we mean a situation in which mechanical tension is the immediate stimulus for axonal elongation, and apparently axonal initiation and specification as well. Clearly myriad longer-time-scale regulators are also necessary, such as appropriate trophic factors, growth-associated proteins, and specializations of the cytoskeleton. But with all that in place, it is undeniable that there are situations in which mechanical tension is the determining stimulus leading to formation and elongation of an axon. But how does this work? What is it in an axon that the mechanical signal acts upon and how is this initial response transduced into a cascade of biochemical and cellular changes? The conditions for the various experimental "towing" interventions apparently disqualify the typical mechanotransduction pathways. In particular, axons are suspended in the culture medium during most protocols to experimentally elongate axons, i.e., the axon is largely isolated during towing. This argues that the tension-sensing mechanism is entirely contained within the axon. So, for example, adhesions or changes of adhesion to a substrate, probably the most widely cited subprocess of cellular mechanotransduction (Ingber, 2006; Hoffman et al., 2011; Iskratsch et al., 2014), apparently do not directly contribute to tension-induced mass addition. Similarly, there are no changes in cellular motility; no changes in cell–cell interactions; and no changes in cell stiffness (again, a Newtonian dashpot). These "disqualifications" highlight the possibly unique status of neuronal elongation in response to tension. We can only speculate on the possible mechanism.

From a purely geometric standpoint, a nerve cell that produces 1 mm of axon in a day (a typical rate in a towing experiment) increases its length by several orders of magnitude more than its radius making longitudinal addition of material the dominant factor in response to pulling. Thus, longitudinal elements such as microtubules, intermediate filaments, and actin filaments, should be selectively up-regulated in a towed neuron, to a much greater

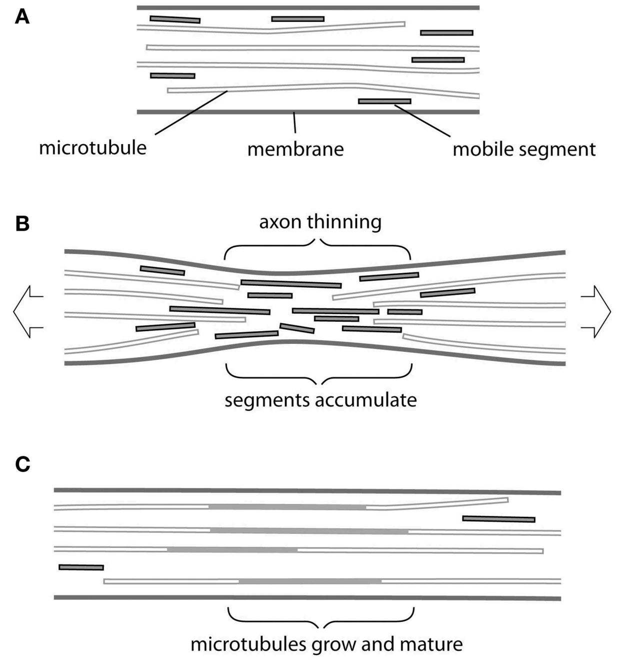

FIGURE 1 | Possible mechanism of tension-driven axon growth. **(A)** Region of axon is shown containing long and short microtubules. Short microtubule segments (red) are rapidly transported in both anterograde and retrograde direction by molecular motors. Note that neurofilaments, which behave in a similar fashion, are omitted for clarity. **(B)** Tension is created in the axon by pulling. This causes the axon to become thinner and long microtubules to be drawn apart longitudinally. At the same time thinning causes microtubules to be pushed together laterally. Rapid transport is no longer possible across this region and mobile segments build up in a traffic jam. **(C)** The accumulated microtubule segments rearrange and add to free ends. Eventually new lengths of microtubule become stabilized by associated proteins, causing their lateral spacing to increase and the axonal diameter to return to its original value.

degree than components of the cytosol or nucleus. Moreover, since the bulk of this synthesis will take place in the cell soma, we also anticipate a major increase in the transport of these proteins and their assembly at the site of growth.

Providentially, recent findings concerning the transport and assembly of cytoskeletal elements in an axon seem to offer a possible mechanism (**Figure 1**). At steady state (**Figure 1A**), short segments of both microtubules and neurofilaments have been observed to move rapidly within the axon in either direction, driven by molecular motors, and to be able to add to more static structures (Wang and Brown, 2002; Baas et al., 2006; Brown and Jung, 2013). These motile segments therefore offer a potential source for mass addition, available at short notice at any point along the axon. Conceivably they could even underpin the notional telescopic mechanism for elongation mentioned above. But how could tension cause mobile segments of microtubules and neurofilaments to accumulate at the right location and when required?

The simplest answer seems to us to be thinning of the axon during stretch (**Figure 1B**). Here, we are focused on stretch that does not cause evidence of injury (Loverde and Pfister, 2015, this issue). Although in such cases the final diameter of axons produced by towing is reported to be normal, in every series of experiments there are instances in which thinning and eventual breakage of neurites occurs. This was especially noticeable in axons towed rapidly (Fass and Odde, 2003) and—interestingly—also conspicuous following treatment with the microtubule poison vinblastine (Zheng et al., 1993). If we consider that, even in the hands of the most skilled operator, some degree of thinning must occur then we have a plausible first step for our response. Tension will draw microtubules and neurofilaments apart longitudinally and possibly also cause them to break (Tang-Schomer et al., 2012). At the same time these cytoskeletal elements will be forced closer together by the thinning of the axon, so that the space between them available for transport will be reduced. It may be noted that, compaction of microtubules and neurofilaments was directly observed in thinned regions of axons following stretching and fast-freezing (Ochs et al., 1997). Breakage and compaction conspire to impede the progress of shorter more mobile segments of microtubules and neurofilaments, which will therefore pile up at the site of constriction in a "traffic jam" (**Figure 1B**). We can then imagine the normal process of maturation taking place (**Figure 1C**) in which the accumulated segments add to the cytoskeletal framework of the axon and acquire a complement of associated proteins, such as the newly described complex between ankyrin and MAP1B (Stephan et al., 2015). Spaces between microtubules and neurofilaments will be restored and new channels created. Transport will resume and the original axon diameter will return to its original value… at this point tension will have caused the axon to grow.

Clearly this description omits many essential steps. Upregulation of the synthesis of tubulin and neurofilament protein must occur in the cell body together with that of actin filaments and membrane components such as channels. These all have to be transported into the axon and assembled in the correct location. But the notion of an accumulation of cytoskeletal and membrane components triggered by axon thinning and their subsequent rearrangement and maturation could explain the remarkable and possibly unique response of neurons to tension.

Acknowledgments

We would like to thank Maximillian Jakobs for insightful comments. SH would like to thank Phillip Lamoureux and Robert E. Buxbaum for their productive collaborations over many years.

References

Baas, P. W., Vidya Nadar, C., and Myers, K. A. (2006). Axonal transport of microtubules: the long and short of it. *Traffic* 7, 490–498. doi: 10.1111/j.1600-0854.2006.00392.x

Bray, D. (1979). Mechanical tension produced by nerve cells in tissue culture. *J. Cell Sci.* 37, 391–410.

Bray, D. (1984). Axonal growth in response to experimentally applied mechanical tension. *Dev. Biol.* 102, 379–389. doi: 10.1016/0012-1606(84)90202-1

Brown, A., and Jung, P. (2013). A critical reevaluation of the stationary axonal cytoskeleton hypothesis. *Cytoskeleton* 70, 1–11. doi: 10.1002/cm.21083

Chada, S., Lamoureux, P., Buxbaum, R. E., and Heidemann, S. R. (1997). Cytomechanics of neurite outgrowth from chick brain neurons. *J. Cell Sci.* 110, 1179–1186.

Fass, J. N., and Odde, D. J. (2003). Tensile force-dependent neurite eicitation via anti-[beta]1 integrin antibody-coated magnetic beads. *Biophys. J.* 85, 623–636. doi: 10.1016/S0006-3495(03)74506-8

Franze, K. (2013). The mechanical control of nervous system development. *Development* 140, 3069–3077. doi: 10.1242/dev.079145

Gilmour, D., Knaut, H., Maischein, H.-M., and Nüsslein-Volhard, C. (2004). Towing of sensory axons by their migrating target cells *in vivo*. *Nat. Neurosci.* 7, 491–492. doi: 10.1038/nn1235

Harrison, R. G. (1935). On the origin and development of the nervous system studied by the methods of experimental embryology. *Proc. R. Soc. Lond. B* 118, 155–196. doi: 10.1098/rspb.1935.0053

Hoffman, B. D., Grashoff, C., and Schwartz, M. A. (2011). Dynamic molecular processes mediate cellular mechanotransduction. *Nature* 475, 316–323. doi: 10.1038/nature10316

Ingber, D. E. (2006). Cellular mechanotransduction: putting all the pieces together again. *FASEB J.* 20, 811–827. doi: 10.1096/fj.05-5424rev

Iskratsch, T., Wolfenson, H., and Sheetz, M. P. (2014). Appreciating force and shape—the rise of mechanotransduction in cell biology. *Nat. Rev. Mol. Cell Biol.* 15, 825–833. doi: 10.1038/nrm3903

Lamoureux, P. L., Ruhel, G., Buxbaum, R. E., and Heidemann, S. R. (2002). Mechanical tension can specify axonal fate in hippocampal neurons. *J. Cell Biol.* 159, 499–508. doi: 10.1083/jcb.200207174

Ochs, S., Pourmand, R., Jersild, R. A., and Friedman, R. N. (1997). The origin and nature of beading: a reversible transformation of the shape of nerve fibers. *Progr. Neurobiol.* 52, 391–426. doi: 10.1016/S0301-0082(97)00022-1

O'Toole, M. R., Lamoureux, P. L., and Miller, K. E. (2008). A physical model of axonal elongation: force, viscosity, and adhesions govern the mode of outgrowth. *Biophys. J.* 94, 2610–2620. doi: 10.1529/biophysj.107.117424

Pfister, B. J., Bonislawski, D. P., Smith, D. H., and Cohen, A. S. (2006). Stretch-grown axons retain the ability to transmit active electrical signals. *FEBS Lett.* 580, 3525–3531. doi: 10.1016/j.febslet.2006.05.030

Pfister, B. J., Iwata, A., Meaney, D. F., and Smith, D. H. (2004). Extreme stretch growth of integrated axons. *J. Neurosci.* 24, 7978–7983. doi: 10.1523/JNEUROSCI.1974-04.2004

Smith, D. H. (2009). Stretch growth of integrated axon tracts: extremes and exploitations. *Progr. Neurobiol.* 89, 231–239. doi: 10.1016/j.pneurobio.2009.07.006

Steketee, M. B., Oboudiyat, C., Daneman, R., Trakhtenberg, E., Lamoureux, P., Weinstein, J. E., et al. (2014). Regulation of intrinsic axon growth ability at retinal ganglion cell growth cones. *Invest. Ophthalmol. Vis. Sci.* 55, 4369–4377. doi: 10.1167/iovs.14-13882

Stephan, R., Goellner, B., Moreno, E., Frank, C. A., Hugenschmidt, T., Genoud, C., et al. (2015). Hierarchical microtubule organization controls axons caliber and transport and determines synaptic structure and stability. *Dev. Cell* 33, 5–21. doi: 10.1016/j.devcel.2015.02.003

Suter, D. M., and Miller, K. E. (2011). The emerging role of forces in axonal elongation. *Progr. Neurobiol.* 94, 91–101. doi: 10.1016/j.pneurobio.2011.04.002

Tang-Schomer, M. D., Johnson, V. E., Baas, P. W., Stewart, W., and Smith, D. H. (2012). Partial interruption of axonal transport due to microtubule breakage accounts for the formation of periodic varicosities after traumatic axonal injury. *Exp. Neurol.* 233, 364–372. doi: 10.1016/j.expneurol.2011.10.030

Wang, L., and Brown, A. (2002). Rapid movement of microtubules in axons. *Curr. Biol.* 12, 1496–1501. doi: 10.1016/S0960-9822(02)01078-3

Weiss, P. (1941). Nerve patterns: the mechanics of nerve growth. *Growth* 5 (Suppl. Third Growth Symposium), 153–203.

Zheng, J., Buxbaum, R. E., and Heidemann, S. R. (1993). Investigation of microtubule assembly and organization accompaying tension-induced initiation. *J. Cell Sci.* 104, 1239–1250.

Zheng, J., Lamoureux, P. L., Santiago, V., Dennerll, T., Buxbaum, R. E., and Heidemann, S. R. (1991). Tensile regulation of axonal elongaton and initiation. *J. Neurosci.* 11, 117–1125.

Conflict of Interest Statement: The authors declare that the research was conducted in the absence of any commercial or financial relationships that could be construed as a potential conflict of interest.

frontiers
in Cellular Neuroscience

ORIGINAL RESEARCH
published: 05 August 2015
doi: 10.3389/fncel.2015.00292

Stretch induced hyperexcitability of mice callosal pathway

Anthony Fan [1], *Kevin A. Stebbings* [2], *Daniel A. Llano* [2,3,4,5] *and Taher Saif* [1]*

[1] Department of Mechanical Science and Engineering, University of Illinois, Urbana, IL, USA, [2] Neuroscience Program, University of Illinois, Urbana, IL, USA, [3] Department of Molecular and Integrative Physiology, University of Illinois, Urbana, IL, USA, [4] Beckman Institute, University of Illinois, Urbana, IL, USA, [5] College of Medicine, University of Illinois, Urbana, IL, USA

Memory and learning are thought to result from changes in synaptic strength. Previous studies on synaptic physiology in brain slices have traditionally been focused on biochemical processes. Here, we demonstrate with experiments on mouse brain slices that central nervous system plasticity is also sensitive to mechanical stretch. This is important, given the host of clinical conditions involving changes in mechanical tension on the brain, and the normal role that mechanical tension plays in brain development. A novel platform is developed to investigate neural responses to mechanical stretching. Flavoprotein autofluoresence (FA) imaging was employed for measuring neural activity. We observed that synaptic excitability substantially increases after a small (2.5%) stretch was held for 10 min and released. The increase is accumulative, i.e., multiple stretch cycles further increase the excitability. We also developed analytical tools to quantify the spatial spread and response strength. Results show that the spatial spread is less stable in slices undergoing the stretch-unstretch cycle. FA amplitude and activation rate decrease as excitability increases in stretch cases but not in electrically enhanced cases. These results collectively demonstrate that a small stretch in physiological range can modulate neural activities significantly, suggesting that mechanical events can be employed as a novel tool for the modulation of neural plasticity.

Keywords: neuromechanics, acute brain slice, hyperexcitability, plasticity, mechanical stretch, flavoproteins autofluorescence

Edited by:
Kyle Miller,
Michigan State University, USA

Reviewed by:
Katsuei Shibuki,
Niigata University, Japan
Bryan Pfister,
New Jersey Institute of Technology, USA

****Correspondence:***
Taher Saif,
Mechanical Science and Engineering, University of Illinois, 1206 W. Green St., Urbana, IL 61801, USA
saif@illinois.edu

Received: *30 April 2015*
Accepted: *15 July 2015*
Published: *05 August 2015*

Citation:
Fan A, Stebbings KA, Llano DA and Saif T (2015) Stretch induced hyperexcitability of mice callosal pathway. Front. Cell. Neurosci. 9:292. doi: 10.3389/fncel.2015.00292

Introduction

Modulation of neuronal communications has traditionally been viewed as chemically induced (Kandel et al., 2012). However, recent evidence shows that mechanical cues influence many biological processes (Wang et al., 2009). Neurons are particularly sensitive to their mechanical micro-environment. For example, ion channels are mechano-sensitive, such that a high-enough stress induces structural changes in a protein complex, and hence a change in functionality (Sachs, 2010). This has been shown experimentally in a variety of systems (Pfister et al., 2006; Cohen et al., 2007; Morris, 2011). In addition, growth of neurons can be induced by an applied stretch (Pfister et al., 2004). For example, dorsal root ganglion neurons are able to respond to a steady stretch and adjust their length to as far as a thousand times their original length. Application of stretch in the physiological range to frog neuromuscular junctions increases the frequency of spontaneous activities and the amplitude of evoked activities (Chen and Grinnell, 1995) within tens of milliseconds. Embryonic drosophila motor neurons actively maintain a rest tension of about a nano-Newton, and the loss of that tension prevents neurotransmitter vesicle clustering at the presynaptic terminal (Siechen et al., 2009). Finally, stretching the axon of the motor neurons by 5% for 30 min increases vesicle clustering by 200% (Siechen et al., 2009).

Central nervous system neurons are also subjected to large mechanical stretches and tension with varying rates during development, tumor growth and injuries, and brain swelling. It has been shown that tension is able to direct the growth of primary hippocampal neuron in 2-D culture (Lamoureux et al., 2002). CNS axons can also be stretch grown to 1 cm in length (Smith et al., 2001). Various groups have looked at the effect of traumatic strain, strain rate, and stress on cell death regulatory mechanism (Morrison et al., 2011; Franze et al., 2013) in animal models (Santhakumar et al., 2001), dissociated primary culture (Patel et al., 2014), and cortical cell culture (Goforth et al., 2011; Ferrario et al., 2013). However, the effects of mechanical stretches at the physiological level on long and short term synaptic functions, in particular, neuronal excitability remain unclear.

Although it has been speculated that mechanical forces at the physiological level play a role in brain morphology (Van Essen, 1997) and function (Tyler, 2012), no direct observations have yet been made to demonstrate their effect on brain functionality. In this study, we show, using untreated mouse brain coronal slices, that the history of both a small stretch and a small stretch rate can substantially modulate evoked and spontaneous neural activities in the callosal pathway. We chose the coronal preparation of the callosal axon pathway for its strong axon projection bridging the 2 hemispheres. The pathway consists of a large number of axonal projections. Thus, the preparation is appropriate for testing the hypothesis that mechanical stretch along the pathway will affect its function, in particular its excitability. We developed an experimental setup that allows us to apply a prescribed amount of stretch in one direction across the brain slice, modeling an increased physiological tension along the callosal axonal projections. Concurrently, the setup allows evaluation of spontaneous and electrically evoked neural activities. These activities are quantified by imaging flavoprotein autofluorescence (FA), which originates from the change of oxidation state of mitochondrial flavoproteins upon neuronal activation (Shibuki et al., 2003; Reinert et al., 2007).

Materials and Methods

Brain Slicing

One month old mice of both sexes were obtained from the in-house animal facility at Beckman Institute for Advanced Science and Technology at the University of Illinois. The animal was deeply anesthetized with ketamine (100 mg/kg) and xylazine (3 mg/kg) and a transcardial perfusion was subsequently performed with chilled oxygenated (95% O2/5% CO2) slicing solution [sucrose (234 mM), glucose (11 mM), NaHCO3(26 mM), KCl (2.5 mM), NaH2PO4●H2O (125 mM), MgCl2●6H2O (10 mM), and CaCl2●2H2O (0.5 mM)] at 4°C. The mouse was then decapitated and its brain was removed from the skull. The aligned brain tissue was submerged in chilled slicing fluid in a vibration slicer. Obtained slices 600 μm thick were left in a warm (32°C) artificial cerebrospinal fluid (aCSF) [NaHCO3 (26 mM), KCl (2.5 mM), glucose (10 mM), NaCl (126 mM), NaH2PO4●H2O (1.25 mM), MgCl2●6H2O (3 mM), and CaCl22H2O (1.1 mM)] bath for an hour before experiments. We have previously found that 600 μm thick slices prepared in a similar fashion are robustly viable (Llano et al., 2014). In this study, all data are obtained from the callosal pathway. All procedures were approved by the Institutional Animal Care and Use Committee at the University of Illinois. All animals were housed in animal care facilities approved by the American Association for Accreditation of Laboratory Animal Care. Every attempt was made to minimize the number of animals used and to reduce suffering at all stages of the study.

Stretching Mechanism

Slices were gripped and made stationary by a micro-vice on each side of the perfusion stage as depicted in **Figures 1A–C**. This was intended to avoid the use of an adherent stretchable substrate leading to a mismatch in elastic properties. Each micro-vice is connected to the frame of the recording chamber. A power screw mechanism controlled by a stepper motor is used to actuate the micro-vices toward or away from each other. Each clockwise turn of the screw would lead to a linear retraction of 1/80 inches and vice versa, hence stretching/relaxing the mounted slice. Geometries were optimized so that the whole device could be fit under the fluorescence microscope used for imaging during the experiment. The inlet and outlet attached to the recording chamber enable aCSF [NaHCO3 (26 mM), KCl (2.5 mM), glucose (10 mM), NaCl (126 mM), NaH2PO4●H2O (1.25 mM), MgCl2●6H2O (2 mM), and CaCl2●2H2O (2 mM)] to perfuse the slice at a constant flow rate with no apparent waste accumulation.

Flavoprotein Autofluorescence Imaging

FA was used in this study to track neuronal activities. Briefly, oxidation of mitochondrial flavoproteins is induced by influx of calcium ions upon neuronal activation (Shibuki et al., 2003). The oxidized flavoproteins fluoresce green under blue light. By tracking this green autofluorescence, neural activity could be measured. We and others have shown that it is a highly sensitive marker of neuronal activation and is quantitative (Reinert et al., 2007; Llano et al., 2009, 2012). Importantly, and unlike other imaging methods, the FA imaging signals remain stable for hours in a slice preparation (Shibuki et al., 2003). This permits a series of manipulations to be done in the tissue to investigate potential mechanisms by which micro-stretch affects neuronal activity. It has been shown that 80% of the FA signal comes from postsynaptic activations (Reinert et al., 2004; Llano et al., 2009). The method provides a rapid assessment of neuronal activation and carries several advantages compared to other imaging techniques that involve dye loading. Dye loading (e.g., calcium-sensitive or voltage-sensitive dyes) creates substantial changes in signal strength over time and potential heterogeneities over the tissue, depending on dye uptake (Lajtha et al., 2007). Electrophysiological measurements are of limited use in the current experiments because upon the induction of stretch, slippage might occur between the electrode-tissue interface. In this study, the slice was put under an epifluorescence

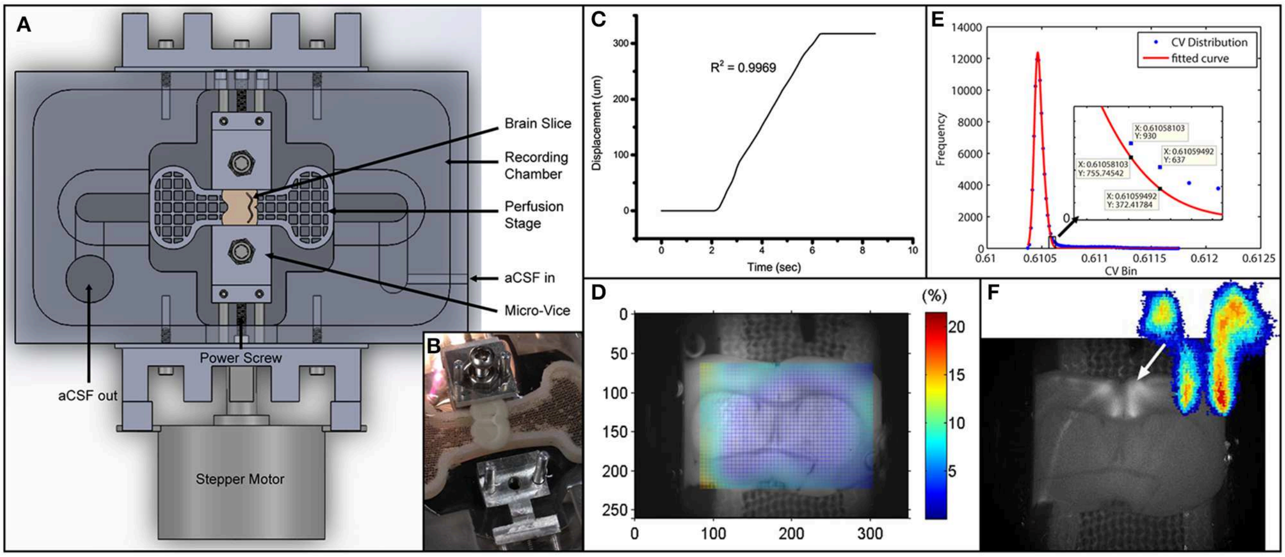

FIGURE 1 | Experimental setup and data analysis methods. (A) Schematics depicting the entire setup. Micro-vices are actuated by a power screw mechanism in which a rotation of the screw will result in a uniaxial translation. **(B)** Picture of device with brain slice secured on one end. **(C)** Displacement vs. time plot depicting the stretch applied during the experiment. R^2-value describes a linear fit to the increasing region. The displacement is 317.5 µm over 4 s, giving a stretch rate of 79.4 µm/s. **(D)** Digital image correlation (see Materials and Methods) was used to obtain displacement fields from videos. The color map here plots the effective strain (Equation 2) over the brain slice preparation. **(E)** I_{CV} of all pixels are plotted as a histogram in blue circles. Red line depicts a 2-term Gaussian fit. The right hand side is magnified in the subplot. Threshold value based on Equation (3) is sandwiched between the 2 data labels. **(F)** Grayscale image was obtained by performing a standard deviation projection in ImageJ. The heat map was generated by plotting I_{CV}^{p}. Sparse outliers away from the main area were also trimmed.

microscope [Olympus BX51 with a Prior Lumen 200 light source] using an UMNIB Olympus filter cube (470–490-nmexcitation, 505-nm dichroic, and 515-nm emission long pass) and other supplementary optics (Theyel et al., 2011). Images were acquired with a CCD camera [QImaging EXi with Firewire interface] at 4 frames per second. Image analyses were done in ImageJ and MATLAB.

Electrical and Chemical Stimulation

In all experiments, 800 nM of SR95531 (Tocris Bioscience, Bristol, UK), antagonist of the neuroinhibitor $GABA_A$, was added to the aCSF. SR95531 lowers the activation barrier for neuronal firing making the callosal system hyperexcitable to gain a measureable signal to stimulation. To stimulate, we used in-bath tungsten electrodes that did not directly contact the slice. Electrical pulse train stimulations were applied every 10 s for 50 repetitions in all experiments. Each stimulation is a train of 2ms pulses at 40 Hz for 1 s. Amplitudes varied from 1 to 6 mA to achieve an initial excitability of around 10% in every experiment. Excitability is defined as the number of FA responses over the number of stimulations.

Strain Field Calculation

Strain could be defined with different reference points. Here, we provided measurements of two strain values. The global strain was calculated based on the displacement of the micro-vices alone. It is the distance traveled by the moving micro-vice over the original separation between the 2 micro-vices.

We also measured the strain field in the region with FA responses using digital image correlation (DIC) analysis (Jones et al., 2014). We called this the local strain. Briefly, every image (except the first one) in an image sequence was divided into small subregions. Each subregion was treated as rigid (no deformation whatsoever). These subregions were then compared to the first image in the sequence to find the location of maximum correlation. This way a displacement vector could be formulated for each subregion in every image. The displacement vectors could then be interpolated and smoothed to give a numerical displacement field. The displacement values (u) were then formulated into a 2-D strain tensor field (**Figure 1D**), given the plane stress assumption, using the following strain-displacement relationship:

$$\epsilon_{\alpha\beta}=\frac{1}{2}(\frac{\partial u_{\alpha}}{\partial X_{\beta}}+\frac{\partial u_{\beta}}{\partial X_{\alpha}}), \tag{1}$$

where X is the coordinate system, and $\alpha\beta = 1, 2$ define the in-plane coordinates. When the 2 indices are the same, i.e., $\alpha = \beta = 1 \; or \; 2$, it is denoting the axial strains. When the 2 indices are different, i.e., $\alpha \neq \beta$, it is the shear component induced by the inhomogeneity of the brain slice. To summarize the strain field, essentially a 2-by-2 tensor, we adopted the effective strain convention. Effective strain (ϵ_e), reported as local strain in text, can be defined as:

$$\epsilon_e = \sum_{\beta=1}^{2}\sum_{\alpha=1}^{2}\sqrt{\frac{2}{3}\epsilon_{\alpha\beta}\epsilon_{\alpha\beta}}. \tag{2}$$

The local effective strain serves to account for also the shear components in the local region, whereas the global strain has only axial components. Global strain is what is applied, while local strain is the resulting strain level in the region of interest.

Quantification of Evoked Activation

A criterion is required to identify the active pixels for an accurate representation of the spatial and temporal FA activation. We used the coefficient of variation, I_{cv}, (standard deviation over mean) of temporal intensities of each pixel to find the active pixels in our image sequences. To determine the threshold for quantification of activation area, we plotted the I_{cv} distribution into a histogram, $H[I_{cv}]$, and fit the profile to a two-term Gaussian function, $G(I_{cv})$. The selection of two-term Gaussian was because all images could be segmented into a darker region and a brighter region. The Gaussian distribution could then capture random noises fluctuating around the respective mean. The right tail (with larger values) is expected to deviate from the normal distribution because of the fluorescing pixels, and we use this point of deviation as our I_{cv} threshold value (**Figure 1E**). The point of deviation, I_{cv}^{p}, is defined as:

$$I_{cv}^{p}{:}I_{cv} \rightarrow \frac{H-G}{G} > 0.5. \qquad (3)$$

It is essentially when the actual distribution (H) exceeds the Gaussian (G) by 50%. To quantify the time profile of activation of the activated region (**Figure 1F**), spatial averaging of intensity was used. The change in activation is quantified by $\frac{\Delta f}{f_0}$, defined as the change in fluorescence over baseline fluorescence.

During the measurement of spontaneous activities, the slice was constantly moving. This led to a problem of uneven lighting as we progressed through the image sequence, affecting the FA signal. In an effort to correct this artifact, we established and reported the adjusted intensity. The adjusted intensity I_{adj} is defined as:

$$I_{adj}\,[t] = \sum_{x_i,y_i\in A}^{N} \frac{I[x_i,y_i,t]}{N} - \left(\sum_{x_i=x_{min}}^{x_{max}} \sum_{y_i=y_{min}}^{y_{max}} \frac{I\left[x_i,y_i,t\right]}{\Delta x\Delta y - N} - \sum_{x_i,y_i\in A}^{N} \frac{I\left[x_i,y_i,t\right]}{\Delta x\Delta y - N} \right), \qquad (4)$$

where A denotes the activation area. x_{max}, x_{min}, y_{max}, and y_{min} are the limit points of the smallest rectangle enclosing the entire activation area. $\Delta x = x_{max} - x_{min}$. $\Delta y = y_{max} - y_{min}$. This could be interpreted as the signal minus the average background intensity. The first term in Equation (4) denotes the signal averaged over the activation area. The second term denotes averaged background intensity.

Results

Flavoprotein Autofluorescence before Stretch and after Stretch

Using the platform we developed (**Figure 1A**), the brain slice was gently gripped and tensed by the micro-vices until no edge slippage was observed ensuring that the prescribed stretch was entirely applied onto the slice. (see **Figure 1B** and Materials and Methods for detailed description). As baseline measurement, we took a fluorescence video of 500 s long recording the response of the slice to 50 stimulation pulse trains, each 10 s apart. The slice was subsequently stretched by 317.5 μm (or 4.2% of total the length of the slice) over 4 s (**Figure 1C**). Using the DIC methods (see Materials and Methods), effective strain at responsive area was found to be 2.5% (**Figure 1D**), while edge-to-edge global strain is 4.2%. The stretch was maintained for 10 min and then entirely released. *No measurement was made while the slice was being held stretched.* After the slice was released from stretch, we performed the baseline measurement again. This stretch-baseline-cycle was repeated for 4 more times. This paradigm was applied to 4 independent slices from 4 animals.

To ensure that the extra excitability is not due to sensitization to electrical stimulations or degeneration of tissue health, control slices were subjected to the same series of manipulation, without the stretch. The control paradigm was applied to 3 independent slices from 3 animals.

Stretch Effects on Excitability

Excitability here is defined as the ratio of number of times the slice responds (detected using FA) to the number it is electrically stimulated. Thus, excitability gives the probability of FA response. We found that in all slices undergoing the stretch-baseline-cycle ($n = 4$), excitability increases after every cycle to ultimately 3 times of the original probability (**Figure 2A**). It thus seems that the slice “remembers” its past history of stretch, and its current excitability results from a cumulative effect of its past stretches. Normalized baseline measurements from the control group ($n = 3$) are plotted next to stretched group. We fit a linear regression to each experiment individually, and the averaged slope is reported in **Figure 2B** comparing the slope in stretched and control slices. We found that the stretched slices showed a significant increase in excitability compared to control slices ($p = 0.013$).

Stretch Effects on Spatial and Temporal Activation

We note that the area of activation of the slice fluctuates in the stretched group (**Figure 3A**). Further looking into the spatial distribution and the strength of variation in the activation area, we observed a shift in the location of maximum activity in the stretched group. An example is shown in **Figure 3A**, with the stretched group at the top row and the control group at the bottom. It is thus possible that the stretch applied and released in between the 2 baseline measurements can lead to a spatial reconfiguration of excitability.

Temporal activation profile, $\frac{\Delta \mathrm{f}}{\mathrm{f}_0}$, is plotted against time. The amplitude of each fluorescence peak is obtained by subtracting the value preceding the stimulation to the peak $\frac{\Delta f}{f_0}$ value. The first activation amplitude, i.e., the first electrical stimulation after the stretch is released, in each baseline measurement is found to be steady (**Figure 3B**). However, the average activation amplitude is found to decrease after each stretch-baseline cycle. The control amplitudes remain unchanged (**Figure 3C**). We fit a linear regression to the amplitudes in each experiment individually, and

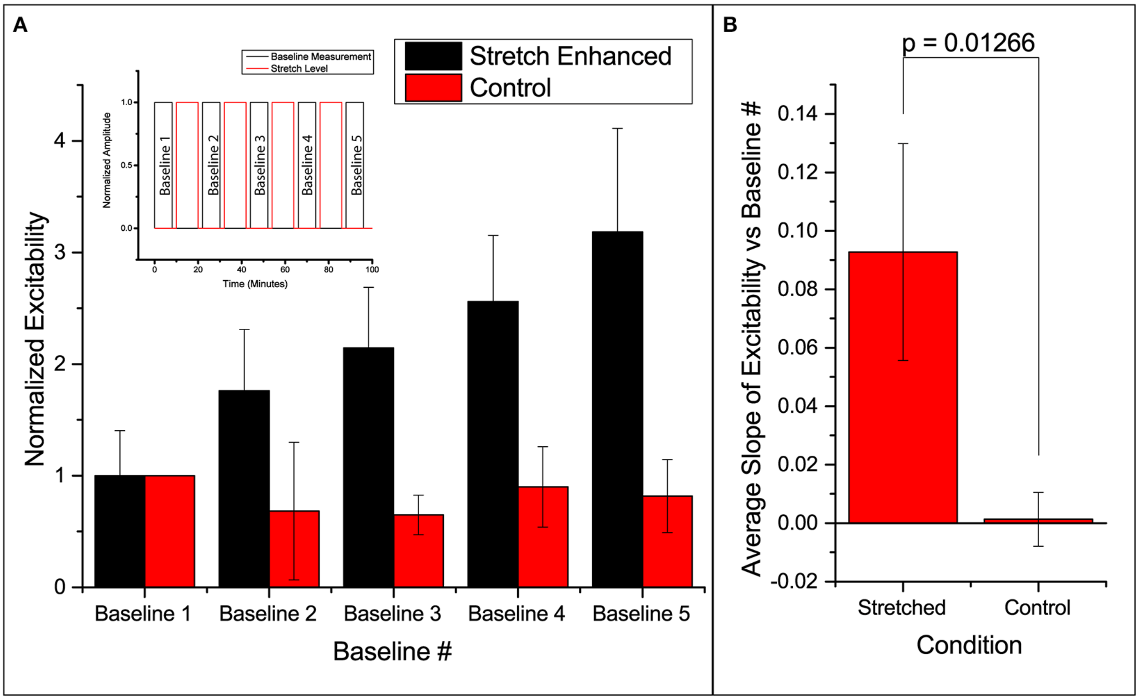

FIGURE 2 | Enhanced excitability of callosal pathway by stretch alone and the 2 control schemes. (A) Normalized probability of response of stretched group and control group. The stretched data set here is individually normalized to the average probability of the first baseline. This serves to show the variation in the starting probability of response, as given in the error bar. All subsequent column plots are normalized to the first baseline probability within individual experimental data set, leading to an error bar magnitude of 0. Subfigure includes a schematic of the paradigm. **(B)** The slopes of excitability vs. baseline # in each independent data set are averaged and reported here. This serves to compare the increase in excitability of the stretched and control groups. All error bars in SD. *P*-value obtained from 2-tail *t*-test with unequal variance.

the averaged slope is reported in **Figure 3D**. All stretched slices show significant negative slope compared to controls ($p = 0.041$) and a significant negative slope of the temporal activation rate ($p = 0.028$, **Figure 3E**). The temporal activation rate serves as a secondary measurement of the temporal activation. It is equivalent to the maximum rate $\frac{d\left(\frac{\Delta f}{f_0}\right)}{dt}$ when the FA signal is ascending to the peak value (FA amplitude).

The attenuations in the signal appear to correlate with the number of FA responses. This leads to the question whether the attenuation of activation amplitude and rate is simply due to the increase in the number of FA responses or is actually induced by the stretching paradigm. To address this question, we artificially increased the probability of FA response by increasing the applied electrical stimulation ($n = 4$). A linear regression is fit to the amplitude/rate vs. excitability profile in individual experiment separately (**Figures 3F,G**). The average slope (slightly positive but approaching zero) shows that the activation amplitude and rate do not change with electrical stimulation alone. This is possibly because at subthreshold stimulations, increasing electrical current does not lead to an FA response with a larger amplitude. The extra energy is exhausted by the higher number of FA occurrences. Thus, we conclude that the attenuation of the signals is due to the stretching paradigm rather than a consequence of electrical stimulation, suggesting that the stretching manipulation might have lowered the energy barrier for synaptic activation leading to hyperexcitability.

Spontaneous Activities due to Stretch Alone

By introducing a higher concentration of SR95531, it would lead to spontaneous FA activities previously not observed. A separate slice was stretched with time (**Figure 4A**) in a stepwise fashion in 3 cycles with a higher dose of SR95531 (2 μM). There was a 5-min time gap between each cycle. No electrical stimulation was applied here. The slice was imaged during the entire span of the cycles and FA data were analyzed as described in Equation (4) (see Materials and Methods).

The $\frac{\Delta f}{f_0}$ plots show a close correspondence between stretching impulse (strain rate > 0) and induced flavoprotein activities in all three cycles of stretch (**Figure 4A**). Some spontaneous FA signals could be observed when the slice was not stretched or when simply held stretched, i.e., strain rate $= 0$. No activity was observed during the relaxation steps (strain rate < 0). Out of the 11 stretching steps, 6 (50%) led to an immediate FA response; two others led to FA responses within 13 s (**Figure 4B**). The results suggest that a brain slice is sensitive to also stretch impulses.

Discussion

The probability of neural response to electrical stimulation can be increased by applying a stronger electrical stimulus or by

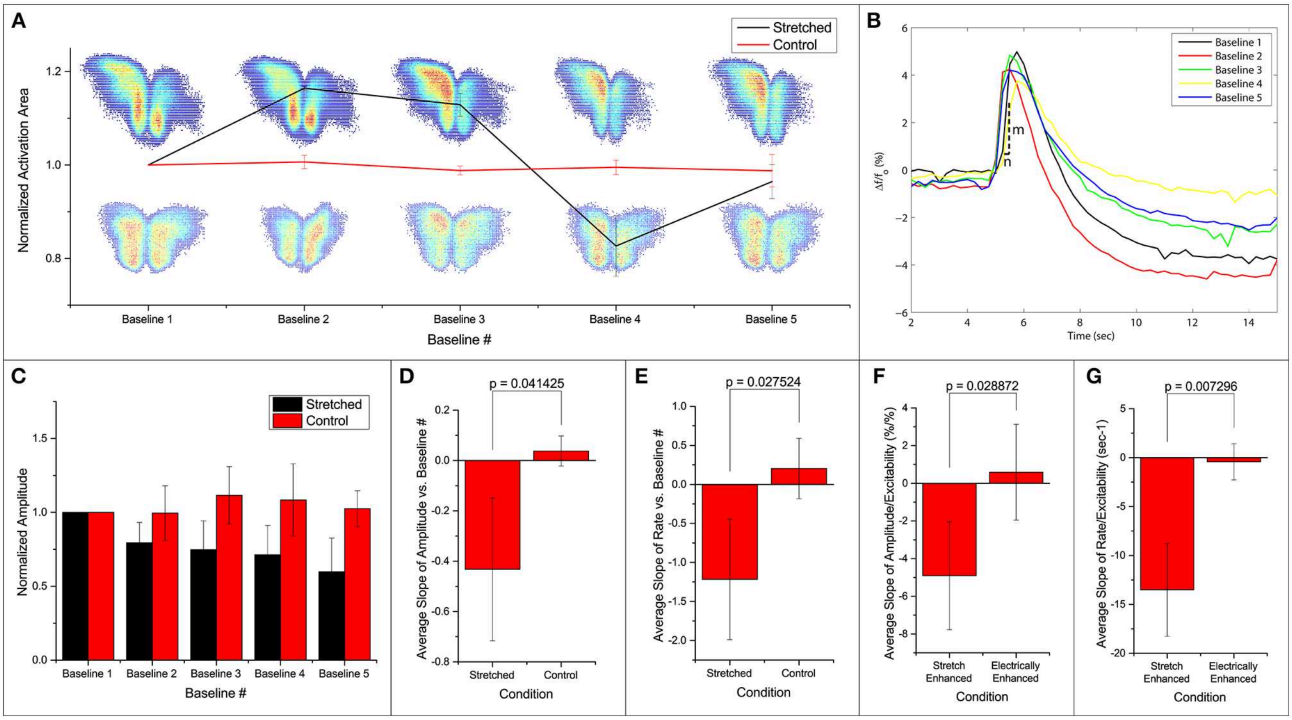

FIGURE 3 | Fluorescence intensities are averaged over the calculated activation areas. (A) Spatial activities in subsequent baseline measurements. Normalized activation area of the stretched and control groups are plotted. Two examples of activation areas: stretched on top, and control at the bottom. **(B)** An example of the $\frac{\Delta f}{f_0}$ signal in one stretch experiment. Each line denotes the first FA response (out of 50 stimulations) in baseline 1–5 as labeled. All measurements are made when stretch is zero. After each baseline measurement, slice is held stretched for 10 min and then brought back to the original position before the next baseline measurement commences. Activation rate is defined as $\frac{m}{n}$. **(C)** Normalized average amplitudes are plotted for the stretched and control groups. Slope of **(D,F)** amplitude and **(E,G)** rate vs. baseline measurement number and excitability from each experiment is averaged and compared. All error bars in SD. *P*-values obtained from 2-tail t-test with unequal variance.

applying the stimulus more frequently (Bikson et al., 2004). Long-term potentiation (LTP) has been shown to be induced by a tetanic stimulation in which frequency is usually in the range of 100Hz (Malenka and Bear, 2004). Long-term depression (LTD), on the other hand, can be induced by a low frequency stimulation in the range of 10 Hz (Malenka and Bear, 2004). The actual frequency that is required to induce plasticity is pathway-dependent and species-dependent (Malenka and Bear, 2004). At intermediate frequencies, synaptic transmission is usually memoryless, i.e., the same electrical stimulus will give the same probability/strength of neural responses regardless of what the pathway was subjected to before (Bliss and Lomo, 1973).

Here we show that by maintaining a small stretch for 10 min, we can increase this probability of neural response. Note that this is not the same as LTP, since LTP describes the changes in strength of postsynaptic response, whereas we are reporting excitability. Nonetheless, in both LTP and the stretch-enhanced excitability, the electrically evoked activity has a higher probability in surpassing the activation threshold.

It is not yet known whether the changes in probability, amplitude or rate of the FA response correlate with similar change in the underlying electrophysiological response. However, it has been shown that there is a strong correspondence in the strength of the 2 signals under normal conditions (Shibuki et al., 2003; Reinert et al., 2004; Llano et al., 2009). It has also been shown that only 15% of the FA signal is left when postsynaptic glutamate receptors are blocked (Reinert et al., 2004; Llano et al., 2012). Therefore, it is likely the increase in excitability we see here are due to direct/indirect enhancement in postsynaptic activity—either as a result of more vesicles being released from the presynaptic terminal upon the same stimulation, or the mechanism of receiving the vesicles has become more efficient.

Previous finding reports that a 5% stretch in embryonic Drosophila axons of motor neurons results in a 200% increase in neurotransmitter vesicle clustering at the presynaptic terminal of neuromuscular junctions. It takes about 20 min for the increased clustering to occur (Siechen et al., 2009; Ahmed et al., 2012). In our case, the stretch was held for 10 min. Arguably, the difference could be attributed to the different species and the different neural structures (neuromuscular vs. neural-neural). It is thus possible that the increased clustering of synaptic vesicles can lead to a higher docking ratio, more frequent spontaneous release, and larger release upon stimulation (Dobrunz, 2002). This could explain the higher excitability upon completion of a stretch-baseline cycle.

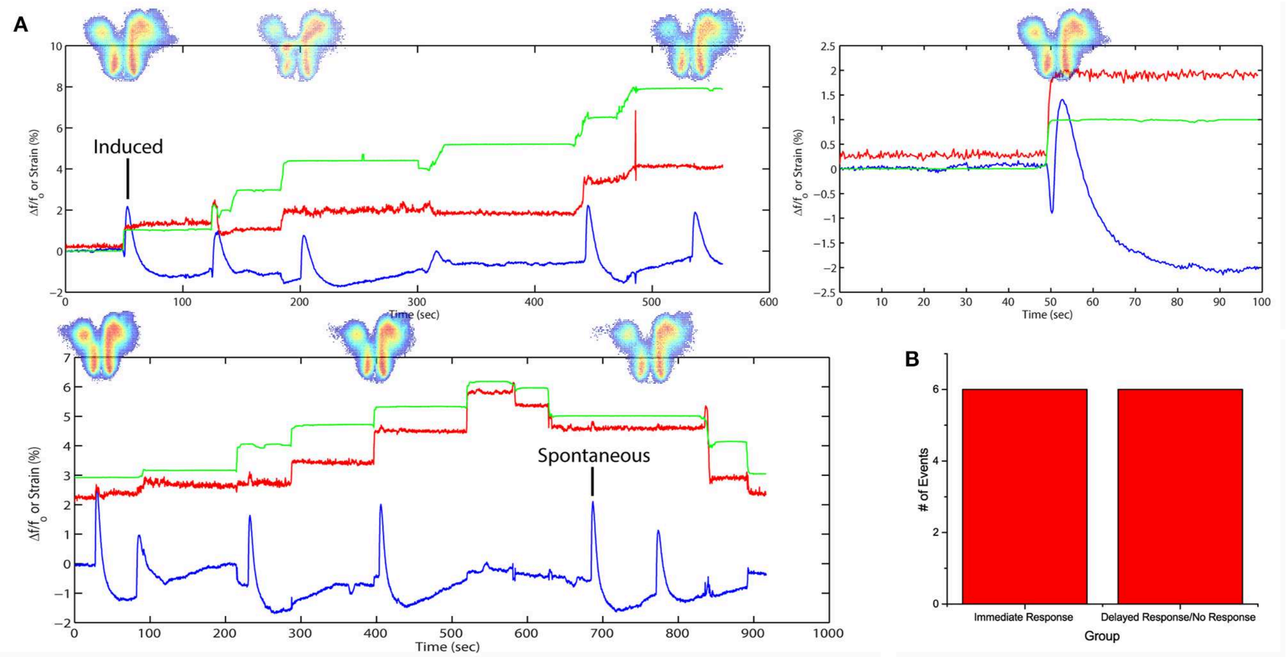

FIGURE 4 | Stretch effects alone without electrical stimulation. (A) Processed average intensities are plotted against time. Red lines denote effective strain level at activation area. Green lines denote effective strain level globally, defined by the position of the micro-vices. Activation area examples are placed aligned to respective peaks. An example is given for induced and spontaneous activation respectively. **(B)** All fluorescence occurrences are grouped into 2 groups: (1) immediate firing after stretch application, (2) delayed firing or no firing before the next stretch.

The increased response due to stretch could be because of postsynaptic modifications, in particular, that stretch results in increased clustering of neurotransmitter receptors (AMPA and/or NMDA) in the postsynaptic density, similar to LTP (Bear et al., 1987). This increases the probability of neuronal activity due to a given electrical stimulation and hence a given presynaptic release of neurotransmitter. It has been shown that integrin activities (to be discussed) lead to phosphorylation of CamKII (Charrier et al., 2010), known to be critical in LTP (Lisman et al., 2012).

Cell-cell adhesion protein molecules facilitate force transfer in neighboring cells by acting as an anchor (Wang et al., 2009). Many of these protein complexes are found in neural pathways (Mobley et al., 2009). Increased mechanical tension can lead to a structural change in these molecules leading to downstream signaling cascades. One study has attributed the high stretch sensitivity of motor nerve terminals to integrin, a cell-cell adhesion protein (Chen and Grinnell, 1995). In that study, both the evoked amplitude and the frequency of spontaneous activity increase significantly with the application of stretch on frog muscle. The increase is linear with respect to the magnitude of the stretch applied. The known integrin inhibitors, such as peptides containing the Arg-Gly-Asp (RGD) sequence, suppressed the stretch sensitivity. Enhancement of transmitter release occurs within a few milliseconds of the stretch application, which might affect the stretch-rate sensitivity of neuronal response, i.e., increased responsiveness at faster rate of stretch.

Stretch or tension can also increase ionic conductances, similar to peripheral mechanotransducers (Sachs, 1991), either pre- or post-synaptically. Collectively, or individually, alterations in ionic conductances could lower the activation barrier for action potentials or increase postsynaptic sensitivity to presynaptic activity. The change of conductance due to stretch is expected to be instantaneous. Thus, this mechanism should also result in strain-rate sensitivity, possibly providing an explanation for the similar sensitivity we observed.

There are also clinical implications to this work. Stretching of axons is seen in a large number of clinical conditions, including hydrocephalus, traumatic brain injury and other forms of brain injury leading to edema (e.g., stroke, tumors, infection). The current results imply that even small amounts of stretch can lead to major changes in neuronal function, and may explain hyperexcitability phenomena, such as seizures, that can be seen during these states. We note that some studies have shown that traumatic levels of stretch typically lead to hypoexcitability (Goforth et al., 2011; Ferrario et al., 2013). It is thus possible that different strength of mechanical stimuli can lead to opposite outcomes. Future work will clarify the mechanisms of the changes we observed, and may therefore lead to novel therapeutics to deal with these stretch-induced hyperexcitability.

Author Contributions

AF, KS, DL, TS designed research. AF, KS performed research. AF contributed unpublished reagents/analytic tools. AF, TS analyzed data. AF, TS wrote the paper. All authors read and reviewed the paper.

Acknowledgments

This work was funded by the National Science Foundation (NSF 1300808) Grant 0965918 IGERT at UIUC: Training the Next Generation of Researchers in Cellular and Molecular Mechanics and Bio-Nanotechnology.

References

Ahmed, W. W., Li, T. C., Rubakhin, S. S., Chiba, A., Sweedler, J. V., and Saif, T. A. (2012). Mechanical tension modulates local and global vesicle dynamics in neurons. *Cell. Mol. Bioeng.* 5, 155–164. doi: 10.1007/s12195-012-0223-1

Bear, M. F., Cooper, L. N., and Ebner, F. F. (1987). A physiological basis for a theory of synapse modification. *Science* 237, 42–48. doi: 10.1126/science.3037696

Morrison, B. III., Elkin, B. S., Doll'e, J. P., and Yarmush, M. L. (2011). *In vitro* models of traumatic brain injury. *Annu. Rev. Biomed. Eng.* 13, 91–126. doi: 10.1146/annurev-bioeng-071910-124706

Bikson, M., Inoue, M., Akiyama, H., Deans, J. K., Fox, J. E., Miyakawa, H., et al. (2004). Effects of uniform extracellular DC electric fields on excitability in rat hippocampal slices *in vitro*. *J. Physiol.* 557, 175–190. doi: 10.1113/jphysiol.2003.055772

Bliss, T. V., and Lomo, T. (1973). Long-lasting potentiation of synaptic transmission in the dentate area of the anaesthetized rabbit following stimulation of the perforant path. *J. Physiol.* 232, 331–356. doi: 10.1113/jphysiol.1973.sp010273

Charrier, C., Machado, P., Tweedie-Cullen, R. Y., Rutishauser, D., Mansuy, I. M., and Triller, A. (2010). A crosstalk between β1 and β3 integrins controls glycine receptor and gephyrin trafficking at synapses. *Nat. Neurosci.* 13, 1388–1395. doi: 10.1038/nn.2645

Chen, B. M., and Grinnell, A. D. (1995). Integrins and modulation of transmitter release from motor nerve terminals by stretch. *Science* 269, 1578–1580. doi: 10.1126/science.7667637

Cohen, A. S., Pfister, B. J., Schwarzbach, E., Grady, M. S., Goforth, P. B., and Satin, L. S. (2007). Injury-induced alterations in CNS electrophysiology. *Prog. Brain Res.* 161, 143–169. doi: 10.1016/S0079-6123(06)61010-8

Dobrunz, L. E. (2002). Release probability is regulated by the size of the readily releasable vesicle pool at excitatory synapses in hippocampus. *Int. J. Dev. Neurosci.* 20, 225–236. doi: 10.1016/S0736-5748(02)00015-1

Ferrario, C. R., Ndukwe, B. O., Ren, J., Satin, L. S., and Goforth, P. B. (2013). Stretch injury selectively enhances extrasynaptic, GluN2B-containing NMDA receptor function in cortical neurons. *J. Neurophysiol.* 110, 131–140. doi: 10.1152/jn.01011.2012

Franze, K., Janmey, P. A., and Guck, J. (2013). Mechanics in neuronal development and repair. *Annu. Rev. Biomed. Eng.* 15, 227–251. doi: 10.1146/annurev-bioeng-071811-150045

Goforth, P. B., Ren, J., Schwartz, B. S., and Satin, L. S. (2011). Excitatory synaptic transmission and network activity are depressed following mechanical injury in cortical neurons. *J. Neurophysiol.* 105, 2350–2363. doi: 10.1152/jn.00467.2010

Jones, E. M. C., Silberstein, M. N., White, S. R., and Sottos, N. R. (2014). In situ measurements of strains in composite battery electrodes during electrochemical cycling. *Exp. Mech.* 54, 971–985. doi: 10.1007/s11340-014-9873-3

Kandel, E., Schwartz, J., Jessell, T., Siegelbaum, S., and Hudspeth, A. J. (2012). *Principles of Neural Science, 5th Edn*. New York, NY: McGraw Hill Professional.

Lajtha, A., Gibson, G. E., and Dienel, G. A. (2007). *Handbook of Neurochemistry and Molecular Neurobiology*. New York, NY: Springer.

Lamoureux, P., Ruthel, G., Buxbaum, R. E., and Heidemann, S. R. (2002). Mechanical tension can specify axonal fate in hippocampal neurons. *J. Cell Biol.* 159, 499–508. doi: 10.1083/jcb.200207174

Lisman, J., Yasuda, R., and Raghavachari, S. (2012). Mechanisms of CaMKII action in long-term potentiation. *Nat. Rev. Neurosci.* 13, 169–182. doi: 10.1038/nrn3192

Llano, D. A., Slater, B. J., Lesicko, A. M., and Stebbings, K. A. (2014). An auditory colliculothalamocortical brain slice preparation in mouse. *J. Neurophysiol.* 111, 197–207. doi: 10.1152/jn.00605.2013

Llano, D. A., Theyel, B. B., Mallik, A. K., Sherman, S. M., and Issa, N. P. (2009). Rapid and sensitive mapping of long-range connections *in vitro* using flavoprotein autofluorescence imaging combined with laser photostimulation. *J. Neurophysiol.* 101, 3325–3340. doi: 10.1152/jn.91291.2008

Llano, D. A., Turner, J., and Caspary, D. M. (2012). Diminished cortical inhibition in an aging mouse model of chronic tinnitus. *J. Neurosci.* 32, 16141–16148. doi: 10.1523/JNEUROSCI.2499-12.2012

Malenka, R. C., and Bear, M. F. (2004). LTP and LTD: an embarrassment of riches. *Neuron* 44, 5–21. doi: 10.1016/j.neuron.2004.09.012

Mobley, A. K., Tchaicha, J. H., Shin, J., Hossain, M. G., and McCarty, J. H. (2009). Beta8 integrin regulates neurogenesis and neurovascular homeostasis in the adult brain. *J. Cell Sci.* 122, 1842–1851. doi: 10.1242/jcs.043257

Morris, C. E. (2011). Voltage-gated channel mechanosensitivity: fact or friction? *Front. Physiol.* 2:25. doi: 10.3389/fphys.2011.00025

Patel, T. P., Ventre, S. C., Geddes-Klein, D., Singh, P. K., and Meaney, D. F. (2014). Single-neuron NMDA receptor phenotype influences neuronal rewiring and reintegration following traumatic injury. *J. Neurosci.* 34, 4200–4213. doi: 10.1523/JNEUROSCI.4172-13.2014

Pfister, B. J., Bonislawski, D. P., Smith, D. H., and Cohen, A. S. (2006). Stretch-grown axons retain the ability to transmit active electrical signals. *FEBS Lett.* 580, 3525–3531. doi: 10.1016/j.febslet.2006.05.030

Pfister, B. J., Iwata, A., Meaney, D. F., and Smith, D. H. (2004). Extreme stretch growth of integrated axons. *J. Neurosci.* 24, 7978–7983. doi: 10.1523/JNEUROSCI.1974-04.2004

Reinert, K. C., Dunbar, R. L., Gao, W., Chen, G., and Ebner, T. J. (2004). Flavoprotein autofluorescence imaging of neuronal activation in the cerebellar cortex *in vivo*. *J. Neurophysiol.* 92, 199–211. doi: 10.1152/jn.01275.2003

Reinert, K. C., Gao, W., Chen, G., and Ebner, T. J. (2007). Flavoprotein autofluorescence imaging in the cerebellar cortex *in vivo*. *J. Neurosci. Res.* 85, 3221–3232. doi: 10.1002/jnr.21348

Sachs, F. (1991). Mechanical transduction by membrane ion channels: a mini review. *Mol. Cell. Biochem.* 104, 57–60. doi: 10.1007/BF00229804

Sachs, F. (2010). Stretch-activated ion channels: what are they? *Physiology* 25, 50–56. doi: 10.1152/physiol.00042.2009

Santhakumar, V., Ratzliff, A. D., Jeng, J., Toth, Z., and Soltesz, I. (2001). Long-term hyperexcitability in the hippocampus after experimental head trauma. *Ann. Neurol.* 50, 708–717. doi: 10.1002/ana.1230

Shibuki, K., Hishida, R., Murakami, H., Kudoh, M., Kawaguchi, T., Watanabe, M., et al. (2003). Dynamic imaging of somatosensory cortical activity in the rat visualized by flavoprotein autofluorescence. *J. Physiol.* 549, 919–927. doi: 10.1113/jphysiol.2003.040709

Siechen, S., Yang, S., Chiba, A., and Saif, T. (2009). Mechanical tension contributes to clustering of neurotransmitter vesicles at presynaptic terminals. *Proc. Natl. Acad. Sci. U.S.A.* 106, 12611–12616. doi: 10.1073/pnas.0901867106

Smith, D. H., Wolf, J. A., and Meaney, D. F. (2001). A new strategy to produce sustained growth of central nervous system axons: continuous mechanical tension. *Tissue Eng.* 7, 131–139. doi: 10.1089/107632701300062714

Theyel, B. B., Llano, D. A., Issa, N. P., Mallik, A. K., and Sherman, S. M. (2011). *In vitro* imaging using laser photostimulation with flavoprotein autofluorescence. *Nat. Protoc.* 6, 502–508. doi: 10.1038/nprot.2011.315

Tyler, W. J. (2012). The mechanobiology of brain function. *Nat. Revie. Neurosci.* 13, 867–878. doi: 10.1038/nrn3383

Van Essen, D. C. (1997). A tension-based theory of morphogenesis and compact wiring in the central nervous system. *Nature* 385, 313–318. doi: 10.1038/385313a0

Wang, N., Tytell, J. D., and Ingber, D. E. (2009). Mechanotransduction at a distance: mechanically coupling the extracellular matrix with the nucleus. *Nat. Rev. Mole. Cell Biol.* 10, 75–82. doi: 10.1038/nrm2594

Conflict of Interest Statement: The authors declare that the research was conducted in the absence of any commercial or financial relationships that could be construed as a potential conflict of interest.

frontiers in Cellular Neuroscience

ORIGINAL RESEARCH
published: 16 July 2015
doi: 10.3389/fncel.2015.00271

An electromechanical model of neuronal dynamics using Hamilton's principle

Corina S. Drapaca *

Department of Engineering Science and Mechanics, Pennsylvania State University, University Park, PA, USA

Damage of the brain may be caused by mechanical loads such as penetration, blunt force, shock loading from blast, and by chemical imbalances due to neurological diseases and aging that trigger not only neuronal degeneration but also changes in the mechanical properties of brain tissue. An understanding of the interconnected nature of the electro-chemo-mechanical processes that result in brain damage and ultimately loss of functionality is currently lacking. While modern mathematical models that focus on how to link brain mechanics to its biochemistry are essential in enhancing our understanding of brain science, the lack of experimental data required by these models as well as the complexity of the corresponding computations render these models hard to use in clinical applications. In this paper we propose a unified variational framework for the modeling of neuronal electromechanics. We introduce a constrained Lagrangian formulation that takes into account Newton's law of motion of a linear viscoelastic Kelvin–Voigt solid-state neuron as well as the classic Hodgkin–Huxley equations of the electronic neuron. The system of differential equations describing neuronal electromechanics is obtained by applying Hamilton's principle. Numerical simulations of possible damage dynamics in neurons will be presented.

Keywords: electromechanics, dynamic stiffness, Kelvin–Voight model, Hodgkin–Huxley model, Hamilton's principle

Edited by:
Daniel Marcel Suter,
Purdue University, USA

Reviewed by:
Ellen Kuhl,
Stanford University, USA
M. Taher A. Saif,
University of Illinois at
Urbana-Champaign, USA

Correspondence:
Corina S. Drapaca,
Department of Engineering Science
and Mechanics, Pennsylvania State
University, 212 Earth-Engineering
Science Building, University Park,
PA 16803, USA
csd12@psu.edu

Received: *02 May 2015*
Accepted: *29 June 2015*
Published: *16 July 2015*

Citation:
Drapaca CS (2015) An electromechanical model of neuronal dynamics using Hamilton's principle. Front. Cell. Neurosci. 9:271. doi: 10.3389/fncel.2015.00271

Introduction

Brain tissue is an inhomogeneous, multi-scale composite material composed of interconnected networks of blood vessels, neuron, and glia cells submerged in cerebrospinal fluid. Effects of mechanical and/or electro-chemical stresses and deformations on brain vary widely depending on the cell types, mechanical and bio-chemical characteristics of the cells, as well as cell's mechanosensitivity and mechanotransduction abilities. For instance, brain damage may take many different forms. For neurons, damage might include breakage of cytoskeleton networks in dendrites or axons, membrane rupture, separation of synaptic connections, or severance of dendritic or axonal projections. For the vascular system, damage might be puncture of macro or micro capillaries, or restrictions that alter perfusion on various scales. Depending on severity, most of these mechanical injuries will be followed by short or long term chemical imbalances and/or functional impairments or even death.

Given the high complexity of brain's structure and dynamics, designing, performing, and interpreting experiments on brain *in vivo* at various time and length scales continue to be very challenging and as a result the mechanisms that govern the interconnected electro-chemo-mechanical processes that result in brain damage and ultimately loss of functionality remain poorly understood. Mathematical models and corresponding computer simulations can increase our comprehension on brain damage processes (and, in general, on neurological diseases and neurodegeneration) and help design better experiments for measurements and hypothesis testing that ultimately will lead to improved medical diagnostic and therapeutic protocols. In the last few decades a multitude of mathematical models have been proposed to study brain biomechanics and, independently, brain bio-chemistry at cell as well as tissue levels. The majority of these models are mentioned in the comprehensive reviews of brain biomechanics and mechanobiology by Goldsmith (2001) and Goriely et al. (2015). Recently, models that link brain biomechanics to its bio-chemistry have also started to be developed (Drapaca and Fritz, 2012; Lang et al., 2015). Such coupled models are essential in enhancing the understanding of brain mechanisms such as the onset of normal pressure hydrocephalus due to ionic imbalances and in the absence of an elevated intracranial pressure (Drapaca and Fritz, 2012), and the propagation of damage in brain tissue caused by edema and lack of proper oxygenation (Lang et al., 2015). However, the lack of experimental data required by these very advanced mathematical models as well as the complexity of the corresponding computations render these models hard to use in today's clinical applications. In addition, these coupled models have been built at tissue level and thus they cannot predict the mechano-chemical responses of brain cells to mechanical and/or electro-chemical events that happen at tissue and organ scales.

The latest survey of the literature on brain biomechanics and mechanobiology by Goriely et al. (2015) emphasizes the current need in the field of brain research for the development of *"bottom-up"* mathematical models that link brain mechanics and function at each relevant length scale as well as across scales, incorporate anatomically accurate geometry and connections of cells and cerebral vasculature, and ultimately allow information from molecular and cellular levels to propagate to tissue and organ levels and *vice versa*. One possible first step in building such a bottom-up model is to start at the cell level and create an electromechanical model of neuronal dynamics. The aim of this paper is therefore to develop a lower-dimensional electromechanical model of a neuron which (1) is simple enough so that its predictions may be experimentally verified, and (2) could be used as a foundation model for more advanced multi-scaling (bottom-up) mathematical models. We assume that the electro-chemical activity of a neuron is described by the classic Hodgkin–Huxley equations (Hodgkin and Huxley, 1952) and that from a mechanical point of view the neuron behaves like a linear visco-elastic Kelvin–Voigt solid. The assumption of linear viscoelastic neuron is supported by experimental evidence reported by Lu et al. (2006) and Grevesse et al. (2015). In order to couple the Kelvin–Voigt mechanical model and the Hodgkin–Huxley electric model we will use a constraint Lagrangian formulation and the non-conservative form of Hamilton's principle. This approach will give us the coupled equations of motion by minimizing a special integral functional (action) whose integrand is made of kinetic and potential energies (Lagrangian) and the work done by the forces acting on the neuron. Although Hamilton's principle has been used in classical mechanics for a very long time (see for instance Lanczos, 1986), and recently has been applied to model neuronal electro-chemical activities (Dickel, 1989; Paninski, 2006; Wilson and Steyn-Ross, 2008; Chuankui, 2012) and ion transport through cell's membrane (Eisenberg et al., 2010), the principle has not been used to link neuron's mechanics and its electro-chemistry until now. The proposed electromechanical model has the following desirable features: (1) incorporates relevant macroscopic (cell level) and microscopic (ionic level) mechanical and electrical information, (2) facilitates the study of the dynamics of neuronal stiffness due to the evolutions of microstructural components, and (3) highlights neuronal mechanotransduction. We test the performance of our model in numerical simulations of neuronal mechanical insults. Although today it is well-known and accepted that traumatic brain injuries change the mechanics and electrophysiology of neurons on short and long time scales (see for instance Goriely et al., 2015, and the references within), the focus of the experimentalists as well as the modelers has been primarily on the mechanical characterization of the neuronal damage, and therefore a direct liaison between the neuronal mechanical properties and its altered functions has not been established yet. Our numerical simulations clearly show neuronal mechanotransduction: for initially applied displacements and speeds of magnitudes comparable to the size of the neuron, action potentials are observed, while very fast initially applied speeds (jabbing) inhibit the action potentials and this case might describe one possible neuronal damage dynamics following a serious mechanical injury. In addition, we notice that our proposed dynamics for the stiffness of a neuron appears to be in agreement with the experimental observations of healthy neurons reported by Zou et al. (2013).

The paper is organized as follows. In Section Mathematical Model we present our mathematical model, and in Section Results we show some relevant numerical simulations. The paper ends with a section containing concluding remarks and future directions.

Mathematical Model

We model the axon as a axi-symmetric circular cylinder made of an inner core filled with the intracellular space and an outer layer filled with the cell's membrane (**Figure 1**). Both the intracellular space and the membrane are assumed to be homogeneous such that the study of neuronal electromechanics can be reduced to the study of a simple electromechanical element that we introduce here. Our novel low-dimensional electromechanical model of a neuron couples a spring-dashpot-mass mechanical model of the neuron and an electric circuit model of cell's membrane (**Figure 1**). Inspired by recent experimental findings by Lu et al. (2006) and Grevesse et al. (2015) we model the macroscopic material neuron as a linear visco-elastic Kelvin–Voigt solid. We use the classic Hodgkin–Huxley equations (Hodgkin and Huxley, 1952) to model the macroscopic electric dynamics of neuron's membrane. The linkage between the Kelvin–Voigt and

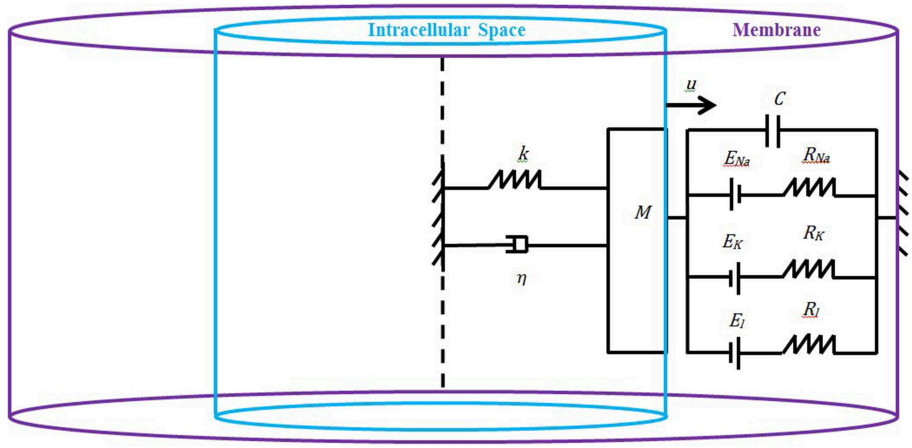

FIGURE 1 | Schematic of the proposed model: the neuron is an axi-symmetric homogeneous circular cylinder whose inner core is the intracellular space (light blue), and the outer layer is the membrane (purple). Due to the symmetry (dashpot line) and material homogeneity, it is enough to study half of the neuron whose properties are encapsulated into a spring-dashpot-mass mechanical system with the spring and dashpot connected in parallel (Kelvin–Voigt model), and the membrane is represented as an electric circuit governed by the classic Hodgkin–Huxley equations.

Hodgkin–Huxley models is achieved by using a Lagrangian formulation and Hamilton's principle as follows.

We start by introducing a Lagrangian of the form:

$$\mathcal{L} = \frac{1}{2}M\dot{u}^2 + \frac{1}{2}\tilde{a}\dot{m}^2 + \frac{1}{2}\tilde{b}\dot{n}^2 + \frac{1}{2}\tilde{c}\dot{h}^2 - \frac{1}{2C\,(u)}{q_C}^2 - \frac{1}{2}k\left(m, n, h\right)\, u^2, \tag{1}$$

where M is half of the constant mass of the neuron of constant cross-sectional area A, $u(t)$ is the macroscopic (cell level) displacement that depends on time t, $k(m, n, h)$ is the macroscopic spring constant (can be interpreted as a "rescaled" stiffness, as we will show in the results section), $C(u)$ is the macroscopic capacitance of membrane's lipid bilayer modeled as a capacitor of electric charge q_C , and $\tilde{a}$, $\tilde{b}$, and $\tilde{c}$ are positive constants with physical units of Joules. Lastly, $m(t)$, $n(t)$, and $h(t)$ are time-dependent variables between 0 and 1 representing the activations of the Na+ and K+ channels and, respectively, the inactivation of Na+ channel. For simplicity, we denote by $\dot{f} = \frac{df}{dt}$ the first order time derivative of a generic function $f(t)$. The first term of the Lagrangian $\mathcal{L}$ in Formula (1) is the macro-kinetic mechanical energy, while the second, third and fourth terms are micro-kinetic electric energies. The fifth term in Formula (1) represents a macro-potential electric energy and the last term of $\mathcal{L}$ is a macro-potential mechanical energy.

Following the variational formulations for electric circuits (Ober-Blöbaum et al., 2013) and for neurons (Chuankui, 2012) we introduce q_{Na}, q_K , and q_l, the electric charges of Na^+, K^+ and leakage channels, respectively. The law of charge conservation provides the following constraint:

$$q_C + q_{Na} + q_K + q_l = 0. \tag{2}$$

We take q_{Na}, q_K, q_l, m, n, h, and u as generalized coordinates. By replacing q_C from Formula (2) into the Lagrangian expression (1) we can calculate the variation of the Lagrangian $\mathcal{L}$ as follows:

$$\begin{aligned}\delta\mathcal{L} &= lim_{\varepsilon\to 0}\,\mathcal{L}\left(q_{Na}+\varepsilon\delta q_{Na}, q_K + \varepsilon\delta q_K, q_l + \varepsilon\delta q_l, m + \varepsilon\delta m,\right.\\ &\quad \left. n + \varepsilon\delta n, h + \varepsilon\delta h, u + \varepsilon\delta u\right)\\ &= M\dot{u}\delta\dot{u} + \tilde{a}\dot{m}\delta\dot{m} + \tilde{b}\dot{n}\delta\dot{n} + \tilde{c}\dot{h}\delta\dot{h} + \frac{1}{C}q_C\left(\delta q_{Na}\right.\\ &\quad \left. + \delta q_K + \delta q_l\right) + \frac{1}{2C^2}\frac{dC}{du}{q_C}^2\delta u - ku\delta u\\ &\quad -\frac{1}{2}\left(\frac{\partial k}{\partial m}u^2\delta m + \frac{\partial k}{\partial n}u^2\delta n + \frac{\partial k}{\partial h}u^2\delta h\right),\end{aligned} \tag{3}$$

where δq_{Na}, δq_K, δq_l, δm, δn, δh, and δu are variations of the generalized coordinates.

We further define the virtual work done by non-conservative forces as (Ober-Blöbaum et al., 2013; Cusumano et al., 2015):

$$\begin{aligned}\delta W &= -\left(R_{Na}\dot{q}_{Na}\delta q_{Na} + R_K\dot{q}_K\delta q_K + R_l\dot{q}_l\delta q_l\right.\\ &\quad \left.+\eta\dot{u}\delta u\right) + \left(-E_{Na}\delta q_{Na} - E_K\delta q_K - E_l\delta q_l + F_m\delta m\right.\\ &\quad \left.+F_n\delta n + F_h\delta h + f\delta u\right)\end{aligned} \tag{4}$$

In Formula (4) the terms inside the first set of parentheses represent dissipative forces due to the resistors of resistances R_{Na}, R_K, R_l in the Hodgkin–Huxley model, and due to the linear dashpot in the Kelvin–Voigt model whose damping coefficient is η (can be interpreted as a "rescaled" dynamic viscosity, as we will show in the results section). The second set of parentheses in Formula (4) contains the following generalized forces: the reverse potentials E_{Na}, E_K, E_l of the Hodgkin–Huxley model, an externally applied mechanical force f, and forces F_m, F_n, F_h which are work conjugates of the gating variables m, n, and respectively h. The choice of signs in Formula (4) guarantees that the virtual work δW is thermodynamically consistent.

We employ now the non-conservative form of Hamilton's principle:

$$\int_{t_1}^{t_2} (\delta\mathcal{L} + \delta W)\, dt = 0, \tag{5}$$

where the variations $\delta q_{Na}, \delta q_K, \delta q_l, \delta m, \delta n, \delta h,$ and δu are independent and vanish at the arbitrary times $t_1,\ t_2$. By replacing Formulas (3) and (4) into the Hamilton's principle, Equation (5), using integration by parts, the independence of the variations $\delta q_{Na}, \delta q_K, \delta q_l, \delta m, \delta n, \delta h, \delta u$ and the fact that these variations are zero at t_1, t_2, we obtain the following Euler-Lagrange differential equations:

$$M\ddot{u} + \eta\dot{u} + ku - \frac{1}{2}\frac{dC}{du}V^2 = f \tag{6}$$

$$R_{Na}\dot{q}_{Na} = V - E_{Na} \tag{7}$$

$$R_K\dot{q}_K = V - E_K \tag{8}$$

$$R_l\dot{q}_l = V - E_l \tag{9}$$

$$\tilde{a}\ddot{m} + \frac{1}{2}\frac{\partial k}{\partial m}u^2 = F_m \tag{10}$$

$$\tilde{b}\ddot{n} + \frac{1}{2}\frac{\partial k}{\partial n}u^2 = F_n \tag{11}$$

$$\tilde{c}\ddot{h} + \frac{1}{2}\frac{\partial k}{\partial h}u^2 = F_h \tag{12}$$

where $V = q_C/C$ is the potential of the capacitor.

Lastly, Kirchhoff's current law needs to be added to the system of Equations (6–12) (Ober-Blöbaum et al., 2013). Replacing Equations (7–9) into Kirchhoff current law yields the well-known Hodgkin–Huxley equation for the membrane potential:

$$C\dot{V} = I - \frac{1}{R_{Na}}(V - E_{Na}) - \frac{1}{R_K}(V - E_K) - \frac{1}{R_l}(V - E_l), \tag{13}$$

where I is a known external current applied on the membrane.

The unknown functions $u,\ V,\ m, n,$ and h can be found by solving the coupled Equations (6, 10–13) with appropriate initial conditions. However, in order to solve these equations we need to provide expressions for $F_m,\ F_n,\ F_h,\ \tilde{a},\ \tilde{b}, \tilde{c},\ C(u),\ k(m, n, h)$. These expressions are very difficult to prescribe due to insufficient knowledge of neuronal mechanotransduction processes. Thus, for the sake of simplicity, we take $f = 0$ in Equation (6), and replace Equations (10–12) by the classic Hodgkin–Huxley equations for $m,\ n,\ h$ (Dayan and Abbott, 2001):

$$\begin{aligned}\dot{m} &= \alpha_m(1-m) - \beta_m m\\ \dot{n} &= \alpha_n(1-n) - \beta_n n\\ \dot{h} &= \alpha_h\left(1-h\right) - \beta_h h\end{aligned}$$

where

$$\alpha_m = \frac{0.1(V+40)}{1-exp\left(-0.1(V+40)\right)},\ \beta_m = 4exp\left(-0.0556(V+65)\right),$$

$$\alpha_n = \frac{0.01(V+55)}{1-exp\left(-0.1(V+55)\right)},\ \beta_n = 0.125exp\left(-0.0125(V+65)\right),$$

$$\alpha_h = 0.07exp\left(-0.05(V+65)\right),\ \beta_h = \frac{1}{1+exp\left(-0.1(V+35)\right)}.$$

In addition, we take (Dayan and Abbott, 2001):

$$\frac{1}{R_{Na}} = g_{Na}m^3h\tilde{A},\ \frac{1}{R_K} = g_K n^4\tilde{A},\ \frac{1}{R_l} = g_l\tilde{A}, \tag{14}$$

with $\tilde{A}$ the surface area of the neuron, and g_{Na}, g_K, g_l the maximal conductances of the Na^+, K^+ and respectively leakage currents.

We propose further expressions for $C(u)$ and $k(m, n, h)$. According to Dayan and Abbott (2001) the capacitance is proportional to the surface area of the membrane and since our model is one-dimensional we could for instance assume that the membrane acts like a parallel-plate capacitor. Thus we have:

$$C = c_m\tilde{A} = \frac{\epsilon\tilde{A}}{r+u} = \frac{\epsilon\tilde{A}}{r\left(1+u/r\right)} \approx \frac{\epsilon\tilde{A}}{r}\left(1-\frac{u}{r}\right), \tag{15}$$

where c_m is the specific membrane capacitance, ϵ is membrane's permittivity, and r is the thickness of the membrane. Regarding the expression for the dynamic spring constant $k(m, n, h)$, we hypothesize that the cell stiffens during an action potential. Such an assumption appears to be supported by the observations made by Hille (2001) and Zou et al. (2013). During activation, the neuron stiffens due to the pulling on cytoskeletal elements by the swelling of the cell (Zou et al., 2013), and by the gates in ion channels that act as protein motors (Hille, 2001). According to Formula (14), Na^+ conductance uses three gates of type m and one gate of type h, while K^+ conductance uses four gates of type n and we could for instance assume that:

$$k\left(m, n, h\right) = k_0\left(1 + m^3(1-h)n^4\right), \tag{16}$$

where k_0 is the spring constant in the inactive state of the neuron.

We observe that in the proposed model the electromechanical coupling is achieved through Equations (6, 10–12), and through Expressions (15–16).

Results

In our simulations we used the following parameters taken from Dayan and Abbott (2001):

$$E_{Na} = 50mV,\ E_K = -77mV,\ E_l = -54.387mV,$$
$$g_{Na} = 1.2\frac{mS}{mm^2},\ g_K = 0.36\frac{mS}{mm^2},\ g_l = 0.003\frac{mS}{mm^2}.$$

The thickness of the membrane is $r = 4$ nm, the radius of the neuron is $r_0 = 2\mu m$ (Dayan and Abbott, 2001), an average Young's modulus (stiffness) of the neuron is $E_0 = 200Pa$ (Lu et al., 2006; Zou et al., 2013), half of the neuronal mass is $M = 0.1ng$ (Corbin et al., 2014). The specific membrane capacitance for a neuron in mechanical equilibrium ($u = 0$) is $0.01\frac{\mu F}{mm^2}$ and thus from Formula (15) we have:

$$c_m = 0.01\left(1 - \frac{u}{r}\right)\frac{\mu F}{mm^2}.$$

We also used a value of $\mu = 4mPa \cdot s$ for the dynamic viscosity of the neuron (this value was found by Park et al. (2010) for non-neuronal cells).

Under the assumption that the neuron has a circular cylindrical shape, the cross-sectional area is $A = \pi r_0{}^2$. Then the spring constant of an inactive neuron is calculated from equating two different representations of the restoring force in a linear elastic spring: $k_0 u = E_0 \frac{u}{r_0} A$. Thus $k_0 = E_0 \frac{A}{r_0}$. Similarly, the damping constant is calculated from the shear force to be: $\eta = \mu \frac{A}{r_0}$. Lastly, in all numerical simulations we applied a constant external current per unit (surface) area of $0.1 \frac{\mu A}{mm^2}$.

Because of the numerical stiffness of Equation (6) we solved instead $M\ddot{u} + \eta\dot{u} + ku = 0$, with k given by Formula (16), and we solved the classic Hodgkin–Huxley equations with C given by Formula (15). We notice that this simplification preserves a weaker coupling between the mechanical and electrical behaviors of the neuron expressed by Formulas (15) and (16).

We re-wrote $M\ddot{u} + \eta\dot{u} + ku = 0$ as a system of first order differential equations:

$$\dot{u} = d, \dot{d} = -\frac{\eta}{M} d - \frac{k}{M} u \tag{17}$$

and used Matlab built-in function **ode15s** that solves stiff ordinary differential equations. The function **ode15s** uses a modified linear multistep backward difference formula of order up to five known to have good stability and changes the stepsize of the discretization adaptively according to a numerical scheme that calculates relative and absolute error tolerances (Shampine and Reichelt, 1997).

The Hodgkin–Huxley equations were solved with the following initial conditions:

$$V(0) = -65mV, m(0) = \frac{\alpha_m\left(V(0)\right)}{\alpha_m\left(V(0)\right) + \beta_m\left(V(0)\right)},$$
$$n(0) = \frac{\alpha_n(V(0))}{\alpha_n\left(V(0)\right) + \beta_n(V(0))}, h(0) = \frac{\alpha_h(V(0))}{\alpha_h\left(V(0)\right) + \beta_h(V(0))}.$$

We solved System (17) using two sets of initial conditions:

$$\text{Set1}: u(0) = 1nm,\ d(0) = \dot{u}(0) = 10nm/ms$$
$$\text{Set2}: u(0) = 0, d(0) = \dot{u}(0) = 1nm/\mu s$$

Working with Matlab's default values for the relative error tolerance (10^{-3}) and the absolute error tolerance (10^{-6}), the function **ode15s** solved System (17) and the classic Hodgkin–Huxley equations coupled by Formulas (15) and (16) using a minimum (maximum) stepsize of 0.0051 ms (1.0076 ms) for the initial conditions in Set 1, and a minimum (maximum) stepsize of 0.00075 ms(0.0067 ms) for the initial conditions in Set 2. In **Figures 2**, **3** we show the evolutions of the voltage, gaiting variables, displacement and Young's modulus for Set 1 respectively, Set 2. For initial conditions in Set 1, we observe that the action potentials occur and the Young's modulus and the displacement variations appear to be physically admissible and possibly within a healthy range. The dynamics of the stiffness of a neuron is in agreement with the experimental observations in the normally functioning regime reported by Zou et al. (2013). However, for the initial conditions in Set 2 which mimic a more serious traumatic event, not only that the action potentials do not happen anymore (**Figure 3A**) but also sustained big oscillations of the displacement field are noticed (**Figure 3C**). In this case the gating variables (**Figure 3B**) as well as the Young's modulus (**Figure 3D**) remain almost constant. The solutions obtained using the initial conditions in Set 2 might show damaging effects of a very fast initial speed (jabbing) on the material structure and electro-chemical activity of a neuron. As it is apparent from **Figures 2**, **3**, the proposed model is able to capture neuronal mechanotransduction. In **Figure 4** we show the evolutions of the displacements obtained using the two sets of initial conditions during 1 ms. While the oscillations are quickly attenuated for Set 1 of initial conditions (**Figure 4A**) which allows the action potential to develop soon afterwards, for the initial conditions of Set 2 the amplitudes of the oscillations of the displacement field are much higher than in the previous case and do not appear to diminish in time. Also, the membrane's depolarization does not occur in this case (**Figure 4B**).

Conclusions and Future Directions

In this paper we proposed a new electromechanical model that couples the mechanical behavior and electro-chemical activity of a neuron and investigated neuronal mechanotranduction through numerical simulations. The neuron was modeled as a liner-viscoelastic Kelvin–Voigt solid whose electro-chemical activity was described by the classic Hodgkin–Huxley equations. We used a Lagrangian formulation and Hamilton's principle to obtain the coupled equations of motion. This approach has the advantage that it can link macroscopic (cell level) as well as microscopic (ionic level) mechanical and electrical information and thus it can describe neuronal mechanotransduction. In addition we assumed that the membrane's capacitance depends on the mechanical displacement of the neuron, while the Young's modulus of the neuron depends on the gating variables in the Hodgkin–Huxley model. Our numerical simulations were done in Matlab using the built-in function **ode15s** to solve a simplified version of our differential equations. When a constant external electric current was applied and the initial displacement and speed were of orders of magnitude comparable to the size of the neuron, the action potentials occurred and looked similar to the ones observed in healthy neurons. In this case the dynamics of the neuron's stiffness appeared to be in agreement with experimental measurements done on healthy neurons (Zou et al., 2013). However, for very fast initial speeds which could model a serious traumatic event and in the presence of a constant applied external current, high persisting oscillations in the mechanical displacement of the neuron were observed and the action potentials did not happen, suggesting possible structural and functional damage of the neuron.

One of the limitations of the proposed model is coming up with physically relevant expressions that couple capacitance and displacement and respectively stiffness and gating variables, because there are no experimental observations that could guide

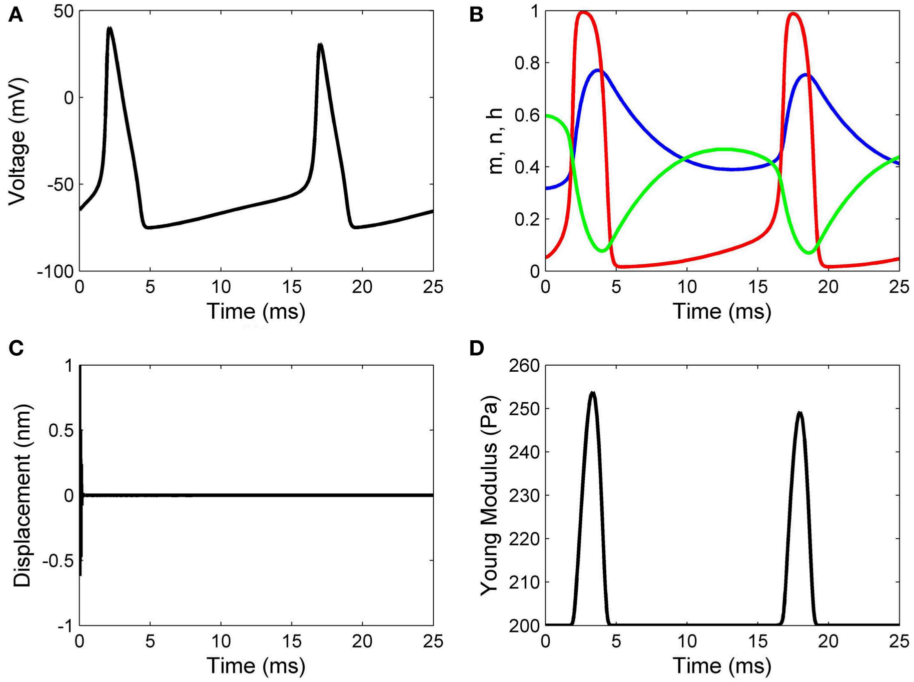

FIGURE 2 | Results for initial displacement of 1 nm and initial speed of 10 nm/ms: (A) voltage, (B) functions n (blue line), m (red line), and h (green line), (C) displacement, and (D) Young's modulus.

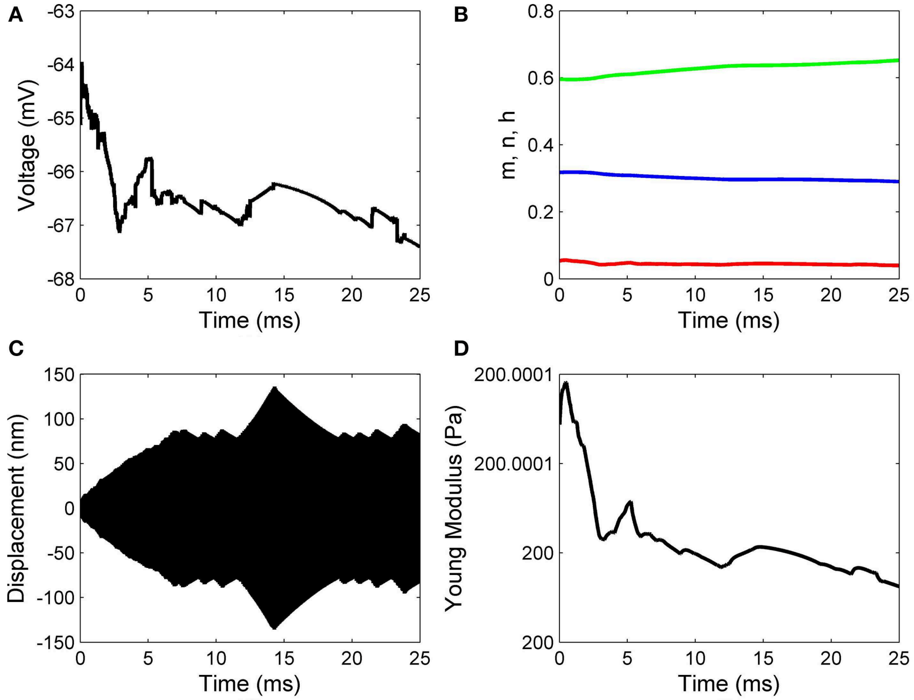

FIGURE 3 | Results for zero initial displacement and initial speed of 1 nm/μs: (A) voltage, (B) functions n (blue line), m (red line), and h (green line), (C) displacement, and (D) Young's modulus.

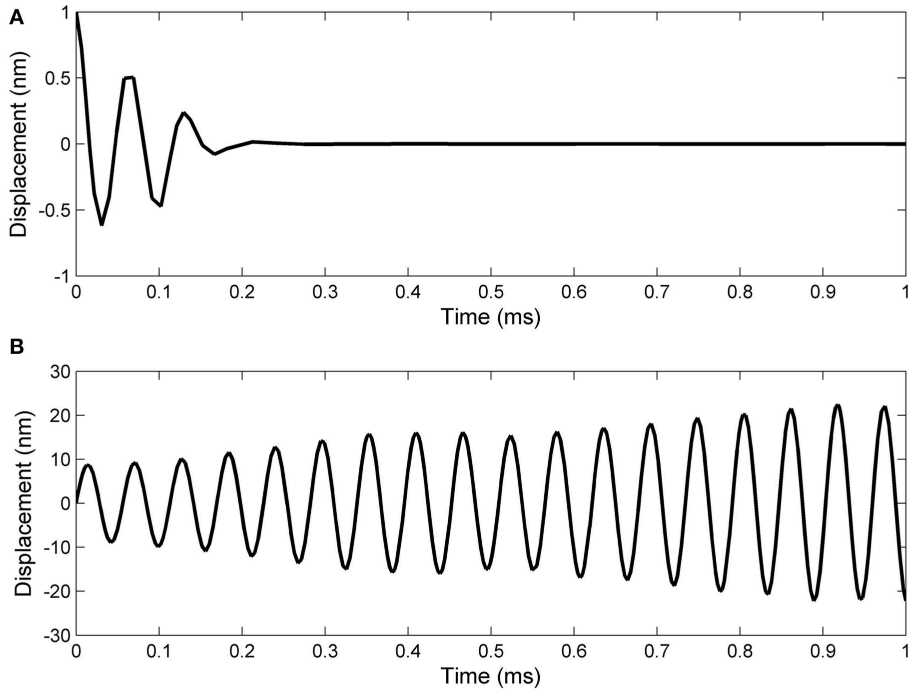

FIGURE 4 | A closer look at the displacement evolution during 1 ms in the following cases: (A) initial displacement of 1 nm and initial speed of 10 nm/ms; (B) zero initial displacement and initial speed of 1 nm/μs.

us. However, given the simplicity of the proposed model, we hope that our approach will inspire future experimental work that will provide empirical relationships among the model's mechanical and electrical parameters. Another limitation of our approach is the use of the Matlab built-in function **ode15s** to solve the proposed system of stiff differential equations. Shampine and Bogacki (1989) advised caution in drastically reducing the stepsize in the discretization implemented in **ode15s** since this action may in fact increase numerical error and cause instabilities in the solutions.

In our future work we plan to develop a better numerical solver that will allow us to solve the fully coupled differential equations which are numerically stiff. In addition, we will perform the bifurcation analysis of the model. Lastly, we intend to incorporate in our model ion transport through cell's membrane using the variational formulation from Eisenberg et al. (2010).

References

Chuankui, Y. (2012). "A neuron model based on Hamilton principle and energy coding," in *Proceedings of the 2011 2nd International CACS*, *AISC*, Vol. 145 (Berlin; Heidelberg: Springer), 395–401.

Corbin, E. A., Millet, L. J., Keller, K. R., King, W. P., and Bashir, R. (2014). Measuring physical properties of neuronal and glial cells with resonant microsensors. *Anal. Chem*. 86, 4864–4872. doi: 10.1021/ac5000625

Cusumano, J. P., Roy, A., and Li, Q. (2015). Damage dynamics, rate laws, and failure statistics viat Hamilton's principle. *Meccanica* 50, 77–98. doi: 10.1007/s11012-014-0055-2

Dayan, P., and Abbott, L. F. (2001). *Theoretical Neuroscience Computational and Mathematical Modeling of Neural Systems*. Cambridge, MA: The MIT Press.

Dickel, G. (1989). Hamilton's principle of least action in nervous excitation. *J. Chem. Soc. Faraday Trans.* 85, 1463–1468. doi: 10.1039/f19898501463

Drapaca, C. S., and Fritz, J. S. (2012). A mechano-electro chemical model of brain neuro-mechanics: application to normal pressure hydrocephalus. *Int. J. Numer. Anal. Model. B* 3, 82–93.

Eisenberg, B., Hyon, Y.-K., and Liu, C. (2010). Energy variational analysis of ions in water and channels: field theory for primitive models of complex ionic fluids. *J. Chem. Phys.* 133, 104104. doi: 10.1063/1.3476262

Goldsmith, W. (2001). The state of head injury biomechanics: past, present, and future: part 1. *Crit. Rev. Biomed. Eng.* 29, 441–600. doi: 10.1615/CritRevBiomedEng.v29.i56.10

Goriely, A., Geers, M. G. D., Holzapfel, G. A., Jayamohan, J., Jerusalem, A., Sivaloganathan, S., et al. (2015). Mechanics of the brain: perspectives, challenges, and opportunities. *Biomech. Model. Mechanobiol.* doi: 10.1007/s10237-015-0662-4. [Epub ahead of print].

Grevesse, T., Dabiri, B. E., Parker, K. K., and Gabriele, S. (2015). Opposite rheological properties of neuronal microcompartments predict axonal vulnerability in brain injury. *Sci. Rep.* 5:9475. doi: 10.1038/srep09475

Hille, B. (2001). *Ion Channels of Excitable Membranes*, *3rd Edn*. Sunderland, MA: Sinauer Associates Inc.

Hodgkin, A. L., and Huxley, A. F. (1952). A qualitative description of membrane current and its application to conduction and excitation in nerve. *J. Physiol.* 117, 500–544. doi: 10.1113/jphysiol.1952.sp004764

Lanczos, C. (1986). *The Variational Principles of Mechanics*, *4th Edn*. Mineola, NY: Dover Publications Inc.

Lang, G. E., Vella, D., Waters, S. L., and Goriely, A. (2015). Propagation of damage in brain tissue: coupling the mechanics of oedema and oxygen delivery. *Biomech. Model. Mechanobiol.* doi: 10.1007/s10237-015-0665-1. [Epub ahead of print].

Lu, Y. B., Franze, K., Seifert, G., Steinhauser, C., Kirchhoff, F., Wolburg, H., et al. (2006). Viscoelastic properties of individual glial cells and neurons in the CNS. *Proc. Natl. Acad. Sci. U.S.A.* 103, 17759–17764. doi: 10.1073/pnas.0606150103

Ober-Blöbaum, S., Tao, M., Cheng, M., Owhadi, H., and Marsden, J. E. (2013). Variational integrators for electric circuits. *J. Comput. Phys.* 242, 498–530. doi: 10.1016/j.jcp.2013.02.00

Paninski, L. (2006). The most likely voltage path and large deviations approximations for integrate-and-fire neurons. *J. Comp. Neurosci.* 21, 71–87. doi: 10.1007/s10827-006-7200-4

Park, K., Larry, J. M., Kim, N., Li, H., Jin, X., Popescu, G., et al. (2010). Measurement of adherent cell mass and growth. *Proc. Natl. Acad. Sci. U.S.A.* 107, 20691–20696. doi: 10.1073/pnas.1011365107

Shampine, L. F., and Bogacki, P. (1989). The effect of changing the stepsize in linear multistep codes. *SIAM J. Sci. Stat. Comput.* 10, 1010–1023. doi: 10.1137/0910060

Shampine, L. F., and Reichelt, M. W. (1997). The MATLAB ODE suite. *SIAM J. Sci. Comput.* 18, 1–22. doi: 10.1137/S1064827594276424

Wilson, M. T., and Steyn-Ross, D. A. (2008). Subthreshold dynamics of a single neuron from a Hamiltonian perspective. *Phys. Rev. E* 78:061908. doi: 10.1103/PhysRevE.78.061908

Zou, S., Chisholm, R., Tauskela, J. S., Mealing, G. A., Johnston, L. J., and Morris, C. E. (2013). Force spectroscopy measurements show that cortical neurons exposed to excitotoxic agonists stiffen before showing evidence of bleb damage. *PLoS ONE* 8:e73499. doi: 10.1371/journal.pone.0073499

Conflict of Interest Statement: The author declares that the research was conducted in the absence of any commercial or financial relationships that could be construed as a potential conflict of interest.

frontiers
in Cellular Neuroscience

GENERAL COMMENTARY
published: 28 August 2015
doi: 10.3389/fncel.2015.00339

Corrigendum: An electromechanical model of neuronal dynamics using Hamilton's principle

Corina S. Drapaca *

Department of Engineering Science and Mechanics, Pennsylvania State University, University Park, PA, USA

Keywords: electromechanics, dynamicstiffness, Kelvin–Voightmodel, Hodgkin–Huxleymodel, Hamilton's principle

OPEN ACCESS

Edited by:
Daniel Marcel Suter,
Purdue University, USA

Reviewed by:
Ellen Kuhl,
Stanford University, USA

****Correspondence:***
Corina S. Drapaca,
csd12@psu.edu

Received: *30 July 2015*
Accepted: *17 August 2015*
Published: *28 August 2015*

Citation:
Drapaca CS (2015) Corrigendum: An electromechanical model of neuronal dynamics using Hamilton's principle. Front. Cell. Neurosci. 9:339. doi: 10.3389/fncel.2015.00339

A corrigendum on

An electromechanical model of neuronal dynamics using Hamilton's principle
by Drapaca, C. S. (2015). Front. Cell. Neurosci. 9:271. doi: 10.3389/fncel.2015.00271

In Equation (3) the limit $\lim_{\varepsilon \to 0} \mathcal{L}$ should be replaced by $\lim_{\varepsilon \to 0} d\mathcal{L} / d\varepsilon$.

Conflict of Interest Statement: The author declares that the research was conducted in the absence of any commercial or financial relationships that could be construed as a potential conflict of interest.

frontiers in Cellular Neuroscience

ORIGINAL RESEARCH
published: 24 August 2015
doi: 10.3389/fncel.2015.00308

Developmental axon stretch stimulates neuron growth while maintaining normal electrical activity, intracellular calcium flux, and somatic morphology

Joseph R. Loverde [1, 2] ***and Bryan J. Pfister*** [1]*

[1] Department of Biomedical Engineering, Center for Injury Bio-mechanics, Materials and Medicine, New Jersey Institute of Technology, Newark, NJ, USA, [2] Department of Chemistry and Life Sciences, Center for Molecular Science, United States Military Academy, West Point NY, USA

Edited by:
Kyle Miller,
Michigan State University, USA

Reviewed by:
Xiao-Feng Zhao,
University of Michigan, USA
Steven R. Heidemann,
Michigan State University, USA
Dennis Bray,
University of Cambridge, UK

****Correspondence:***
Bryan J. Pfister,
Department of Biomedical Engineering, New Jersey Institute of Technology, 323 Martin Luther King Jr. Boulevard, University Heights, Newark, NJ 07102-1982, USA
pfister@njit.edu

Received: *29 May 2015*
Accepted: *27 July 2015*
Published: *24 August 2015*

Citation:
Loverde JR and Pfister BJ (2015) Developmental axon stretch stimulates neuron growth while maintaining normal electrical activity, intracellular calcium flux, and somatic morphology. Front. Cell. Neurosci. 9:308. doi: 10.3389/fncel.2015.00308

Elongation of nerve fibers intuitively occurs throughout mammalian development, and is synchronized with expansion of the growing body. While most tissue systems enlarge through mitosis and differentiation, elongation of nerve fibers is remarkably unique. The emerging paradigm suggests that axons undergo stretch as contiguous tissues enlarge between the proximal and distal segments of spanning nerve fibers. While stretch is distinct from growth, tension is a known stimulus which regulates the growth of axons. Here, we hypothesized that the axon stretch-growth process may be a natural form of injury, whereby regenerative processes fortify elongating axons in order to prevent disconnection. Harnessing the live imaging capability of our axon stretch-growth bioreactors, we assessed neurons both during and following stretch for biomarkers associated with injury. Utilizing whole-cell patch clamp recording, we found no evidence of changes in spontaneous action potential activity or degradation of elicited action potentials during real-time axon stretch at strains of up to 18% applied over 5 min. Unlike traumatic axonal injury, functional calcium imaging of the soma revealed no shifts in free intracellular calcium during axon stretch. Finally, the cross-sectional areas of nuclei and cytoplasms were normal, with no evidence of chromatolysis following week-long stretch-growth limited to the lower of 25% strain or 3 mm total daily stretch. The neuronal growth cascade coupled to stretch was concluded to be independent of the changes in membrane potential, action potential generation, or calcium flux associated with traumatic injury. While axon stretch-growth is likely to share overlap with regenerative processes, we conclude that developmental stretch is a distinct stimulus from traumatic axon injury.

Keywords: axon stretch-growth, neuron development, nerve, regeneration, trauma, injury

Introduction

The development of meter-long axons within the nervous system is an extraordinary, yet unresolved biological phenomenon. The most widely studied mechanism of axon growth has been the migration and extension of growth cones during early development. However, following growth cone extension, axons continue to grow in synchrony with the expansion of the body and mitotic tissues. The preeminent regulatory mechanism for such symbiotic interaction is the biomechanical stretching of axons, a known stimulus of neuronal growth (Weiss, 1941; Bray, 1979, 1984; Dennerll et al., 1989; Zheng et al., 1991; Lamoureux et al., 1992, 2010, 2011; Chada et al., 1997). Notably, the technique of axon stretch-growth (ASG) has emerged as the sole method capable of producing 10 cm long axon tracts *in vitro* (Pfister et al., 2004, 2006).

Interestingly, the dramatic growth incurred by stretch resembles the robust regeneration induced by axonal injury. For example, surgical ligation of the peripheral process of DRG neurons increases regeneration of the central branch 100-fold compared to control neurons (Richardson and Issa, 1984). Preconditioning lesions amplify growth following subsequent injury enough to drive axon extension within inhibitory growth environments (Qiu et al., 2005; Hoffman, 2010). Conceivably, stressors such as surgery or injury temporarily mimic the stress of development, driving mechanisms that normally accommodate the synchrony of body and nervous system growth. In turn, the stretch-growth process may be regarded as a form of natural trauma within intact neurons, whereby distressed axons undergo fortifying growth to prevent disconnection.

While developmental stretch and traumatic injury may both serve as stressors that stimulate axon growth, many variables exist within the scope of such stimuli. Developmental stretch is associated with cumulative and low amplitude deformation applied systemically over long time periods. For instance, the crown-rump length of a developing fetus elongates at peak rates of 2 mm/d in the second trimester (Aviram et al., 2004), and infants continue to grow at a rate of 1 mm/d during the first 3 months of life. Conversely, traumatic injury connotes rapid, high amplitude deformation applied to distinct nerve segments, which causes quantifiable cellular changes on the order of seconds to milliseconds (LaPlaca et al., 1997; LaPlaca and Thibault, 1998; Magou et al., 2011). Critically, if stretch-growth is indeed within the spectra of trauma, it may be sub-injurious if axon growth occurs proportionally with expansion of the growing body. Alternatively, it is plausible that accrued stretch periodically manifests as an internal injury, leading to disproportionate spurts of fortifying axon growth.

Here, we used biomarkers associated with traumatic injury to evaluate if developmental axon stretch may be a form of injury. The phenotypic cascade that follows axon injury has been well-characterized, and several useful biomarkers may be detected within the cytoplasm of injured neurons. Upon insult, rapid membrane depolarization initiates a cascade of bursting action potentials (injury discharge), which are accompanied by large and sustained increases in free intracellular calcium (LaPlaca and Thibault, 1998; Limbrick et al., 2003; Iwata et al., 2004; Weber, 2004). Primary injury also leads to delayed, secondary injuries, which occur within the ensuing days to months. The chromatolytic reaction is a classic manifestation of secondary injury, and is marked by eccentric and misshapen nuclei within swollen cytoplasms (Goldstein et al., 1987; Croul et al., 1988; McIlwain and Hoke, 2005; Hanz and Fainzilber, 2006). These changes are commonly associated with temporary regenerative cascades lasting the order of 1–2 months, after which growth slows.

Thresholds for mild to moderate injury are not well-defined, and it is unknown where developmental stretch may fit within the spectra of trauma. Accordingly, we analyzed neurons for changes in electrophysiological activity and free intracellular calcium during real-time axon stretch. Further, the cytoplasmic and nuclear morphology of stretch-grown neurons was analyzed at end-points following prolonged periods of mild, moderate or excessive stretch paradigms to assess for the presence of chromatolysis.

Materials and Methods

Cell Culture

Rat cervical dorsal root ganglion (DRGs) neurons were isolated from E16 Sprague Dawley rat pups and dissociated in 0.25 g/L trypsin for 30 min. Cultures were maintained in Neurobasal medium (Life Technologies, Carlsbad, CA) supplemented with 2% B-27, 0.5 mM l-glutamine, 2.5 g/L d-glucose, 1% FBS-HI, 20 ng/mL 7S NGF, 20 μM FdU, and 20 μM Uridine. Cultures were replenished every 2–3 days by replacing 50% of the culture volume with fresh media. All protocols were approved by the Rutgers University-Newark Institutional Animal Care and Use Committee.

Unidirectional Axon Stretch-growth of Dissociated Neurons

Utilizing custom live imaging bioreactors previously described (Loverde et al., 2011a,b), our stretch-growth technique was modified in order to allow for analysis of neuronal somata during axon stretch. In this device, a glass coverslip serves as the bottom culture substrate which allows for optimal imaging of cells on top of an inverted microscope. Dissociated cells were seeded onto the glass coverslip where growth cones extended and adhered to Aclar manipulating substrates, **Figure 1**. The Aclar is subsequently displaced by a computer controlled stepper system that applies stretch to the bridging axons.

The bioreactor culture surfaces, including the glass coverslip and Aclar manipulating substrates (2 mil UltRx2000, Honeywell, Morristown, NJ) were cleaned 2 days prior to coating using cotton swabs dipped in 50% acetone. On the day of seeding, substrates were coated with high molecular weight poly-d-lysine (354210, Becton Dickinson, Bedford MA) at 60 μg/cm^2 in PBS w/Ca^{2+} and Mg^{2+} for 1 h. To assist with the accuracy of plating small numbers of cells, barriers were created from polydimethylsiloxane elastomer (PDMS, NuSil Technology LLC, Carpinteria, CA). PDMS was cured in 100 mm dishes and blocks (7.5 × 5× 3 mm) were cut with a scalpel. The blocks were temporarily positioned at the seeding area of the coverslip after coating, **Figure 1A**. For each bioreactor, dissociated neurons were seeded onto the coverslip against the blocks in 15 μL drops (∼25,000 cells/drop). After 1 h, blocks were removed and culture lanes were filled with media. Next, the manipulating substrates were repositioned to within 200–500 μm of adherent cells using the stepper motor system. The system was then immobilized for 4–5 days while growth cones extended and adhered to Aclar manipulating substrates, **Figure 1B**. Finally, stretch was initiated at the rates specified herein for real-time or end-point analysis, **Figure 1C**.

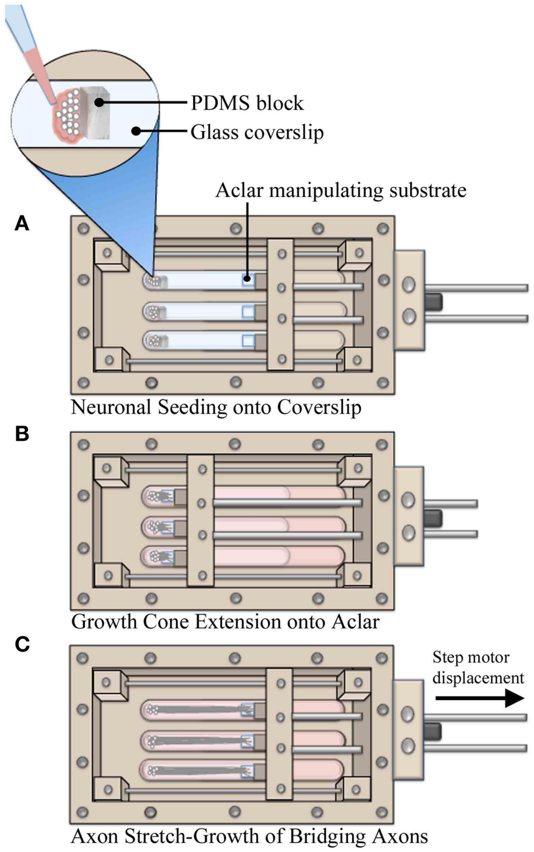

FIGURE 1 | Axon stretch-growth methodology. (A) Neurons were seeded against PDMS barriers to create culture homogeneity such that all cell bodies were positioned on coverglass. Precise positioning of PDMS within multiple culture lanes also set consistent spacing between cells and Aclar substrates, resulting in consistent pre-stretch axon lengths. **(B)** Aclar substrates were positioned within 250–500 μm of the seeded cells to allow for growth cone extension and adhesion while the system was held statically over 4–5 days. **(C)** Stretch was applied by manipulating Aclar substrates away from the seeding area, applying strain to bridging axons.

Real-time Analysis of Axon Stretch-growth

Whole-cell patch clamp and functional calcium imaging experiments were performed in real-time while axons were actively being stretched. However, prior to real-time experimentation, it was necessary to distinguish which neurons had successfully extended and adhered to Aclar manipulating substrates. Accordingly, real-time experiments were initially stretch-grown in an incubator over 2 days to 1 mm in length. This allowed the distinction between stretch-grown and non-stretch-grown axons and the corresponding neuronal somata for subsequent real-time experimentation. Following initial stretch-growth, cultures were given ≥24 h to rest and re-establish basal axon tension. Stretch-grown neurons spanning 1 mm in length in the resting state are referred to as the "Resting" group.

The "Real-time" stretch protocol used in the electrophysiology and calcium imaging experiments is outlined in **Table 1**. For practicality, and to complete experiments within reasonable time periods, we developed a real-time stretch sequence that considers stretch rate and the accumulation of applied strain. Briefly, stretching starts with a mild axon strain of 1% applied over 1 min, and increases to 3.6, 7.2, 12, and 18% strain over the following 4 min (strain = change in axon length/original length), **Table 1**. Importantly, this paradigm provided high resolution recording at low axon strain, which is likely to be representative of the stretch-growth process *in vivo*. Further, this paradigm also provided for recording at relatively higher axon strain, where injury is more likely to occur.

At the end of each real time experiment, stretched cultures were returned to the incubator for 3–4 days and subsequently analyzed at rest. Neurons which underwent both initial stretch-growth and real-time stretch were referred to as the "Post real-time" group. For electrophysiology experiments, control cells were patched within tissue culture dishes. For calcium imaging experiments, sham neurons were cultured within stretch-growth bioreactors not exposed to stretch.

TABLE 1 | Stretch paradigm for real-time analysis of stretch-mediated events.

Time (Minute)	Step motor step size (μm)	Number of steps	Inter-step delay (s)	Stretch rate (μm/min)	Accumulated stretch (μm)	Accumulated strain* (%)
1	0	0	0	0	0	0
2	2	6	10	12	12	1.2
3	4	6	10	24	36	3.6
4	6	6	10	36	72	7.2
5	8	6	10	48	120	12
6	10	6	10	60	180	18

** Based on initial axon length of 1 mm.*

Whole-cell Patch Clamp Recording

For this study, a customized stationary microscope stage was developed to fix the stretch-growth bioreactor together with the patch clamp head stage to a Nikon Eclipse TE-2000 microscope, **Figure 2**. Whole-cell recordings were acquired using an Axon MultiClamp 700B amplifier (Molecular Devices, Sunnyvale, CA) in current clamp mode. Measurements of membrane potential were digitized at 25 kHz using an Axon Digidata 1440A and filtered at 10 kHz using a low-pass 8-pole Bessel filter. Recordings were obtained using patch electrodes with a resistance of 4–6 MΩ. Electrodes were filled with intracellular solution consisting of 120 mM KCl, 0.2 mM EGTA, 30 mM HEPES, 5 mM Na-ATP, 0.4 mM Na_2-GTP, 5 mM $MgCl_2$, 0.1 mM NaH_2PO_4 in water adjusted to pH 7.2. Extracellular solution consisted of PBS w/Ca^{2+} and Mg^{2+} at room temperature. Input resistance (Rm) was calculated by injecting a 50 pA hyperpolarizing current and measuring the change in voltage. Current stimulated action potentials were elicited by injecting brief 3 ms depolarizing currents (100–900 pA).

A limitation of patch clamp recording of cultures undergoing real-time axon stretch is the ability to only patch one cell per bioreactor during stretch. Accordingly, stringent criteria were established to select for the most reliable patches. Analyzed cells maintained flat natural RMP ≤ -50 mV throughout testing without holding current ($\geq$10 min), and were capable of elicited action potentials upon injection of depolarizing current <1 nA. Action potentials were analyzed by comparing depolarizing current, activation threshold, peak voltage, after-hyperpolarization voltage (AHP), amplitude, duration (APD_{50}), and rise and fall times (10–90%).

Functional Calcium Imaging

Utilizing time-lapse microscopy, neuronal somata were monitored for changes in intracellular calcium flux during real-time axon stretch as outlined in **Table 1**. Prior to analysis, cells were rinsed and loaded with 3.2 μM Fluo-4AM (F-14201, Invitrogen), using an equal volume of Pluronic F-127 detergent (P-3000MP, Invitrogen) for 30 min at 37°C. After loading, cells were rinsed with culture media and incubated an additional 30 min for de-esterification. Finally, cells were rinsed with PBS and promptly setup for time-lapse imaging. Importantly, Fluo-4 exhibits a large fluorescence intensity increase upon binding free calcium. Since free intracellular calcium concentrations are normally low due to sequestration in organelles, spontaneous cytosolic increases are readily detectible (Smetters et al., 1999).

Cells were imaged on a Nikon Eclipse TE-2000 inverted microscope using a 75 watt xenon arc lamp and a CoolSNAP EZ CCD camera (Photometrics, Tucson, AZ). The microscope was set to take images at 2 Hz with an exposure time of 100–200 ms

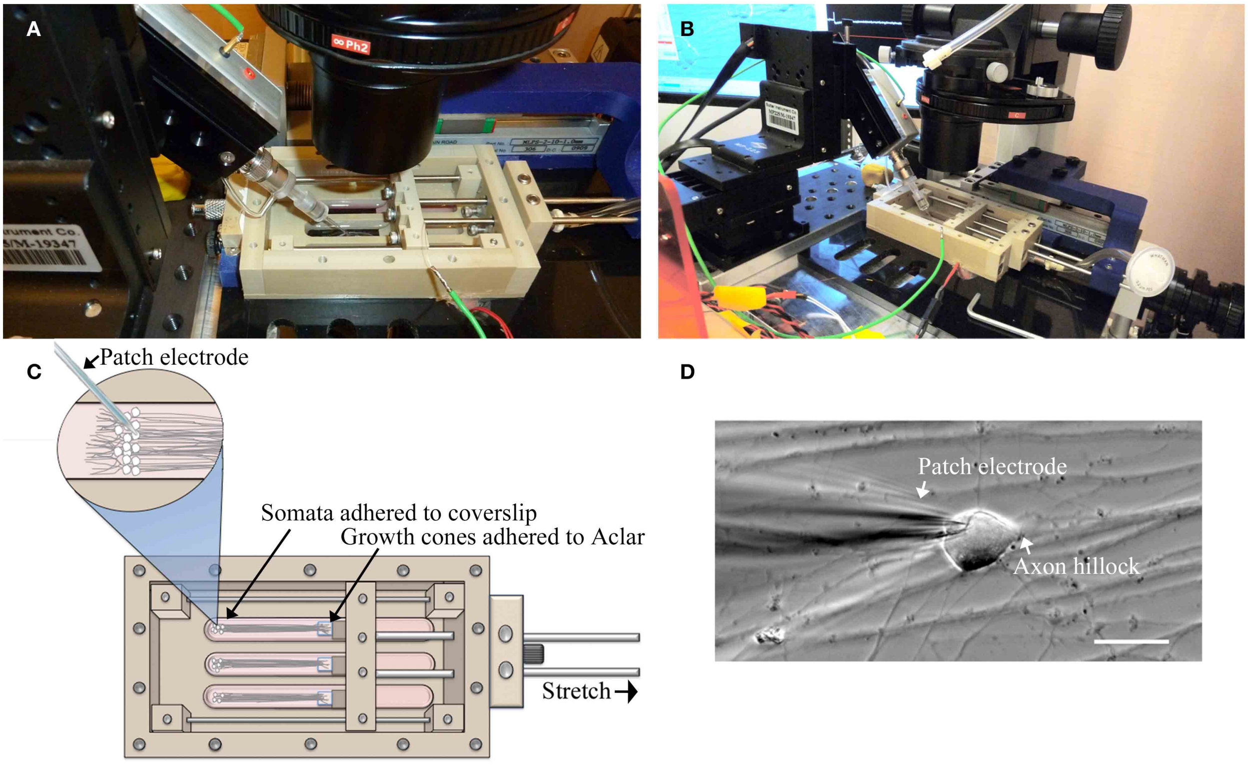

FIGURE 2 | Patch-clamp recording of neuronal somata during axon stretch. (A) Patch-clamp head stage positioning within an elongated well of a customized stretch-grown bioreactor. **(B)** Overview of head-stage, linear motion table, and stretch-growth bioreactor fixed to a customized microscope stage. **(C)** Orientation of somata, growth cones, and patch electrode within bioreactor. **(D)** Patch clamp of a stretch-grown cell, bar = 25 μm.

using a Lambda SC Smart Shutter (Sutter Instruments, Novato, CA). To minimize photoactivation and bleaching of cells, #4 and #8 ND filters were used to attenuate light, while 2 × 2 camera binning was used to boost recording sensitivity.

Fluorescent time-lapse sequences were analyzed using ImageJ (Schneider et al., 2012). For each experiment, image sequences (stacks) were registered using the "StackReg" plug-in (Thévenaz et al., 1998) set to rigid body transformation to correct for movement. Next, a cell-free background region was selected and measured across the entire image sequence using the "Measure Stack" plug-in (by Bob Dougherty). Background intensity values were saved in an Excel spreadsheet (Microsoft, Redmond, WA) and averaged. Finally, the circumference of stretch grown somata were individually traced using the oval selection tool and intensity values were recorded similarly to background. Average background intensity was subtracted from each cytoplasmic measurement, and the subsequent values were normalized to the first measurement for each cell. Accordingly, reported data represents the ratio of measured fluorescence (F) to baseline fluorescence (F_0), with a (F/F_0) ratio of one reflecting baseline intensity. Graphs of (F/F_0) ratios were plotted to facilitate the visualization of calcium flux. Logic statements written in Excel were used to facilitate calculation of frequency, amplitude, and duration of calcium spikes.

Traumatic Stretch-injury

A sustained rise in intracellular calcium is a known result in an *in vitro* model of traumatic brain injury using cortical neurons and is described elsewhere (Magou et al., 2011). Using the technique described by Magou et al., we evaluated calcium flux in DRG neurons subjected to a traumatic stretch-injury as positive control. Briefly, dissociated DRGs were cultured on thin silicone membranes which were rapidly deformed by applying a pressure pulse. Cultures were stretch-injured at 40% strain at a rate of 30 s^{-1} following 11 DIV. Staining and imaging were performed similarly to stretch-grown cells. For live time-lapse imaging, injuries were delivered at the 1 min mark, similar to the onset of stretch using the real-time stretch protocol (**Table 1**).

Morphology of Stretch-grown Neuronal Somata

These experiments consider the end-point morphology of neuronal somata following varying axon stretch profiles, **Table 2**. A "mild" stretch-growth profile was developed to apply a continuous stretch of 0.25 mm/d over 8 days. A "moderate" stretch-growth profile was developed to target 25% daily strain until reaching a peak of 3 mm/d in order to prevent axon disconnection while maximizing growth. Finally, a "stretch-axotomy" profile was developed to exceed 25% daily strain and cause complete axon disconnection. Importantly, all cells were cultured for an equal time period of 18–19 DIV, since morphological abnormalities are most prominently detected 2–3 weeks following perturbation (Goldstein et al., 1987; Croul et al., 1988; McIlwain and Hoke, 2005).

Dissociated cells were rinsed gently in PBS and fixed in 4% paraformaldehyde for 1 h at room temperature. Phase contrast panoramas were taken prior to labeling in order to trace stretch-grown axons toward their somata. Plasma membranes were labeled with conjugated wheat germ agglutinin (W32464, Invitrogen, Carlsbad, CA) applied dropwise to cover cells at 5 μg/mL for 10 min. Next, 0.1% Triton X-100 and 4% normal goat serum were used to permeabilize cells for 1 h. Neurotrace™ (N-21480, Invitrogen) was diluted 450-fold and applied dropwise to label cell bodies for 20 min, while DAPI (D1306, Invitrogen) was used to counterstain nuclei at 300 nM for 2 min. Confocal sections were taken over the entire height of somata using a 60x oil immersion objective, and rendered into 2D images for analysis with ImageJ. Cross-sectional areas of cytoplasms and nuclei were measured using ImageJ by tracing the circumference and utilizing the measure function.

Statistical Analysis

Data was analyzed for variance using two-tailed unequal variance *t*-tests between mechanically manipulated cells (stretch/injury) vs. non-manipulated cells (controls). Graphed data is reported as mean ± standard deviation.

Results

Unidirectional Axon Stretch-growth of Dissociated Neurons

The modified seeding technique developed here was essential to the experimental procedures requiring high resolution microscopy and access to stationary, dissociated neuronal somata during mechanical stretch of axons. The unidirectional stretch-growth procedure relies upon the ability to seed neurons within close proximity of the manipulating substrates to ensure that a sufficient density of growth cones can reach and extend onto the Aclar. To optimize the density of seeded cells and homogenize the distance between the cells and the Aclar, PDMS blocks were used to temporarily constrain cells at the time of seeding. We targeted a distance of 250 μm between the Aclar and cells, but found that distances up to 500 μm were successful given additional time for growth between the substrates.

Within each experiment, stretch-grown axons attached to manipulating substrates were identified by a characteristic straight and taut appearance following 0.2–1 mm stretch, **Figure 3**. Experimental somata were found by tracing stretch-grown axons from the manipulating substrates back toward the seeding area for subsequent analysis of stretch-mediated events, **Figures 3B,C**. We found that most axons could be traced back to the first few rows of somata closest to the Aclar. Video recordings made during real-time analysis enabled viewing of axon stretch and subsequent displacement of stretch-grown somata at high strain, **Supplementary Videos 1**, **2**.

Growth-promoting Axon Stretch does not Provoke Spontaneous Action Potentials

Gap-free recordings were compared between exceptional cells that met patch inclusion criteria for analysis, including controls (8 DIV, $n = 4$), stretch-grown cells at rest (Resting, 8 DIV, $n = 3$), stretch-grown cells during real-time stretch (Real-Time, 8 DIV, $n = 3$), and cells at rest following real-time stretch (Post-RT, 12 DIV, $n = 3$). Over the course of 2 h of gap-free recordings, the majority of cells did not fire any spontaneous action potentials

TABLE 2 | Stretch rate escalation paradigms for end-point analysis of dissociated embryonic DRG neurons.

	Stretch growth - Mild strain				Stretch growth - Moderate strain				Stretch - Axotomy			
Stretch day	Stretch rate[a] [mm/d]	Daily strain[b,c] [%]	Accumulated Stretch growth [mm]	Axon length[b,d] [mm]	Stretch rate[a] [mm/d]	Daily strain[b,c] [%]	Accumulated Stretch growth [mm]	Axon length[b,d] [mm]	Stretch rate[a] [mm/d]	Daily strain[b,c] [%]	Accumulated Stretch [mm]	Axon length[b,d] [mm]
1	0.25	14	0.25	2.00	0.5	29	0.50	2.25	0.5	29	0.50	2.25
2	0.25	13	0.50	2.25	0.5	22	1.00	2.75	0.5	22	1.00	2.75
3	0.25	11	0.75	2.50	0.75	27	1.75	3.50	0.75	27	1.75	3.50
4	0.25	10	1.00	2.75	0.75	21	2.50	4.25	1	29	2.75	4.50
5	0.25	9	1.25	3.00	1	24	3.50	5.25	1.5	33	4.25	6.00
6	0.25	8	1.50	3.25	1.25	24	4.75	6.50	2	33	6.25	8.00
7	0.25	8	1.75	3.50	1.5	23	6.25	8.00	3	38	9.25	Axotomy
8	0.25	7	2.00	3.75	2	25	8.25	10.00	–	–	–	–
9	0	0	2.00	3.75	2.5	25	10.75	12.50	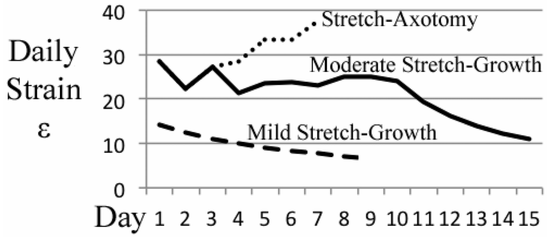			
10	0	0	2.00	3.75	3	24	13.75	15.50				
11	0	0	2.00	3.75	3	19	16.75	18.50				
12	0	0	2.00	3.75	3	16	19.75	21.50				
13	0	0	2.00	3.75	3	14	22.75	24.50				
14	0	0	2.00	3.75	3	12	25.75	27.50				
15	0	0	2.00	3.75	3	11	28.75	30.50				

[a] *Daily stretch is applied in periodic 2 μm steps evenly spaced over 24 h. Stretch rate is adjusted by changing the delay between steps.*

[b] *Based on axon length of 1.75 mm prior to initiation of stretch.*

[c] *Neglecting concomitant daily growth.*

[d] *Based on daily stretch-growth and previous axon length, excluding growth cone migration.*

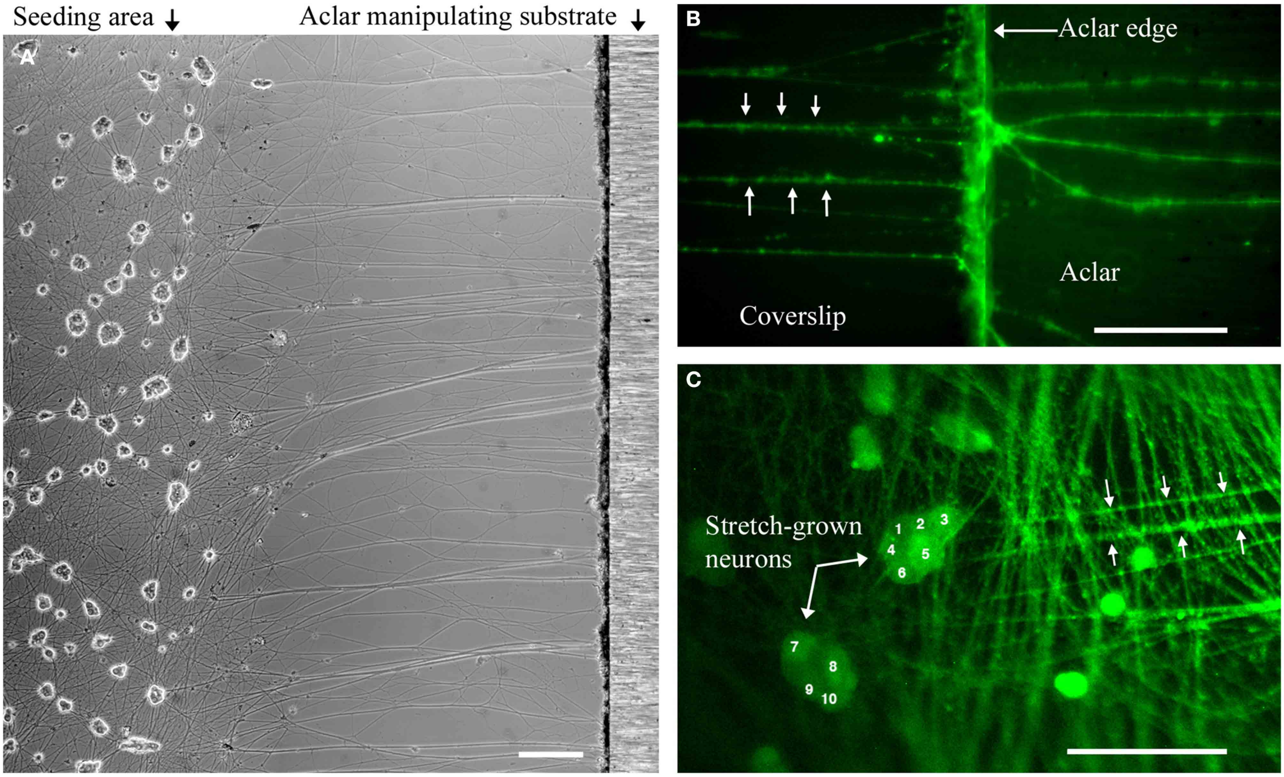

FIGURE 3 | Dissociated stretch-grown neurons. (A) Stretch-grown neurons following 1 mm stretch-growth, bar = 250 μm. **(B)** Neurons stained with Fluo-4AM were traced from the Aclar manipulating substrate back to the cell seeding area, bar = 50 μm. **(C)** Cell seeding area containing somata of stretch grown neurons. Bar = 100 μm.

(SAPs), **Figure 4A**. We found a single cell which fired two SAPs during real-time stretch after repeating the real-time stretching protocol twice, **Figure 4B**. A second cell fired five SAPs during static observation while at rest within the "Post-RT" condition, **Figure 4C**.

Three cells within the "Resting" condition did not fire any SAPs during gap-free recording prior to real-time stretch. Upon application of real-time stretch, two cells reached axonal strains of 5–18% before being pulled out of patch electrodes. While these cells did not exhibit any SAPs throughout recording, they maintained normal resting membrane potential, and retained the ability to fire elicited action potentials within the stretched state while stretching was paused briefly. Stepper motor interference revealed that patch loss occurred synchronously with a stretch step upon reaching 5% strain in one cell, while the patch was lost gradually beginning at 18% strain in a second cell (not shown).

In a third cell stretched during "Real-time" recording, patch was maintained throughout the entire stretching routine, and no SAPs were found up to 18% strain (**Table 1**). Since patch was maintained after completing the experiment, we repeated the stretching protocol and found that the patch was maintained up to an applied axon strain of 52% with no sign of degradation. Two SAPs were recorded during "Real-time" stretch upon reaching an applied strain of 21.5%, after which stretching was paused for additional recording, **Figure 4B**. No spontaneous activity occurred beyond 21.5%, despite further increases in strain. Membrane potential remained unaffected by stretch, and elicited action potentials appeared normal during brief pauses in stretching. Notably, most axons were thinning and began to disconnect at 52% strain, **Supplementary Video 3**. We manipulated the patch electrode away from the cell and found that the membrane could be stretched 50 μm before disconnecting, **Supplementary Video 4**. Results suggest that while stretch can provoke isolated SAPs at high strain, stretch within the context of stretch-growth does not alter membrane potential or play a role in the initiation of spontaneous action potentials.

Analysis of stretch-grown cells at rest revealed that stretch-growth did not increase spontaneous activity. In one instance, a "Post real-time" cell at rest fired five SAPs over 5 min of gap-free recording without any notable period, **Figure 4C**. A comparison of the SAP waveforms attained from the "Real-time" stretched cell and the "Post real-time" cell at rest revealed a 12.6 mV reduction in amplitude in the cell within the stretched state, **Figure 4D**.

Stimulated Action Potentials are Unaffected by Applied Axon Strain

A comparison of spontaneous action potentials (data from gap-free recordings above) revealed a 12.6 mV reduction in

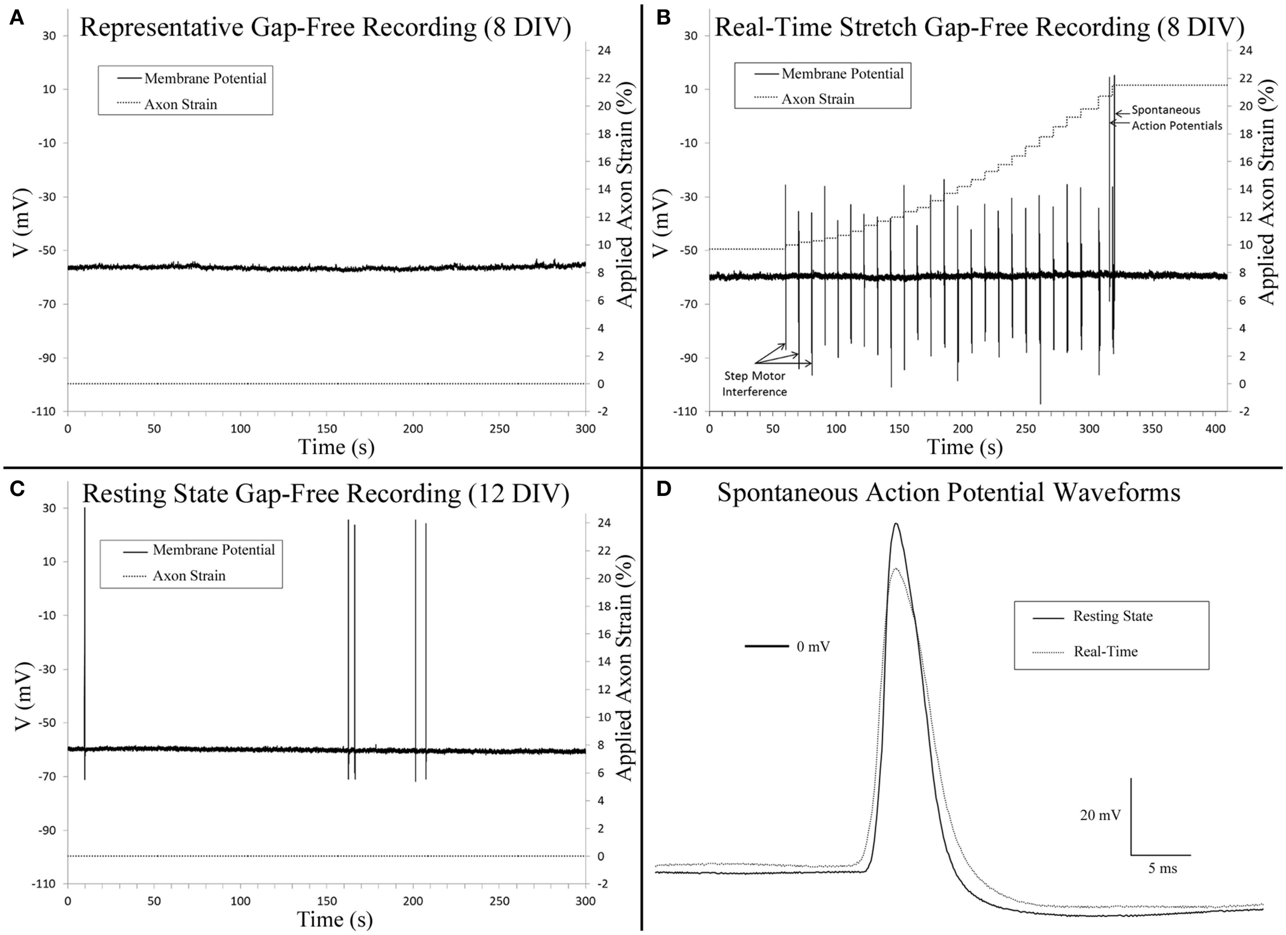

FIGURE 4 | Gap-free patch clamp recording. (A) Cervical DRG neurons generally did not fire spontaneous action potentials within 10 min recordings. **(B)** Isolated spontaneous action potentials were evident in a single cell during real-time stretch upon reaching an axon strain of 21.5%. Step motor interference reflects programmed stretch steps which occur at a frequency of 0.1 Hz (**Table 1**). Control recordings confirmed that interference spikes originated from the stepper motor and not cells. **(C)** A single cell at rest fired five spontaneous action potentials. **(D)** A comparison of spontaneous action potentials obtained from **(B,C)** revealed that peak voltage was reduced by 11.6 mV in the cell undergoing real-time stretch.

action potential amplitude in the cell under applied tension. Accordingly, we investigated the effect of applied axon strain on stimulated action potential properties. Using the cell which reached a cumulative 52% axon strain, we compared stimulated action potentials acquired during brief pauses in stretching that occurred at 5, 10, 21.5, 37, and 52% axon strain, **Figure 5**. Initial depolarizing current at 5% axon strain required 600 pA and corresponded to a peak action potential voltage of 25 mV. Subsequent action potentials were all elicited at 500 pA and corresponded to peak voltages ranging from 19 to 16 mV as strain was increased from 10 to 52%. Therefore, at 500 pA, peak voltage decreased by 3 mV as strain was increased 42%. Membrane resistance (R_m) varied from 287 to 349 MΩ, while action potential durations (APD_{50}) and fall times (10–90%) fluctuated nominally from 4 to 4.5 ms and 3.7 to 4.0 ms, respectively, all without correlation to strain. Rise times were not calculated due to current stimulation artifact. Notably, current stimulated action potentials virtually mirrored the 2 SAPs acquired during real-time stretch, which peaked at 15 mV upon reaching 21.5% strain. These results suggest there is little to no correlation between action potential morphology and applied axon strain.

Neurons Retain the Ability to Fire Action Potentials Both during and Following Stretch-growth

Stimulated action potentials were compared between controls (8 DIV, $n = 4$), stretch-grown cells at rest (Resting, 8 DIV, $n = 3$), stretch grown cells during real-time stretch (Real-Time, 8 DIV, $n = 3$), and cells at rest following real-time stretch (Post-RT, 12 DIV, $n = 3$), **Figure 6**. Since, we found that applied axon strain had no effect on stimulated action potential morphology (analysis above), we combined stimulated action potential data from all "Real-time" cells into a single group, irrespective of applied strain.

We found a significant difference in the action potential amplitudes of real-time stretched cells compared to controls ($p = 0.005$), **Figure 6F**. While resting membrane potential

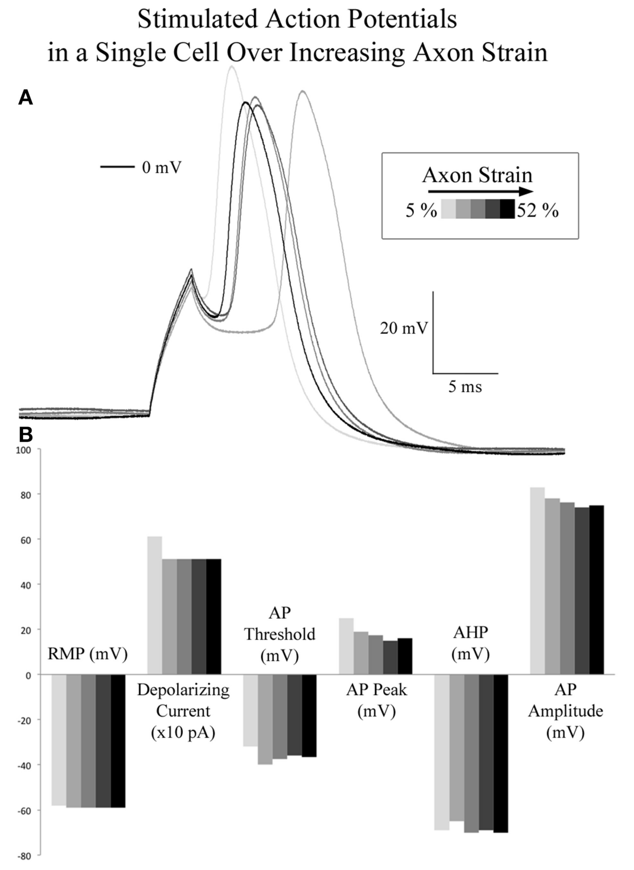

FIGURE 5 | Current stimulated action potentials during real-time axon stretch. (A) Overlaid current stimulated action potential traces corresponding to 5, 10, 21, 37, and 52% axon strain in a single cell. **(B)** Action potential attributes did not correlate with axon strain. At 500 pA depolarizing current, peak voltage decreased by 3 mV as strain was increased 42%.

decreased from −53.9 ± 3.9 mV in non-stretched controls to −56.5 ± 2.4 mV in the real-time group, **Figure 6A**, peak action potential voltage decreased from 38.4 ± 1.8 mV in controls to 15.6 ± 3.4 mV in the real-time group, **Figure 6D**. Accordingly, action potential amplitudes were reduced by an average of 19 mV in real-time stretched cells, largely due to differences in peak voltage. We also found a significant difference in the activation threshold of "Post real-time" cells, **Figure 6C**. The activation threshold decreased from −25.3 ± 1.2 mV in controls to −34.4 ± 2.9 mV in "Post real-time" cells ($p = 0.02$). We believe the difference in activation threshold may be due to the advanced age of "Post real-time" cells which were patched 3–4 days following real-time stretch. Notably, the action potential amplitudes of "Post real-time" cells appeared normal, and averaged 89 ± 15.6 mV similar to non-stretched controls. Ultimately, we believe action potential amplitudes recorded during real-time stretch were reduced due to patch integrity issues instead of physiological changes. No significant differences were found in depolarizing current, after-hyperpolarization voltage, action potential duration, or rise-decay times (10–90% not shown) in any evaluated group.

The Prevalence of Spontaneous Calcium Flux in Stretch-grown Neurons is Distinct from Injury

Control cells never exposed to stretch were analyzed for spontaneous calcium influx within sham bioreactors. Following 8 DIV, we found that 50% of control cells underwent spontaneous calcium influx within 10 min recordings, with a total incidence of between 0 to 144 spikes per cell, and a median of 0.6 spikes/min ($n = 54$). In order to reduce the background of constitutively spiking cells in experimental datasets, we screened out cells which spiked during the first minute of all time-lapse recordings, **Figure 7**. For controls, 12 cells were removed which lowered the median spiking frequency from 0.6 to 0.1 spikes/min. For analysis of trends associated with stretch-growth, soma were monitored during real-time stretch as outlined in **Table 1**. As positive control, a traumatic stretch-injury group was evaluated for comparison to stretch-grown cells in addition to non-stretched controls. Using data collected from real-time recordings (Control, Real-time stretch, Injury), we calculated the prevalence and average frequency of spiking over 1 min "binned" periods for 6 min starting at the time of stretch-growth or injury, **Figures 8A,B**.

Utilizing the "binned" dataset, we found that between 7 and 19% of control cells spiked during each minute of recording ($n = 42$), **Figure 8A**. A slightly wider range of 4–35% was found during real-time stretch ($n = 23$, 11 DIV) with a higher prevalence noted above 11% strain (5 min). In injured cells, a remarkable 93% of screened cells ($n = 14$, 11 DIV) spiked at the time of injury (1 min mark, **Supplementary Video 5**), after which spiking prevalence dropped to the 7–21% range similar to controls for the duration of recording.

For spiking cells, the average frequency of spiking ranged from 1.6 to 5 spikes/min in controls and 2 to 5.3 spikes/min in cells undergoing real-time stretch, with higher frequencies occurring toward the end of recording in both groups, **Figure 8B**. Injured cells spiked at a rate of 1.6–4.7 spikes/min similar to controls, remarkably, also trending toward higher frequencies at the end of the experiment instead of at the time of injury. While real-time stretched cells spiked at insignificantly higher rates with increasing strain, we believe increases in spiking frequency were also related to the assay since increases occurred in all groups over time.

We noted that one stretch-grown culture at rest for 2 days did not contain any constitutively spiking cells in the first minute of recording ($n = 20$, 8 DIV). Further, upon application of stretch, only a single cell underwent spontaneous calcium influx, (6 min mark, **Supplementary Video 2**). In contrast, 15% of stretch-grown cells spiked during the first minute of recording in cultures at rest for 5 days ($n = 27$, 11 DIV), which closely approximated controls. In total, 43 screened cells were monitored during real-time stretch between 8 and 11 DIV, and only 15 unique cells spiked during the stretch-growth assay. As a direct comparison, 15 of 42 unique control cells, and 14 of 15 injured cells spiked in the same period. While real-time stretched cells spiked more frequently on day 11 than day 8, the phenotype of spiking cells resembled controls more so than injury. Ultimately, we could not provoke ubiquitous changes in spiking using the rates and limits established for the stretch-growth

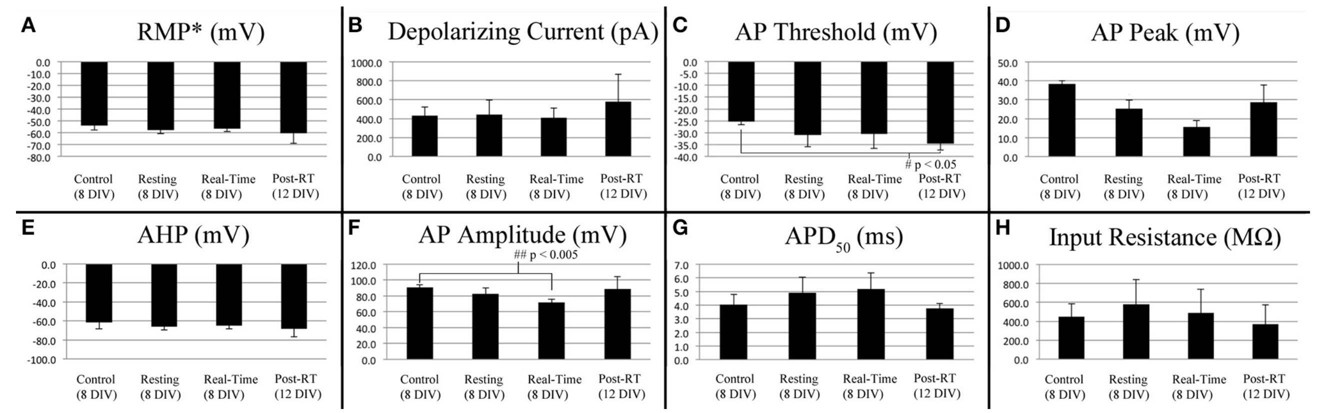

FIGURE 6 | Current stimulated action potential attributes. Data represents averages attained from non-stretched controls (8 DIV, $n = 4$), stretch-grown cells at rest following initial stretch-growth (Resting, 8 DIV, $n = 3$), stretch grown cells during real-time stretch (Real-Time, 8 DIV, $n = 3$), and cells at rest 3–4 days following real-time stretch (Post-RT, 12 DIV, $n = 3$). **(A)** Resting membrane potential, **(B)** Depolarizing current, **(C)** Activation threshold, **(D)** Peak voltage, **(E)** After-hyperpolarization voltage, **(F)** Amplitude, **(G)** Action potential duration at 50% amplitude, **(H)** Input resistance. Graphs show mean ± standard deviation; *uncorrected.

method, whereas we were successful with the stretch-injury method.

Spontaneous Calcium Spikes in Stretch-grown Neurons Exhibit Normal Amplitude and Duration

Utilizing the "binned" analysis method, we calculated the average amplitude and duration of calcium spikes over 1 min periods for comparison between experiment groups, **Figures 8C,D**. While amplitude was not normalized between groups, we found that the range was comparable between experiments. The average amplitude ranged from 0.21 to 0.53 F/F_0 in controls and 0.31 to 0.66 F/F_0 in stretched cells with an insignificant increase beginning at 11% strain. In injured cells, the average amplitude of spikes ranged from 0.13 to 1.13 F/F_0, which peaked significantly at the time of injury ($p = 0.003$, 2 vs. 7 min), **Figures 7C**, **8C**. Following injury, 95% of cells ($n = 20$, including constitutively spiking cells) did not return to the original fluorescence baseline, but rather a higher offset baseline. Despite a dramatic increase in amplitude at the time of injury, pre- and post-injury calcium spiking amplitudes were the lowest recorded throughout experimentation, perhaps due to imaging through silicone culture substrates instead of coverglass used for controls and stretch-grown cells.

Calcium spike duration, as measured from the time of onset until return to baseline, was consistent in controls and ranged from 1.03 to 4.34 s on average, **Figure 8D**. We did not notice any trends in spike duration associated with real-time stretch following 11 DIV, as the range fluctuated from 2.58 to 5.21 s on average. In contrast, there was a significantly higher spike duration in injured cells at the time of injury than after injury ($p = 0.02$, 2 min vs. 7 min). The average spike duration at the time of injury was 6.16 ± 5.15 s, which returned to control levels immediately thereafter in subsequent spikes.

We also found that in addition to intracellular calcium spiking in somata, many axons also increased in fluorescence intensity within injured cultures, **Figure S1** in Supplementary Material. While some axons increased in intensity homogenously following injury, anterograde and retrograde pulses appeared to increase in others, **Supplementary Video 5**. Although we did not measure axonal calcium flux using the stretch-growth method, we did not find remarkable changes within the proximal segments of cells undergoing stretch.

Anecdotally, we removed outliers from our datasets which had large calcium transients that resembled waves instead of spikes. Calcium waves had durations on the order of minutes, and only presented in 1–2 cells per culture. Following 8 DIV, we found a single cell illuminate after reaching 18% strain which had a duration of over 2 min (6 min mark, **Supplementary Video 2**). Similarly, we found a second cell in a day 11 culture with a large calcium wave that began after reaching just 4% strain, yet had a longer duration of 6 min. We found equivalent waves in control cultures, as well as injured cultures, and so these cells were omitted from analyzed data.

Stretch-grown Neurons Maintain Normal Somatic Morphology

Cross-sectional areas of nuclei and cytoplasms were compared after 2 weeks in culture following mild, moderate, or excessive stretch routines, **Table 2**. Mild and moderate profiles were considered to be stretch-growth profiles since they limited strain to 14 and 25%, respectively, and resulted in cultures with no axon disconnection. Alternatively, the stretch-axotomy profile ramped to 38% peak strain and resulted in completely axotomized cultures. Significant differences were found in the cytoplasmic cross-sectional areas of stretch-axotomized neurons, but no differences were found in the stretch-growth groups compared to controls, **Figure 9**. Non-stretched control cytoplasmic areas measured 299 ± 177 μm^2 ($n = 161$), while the 14 and 25% stretch-growth groups measured 325 ± 158 μm^2 ($n = 38$, $p = 0.37$) and 316 ± 156 μm^2 ($n = 216$, $p = 0.32$), respectively. Stretch-axotomized neurons disconnected by day 8, and had an average cross-sectional area of 463 ± 178 μm^2

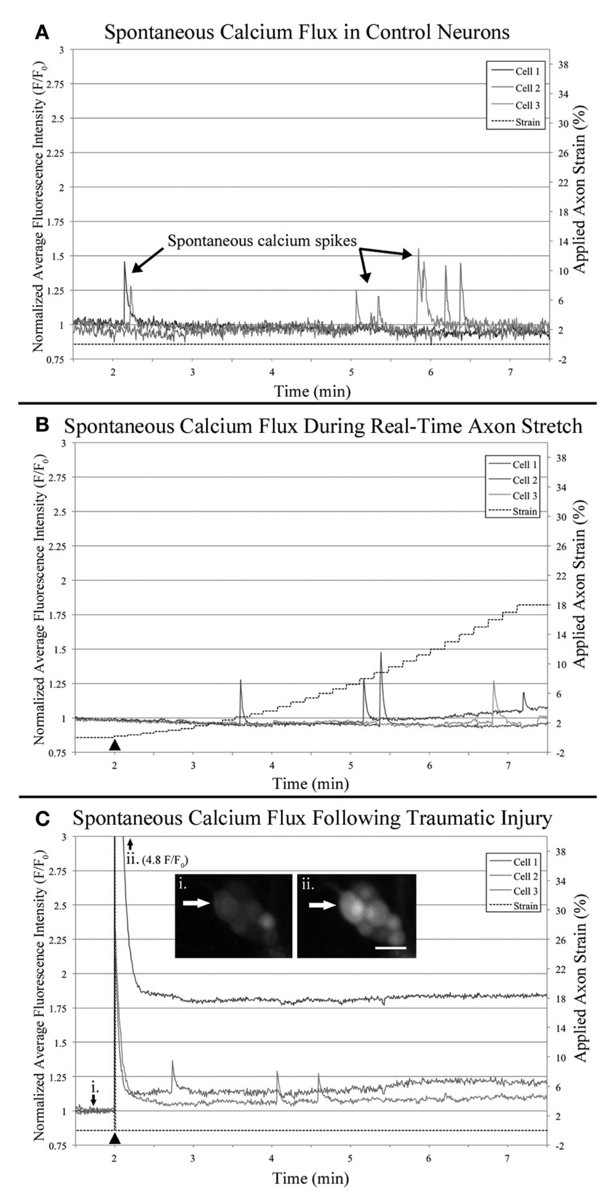

FIGURE 7 | Functional calcium imaging. Cells were loaded with Fluo-4AM and imaged over 10 min time-lapse sequences which were quantified and plotted. All cells which spiked during the first minute of recording were excluded from analysis to reduce background noise. Examples plots represent: **(A)** Control neurons within sham bioreactors, **(B)** Neurons undergoing real-time stretch, and **(C)** Stretch-injured cells subjected to 40% strain over 30 s^{-1}, (i) before injury, (ii) immediately after injury. Bar = 25 μm.

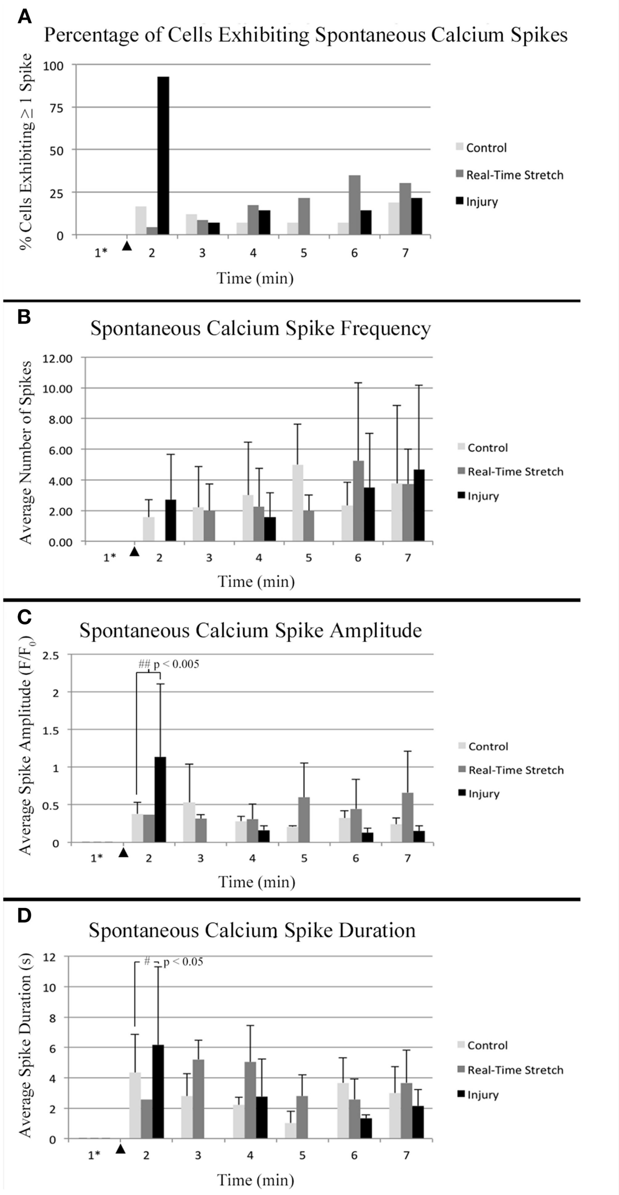

FIGURE 8 | Intracellular calcium flux. Quantified data from control neurons ($n = 42$, 8 DIV), real-time stretched cells ($n = 11$, 11 DIV), and stretch-injured cells ($n = 14$, 11 DIV) was averaged over 1-min periods for analysis of trends associated with experimental perturbation. **(A)** The prevalence of spiking increased ubiquitously in injured cells at the time of injury. **(B)** The frequency of spikes, in spiking cells, tended to increase in all cells over time. **(C)** The amplitude of calcium spikes was significantly larger in injured cells at the time of injury than during subsequent spikes. **(D)** The duration of calcium spikes at the time of injury was significantly longer at the time of injury than in subsequent spikes. Graphs show mean ± standard deviation. ▲ Time of injury in injured cells/start of real-time stretch in stretch-grown cells. *Cells that spiked during the first minute of recordings were excluded from analysis.

($n = 51$, $p < 0.0001$), which was significantly larger than control and stretch-growth groups. These results suggest clear differences exist between membrane-preserving stretch vs. membrane-compromising levels of stretch.

The nuclei of cells undergoing mild stretch-growth and stretch-axotomy were significantly larger than that of control neurons. Control nuclei measured $83 \pm 20\,\mu\text{m}^2$ ($n = 161$) while mild stretch-growth nuclei measured $101 \pm 32\,\mu\text{m}^2$ ($n = 38$, $p = 0.002$) and stretch-axotomy measured $112 \pm 27\,\mu\text{m}^2$ ($n = 51$, $p < 0.0001$). Interestingly, moderate stretch-growth nuclei measured $86 \pm 19\,\mu\text{m}^2$ ($n = 216$, $p = 0.14$) and were not significantly different than controls.

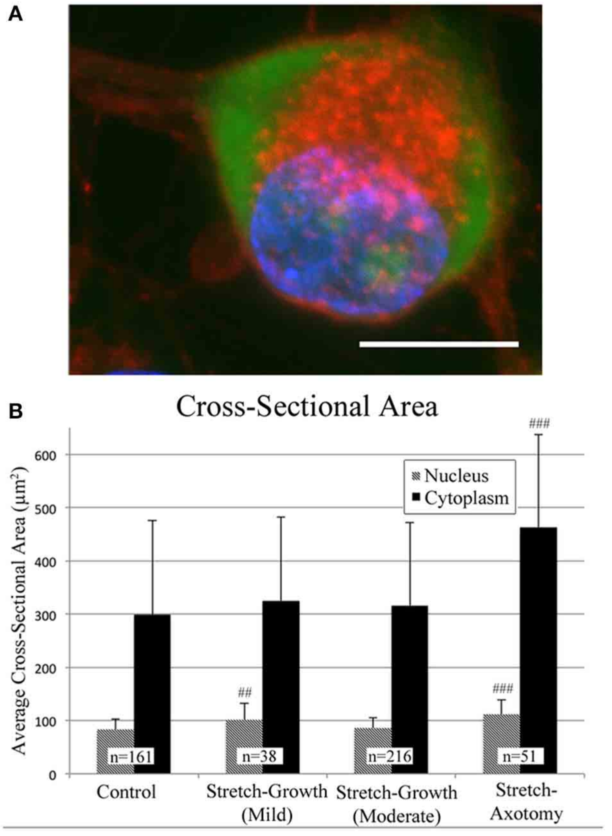

FIGURE 9 | Morphological analysis of soma following axon stretch. (A) Example of a DRG neuron as stained for analysis using wheat germ agglutinin (red), Nissl stain (green), and DAPI (blue); bar = 10 µm. **(B)** Mild and moderate stretch-growth paradigms resulted in normal cytoplasmic cross-sectional areas. Stretch-axotomized neurons had significantly larger cytoplasms and nuclei compared to controls ($p < 0.0001$ for cytoplasms and nuclei). '##' and '###' indicate $p < 0.005$ and $p < 0.0005$, respectively, compared to controls.

Discussion

Previously, it was found that neurons were able to conduct fast axonal transport at acute strains of up to ~25%, but higher strain resulted in pathologic occlusion (Loverde et al., 2011a). Notably, these strain thresholds were evaluated over the course of 1–2 h in order to assess for acute changes in transport. In our experience, growth occurs within hours of stretch, and is evident well before reaching 25% strain. Here, we applied exponential strain that reached 18% within 10 min real-time recordings to determine if the stimulus of stretch may be considered injurious.

Whole-cell patch clamp recording and functional calcium imaging were used to investigate if applied strain alters membrane potential or calcium homeostasis. Our results suggest that strain associated with stretch-growth does not cause changes in membrane potential, spontaneous electrophysiological activity, or intracellular calcium flux as would be expected following injury. We also analyzed the morphology of somata following long-term stretch routines to determine if stretch-growth initiates secondary injury. Our results revealed enlargement of the cytoplasms of stretch-axotomized neurons, but not stretch-grown neurons. Together, these results support that mechanical stretch of axons does not connote injury within the rates and limits established for stretch-growth. Further, signaling changes associated with electrophysiology or calcium flux do not appear to be linked to the stretch-growth process.

Live Imaging of Dissociated Stretch-grown Cultures

Our technique for axon stretch-growth results in a heterogeneous experimental culture containing both stretch-grown axons attached to Aclar, and non-stretch-grown axons that remain on the coverslip. To identify neurons undergoing stretch for analysis, bridging neurons were initially stretch-grown to approximately 1 mm in length and axons were individually traced to corresponding somata. For analysis under stretching conditions, stretch-grown neurons were allowed to rest for at least 24 h prior to the re-initiation of stretch under experimental observation. Crucially, initial stretch-growth was not expected to interfere with subsequent experimentation, as stretch-grown neurons halt growth and re-establish resting tension within minutes to hours following pauses in stretching (Dennerll et al., 1989; Lamoureux et al., 2011). Consequently, resuming stretch of previously stretch-grown neurons at rest was expected to be equivalent to the initial stretching stimulus.

For the techniques used in this study: whole-cell patch clamp, functional calcium imaging, and fluorescence microscopy, neuronal somata were required to be located on the coverslip bottom of the bioreactor. Accordingly, a new method was developed to seed neuronal somata at optimal density and distance of the manipulating substrates. The PDMS-barrier seeding method resulted in healthy populations of neuronal somata, while providing for axons of equivalent length between culture lanes and experiments. Importantly, this technique also restricted somata to the coverslip, which eliminated the need to differentiate between axons originating from the Aclar.

Electrophysiology of Cells Undergoing Real-time Axon Stretch

No reproducible evidence was found for an increase in spontaneous activity due to axon stretch. While stretch may trigger isolated spontaneous depolarization at high axon strains (~21.5% in one case), it is unlikely that neurons ever reach such thresholds during development due to concomitant cellular growth. Notably, we found a reduction in the action potential amplitude of cells within the stretched-state. A plausible explanation is that the continuity of whole-cell patches degraded with axon strain and microscopic cellular movement. In many cases not presented, cells were marginally pulled out of recording electrodes, which resulted in rises in membrane potential and reductions in current stimulated peak voltage. Here, in a cell with a robust patch that reached 52% axon strain, we did not find correlated changes in membrane potential or peak voltage as strain was increased. Conceivably, action potential voltage may have been a more sensitive indicator of patch degradation than membrane potential, which suggests that the majority of real-time patches may have been compromised due to culture movement. Notably, the action potential amplitudes of stretch-grown cells at rest were normal, supporting that stretch does not reduce action potential amplitude.

Functional Calcium Imaging

Similar to patch clamp recording, functional calcium imaging was used to analyze groups of neurons to determine if changes in spontaneous activity occurred as a result of stretch. Throughout the evaluation of multiple stretch-grown cultures, no reproducible changes in spiking activity were provoked by stretch within the context of stretch-growth. These results corroborate patch clamp recordings, as changes in both spontaneous action potentials and calcium spikes were not prevalent or reproducible. While stretch-growth appeared to increase the spiking rate of a small percentage of quiescent cells, the prevalence and frequency of spiking was not significantly different from controls. Conversely, the prevalence of spiking in injured cells was nearly homogenous at the time of injury, signifying a marked difference between growth-promoting stretch and traumatic injury.

We analyzed the amplitude and duration of calcium spikes during axon stretch to determine if strain altered the dynamics of calcium flux. No significant differences were found between controls and real-time stretched cells. Conversely, significant differences were found in the amplitude and duration of injured cells at the time of injury. Notably, injured cells underwent sustained increases in baseline calcium which lasted for the duration of recording. While cellular movement complicated measurement of basal calcium levels in some stretch-grown cells, **Figure 7B** (Cell #3, >7 min), we did not find rises in baseline calcium to be associated with the stretch-growth process.

During patch clamp analysis, we repeated our real-time stretch paradigm in order to increase strain beyond 18% where possible. In doing so, we found spontaneous action potentials in one cell at 21.5% strain. Anecdotally, we briefly increased strain beyond 18% during functional calcium imaging, but could not stimulate ubiquitous changes similar to injury. We noted, however, that older cultures appeared to have a greater prevalence of spontaneous activity than younger cultures. We also noted that cells appeared to be responsive to fluorescent light, and so light exposure was minimized while camera sensitivity was maximized. Despite these efforts, we still noticed a slight trend toward higher spiking frequencies at the end of 10 min experiments, and so we limited the scope of our analysis to 1 min following the conclusion of real-time stretch at 18% strain, while utilizing the same analysis window for control and injury groups.

Somatic Morphology

During early experimentation, it was quickly discovered that dissociated embryonic cells were incapable of growth at the applied strain rates developed for explants. Whereas explants could reach and sustain a unidirectional stretch-growth rate of 3 mm/d by day 7, dissociated cells required 10 days to reach equivalent rates. While stretch-growth paradigms were optimized, the resultant morphology of neuronal somata were analyzed following mild, moderate, or excessive stretching profiles. Notably, since cultures were maintained in medium containing NGF with minimal serum, we assumed that after 2 weeks in culture only nociceptive TrkA^+ neurons survived, but did not otherwise verify subtype. Confocal microscopy of stretch-grown neurons revealed no discernible differences in the morphology of embryonic somata following mild or moderate stretch-growth compared with controls. Conversely, excessive stretch caused a significant increase in the cytoplasmic cross-sectional area of axotomized neurons. Interestingly, we also found a slight increase in the dimensions of nuclei of mildly stretch-grown neurons, suggesting differences may exist in the growth of neurons stretch-grown at different rates.

Curiously, it was found by another group that mechanically elongated adult DRG neurons show evidence of chromatolysis following limb elongation (Safonova and Kovalenko, 2005). While these results appear contradictory to ours, adult neurons were stretch grown at a rate of 3 mm/d for 10 days *in vivo*. In our experience, the maximum stretch-growth rate for adult neurons was 2 mm/d *in vitro* using rat neurons (Loverde et al., 2011a). Admittedly, we did not evaluate adult neurons for signs of injury, nor did we evaluate pathologic levels of stretch prior to axotomy here. However, we found cytoplasmic swelling in stretch-axotomized neurons, but did not find evidence of pathology in neurons stretch-grown within their growth capacity. We theorize that adult neurons stretch-grown at rates within their growth capacity would not show signs of injury.

Developmental Axon Stretch vs. Traumatic Axon Injury

While both stretch and injury have been established as stimuli capable of increasing axon growth, a key divergence between these methods is the rupture of membrane that is associated with injury. In our stretch-axotomy paradigm, we exceeded the maximum growth capacity of embryonic DRGs, which caused subsequent disconnection and a chromatolytic phenotype. Accordingly, stretch at any rate which compromises membrane integrity should be interpreted as injurious. Importantly, since the rate of developmental body growth is well within the neuronal stretch-growth capacity, growth of axons occurs prior to reaching levels of strain that may be regarded as injurious. DRG neurons appear to be capable of maintaining a homeostasis between body growth and axon growth that differentiates the stimulus of stretch from injury.

We speculate that the growth cascade stimulated by stretch may be mutually provoked by injury. It is forthcoming that stretch-growth is a developmental stress response, and is likely to be provoked by an array of extrinsic perturbations. Indeed, while stretch-growth of axons does not appear injurious, it is likely still within the spectra of trauma. The therapeutic potential of the stretch-growth model is significant, in that the adaptive signaling changes which promote axon growth may be isolated from the maladaptive changes that accompany injury models. Parallel study of the stretch-growth and regenerative growth processes may serve to decipher between the requisite signals needed to regulate long-term axon growth.

Author Contributions

JL conceived experiments, performed experiments, analyzed data, wrote paper. BP conceived experiments, wrote paper.

Acknowledgments

This work was supported by the New Jersey Commission on Brain Injury Research 07-3204-BIR-E-0 and the NSF CAREER CBET-0747615. We thank Dr. Josh Berlin and Dr. George Magou for providing technical expertise in functional calcium imaging and patch clamp recording. We also thank Dr. Kyle Miller for his mentorship on axon stretch and experimental methodologies. We also thank Mr. John Hoinowski, NJIT Biomedical Engineering Design Studio, for his help in the fabrication of customized device components. Finally, we thank John Blum from Honeywell for providing Aclar film samples.

Supplementary Material

The Supplementary Material for this article can be found online at: http://journal.frontiersin.org/article/10.3389/fncel.2015.00308

Figure S1 | Calcium increases following traumatic stretch injury. (A) Before injury, fluorescence intensity of Fluo-4AM is extremely weak in axons compared to somata. **(B)** Immediately following injury, increases in fluorescence intensity occur in both the soma and axons (arrow). **(C)** Nine minutes post-injury, fluorescence increases persist in a percentage of somata (arrow heads) and axons. Bar = 25 μm.

Supplementary Video 1 | Patch-clamp recording during real-time axon stretch. Subtle movement of neuronal somata occurs during real-time axon stretch.

Supplementary Video 2 | Functional calcium imaging of real-time axon stretch (8 DIV). A rise in intracellular calcium can be seen in a single cell after reaching 18% strain (6 min mark, see arrow). Bar = 25 μm.

Supplementary Video 3 | Stretch-grown cultures following excessive stretch. Axons thin pathologically following excessive strain which reached 52%.

Supplementary Video 4 | Membrane elasticity of neuronal somata. Following patch clamp recording, a recording electrode is manipulated away from a cell while the membrane remains intact and undergoes 50 μm stretch.

Supplementary Video 5 | Functional calcium imaging of traumatic stretch injury. A traumatic stretch-injury causes ubiquitous calcium spiking at the time of stretch-injury (1 min mark).

References

Aviram, R., Shpan, D. K., Markovitch, O., Fishman, A., and Tepper, R. (2004). Three-dimensional first trimester fetal volumetry: comparison with crown rump length. *Early Hum. Dev.* 80, 1–5. doi: 10.1016/j.earlhumdev.2004.02.005

Bray, D. (1979). Mechanical tension produced by nerve cells in tissue culture. *J. Cell Sci.* 37, 391–410.

Bray, D. (1984). Axonal growth in response to experimentally applied mechanical tension. *Dev. Biol.* 102, 379–389. doi: 10.1016/0012-1606(84)90202-1

Chada, S., Lamoureux, P., Buxbaum, R. E., and Heidemann, S. R. (1997). Cytomechanics of neurite outgrowth from chick brain neurons. *J. Cell Sci.* 110, 1179–1186.

Croul, S. E., Mezitis, S. G., and Gonatas, N. K. (1988). An anti-organelle antibody in pathology. The chromatolytic reaction studied with a monoclonal antibody against the Golgi apparatus. *Am. J. Pathol.* 133, 355–362.

Dennerll, T. J., Lamoureux, P., Buxbaum, R. E., and Heidemann, S. R. (1989). The cytomechanics of axonal elongation and retraction. *J. Cell Biol.* 109, 3073–3083. doi: 10.1083/jcb.109.6.3073

Goldstein, M. E., Cooper, H. S., Bruce, J., Carden, M. J., Lee, V. M., and Schlaepfer, W. W. (1987). Phosphorylation of neurofilament proteins and chromatolysis following transection of rat sciatic nerve. *J. Neurosci.* 7, 1586–1594.

Hanz, S., and Fainzilber, M. (2006). Retrograde signaling in injured nerve–the axon reaction revisited. *J. Neurochem.* 99, 13–19. doi: 10.1111/j.1471-4159.2006.04089.x

Hoffman, P. N. (2010). A conditioning lesion induces changes in gene expression and axonal transport that enhance regeneration by increasing the intrinsic growth state of axons. *Exp. Neurol.* 223, 11–18. doi: 10.1016/j.expneurol.2009.09.006

Iwata, A., Stys, P. K., Wolf, J. A., Chen, X. H., Taylor, A. G., Meaney, D. F., et al. (2004). Traumatic axonal injury induces proteolytic cleavage of the voltage-gated sodium channels modulated by tetrodotoxin and protease inhibitors. *J. Neurosci.* 24, 4605–4613. doi: 10.1523/JNEUROSCI.0515-03.2004

Lamoureux, P., Heidemann, S., and Miller, K. E. (2011). Mechanical manipulation of neurons to control axonal development. *J. Vis. Exp.* e2509. doi: 10.3791/2509

Lamoureux, P., Heidemann, S. R., Martzke, N. R., and Miller, K. E. (2010). Growth and elongation within and along the axon. *Dev. Neurobiol.* 70, 135–149. doi: 10.1002/dneu.20764

Lamoureux, P., Zheng, J., Buxbaum, R. E., and Heidemann, S. R. (1992). A cytomechanical investigation of neurite growth on different culture surfaces. *J. Cell Biol.* 118, 655–661. doi: 10.1083/jcb.118.3.655

LaPlaca, M. C., Lee, V. M., and Thibault, L. E. (1997). An *in vitro* model of traumatic neuronal injury: loading rate-dependent changes in acute cytosolic calcium and lactate dehydrogenase release. *J. Neurotrauma* 14, 355–368. doi: 10.1089/neu.1997.14.355

LaPlaca, M. C., and Thibault, L. E. (1998). Dynamic mechanical deformation of neurons triggers an acute calcium response and cell injury involving the N-methyl-D-aspartate glutamate receptor. *J. Neurosci. Res.* 52, 220–229.

Limbrick, D. D. Jr., Sombati, S., and Delorenzo, R. J. (2003). Calcium influx constitutes the ionic basis for the maintenance of glutamate-induced extended neuronal depolarization associated with hippocampal neuronal death. *Cell Calcium* 33, 69–81. doi: 10.1016/S0143-4160(02)00054-4

Loverde, J. R., Ozoka, V. C., Aquino, R., Lin, L., and Pfister, B. J. (2011a). Live imaging of axon stretch growth in embryonic and adult neurons. *J. Neurotrauma* 28, 2389–2403. doi: 10.1089/neu.2010.1598

Loverde, J. R., Tolentino, R. E., and Pfister, B. J. (2011b). Axon stretch growth: the mechanotransduction of neuronal growth. *J. Vis. Exp.* e2753. doi: 10.3791/2753

Magou, G. C., Guo, Y., Choudhury, M., Chen, L., Hususan, N., Masotti, S., et al. (2011). Engineering a high throughput axon injury system. *J. Neurotrauma* 28, 2203–2218. doi: 10.1089/neu.2010.1596

McIlwain, D. L., and Hoke, V. B. (2005). The role of the cytoskeleton in cell body enlargement, increased nuclear eccentricity and chromatolysis in axotomized spinal motor neurons. *BMC Neurosci.* 6:19. doi: 10.1186/1471-2202-6-19

Pfister, B. J., Iwata, A., Meaney, D. F., and Smith, D. H. (2004). Extreme stretch growth of integrated axons. *J. Neurosci.* 24, 7978–7983. doi: 10.1523/JNEUROSCI.1974-04.2004

Pfister, B. J., Iwata, A., Taylor, A. G., Wolf, J. A., Meaney, D. F., and Smith, D. H. (2006). Development of transplantable nervous tissue constructs comprised of stretch-grown axons. *J. Neurosci. Methods* 153, 95–103. doi: 10.1016/j.jneumeth.2005.10.012

Qiu, J., Cafferty, W. B., McMahon, S. B., and Thompson, S. W. (2005). Conditioning injury-induced spinal axon regeneration requires signal transducer and activator of transcription 3 activation. *J. Neurosci.* 25, 1645–1653. doi: 10.1523/JNEUROSCI.3269-04.2005

Richardson, P. M., and Issa, V. M. (1984). Peripheral injury enhances central regeneration of primary sensory neurones. *Nature* 309, 791–793. doi: 10.1038/309791a0

Safonova, G. D., and Kovalenko, A. P. (2005). Morpho-functional characteristic of dog spinal ganglion neurons in post-distraction period. *Morfologiia* 127, 44–47.

Schneider, C. A., Rasband, W. S., and Eliceiri, K. W. (2012). NIH Image to ImageJ: 25 years of image analysis. *Nat. Methods* 9, 671–675. doi: 10.1038/nmeth.2089

Smetters, D., Majewska, A., and Yuste, R. (1999). Detecting action potentials in neuronal populations with calcium imaging. *Methods* 18, 215–221. doi: 10.1006/meth.1999.0774

Thévenaz, P., Ruttimann, U. E., and Unser, M. (1998). A pyramid approach to subpixel registration based on intensity. *IEEE Trans. Image Process.* 7, 27–41. doi: 10.1109/83.650848

Weber, J. T. (2004). Calcium homeostasis following traumatic neuronal injury. *Curr. Neurovasc. Res.* 1, 151–171. doi: 10.2174/1567202043480134

Weiss, P. (1941). “Nerve patterns: the mechanics of nerve growth,” in *Growth, Third Growth Symposium*, 163–203.

Zheng, J., Lamoureux, P., Santiago, V., Dennerll, T., Buxbaum, R. E., and Heidemann, S. R. (1991). Tensile regulation of axonal elongation and initiation. *J. Neurosci.* 11, 1117–1125.

Conflict of Interest Statement: The authors declare that the research was conducted in the absence of any commercial or financial relationships that could be construed as a potential conflict of interest.

frontiers in Cellular Neuroscience

ORIGINAL RESEARCH
published: 26 August 2015
doi: 10.3389/fncel.2015.00333

Cdc42 and RhoA reveal different spatio-temporal dynamics upon local stimulation with Semaphorin-3A

Federico Iseppon[1], *Luisa M. R. Napolitano*[1, 2], *Vincent Torre*[1]* and *Dan Cojoc*[3]*

[1] Neurobiology Sector, International School for Advanced Studies, Trieste, Italy, [2] Structural Biology Laboratory, Elettra-Sincrotrone Trieste S.C.p.A., Trieste, Italy, [3] Institute of Materials – National Research Council, Trieste, Italy

Small RhoGTPases, such as Cdc42 and RhoA, are key players in integrating external cues and intracellular signaling pathways that regulate growth cone (GC) motility. Indeed, Cdc42 is involved in actin polymerization and filopodia formation, whereas RhoA induces GC collapse and neurite retraction through actomyosin contraction. In this study we employed Förster Resonance Energy Transfer (FRET) microscopy to study the spatio-temporal dynamics of Cdc42 and RhoA in GCs in response to local Semaphorin-3A (Sema3A) stimulation obtained with lipid vesicles filled with Sema3A and positioned near the selected GC using optical tweezers. We found that Cdc42 and RhoA were activated at the leading edge of NG108-15 neuroblastoma cells during spontaneous cycles of protrusion and retraction, respectively. The release of Sema3A brought to a progressive activation of RhoA within 30 s from the stimulus in the central region of the GC that collapsed and retracted. In contrast, the same stimulation evoked waves of Cdc42 activation propagating away from the stimulated region. A more localized stimulation obtained with Sema3A coated beads placed on the GC, led to Cdc42 active waves that propagated in a retrograde manner with a mean period of 70 s, and followed by GC retraction. Therefore, Sema3A activates both Cdc42 and RhoA with a complex and different spatial-temporal dynamics.

Keywords: RhoA, Cdc42, FRET, local stimulation, Semaphorin-3A, GC retraction, NG108-15 cell line

Edited by:
Daniel Marcel Suter,
Purdue University, USA

Reviewed by:
Timothy Gomez,
University of Wisconsin, USA
Gianluca Gallo,
Temple University, USA

Correspondence:
Vincent Torre,
Neurobiology Sector, International School for Advanced Studies, via Bonomea 265, Trieste 34136, Italy
torre@sissa.it;
Dan Cojoc,
Institute of Materials – National Research Council, Area Science Park, Basovizza, Trieste 34149, Italy
cojoc@iom.cnr.it

Received: *29 April 2015*
Accepted: *10 August 2015*
Published: *26 August 2015*

Citation:
Iseppon F, Napolitano LMR, Torre V and Cojoc D (2015) Cdc42 and RhoA reveal different spatio-temporal dynamics upon local stimulation with Semaphorin-3A.
Front. Cell. Neurosci. 9:333.
doi: 10.3389/fncel.2015.00333

Introduction

Axon outgrowth and guidance depend on the ability of growth cones (GCs) to detect molecular guidance cues in their extracellular environment and to respond with a dynamic remodeling of the cytoskeleton. It is well-established that repulsive GCs turning arises from the disruption and loss of F-actin superstructures and actomyosin contraction, while attractive GC turning entails asymmetrical incorporation of actin on the side of the GC close to the chemoattractant (Dent et al., 2011). The Rho protein family members of small GTPases act as molecular switches to control signal transduction pathways by cycling between a GDP-bound, inactive form, and a GTP-bound, active form (Raftopoulou and Hall, 2004). In their active state, they have a key role in the cytoskeleton reorganization as they act downstream of most guidance cue receptors (Hall, 1998; Luo, 2000; Dickson, 2001; Jaffe and Hall, 2005). In neurons, the Rho family members RhoA and Cdc42 regulate GC extension and axon outgrowth: RhoA triggers actin cytoskeleton rearrangement to support GC collapse and neurite retraction (Thies and Davenport, 2003; Wu et al., 2005), whereas Cdc42 promotes neurite outgrowth and GC filopodia formation (Ahmed et al., 2006; Hall and Lalli, 2010). However, the activation of the RhoA pathway has growth-promoting effects in cortical and hippocampal cell axons (Ahnert-Hilger et al., 2004; Ohnami et al., 2008).

The secreted guidance cue is Semaphorin-3A (Sema3A), a repulsive guidance molecule that generally causes GC collapse in neurons through microtubule and actin reorganization (Fan and Raper, 1995; Goshima et al., 2002; Tran et al., 2007; Zhou et al., 2008), helping steer both axons and migrating cells along the correct trajectory. Sema3A is thought to act as a dimer (Wong et al., 1999) binding to the complex of receptors neuropilin1/plexinA1, to initiate signal transduction pathways (Adams et al., 1997; Takahashi et al., 1997). Intracellular signaling of Sema3A has been extensively studied, also quite recently (Jongbloets and Pasterkamp, 2014; Worzfeld and Offermanns, 2014). In DRG neurons, Sema3A stimulation induces GC collapse of sensory neurons through RhoA effector ROCK and intra-axonal translation of RhoA mRNA, which, through an axonal 3′UTR targeting element, is localized in developing axons and GCs (Wu et al., 2005; Hengst et al., 2006). This local translation is a condition necessary and sufficient to allow Sema3A-mediated GC collapse. In contrast, the role of Cdc42 in Sema3A collapse response is still unclear with reported contradictory results (Jin and Strittmatter, 1997; Kuhn et al., 1999).

Bath application of Sema3A has several drawbacks: the entire neuron is exposed to Sema3A and the response could involve both the entire neuron and the GC (Brown et al., 2009). In the present study, we combined the sensitized emission Förster Resonance Energy Transfer (FRET) technique with local stimulation to observe the spatial and temporal activation of RhoA and Cdc42 following localized stimulation with Sema3A. We used two types of vectors for local delivery of molecules: microbeads and micro-sized lipid vesicles. Silica microbeads have been covalently functionalized on their surface with Sema3A and placed on the GC of interest with a sub-micrometric precision, allowing a more localized stimulation for 30 s. Thus, Sema3A beads were able to induce a localized response to Sema3A, although the guidance molecule was not in its native form. We then used lipid vesicles encapsulating Sema3A that were trapped with optical tweezers in front of the exploring GC and broken with short UV laser pulse. In this way we studied the delivery of Sema3A in its native form but with a less precise spatial localization of its delivery.

In this paper, we examine the role of RhoA and Cdc42 in NG108-15 neuroblastoma cells and we show that they are both involved in Sema3A morphological changes with specific spatio-temporal dynamics; we also show that Cdc42 (but not RhoA) exhibits a complex wave behavior. Although the existence of different models that prove both a crosstalk and a negative feedback between the Rho GTPases (Holmes et al., 2012; Marèe et al., 2012) is confirmed, our data support a more dynamic pattern for Cdc42 that reflects a higher degree of complexity for the Rho GTPase signaling.

Materials and Methods

Cell Cultures and Transfection

NG108-15 neuroblastoma cells were purchased from Sigma Aldrich and grown in Dulbecco's modified Eagle's medium (DMEM) with 10% (v/v) fetal bovine serum (FBS) (Invitrogen), 100 μg/ml streptomycin and 100 units/ml in penicillin in a 5% CO_2atmosphere at 37°C. For live cell imaging studies, cells were seeded on glass coverslips, coated for 3 h with laminin (50 μg/ml, L2020 Sigma) in 12-multiwell plates. Cells were transfected 24 h later with intermolecular RhoA/Cdc42 FRET sensors (Murakoshi et al., 2011) using Metafectene reagent (Biontex Laboratories) following the manufacturer's protocol and imaged 1 day after transfection. mEGFP-RhoA-C1 (Addgene plasmid #29674), mEGFP-Cdc42-C1 (Addgene plasmid #29673), mCherry-Rhotekin(8–89)-mCherry-C1 (Addgene plasmid #29675) and mCherry-Pak3(60–113)/S74A/F84A-mCherry-C1 (Addgene plasmid #29676) were a gift from Ryohei Yasuda (Murakoshi et al., 2011).

Immunofluorescence

All these steps were performed at room temperature (20–22°C) and coverslips were rinsed with phosphate-buffered saline (PBS) between each step. Cells were fixed in freshly prepared 4% paraformaldehyde containing 0.15% picric acid in PBS, permeabilized in 0.1% Triton X-100 for 10 min and blocked with 0.5% BSA (all from Sigma-Aldrich, St.Louis, MO) in PBS for 1 h. Cells were then incubated with primary goat polyclonal antibody against neuropilin1 (Santa Cruz Biotechnology, Santa Cruz, CA) and rabbit polyclonal antibody against plexinA1 (Santa Cruz Biotechnology, Santa Cruz, CA) for 1 h. The secondary antibodies were donkey anti-rabbit 488 and donkey anti-goat 594 Alexa (Invitrogen, Life Technologies, Gaithersburg, MD, USA) and the incubation time was 30 min. Nuclei were stained with 2 μg/ml Hoechst 33342 (Sigma-Aldrich, St.Louis, MO) in PBS for 5 min. Coverslips were inverted and mounted on the glass side using Vectashield Mounting Medium and were then examined on a Leica DM6000 microscope (Leica Microsystems GmbH, Germany) using a 100× magnification and 1.42 NA oil-immersion objective. Fluorescent images were processed using Leica LCS Lite and Image J by W. Rasband (developed at the U.S. National Institutes of Health and available at http://rsbweb.nih.gov/ij/). For the colocalization analysis, each image was captured applying the same exposure and gain settings per channel and using Volocity 5.4 3D imaging software (PerkinElmer, Coventry, UK).

Vesicle Preparation

Detailed experimental procedures are described in our companion papers (Pinato et al., 2011, 2012). Single vesicles, with a diameter of 1–5 μm, were obtained with the lipid film hydration method using a hydration solution containing BSA or Sema3A, and were then identified, trapped and positioned at the location of interest (Ichikawa and Yoshikawa, 2001).

Beads Functionalization and Immunohistochemistry

1.5 μm large silica beads coated with COOH groups (Kisker-biotech, cat. PSi-1.5COOH) were functionalized using PolyLink

Protein Coupling Kit (Bangs Laboratories Inc., cat. PL01N), following the manufacturers protocol. Briefly, about 1.4×10^5 beads were incubated with 500 ng of Sema3A, in the presence of 20 μg/μL EDAC for 1 h, at room temperature and stored in Storage Buffer at 4°C.

Coated and un-coated microspheres were washed in PBS and incubated for 1 h, at room temperature, with anti-Sema3A (1:50, Sigma). Beads were then centrifuged, washed and incubated for 30 min, at room temperature, with donkey anti-goat Alexa 594 (Invitrogen) and finally analyzed using Fluorescence Microscopy (Nikon Eclipse TE-2000-E).

Optical Manipulation and FRET Microscopy Setup

Local delivery was achieved by optical trapping and manipulation of single vesicles at a specific position nearby the cells, followed by vesicles photolysis, to release active molecules. To increase the localization of the stimulus, single beads were optically trapped and maintained in contact with the GCs for 30 s. RhoGTPases activation was monitored by FRET microscopy. The setup, depicted in **Figure 1**, was developed around an inverted microscope (Nikon Eclipse TE-2000-E) adding three modules: (1) Infrared (IR) laser tweezers (custom built); (2) Ultraviolet (UV) laser micro-dissection system (MMI- CellCut Plus, MMI, Zurich, Switzerland); (3) Image splitter (OptoSplit II LS, Cairn Research, UK).

The first two modules are described in detail in our companion papers (Pinato et al., 2011, 2012). The trapping laser beam, generated by a 1064 nm fiber laser, is aligned with the micro-dissection UV beam and then focused on the sample through the same lens (Nikon, 60X water immersion, numerical aperture NA-1.2). The fluorescence path includes a 100 W Hg Lamp, excitation filters for EGFP (445/30 nm, Chroma, USA) and mCherry (550/30 nm). Light emitted by the sample is directed to the image splitter, where a dichroic mirror (585 nm) splits the light into Donor (EGFP) and Acceptor (mCherry) channels. After passing through the emission filters (EGFP: 515/30 nm; mCherry: 625/30 nm) each of the two beams is imaged on one of the two halves of a sCMOS sensor (Orca Flash 4.0, Hamamatsu), thus allowing the acquisition of the donor and of FRET emissions simultaneously. All live cells and FRET microscopy experiments were performed on the setup previously described. Imaging was performed in a Ringer's Solution and during the experiments cells were kept at 37°C, using a temperature controller (TempControl 37-2, PeCon, Germany). Experiments with the same coverslip always lasted less than 60 min. For bath applied stimulation assays time-lapse DIC images were acquired every 500 ms with a Nikon, 20X (NA: 0.25) objective in case of population studies, and with a Nikon, 60X (NA: 1.2) objective in case of single cell studies, from 90 s before adding the Sema3A to 20 min after it. For local stimulation assays, we trapped the lipid vesicle or the bead with the optical tweezers and we positioned it in front of, or in contact with, the selected GC. We then acquired simultaneously the Donor and Acceptor (FRET) channels for 15 min after the vesicle photolysis. All acquisitions were done with the sCMOS sensor at 16-bit depth. The exposure time for the FRET channels acquisition was 1 s at binning 4 × 4.

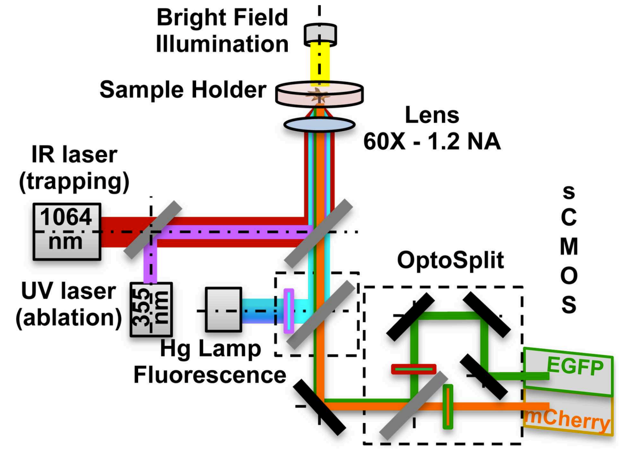

FIGURE 1 | Optical manipulation and FRET imaging setup. The IR laser beam (1064 nm) is aligned to the UV laser micro-dissection beam (355 nm) and then both are directed into the pupil of the microscope objective (60X - 1.2 NA). The sample is illuminated both by a white light source and a Hg fluorescence lamp. The light coming from the Donor and the Acceptor fluorophores in the sample is separated by a dual emission image splitter and the two images are formed on the two halves of the sCMOS camera sensor.

Ratiometric Corrections and Image Analysis

Ratiometric corrections and ratio calculations to generate activity images were performed using the Biosensors 2.1 MATLAB package (Danuser laboratory: http://lccb.hms.harvard.edu/software.html). All images were sequentially shading-corrected and background-subtracted; an optional photobleaching correction was also applied. Binary masks, with values equal to 1 inside the cells and 0 elsewhere, were extracted by thresholding the EGFP image (since it presented the highest signal-to-noise ratio). Control cells expressing either EGFP alone or mCherry alone were used to obtain bleedthrough coefficients necessary for the correction of the FRET image. The final ratio image, obtained dividing the completely corrected FRET image by the EGFP image, was used as a measure for the RhoA and Cdc42 activity.

Further image analysis was performed by ImageJ and custom-built codes were written in Matlab (Mathworks). To describe RhoA and Cdc42 activation, rectangular areas (size 10 × 20 μm) were generated selecting regions of interest in the normal direction with respect to the edge dynamics of the GCs; montage images were then composed by taking one image every 60 or 120 s for the entire duration of the experiment. The quantification of the FRET ratio was performed in stalling, protruding and retracting regions of the cell edge, and the results were normalized by the mean intensity of the ratio in the stalling regions. To measure the temporal dynamics of RhoA and Cdc42, a square area of $4\,\mu m^2$ was selected in the region of interest previously considered for image montages, so that no movement of the edge could interfere with the measurements; the intensity was calculated for every time point and then the measurements were normalized using the following equation:

$\Delta F = \frac{F-F_0}{F_0}$, where F is the intensity at the time point t and F_0 is the intensity at the first frame. Cell edges were detected for each frame by intensity-thresholding of the Ratio final image and edge dynamics were calculated along the central line of the rectangles, previously considered for the image montages. Edge and RhoGTPases activation dynamics were then plotted together in a graph, as a function of time. To measure the period of the waves in the different cases, one or more areas were selected in the retracting GCs, as previously described for temporal dynamics measurements, and then the wave period was calculated extrapolating the time between two maxima from the intensity vs. time plots.

Statistical Analysis

All quantitative results have been obtained from at least three independent experiments and expressed as the mean ± SEM. Experimental data were analyzed by Student's *t*-test and One-Way analysis of variance (ANOVA). Differences among samples were considered statistically significant when $p < 0.05$.

Results

The Spontaneous Dynamics of RhoA and Cdc42 in NG108-15 Cell Line

NG108-15 neuroblastoma cells are a good model system for neuronal signaling and growth (Smalheiser, 1991a,b; Goshima et al., 1993; Tsuji et al., 2011). In the absence of adherent or diffusive signaling gradients, NG108-15 cells exhibit both a complete collapse of the GC followed by a full or partial retraction of the neurite and the transient collapse of the GC structures (Rauch et al., 2013). Therefore, to measure the spontaneous activity of RhoA and Ccd42 in GCs, we transiently overexpressed in NG108-15 cells the intermolecular RhoA/Cdc42 probes based on FRET (Murakoshi et al., 2011). These probes consist of two components: wild type RhoA/Cdc42 tagged with monomeric enhanced green fluorescent protein (mEGFP) and their binding partner, Rho GTPase binding domain (RBD) of Rhotekin/Pak3, doubly tagged with mCherry (mCherry-RBD-mCherry) (Murakoshi et al., 2011). The expression of the intermolecular RhoA/Cdc42 probes was carefully titrated to levels that did not alter the normal neurite outgrowth. GFP, mCherry and FRET images were captured 18-20 h post-transfection using a Dual-view image splitting device. After background and spectral bleed-through correction, the GFP/mCherry ratio was measured and correlated with the activation levels of RhoA and Cdc42 during spontaneous protrusion and retraction events.

NG108-15 neuroblastoma cell line shows neurite outgrowth when plated on glass slides that have been coated with laminin. To examine the effect of RhoA and Cdc42 transfection on NG108-15 cells, we compared the morphologies of cells transfected with either RhoA or Cdc42 (Figures S1A,B). Transfection of Cdc42 induced significant neurite outgrowth compared with RhoA transfected cells that appeared more flatted (Figures S1A–D). Furthermore, most of the Cdc42-transfected cells were polarized with long neurite-like processes that were generally branched and exhibited micro-spikes along their length (Figures S1B–D).

In RhoA transfected cells, we observed that elevated RhoA activity (**Figures 2A,B**; mean FRET ratio: 1.109) correlates with edge retraction, whereas reduced RhoA activity (**Figures 2A,B**; mean FRET ratio: 0.831) leads to edge protrusion. To investigate how spontaneous RhoA activity relates to edge dynamics, we scanned RhoA activity in both protrusion (**Figures 2C,D**) and retraction regions (**Figures 2C,E**) of one representative cell at 60 s intervals. This confirmed that edge retraction coincides with a boost in RhoA activity compared with a protrusion event.

Cdc42 activity has been implicated in the regulation of filopodia and lamellipodia extension in many cell types (Nobes and Hall, 1995; Peng et al., 2003; Nalbant et al., 2004; Myers et al., 2012). We then imaged Cdc42 transfected cells and we found that membrane-ruffling and filopodia extension strongly correlate with hot spots of Cdc42 activity (**Figure 3B**; mean FRET ratio of 1.061) with respect to cell edges without protrusions

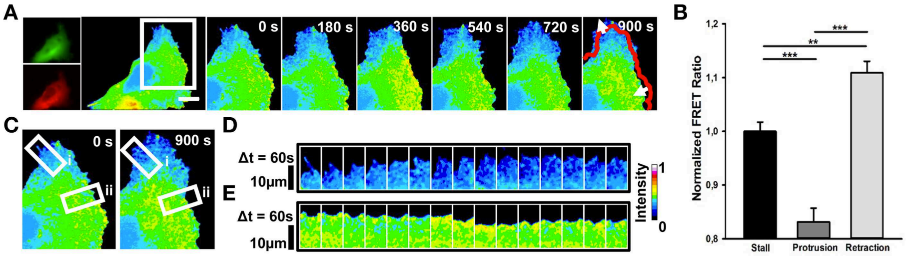

FIGURE 2 | Spontaneous RhoA dynamics in NG108-15 cells. **(A)** Ratiometric FRET live imaging of a representative RhoA-FRET neuroblastoma cell (n = six experiments). Consecutive frames were taken every second (left: generation of a ratiometric image) for 15 min. Insets on the right show a time series (1 frame every 3 min) of the magnified region denoted by the white box in the left image. Arrows indicate protrusion and retraction directions. The red line shows the initial edge profile. Scale Bar: 20 μm. **(B)** Quantification of mean RhoA activity (FRET ratio) in 50 stalling, protruding and retracting sections along the cell edge from RhoA neuroblastoma cells from two experiments. $^{**}p < 0.01$, $^{***}p < 0.001$ using ANOVA test (**C–E**) Montage images showing the dynamics of RhoA activation in protruding **(D)** and retracting sections **(E)** along the cell edge. **(C)** Images showing the regions of interest selected for the montage (white boxes) (i, protruding region; ii, retracting region). **(D,E)** Montage images highlighting a low RhoA activity in protruding regions **(D)** and a higher RhoA activity in retracting ones **(E)**. Intensity scale on the right in **(D)** applies to **(A,C–E)**.

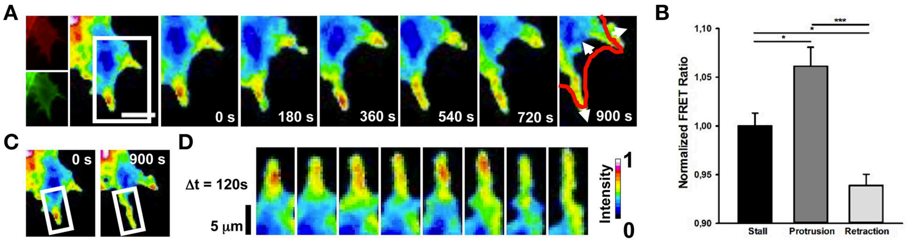

FIGURE 3 | Spontaneous Cdc42 dynamics in NG108-15 cells. **(A)** Ratiometric FRET live imaging of a representative Cdc42-FRET neuroblastoma cell (n = six experiments). Consecutive frames were taken every second (left: generation of a ratiometric image) for 15 min. Insets on the right show a time series (1 frame every 3 min) of the magnified region denoted by the white box in the left image. Arrows indicate protrusion and retraction directions. The red line shows the initial GC profile. Scale Bar: 20 μm. **(B)** Quantification of mean Cdc42 activity (FRET ratio) in 30 stalling, protruding and retracting sections along the cell edge from Cdc42 neuroblastoma cells from two experiments. $^{*}p < 0.05$, $^{***}p < 0.001$ using ANOVA test **(C,D)** Montage images showing the dynamics of Cdc42 activation in a protruding region of the cell. **(C)** Images showing the region of interest selected for the montage (white boxes). **(D)** Montage images highlighting hotspots of Cdc42 in the protruding region. Intensity scale on the right in **(D)** applies to **(A,C,D)**.

(**Figure 3B**; mean FRET ratio of 0.938) (**Figure 3**). Therefore, these findings indicate that a selective activation of RhoA and Cdc42 correlates spatially and temporally with retraction and extension events in NG108-15 cell line.

Sema3A Induces GC Retraction in NG108-15 Cell Line

In order to study the NG108-15 behavior after Sema3A stimulation, we first observed the distribution of Sema3A receptors neuropilin1 and plexinA1 using immunofluorescence microscopy after double staining with antibodies against neuripilin1 and plexinA1: both the Sema3A receptors were found in GCs of NG108-15 cell line (Figure S1E). This observation was consistent with the distribution of neuropilin1 and plexinA1 shown for hippocampal neurons (Pinato et al., 2012). Since bath application of Sema3A could have several drawbacks (Brown et al., 2009), we examined the effect of local stimulation with Sema3A filled lipid vesicles on GC in NG108-15 cells. We had previously demonstrated that local stimulation with vesicles encapsulating guidance molecules can allow a controlled spatiotemporal stimulation of hippocampal neurons that mimics better the natural behavior of the guidance molecules themselves (Pinato et al., 2012).

Lipid vesicles, with a diameter varying between 1 and 5 μm, were encapsulated with 10^3–10^4 molecules of Sema3A (Pinato et al., 2011, 2012). Local stimulation with lipid vesicles encapsulating Sema3A led to a rapid collapse and retraction of the GC (**Figures 4A,C**): retraction was already detectable at 100 s after stimulation with Sema3A and reached a plateau between 5 and 6 min. After local stimulation with BSA, no comparable retraction was observed (**Figures 4B,D**).

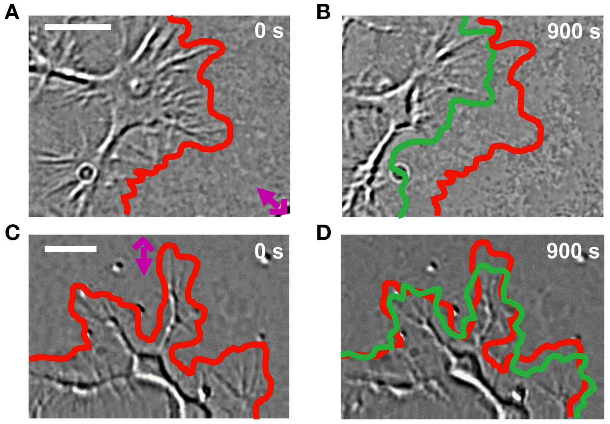

FIGURE 4 | GC behavior of NG108-15 cells stimulated with Sema3A. **(A,B)** DIC images of a representative cell locally stimulated with lipid vesicles encapsulating 1 μM of Sema3A at 0 **(A)** and 900 s **(B)** from the delivery. The red and green lines represent respectively the initial and final GC profile. The pink cross with the arrow represents the position of the liposome. **(C,D)** The same as in **(A,B)**, but the representative cell is locally stimulated with lipid vesicles encapsulating 1 μM of BSA. Frames were taken every second for 15 min in both cases. Contrast and brightness enhancement were applied to all images, followed by bandpass filtering of the spatial frequencies to enhance the edge contrast.

Local Stimulation by Sema3A Induces RhoA Activation Followed By the GC Retraction

To investigate the spatio-temporal activation of RhoA after local stimulation with Sema3A, we combined FRET with optical tweezers set-up to induce the local delivery of vesicles encapsulating Sema3A (**Figure 1**-see Methods section). Local application of Sema3A leads to an increase of RhoA activity in the central region of the GC followed by GC collapse and retraction (**Figure 5A** and Supplementary Movie 1). Ratiometric FRET imaging highlighted that RhoA activity increases rapidly, within 30 s after Sema3A local stimulation, reaching the maximum value within 400 s (**Figures 5B,C**). A more detailed analysis of the time dependence of RhoA activity and GC edge retraction showed that the GC begins to retract within 100–120 s after Sema3A local stimulation, reaching a complete collapse and retraction within 15 min (**Figure 5D**; data from five experiments). The delay between the increase of RhoA activity and the GC retraction can be explained with the recruitment of RhoA binding proteins necessary for cytoskeletal rearrangement. When we stimulated RhoA transfected cells with vesicles encapsulating

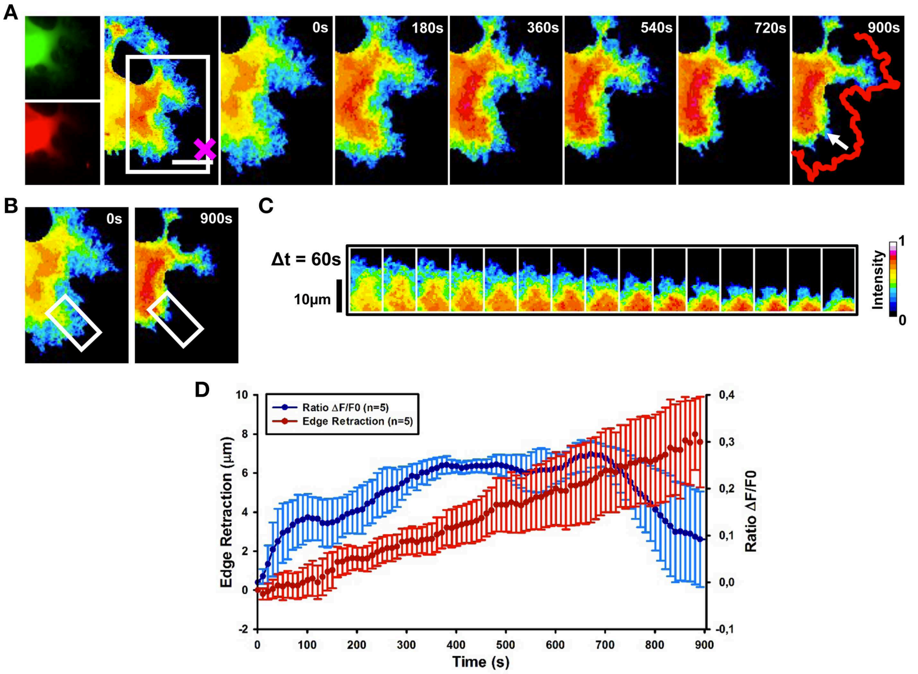

FIGURE 5 | RhoA activation dynamics upon local release of Sema3A. **(A)** Ratiometric FRET live imaging of a representative RhoA-FRET neuroblastoma cell upon Sema3A stimulation. Frames were taken every second (left: generation of a ratiometric image) for 15 min (the cross indicates the position of the lipid vesicle filled with Sema3A). Insets on the right show a time series (1 frame every 3 min) of the magnified region denoted by the white box in the left image. Arrow indicates the retraction direction. The red line shows the initial edge profile. Scale Bar: 20 μm. **(B,C)** Montage images showing the dynamics of RhoA activation in the stimulated cell GCs. **(B)** Images showing the region of interest selected for the montage (white boxes). **(C)** Montage images highlighting a progressive increase of RhoA activation in the retracting GC. Images were taken at 60 s intervals. Intensity scale on the right in **(C)** applies to **(A–C)**. **(D)** Plot of average RhoA activity ($\Delta F/F_0$) from five experiments. RhoA dynamics was followed for 15 min after Sema3A stimulation. FRET ratio is represented as a blue line; edge retraction is defined as a red line. Data are shown as Mean ± SEM.

BSA (Figures S2A–C), no comparable retraction (**Figure 2**) was observed.

Thus, our results strongly suggest that Sema3A local stimulation leads to an activation of RhoA associated to GC collapse and retraction.

Cdc42 Activation Exhibits a Wave-like Behavior

We then determined the spatial and temporal dynamics of activated Cdc42 in response to Sema3A local delivery (Supplementary Movie 2). Ratiometric FRET imaging showed that Cdc42 activity decreases within 60 s from Sema3A stimulation almost in synchrony with the cell edge retraction (**Figures 6A,B,D,E** and Figure S3; data from seven experiments).

In 43% of cases, we observed that in the region far from the stimulus Cdc42 activity increases within 120 s after Sema3A stimulation followed by edge advancement, lamellipodia ruffling and filopodia extension (**Figures 6A–C,F**). Plotting Cdc42 activity against time showed waves of active Cdc42 between the front and back of the protruding region, with a mean period of 155 ± 9 s (**Figures 7C,E**; data from three experiments). The delay between Cdc42 activation and Sema3A stimulation indicates that the protrusion event in the region far from the local release of Sema3A is a reaction to the repulsive stimulus. Consistently, BSA local stimulation seemed not to affect the activity of Cdc42 in transfected cells (Figures S2D–F).

In order to better characterize Cdc42 activity in response to Sema3A local stimulation, we used 1.5 μm microbeads coated with Sema3A that allow a more localized stimulation (D'Este et al., 2011) (Figure S4). Live FRET imaging of GCs transfected with Cdc42 and stimulated with Sema3A-beads showed the appearance of recurring waves of active Cdc42 almost in synchrony with the retraction of the GC (**Figure 7A**). Plotting Cdc42 intensity against time from three different areas of the stimulated GC revealed a burst of Cdc42 activity within 100–120 s from the local stimulation and highlighted the propagation of Cdc42 traveling waves from the front to the back of the retracting GC (**Figure 7B**). In spontaneous GC collapse and retraction we observed again Cdc42 active waves, but with a different periodicity (Beads: 70 ± 5 s vs. Spontaneous: 110 ± 10 s) (**Figures 7D,E**). Indeed, we found that Cdc42 active waves have different periods in all three cases described herein (Lipid vesicles, Spontaneous, and Coated Beads) reflecting the different cellular behavior in response to the stimulus applied (Holmes et al., 2012; Marèe et al., 2012).

Taken together, these findings show that (a) Cdc42 has a traveling wave behavior with a different periodicity, highlighting

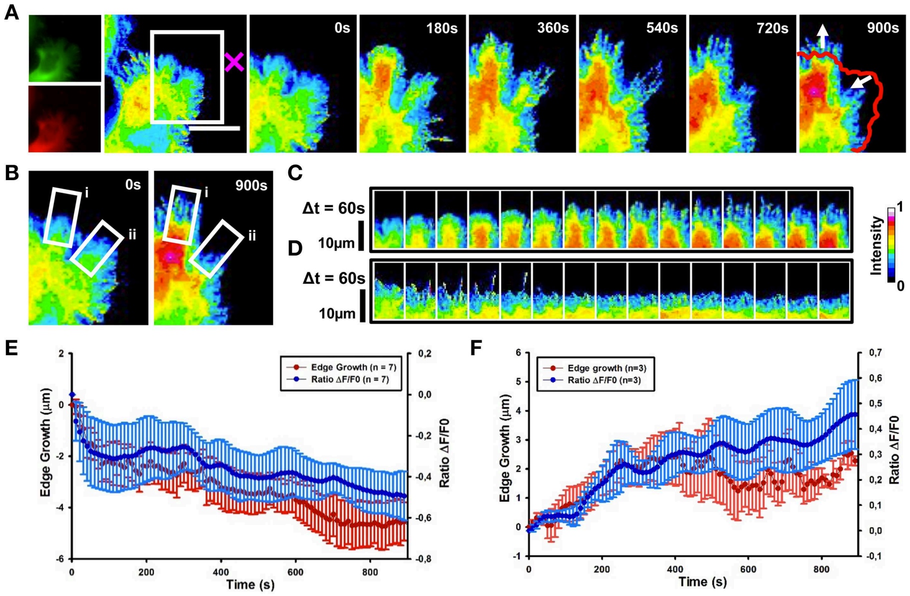

FIGURE 6 | Cdc42 dynamics upon local delivery of Sema3A. (A) Cdc42 activity determined by ratiometric FRET live imaging. Frames were taken every second (left: generation of a ratiometric image) for 15 min after stimulation (the cross indicates the position of the lipid vesicle encapsulating Sema3A). Insets on the right show a time series (1 frame every 3 min) of the magnified region denoted by the white box in the left image. Arrows indicate retraction and protrusion directions. The red line shows the initial edge profile. Scale Bar: 20 μm. **(B–D)** Montage images showing the dynamics of Cdc42 activity in protruding and retracting regions of the cell. **(B)** Images showing the regions of interest selected for the montage (white boxes) (i, protruding region; ii, retracting region). **(C,D)** Montage images highlighting a decrease of Cdc42 activity in the retracting region of the cell facing the lipid vesicle filled with Sema3A **(C)** and an increase of Cdc42 activity in the protruding region, away from the vesicle **(D)**. Images are taken at 60 s intervals. Intensity scale on the right in **(D)** applies to **(A–D)**. **(E)** Plot of average Cdc42 activity ($\Delta F/F_0$) vs. edge growth from seven experiments. Negative values are defined as retraction. FRET ratio is represented as a blue line; edge growth is defined as a red line. **(F)** The same as in **(E)**, but in this case data are obtained from three experiments. Positive values are defined as edge protrusion. Data are shown as Mean ± SEM.

its complex spatio-temporal dynamic; (b) that, in all the cases observed, a variation of Cdc42 activity upon Sema3A stimulation is accomplished with a leading edge retraction in the region of the stimulus; (c) that, in few cases, Sema3A local release induces the formation of active Cdc42 waves away from Sema3A stimulation that produced new lamellipodia and filopodia.

Discussion

By combining FRET with local stimulation we have demonstrated that local delivery of Sema3A induces an activation of RhoA followed by a rapid GC retraction. The use of two different approaches (beads and liposome vesicles) for Sema3A local stimulation of Cdc42 transfected cells, both based on optical manipulation, led to a better characterization of Cdc42 wave behavior. Sema3A release from the vesicles induced a decrease in Cdc42 activity followed by an edge retraction. In regions distant from the stimulus, active waves of Cdc42 resulted in a marked increase in cell dynamic with lamellipodia-ruffling and filopodia extension. Using 1.5-μm diameter Sema3A-immobilized microbeads, we observed again Cdc42 active waves that here resulted in GC retraction. In previous papers (Pinato et al., 2011, 2012), the local delivery was used to estimate the minimum number of Sema3A and Netrin1 molecules necessary to induce retraction and growth, respectively. The present study expands previous observations by combining for the first time local stimulation with the FRET technique underlying a fine spatial and temporal regulation of RhoGTPase activities after Sema3A stimulus.

RhoA and Cdc42 Have a Different Spontaneous Activity in NG108-15 Neuroblastoma Cells

Rho GTPases are key molecular switches that affect multiple cellular functions including cell migration and polarity, vesicle trafficking, cytokinesis and endocytosis (Etienne-Manneville and Hall, 2002; Govek et al., 2005; Boureux et al., 2007; Haesman and Ridley, 2008; Pertz, 2010). They are important players in the transmission and integration of signals that control the cytoskeleton: in response to extracellular signals, they induce changes in the organization of actin cytoskeleton to allow different biological processes like morphogenesis, chemotaxis, axonal guidance, and cell cycle progression (Ridley and Hall, 1992; Gallo and Letourneau, 2004; Sit and Manser, 2011; Gomez and Letourneau, 2014). In N1E-115 neuroblastoma cell line, Cdc42 promotes the formation of filopodia and lamellipodia, whereas RhoA causes GC collapse and neurite retraction (Kozma et al., 1997; van Leeuwen et al., 1997; Sarner et al., 1997). Consistent with this view, on a laminin

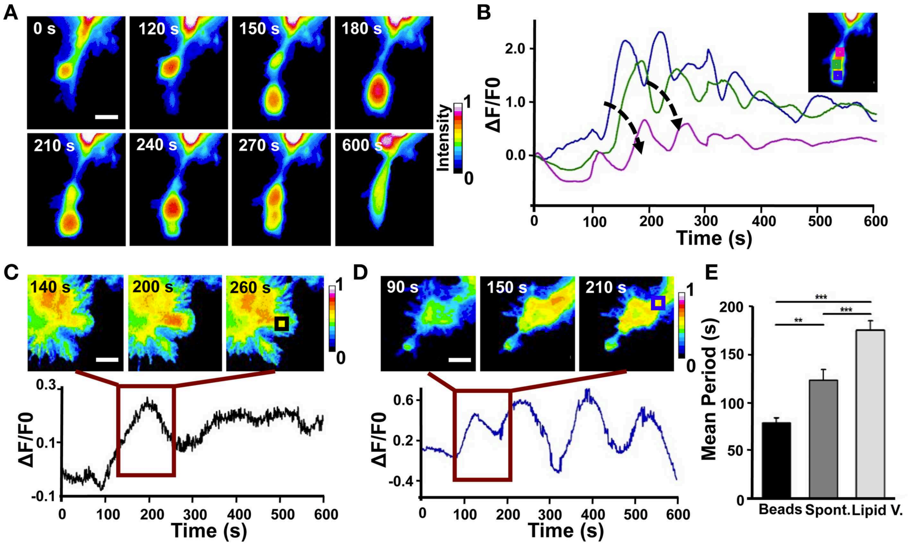

FIGURE 7 | Analysis of Cdc42 wave-like behavior. (A) Time series of the active Cdc42 retrograde waves upon local stimulation with Sema3A-coated beads (Representative of three experiments). **(B)** Plot of average Cdc42 activity ($\Delta F/F_0$) in the regions defined by the colored squares in the inset image at the top right. The analyzed cell is the same shown in **(A)**. Arrows indicate the temporal progression of the oscillations. **(C)** Top: Time series (1 frame every 60 s) of the Cdc42 oscillatory behavior upon local stimulation with lipid vesicles filled with Sema3A for the time defined by the dark red square in the bottom plot; Bottom: Plot of average Cdc42 activity ($\Delta F/F_0$) in the region defined as a black square in the image at the top right. **(D)** Top: Time series (1 frame every 60 s) of the Cdc42 wave behavior during spontaneous motion for the time defined by the dark red square in the bottom plot. Bottom: Plot of average Cdc42 activity ($\Delta F/F_0$) in the region defined as a blue square in the image at the top right. **(E)** Quantification of the period of the oscillations both during spontaneous motion and upon local stimulation. Mean period ± SEM of 10 periods from 3 experiments for bead stimulation, 10 periods from 2 experiments for spontaneous motion and 10 periods from 3 experiments for lipid vesicles stimulation. $^{**}p < 0.01$, $^{***}p < 0.01$ using ANOVA test. Scalebars in **(A,C,D)**: 10 μm.

substrate, NG108-15 cells expressing Cdc42 exhibited long processes with rather simple GCs and branched neurites with several actin microspikes along their length. On the contrary, expression of RhoA often resulted in cell rounding and flattening without the appearance of stress fibers or focal contact (Figure S1). Spatial and temporal monitoring of spontaneous activity of RhoA and Cdc42 in NG108-15 cells allowed us to directly compare cell motility with levels of active RhoA and Cdc42. We found that filopodia and lamellipodia protrusions correlate with Cdc42 activation in these subcellular domains (**Figure 3**), whereas RhoA activity increases and decreases in synchrony with cell leading edge retraction and protrusion (**Figure 2**).

Local Release of Sema3A Induces a Rapid GC Collapse and Retraction

The role of Rho-family GTPases in response to several guidance cue stimulations has been extensively studied in order to address their role in F-actin dynamics and organization that determine axon guidance, GC behavior and axon extension (Gallo and Letourneau, 2004). Attractive cues such as brain-derived neurotrophic factor (BDNF) activate Cdc42 and Rac (Yuan et al., 2003; Cheung et al., 2007; Myers et al., 2012; Tep et al., 2012), whereas repulsive cues like Slit or Eph/ephrin have been shown to induce a reduction of Cdc42 activity at GC periphery and an activation of RhoA/ROCK pathway respectively (Wahl et al., 2000; Myers et al., 2012; Takeuchi et al., 2015). However, it is well-established that small GTPases are important components of Semaphorin (Sema)/plexin axon guidance signaling (Kruger et al., 2005; Tran et al., 2007). The Sema family of secreted, transmembrane and GPI-linked proteins is one of the largest families of axon guidance cues and guides the growing axons by repelling them or preventing them from entering certain regions (Yazdani and Terman, 2006). The prototypic member of this family is the diffusible repulsive guidance cue Sema3A that induces collapse of GCs through the interaction with its receptor plexinA1 (Fan and Raper, 1995; Nakamura et al., 2000; Brown and Bridgman, 2009). In our experiments, Sema3A local delivery leads to a rapid GC collapse and retraction in NG108-15 neuroblastoma cell line (**Figure 4**) in agreement with similar experiments in DRG neurons (Brown et al., 2009).

Sema3A Local Stimulation Activates RhoA and Cdc42 with Specific Spatio-temporal Dynamics

Previous findings have indicated an inhibitory role for RhoA in inducing neurite extension (Kozma et al., 1997; Dickson, 2001; Wu et al., 2005). Consistently, we found that Sema3A local release leads to RhoA activation within 30 s, causing a delayed GC retraction (100–120 s from stimulation) with a correlation between the levels of RhoA activity and Sema3A-induced morphological changes (**Figure 5**). This delay suggests that GC collapse and retraction could require RhoA recruitment of its binding partners.

In Cdc42 transfected cells, local delivery of Sema3A caused a decrease of Cdc42 activity within 60 s from the stimulation (**Figure 6**). Cdc42 showed a wave behavior with a retrograde flow that proceeded almost in synchrony with cell retraction toward the repulsive cue (**Figure 6**). In a few cases, Sema3A local release induced the formation of active Cdc42 propagating waves away from Sema3A stimulation that generated new lamellipodia and filopodia suggesting a role for Cdc42 as an important component of actin *t*-waves (Lim et al., 2008; Flynn et al., 2009; Mori et al., 2011; Allard and Mogilner, 2013) (**Figure 6**).

Local stimulation with Sema3A coated beads induced the formation of active Cdc42 waves that propagated from the edge of the GC to the center of the cell with a period of 70 s (**Figure 7**). The same active Cdc42 waves were found in spontaneous GC collapse and retraction in response to repellent signals naturally occurring in neuronal cell culture, but with a mean period of 110 s (Rauch et al., 2013). How differently Sema3A stimulation can influence Cdc42 wave behavior is still an open question. One possibility is that these different Cdc42 dynamic wave patterns reflect the heterogeneity of the cell population or differential activity states of the cell. Alternatively, bead mechanical stimulation could induce calcium oscillations within the cell that influence actin *t*-waves through the modulation of Cdc42 activity (Wu et al., 2013). Although previous models have highlighted a fine spatio-temporal crosstalk between Rho GTPases that exhibit sustained polarization by a wave-pinning mechanism (Mori et al., 2008; Holmes et al., 2012; Marèe et al., 2012), our data show a wave-propagation mechanism for Cdc42 but not for RhoA and provide clear evidence for a higher degree of complexity in Rho GTPase signaling network (Pertz, 2010).

Our findings clearly indicate that the combination of the FRET technique with local stimulation provides new tools for the study of cytoskeleton rearrangements in response to guidance cue stimulations, highlighting the dynamic spatial and temporal regulation of Rho GTPases.

Acknowledgments

We acknowledge the financial support of the NEUROSCAFFOLDS Project n.604263 within the Seventh Framework Programme for Research of the European Commission. We also acknowledge the financial support of the SI-CODE project of the Future and Emerging Technologies (FET) programme within the Seventh Framework Programme for Research of the European Commission, under FET-Open grant number: FP7-284553.

Supplementary Material

The Supplementary Material for this article can be found online at: http://journal.frontiersin.org/article/10.3389/fncel.2015.00333

References

Adams, R. H., Lohrum, M., Klostermann, A., Betz, H., and Püschel, A. W. (1997). The chemorepulsive activity of secreted semaphorins is regulated by furin-dependent proteolytic processing. *EMBO J.* 16, 6077–6086. doi: 10.1093/emboj/16.20.6077

Ahmed, I., Calle, Y., Iwashita, S., and Nur-E-Kamal A. (2006). Role of Cdc42 in neurite outgrowth of PC12 cells and cerebellar granule neurons. *Mol. Cell. Biochem.* 281, 17–25. doi: 10.1007/s11010-006-0165-9

Ahnert-Hilger, G., Höltje, M., Grosse, G., Pickert, G., Mucke, C., Nixdorf-Bergweiler, B., et al. (2004). Differential effects of Rho GTPases on axonal and dendritic development in hippocampal neurones. *J. Neurochem.* 90, 9–18. doi: 10.1111/j.1471-4159.2004.02475.x

Allard, J., and Mogilner, A. (2013). Traveling waves in actin dynamics and cell motility. *Curr. Opin. Cell Biol.* 25, 107–115. doi: 10.1016/j.ceb.2012.08.012

Boureux, A., Vignal, E., Faure, S., and Fort, P. (2007). Evolution of the Rho family of ras-like GTPases in eukaryotes. *Mol. Biol. Evol.* 24, 203–216. doi: 10.1093/molbev/msl145

Brown, J. A., and Bridgman, P. C. (2009). Disruption of the cytoskeleton during Semaphorin 3A induced growth cone collapse correlates with differences in actin organization and associated binding proteins. *Dev. Neurobiol.* 69, 633–646. doi: 10.1002/dneu.20732

Brown, J. A., Wysolmerski, R. B., and Bridgman, P. C. (2009). Dorsal root ganglion neurons react to semaphorin 3A application through a biphasic response that requires multiple myosin II isoforms. *Mol. Biol. Cell* 20, 1167–1179. doi: 10.1091/mbc.E08-01-0065

Cheung, Z. H., Chin, W. H., Chen, Y., Ng, Y. P., and Ip, N. Y. (2007). Cdk5 is involved in BDNF-stimulated dendritic growth in hippocampal neurons. *PLoS Biol.* 5:e63. doi: 10.1371/journal.pbio.0050063

Dent, E. W., Gupton, S. L., and Gertler, F. B. (2011). The growth cone cytoskeleton in axon outgrowth and guidance. *Cold Spring Harb. Perspect. Biol.* 3:a001800. doi: 10.1101/cshperspect.a001800

D'Este, E., Baj, G., Beuzer, P., Ferrari, E., Pinato, G., Tongiorgi, E., et al. (2011). Use of optical tweezers technology for long-term, focal stimulation of specific subcellular neuronal compartments. *Integr. Biol. (Camb.)* 3, 568–577. doi: 10.1039/c0ib00102c

Dickson, B. J. (2001). Rho GTPases in growth cone guidance. *Curr. Opin. Neurobiol.* 11, 103–110. doi: 10.1016/S0959-4388(00)00180-X

Etienne-Manneville, S., and Hall, A. (2002). Rho GTPases in cell biology. *Nature* 420, 629–635. doi: 10.1038/nature01148

Fan, J., and Raper, J. A. (1995). Localized collapsing cues can steer growth cones without inducing their full collapse. *Neuron* 14, 263–274. doi: 10.1016/0896-6273(95)90284-8

Flynn, K. C., Pak, C. W., Shaw, A. E., Bradke, F., and Bamburg, J. R. (2009). Growth cone-like waves transport actin and promote axonogenesis and neurite branching. *Dev. Neurobiol.* 69, 761–779. doi: 10.1002/dneu.20734

Gallo, G., and Letourneau, P. C. (2004). Regulation of growth cone actin filaments by guidance cues. *J. Neurobiol.* 58, 92–102. doi: 10.1002/neu.10282

Gomez, T. M., and Letourneau, P. C. (2014). Actin dynamics in growth cone motility and navigation. *J. Neurochem.* 129, 221–234. doi: 10.1111/jnc.12506

Goshima, Y., Ito, T., Sasaki, Y., and Nakamura, F. (2002). Semaphorins as signals for cell repulsion and invasion. *J. Clin. Invest.* 109, 993–998. doi: 10.1172/JCI0215467

Goshima, Y., Ohsako, S., and Yamauchi, T. (1993). Overexpression of Ca2+/calmodulin-dependent protein kinase II in Neuro2a and NG108-15 neuroblastoma cell lines promotes neurite outgrowth and growth cone motility. *J. Neurosci.* 13, 559–567.

Govek, E. E., Newey, S. E., and Van Aelst, L. (2005). The role of the Rho GTPases in neuronal development. *Genes Dev.* 19, 1–49. doi: 10.1101/gad.1256405

Haesman, S. J., and Ridley, A. J. (2008). Mammalian Rho GTPases: new insights into their functions from *in vivo* studies. *Nat. Rev. Mol. Cell. Biol.* 9, 690–701. doi: 10.1038/nrm2476

Hall, A. (1998). Rho GTPases and the actin cytoskeleton. *Science* 279, 509–514. doi: 10.1126/science.279.5350.509

Hall, A., and Lalli, G. (2010). Rho and Ras GTPases in axon growth, guidance, and branching. *Cold Spring Harb. Perspect. Biol.* 2:a001818. doi: 10.1101/cshperspect.a001818

Hengst, U., Cox, L. J., Macosko, E. Z., and Jaffrey, S. R. (2006). Functional and selective RNA interference in developing axons and growth cones. *J. Neurosci.* 26, 5727–5732. doi: 10.1523/JNEUROSCI.5229-05.2006

Holmes, W. R., Carlsson, A. E., and Edelstein-Keshet, L. (2012). Regimes of wave type patterning driven by refractory actin feedback: transition from static polarization to dynamic wave behaviour. *Phys. Biol.* 9:046005. doi: 10.1088/1478-3975/9/4/046005

Ichikawa, M., and Yoshikawa, K. (2001). Optical transport of a single cell-sized liposome. *Appl. Phys. Lett.* 79, 4598–4600. doi: 10.1063/1.1430026

Jaffe, A. B., and Hall, A. (2005). Rho GTPases: biochemistry and biology. *Annu. Rev. Cell Dev. Biol.* 21, 247–269. doi: 10.1146/annurev.cellbio.21.020604.150721

Jin, Z., and Strittmatter, S. M. (1997). Rac1 mediates collapsin-1-induced growth cone collapse. *J. Neurosci.* 17, 6256–6263

Jongbloets, B. C., and Pasterkamp, R. J. (2014). Semaphorin signalling during development. *Development* 141, 3292–3297. doi: 10.1242/dev.105544

Kozma, R., Sarner, S., Ahmed, S., and Lim, L. (1997). Rho family GTPases and neuronal growth cone remodelling: relationship between increased complexity induced by Cdc42Hs, Rac1, and acetylcholine and collapse induced by RhoA and lysophosphatidic acid. *Mol. Cell. Biol.* 17, 1201–1211.

Kruger, R. P., Aurandt, J., and Guan, K. L. (2005). Semaphorins command cells to move. *Nat. Rev. Mol. Cell. Biol.* 6, 789–800. doi: 10.1038/nrm1740

Kuhn, T. B., Brown, M. D., Wilcox, C. L., Raper, J. A., and Bamburg, J. R. (1999). Myelin and collapsin-1 induce motor neuron growth cone collapse through different pathways: inhibition of collapse by opposing mutants of rac1. *J. Neurosci.* 19, 1965–1975.

van Leeuwen, F. N., Kain, H. E., Kammen, R. A., Michiels, F., Kranenburg, O. W., and Collard, J. G. (1997). The guanine nucleotide exchange factor Tiam1 affects neuronal morphology; opposing roles for the small GTPases Rac and Rho. *J. Cell Biol.* 139, 797–807. doi: 10.1083/jcb.139.3.797

Lim, L. B., Bu, W., Goh, W. I., Koh, E., Ong, S. H., Pawson, T., et al. (2008). The Cdc42 Effector IRSp53 generates filopodia by coupling membrane protrusion with actin dynamics. *J. Biol. Chem.* 283, 20454–20472. doi: 10.1074/jbc.M710185200

Luo, L. (2000). Rho GTPases in neuronal morphogenesis. *Nat. Rev. Neurosci.* 1, 173–180. doi: 10.1038/35044547

Marèe, A. F., Grieneisen, V. A., and Edelstein-Keshet, L. (2012). How cells integrate complex stimuli: the effect of feedback from phosphoinositides and cell shape on cell polarization and motility. *PLoS Comput. Biol.* 8:e1002402. doi: 10.1371/journal.pcbi.1002402

Mori, Y., Jilkine, A., and Edelstein-Keshet, L. (2008). Wave-pinning and cell polarity from a bistable reaction-diffusion system. *Biophys. J.* 94, 3684–3697. doi: 10.1529/biophysj.107.120824

Mori, Y., Jilkine, A., and Edelstein-Keshet, L. (2011). Asymptotic and bifurcation analysis of wave-pinning in a reaction-diffusion model for cell polarization. *SIAM J. Appl. Math.* 71, 1401–1427. doi: 10.1137/10079118X

Murakoshi, H., Wang, H., and Yasuda, R. (2011). Local, persistent activation of Rho GTPases during plasticity of single dendritic spines. *Nature* 472, 100–104. doi: 10.1038/nature09823

Myers, J. P., Robles, E., Ducharme-Smith, A., and Gomez, T. M. (2012). Focal adhesion kinase modulates Cdc42 activity downstream of positive and negative axon guidance cues. *J. Cell Sci.* 125, 2918–2929. doi: 10.1242/jcs.100107

Nakamura, F., Kalb, R. G., and Strittmatter, S. M. (2000). Molecular basis of semaphorin-mediated axon guidance. *J. Neurobiol.* 44, 219–229. doi: 10.1002/1097-4695(200008)44:2<219::AID-NEU11>3.0.CO;2-W

Nalbant, P., Hodgson, L., Kraynov, V., Toutchkine, A., and Hahn, K. M. (2004). Activation of endogenous Cdc42 visualized in living cells. *Science* 305, 1615–1619. doi: 10.1126/science.1100367

Nobes, C. D., and Hall, A. (1995). Rho, rac and cdc42 GTPases: regulators of actin structures, cell adhesion and motility. *Biochem. Soc. Trans.* 23, 456–459. doi: 10.1042/bst0230456

Ohnami, S., Endo, M., Hirai, S., Uesaka, N., Hatanaka, Y., Yamashita, T., et al. (2008). Role of RhoA in activity-dependent cortical axon branching. *J. Neurosci.* 28, 9117–9121. doi: 10.1523/JNEUROSCI.1731-08.2008

Peng, J., Wallar, B. J., Flanders, A., Swiatek, P. J., and Alberts, A. S. (2003). Disruption of the Diaphanous-related formin Drf1 gene encoding mDia1 reveals a role for Drf3 as an effector for Cdc42. *Curr. Biol.* 13, 534–545. doi: 10.1016/S0960-9822(03)00170-2

Pertz, O. (2010). Spatio-temporal Rho GTPase signaling - where are we now? *J. Cell Sci.* 123, 1841–1850. doi: 10.1242/jcs.064345

Pinato, G., Cojoc, D., Lien, L. T., Ansuini, A., Ban, J., D'Este, E., et al. (2012). Less than 5 Netrin-1 molecules initiate attraction but 200 Sema3A molecules are necessary for repulsion. *Sci. Rep.* 2:675. doi: 10.1038/srep00675

Pinato, G., Raffaelli, T., D'Este, E., Tavano, F., and Cojoc, D. (2011). Optical delivery of liposome encapsulated chemical stimuli to neuronal cells. *J. Biomed. Opt.* 16, 095001. doi: 10.1117/1.3616133

Raftopoulou, M., and Hall, A. (2004). Cell migration: Rho GTPases lead the way. *Dev. Biol.* 265, 23–32. doi: 10.1016/j.ydbio.2003.06.003

Rauch, P., Heine, P., Goettgens, B., and Käs, J. A. (2013). Different modes of growth cone collapse in NG 108-15 cells. *Eur. Biophys. J.* 42, 591–605. doi: 10.1007/s00249-013-0907-z

Ridley, A. J., and Hall, A. (1992). The small GTP-binding protein rho regulates the assembly of focal adhesions and actin stress fibers in response to growth factors. *Cell* 70, 389–399. doi: 10.1016/0092-8674(92)90163-7

Sarner, S., Kozma, R., Ahmed, S., and Lim, L. (1997). Phosphatidylinositol 3-Kinase, Cdc42, and Rac1 act downstream of ras in integrin-dependent neurite outgrowth in N1E-115 neuroblastoma cells. *Mol. Cell. Biol.* 20, 158–172. doi: 10.1128/MCB.20.1.158-172.2000

Sit, S. T., and Manser, E. (2011). Rho GTPases and their role in organizing the actin cytoskeleton. *J. Cell Sci.* 124, 679–683. doi: 10.1242/jcs.064964

Smalheiser, N. R. (1991a). Cell attachment and neurite stability in NG108-15 cells: what is the role of microtubules? *Brain Res. Dev. Brain Res.* 58, 271–282. doi: 10.1016/0165-3806(91)90015-B

Smalheiser, N. R. (1991b). Role of laminin in stimulating rapid-onset neurites in NG108-15 cells: relative contribution of attachment and motility responses. *Brain Res. Dev. Brain Res.* 62, 81–89. doi: 10.1016/0165-3806(91)90192-L

Takahashi, T., Nakamura, F., and Strittmatter, S. M. (1997). Neuronal and non-neuronal collapsin-1 binding sites in developing chick are distinct from other semaphorin binding sites. *J. Neurosci.* 17, 9183–9193.

Takeuchi, S., Katoh, H., and Negishi, M. (2015). Eph/ephrin reverse signalling induces axonal retraction through RhoA/ROCK pathway. *J. Biochem.* pii: mvv042. doi: 10.1093/jb/mvv042

Tep, C., Kim, M. L., Opincariu, L. I., Limpert, A. S., Chan, J. R., Appel, B., et al. (2012). Brain-derived neurotrophic factor (BDNF) induces polarized signaling of small GTPase (Rac1) protein at the onset of Schwann cell myelination through partitioning-defective 3 (Par3) protein. *J. Biol. Chem.* 287, 1600–1608. doi: 10.1074/jbc.M111.312736

Thies, E., and Davenport, R. W. (2003). Independent roles of Rho-GTPases in growth cone and axonal behavior. *J. Neurobiol.* 54, 358–369. doi: 10.1002/neu.10135

Tran, T. S., Kolodkin, A. L., and Bharadwaj, R. (2007). Semaphorin regulation of cellular morphology. *Annu. Rev. Cell Dev. Biol.* 23, 263–292. doi: 10.1146/annurev.cellbio.22.010605.093554

Tsuji, T., Higashida, C., Yoshida, Y., Islam, M. S., Dohmoto, M., Koizumi, K., et al. (2011). Ect2, an ortholog of Drosophila's pebble, negatively regulates neurite outgrowth in neuroblastoma x glioma hybrid NG108-15 cells. *Cell. Mol. Neurobiol.* 31, 663–668. doi: 10.1007/s10571-011-9668-3

Wahl, S., Barth, H., Ciossek, T., Aktories, K., and Mueller, B. K. (2000). Ephrin-A5 induces collapse of growth cones by activating Rho and Rho kinase. *J. Cell Biol.* 149, 263–270. doi: 10.1083/jcb.149.2.263

Wong, J. T., Wong, S. T., and O'Connor, T. P. (1999). Ectopic semaphorin-1a functions as an attractive guidance cue for developing peripheral neurons. *Nat. Neurosci.* 2, 798–803. doi: 10.1038/12168

Worzfeld, T., and Offermanns, S. (2014). Semaphorins and plexins as therapeutic targets. *Nat. Rev. Drug Discov.* 13, 603–621. doi: 10.1038/nrd4337

Wu, K. Y., Hengst, U., Cox, L. J., Macosko, E. Z., Jeromin, A., Urquhart, E. R., et al. (2005). Local translation of RhoA regulates growth cone collapse. *Nature* 436, 1020–1024. doi: 10.1038/nature03885

Wu, M., Wu, X., and De Camilli, P. (2013). Calcium oscillations-coupled conversion of actin travelling waves to standing oscillations. *Proc. Natl. Acad. Sci. U.S.A.* 110, 1339–1344. doi: 10.1073/pnas.1221538110

Yazdani, U., and Terman, J. R. (2006). The semaphorins. *Genome Biol.* 7:211. doi: 10.1186/gb-2006-7-3-211

Yuan, X. B., Jin, M., Xu, X., Song, Y. Q., Wu, C. P., Poo, M. M., et al. (2003). Signalling and crosstalk of Rho GTPases in mediating axon guidance. *Nat. Cell Biol.* 5, 38–45. doi: 10.1038/ncb895

Zhou, Y., Gunput, R. A., and Pasterkamp, R. J. (2008). Semaphorin signaling: progress made and promises ahead. *Trends Biochem. Sci.* 33, 161–170. doi: 10.1016/j.tibs.2008.01.006

Conflict of Interest Statement: The authors declare that the research was conducted in the absence of any commercial or financial relationships that could be construed as a potential conflict of interest.

frontiers
in Cellular Neuroscience

REVIEW
published: 30 September 2015
doi: 10.3389/fncel.2015.00381

Regulation of cytoskeletal dynamics by redox signaling and oxidative stress: implications for neuronal development and trafficking

*Carlos Wilson and Christian González-Billault**

Department of Biology, Faculty of Sciences, Universidad de Chile, Santiago, Chile

A proper balance between chemical reduction and oxidation (known as redox balance) is essential for normal cellular physiology. Deregulation in the production of oxidative species leads to DNA damage, lipid peroxidation and aberrant post-translational modification of proteins, which in most cases induces injury, cell death and disease. However, physiological concentrations of oxidative species are necessary to support important cell functions, such as chemotaxis, hormone synthesis, immune response, cytoskeletal remodeling, Ca^{2+} homeostasis and others. Recent evidence suggests that redox balance regulates actin and microtubule dynamics in both physiological and pathological contexts. Microtubules and actin microfilaments contain certain amino acid residues that are susceptible to oxidation, which reduces the ability of microtubules to polymerize and causes severing of actin microfilaments in neuronal and non-neuronal cells. In contrast, inhibited production of reactive oxygen species (ROS; e.g., due to NOXs) leads to aberrant actin polymerization, decreases neurite outgrowth and affects the normal development and polarization of neurons. In this review, we summarize emerging evidence suggesting that both general and specific enzymatic sources of redox species exert diverse effects on cytoskeletal dynamics. Considering the intimate relationship between cytoskeletal dynamics and trafficking, we also discuss the potential effects of redox balance on intracellular transport via regulation of the components of the microtubule and actin cytoskeleton as well as cytoskeleton-associated proteins, which may directly impact localization of proteins and vesicles across the soma, dendrites and axon of neurons.

Keywords: redox, cytoskeleton, neurons, development, trafficking

Edited by:
Daniel Marcel Suter,
Purdue University, USA

Reviewed by:
Laura Anne Lowery,
Boston College, USA
Mary Halloran,
University of Wisconsin, USA
Stephanie L. Gupton,
University of North Carolina
at Chapel Hill, USA

****Correspondence:***
Christian González-Billault,
Department of Biology, Faculty
of Sciences, Universidad de Chile,
Las Palmeras 3425,
7800024 Santiago, Chile
chrgonza@uchile.cl

Received: *26 June 2015*
Accepted: *11 September 2015*
Published: *30 September 2015*

Citation:
Wilson C and González-Billault C (2015) Regulation of cytoskeletal dynamics by redox signaling and oxidative stress: implications for neuronal development and trafficking. Front. Cell. Neurosci. 9:381. doi: 10.3389/fncel.2015.00381

The Nervous System as a Target for Oxidative Species

The chemical reduction-oxidation (redox) balance commands physiological and pathological responses at different levels ranging from cells to tissues to biological systems. Among organs, the brain is especially vulnerable to oxidation for three main reasons. First, the brain consumes high levels of O_2—up to 20% of the amount used by the entire body (Sparaco et al., 2006). Given that the brain represents only 2% of the total body mass, metabolites derived from O_2 in the brain are highly concentrated in a restricted space, increasing the risk of oxidation. Second, Fe^{2+} is abundant in many specific areas of the brain (Gerlach et al., 1994), contributing to non-reversible oxidation. Fe^{2+}, the redox-active form of iron, catalyzes the conversion of hydrogen peroxide (H_2O_2) into the hydroxyl radical ($HO\oplus$) through the Fenton reaction. The hydroxyl radical represents the most chemically reactive of all reactive oxygen species (ROS; Núñez et al., 2012). Finally, the brain lacks effective mechanisms to remove accumulated pro-oxidative molecules (Halliwell, 1992). Together, these factors necessitate that the brain must utilize effective biochemical measures to counter oxidative stress.

Increased oxidation of molecules in both central and peripheral neurons is often associated with aging, oxidative stress and disease (Andersen, 2004). The term oxidative stress was coined to reflect an imbalance between oxidative and reductive molecules that leads to increased accumulation of pro-oxidant species, with deleterious consequences in most cases (Sies, 1997). This is the case for several neuronal pathologies, including Parkinson's disease, Alzheimer's disease, Huntington's disease and amyotrophic lateral sclerosis (Andersen, 2004). Most sporadic versions of these pathologies are linked to aging and have a documented positive correlation between oxidative stress and development of pathology.

Although oxidation of intracellular components owing to increased oxidative stress is a natural consequence of long-term exposure to pro-oxidant conditions, it is important to remember that physiological synthesis of oxidative species is required for normal cellular function (Rhee, 2006; Dáux and Toledano, 2007). The innate immune response depends on proper synthesis of ROS produced by NADPH oxidases (NOXs). Particularly, phagocytosis, chemotaxis and cellular locomotion of immune cells require basal ROS synthesis (Lambeth, 2004). Other processes requiring physiological concentrations of ROS include thyroid hormone synthesis, Ca^{2+} homeostasis, ion channel dynamics and cytoskeletal remodeling (Bedard and Krause, 2007; Hidalgo and Nunez, 2007; Espinosa et al., 2009; Sakai et al., 2012; Contreras-Ferrat et al., 2014).

In the central nervous system (CNS), enzymatic production of physiological levels of ROS contributes to synaptic plasticity and memory consolidation (Knapp and Klann, 2002; Massaad and Klann, 2011). Genetic models in which $gp91^{phox}$ and $p47^{phox}$ proteins are inactivated (the catalytic and one of the regulatory subunits of the NOX complex, respectively) exhibit abnormal long-term potentiation responses after electrical stimulation, which is an *ex vivo* paradigm to evaluate synaptic plasticity in hippocampal neurons (Kishida et al., 2006). $gp91^{phox}$ and $p47^{phox}$ knockout mice also have decreased consolidation of spatial memory, suggesting a neuronal disorder owing to impaired NOX activity and ROS signaling (Kishida et al., 2006). Humans with chronic granulomatous disease (CGD), an inherited syndrome caused by point mutations in the NOXs proteins $gp91^{phox}$, $p47^{phox}$, $p67^{phox}$ and $p22^{phox}$, affecting the immune response to pathogens, develop cognitive impairments and reduced intellectual coefficients compared with healthy control individuals (Pao et al., 2004). CGD develops during childhood and often requires repeated long-term hospitalization throughout life. It has been proposed that the intellectual deficits in CGD children could be linked to irregular school attendance and that this could even be the main cause for their low intellectual coefficients. However, other infectious diseases with similar periods of hospitalization do not result in cognitive deficits, suggesting that CGD patients develop specific neuronal alterations mainly attributable to reduced NOX activity and decreased ROS synthesis (Pao et al., 2004).

Taken together, these observations suggest that basal physiological ROS synthesis is required for normal cellular function, including the regulation of neurotransmission, but that high and unregulated ROS concentrations lead to oxidative stress and disease.

General Overview of Redox Balance

Intracellular Sources of ROS

The main oxidative species derived from O_2 are H_2O_2, $HO\oplus$ and the superoxide anion ($O_2\oplus^-$) and are collectively called ROS (Bedard and Krause, 2007). Nitrogen (N_2), the principal gas in the atmosphere we breathe, also induces intracellular oxidation via the production of physiologically reactive nitrogen species (Weidinger and Kozlov, 2015).

The main sources of intracellular ROS are mitochondria and NOXs. In mitochondria, complexes I and III of the electron transfer chain produce the short-lived $O_2\oplus^-$, a radical derived from O_2 (Murphy, 2009; Bigarella et al., 2014). No intracellular signaling pathway that regulates mitochondrial superoxide synthesis has yet been described, suggesting that mitochondria could be a source of constitutive ROS production. Synthesis and release of ROS from mitochondria depend on the tissue and its intrinsic metabolism. Mitochondrial dysfunction quickly leads to oxidative stress that targets DNA, membrane lipids and proteins, directly affecting cell physiology (Tahara et al., 2009).

NOXs represent the other major cellular source of ROS (Bedard and Krause, 2007). The NOX family includes seven members that catalyze the production of $O_2\oplus^-$ in an NADPH-dependent reaction. The family is composed of five canonical NOXs (NOX1 to NOX5) and two dual oxidases (Duox1 and Duox2; Lambeth et al., 2007). NOXs represent the main enzymatic source of ROS, and several signal transduction pathways are involved in their regulation (Dang et al., 2001; Park et al., 2001; Chen et al., 2003; Hoyal et al., 2003). NOX1, NOX2 and NOX4 are expressed in the CNS (Sorce and Krause, 2009), with NOX2 being the principal enzyme expressed in neurons. NOX2 can produce superoxide by itself but requires interaction with regulatory proteins for stabilization and to increase ROS levels under physiological circumstances. Together with its partners $p22^{phox}$, $p47^{phox}$, $p67^{phox}$ and $p40^{phox}$, NOX2 synthesizes superoxide to meet the physiological requirements of neurons (Bokoch and Diebold, 2002; Glogauer et al., 2003; Nauseef, 2004; Decoursey and Ligeti, 2005).

ROS as Signaling Molecules

Superoxide reactivity is fairly low, mainly owing to its short life-time and restricted diffusion area (Weidinger and Kozlov, 2015). However, superoxide can be converted to H_2O_2 either spontaneously or enzymatically via superoxide dismutase

(Núñez et al., 2012). H_2O_2, the most stable ROS, is converted to H_2O by several antioxidant enzymes, e.g., glutathione peroxidase and catalase, and this is likely the reason why oxidative modifications induced by H_2O_2 are transient and reversible (Weidinger and Kozlov, 2015). Thus, under normal conditions, the synthesis of superoxide and H_2O_2 are enzymatically regulated and their levels remain under a physiological threshold. In the presence of Fe^{2+}, however, H_2O_2 is rapidly converted to $HO\oplus$ through the Fenton reaction (Núñez et al., 2012). Hydroxyl radicals modify molecules in a non-reversible way, leading to permanent modifications of proteins and other targets. To consider ROS as signaling molecules, they should meet certain spatial and regulatory criteria, namely they should be produced locally and their levels regulated by intracellular molecular systems. According to these criteria, superoxide and H_2O_2, but not $HO\oplus$, are considered signaling molecules (Dáux and Toledano, 2007; Janssen-Heininger et al., 2008; Gerich et al., 2009).

Regulation of Protein Function by Oxidation via Post-Translational Modification

Cysteine thiol groups (SH) of proteins are the main targets for oxidation (Stadtman and Berlett, 1997). In general terms, oxidation of SH groups leads to glutathionylation, nitrosylation and disulfide bond formation. These modifications are enzymatically reversed through the glutaredoxin (Grx), thioredoxin and peroxiredoxin systems, among others (Ghezzi, 2005; Shelton et al., 2005; Janssen-Heininger et al., 2008). Oxidation also leads to sulfenic acid formation and protein carbonylation, two non-reversible modifications that permanently affect protein structure and function (Bigarella et al., 2014).

The functions of several proteins, including cytoskeletal proteins, depend on ROS signaling and oxidation (Sparaco et al., 2006). Several studies have shown that redox balance affects both *in vitro* and *in vivo* cytoskeletal dynamics, which directly impacts cell morphology and morphometrics. In neurons, cytoskeletal rearrangement commands cell development, polarization and neurotransmission (Jaworski et al., 2009; Hoogenraad and Akhmanova, 2010; Stiess and Bradke, 2011; Caceres et al., 2012; Gonzalez-Billault et al., 2012). Neurons are highly polarized cells, having a cell body from which emerge several dendrites and an axon to establish functional communication networks with other neurons and glial cells (Caceres et al., 2012). Acquisition of this morphology depends directly on the dynamics of actin microfilaments and microtubules (Neukirchen and Bradke, 2011). Given the influence of the redox state on neuronal function and its potential role in modifying the cytoskeleton, it is interesting to review the contribution of the redox balance to cytoskeletal organization in neurons.

Contribution of Redox Balance to Organization of the Neuronal Cytoskeleton

Redox State of Neuronal Cytoskeleton Proteins

The main components of the neuronal cytoskeleton network, namely actin microfilaments, microtubules and neurofilaments, are susceptible to oxidation (Sparaco et al., 2006). Post-mortem histological studies from non-pathological human samples have revealed a basal pool of glutathionylated proteins in the prefrontal cortex, cerebellum and spinal cord. Cellular analysis of the prefrontal cortex revealed that neurons are more highly glutathionylated than oligodendrocytes and astrocytes. Biochemical analysis revealed that actin, tubulin and neurofilaments are glutathionylated, suggesting that the redox state of neurons and cytoskeletal proteins under basal conditions is slanted toward oxidation (Sparaco et al., 2006). The relevance of cytoskeleton oxidation depends on the spatiotemporal context in which a defined modification occurs as well as the source of the ROS. Whereas physiological ROS production is needed for proper cytoskeleton polymerization, oxidation tends to disrupt polymerization and impair cytoskeletal dynamics under oxidative stress conditions (Munnamalai and Suter, 2009; Hung et al., 2010; Morinaka et al., 2011; Wilson et al., 2015).

Actin Modification and Regulation of F-Actin Dynamics by Oxidative Species

Intracellular ROS production is needed for proper cell migration and chemotaxis, which are actin-dependent processes (Roberts et al., 1999; Ambruso et al., 2000; Kim and Dinauer, 2001). Actin monomers contain 5 Cys and 16 Met residues (Dalle-Donne et al., 2002, 2003). Of these, only Cys 374 is fully exposed to the cytoplasm (Dalle-Donne et al., 2003). By contrast, Met 44, 47 and 355 are prominently exposed to the cytoplasm and Met 176, 190, 227 and 260 are also susceptible to the action of oxidative molecules (Dalle-Donne et al., 2002). *In vitro* assays suggested that an oxidative environment inhibits actin polymerization (Dalle-Donne et al., 2003). In addition, both Cys and Met residues can be carbonylated after *in vitro* treatment with hypochlorous acid (HOCl), a common derivative product released by leukocytes during the initial phase of the immune response. This polymerization assay was designed to recapitulate *in vitro* the exact oxidative environment of the immune cell response; importantly, this environment inhibits actin polymerization (Dalle-Donne et al., 2001). This analysis also revealed that specific glutathionylation at Cys 374 decreases actin polymerization (Dalle-Donne et al., 2003). In neutrophils, glutaredoxin 1 (Grx1), a deglutathionylating enzyme that reduces oxidized Cys residues, is needed to maintain actin dynamics (Sakai et al., 2012). ROS depletion using the NOX inhibitor diphenyleneiodonium or Grx1 overexpression decreases actin glutathionylation, increases the amount of filamentous actin (F-actin) and impairs proper cellular migration. In contrast, loss of Grx1 function via knockdown and knockout strategies increases the amount of glutathionylated actin and decreases the level of F-actin. Sakai et al. (2012) proposed that physiological levels of ROS and redox balance regulate actin dynamics, which are required for chemotaxis and migration of immune cells. On the other hand, physiological ROS levels induce local membrane protrusions in marsupial kidney epithelium Ptk1 cells in a mechanism that involves cofilin, the actin-related protein 2/3 complex (Arp2/3) and the extracellular signal–regulated kinase (ERK), thereby enhancing the retrograde flow of actin at the leading edge of these migrating cells (Taulet et al., 2012).

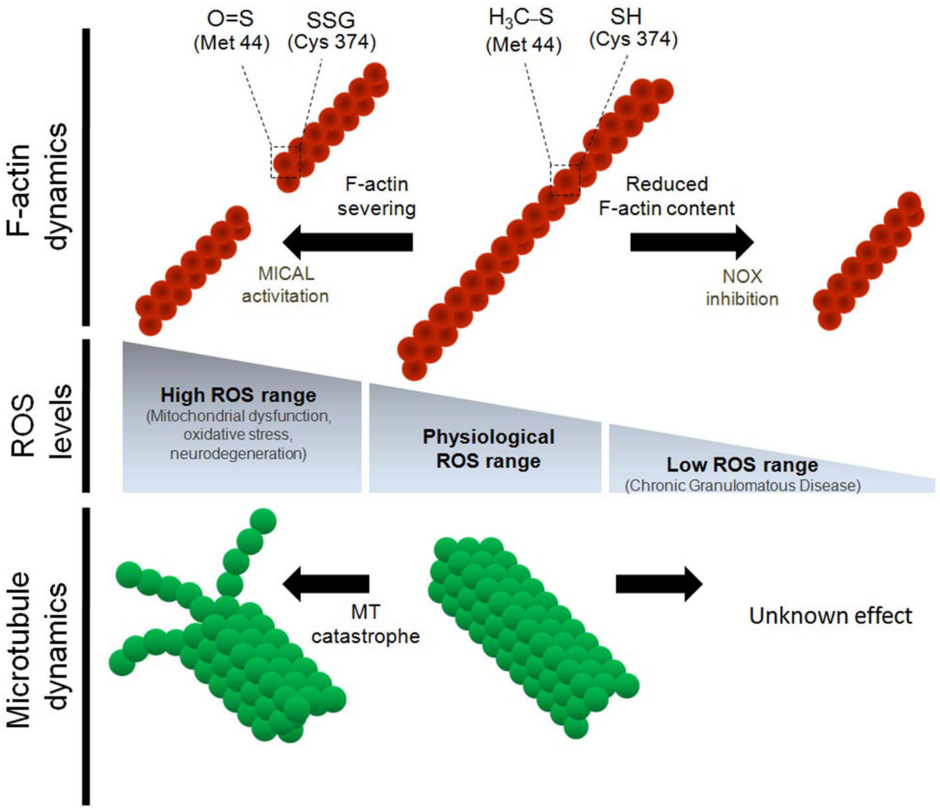

FIGURE 1 | Regulation of the cytoskeleton dynamics by differential reactive oxygen species (ROS) levels. Physiological concentrations of ROS are needed for proper F-actin and microtubule dynamics both *in vitro* and *in vivo*. Oxidative stress induces the severing of F-actin and impairs microtubule polymerization. In the particular case of actin monomers, both Cys 374 and Met 42 residues are targets for oxidative molecules during oxidative stress conditions. Oxidation of Cys 374 leads to actin glutathionylation. On the other hand, oxidation of Met 44, which occurs specifically by MICAL1, leads to Met oxidation and severing of the actin filaments (Hung et al., 2011). Despite both α and β tubulin have several Cys residues that are susceptible to oxidation, it has not been described which Cys residues of tubulin monomers are modified by oxidation. In contrast, down-regulation of ROS synthesis, mainly through NOX inhibition, decreases the F-actin content and alters the dynamic properties of the actin cytoskeleton. None of the post-translational modification of actin monomers have been described after NOX inhibition and ROS down-regulation. Finally, the effect of the inhibition of ROS synthesis (below physiological levels) on microtubule dynamics has not been explored.

Figure 1 summarizes the effect of the oxidative power on actin polymerization and F-actin dynamics.

ROS also target the actin cytoskeleton in neuronal cells. The Semaphorin/Plexin signaling pathway represents a major repulsive cue for axonal guidance (Hung and Terman, 2011). Semaphorin 3A (Sema3A) signaling induces a local increase in H_2O_2 at the growth cones of dorsal root ganglion neurons by activating MICAL1 and MICAL3 (Morinaka et al., 2011). MICAL1 is a binding partner for the cytosolic domain of Plexin A, a Sema3A receptor (Terman et al., 2002). The principal target of MICAL1 is actin (Hung et al., 2010, 2011; Giridharan and Caplan, 2014). In bristle cells of Drosophila melanogaster, oxidation of actin at Met 44 by MICAL1 severs actin filaments (Hung et al., 2011). MICAL1-dependent actin oxidation is reversed by Selenoprotein R (SelR) activation, restoring F-actin dynamics and polymerization (Hung et al., 2013). After neuronal injury, Sema3A levels rise above normal levels to inhibit the ability of axons to regenerate and regrow. These findings represent a redox mechanism by which Sema3A induces the collapse of axonal growth cones and impedes axon guidance, supporting the hypothesis that redox imbalance—particularly oxidative stress—leads to neuronal damage. Therefore, MICAL1 contributes to axonal pathfinding by regulating ROS signaling at dorsal root ganglion growth cones. In addition to directly regulating the actin redox balance, MICAL1 may modify actin dynamics by promoting interaction between proteins. MICAL1 interacts with Cas and CasL proteins, which may be involved in cross-talk between actin and intermediate filaments (Suzuki et al., 2002). Moreover, MICAL1 negatively regulates the nuclear dbf2-related kinase NDR2 in non-neuronal cells (Zhou et al., 2011). NDR1 and NDR2 contribute to targeting the Par3/Par6/aPKC complex to growing axons, a mechanism that promotes neuronal polarity (Yang et al., 2014). Together, these findings suggest that MICAL1 both directly and indirectly regulates the neuronal actin cytoskeleton, contributing to neuronal function and development under both normal and stress conditions.

In the marine mollusk Aplysia, NOX-derived ROS are required to maintain proper F-actin dynamics in the growth cones of bag cells (Munnamalai and Suter, 2009; Munnamalai et al., 2014). Inhibition of NOX activity using pharmacological inhibitors like apocynin, diphenyleneiodonium and VAS2870 reduce F-actin content in these growth cones and reduce both retrograde actin flow and neurite outgrowth, supporting the idea that actin dynamics and neurite elongation require basal NOX activity (Munnamalai and Suter, 2009). Cultured embryonic hippocampal neurons that express the mutant P156Q $p22^{phox}$, which down-regulates ROS synthesis by the NOX complex, show a decrease in the number, length and lifetime of filopodia at axonal growth cones (Wilson et al., 2015). Moreover, lamellar actin organization of stage 1 neurons, the initial morphology from which neurons develop, is disrupted after loss of NOX function (Wilson et al., 2015). Together, this evidence supports the hypothesis that local ROS signaling is needed to maintain normal F-actin dynamics in neurons and is consistent with other reports proposing that ROS are needed to support membrane protrusions, lamellar structures and filopodia at the leading edge of migrating cells (Taulet et al., 2012). Interestingly, NOX2 and $p40^{phox}$co-distribute with F-actin at the growth cone of neuronal bag cells in Aplysia, suggesting that local ROS production may be involved in neurite outgrowth (Munnamalai et al., 2014). NOXs are expressed in axons and dendrites of embryonic and adult neurons, suggesting that local ROS synthesis that may be involved in filopodial dynamics and neurite growth (Tejada-Simon et al., 2005; Wilson et al., 2015). **Figure 2** summarizes the differential effect of ROS on the organization of the growth cones of axons.

Tubulin Modification and Regulation of Microtubule Dynamics by Oxidative Species

α-Tubulin and β-tubulin contain 12 and 8 Cys residues, respectively, and each of these residues can be oxidized by endogenous and exogenous oxidizing agents (Luduena and Roach, 1991; Löwe et al., 2001; Landino et al., 2002, 2004a). The functions of these Cys residues are linked to GTP binding, microtubule polymerization and drug response (Mellon and Rebhun, 1976; Luduena et al., 1985; Luduena and Roach, 1991). In *in vitro* polymerization assays using purified tubulin from adult bovine brain, oxidative species added to the reaction medium dramatically reduced tubulin polymerization. Peroxynitrite ($ONOO^-$), a ROS produced from the reaction between superoxide and nitric oxide (NO⊕), progressively oxidizes the thiol groups of tubulin monomers, thereby decreasing the ability of microtubules to polymerize *in vitro* (Landino et al., 2007). The same results were obtained with NO⊕ and nitroxyl donors. Moreover, $ONOO^-$ promotes disulfide bond formation between α- and β-tubulin (Landino et al., 2004a). In addition, *in vitro* assays revealed that tubulin is glutathionylated after treatment with $ONOO^-$, and that this modification is reversed by the glutathione/glutathione reductase system, composed of glutathione, glutathione reductase, Grx and NADPH (Landino et al., 2004a). The reversal of tubulin glutathionylation by this system is interesting because intracellular signaling pathways may modulate microtubule polymerization in a reversible manner. **Figure 1** summarizes the effect of high oxidative power on microtubule dynamics. However, the inhibition of ROS synthesis below a physiological range has not been explored in terms of tubulin modifications nor microtubule dynamics.

Another layer of regulation is provided by proteins that stabilize or destabilize microtubules. Microtubule-associated protein 2 (MAP2) and tau are MAPS that specifically regulate MT polymerization in dendrites and axon. MAP2 and tau contain one and seven Cys residues, respectively (Lewis et al., 1988). Oxidation of MAP2 and tau Cys residues decreases microtubule polymerization *in vitro*, suggesting that redox balance regulates tubulin not only through direct interaction but also by regulating their stabilization by MAPs (Landino et al., 2004b). It is plausible that oxidized/reduced MAPs present differential microtubule stabilization. Moreover, binding of MAPs to microtubules may promote differential regulation of molecular motors in axons and dendrites (Dixit et al., 2008), affecting trafficking and cargo destination. Therefore, redox-dependent MAP modifications may be an additional mechanism for regulating cytoskeletal dynamics in neurons. Indeed, increased nitrosylation of MAP1B at Cys 2457 is involved in neurite retraction through a mechanism that couples microtubule stability and dynein function (Stroissnigg et al., 2007; Villarroel-Campos and Gonzalez-Billault, 2014).

Microtubule function depends on its intrinsic polymerization properties (Mitchison and Kirschner, 1984, 1988) as well as the specific tubulin isotype (Kavallaris, 2010) and post-translational modifications (Janke, 2014). Microtubule proteins can be modified by redox state, but understanding the functional consequences of such modifications can be challenging. For example, tubulin modifications induced by $ONOO^-$ treatment *in vitro* can be difficult to interpret because $ONOO^-$is unstable at physiological pH, and thus *in vitro* microtubule polymerization assays are performed at basic pH (typically pH 10). In addition, tubulin is glutathionylated in both cell-specific and tissue-specific ways (Sparaco et al., 2006, 2009). Prefrontal cortex, cerebellum and spinal cord tissue samples from non-pathological humans exhibit tubulin glutathionylation under basal conditions. In addition, after treatment with oxidized glutathione, neurons are preferentially glutathionylated compared with astrocytes and oligodendrocytes (Sparaco et al., 2006). Thus, it seems that tubulin Cys residues can be modified by redox balance in both *in vitro* and *in vivo* contexts.

Neurite outgrowth is affected by tubulin oxidation in cellular models. In the motor neuron-derived neuroblastoma cell line NSC34, oxidation induced by oxidized glutathione promote the formation of retraction bulbs and thin axon-like processes (Carletti et al., 2011). Under these conditions, glutathionylated tubulin levels are increased and interestingly, tyrosination of α-tubulin is simultaneously decreased. These findings suggest that an oxidative cytoplasmic environment induces tubulin glutathionylation, leading to neurite retraction and degeneration.

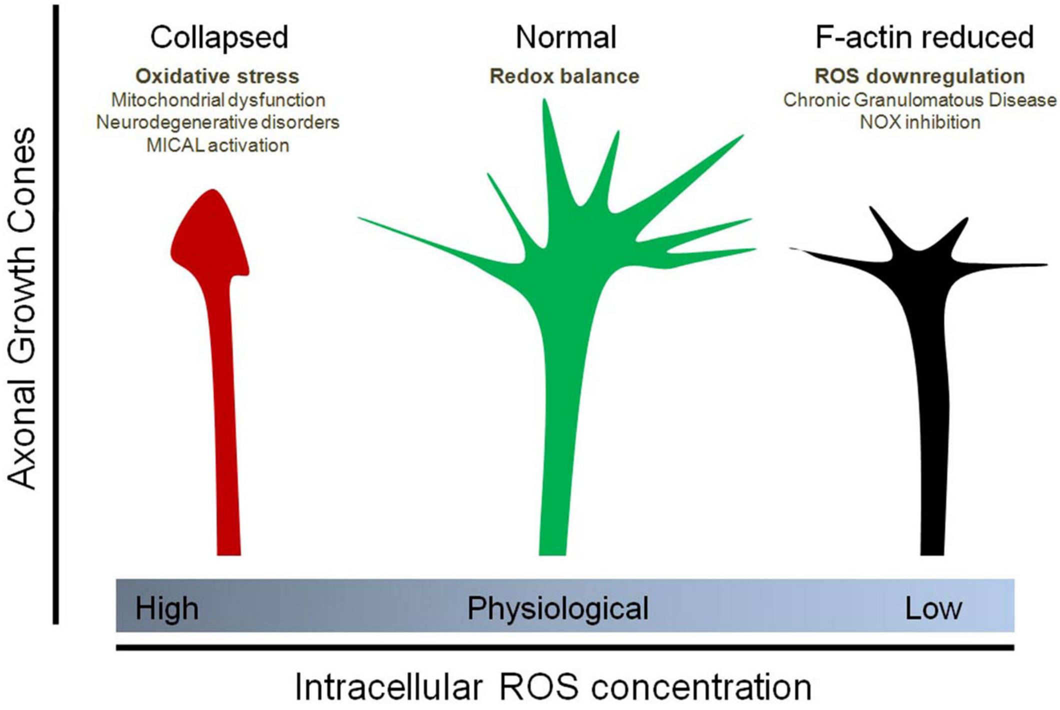

FIGURE 2 | Effect of physiological and non-physiological ROS on axonal growth cone organization. Oxidative stress (due to mitochondrial dysfunction, Sema3A/Plexin signaling and MICAL1 activation, neurodegenerative disorders, among others) induces the collapse of the axonal growth cones of neurons. In contrast, down-regulation of ROS synthesis, particularly due to NOX inhibition as well as Chronic Granulomatous Disease (CGD), decreases the F-actin content at the growth cone and affect filopodial dynamics by decreasing the number and length of filopodia at the axonal growth cone. Physiological concentrations of ROS, principally maintained by NOX enzymes and basal mitochondrial activity, are needed for a proper organization of the growth cones. In this context, the implicances for vesicular trafficking due to altered cytoskeleton dynamics has not been explored.

Moreover, in Friedrich's ataxia, a neuropathological condition characterized by degeneration of spinal cord pathways, immunohistochemical studies in motor neurons revealed co-distribution of tyrosinated tubulin and glutathionylated proteins (Sparaco et al., 2009). In the future, it will be necessary to establish whether there is a causal relationship between tubulin glutathionylation and changes in microtubule dynamics.

Studies in cultured primary neurons exploring phenotypes and mechanisms underlying the regulation of microtubule dynamics by redox state are still preliminary. However, there is some indirect evidence suggesting a putative link between microtubule polymerization and ROS balance. CRMP-2, a molecular regulator of microtubule polymerization, is oxidized at Cys 504, inducing homodimerization. These dimers can form a transient complex with thioredoxin, which creates a docking site for the protein kinase GSK3-β. GSK3-β-dependent CRMP-2 phosphorylation is linked to growth cone collapse in cultured dorsal root ganglion cells, recapitulating some molecular pathways involved in the initial steps of neurodegeneration (Morinaka et al., 2011). Therefore, new research may help establish a direct link between regulation of microtubule dynamics and redox balance in neuronal systems.

Participation of Oxidative Species in the Central Nervous System and Neuronal Development

Genetic models that reduce ROS production in the nervous system, such as gp91^{phox} and p47^{phox} knockout mice, are characterized by a macroscopically normal brain overall, including the cerebral cortex and hippocampus (Kishida et al., 2006). However, they display cognitive impairments as well as impaired synaptic plasticity, a phenomenon that involves, among other molecular events, cytoskeletal remodeling (Kishida et al., 2006). Therefore, a complete understanding of the contribution of ROS to normal nervous system physiology is important. Some insights have emerged in the last few years. For example, ROS levels have been shown to contribute to the commitment of neuronal progenitors to differentiate into mature neurons (Forsberg et al., 2013; Quadrato and Di Giovanni, 2013; Forsberg and Di Giovanni, 2014). Along the same line, loss of NOX function (using either neurons from NOX2 knockout mice or NOX2 knockdown in cultured neurons) has been shown to decrease the proliferation rate and number of neural stem cells *in vivo* and *in vitro*, suggesting that physiological ROS levels derived from NOX2 are needed to maintain a basal population of adult hippocampal neuronal progenitors (Dickinson et al., 2011). It was recently observed that inhibition of NOX functions alter normal neuronal polarization and reduces axonal growth (Wilson et al., 2015). Similarly, differentiation of cerebellar granule neurons involves glutathione homeostasis and NOX activity (Olguín-Albuerne and Morán, 2015). Of note, MICAL1 knockout mice exhibit abnormal mossy fiber lamination, aberrant F-actin content and decreased Rab6 trafficking to the growth cones of hippocampal neurons, suggesting a role in the development of mossy fiber axons and of specific sub-areas of the hippocampus and supporting the notion that redox balance is needed for development of brain tissues (Van Battum et al., 2014). Together, these lines of evidence support a new hypothesis in the field of ROS, that the physiological and controlled production of ROS is needed for signaling and development in neurons. In the future, it will be important to address *in vivo* functions for ROS from various sources and their involvement in neuronal differentiation, migration and axonal guidance.

A major challenge in this field is to understand the specificity that redox imbalance have on cytoskeleton proteins compared to DNA or lipids. This is especially important considering that modifications on these molecules could also affect neuronal functions and morphology. In fact, ROS contributes to the transcription of several genes associated with metabolism, cell cycle and development (Bigarella et al., 2014), supporting the notion that ROS have pleiotropic effects on sub-cellular components. Moreover, there are technical concerns about the quantification of ROS in cells. Both ROS and cytoskeleton proteins are dynamic cellular elements with short life-times. Thus, it is hard to establish a correlation between local synthesis of ROS and the oxidation of actin filaments and microtubules in a living cell. New genetic tools based on fluorescence microscopy have emerged in the last years to measure ROS levels (Mishin et al., 2015). Genetically encoded probes to measure ROS combined with cytoskeleton biosensors will be necessary to define the spatial and temporal association between ROS synthesis and cytoskeleton remodeling.

Emerging Concepts in the Contribution of Redox Balance to Vesicle Trafficking

Intracellular trafficking is highly dependent on actin microfilaments, microtubules and molecular motors such as myosin, kinesin and dynein. In addition, members of the Rab family of small GTPases are essential for targeting components to discrete domains within cells. Several Rab proteins derived from the trans-Golgi network, the early/late endosome and recycling endosomes regulate neurite outgrowth and development (Villarroel-Campos et al., 2014). In preceding sections, we discussed how changes in ROS content may target tubulin and actin dynamics to regulate the tracks for intracellular trafficking. However, the link between redox balance and the vesicle components involved in neuronal trafficking remains poorly understood.

Several studies correlate MICAL activity with trafficking. It has been recovered as an interacting partner for several members of the Rab family in yeast two-hybrid experiments (Fukuda et al., 2008). MICAL1 deletion leads to aberrant destination of the IgCAM cell adhesion molecules to the growth cones of cultured hippocampal neurons in a Rab6- and actin-dependent mechanism, establishing a link between redox state and vesicle trafficking in neurons (Van Battum et al., 2014). Interestingly, MICAL1 interacts with Rab1, which is involved in vesicle trafficking from the endoplasmic reticulum to the Golgi (Fischer et al., 2005). Additionally, MICAL3 interacts with Rab8, which in turns interacts with Rab6 to promote exocytosis of secretory vesicles (Van Battum et al., 2014). Moreover, expression of a mutant isoform of MICAL3 in HeLa cells induces accumulation of vesicles at the cell cortex by inhibiting vesicle docking with the plasma membrane, ultimately decreasing release of vesicle contents (Grigoriev et al., 2011). This suggests a link between Rab-dependent vesicle trafficking and ROS. Zinc deficiency has been shown to decrease tubulin polymerization via oxidation of tubulin thiol groups (Mackenzie et al., 2011). Interestingly, tubulin oxidation also impairs translocation of the transcription factor NFκB to the nucleus, suggesting a link between redox state and microtubule-dependent trafficking in a cellular model (Mackenzie et al., 2011).

In addition to ROS, NO also plays a role in terms of neuronal function and vesicle trafficking. A recent report suggest that NO reduces the expression of the molecular motors KIF5 and KIF21B and it decreases the length of the axons of cultured cortical neurons (Redondo et al., 2015). Authors hypothesize that NO exposure could affect KIF-dependent vesicle trafficking required for normal axonal growth. In fact, axonal retraction and NO release are key issues in some neurodegenerative disorders, like Parkinson's disease (More et al., 2013; Tripathy et al., 2015). However, authors did not explored vesicle movement after NO exposure and this issue does not allow to conclude a direct effect of NO on axonal trafficking through cytoskeleton regulation. Moreover, G-protein coupled receptors that respond to NO (NO/CG) contributes positively to the physiology of neurons and neurotransmission (Hardingham et al., 2013; Russwurm et al., 2013). In summary, oxidative molecules signaling is an emerging concept in the field of cytoskeleton regulation and further studies will be required to understand the contribution to the vesicle trafficking and its impact on the physiology of neurons.

Concluding Remarks and Future Perspectives

ROS influence many different cellular functions under both physiological and pathological conditions. The targets of ROS include DNA, lipids and proteins. Among these, cytoskeletal proteins can be modified *in vitro* and *in vivo* by redox molecules. An imbalance between oxidative and reductive species leads to oxidative stress, which affects the polymerization of both F-actin and microtubules. In contrast, down-regulation of ROS also affects normal cytoskeletal organization, impacting the morphology, development and physiology of cells and neurons. Neuronal development and specification of neuronal compartments depend on redox homeostasis, in a mechanism that involves regulation of the actin cytoskeleton by the NOX complex. Further exploration of the role of redox balance in regulating microtubule dynamics in cellular models is required. Abnormal polymerization of actin microfilaments and microtubules directly affects vesicle trafficking and specific cargo delivery throughout the soma, dendrites and axon. However, the regulation of vesicle trafficking and protein sorting by redox balance represents an unexplored field despite strong evidence in several cellular contexts that cytoskeletal proteins are targets of oxidative species. Moreover, the contribution of redox balance to the interaction between the cytoskeleton and cytoskeleton-associated proteins such as myosins, dyneins and kinesin molecular motors has not been studied, and such analysis may reveal direct effects on vesicle trafficking and cargo destination. New evidence has emerged concerning the dissection of the cellular sources of ROS that can modulate cytoskeletal dynamics. The development of new ratiometric microscopy tools to characterize the spatiotemporal production of ROS may give other important clues about how redox balance controls neuronal physiology.

Funding

This work was funded by CONICYT doctoral fellowship 21120221 to CW and by grants ACT-1114 and Fondecyt 1140325 to CG-B.

References

Ambruso, D. R., Knall, C., Abell, A. N., Panepinto, J., Kurkchubasche, A., Thurman, G., et al. (2000). Human neutrophil immunodeficiency syndrome is associated with an inhibitory Rac2 mutation. *Proc. Natl. Acad. Sci. U S A* 97, 4654–4659. doi: 10.1073/pnas.080074897

Andersen, J. K. (2004). Oxidative stress in neurodegeneration: cause or consequence?. *Nat. Med.* 10(Supplement), S18–S25. doi: 10.1038/nrn1434

Bedard, K., and Krause, K. H. (2007). The NOX family of ROS-generating NADPH oxidases: physiology and pathophysiology. *Physiol. Rev.* 87, 245–313. doi: 10.1152/physrev.00044.2005

Bigarella, C. L., Liang, R., and Ghaffari, S. (2014). Stem cells and the impact of ROS signaling. *Development* 141, 4206–4218. doi: 10.1242/dev.107086

Bokoch, G. M., and Diebold, B. A. (2002). Current molecular models for NADPH oxidase regulation by Rac GTPase. *Blood* 100, 2692–2696. doi: 10.1182/blood-2002-04-1149

Caceres, A., Ye, B., and Dotti, C. G. (2012). Neuronal polarity: demarcation, growth and commitment. *Curr. Opin. Cell Biol.* 24, 547–553. doi: 10.1016/j.ceb.2012.05.011

Carletti, B., Passarelli, C., Sparaco, M., Tozzi, G., Pastore, A., Bertini, E., et al. (2011). Effect of protein glutathionylation on neuronal cytoskeleton: a potential link to neurodegeneration. *Neuroscience* 192, 285–294. doi: 10.1016/j.neuroscience.2011.05.060

Chen, Q., Powell, D. W., Rane, M. J., Singh, S., Butt, W., Klein, J. B., et al. (2003). Akt phosphorylates p47phox and mediates respiratory burst activity in human neutrophils. *J. Immunol.* 170, 5302–5308. doi: 10.4049/jimmunol.170.10.5302

Contreras-Ferrat, A., Llanos, P., Vasquez, C., Espinosa, A., Osorio-Fuentealba, C., Arias-Calderon, M., et al. (2014). Insulin elicits a ROS-activated and an IP(3)-dependent Ca(2)(+) release, which both impinge on GLUT4 translocation. *J. Cell Sci.* 127, 1911–1923. doi: 10.1242/jcs.138982

Dalle-Donne, I., Giustarini, D., Rossi, R., Colombo, R., and Milzani, A. (2003). Reversible S-glutathionylation of Cys 374 regulates actin filament formation by inducing structural changes in the actin molecule. *Free Radic. Biol. Med.* 34, 23–32. doi: 10.1016/s0891-5849(02)01182-6

Dalle-Donne, I., Rossi, R., Giustarini, D., Gagliano, N., Di Simplicio, P., Colombo, R., et al. (2002). Methionine oxidation as a major cause of the functional impairment of oxidized actin. *Free Radic. Biol. Med.* 32, 927–937. doi: 10.1016/s0891-5849(02)00799-2

Dalle-Donne, I., Rossi, R., Giustarini, D., Gagliano, N., Lusini, L., Milzani, A., et al. (2001). Actin carbonylation: from a simple marker of protein oxidation to relevant signs of severe functional impairment. *Free Radic. Biol. Med.* 31, 1075–1083. doi: 10.1016/s0891-5849(01)00690-6

Dang, P. M., Fontayne, A., Hakim, J., El Benna, J., and Perianin, A. (2001). Protein kinase C zeta phosphorylates a subset of selective sites of the NADPH oxidase component p47phox and participates in formyl peptide-mediated neutrophil respiratory burst. *J. Immunol.* 166, 1206–1213. doi: 10.4049/jimmunol.166.2.1206

Dáux, B., and Toledano, M. B. (2007). ROS as signalling molecules: mechanisms that generate specificity in ROS homeostasis. *Nat. Rev. Mol. Cell Biol.* 8, 813–824. doi: 10.1038/nrm2256

Decoursey, T. E., and Ligeti, E. (2005). Regulation and termination of NADPH oxidase activity. *Cell. Mol. Life Sci.* 62, 2173–2193. doi: 10.1007/s00018-005-5177-1

Dickinson, B. C., Peltier, J., Stone, D., Schaffer, D. V., and Chang, C. J. (2011). Nox2 redox signaling maintains essential cell populations in the brain. *Nat. Chem. Biol.* 7, 106–112. doi: 10.1038/nchembio.497

Dixit, R., Ross, J. L., Goldman, Y. E., and Holzbaur, E. L. (2008). Differential regulation of dynein and kinesin motor proteins by tau. *Science* 319, 1086–1089. doi: 10.1126/science.1152993

Espinosa, A., Garcia, A., Hartel, S., Hidalgo, C., and Jaimovich, E. (2009). NADPH oxidase and hydrogen peroxide mediate insulin-induced calcium increase in skeletal muscle cells. *J. Biol. Chem.* 284, 2568–2575. doi: 10.1074/jbc.m804249200

Fischer, J., Weide, T., and Barnekow, A. (2005). The MICAL proteins and rab1: a possible link to the cytoskeleton?. *Biochem. Biophys. Res. Commun.* 328, 415–423. doi: 10.1016/j.bbrc.2004.12.182

Forsberg, K., and Di Giovanni, S. (2014). Cross talk between cellular redox status, metabolism and p53 in neural stem cell biology. *Neuroscientist* 20, 326–342. doi: 10.1177/1073858413514634

Forsberg, K., Wuttke, A., Quadrato, G., Chumakov, P. M., Wizenmann, A., and Di Giovanni, S. (2013). The tumor suppressor p53 fine-tunes reactive oxygen species levels and neurogenesis via PI3 kinase signaling. *J. Neurosci.* 33, 14318–14330. doi: 10.1523/jneurosci.1056-13.2013

Fukuda, M., Kanno, E., Ishibashi, K., and Itoh, T. (2008). Large scale screening for novel rab effectors reveals unexpected broad Rab binding specificity. *Mol. Cell. Proteomics* 7, 1031–1042. doi: 10.1074/mcp.m700569-mcp200

Gerich, F. J., Funke, F., Hildebrandt, B., Fasshauer, M., and Muller, M. (2009). H(2)O(2)-mediated modulation of cytosolic signaling and organelle function in rat hippocampus. *Pflugers Arch.* 458, 937–952. doi: 10.1007/s00424-009-0672-0

Gerlach, M., Ben-Shachar, D., Riederer, P., and Youdim, M. B. (1994). Altered brain metabolism of iron as a cause of neurodegenerative diseases? *J. Neurochem.* 63, 793–807. doi: 10.1046/j.1471-4159.1994.63030793.x

Ghezzi, P. (2005). Regulation of protein function by glutathionylation. *Free Radic. Res.* 39, 573–580. doi: 10.1080/10715760500072172

Giridharan, S. S., and Caplan, S. (2014). MICAL-family proteins: complex regulators of the actin cytoskeleton. *Antioxid. Redox Signal.* 20, 2059–2073. doi: 10.1089/ars.2013.5487

Glogauer, M., Marchal, C. C., Zhu, F., Worku, A., Clausen, B. E., Foerster, I., et al. (2003). Rac1 deletion in mouse neutrophils has selective effects on neutrophil functions. *J. Immunol.* 170, 5652–5657. doi: 10.4049/jimmunol.170.11.5652

Gonzalez-Billault, C., Munoz-Llancao, P., Henriquez, D. R., Wojnacki, J., Conde, C., and Caceres, A. (2012). The role of small GTPases in neuronal morphogenesis and polarity. *Cytoskeleton (Hoboken)* 69, 464–485. doi: 10.1002/cm.21034

Grigoriev, I., Yu, K. L., Martinez-Sanchez, E., Serra-Marques, A., Smal, I., Meijering, E., et al. (2011). Rab6, Rab8 and MICAL3 cooperate in controlling docking and fusion of exocytotic carriers. *Curr. Biol.* 21, 967–974. doi: 10.1016/j.cub.2011.04.030

Halliwell, B. (1992). Reactive oxygen species and the central nervous system. *J. Neurochem.* 59, 1609–1623. doi: 10.1111/j.1471-4159.1992.tb10990.x

Hardingham, N., Dachtler, J., and Fox, K. (2013). The role of nitric oxide in pre-synaptic plasticity and homeostasis. *Front. Cell. Neurosci.* 7:190. doi: 10.3389/fncel.2013.00190

Hidalgo, C., and Nunez, M. T. (2007). Calcium, iron and neuronal function. *IUBMB Life* 59, 280–285. doi: 10.1080/15216540701222906

Hoogenraad, C. C., and Akhmanova, A. (2010). Dendritic spine plasticity: new regulatory roles of dynamic microtubules. *Neuroscientist* 16, 650–661. doi: 10.1177/1073858410386357

Hoyal, C. R., Gutierrez, A., Young, B. M., Catz, S. D., Lin, J. H., Tsichlis, P. N., et al. (2003). Modulation of p47PHOX activity by site-specific phosphorylation: Akt-dependent activation of the NADPH oxidase. *Proc. Natl. Acad. Sci. U S A* 100, 5130–5135. doi: 10.1073/pnas.1031526100

Hung, R. J., Pak, C. W., and Terman, J. R. (2011). Direct redox regulation of F-actin assembly and disassembly by Mical. *Science* 334, 1710–1713. doi: 10.1126/science.1211956

Hung, R. J., Spaeth, C. S., Yesilyurt, H. G., and Terman, J. R. (2013). SelR reverses Mical-mediated oxidation of actin to regulate F-actin dynamics. *Nat. Cell Biol.* 15, 1445–1454. doi: 10.1038/ncb2871

Hung, R. J., and Terman, J. R. (2011). Extracellular inhibitors, repellents and semaphorin/plexin/MICAL-mediated actin filament disassembly. *Cytoskeleton (Hoboken)* 68, 415–433. doi: 10.1002/cm.20527

Hung, R. J., Yazdani, U., Yoon, J., Wu, H., Yang, T., Gupta, N., et al. (2010). Mical links semaphorins to F-actin disassembly. *Nature* 463, 823–827. doi: 10.1038/nature08724

Janke, C. (2014). The tubulin code: molecular components, readout mechanisms and functions. *J. Cell Biol.* 206, 461–472. doi: 10.1083/jcb.201406055

Janssen-Heininger, Y. M., Mossman, B. T., Heintz, N. H., Forman, H. J., Kalyanaraman, B., Finkel, T., et al. (2008). Redox-based regulation of signal transduction: principles, pitfalls and promises. *Free Radic. Biol. Med.* 45, 1–17. doi: 10.1016/j.freeradbiomed.2008.03.011

Jaworski, J., Kapitein, L. C., Gouveia, S. M., Dortland, B. R., Wulf, P. S., Grigoriev, I., et al. (2009). Dynamic microtubules regulate dendritic spine morphology and synaptic plasticity. *Neuron* 61, 85–100. doi: 10.3410/f.1145052.605000

Kavallaris, M. (2010). Microtubules and resistance to tubulin-binding agents. *Nat. Rev. Cancer* 10, 194–204. doi: 10.1038/nrc2830

Kim, C., and Dinauer, M. C. (2001). Rac2 is an essential regulator of neutrophil nicotinamide adenine dinucleotide phosphate oxidase activation in response to specific signaling pathways. *J. Immunol.* 166, 1223–1232. doi: 10.4049/jimmunol.166.2.1223

Kishida, K. T., Hoeffer, C. A., Hu, D., Pao, M., Holland, S. M., and Klann, E. (2006). Synaptic plasticity deficits and mild memory impairments in mouse models of chronic granulomatous disease. *Mol. Cell. Biol.* 26, 5908–5920. doi: 10.1128/mcb.00269-06

Knapp, L. T., and Klann, E. (2002). Role of reactive oxygen species in hippocampal long-term potentiation: contributory or inhibitory? *J. Neurosci. Res.* 70, 1–7. doi: 10.1002/jnr.10371

Lambeth, J. D. (2004). NOX enzymes and the biology of reactive oxygen. *Nat. Rev. Immunol.* 4, 181–189. doi: 10.1038/nri1312

Lambeth, J. D., Kawahara, T., and Diebold, B. (2007). Regulation of Nox and Duox enzymatic activity and expression. *Free Radic. Biol. Med.* 43, 319–331. doi: 10.1016/j.freeradbiomed.2007.03.028

Landino, L. M., Hasan, R., Mcgaw, A., Cooley, S., Smith, A. W., Masselam, K., et al. (2002). Peroxynitrite oxidation of tubulin sulfhydryls inhibits microtubule polymerization. *Arch. Biochem. Biophys.* 398, 213–220. doi: 10.1006/abbi.2001.2729

Landino, L. M., Koumas, M. T., Mason, C. E., and Alston, J. A. (2007). Modification of tubulin cysteines by nitric oxide and nitroxyl donors alters tubulin polymerization activity. *Chem. Res. Toxicol.* 20, 1693–1700. doi: 10.1021/tx7001492

Landino, L. M., Moynihan, K. L., Todd, J. V., and Kennett, K. L. (2004a). Modulation of the redox state of tubulin by the glutathione/glutaredoxin reductase system. *Biochem. Biophys. Res. Commun.* 314, 555–560. doi: 10.1016/j.bbrc.2003.12.126

Landino, L. M., Robinson, S. H., Skreslet, T. E., and Cabral, D. M. (2004b). Redox modulation of tau and microtubule-associated protein-2 by the glutathione/glutaredoxin reductase system. *Biochem. Biophys. Res. Commun.* 323, 112–117. doi: 10.1016/j.bbrc.2004.08.065

Lewis, S. A., Wang, D. H., and Cowan, N. J. (1988). Microtubule-associated protein MAP2 shares a microtubule binding motif with tau protein. *Science* 242, 936–939. doi: 10.1126/science.3142041

Löwe, J., Li, H., Downing, K. H., and Nogales, E. (2001). Refined structure of alpha beta-tubulin at 3. 5 A resolution. *J. Mol. Biol.* 313, 1045–1057. doi: 10.2210/pdb1jff/pdb

Luduena, R. F., and Roach, M. C. (1991). Tubulin sulfhydryl groups as probes and targets for antimitotic and antimicrotubule agents. *Pharmacol. Ther.* 49, 133–152. doi: 10.1016/0163-7258(91)90027-j

Luduena, R. F., Roach, M. C., Jordan, M. A., and Murphy, D. B. (1985). Different reactivities of brain and erythrocyte tubulins toward a sulfhydryl group-directed reagent that inhibits microtubule assembly. *J. Biol. Chem.* 260, 1257–1264.

Mackenzie, G. G., Salvador, G. A., Romero, C., Keen, C. L., and Oteiza, P. I. (2011). A deficit in zinc availability can cause alterations in tubulin thiol redox status in cultured neurons and in the developing fetal rat brain. *Free Radic. Biol. Med.* 51, 480–489. doi: 10.1016/j.freeradbiomed.2011.04.028

Massaad, C. A., and Klann, E. (2011). Reactive oxygen species in the regulation of synaptic plasticity and memory. *Antioxid. Redox Signal.* 14, 2013–2054. doi: 10.1089/ars.2010.3208

Mellon, M. G., and Rebhun, L. I. (1976). Sulfhydryls and the in vitro polymerization of tubulin. *J. Cell Biol.* 70, 226–238. doi: 10.1083/jcb.70.1.226

Mishin, A. S., Belousov, V. V., Solntsev, K. M., and Lukyanov, K. A. (2015). Novel uses of fluorescent proteins. *Curr. Opin. Chem. Biol.* 27, 1–9. doi: 10.1016/j.cbpa.2015.05.002

Mitchison, T., and Kirschner, M. (1984). Dynamic instability of microtubule growth. *Nature* 312, 237–242. doi: 10.1038/312237a0

Mitchison, T., and Kirschner, M. (1988). Cytoskeletal dynamics and nerve growth. *Neuron* 1, 761–772. doi: 10.1016/0896-6273(88)90124-9

More, S. V., Kumar, H., Kim, I. S., Song, S. Y., and Choi, D. K. (2013). Cellular and molecular mediators of neuroinflammation in the pathogenesis of Parkinson's disease. *Mediators Inflamm.* 2013:952375. doi: 10.1155/2013/952375

Morinaka, A., Yamada, M., Itofusa, R., Funato, Y., Yoshimura, Y., Nakamura, F., et al. (2011). Thioredoxin mediates oxidation-dependent phosphorylation of CRMP2 and growth cone collapse. *Sci. Signal* 4:ra26. doi: 10.1126/scisignal.2001127

Munnamalai, V., and Suter, D. M. (2009). Reactive oxygen species regulate F-actin dynamics in neuronal growth cones and neurite outgrowth. *J. Neurochem.* 108, 644–661. doi: 10.1111/j.1471-4159.2008.05787.x

Munnamalai, V., Weaver, C. J., Weisheit, C. E., Venkatraman, P., Agim, Z. S., Quinn, M. T., et al. (2014). Bidirectional interactions between NOX2-type NADPH oxidase and the F-actin cytoskeleton in neuronal growth cones. *J. Neurochem.* 130, 526–540. doi: 10.1111/jnc.12734

Murphy, M. P. (2009). How mitochondria produce reactive oxygen species. *Biochem. J.* 417, 1–13. doi: 10.1042/bj20081386

Nauseef, W. M. (2004). Assembly of the phagocyte NADPH oxidase. *Histochem. Cell Biol.* 122, 277–291. doi: 10.1007/s00418-004-0679-8

Neukirchen, D., and Bradke, F. (2011). Neuronal polarization and the cytoskeleton. *Semin. Cell Dev. Biol.* 22, 825–833. doi: 10.1016/j.semcdb.2011.08.007

Núñez, M. T., Urrutia, P., Mena, N., Aguirre, P., Tapia, V., and Salazar, J. (2012). Iron toxicity in neurodegeneration. *Biometals* 25, 761–776. doi: 10.1007/s10534-012-9523-0

Olguín-Albuerne, M., and Morán, J. (2015). ROS produced by NOX2 control *in vitro* development of cerebellar granule neurons development. *ASN Neuro.* 7:1759091415578712. doi: 10.1177/1759091415578712

Pao, M., Wiggs, E. A., Anastacio, M. M., Hyun, J., Decarlo, E. S., Miller, J. T., et al. (2004). Cognitive function in patients with chronic granulomatous disease: a preliminary report. *Psychosomatics* 45, 230–234. doi: 10.1176/appi.psy.45.3.230

Park, H. S., Lee, S. M., Lee, J. H., Kim, Y. S., Bae, Y. S., and Park, J. W. (2001). Phosphorylation of the leucocyte NADPH oxidase subunit p47(phox) by casein kinase 2: conformation-dependent phosphorylation and modulation of oxidase activity. *Biochem. J.* 358, 783–790. doi: 10.1042/0264-6021:3580783

Quadrato, G., and Di Giovanni, S. (2013). Waking up the sleepers: shared transcriptional pathways in axonal regeneration and neurogenesis. *Cell. Mol. Life Sci.* 70, 993–1007. doi: 10.1007/s00018-012-1099-x

Redondo, J., Hares, K., Wilkins, A., Scolding, N., and Kemp, K. (2015). Reductions in kinesin expression are associated with nitric oxide-induced axonal damage. *J. Neurosci. Res.* 93, 882–892. doi: 10.1002/jnr.23556

Rhee, S. G. (2006). Cell signaling. H2O2, a necessary evil for cell signaling. *Science* 312, 1882–1883. doi: 10.1126/science.1130481

Roberts, A. W., Kim, C., Zhen, L., Lowe, J. B., Kapur, R., Petryniak, B., et al. (1999). Deficiency of the hematopoietic cell-specific Rho family GTPase Rac2 is characterized by abnormalities in neutrophil function and host defense. *Immunity* 10, 183–196. doi: 10.1016/s1074-7613(00)80019-9

Russwurm, M., Russwurm, C., Koesling, D., and Mergia, E. (2013). NO/cGMP: the past, the present and the future. *Methods Mol. Biol.* 1020, 1–16. doi: 10.1007/978-1-62703-459-3_1

Sakai, J., Li, J., Subramanian, K. K., Mondal, S., Bajrami, B., Hattori, H., et al. (2012). Reactive oxygen species-induced actin glutathionylation controls actin dynamics in neutrophils. *Immunity* 37, 1037–1049. doi: 10.1016/j.immuni.2012.08.017

Shelton, M. D., Chock, P. B., and Mieyal, J. J. (2005). Glutaredoxin: role in reversible protein s-glutathionylation and regulation of redox signal transduction and protein translocation. *Antioxid. Redox Signal.* 7, 348–366. doi: 10.1089/ars.2005.7.348

Sies, H. (1997). Oxidative stress: oxidants and antioxidants. *Exp. Physiol.* 82, 291–295. doi: 10.1113/expphysiol.1997.sp004024

Sorce, S., and Krause, K. H. (2009). NOX enzymes in the central nervous system: from signaling to disease. *Antioxid. Redox Signal.* 11, 2481–2504. doi: 10.1089/ars.2009.2578

Sparaco, M., Gaeta, L. M., Santorelli, F. M., Passarelli, C., Tozzi, G., Bertini, E., et al. (2009). Friedreich's ataxia: oxidative stress and cytoskeletal abnormalities. *J. Neurol. Sci.* 287, 111–118. doi: 10.1016/j.jns.2009.08.052

Sparaco, M., Gaeta, L. M., Tozzi, G., Bertini, E., Pastore, A., Simonati, A., et al. (2006). Protein glutathionylation in human central nervous system: potential role in redox regulation of neuronal defense against free radicals. *J. Neurosci. Res.* 83, 256–263. doi: 10.1002/jnr.20729

Stadtman, E. R., and Berlett, B. S. (1997). Reactive oxygen-mediated protein oxidation in aging and disease. *Chem. Res. Toxicol.* 10, 485–494. doi: 10.1021/tx960133r

Stiess, M., and Bradke, F. (2011). Neuronal polarization: the cytoskeleton leads the way. *Dev. Neurobiol.* 71, 430–444. doi: 10.1002/dneu.20849

Stroissnigg, H., Trancíková, A., Descovich, L., Fuhrmann, J., Kutschera, W., Kostan, J., et al. (2007). S-nitrosylation of microtubule-associated protein 1B mediates nitric-oxide-induced axon retraction. *Nat. Cell Biol.* 9, 1035–1045. doi: 10.1038/ncb1625

Suzuki, T., Nakamoto, T., Ogawa, S., Seo, S., Matsumura, T., Tachibana, K., et al. (2002). MICAL, a novel CasL interacting molecule, associates with vimentin. *J. Biol. Chem.* 277, 14933–14941. doi: 10.1074/jbc.M111842200

Tahara, E. B., Navarete, F. D., and Kowaltowski, A. J. (2009). Tissue-, substrate- and site-specific characteristics of mitochondrial reactive oxygen species generation. *Free Radic. Biol. Med.* 46, 1283–1297. doi: 10.1016/j.freeradbiomed.2009.02.008

Taulet, N., Delorme-Walker, V. D., and Dermardirossian, C. (2012). Reactive oxygen species regulate protrusion efficiency by controlling actin dynamics. *PLoS One* 7:e41342. doi: 10.1371/journal.pone.0041342

Tejada-Simon, M. V., Serrano, F., Villasana, L. E., Kanterewicz, B. I., Wu, G. Y., Quinn, M. T., et al. (2005). Synaptic localization of a functional NADPH oxidase in the mouse hippocampus. *Mol. Cell. Neurosci.* 29, 97–106. doi: 10.1016/j.mcn.2005.01.007

Terman, J. R., Mao, T., Pasterkamp, R. J., Yu, H. H., and Kolodkin, A. L. (2002). MICALs, a family of conserved flavoprotein oxidoreductases, function in plexin-mediated axonal repulsion. *Cell* 109, 887–900. doi: 10.1016/s0092-8674(02)00794-8

Tripathy, D., Chakraborty, J., and Mohanakumar, K. P. (2015). Antagonistic pleiotropic effects of nitric oxide in the pathophysiology of Parkinson's disease. *Free Radic. Res.* 49, 1129–1139. doi: 10.3109/10715762.2015.1045505

Van Battum, E. Y., Gunput, R. A., Lemstra, S., Groen, E. J., Yu, K. L., Adolfs, Y., et al. (2014). The intracellular redox protein MICAL-1 regulates the development of hippocampal mossy fibre connections. *Nat. Commun.* 5:4317. doi: 10.1038/ncomms5317

Villarroel-Campos, D., Gastaldi, L., Conde, C., Caceres, A., and Gonzalez-Billault, C. (2014). Rab-mediated trafficking role in neurite formation. *J. Neurochem.* 129, 240–248. doi: 10.1111/jnc.12676

Villarroel-Campos, D., and Gonzalez-Billault, C. (2014). The MAP1B case: an old MAP that is new again. *Dev. Neurobiol.* 74, 953–971. doi: 10.1002/dneu.22178

Weidinger, A., and Kozlov, A. V. (2015). Biological activities of reactive oxygen and nitrogen species: oxidative stress versus signal transduction. *Biomolecules* 5, 472–484. doi: 10.3390/biom5020472

Wilson, C., Núñez, M. T., and González-Billault, C. (2015). Contribution of NADPH-oxidase to the establishment of hippocampal neuronal polarity in culture. *J. Cell Sci.* 128, 2989-2995. doi: 10.1242/jcs.168567

Yang, R., Kong, E., Jin, J., Hergovich, A., and Püschel, A. W. (2014). Rassf5 and Ndr kinases regulate neuronal polarity through Par3 phosphorylation in a novel pathway. *J. Cell Sci.* 127, 3463–3476. doi: 10.1242/jcs.146696

Zhou, Y., Adolfs, Y., Pijnappel, W. W., Fuller, S. J., Van der Schors, R. C., Li, K. W., et al. (2011). MICAL-1 is a negative regulator of MST-NDR kinase signaling and apoptosis. *Mol. Cell. Biol.* 31, 3603–3615. doi: 10.1128/mcb.01389-10

Conflict of Interest Statement: The authors declare that the research was conducted in the absence of any commercial or financial relationships that could be construed as a potential conflict of interest.

frontiers
in Cellular Neuroscience

REVIEW
published: 30 June 2015
doi: 10.3389/fncel.2015.00241

TIPsy tour guides: how microtubule plus-end tracking proteins (+TIPs) facilitate axon guidance

*Elizabeth A. Bearce, Burcu Erdogan and Laura Anne Lowery**

Department of Biology, Boston College, Chestnut Hill, MA, USA

The growth cone is a dynamic cytoskeletal vehicle, which drives the end of a developing axon. It serves to interpret and navigate through the complex landscape and guidance cues of the early nervous system. The growth cone's distinctive cytoskeletal organization offers a fascinating platform to study how extracellular cues can be translated into mechanical outgrowth and turning behaviors. While many studies of cell motility highlight the importance of actin networks in signaling, adhesion, and propulsion, both seminal and emerging works in the field have highlighted a unique and necessary role for microtubules (MTs) in growth cone navigation. Here, we focus on the role of singular pioneer MTs, which extend into the growth cone periphery and are regulated by a diverse family of microtubule plus-end tracking proteins (+TIPs). These +TIPs accumulate at the dynamic ends of MTs, where they are well-positioned to encounter and respond to key signaling events downstream of guidance receptors, catalyzing immediate changes in microtubule stability and actin cross-talk, that facilitate both axonal outgrowth and turning events.

Keywords: +TIPs, axon guidance, growth cone, microtubule dynamics, cytoskeleton

OPEN ACCESS

Edited by:
Daniel Marcel Suter,
Purdue University, USA

Reviewed by:
Phillip R. Gordon-Weeks,
King's College London, UK
Fengquan Zhou,
Johns Hopkins University, USA

***Correspondence:**
Laura Anne Lowery,
Department of Biology, Boston College, 140 Commonwealth Avenue, Chestnut Hill, MA 02467, USA
laura.lowery@bc.edu

Received: *28 April 2015*
Accepted: *15 June 2015*
Published: *30 June 2015*

Citation:
Bearce EA, Erdogan B and Lowery LA (2015) TIPsy tour guides: how microtubule plus-end tracking proteins (+TIPs) facilitate axon guidance.
Front. Cell. Neurosci. 9:241.
doi: 10.3389/fncel.2015.00241

Introduction

The young neuron faces a complex journey. Extending a single, properly guided axon through the developing embryo involves intricate orchestration of growth, retraction, and turning events. To navigate this landscape, the axon is equipped with a responsive cytoskeletal vehicle called the growth cone, which uses a well-organized network of actin filaments to maneuver and power forward. In order to choose the right course, the axon is presented with a multitude of external, chemotropic cues, which must be detected and then effectively translated into an appropriate mechanical response (**Figure 1A**). The spatially-restricted stabilization of microtubules (MTs) has long been established to be integral for turning behaviors. Evidence has emerged only more recently that suggests that their plus-end tracking proteins (+TIPs) intercede as signal transduction "tour guides" during axon guidance. Utilizing their capacity to interface with both microtubule and actin cytoskeletons, as well as their close-proximity to the cortical guidance cascades, +TIPs are well-positioned to inform and direct growth cone behaviors. In this review, we highlight seminal and current works on +TIP-mediated signal transduction and regulation of cytoskeletal dynamics in axon elongation and turning events.

The Growth Cone Cytoskeletal Vehicle

The basic organization of the growth cone cytoskeleton has been well-characterized (Geraldo and Gordon-Weeks, 2009; Lowery and Van Vactor, 2009; Dent et al., 2011; Hur et al., 2012; **Figure 1B**).

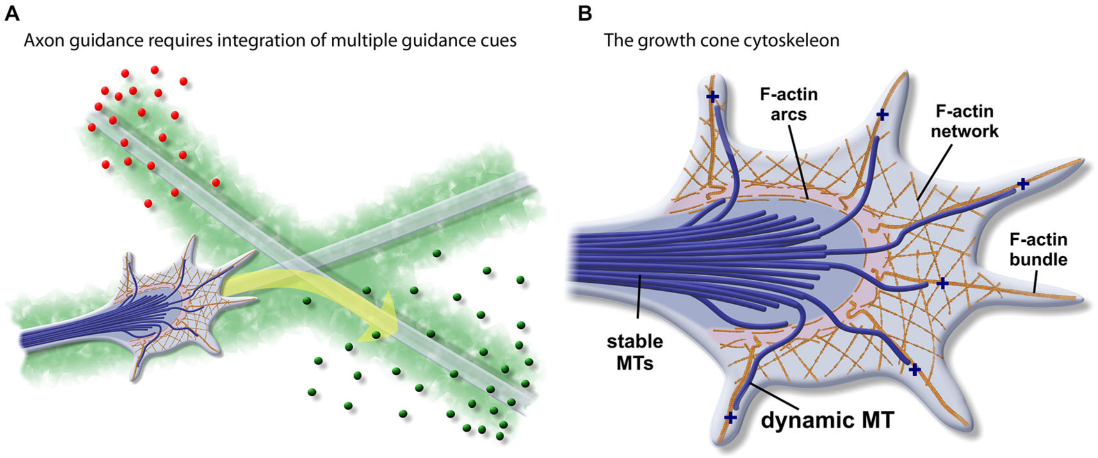

FIGURE 1 | The growth cone cytoskeleton. (A) The axon has to travel a complex landscape which presents a multitude of external chemotropic cues (e.g., red and green circles represent diffusible cues, light green represents substrate-bound cues). To properly interpret and navigate these signals, the axon is equipped with a dynamic cytoskeletal vehicle called the growth cone. **(B)** Structural organization of the growth cone cytoskeleton: Bundled, stable Microtubules (MTs) extend through the axon, entering the growth cone "wrist." These terminate in the growth cone "central" domain, surrounded by a cage of F-actin arcs. F-actin bundles extend into the growth cone "fingers" (filopodia) to sample the environment. Between the filopodia there exist a series of cortical actin networks which create the lamellipodial veils. A subset of MTs can escape the central domain, to trace along F-actin structures and explore the growth cone periphery. The dynamic plus-ends of MTs are decorated by set of proteins called plus-end tracking proteins (+TIPs) (not shown). Concentration of +TIPs at the dynamic leading edge is particularly important as they come in close contact with signaling cascades that are triggered by external cues.

The bundled MTs of the axon shaft give way to the contractile actomyosin "wrist" at the base of the growth cone. In the growth cone central domain, stable MTs are corralled into a dense cluster by actin arcs. Filamentous (F)-actin bundles extend into the growth cone periphery, forming the filopodia "fingers." Cortical actin networks surround the filopodia, forming lamellipodia-like veils. Singular dynamic, pioneer MTs escape the central domain with their dynamic "plus-ends" oriented towards the filopodial tips. These MTs transiently couple to the F-actin-based filopodial tracks, allowing them to explore the outer reaches of the actin cytoskeleton (Schaefer et al., 2002). The positioning of these MTs within the growth cone periphery allows them to aid in vesicle transport, couple to actin networks, and encounter signaling molecules.

Microtubules in Axon Outgrowth and Turning

Both actin and MTs play a critical role in coordinated growth cone motility and steering. It is generally accepted that F-actin networks, by way of F-actin treadmilling and adhesion dynamics, provide protrusion and motility to the growth cone vehicle (Dent et al., 2011). However, early studies of growth cone dynamics noted that singular MTs were capable of escaping the central growth cone domain, and that the orientation of these MTs often predicted the direction of subsequent outgrowth (Sabry et al., 1991; Tanaka et al., 1995). When focus was drawn to these "pioneer" MTs of the growth cone periphery, it became evident that their selective stabilization could impact growth cone navigation events. Localized application of the microtubule stabilizing drug, Taxol, was sufficient to induce growth cone turning towards the site of administration, whereas the opposite turning effect was seen with administration of a MT-depolymerizing drug, Nocodazole (Buck and Zheng, 2002). Attractive turning could be extinguished by subsequent inhibition of either actin or Rho GTPases, indicating that this initial stabilization of MTs precedes and facilitates actin remodeling, potentially through subsequent activation of Rho GTPases (Buck and Zheng, 2002). While these studies highlighted an important role for pioneer MTs in axon outgrowth and turning events, thus establishing MTs as important navigators of the growth cone vehicle, it was not immediately clear how biologically-relevant extracellular guidance cues might result in targeted, downstream changes in growth cone MT stability. However, the more general question of how MTs are stabilized, destabilized, or otherwise modulated has long been a topic of interest in many biological contexts.

+TIPs Decorate the Ends of MTs and Contribute to their Dynamic Instability

MTs are subject to regulation by a multitude of MT associated proteins (MAPs), which act to nucleate, stabilize, destabilize, sever, bundle, or additionally modify MT behaviors (Andersen, 2000; Akhmanova and Steinmetz, 2008). A subset of these, which selectively ride along, or "track" the dynamic MT plus-end, are appropriately-named the +TIPs (Akhmanova and Steinmetz, 2008). But +TIPs are not passive hitchhikers; rather, they are themselves dynamic and interactive, undergoing phosphorylation and other modifications which can induce MT-actin crosslinking, interactions with focal adhesion scaffolding, or rapid dissociation from the plus-end. Their malleable behaviors make them ideal "first responders" within axon guidance pathways, serving as informative translators along the journey. Here, we present a collection of evidence to substantiate

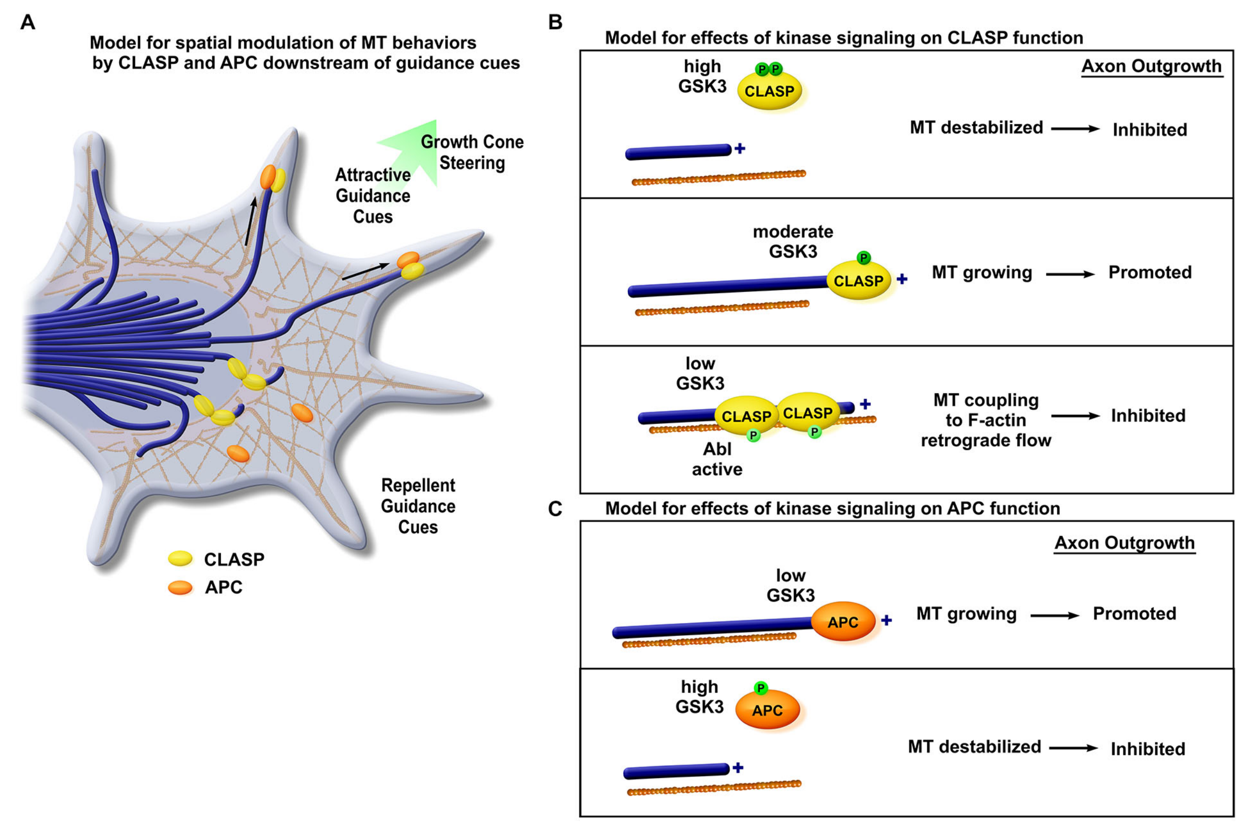

FIGURE 2 | Phosphorylation dependent +TIPs spatial distribution along MT is key to axon outgrowth and steering. (A) Spatial distribution of CLASP and APC is key to the modulation of MT dynamic behavior and generation of the navigational response. Asymmetrically-distributed guidance signals differentially regulate +TIP localization. On the side of attractive guidance cues, CLASP and APC demonstrate MT plus-end binding and promote axon outgrowth. Faced with repellent cues, APC dissociates from MTs and CLASP shows lattice binding, inhibiting axon outgrowth. **(B)** Distribution of CLASP is modulated by phosphorylation by kinases. High levels of GSK3 activity lead to two sites of phosphorylation of CLASP, which then dissociates from MTs causing MT destabilization and axon outgrowth inhibition (upper panel). Moderate GSK3 activity promotes a single site of phosphorylation of CLASP, facilitating CLASP plus-end localization and axon growth (middle panel). With low levels of GSK3, CLASP remains unphosphorylated, and CLASP binds to the MT lattice, inhibiting axon growth by coupling MTs to F-actin retrograde flow. A similar phenotype is observed when CLASP is exposed to high levels of Abl activity, which leads to phosphorylation at a different site (lower panel). **(C)** Phosphorylation-dependent APC distribution. Low GSK3 activity allows APC to remain unphosphorylated, promoting its association with plus-ends, facilitating axon growth (upper panel). However, under high GSK3 activity, phosphorylated APC dissociates from MTs and causes MT destabilization of MTs and axon growth inhibition (lower panel).

a role for +TIPs as molecular tour guides during axon elongation and turning events.

The +TIP of the Iceberg: Cytoplasmic Linker Associated Protein (CLASP) and Adenomatous Polyposis Coli (APC) Emerge as Axon Guidance Modulators

The first formative links between MT plus-end regulation and extracellular signaling cues were forged when two disparate +TIPs were simultaneously shown to possess distinct roles in relaying information downstream of axon guidance signaling events (**Figure 2**). Utilizing an elegant, *in vivo* genetic screen in the *Drosophila* retina, Lee et al. showed that *mast/orbit*, an ortholog to the MAP, cytoplasmic linker associated protein 1 (CLASP 1), cooperates with Abelson tyrosine kinase (*Abl*), a downstream signaling molecule involved in the Slit repellent pathway (Lee et al., 2004). This genetic interaction was fortified when *mast/orbit* and *Abl* zygotic loss-of-function mutants displayed an identical ectopic central nervous system midline crossing phenotype and similar deficits in motor axon pathfinding within the peripheral nervous system. To gain a mechanistic understanding of the function of CLASP within growth cones, and to elucidate why manipulation of this +TIP might result in an axon guidance phenotype, GFP-CLASP was expressed in growth cones of *Xenopus laevis* (an ideal system for imaging cytoskeletal dynamics due to their large size and ease of neuronal culturing (Stout et al., 2014)). CLASP was found to localize to growing MT plus-ends specifically within the growth cone and preferentially track the ends of pioneer MTs which ran along actin filopodia, where CLASP would theoretically be exposed to Abl signaling cues. Overexpression of CLASP, however, demonstrated severe central-zone MT looping, where MTs were unable to escape into the growth cone periphery, and growth cone advance was significantly reduced. Together, these data provided strong evidence that CLASP was implicated downstream of Abl kinase signaling events to regulate growth cone MT dynamics.

Separately, Zhou et al. provided evidence that interactions between pioneer MTs and the +TIP APC were facilitated downstream of the axonal outgrowth signaling molecule nerve growth factor (NGF) in murine dorsal root ganglion neurons (Zhou et al., 2004; **Figure 2**). This was the first record of a role for APC in the nervous system, though its plus-end localization had previously been shown in other cell types (Zumbrunn et al., 2001). Here, APC was shown to localize strongly to MT plus-ends in growth cones. However, this association could be reduced if NGF was removed, leading to the hypothesis that APC bound to plus-ends in response to localized inactivation of one of NGF's downstream signaling effectors, GSK3. This was tested with numerous pharmacological inhibitors and mutant constructs, which verified that APC operated directly downstream of GSK3b to locally-stabilize MTs when GSK3 was inactive. This selective stabilization occurred simultaneously with actin remodeling. Together, these data supported a model for APC promoting axonal elongation, downstream of signaling cues.

Expanded Roles of CLASP: Navigating Downstream of Two Kinases

Subsequent explorations of CLASP's role in axon outgrowth and guidance have expanded details of its regulation to include modulation not only by Abl, but by GSK3, as well. While significant progress has been made in understanding the interplay between these two guidance cascades, early studies examining the role of CLASP on a cellular level initially painted a muddled picture.

First, it was not exceedingly clear what role CLASP played in axon elongation. Lee et al. (2004) associated it genetically with Slit, and consequently, with repulsive turning events. However, CLASP was already known to be a MT stabilizing protein in multiple systems (Lemos et al., 2000; Akhmanova et al., 2001; Galjart, 2005). Therefore, a role in repulsive turning seemed to go against seminal observations that localized MT-stabilization would promote outgrowth and attractive turning (Buck and Zheng, 2002). When CLASP was then found to be a substrate of GSK3, this added another layer of complexity; GSK3 had been implicated in both promoting and inhibiting axon elongation (Owen and Gordon-Weeks, 2003; Zhou et al., 2004). Solutions to these controversies were somewhat intertwined, as later work would reveal that CLASP was not solely a +TIP, but additionally possessed a MT lattice-binding activity. Signaling events downstream of guidance cues, through GSK3 and Abl, could control the switch between these two modes of MT interaction.

When Hur et al. (2011) examined GSK3 phosphorylation of CLASP in the growth cone, they showed that rather than complete GSK3 inactivation, a balance of GSK3 inhibition was necessary to allow axon outgrowth. Thus, an understandable model finally emerged (Hur et al., 2011; **Figure 2**). There were two separate sites available for phosphorylation of CLASP by GSK3. In cases of highly-active GSK3, both sites were phosphorylated, CLASP dissociated from MTs, and axon outgrowth was reduced. Where only one site was phosphorylated, plus-end binding was optimized, promoting MT stability and axon elongation. However, when GSK3 was entirely inactive, CLASP remained dephosphorylated at these sites, which enabled strong association to the MT lattice. MTs then accumulated within the central growth cone, and axon outgrowth was stunted. This phenotype could be largely rescued by the myosin-II inhibitor blebbistatin, indicating that MTs were being excessively-coupled to F-actin retrograde flow. These findings in neurons were consistent with previous studies of CLASP regulation by GSK3 in non-neuronal cells (Akhmanova et al., 2001; Wittmann and Waterman-Storer, 2005; Kumar et al., 2009, 2012). Separately, CLASP depletion in the growth cone was also shown to strongly perturb actin organization, resulting in collapsed, weakened F-actin architecture within lamellipodial veils (Marx et al., 2013), supporting an idea that balanced CLASP-plus-end and CLASP-lattice (and F-actin) interactions are necessary for optimal growth cone structural integrity.

Subsequent biochemical studies of CLASP phosphorylation by Abl demonstrated similar functional interactions, in that Abl phosphorylation also occurred within a domain that mediated both MT and actin binding, and was thus also able to "toggle" CLASP behavior (Engel et al., 2014). Overexpression of constitutively-active Abl resulted in a phenotype that mirrored GSK3 inhibition, with decreased CLASP localization at MT plus-ends, accumulation of CLASP with actin-rich structures in the central growth cone domain, and growth cone pausing (Engel et al., 2014). While it was already well-established that Abl signaling regulates F-actin organization by Ena/VASP (Gertler et al., 1995; Wills et al., 1999; Bashaw et al., 2000; Lin et al., 2009), this work suggests that Abl regulation of CLASP may also affect F-actin organization, once again highlighting the complex interplay at work within the growth cone cytoskeleton.

APC: A Jack of all Trades, and Putative Growth Cone Synthesis Hub

Similar to CLASP, APC was established as a +TIP which was thought to stabilize MTs even prior to its implications in axon guidance, and it had already been speculated that its phosphorylation state may affect its association to MTs (Smith et al., 1994; Su et al., 1995; White, 1997; Zumbrunn et al., 2001). Like other plus-end stabilizing proteins, APC was found to be greatly enriched in the nervous system during axon growth and navigation (Bhat et al., 1994; Koester et al., 2007). A series of works emerged that pointed to GSK3-modulated APC in multiple roles within the early nervous system, including neuronal polarity, migration, and axon specification, providing some added assurance that this interaction was an important regulator of MT dynamics in neural development (Dobashi et al., 2000; Shi et al., 2004; Koester et al., 2007; Purro et al., 2008; Eom et al., 2014; Mohn et al., 2014; Onouchi et al., 2014). APC preferential localization was shown to accumulate on the "turning" side of the growth cone as it encountered a substrate border, predicting turning behavior (Koester et al., 2007; **Figure 2**). Evidence in mouse neurons also pointed towards a role for APC downstream of Wnt signaling, as growth cone pausing, MT looping, and reduction in APC plus-end localization can also be induced by Wnt3a (Purro et al., 2008). But this newer function in axon guidance (Zhou et al., 2004) did not come without discourse: the dominant negative strategies that first identified APC as a candidate for axon guidance in murine models met some critique when complete ablation of the APC ortholog in *Drosophila* neuronal precursors caused perceptible effects on polarity and axon outgrowth of some but not all neurons (Rusan et al., 2008).

However, recent findings pointing to a role for APC in translation might explain the discrepancy between these previous experiments. APC gained new acclaim as strong evidence emerged that it serves not only as a MT-effector, but also as an RNA-binding protein in neurons (Preitner et al., 2014). A HITS-CLIP interactome generated from RNA targets of APC revealed a large pool of highly-interrelated cytoskeletal mRNAs, opening up the provocative possibility that APC may sequester localized cytoskeletal protein factories, an idea supported by demonstration of its ability to facilitate local synthesis of an axon-specific tubulin isotype, beta2B-tubulin (Preitner et al., 2014). This is especially intriguing when taken into consideration with evidence that APC contains a region on its N-terminal that permits self-association and clustering (Li et al., 2008), which could potentially greatly amplify the amount of mRNA sequestered in one peripheral region. The capacity of APC to localize mRNA could explain the discrepancy noted between earlier murine and *Drosophila* studies of plus-end function and axon outgrowth, as the *Drosophila* studies deleted APC, while the murine experiments disrupted APC-MT plus-end interactions without ablating it, potentially contributing to mislocalization of APC-interacting mRNAs. This mRNA-localization function is thus far unique among +TIPs, but represents an enticing possibility that some members of the family could not only modulate turning events, but also direct local translation and thereby facilitate rapid outgrowth from these regions of stabilized, pioneer MTs. This possibility is further bolstered by the fact that a screen for CLASP interactors identified multiple RNA processing factors (Lowery et al., 2010), although a direct role for CLASP in translation regulation remains to be seen.

A New Team of Tour Guides: An Expanding Family of Tip-trackers Shows Promise as Regulators of Axon Guidance

The initial explorations on CLASP and APC paved the way for further genetic and cell biological approaches investigating +TIP function within the growth cone. These studies began to quickly reveal a growing cast of +TIPs that contribute far beyond their prescribed roles in MT stability. It is now apparent that their functions include coupling MT dynamics to F-actin networks, promoting or inhibiting axonal outgrowth, and facilitating growth cone turning, as described in more detail below (**Figure 3**).

XMAP215

XMAP215 was initially identified as a MT-growth enhancing protein isolated from *Xenopus* egg extracts (Gard and Kirschner, 1987), and it remains the best-characterized MT polymerase, highly-conserved in all eukaryotes (Charrasse et al., 1996; Lee et al., 2001; Brouhard et al., 2008; Podolski et al., 2014). Affinity of XMAP215 for the MT plus-end is unique compared to many +TIPs, in that its localization does not depend upon EB1 (Brouhard et al., 2008). Rather, XMAP215 localizes to the far-distal plus-end, beyond EB1 (Maurer et al., 2014). While XMAP215 has been well-characterized *in vitro*, only a handful of studies have examined its function *in vivo*.

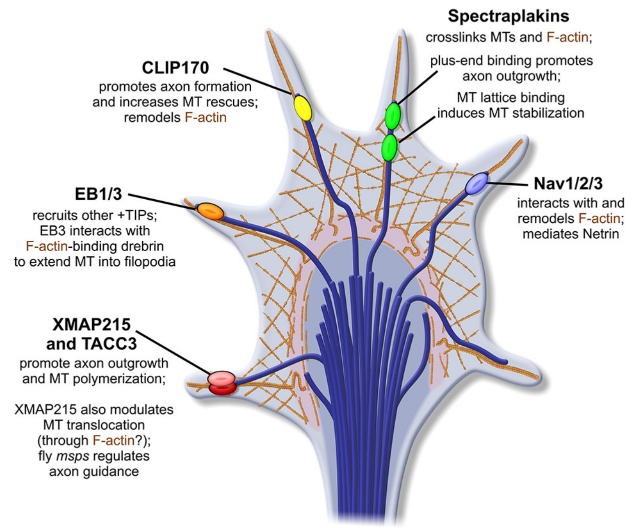

FIGURE 3 | Additional +TIPs in axon outgrowth and guidance. A brief synopsis of other presently-identified +TIPs that function in axon outgrowth and guidance, highlighting some of their known interactions: note that a number of these proteins demonstrate an ability to facilitate MT-F-actin coupling.

Initial studies of XMAP215-family members using neuronal cultures have confirmed its canonical role as a MT polymerase in neurons (van der Vaart et al., 2012; Lowery et al., 2013), but have also highlighted a novel growth cone-specific function for XMAP215 (Lowery et al., 2013). The mammalian ortholog, ch-TOG, was first shown to be important for promoting MT growth velocity, reducing MT catastrophe frequency in neurons, and enhancing axonal outgrowth (van der Vaart et al., 2012). However, in a separate study using *Xenopus laevis*, data gathered from growth cones after only partial inhibition of XMAP215 function revealed an unexpected function of this canonical +TIP. While partial knockdown did result in an increased rate of MT catastrophe (consistent with the ch-TOG study), MTs also exhibited a counterintuitive increase in MT plus-end velocities selective to growth cones (Lowery et al., 2013). Analysis by quantitative fluorescent speckle microscopy illustrated that differences in overall MT translocation/sliding, rather than MT polymerization, were a major contributor to the measured plus-end velocity change in the XMAP215 KD. In control growth cones, net translocation of MTs favored retrograde movement, attributed to frequent coupling of MTs to F-actin retrograde flow (Lowery et al., 2013). However, partial XMAP215 knockdown tipped the scales in favor of anterograde MT translocation. This finding indicated a previously undescribed role for XMAP215 in affecting MT translocation within the growth cone, possibly by mediating F-actin-MT crosslinking events. The balance of anterograde MT polymerization and MT sliding behaviors vs. the "drag" elicited by coupling to F-actin retrograde flow is thought to be instrumental in neurite and axon extension (Schaefer et al., 2002, 2008; Myers et al., 2006; Lee and Suter, 2008; Lu et al., 2013, 2015). Spatial regulation of MT polymer movements also likely contributes to axon guidance as well, although this remains to be explicitly shown. It is not entirely clear whether the role of XMAP215 in affecting MT sliding is direct or through additional intermediates, given that the *Drosophila* XMAP215 ortholog, *msps*, shows a genetic interaction with CLASP (Lowery et al., 2010), which is known to mediate MT-F-actin crosslinking (see above).

In fact, XMAP215 originally emerged as a prime candidate for modulating axon guidance when dual genetic and proteomic screens to identify CLASP interactors in *Drosophila* revealed that *msps* genetically antagonizes CLASP function and contributes to axon guidance in the embryonic CNS (Lowery et al., 2010). Overexpression of *msps* was also able to ameliorate a peripheral motor neuron "bypass" phenotype seen in *Abl* gain-of-function mutants (Lowery et al., 2010), further substantiating the role of an XMAP215-family member in axon guidance. However, only this single genetic study has thus far demonstrated a possible connection between XMAP215 and axon guidance. Accordingly, there is still an enduring motive to further define the cell biological functions of XMAP215 in growth cones, and deduce how these may ultimately mediate steering mechanisms.

Transforming Acidic Coiled Coil (TACC3)

An ortholog to TACC3, member of the Transforming Acidic Coiled Coil (TACC) family (Piekorz et al., 2002; Aitola et al., 2003; Gergely et al., 2003), was similarly identified alongside XMAP215 in a screen for genetic interactors of CLASP in *Drosophila* (Long et al., 2013). Prior to this finding, the cytoskeletal functions of TACC3 were well-characterized primarily at the centrosome and mitotic spindle, where TACC3 is necessary for XMAP215 recruitment and astral and spindle MT elongation (Lee et al., 2001; Peset and Vernos, 2008; Lioutas and Vernos, 2013; Thakur et al., 2014). Thus, on one hand, the appearance of TACC3 in an interactome with XMAP215 was not entirely unintuitive. However, TACC3's functions at the mitotic spindle were not specifically attributed to any plus-end regulatory capacity, and its presence at MT nucleation sites could not justify any function in guidance or outgrowth of post-mitotic neurons. Nonetheless, a subsequent examination confirmed that knocking down TACC3 in *Xenopus laevis* could drive significant decrease in axonal outgrowth length *in vitro* (Nwagbara et al., 2014). In live cells, TACC3 was shown to localize to the far-distal MT plus-end in embryonic neurons, where it co-localizes with XMAP215. Manipulation of TACC3 appeared to govern the fluorescent intensity of XMAP215 comets, suggesting that TACC3 recruits XMAP215 to the distal plus-ends of interphase MTs. It is likely this recruitment of XMAP215 that drives MT plus-end velocities; thus, TACC3's function at the MT plus-end may be similar to its role at the mitotic spindle. Further studies will be useful to see if this XMAP215 recruitment can be spatially-regulated or modified downstream of signaling factors, as this could emerge as a potent mechanism to drive rapid MT extension, perhaps towards a chemoattractive gradient.

End-binding (EBs)

The majority of +TIPs, including CLASP and APC, as well as others described below (the Spectraplakins, and the Navigators), do not actually bind to the MT plus-end or MT lattice directly. Instead, they localize via domains that target to plus-end scaffold proteins known as the end-binding (EB) proteins (Akhmanova and Steinmetz, 2008; Honnappa et al., 2009). It is worth noting that much of the MT plus-end dynamics studies that are so integral to cell biological ventures today are made possible by tracking and analysis of fluorescent EB1/3 constructs. This technique was first employed to track live, forward movement of MT polymerization in a study that examined MT directionality in various compartments of the young neuron, including the cell body, dendrites, and growth cone (Stepanova et al., 2003). Thus, EB1/3 association to the plus-end, which was confirmed to occur autonomously (Bieling et al., 2007), is crucial for many other +TIP interactions. For that reason alone, their role in axon guidance must be critical, albeit somewhat difficult to tease out from the complex of proteins that associate with them.

Another additional point of EB plus-end function comes from its interaction with drebrin (Geraldo et al., 2008), an actin binding protein. In immunoprecipitation assays, EB3 but not EB1, can immunoprecipitate drebrin from the growth cone cytosol. Drebrin shows strong immunolabeling with F-actin bundles in the proximal regions of filopodia. Colocalization of the two proteins appeared to occur when the distal tip of pioneer MTs came in contact with these F-actin bundles. The functional outcome of this interaction was tested with expression of a portion of EB3 that binds drebrin but not MTs; notably, these neurons were unable to extend growth cones. When drebrin was depleted, growth cones demonstrated abnormal MT bundling in the central domain, which prevented MT protrusion into filopodia. Together, these data demonstrate a drebrin–EB3, interaction is essential for MT extension into filopodia (Geraldo et al., 2008), which may be pivotal for interaction with localized signaling cascades.

Interestingly, classical or structural MAPs (MAP1B, Tau), which do not strongly associate the plus-end, can function within neurons to compete off or sequester EB1/3 proteins from the plus-end (Tortosa et al., 2013; Sayas and Avila, 2014). This grants these lattice-binding proteins the capacity to modulate an aspect of +TIP localization. Given that MAP1B and Tau association to the MT lattice are, in turn, regulated by GSK3 (Lovestone et al., 1994; Goold et al., 1999; Owen and Gordon-Weeks, 2003), this provides an additional opportunity for signaling cascades to modulate essentially all +TIPs simultaneously via their dependence on EB1.

Cytoplasmic Linker Protein (CLIP-170)

Cytoplasmic Linker Protein (CLIP)-170, initially named for both its size and an association to cytoplasmic endocytic vesicles

(Pierre et al., 1992), offers a myriad of potential signaling interactions, though precisely how these may function in axon guidance is still unfolding. Genetically and proteomically, CLIP-170 interacts with both CLASP and IQGAP (Fukata et al., 2002; Galjart, 2005), an actin-modulator downstream of Cdc42 and Rac1 (Swiech et al., 2011). This IQGAP-CLIP-170 interaction, in tandem with interactions with dynamic MTs, has been demonstrated to regulate actin during dendritic arborization (Swiech et al., 2011). While such a relationship has not been demonstrated explicitly during axon guidance, there have been several insights that point towards CLIP-170 having a role in F-actin remodeling in the growth cone (**Figure 3**).

During axon specification, inhibition of CLIP-170 was sufficient to inhibit axon formation (Neukirchen and Bradke, 2011). Likewise, overexpression could prompt the formation of multiple axons, highlighting a role for CLIP-170 in axon specification. The ability to accomplish this was attributed to a role for CLIP-170 in very modest stabilization of MTs, and specifically, a capacity to marginally increase MT rescue behaviors. This slight increase in stability facilitated the "push" of MTs to enter into the growth cone periphery. Actin phenotypes were also noted in growth cones that expressed a dominant negative CLIP-170, in that actin arcs appeared more robust and less penetrable by central MTs. Actin arc formation and trapping of MTs in the central zone in absence of CLIP-170 could be rescued with a brief treatment of actin depolymerizing drug, upon which axon elongation could resume (Neukirchen and Bradke, 2011).

Additionally, another examination of CLIP-170 in the axon showed that expressing a dominant negative version of CLIP-170 counterintuitively increased the growth rate and total growth distance of EB1-GFP comets (Stepanova et al., 2010), which could indicate changes in MT translocation (similar to those demonstrated with XMAP215) suggesting a decrease in transient coupling to F-actin retrograde flow. Given that CLIP-170 and CLASP interact (Akhmanova et al., 2001; Drabek et al., 2006), and CLASP is capable of performing just such a MT-actin crosslink (Drabek et al., 2006; Tsvetkov et al., 2007; Engel et al., 2014), it will be crucial to investigate the molecular underpinnings of a putative MT-actin link. While it may occur through CLASP, it is possible that CLIP-170 is also capable of this sort of crosslink independently of CLASP, perhaps through its interactions with IQGAP.

It is also worthy of consideration that while CLIP-170 is certainly expressed in early neural development, some researchers believe its role to be somewhat inconclusive (Beaven et al., 2015); their findings suggest that CLIP-170 may not factor into growth cone guidance significantly, as its plus-end binding in the nervous system, at least within *Drosophila*, appears greatly diminished compared to other cell types (Beaven et al., 2015). If this does hold true, it would be consistent with a number of other cases where +TIPs function differently in the neuron compared to other cell types (Stepanova et al., 2003; Lowery et al., 2013), emphasizing a continued need to examine +TIP function in the nervous system both in the context of the previous cell biological literature, as well as in its own right.

Spectraplakins

The Spectraplakins demonstrate another family of +TIPs that are simultaneously able to bind MTs and F-actin (Leung et al., 1999; Fuchs and Karakesisoglou, 2001; Suozzi et al., 2012), and this F-actin-MT crosslinking is essential for axon extension (Lee and Kolodziej, 2002). ACF7, a Spectraplakin denoted Short-stop (Shot) in *Drosophila*, demonstrates an explicit axon guidance phenotype, in that deletion leads to motor axons that "stop-short" of their destinations (Vactor et al., 1993) and show defects in MT bundling (Alves-Silva et al., 2012). Similar to CLASP, Shot was shown to demonstrate disparate MT-binding mechanisms: one that allows lattice-binding, thus inducing bundling and MT stabilization, in addition to an EB1-mediated plus-end binding, which promotes axonal outgrowth (Alves-Silva et al., 2012).

While phosphorylation of Shot/ACF7 has not been examined in a neural context, ACF7 was shown to undergo phosphorylation by GSK3 in skin stem cells. This phosphorylation could inhibit MT-binding and disrupt polarized migration (Wu et al., 2011), a process that (like axon guidance) relies on spatiotemporally-regulated signaling and cytoskeletal dynamics (Horwitz and Webb, 2003; Wittmann and Waterman-Storer, 2005; Machacek et al., 2009). This study also demonstrated two sites of ACF7 phosphorylation by GSK3, and both were able to reduce MT-binding affinity (Wu et al., 2011), demonstrating yet another CLASP-like opportunity for a "sweet spot" of modulation, which may balance plus-end binding, lattice-interactions, dynamic-instability, and thus, axon-elongation.

An alternate or complementary means to explain a role for ACF7/Shot in axonal pathfinding was demonstrated by a link to Dual Leucine-zipper bearing Kinase (DLK; Valakh et al., 2013), which is part of a pathway that is crucial in normal apoptotic neuronal "pruning" and in axon regeneration (Tedeschi and Bradke, 2013; Chen et al., 2014a). RNAi against Shot, as well as a separate, hypomorphic Shot mutant, both demonstrated an "overgrown" synaptic phenotype, mediated by over-activation of DLK (Valakh et al., 2013). DLK activation has been shown to occur in response to cytoskeletal destabilization (Valakh et al., 2015). Therefore, either or both of these effects of Shot manipulation, the direct MT-actin perturbation or the downstream activation of DLK, may play into its deficits in pathfinding, a consideration that once again highlights the complex interplays that are required during cytoskeletal regulation.

Navigators

Another class of +TIPs, the candidly-christened Neuron Navigators, were implicated in axonal pathfinding long before they were at all associated with MT plus-ends. Genetic screening in *C. elegans* first identified *unc-53* as critical for both epithelial and axonal guidance; mutant alleles of the gene demonstrated posterior body malformation, in addition to pronounced defects in mechanosensory neuron turning (Hedgecock et al., 1987). Subsequent searches in human, rat, and mouse identified a conserved family of genes, the Neuron Navigators (*NAV1*, *NAV2*, and *NAV3*), which coded for variations of a Calponin homology domain-containing protein which also featured putative actin-binding, signal transduction, and coiled-coil regions (Ishiguro et al., 2002; Maes et al., 2002; Merrill et al., 2002; Stringham et al., 2002; Martínez-López et al., 2005).

While genetic interaction data suggested the NAVs might act as intermediates between extracellular guidance cues and cytoskeletal machinery in axon guidance, especially when considered in tandem with their potential actin and signaling interactions, possible mechanisms were unclear. Localization data was inconsistent. Fluorescent-labeled homologs of NAV2 demonstrated cytosolic and nuclear localization (Ishiguro et al., 2002), whereas NAV3 appeared strictly nuclear (Coy et al., 2002). Intriguingly then, NAV1, which lacked the actin binding regions contained in the other paralogs, was shown to localize strongly to MT plus-ends, via a MT binding domain (MBD; Martínez-López et al., 2005). This localization shared comet-like morphology demonstrated by EB1. The capacity for NAV1 to act as a +TIP was thought to be unique, as initial efforts did not show plus-end localization of NAV2, despite strong conservation of the MBD domain in all Navigators (Muley et al., 2008). However, data gathered from later rounds of live imaging and immunofluorescence with new antibodies finally offered some evidence that NAV1, NAV2, and NAV3 may be true +TIPs, which could compete for plus-end localization with CLIP-170, attributable to an EB1-dependent binding mechanism (van Haren et al., 2009).

Cell biological studies of NAVs indicate that their role in axon pathfinding may stem from an ability to affect cellular-process organization. Compared to EB1, the Navigators exhibited a preferential localization at MT plus-ends in the periphery in multiple cell types, akin to that of CLASP (Martínez-López et al., 2005; Muley et al., 2008; van Haren et al., 2009). NAV1 specifically showed a pronounced enrichment in the peripheral zone of growth cones, though other NAVs were not tested (Martínez-López et al., 2005). However, overexpression of NAVs in non-neural cells induced MT bundling in neurite-like extensions, which were reported to resemble paused growth cones. This MT bundling appeared to occur with MT stabilization, as bundles colocalized strongly with acetylated-tubulin enrichment (Martínez-López et al., 2005; van Haren et al., 2009).

This ability to reorganize MTs is more poignant when coupled with the capacity of NAVs to interact with actin and mediate signaling cues. Early studies demonstrated that neurons transfected with NAV1 RNAi were less responsive to attractive Netrin signaling. Separately, the CH-domain within NAV2 *C. elegans* homolog was shown to directly interact with Abelson Interactor (ABI-1), an Abl substrate which functions in WAVE-complex mediated actin remodeling (Schmidt et al., 2009). The NAV2 homolog in *Drosophila* (Sickie) was suggested to promote axon growth by functioning in a non-canonical Rac GTPase pathway which ultimately facilitates Cofilin activation, providing an F-actin "recycling" mechanism to balance forward polymerization (Abe et al., 2014). To add another layer of intricacy, the MT plus-end localization of NAV1 was shown to be instrumental in enhancing the activity of TRIO, a Rho guanine nucleotide exchange factor which activates Rac1 and RhoG (van Haren et al., 2014); providing yet another platform for NAVs to influence actin remodeling within the growth cone.

Conclusion

The growth cone is able to correctly maneuver through a myriad of extracellular cues, leading its axon accurately through the developing nervous system, turning in response to attractive or repulsive stimuli, and halting when it has arrived at the correct destination. The mechanisms by which this responsive cytoskeletal machine is able to detect and then translate numerous guidance signals are largely unknown. Here, we have illustrated how a subset of +TIPs can interact at the interface of these guidance cues to influence cytoskeletal behaviors. A striking theme behind the +TIPs that are characterized thus far in axon elongation and guidance, beyond their ability to undergo phosphorylation downstream of guidance molecules, is a strongly-shared ability to participate in transient MT-F-actin crosslinks or directly modulate F-actin behaviors (**Figure 3**). This ability offers a "missing link" of sorts, between signaling cascades, selective MT stabilization, and interactions that could then potentially impact filopodial and adhesion dynamics. Thus, cross-linking +TIPs can offer a feasible opportunity for mechanical translation of guidance molecules into axonal outgrowth and turning behaviors.

Stories in Progress

It is almost certain that the relatively small list of +TIP modulators of axon guidance that we describe in this review will not be conclusive. We have neglected, for instance, the kinesins, whose roles and identities have expanded as they are seen increasingly to impact MT behaviors. Several kinesin family members interact with EB proteins (Lee et al., 2008; Gumy et al., 2013; Chen et al., 2014b) and demonstrate an effect on axon outgrowth through these +TIP interactions (Gumy et al., 2013). Additionally, kinesin-5 and kinesin-12 families have also shown commanding involvement in growth cone turning (Baas, 1998; Myers and Baas, 2007; Nadar et al., 2008; Liu et al., 2010), though whether an EB interaction is involved in their localization in this context is not known. Separately, CLIP-115 and CLIP-190 have been investigated in many shared examinations with CLIP-170 (Hoogenraad et al., 2000; Akhmanova et al., 2001; Stepanova et al., 2003; Neukirchen and Bradke, 2011; Beaven et al., 2015), but their individual roles in the growth cone are less well-clarified, and may emerge with time. As new +TIPs are frequently being established in a number of systems, it will be necessary to begin to not only consider their individual interactions in axon guidance, but also to examine their interplay with one another.

Additionally, we have described how numerous +TIPs are phosphorylated downstream of signaling molecules. However, it is clear that our current knowledge of these interactions is over-simplified. For example, a number of GSK3 substrates must first be phosphorylated by priming kinases, and these priming events have been shown to affect signal transduction within the growth cone (Uchida et al., 2005; Cole et al., 2006; Hida et al., 2012). Thus, phosphorylation by priming kinases may offer an additional layer of regulation for +TIP-MT-actin interactions. Indeed, phosphorylation of CLASP2 by CDK has been indicated to precede GSK3 activity and consequently regulate plus-end binding during mitosis (Kumar et al., 2012). Determining how multiple signaling cascades and kinase activities can be integrated constructively to designate a +TIP's localization and behavior may be considered an ultimate pursuit within the field.

Future Directions

Previous cell biological examinations of growth cone behavior and MT dynamics have relied on whole cell knockdown and overexpression of singular +TIPs. While these are not without merit, it is reasonable to imagine that these treatments can elicit misleading or heavy-handed compensatory phenotypes or unintended consequences, especially in the diverse cytoskeletal structures represented within the neuron. Micropipette or caged delivery of guidance molecules may be an enticing alternative to induce subtle, localized +TIP modulations, at least where we are appropriately familiar with their downstream effectors. But new options may emerge as photo-manipulatable (i.e., LOV, KillerRed, or SuperNova tagged) proteins are increasingly utilized, which would allow more targeted study of +TIP function (Bulina et al., 2006; Wu et al., 2009; Takemoto et al., 2013). In the guided growth cone, +TIPs must be regulated in a spatially and temporally-restricted manner. An ability to locally activate a +TIP phosphomimetic could allow a more physiologically-relevant way to recapitulate this, enabling investigation of perhaps one of the most pressing questions—how localized +TIP manipulation might induce changes in growth cone turning.

Efforts should also be made to translate what we know of axon guidance *in vitro*, from the familiarity of our substrate-coated coverglass, to 3-D substrates and haptotaxis gradients, as both are capable of inducing significant cytoskeletal remodeling (Santiago-Medina et al., 2015). Findings within these systems may challenge our current models of guidance and MT regulation. There is also the consideration, however, as microscopy evolves to become faster, finer, and brighter, that many systems are already well-situated for *in vivo* work. The ability to track individual growth cones in remarkable resolution through living brain tissue in zebrafish (St John et al., 2013) and frog (Leung and Holt, 2012) has allowed intricate investigations beyond what is possible with stripe assays and chemotaxis gradients. Additionally, MT plus-end dynamics have recently been imaged *in vivo* in mouse peripheral nerves (Kleele et al., 2014). Where *in vivo* imaging may currently fail to illustrate the finer mechanistic associations between MT plus-ends, F-actin, and assorted +TIPs, a nod must be given to critical advances in super resolution techniques (PALM, STORM, STED). As so many of the interactions on the MT plus-end occur below the diffraction limit of standard confocal microscopy, our current understanding of +TIP interactions is based predominantly on their biochemical interactions. Using super resolution microscopy, in addition to techniques such as FRET analyses, may allow us to model the plus-end scaffold in intricate detail, as has been accomplished with other cellular nanostructures (e.g., Kanchanawong et al., 2010). All of these emerging methodologies will provide new mechanistic insights into how the advance, retraction, and turning of the growth cone vehicle can be orchestrated during axon guidance, and how these behaviors are organized downstream of extracellular cues. Central to this, +TIPs have emerged as molecular tour guides that can inform and direct these axonal behaviors, by modulating their interactions with both actin and MT cytoskeletons in response to signaling cascades. It is evident, then, that future works that expand the breadth and depth of +TIP identification, function, and regulation will be instrumental to our understanding of axon guidance behaviors.

Acknowledgments

We thank John Flanagan, Elizabeth McNeill, David Van Vactor, and members of the Lowery lab for helpful discussions and suggestions. LAL is funded by National Institutes of Health R00 MH095768, and EAB is funded by a National Science Foundation Graduate Research Fellowship. Any opinion, findings, and conclusions or recommendations expressed in this material are those of the authors and do not necessarily reflect the views of the National Science Foundation.

References

Abe, T., Yamazaki, D., Murakami, S., Hiroi, M., Nitta, Y., Maeyama, Y., et al. (2014). The NAV2 homolog Sickie regulates F-actin-mediated axonal growth in Drosophila mushroom body neurons via the non-canonical Rac-Cofilin pathway. *Development* 141, 4716–4728. doi: 10.1242/dev.113308

Aitola, M., Sadek, C. M., Gustafsson, J. A., and Pelto-Huikko, M. (2003). Aint/Tacc3 is highly expressed in proliferating mouse tissues during development, spermatogenesis and oogenesis. *J. Histochem. Cytochem.* 51, 455–469. doi: 10.1177/002215540305100407

Akhmanova, A., Hoogenraad, C. C., Drabek, K., Stepanova, T., Dortland, B., Verkerk, T., et al. (2001). Clasps are CLIP-115 and -170 associating proteins involved in the regional regulation of microtubule dynamics in motile fibroblasts. *Cell* 104, 923–935. doi: 10.1016/s0092-8674(01)00288-4

Akhmanova, A., and Steinmetz, M. O. (2008). Tracking the ends: a dynamic protein network controls the fate of microtubule tips. *Nat. Rev. Mol. Cell Biol.* 9, 309–322. doi: 10.1038/nrm2369

Alves-Silva, J., Sánchez-Soriano, N., Beaven, R., Klein, M., Parkin, J., Millard, T. H., et al. (2012). Spectraplakins promote microtubule-mediated axonal growth by functioning as structural microtubule-associated proteins and EB1-dependent +TIPs (tip interacting proteins). *J. Neurosci.* 32, 9143–9158. doi: 10.1523/JNEUROSCI.0416-12.2012

Andersen, S. S. (2000). Spindle assembly and the art of regulating microtubule dynamics by MAPs and Stathmin/Op18. *Trends Cell Biol.* 10, 261–267. doi: 10.1016/s0962-8924(00)01786-4

Baas, P. W. (1998). The role of motor proteins in establishing the microtubule arrays of axons and dendrites. *J. Chem. Neuroanat.* 14, 175–180. doi: 10.1016/s0891-0618(98)00012-x

Bashaw, G. J., Kidd, T., Murray, D., Pawson, T., and Goodman, C. S. (2000). Repulsive axon guidance: Abelson and enabled play opposing roles downstream of the roundabout receptor. *Cell* 101, 703–715. doi: 10.1016/S0092-8674(00)80883-1

Beaven, R., Dzhindzhev, N. S., Qu, Y., Hahn, I., Dajas-Bailador, F., Ohkura, H., et al. (2015). Drosophila CLIP-190 and mammalian CLIP-170 display reduced microtubule plus end association in the nervous system. *Mol. Biol. Cell* 26, 1491–1508. doi: 10.1091/mbc.E14-06-1083

Bhat, R. V., Baraban, J. M., Johnson, R. C., Eipper, B. A., and Mains, R. E. (1994). High levels of expression of the tumor suppressor gene APC during development of the rat central nervous system. *J. Neurosci.* 14, 3059–3071.

Bieling, P., Laan, L., Schek, H., Munteanu, E. L., Sandblad, L., Dogterom, M., et al. (2007). Reconstitution of a microtubule plus-end tracking system *in vitro*. *Nature* 450, 1100–1105. doi: 10.1038/nature06386

Brouhard, G. J., Stear, J. H., Noetzel, T. L., Al-Bassam, J., Kinoshita, K., Harrison, S. C., et al. (2008). XMAP215 is a processive microtubule polymerase. *Cell* 132, 79–88. doi: 10.1016/j.cell.2007.11.043

Buck, K. B., and Zheng, J. Q. (2002). Growth cone turning induced by direct local modification of microtubule dynamics. *J. Neurosci.* 22, 9358–9367.

Bulina, M. E., Chudakov, D. M., Britanova, O. V., Yanushevich, Y. G., Staroverov, D. B., Chepurnykh, T. V., et al. (2006). A genetically encoded photosensitizer. *Nat. Biotechnol.* 24, 95–99. doi: 10.1038/nbt1175

Charrasse, S., Coubes, P., Arrancibia, S., and Larroque, C. (1996). Expression of the tumor over-expressed ch-TOG gene in human and baboon brain. *Neurosci. Lett.* 212, 119–122. doi: 10.1016/0304-3940(96)12789-0

Chen, C. H., Lee, A., Liao, C. P., Liu, Y. W., and Pan, C. L. (2014a). RHGF-1/PDZ-RhoGEF and retrograde DLK-1 signaling drive neuronal remodeling on microtubule disassembly. *Proc. Natl. Acad. Sci. U S A* 111, 16568–16573. doi: 10.1073/pnas.1410263111

Chen, Y., Rolls, M. M., and Hancock, W. O. (2014b). An EB1-kinesin complex is sufficient to steer microtubule growth *in vitro*. *Curr. Biol.* 24, 316–321. doi: 10.1016/j.cub.2013.11.024

Cole, A. R., Causeret, F., Yadirgi, G., Hastie, C. J., McLauchlan, H., McManus, E. J., et al. (2006). Distinct priming kinases contribute to differential regulation of collapsin response mediator proteins by glycogen synthase kinase-3 *in vivo*. *J. Biol. Chem.* 281, 16591–16598. doi: 10.1074/jbc.m513344200

Coy, J. F., Wiemann, S., Bechmann, I., Bächner, D., Nitsch, R., Kretz, O., et al. (2002). Pore membrane and/or filament interacting like protein 1 (POMFIL1) is predominantly expressed in the nervous system and encodes different protein isoforms. *Gene* 290, 73–94. doi: 10.1016/s0378-1119(02)00567-x

Dent, E. W., Gupton, S. L., and Gertler, F. B. (2011). The growth cone cytoskeleton in axon outgrowth and guidance. *Cold Spring Harb. Perspect. Biol.* 3:a001800. doi: 10.1101/cshperspect.a001800

Dobashi, Y., Katayama, K., Kawai, M., Akiyama, T., and Kameya, T. (2000). APC protein is required for initiation of neuronal differentiation in rat pheochromocytoma PC12 cells. *Biochem. Biophys. Res. Commun.* 279, 685–691. doi: 10.1006/bbrc.2000.4015

Drabek, K., van Ham, M., Stepanova, T., Draegestein, K., van Horssen, R., Sayas, C. L., et al. (2006). Role of CLASP2 in microtubule stabilization and the regulation of persistent motility. *Curr. Biol.* 16, 2259–2264. doi: 10.1016/j.cub.2006.09.065

Engel, U., Zhan, Y., Long, J. B., Boyle, S. N., Ballif, B. A., Dorey, K., et al. (2014). Abelson phosphorylation of CLASP2 modulates its association with microtubules and actin. *Cytoskeleton (Hoboken)* 71, 195–209. doi: 10.1002/cm.21164

Eom, T. Y., Stanco, A., Guo, J., Wilkins, G., Deslauriers, D., Yan, J., et al. (2014). Differential regulation of microtubule severing by APC underlies distinct patterns of projection neuron and interneuron migration. *Dev. Cell* 31, 677–689. doi: 10.1016/j.devcel.2014.11.022

Fuchs, E., and Karakesisoglou, I. (2001). Bridging cytoskeletal intersections. *Genes Dev.* 15, 1–14. doi: 10.1101/gad.861501

Fukata, M., Watanabe, T., Noritake, J., Nakagawa, M., Yamaga, M., Kuroda, S., et al. (2002). Rac1 and Cdc42 capture microtubules through IQGAP1 and CLIP-170. *Cell* 109, 873–885. doi: 10.1016/s0092-8674(02)00800-0

Galjart, N. (2005). CLIPs and CLASPs and cellular dynamics. *Nat. Rev. Mol. Cell Biol.* 6, 487–498. doi: 10.1038/nrm1664

Gard, D. L., and Kirschner, M. W. (1987). A microtubule-associated protein from Xenopus eggs that specifically promotes assembly at the plus-end. *J. Cell Biol.* 105, 2203–2215. doi: 10.1083/jcb.105.5.2203

Geraldo, S., and Gordon-Weeks, P. R. (2009). Cytoskeletal dynamics in growth-cone steering. *J. Cell Sci.* 122, 3595–3604. doi: 10.1242/jcs.042309

Geraldo, S., Khanzada, U. K., Parsons, M., Chilton, J. K., and Gordon-Weeks, P. R. (2008). Targeting of the F-actin-binding protein drebrin by the microtubule plus-tip protein EB3 is required for neuritogenesis. *Nat. Cell Biol.* 10, 1181–1189. doi: 10.1038/ncb1778

Gergely, F., Draviam, V. M., and Raff, J. W. (2003). The ch-TOG/XMAP215 protein is essential for spindle pole organization in human somatic cells. *Genes Dev.* 17, 336–341. doi: 10.1101/gad.245603

Gertler, F. B., Comer, A. R., Juang, J. L., Ahern, S. M., Clark, M. J., Liebl, E. C., et al. (1995). enabled, a dosage-sensitive suppressor of mutations in the Drosophila Abl tyrosine kinase, encodes an Abl substrate with SH3 domain-binding properties. *Genes Dev.* 9, 521–533. doi: 10.1101/gad.9.5.521

Goold, R. G., Owen, R., and Gordon-Weeks, P. R. (1999). Glycogen synthase kinase 3beta phosphorylation of microtubule-associated protein 1B regulates the stability of microtubules in growth cones. *J. Cell Sci.* 112, 3373–3384.

Gumy, L. F., Chew, D. J., Tortosa, E., Katrukha, E. A., Kapitein, L. C., Tolkovsky, A. M., et al. (2013). The kinesin-2 family member KIF3C regulates microtubule dynamics and is required for axon growth and regeneration. *J. Neurosci.* 33, 11329–11345. doi: 10.1523/JNEUROSCI.5221-12.2013

Hedgecock, E. M., Culotti, J. G., Hall, D. H., and Stern, B. D. (1987). Genetics of cell and axon migrations in Caenorhabditis elegans. *Development* 100, 365–382.

Hida, T., Yamashita, N., Usui, H., Nakamura, F., Sasaki, Y., Kikuchi, A., et al. (2012). GSK3β/axin-1/β-catenin complex is involved in semaphorin3A signaling. *J. Neurosci.* 32, 11905–11918. doi: 10.1523/JNEUROSCI.6139-11.2012

Honnappa, S., Gouveia, S. M., Weisbrich, A., Damberger, F. F., Bhavesh, N. S., Jawhari, H., et al. (2009). An EB1-binding motif acts as a microtubule tip localization signal. *Cell* 138, 366–376. doi: 10.1016/j.cell.2009.04.065

Hoogenraad, C. C., Akhmanova, A., Grosveld, F., De Zeeuw, C. I., and Galjart, N. (2000). Functional analysis of CLIP-115 and its binding to microtubules. *J. Cell Sci.* 113, 2285–2297.

Horwitz, R., and Webb, D. (2003). Cell migration. *Curr. Biol.* 13, R756–R759. doi: 10.1016/j.cub.2003.09.014

Hur, E. M., Saijilafu, H., Lee, B. D., Kim, S. J., Xu, W. L., and Zhou, F. Q. (2011). GSK3 controls axon growth via CLASP-mediated regulation of growth cone microtubules. *Genes Dev.* 25, 1968–1981. doi: 10.1101/gad.17015911

Hur, E. M., Saijilafu, H., and Zhou, F. Q. (2012). Growing the growth cone: remodeling the cytoskeleton to promote axon regeneration. *Trends Neurosci.* 35, 164–174. doi: 10.1016/j.tins.2011.11.002

Ishiguro, H., Shimokawa, T., Tsunoda, T., Tanaka, T., Fujii, Y., Nakamura, Y., et al. (2002). Isolation of HELAD1, a novel human helicase gene up-regulated in colorectal carcinomas. *Oncogene* 21, 6387–6394. doi: 10.1038/sj.onc.1205751

Kanchanawong, P., Shtengel, G., Pasapera, A. M., Ramko, E. B., Davidson, M. W., Hess, H. F., et al. (2010). Nanoscale architecture of integrin-based cell adhesions. *Nature* 468, 580–584. doi: 10.1038/nature09621

Kleele, T., Marinković, P., Williams, P. R., Stern, S., Weigand, E. E., Engerer, P., et al. (2014). An assay to image neuronal microtubule dynamics in mice. *Nat. Commun.* 5:4827. doi: 10.1038/ncomms5827

Koester, M. P., Müller, O., and Pollerberg, G. E. (2007). Adenomatous polyposis coli is differentially distributed in growth cones and modulates their steering. *J. Neurosci.* 27, 12590–12600. doi: 10.1523/jneurosci.2250-07.2007

Kumar, P., Chimenti, M. S., Pemble, H., Schönichen, A., Thompson, O., Jacobson, M. P., et al. (2012). Multisite phosphorylation disrupts arginine-glutamate salt bridge networks required for binding of cytoplasmic linker-associated protein 2 (CLASP2) to end-binding protein 1 (EB1). *J. Biol. Chem.* 287, 17050–17064. doi: 10.1074/jbc.M111.316661

Kumar, P., Lyle, K. S., Gierke, S., Matov, A., Danuser, G., and Wittmann, T. (2009). GSK3beta phosphorylation modulates CLASP-microtubule association and lamella microtubule attachment. *J. Cell Biol.* 184, 895–908. doi: 10.1083/jcb.200901042

Lee, H., Engel, U., Rusch, J., Scherrer, S., Sheard, K., and Van Vactor, D. (2004). The microtubule plus end tracking protein Orbit/MAST/CLASP acts downstream of the tyrosine kinase Abl in mediating axon guidance. *Neuron* 42, 913–926. doi: 10.1016/j.neuron.2004.05.020

Lee, M. J., Gergely, F., Jeffers, K., Peak-Chew, S. Y., and Raff, J. W. (2001). Msps/XMAP215 interacts with the centrosomal protein D-TACC to regulate microtubule behaviour. *Nat. Cell Biol.* 3, 643–649. doi: 10.1038/35083033

Lee, S., and Kolodziej, P. A. (2002). Short stop provides an essential link between F-actin and microtubules during axon extension. *Development* 129, 1195–1204.

Lee, T., Langford, K. J., Askham, J. M., Brüning-Richardson, A., and Morrison, E. E. (2008). MCAK associates with EB1. *Oncogene* 27, 2494–2500. doi: 10.1038/sj.onc.1210867

Lee, A. C., and Suter, D. M. (2008). Quantitative analysis of microtubule dynamics during adhesion-mediated growth cone guidance. *Dev. Neurobiol.* 68, 1363–1377. doi: 10.1002/dneu.20662

Lemos, C. L., Sampaio, P., Maiato, H., Costa, M., Omel'yanchuk, L. V., Liberal, V., et al. (2000). Mast, a conserved microtubule-associated protein required for bipolar mitotic spindle organization. *EMBO J.* 19, 3668–3682. doi: 10.1093/emboj/19.14.3668

Leung, L., and Holt, C. E. (2012). Imaging axon pathfinding in Xenopus *in vivo*. *Cold Spring Harb. Protoc.* 2012, 984–991. doi: 10.1101/pdb.prot070003

Leung, C. L., Sun, D., Zheng, M., Knowles, D. R., and Liem, R. K. (1999). Microtubule actin cross-linking factor (MACF): a hybrid of dystonin and dystrophin that can interact with the actin and microtubule cytoskeletons. *J. Cell Biol.* 147, 1275–1286. doi: 10.1083/jcb.147.6.1275

Li, Z., Kroboth, K., Newton, I. P., and Näthke, I. S. (2008). Novel self-association of the APC molecule affects APC clusters and cell migration. *J. Cell Sci.* 121, 1916–1925. doi: 10.1242/jcs.029470

Lin, T. Y., Huang, C. H., Kao, H. H., Liou, G. G., Yeh, S. R., Cheng, C. M., et al. (2009). Abi plays an opposing role to Abl in Drosophila axonogenesis and synaptogenesis. *Development* 136, 3099–3107. doi: 10.1242/dev.033324

Lioutas, A., and Vernos, I. (2013). Aurora A kinase and its substrate TACC3 are required for central spindle assembly. *EMBO Rep.* 14, 829–836. doi: 10.1038/embor.2013.109

Liu, M., Nadar, V. C., Kozielski, F., Kozlowska, M., Yu, W., and Baas, P. W. (2010). Kinesin-12, a mitotic microtubule-associated motor protein, impacts axonal growth, navigation and branching. *J. Neurosci.* 30, 14896–14906. doi: 10.1523/JNEUROSCI.3739-10.2010

Long, J. B., Bagonis, M., Lowery, L. A., Lee, H., Danuser, G., and Van Vactor, D. (2013). Multiparametric analysis of CLASP-interacting protein functions during interphase microtubule dynamics. *Mol. Cell Biol.* 33, 1528–1545. doi: 10.1128/MCB.01442-12

Lovestone, S., Reynolds, C. H., Latimer, D., Davis, D. R., Anderton, B. H., Gallo, J. M., et al. (1994). Alzheimer's disease-like phosphorylation of the microtubule-associated protein tau by glycogen synthase kinase-3 in transfected mammalian cells. *Curr. Biol.* 4, 1077–1086. doi: 10.1016/s0960-9822(00)00246-3

Lowery, L. A., Lee, H., Lu, C., Murphy, R., Obar, R. A., Zhai, B., et al. (2010). Parallel genetic and proteomic screens identify Msps as a CLASP-Abl pathway interactor in Drosophila. *Genetics* 185, 1311–1325. doi: 10.1534/genetics.110.115626

Lowery, L. A., Stout, A., Faris, A. E., Ding, L., Baird, M. A., Davidson, M. W., et al. (2013). Growth cone-specific functions of XMAP215 in restricting microtubule dynamics and promoting axonal outgrowth. *Neural Dev.* 8:22. doi: 10.1186/1749-8104-8-22

Lowery, L. A., and Van Vactor, D. (2009). The trip of the tip: understanding the growth cone machinery. *Nat. Rev. Mol. Cell Biol.* 10, 332–343. doi: 10.1038/nrm2679

Lu, W., Fox, P., Lakonishok, M., Davidson, M. W., and Gelfand, V. I. (2013). Initial neurite outgrowth in Drosophila neurons is driven by kinesin-powered microtubule sliding. *Curr. Biol.* 23, 1018–1023. doi: 10.1016/j.cub.2013.04.050

Lu, W., Lakonishok, M., and Gelfand, V. I. (2015). Kinesin-1-powered microtubule sliding initiates axonal regeneration in *Drosophila* cultured neurons. *Mol. Biol. Cell* 26, 1296–1307. doi: 10.1091/mbc.E14-10-1423

Machacek, M., Hodgson, L., Welch, C., Elliott, H., Pertz, O., Nalbant, P., et al. (2009). Coordination of Rho GTPase activities during cell protrusion. *Nature* 461, 99–103. doi: 10.1038/nature08242

Maes, T., Barceló, A., and Buesa, C. (2002). Neuron navigator: a human gene family with homology to unc-53, a cell guidance gene from Caenorhabditis elegans. *Genomics* 80, 21–30. doi: 10.1006/geno.2002.6799

Martínez-López, M. J., Alcántara, S., Mascaró, C., Pérez-Branguli, F., Ruiz-Lozano, P., Maes, T., et al. (2005). Mouse neuron navigator 1, a novel microtubule-associated protein involved in neuronal migration. *Mol. Cell Neurosci.* 28, 599–612. doi: 10.1016/j.mcn.2004.09.016

Marx, A., Godinez, W. J., Tsimashchuk, V., Bankhead, P., Rohr, K., and Engel, U. (2013). Xenopus cytoplasmic linker-associated protein 1 (XCLASP1) promotes axon elongation and advance of pioneer microtubules. *Mol. Biol. Cell* 24, 1544–1558. doi: 10.1091/mbc.E12-08-0573

Maurer, S. P., Cade, N. I., Bohner, G., Gustafsson, N., Boutant, E., and Surrey, T. (2014). EB1 accelerates two conformational transitions important for microtubule maturation and dynamics. *Curr. Biol.* 24, 372–384. doi: 10.1016/j.cub.2013.12.042

Merrill, R. A., Plum, L. A., Kaiser, M. E., and Clagett-Dame, M. (2002). A mammalian homolog of unc-53 is regulated by all-trans retinoic acid in neuroblastoma cells and embryos. *Proc. Natl. Acad. Sci. U S A* 99, 3422–3427. doi: 10.1073/pnas.052017399

Mohn, J. L., Alexander, J., Pirone, A., Palka, C. D., Lee, S. Y., Mebane, L., et al. (2014). Adenomatous polyposis coli protein deletion leads to cognitive and autism-like disabilities. *Mol. Psychiatry* 19, 1133–1142. doi: 10.1038/mp.2014.61

Muley, P. D., McNeill, E. M., Marzinke, M. A., Knobel, K. M., Barr, M. M., and Clagett-Dame, M. (2008). The atRA-responsive gene neuron navigator 2 functions in neurite outgrowth and axonal elongation. *Dev. Neurobiol.* 68, 1441–1453. doi: 10.1002/dneu.20670

Myers, K. A., and Baas, P. W. (2007). Kinesin-5 regulates the growth of the axon by acting as a brake on its microtubule array. *J. Cell Biol.* 178, 1081–1091. doi: 10.1083/jcb.200702074

Myers, K. A., Tint, I., Nadar, C. V., He, Y., Black, M. M., and Baas, P. W. (2006). Antagonistic forces generated by cytoplasmic dynein and myosin-II during growth cone turning and axonal retraction. *Traffic* 7, 1333–1351. doi: 10.1111/j.1600-0854.2006.00476.x

Nadar, V. C., Ketschek, A., Myers, K. A., Gallo, G., and Baas, P. W. (2008). Kinesin-5 is essential for growth-cone turning. *Curr. Biol.* 18, 1972–1977. doi: 10.1016/j.cub.2008.11.021

Neukirchen, D., and Bradke, F. (2011). Cytoplasmic linker proteins regulate neuronal polarization through microtubule and growth cone dynamics. *J. Neurosci.* 31, 1528–1538. doi: 10.1523/JNEUROSCI.3983-10.2011

Nwagbara, B. U., Faris, A. E., Bearce, E. A., Erdogan, B., Ebbert, P. T., Evans, M. F., et al. (2014). TACC3 is a microtubule plus end-tracking protein that promotes axon elongation and also regulates microtubule plus end dynamics in multiple embryonic cell types. *Mol. Biol. Cell* 25, 3350–3362. doi: 10.1091/mbc.E14-06-1121

Onouchi, T., Kobayashi, K., Sakai, K., Shimomura, A., Smits, R., Sumi-Ichinose, C., et al. (2014). Targeted deletion of the C-terminus of the mouse adenomatous polyposis coli tumor suppressor results in neurologic phenotypes related to schizophrenia. *Mol. Brain* 7:21. doi: 10.1186/1756-6606-7-21

Owen, R., and Gordon-Weeks, P. R. (2003). Inhibition of glycogen synthase kinase 3beta in sensory neurons in culture alters filopodia dynamics and microtubule distribution in growth cones. *Mol. Cell Neurosci.* 23, 626–637. doi: 10.1016/s1044-7431(03)00095-2

Peset, I., and Vernos, I. (2008). The TACC proteins: TACC-ling microtubule dynamics and centrosome function. *Trends Cell Biol.* 18, 379–388. doi: 10.1016/j.tcb.2008.06.005

Piekorz, R. P., Hoffmeyer, A., Duntsch, C. D., McKay, C., Nakajima, H., Sexl, V., et al. (2002). The centrosomal protein TACC3 is essential for hematopoietic stem cell function and genetically interfaces with p53-regulated apoptosis. *EMBO J.* 21, 653–664. doi: 10.1093/emboj/21.4.653

Pierre, P., Scheel, J., Rickard, J. E., and Kreis, T. E. (1992). CLIP-170 links endocytic vesicles to microtubules. *Cell* 70, 887–900. doi: 10.1016/0092-8674(92)90240-d

Podolski, M., Mahamdeh, M., and Howard, J. (2014). Stu2, the budding yeast XMAP215/Dis1 homolog, promotes assembly of yeast microtubules by increasing growth rate and decreasing catastrophe frequency. *J. Biol. Chem.* 289, 28087–28093. doi: 10.1074/jbc.M114.584300

Preitner, N., Quan, J., Nowakowski, D. W., Hancock, M. L., Shi, J., Tcherkezian, J., et al. (2014). APC is an RNA-binding protein and its interactome provides a link to neural development and microtubule assembly. *Cell* 158, 368–382. doi: 10.1016/j.cell.2014.05.042

Purro, S. A., Ciani, L., Hoyos-Flight, M., Stamatakou, E., Siomou, E., and Salinas, P. C. (2008). Wnt regulates axon behavior through changes in microtubule growth directionality: a new role for adenomatous polyposis coli. *J. Neurosci.* 28, 8644–8654. doi: 10.1523/JNEUROSCI.2320-08.2008

Rusan, N. M., Akong, K., and Peifer, M. (2008). Putting the model to the test: are APC proteins essential for neuronal polarity, axon outgrowth and axon targeting? *J. Cell Biol.* 183, 203–212. doi: 10.1083/jcb.200807079

Sabry, J. H., O'connor, T. P., Evans, L., Toroian-Raymond, A., Kirschner, M., and Bentley, D. (1991). Microtubule behavior during guidance of pioneer neuron growth cones *in situ*. *J. Cell Biol.* 115, 381–395. doi: 10.1083/jcb.115.2.381

Santiago-Medina, M., Gregus, K. A., Nichol, R. H., O'toole, S. M., and Gomez, T. M. (2015). Regulation of ECM degradation and axon guidance by growth cone invadosomes. *Development* 142, 486–496. doi: 10.1242/dev.108266

Sayas, C. L., and Avila, J. (2014). Regulation of EB1/3 proteins by classical MAPs in neurons. *Bioarchitecture* 4, 1–5. doi: 10.4161/bioa.27774

Schaefer, A. W., Kabir, N., and Forscher, P. (2002). Filopodia and actin arcs guide the assembly and transport of two populations of microtubules with unique dynamic parameters in neuronal growth cones. *J. Cell Biol.* 158, 139–152. doi: 10.1083/jcb.200203038

Schaefer, A. W., Schoonderwoert, V. T., Ji, L., Mederios, N., Danuser, G., and Forscher, P. (2008). Coordination of actin filament and microtubule dynamics during neurite outgrowth. *Dev. Cell* 15, 146–162. doi: 10.1016/j.devcel.2008.05.003

Schmidt, K. L., Marcus-Gueret, N., Adeleye, A., Webber, J., Baillie, D., and Stringham, E. G. (2009). The cell migration molecule UNC-53/NAV2 is linked to the ARP2/3 complex by ABI-1. *Development* 136, 563–574. doi: 10.1242/dev.016816

Shi, S. H., Cheng, T., Jan, L. Y., and Jan, Y. N. (2004). APC and GSK-3beta are involved in mPar3 targeting to the nascent axon and establishment of neuronal polarity. *Curr. Biol.* 14, 2025–2032. doi: 10.3410/f.1024916.294704

Smith, K. J., Levy, D. B., Maupin, P., Pollard, T. D., Vogelstein, B., and Kinzler, K. W. (1994). Wild-type but not mutant APC associates with the microtubule cytoskeleton. *Cancer Res.* 54, 3672–3675.

Stepanova, T., Slemmer, J., Hoogenraad, C. C., Lansbergen, G., Dortland, B., De Zeeuw, C. I., et al. (2003). Visualization of microtubule growth in cultured neurons via the use of EB3-GFP (end-binding protein 3-green fluorescent protein). *J. Neurosci.* 23, 2655–2664. doi: 10.3410/f.1015054.195569

Stepanova, T., Smal, I., van Haren, J., Akinci, U., Liu, Z., Miedema, M., et al. (2010). History-dependent catastrophes regulate axonal microtubule behavior. *Curr. Biol.* 20, 1023–1028. doi: 10.1016/j.cub.2010.04.024

St John, J. A., Scott, S., Chua, K. Y., Claxton, C., and Key, B. (2013). Growth cone dynamics in the zebrafish embryonic forebrain are regulated by brother of Cdo. *Neurosci. Lett.* 545, 11–16. doi: 10.1016/j.neulet.2013.04.009

Stout, A., D'Amico, S., Enzenbacher, T., Ebbert, P., and Lowery, L. A. (2014). Using plusTipTracker software to measure microtubule dynamics in Xenopus laevis growth cones. *J. Vis. Exp.* 91:e52138. doi: 10.3791/52138

Stringham, E., Pujol, N., Vandekerckhove, J., and Bogaert, T. (2002). unc-53 controls longitudinal migration in C. elegans. *Development* 129, 3367–3379. doi: 10.3410/f.1007456.93808

Su, L. K., Burrell, M., Hill, D. E., Gyuris, J., Brent, R., Wiltshire, R., et al. (1995). APC binds to the novel protein EB1. *Cancer Res.* 55, 2972–2977.

Suozzi, K. C., Wu, X., and Fuchs, E. (2012). Spectraplakins: master orchestrators of cytoskeletal dynamics. *J. Cell Biol.* 197, 465–475. doi: 10.1083/jcb.201112034

Swiech, L., Blazejczyk, M., Urbanska, M., Pietruszka, P., Dortland, B. R., Malik, A. R., et al. (2011). CLIP-170 and IQGAP1 cooperatively regulate dendrite morphology. *J. Neurosci.* 31, 4555–4568. doi: 10.1523/jneurosci.6582-10.2011

Takemoto, K., Matsuda, T., Sakai, N., Fu, D., Noda, M., Uchiyama, S., et al. (2013). SuperNova, a monomeric photosensitizing fluorescent protein for chromophore-assisted light inactivation. *Sci Rep.* 3:2629. doi: 10.1038/srep02629

Tanaka, E., Ho, T., and Kirschner, M. W. (1995). The role of microtubule dynamics in growth cone motility and axonal growth. *J. Cell Biol.* 128, 139–155. doi: 10.1083/jcb.128.1.139

Tedeschi, A., and Bradke, F. (2013). The DLK signalling pathway—a double-edged sword in neural development and regeneration. *EMBO Rep.* 14, 605–614. doi: 10.1038/embor.2013.64

Thakur, H. C., Singh, M., Nagel-Steger, L., Kremer, J., Prumbaum, D., Fansa, E. K., et al. (2014). The centrosomal adaptor TACC3 and the microtubule polymerase chTOG interact via defined C-terminal subdomains in an Aurora-A kinase-independent manner. *J. Biol. Chem.* 289, 74–88. doi: 10.1074/jbc.m113.532333

Tortosa, E., Galjart, N., Avila, J., and Sayas, C. L. (2013). MAP1B regulates microtubule dynamics by sequestering EB1/3 in the cytosol of developing neuronal cells. *EMBO J.* 32, 1293–1306. doi: 10.1038/emboj.2013.76

Tsvetkov, A. S., Samsonov, A., Akhmanova, A., Galjart, N., and Popov, S. V. (2007). Microtubule-binding proteins CLASP1 and CLASP2 interact with actin filaments. *Cell Motil. Cytoskeleton* 64, 519–530. doi: 10.1002/cm.20201

Uchida, Y., Ohshima, T., Sasaki, Y., Suzuki, H., Yanai, S., Yamashita, N., et al. (2005). Semaphorin3A signalling is mediated via sequential Cdk5 and GSK3beta phosphorylation of CRMP2: implication of common phosphorylating mechanism underlying axon guidance and Alzheimer's disease. *Genes Cells* 10, 165–179. doi: 10.1111/j.1365-2443.2005.00827.x

Vactor, D. V., Sink, H., Fambrough, D., Tsoo, R., and Goodman, C. S. (1993). Genes that control neuromuscular specificity in Drosophila. *Cell* 73, 1137–1153. doi: 10.1016/0092-8674(93)90643-5

Valakh, V., Frey, E., Babetto, E., Walker, L. J., and DiAntonio, A. (2015). Cytoskeletal disruption activates the DLK/JNK pathway, which promotes axonal regeneration and mimics a preconditioning injury. *Neurobiol. Dis.* 77, 13–25. doi: 10.1016/j.nbd.2015.02.014

Valakh, V., Walker, L. J., Skeath, J. B., and DiAntonio, A. (2013). Loss of the spectraplakin short stop activates the DLK injury response pathway in Drosophila. *J. Neurosci.* 33, 17863–17873. doi: 10.1523/jneurosci.2196-13.2013

van der Vaart, B., Franker, M. A., Kuijpers, M., Hua, S., Bouchet, B. P., Jiang, K., et al. (2012). Microtubule plus-end tracking proteins SLAIN1/2 and ch-TOG promote axonal development. *J. Neurosci.* 32, 14722–14728. doi: 10.1523/jneurosci.1240-12.2012

van Haren, J., Boudeau, J., Schmidt, S., Basu, S., Liu, Z., Lammers, D., et al. (2014). Dynamic microtubules catalyze formation of navigator-TRIO complexes to regulate neurite extension. *Curr. Biol.* 24, 1778–1785. doi: 10.1016/j.cub.2014.06.037

van Haren, J., Draegestein, K., Keijzer, N., Abrahams, J. P., Grosveld, F., Peeters, P. J., et al. (2009). Mammalian navigators are microtubule plus-end tracking proteins that can reorganize the cytoskeleton to induce neurite-like extensions. *Cell Motil. Cytoskeleton* 66, 824–838. doi: 10.1002/cm.20370

White, R. L. (1997). Colon cancer. Molecular biology of the APC protein. *Pathol. Biol. (Paris)* 45, 240–244.

Wills, Z., Bateman, J., Korey, C. A., Comer, A., and Van Vactor, D. (1999). The tyrosine kinase Abl and its substrate enabled collaborate with the receptor phosphatase Dlar to control motor axon guidance. *Neuron* 22, 301–312. doi: 10.1016/s0896-6273(00)81091-0

Wittmann, T., and Waterman-Storer, C. M. (2005). Spatial regulation of CLASP affinity for microtubules by Rac1 and GSK3beta in migrating epithelial cells. *J. Cell Biol.* 169, 929–939. doi: 10.1083/jcb.200412114

Wu, Y. I., Frey, D., Lungu, O. I., Jaehrig, A., Schlichting, I., Kuhlman, B., et al. (2009). A genetically encoded photoactivatable Rac controls the motility of living cells. *Nature* 461, 104–108. doi: 10.1038/nature08241

Wu, X., Shen, Q. T., Oristian, D. S., Lu, C. P., Zheng, Q., Wang, H. W., et al. (2011). Skin stem cells orchestrate directional migration by regulating microtubule-ACF7 connections through GSK3β. *Cell* 144, 341–352. doi: 10.1016/j.cell.2010.12.033

Zhou, F. Q., Zhou, J., Dedhar, S., Wu, Y. H., and Snider, W. D. (2004). NGF-induced axon growth is mediated by localized inactivation of GSK-3beta and functions of the microtubule plus end binding protein APC. *Neuron* 42, 897–912. doi: 10.3410/f.1019966.227514

Zumbrunn, J., Kinoshita, K., Hyman, A. A., and Näthke, I. S. (2001). Binding of the adenomatous polyposis coli protein to microtubules increases microtubule stability and is regulated by GSK3 beta phosphorylation. *Curr. Biol.* 11, 44–49. doi: 10.1016/s0960-9822(01)00002-1

Conflict of Interest Statement: The authors declare that the research was conducted in the absence of any commercial or financial relationships that could be construed as a potential conflict of interest.

frontiers
in Cellular Neuroscience

REVIEW
published: 07 July 2015
doi: 10.3389/fncel.2015.00244

Mechanochemical regulation of growth cone motility

Patrick C. Kerstein, Robert H. Nichol IV and Timothy M. Gomez*

Neuroscience Training Program, Department of Neuroscience, School of Medicine and Public Health, University of Wisconsin-Madison, Madison, WI, USA

Neuronal growth cones are exquisite sensory-motor machines capable of transducing features contacted in their local extracellular environment into guided process extension during development. Extensive research has shown that chemical ligands activate cell surface receptors on growth cones leading to intracellular signals that direct cytoskeletal changes. However, the environment also provides mechanical support for growth cone adhesion and traction forces that stabilize leading edge protrusions. Interestingly, recent work suggests that both the mechanical properties of the environment and mechanical forces generated within growth cones influence axon guidance. In this review we discuss novel molecular mechanisms involved in growth cone force production and detection, and speculate how these processes may be necessary for the development of proper neuronal morphogenesis.

Keywords: mechanotransduction, axon guidance, TRP channels, substrate rigidity, durotaxis, actin retrograde flow, neuron

Edited by:
Daniel Marcel Suter,
Purdue University, USA

Reviewed by:
Laura Anne Lowery,
Boston College, USA
Stephanie L. Gupton,
University of North Carolina at Chapel Hill, USA

****Correspondence:***
Timothy M. Gomez,
Neuroscience Training Program,
Department of Neuroscience, School of Medicine and Public Health,
University of Wisconsin-Madison,
1111 Highland Avenue, Madison,
WI 53705, USA
tmgomez@wisc.edu

Received: *08 May 2015*
Accepted: *16 June 2015*
Published: *07 July 2015*

Citation:
Kerstein PC, Nichol RH IV and Gomez TM (2015) Mechanochemical regulation of growth cone motility. Front. Cell. Neurosci. 9:244. doi: 10.3389/fncel.2015.00244

Biochemical and Mechanical Signal Cross-talk in Growth Cones

The last two decades of intensive research have identified many families of chemical ligands and corresponding receptors that are required for proper neural network assembly during embryonic development (for review, see Chèdotal and Richards, 2010; Kolodkin and Tessier-Lavigne, 2011). Previous studies in several animal models clearly demonstrate that graded chemical ligands deposited in the environment of developing neurons serve as navigational cues that guide neuronal migration and morphogenesis. Soluble, cell surface and substratum-associated extracellular ligands are known to activate receptors linked to numerous intracellular biochemical signal transduction cascades that regulate motility. Most biochemical signals effect cytoskeletal dynamics and membrane trafficking directly, or indirectly through new protein translation, to control growth cone motility (Vitriol and Zheng, 2012; Shigeoka et al., 2013). Receptors on growth cones for growth factors, guidance cues and adhesive ligands activate signals that both promote and inhibit motility. A diverse and complex web of interacting biochemical signals are activated by individual ligands. Signaling is further complicated *in vivo*, where multiple ligands are encountered concurrently and signals are integrated by growth cones and converted into a proper behavioral output (Dudanova and Klein, 2013).

While chemical cues in the environment quite clearly have complex and varied effects on intracellular signaling, new work shows that the mechanical properties of the cellular micro-environment of developing neurons also influence signaling and motility. Immobilized ligands on cell surfaces or secreted into the extracellular environment provide adhesive support for migrating cells. Cell surface receptors physically link to immobilized ligands with varying affinities (Myers et al., 2011; Hynes and Naba, 2012). Molecular adaptor proteins link receptors to rigid cytoskeletal elements that generate opposing forces. Classic studies showed that growing axons produce both contractile (myosin motor driven) and pushing (cytoskeleton polymerization) forces (Letourneau et al., 1987; Lamoureux et al., 1989; Heidemann et al., 1990). These forces are known to reciprocally influence cell signaling as a feedback homeostatic regulator of cell adhesion, shape and movements. Therefore, there is likely complex cross talk between biochemical and mechanical signaling within motile growth cones. In this review, we discuss our current understanding on roles of the mechanical environment and intracellular forces that govern axon guidance.

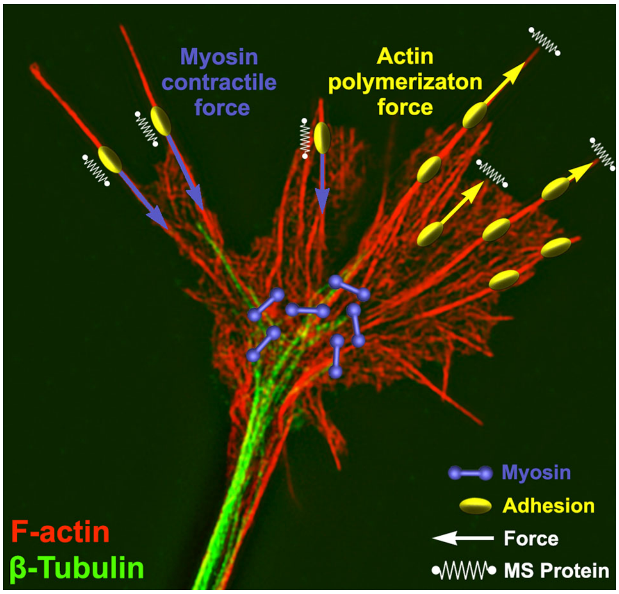

FIGURE 1 | Force generation and force sensing in neuronal growth cones. A neuronal growth cone is labeled for filamentous actin (red) and βI-II tubulin (green) using immunocytochemistry. This super resolution image was captured using structure illumination microscopy as previously described (Santiago-Medina et al., 2015). Overlaying the image are schematic elements depicting myosin dimers (purple) and adhesion complexes (yellow) near the central and peripheral growth cone, respectively. Myosin bound to actin produces a rearward force (purple arrows) on adhesion complexes where mechanosensitive (MS) proteins (parallel springs) detect this force. Adhesion complexes antagonize this rearward force allowing actin polymerization to expand the leading edge membrane (yellow arrows) and stretching a set of membrane MS proteins (perpendicular springs).

Mechanical Force Generation by Growth Cones

The cytomechanical forces that control growth cone motility have been intensely studied for the last 30 years, yet our understanding is still incomplete. Similar to non-neuronal cells, actin and microtubule polymerization play central roles as force-generating polymers in axonal growth cones (**Figure 1**). Complex mechanisms function within growth cones downstream of chemical and mechanical signals to tightly regulate the dynamic assembly and organization of the cytoskeleton (Lowery and van Vactor, 2009; Dent et al., 2011). Leading edge protrusion is thought to be driven largely by F-actin polymerization. Actin polymerization at the leading edge produces tensile forces, which are distributed between plasma membrane protrusion and rearward movement of F-actin bundles (Symons and Mitchison, 1991; Lin et al., 1996; Mogilner and Oster, 2003; Carlier and Pantaloni, 2007). Balance between membrane fluid dynamics and F-actin tensile strength may contribute to the extent of forward protrusion vs. rearward flow of F-actin (**Figure 1**; Bornschlögl, 2013). Conversely, ADF-cofilin mediated depolymerization of F-actin minus ends relieves compressive actin network forces and replenishes G-actin pools needed for further F-actin polymerization at the leading edge (Bamburg, 1999; Marsick et al., 2010; Zhang et al., 2012). A second force that powers F-actin retrograde flow (RF) is myosin-II motor dimers, which centripetally contract antiparallel F-actin networks toward the growth cone central domain (Turney and Bridgman, 2005; Medeiros et al., 2006; Yang et al., 2013; Shin et al., 2014). The contractile force of myosin-II, coupled with the rearward flow of F-actin due to leading edge polymerization, drives F-actin RF in growth cones (Forscher and Smith, 1988; Lin and Forscher, 1995; Brown and Bridgman, 2003). Other F-actin motor proteins, such as myosin I (Wang et al., 2003), V, VI (Suter et al., 2000; Kubota et al., 2010), and X (Berg and Cheney, 2002), also contribute to growth cone movements, morphology and vesicle trafficking.

During axon development and guidance, the equilibrium between actin polymerization and RF is a key regulator of growth cone protrusion and retraction. Increased leading edge protrusion could theoretically result from either increased actin polymerization or decreased myosin-II contraction. On the other hand, leading edge retraction or collapse could result from reduced actin polymerization, increased depolymerization, or increased myosin-II contraction. Another key force that counteracts RF in growth cones, as in non-neuronal cells (Smilenov et al., 1999; Giannone et al., 2009; Thievessen et al., 2013), are clutching forces at cell-substratum adhesions, which physically link to the F-actin cytoskeleton through a number of adaptor and signaling proteins (Suter et al., 1998; Woo and Gomez, 2006; Bard et al., 2008; Shimada et al., 2008; Myers and Gomez, 2011; Santiago-Medina et al., 2013; Toriyama et al., 2013). The molecular "clutch" is thought to restrain myosin-II mediated contractile forces upon the F-actin network to redirect the force of actin polymerization toward membrane protrusion. Many signaling and adaptor proteins target to growth cone point contact adhesions to regulate clutching, which provide numerous possible sites for regulatory control of axon guidance downstream of soluble, immobilized, and mechanical cues (Bard et al., 2008; Myers and Gomez, 2011; Toriyama et al., 2013).

Growth cone point contact adhesions are related to fibroblast focal adhesions, which are multi-functional, macromolecular protein complexes (Smilenov et al., 1999; Bard et al., 2008; Shimada et al., 2008; Geiger et al., 2009; Giannone et al., 2009; Toriyama et al., 2013). However, much less is understood about the molecular regulation and function of growth cone adhesions, and it is likely that these adhesions serve many functions that are unique to growth cones. Point contact adhesions typically assemble within growth cone filopodia that contain parallel bundled actin, have a short lifetime, then disassemble near the base of filopodia (**Figure 2**). Point contact adhesions appear to require integrin engagement, as they are observed primarily in growth cones on extracellular matrix (ECM) proteins (Woo and Gomez, 2006; Myers and Gomez, 2011). The ECM contains many ligands that modulate growth cone motility, such as laminin, tenascin, fibronectin, etc. Each type of ECM ligand activates specific integrin receptors, as we have recently reviewed (Myers et al., 2011). Activation of integrins leads to recruitment of scaffolding and signaling proteins, such as talin, focal adhesion kinase (FAK), paxillin, zyxin, and α-actinin (Gomez et al., 1996; Cluzel et al., 2005; Robles and Gomez, 2006; Myers et al., 2011). In non-neuronal cells, scaffolding proteins link to actin filaments to clutch RF, which supports actin polymerization to drive protrusion of the leading edge (Smilenov et al., 1999; Giannone et al., 2009; Thievessen et al., 2013). Similar clutching of RF likely occurs at growth cone point contacts (Santiago-Medina et al., 2013) and higher density adhesions have been linked to slower RF (Koch et al., 2012). Importantly, since point contact adhesions are modulated by ECM and soluble guidance factors (Woo and Gomez, 2006; Myers and Gomez, 2011; Myers et al., 2012), it is plausible that growth cone guidance is controlled by local changes in RF. Indeed, early studies from Paul Forscher and colleagues suggested that local reduction in RF is correlated with increased growth cone motility (Lin and Forscher, 1995; Lin et al., 1996; Santiago-Medina et al., 2013). For example, reduced RF is correlated with translocation of the growth cone central domain toward areas of strong adhesion of Aplysia neurons in contact with ApCAM-coated beads (Lin and Forscher, 1995; Suter et al., 1998). While the adapter proteins that link and clutch F-actin differ between cell adhesion molecules, such as ApCAM, L1 and N-cadherin, and integrin-ECM adhesions, they both function to restrain RF and promote axon outgrowth (Lin and Forscher, 1995; Suter et al., 1998; Bard et al., 2008; Toriyama et al., 2013).

The inverse relationship between RF and growth cone motility is well established, however there are exceptions to this model. For example, actin RF and motility both increase in Aplysia growth cones stimulated with 5-HT (5-hydroxytryptamine, serotonin; Zhang et al., 2012). This difference may be stimulus dependent, as 5-HT may increase actin polymerization without modulating adhesion dynamics leading to increase actin drag on existing adhesions. This has been described as the viscous slip clutch model (Giannone et al., 2009; Zhang et al., 2012). Conversely, guidance cues such as brain-derived neurotrophic factor (BDNF) and Semaphorin 3A regulate traction forces and actin RF speeds by changing adhesion dynamics (Woo and Gomez, 2006; Myers and Gomez, 2011). However, it is still unclear whether these two mechanisms operate within individual cells, but work in epithelial cells suggests RF rates may slow at focal adhesions through clutching and increases at the leading edge through increased actin polymerization (Gardel et al., 2008). It remains unclear how clutching mechanisms in growth cones depend upon the adhesive environment, soluble guidance cues and cell type.

Increased protrusive forces at the leading edge membrane generated by molecular clutching of F-actin RF, are balanced by adhesive (traction) forces with the cell substratum at adhesion sites (**Figure 3**). Traction forces with the cell substratum have been measured in migrating cells and growth cones using deformable substrata containing fluorescent tracer beads as fiducial marks (Hyland et al., 2014). Early work showed that cells migrate in the direction of the strongest substratum forces

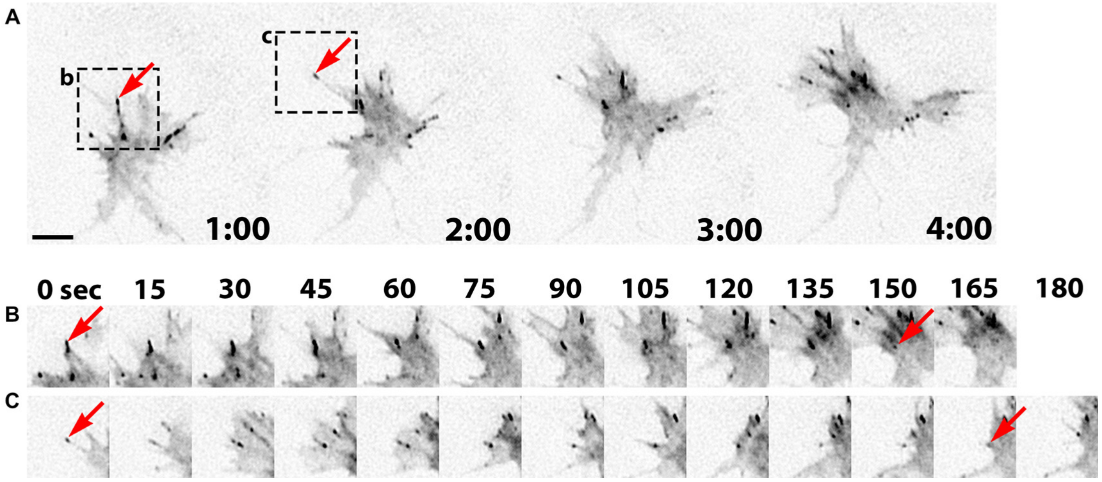

FIGURE 2 | Point contact adhesion dynamics in neuronal growth cones. (A) Inverted contrast images of a *Xenopus* growth cone expressing Paxillin-GFP captured every 1 min over a 4 min period using TIRF microscopy. The arrows and black boxes denote the adhesions viewed in **(B)** and **(C)**. **(B,C)** Images of individual adhesions are displayed at 15 s intervals. The arrows indicate the first and last frames of specific paxillin-GFP puncta. This figure was created with an original timelapse captured for demonstration purposes in this manuscript using techniques previously described (Woo et al., 2009; Myers and Gomez, 2011). Scale bar, 5 μm for all panels.

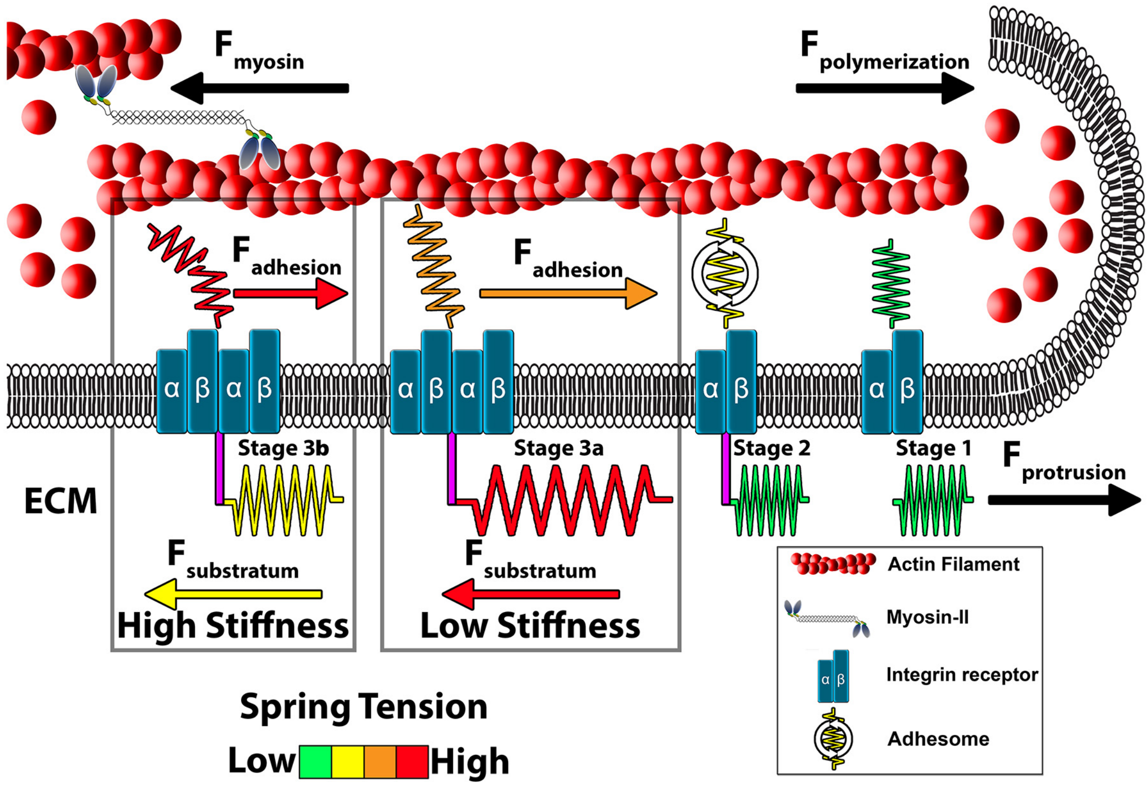

FIGURE 3 | Model of growth cone traction forces on high and low compliant substrata. Distal to the leading edge, active myosin-II generates contractile forces (F_{myosin}) that pulls F-actin rearward. In addition, actin polymerization at the leading edge pushes against the plasma membrane to propel F-actin rearward ($F_{polymerization}$). These forces integrate to drive constitutive retrograde flow (RF) of F-actin filaments at the leading edge. Stage 1 (ligand unbound). The molecular clutch is disengaged in the absence of integrin activation and clustering leading to rapid RF due to unrestrained F_{myosin} and $F_{polymerization}$. Stage 2 (ligand bound). Upon contact with extracellular matrix (ECM) proteins, integrin receptors become activated, cluster and begin recruiting adhesome-related adaptor and signaling proteins. Stage 3 (clutching). Mature point contact adhesions link with actin filaments ($F_{adhesion}$) to restrict RF and generate traction forces ($F_{traction}$) on the substratum. Therefore, forces generated by clutching of RF are distributed between traction forces with the ECM, adhesive forces on point contacts and protrusive forces at the leading edge. Conditions that maintain clutching of RF produce robust protrusion. Stage 3a (low substratum stiffness). On soft substrata, $F_{traction}$ forces are distributed to the elastic substrata at point contact adhesions through substratum displacement, which reduces $F_{adhesion}$ at point contact adhesions. Lower $F_{adhesion}$ at point contacts prevents clutch slippage (breaking), leading to increased protrusion and growth cone translocation. Stage 3b (high stiffness). Little displacement of the ECM occurs on rigid substrata. Subsequently, most force of RF is transferred to $F_{adhesion}$ at point contacts during clutching. The increased force on adhesions results in breaking or disassembly of point contacts via molecular stretching or activation of cellular signals. Fewer and short lived point contacts on rigid ECM disrupts clutching forces necessary for membrane protrusion and rapid outgrowth.

(Lo et al., 2000), which occur at focal adhesions (Plotnikov et al., 2012). In growth cones, these traction forces on the substratum are distributed within the actin-rich peripheral domain, where point contact adhesions are formed (**Figure 1**; Hyland et al., 2014). In response to guidance cues, localized assembly of adhesion complexes likely yield a redistribution of the traction forces on the substratum. This differential increase in traction forces on one side of the growth cone results in preferential growth in that direction. Moreover, the strength of traction forces generated by cells and growth cones increases on more rigid substrata, suggesting homeostatic regulation of force production (Chan and Odde, 2008; Koch et al., 2012). Substratum elasticity regulates integrin activity, internalization and adhesion site assembly (Du et al., 1993; Friedland et al., 2009), which likely accounts for increased traction forces at higher rigidity. Interestingly, growth cones from different neuronal types have been shown to generate different levels of substratum traction stress. For example, CNS hippocampal neurons exhibit rapid RF rates, due to decreased clutching, and can only generate modest peak traction stress. Conversely, dorsal root ganglion (DRG) neurons, which form more point contact adhesions that slow RF, can generate larger traction forces (Koch et al., 2012). These differences in traction stress may be related to the types of elastic environments CNS vs. PNS neurons encounter.

Mechanically Sensitive Proteins within Neuronal Growth Cones

For cells to sense the mechanical properties of their environment they must express proteins that change their conformation in response to mechanical force or tension. Depending on the type of mechanosensitive (MS) protein, conformational changes may lead to modulation of enzymatic activity, accessibility of binding sites for protein-protein interactions, or regulation of ion channel gating. One site where cell mechanosensors are likely concentrated is at integrin receptor-adhesion protein complexes, which function at the interface between the cytoskeleton and ECM (**Figure 4**). Adhesion complexes are spatially and temporally regulated by mechanical strain and substrate elasticity (Pelham and Wang, 1997; Schedin and Keely, 2011), suggesting they provide homeostatic feedback, termed tensional homeostasis. In this section we will discuss several recent reports that demonstrate that individual adhesion proteins and MS ion channels can respond to mechanical forces (**Table 1**).

Several enzymes within adhesion complexes appear to be MS. For example, mechanical forces applied to cells change both the localization and activity of FAK, a key non-receptor tyrosine kinase. Importantly, FAK signaling is necessary for cell behavioral responses to locally applied forces and changes in substratum rigidity (Wang et al., 2001). In growth cones, FAK is essential for point contact adhesion dynamics (assembly/disassembly) and axon guidance (Robles and Gomez, 2006; Woo et al., 2009; Myers and Gomez, 2011) and it is likely that mechanical properties of the environment influence FAK function. For example, FAK activation through deleted in colorectal cancer (DCC) requires both the immobilization of Netrin and acto-myosin contractility, suggesting that the kinase activity of FAK is mechanically dependent. Furthermore, inhibition of FAK during Netrin stimulation disrupts recruitment of adhesion complexes and traction force generation in growth cones (Moore et al., 2012). A second enzyme, receptor-like protein tyrosine phosphatase alpha (RPTP-α), is important for both sensing substratum stiffness and regulating axon extension. RPTP-α co-localizes with αvβ6 integrins where it regulates adhesion signaling by activating Src tyrosine kinases. Specifically on a rigid fibronectin substratum, RPTP-α promotes Src and Cas function and clustering to reinforce adhesion complexes and decrease axon outgrowth of hippocampal neurons (Kostic et al., 2007). However, whether RPTP-α senses substratum stiffness through a direct or indirect mechanism remains unclear.

Scaffolding proteins within adhesion complexes, such as p130Cas, talin, and filamin, also likely act as mechanosensors. Stretching of p130Cas exposes cryptic tyrosine residues that are phosphorylated by Src and Abl kinases and initiate several signaling cascades (Sawada et al., 2006). Loss of p130Cas function in developing neurons leads to aberrant axon pathfinding and dendrite patterning *in vivo* (Huang et al., 2007; Riccomagno et al., 2014). Recent evidence suggest that p130Cas may also be regulated by mechanically-dependent Netrin-DCC signaling during axon guidance (Moore et al., 2012). Similarly, stretching of talin leads to increased binding of the adapter vinculin to reinforce integrin-actin linkages (del Rio et al., 2009; Margadant et al., 2011). Talin has bifunctional roles in growth cones where it is important for the assembly of adhesions and as an integral scaffold within point contact adhesions (Sydor et al., 1996; Kerstein et al., 2013). Disruption of talin function leads to

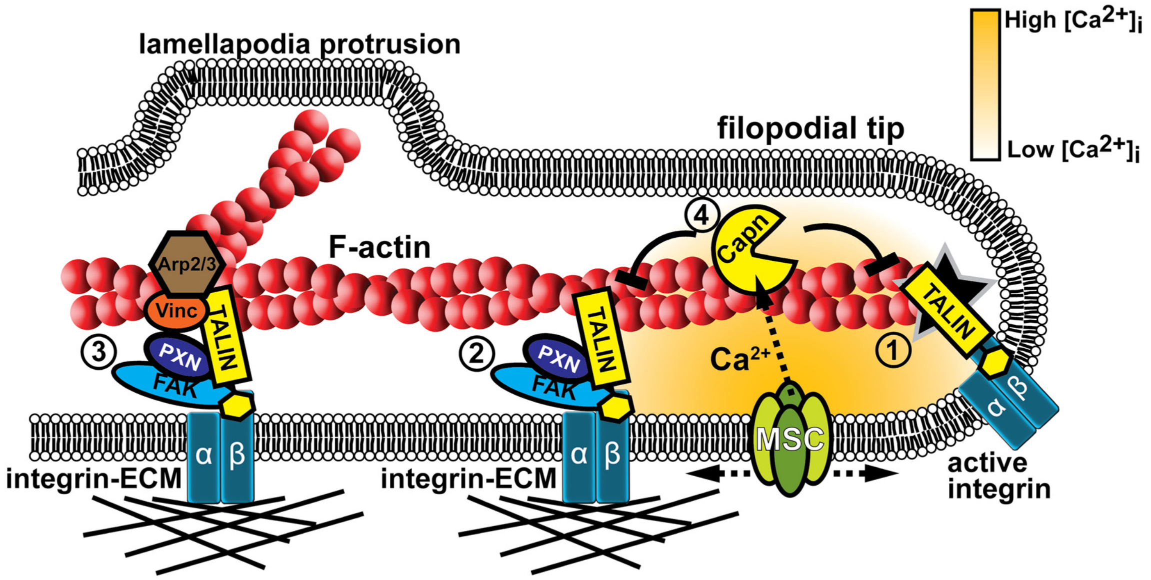

FIGURE 4 | Mechanotranduction within growth cone filopodia involves adhesion and Ca^{2+} signaling. (1) Formation of point contact adhesions are initiated by talin-dependent inside-out activation of integrin receptors. (2) Point contact adhesions form when integrins bind to the ECM and intracellular proteins, such as FAK and paxillin, are recruited to signal and link integrins to the actin cytoskeleton. MS proteins, such as FAK, Talin, and CAS (not shown), are activated during substratum rigidity sensing and signaling for adhesion maturation. (3) Additional proteins are recruited during adhesion maturation, such as vinculin and the actin nucleator Arp2/3. Therefore, mature adhesions act as a signaling nexus for new actin filament polymerization off existing filaments, leading to veil protrusion. (4) Adhesion assembly and maturation can be disrupted when Ca^{2+} flows through MS channels (MSC). Ca^{2+} ions directly activate the protease calpain that targets specific adhesion proteins to inhibit or modulate their function (Kerstein et al., 2013).

changes in filopodial dynamics and reduced growth cone motility (Sydor et al., 1996; Kerstein et al., 2013). In a similar fashion, filamins are scaffolding proteins that are stretched when bound between integrins and F-actin. Tension along filamin unveils cryptic binding sites for many signaling molecules such as RhoA, Rho-associated coiled-coil kinase (ROCK), p21-activated kinase (PAK), and PKC (Furuike et al., 2001; Razinia et al., 2012). In developing animals, mutations in filamins produce premature axon termination, ectopic branching, and aberrant pathfinding *in vivo* (Zheng et al., 2011; Nakamura et al., 2014).

A second set of mechanosensors in growth cones are MS ion channels (**Table 1**). MS channels have been most well studied in hair cells of the auditory system and the primary afferents of the somatosensory system (Geffeney and Goodman, 2012). However, these channels also have important roles in cell motility. MS channels regulate cell migration and growth cone motility through direct control of Ca^{2+} signaling (Lee et al., 1999; Jacques-Fricke et al., 2006; Franze et al., 2009; Wei et al., 2009; Kerstein et al., 2013). Evidence suggest that cell-substratum interactions activate MS channels in motile cells since Ca^{2+} signals localize to adhesion clusters and in areas of high traction forces (**Figure 4**; Gomez et al., 2001; Doyle et al., 2004; Franze et al., 2009). In addition, substratum stiffness modulates Ca^{2+} influx as rigid substrata elicit a higher frequency of Ca^{2+} transients, which inhibits axon extension (Kim et al., 2009; Kerstein et al., 2013). Pharmacological inhibitors of MS channels have strong effects on growth cone motility. MS channel inhibitors such as, GsMTx4, Gd^{3+}, Gentamicin all reduce the frequency of Ca^{2+} transients and accelerate axon extension (Jacques-Fricke et al., 2006; Kerstein et al., 2013). Furthermore, focal force applied to a growth cone induces collapse and retraction of the axon, which is blocked by inhibition of MS channels (Franze et al., 2009).

Recent reports suggest that growth cones express several types of MS ion channels, such as members of the Transient Receptor Potential (TRP) family. TRP channels form both homo- and heterotetrameric cation channels. Increasing evidence suggest an important role for TRP channels for environmental sensing from entire organisms to single cells. TRP channels transduce extracellular stimuli, like mechanical force, into biochemical signals through the influx of the second messenger Ca^{2+} (Wu et al., 2010). Interestingly, several TRP channel subunits that are expressed in developing neurons are believed to be MS, therefore these MS channels may also be important for axon guidance. For example, TRPV2 can be activated by membrane stretch of developing neurons and expression of dominant negative TRPV2 in developing primary motor neurons inhibits axon extension *in vivo* (Shibasaki et al., 2010). However it is unclear how TRPV2 is mechanically activated *in vivo*. One possibility is that substratum rigidity modulates MS channel activity to regulate growth cone motility. Local filopodial Ca^{2+} transients appear to be generated by mechanical activation of transient receptor potential channel 1 (TRPC1), since these signals are reduced when rigidity of the substratum is decreased. In addition, the effects of MS channel blockers on axon outgrowth is lost with knockdown of TRPC1 and partially lost with knockdown of TRPV4 (Kerstein et al., 2013). Importantly, previous findings suggest that TRPC1 is an essential channel for axon pathfinding *in vitro* and *in vivo* (Shim et al., 2005; Wang and Poo, 2005; Wen et al., 2007). Other TRPC channels are also important during axon guidance and have been implicated in cellular mechanotransduction. TRPC5 is activated by hypo-osmotic stimulation and membrane stretch, and inhibited by the MS channel blocker GsMTx4 (Gomis et al., 2008). TRPC5 also plays a critical role in neurite initiation, axogensis, and axon extension (Greka et al., 2003; Hui et al., 2006; Wu et al., 2007; Davare et al., 2009). Similarly, TRPC6 is activated by membrane stretch and inhibited by GsMTx4 (Spassova et al., 2006) and is also important for axon growth and guidance in response to attractive guidance cues (Li et al., 2005). Recent evidence showed an important role for TRPM7 in the regulation on hippocampal axon extension *in vitro* (Turlova et al., 2014). In addition, TRPM7 was previously shown to respond to membrane stretch and fluid sheer force (Oancea et al., 2006; Wei et al., 2009). A major open question in the field is why are so many TRP channels mechanically sensitive. An intriguing new theory suggests that many TRP channels share a gating mechanism that relies on the local tension and shape of the plasma membrane (Liu and Montell, 2015). Furthermore each MS-TRP channel may be specific for a single neuron type. For example, the expression profiles of TRPC subfamily alone vary widely within the nervous system and exhibit even greater variation during development (Riccio et al., 2002; Strübing et al., 2003; Von Niederhäusern et al., 2013). One final possibility is that only a single TRP channel subunit is mechanically sensitive, but it may form tetrameric channels with many different TRP subunits depending on the cell type. This could result in many different channel tetramers being mechanically sensitive, with contribution from one subunit being sufficient to form a MS channel.

MS ion channels outside the TRP channel family may also be important. Piezo (Fam38a/b) ion channels were identified as MS channels in a siRNA based screen in the mechanically excitable Neuro2D cell line (Coste et al., 2010). Piezo1 controls cell migration in non-neuronal cells, possibly through regulating integrin binding activity (McHugh et al., 2010, 2012). However, Piezo1 is mainly expressed in non-neuronal cells, but Piezo2 is expressed neurons and is essential for the sense of touch in vertebrates (Faucherre et al., 2013; Ranade et al., 2014; Woo et al., 2014). Currently our understanding of Piezo2 is limited to adult animals, so future studies will need to address whether this MS channel has a role in neuronal development and growth cone motility.

How mechanical forces are transduced into MS channel gating is uncertain, but may involve coupling with the cytoskeleton (Clark et al., 2007; Hayakawa et al., 2008) interactions with lipids (Anishkin et al., 2014) and second messenger signals (Vriens et al., 2004; Alessandri-Haber et al., 2008). One intriguing site where local mechanical forces may regulate the opening of MS channels is at cell-cell contact sites or integrin adhesions with the ECM (Hayakawa et al., 2008; Kobayashi and Sokabe, 2010; Kazmierczak and Müller, 2012; Eisenhoffer and Rosenblatt, 2013). In support of this notion, both Ca^{2+} signals and TRP channels localize near integrin adhesion sites (Gomez et al., 2001; Matthews et al., 2010; Kerstein et al., 2013). In neurons, these Ca^{2+} signals may act as a feedback mechanism on adhesion assembly and disassembly controlling growth cone motility (Robles et al., 2003; Kerstein et al., 2013). Interestingly, mechanical gating of MS channels likely depends on substratum rigidity and traction forces (Doyle et al., 2004; Munevar et al., 2004; Kerstein et al., 2013). This suggests that differences in the elastic environment of neurons may control their development *in vivo* through regulation of MS channel expression and function. In addition, MS channels may exert homeostatic regulation of the cytoskeleton and adhesion complexes through activation of downstream Ca^{2+} effectors. Previous studies have identified the Ca^{2+} effectors, calcineurin, CaMKII, and calpain as the main signaling pathways that regulate Ca^{2+} dependent growth cone motility and axon guidance (Robles et al., 2003; Wen et al., 2004). However the most intriguing example of mechanical feedback is the Ca^{2+}-dependent protease calpain since it cleaves several adhesion and actin binding proteins to inhibit or modulate their function (**Figure 4**; Franco and Huttenlocher, 2005). Recent studies have shown that axon outgrowth and morphology are regulated through calpain specific cleavage of talin and cortactin, respectively (Mingorance-Le Meur and O'connor, 2009; Kerstein et al., 2013). However, additional calpain targets in growth cones are likely to exist. For example, in non-neuronal cells calpain cleaves the adhesion proteins Src, FAK, and Paxillin and the actin binding proteins Filamin and α-actinin (reviewed in Franco and Huttenlocher, 2005; Chan et al., 2010; Cortesio et al., 2011). It is important to further elucidate the mechanism of feedback inhibition between MS channels and adhesion/cytoskeleton structures particularly in neuronal growth cones.

An interesting area where mechanotransduction has not been studied in growth cones is membrane trafficking. Endocytosis and exocytosis play an important role in growth cone navigation. For example, endocytosis of membrane and surface integrin receptors is required for repulsive growth turning from myelin-associated glycoprotein and semaphorin 3A (Hines et al., 2010; Tojima et al., 2010). Conversely, exocytosis is important for attractive axon turning and increased axon branching (Tojima et al., 2007, 2014; Winkle et al., 2014). Endocytosis and exocytosis may also directly influence mechanical signals. Recent studies showed that during cell migration leading edge protrusions increase plasma membrane tension, which activates further exocytosis to relieve increased tension (Gauthier et al., 2011). However, the mechanism of sensing membrane tension remains unknown. One possibility is that membrane tension activates MS ion channels. Consistent with this, hypotonic solutions induce cell swelling and increase membrane tension, which activates Ca^{2+} influx through MS channels in growth cones (Jacques-Fricke et al., 2006; Kerstein et al., 2013). Another possibility is that membrane tension is required for the localization of leading edge signaling proteins such as the GTPase Rac1 and the SCAR/WAVE complex, as shown recently in neutrophils (Houk et al., 2012). Unfortunately, our understanding of the relationship membrane tension and trafficking is limited in neuronal growth cones and a considerable amount of work remains before a mechanism is completely understood.

Mechanical Properties of the Environment Regulate Cell Migration and Axon Growth

Pioneering studies on the mechanisms of growth cone guidance performed both *in vitro* and *in vivo* focused on the role of cell adhesion as a principal determinant of pathfinding (Gomez et al., 1996; Woo and Gomez, 2006; Bard et al., 2008; Bechara et al., 2008; Myers et al., 2011). Using patterned substrata of differential adhesivity, investigators showed that growth cones could be directed *in vitro* simply by differences in adhesion (Hammarback et al., 1985; Gomez and Letourneau, 1994). These early experiments implied that axons may be targeted *in vivo* by adhesive interactions with extracellular ligands. A number of different cell recognition molecules on the surface of growth cones are known to have adhesive properties (Rutishauser, 1985; Lagenaur and Lemmon, 1987; Schmidt et al., 1995), which function to stabilize leading edge protrusions. While it is still uncertain the relative contributions of adhesion vs. biochemical signaling in the control of axon pathfinding *in vivo*, it is likely that differential cell adhesion has some influence (Caudy and Bentley, 1986a,b; O'Connor et al., 1990).

In addition to the classical ECM components, axon guidance cues are immobilized in the extracellular environment to some extent. While this includes large ECM proteins and cell surface adhesion molecules, small secreted growth factors and chemokines are also likely immobilized. Growing evidence suggests that growth factors bind with high specificity to fibronectin type III repeats and heparin sulfate glycosaminoglycans contained within many ECM proteins such as fibronectin, tenascin, and laminin (Hynes, 2002, 2009). Growth factor binding to the ECM likely serves to localize or concentrate soluble factors [e.g., fibroblast growth factor (FGF), Wnt, bone morphogenic proteins (BMPs)] near the cell binding sites and help establish stable gradients necessary for pattern formation *in vivo*. In some cases, growth factor receptors may cooperate with cell adhesion receptors (e.g., integrin) for cell binding, as has been demonstrated for a5ß1 and vascular endothelial growth factor (VEGF) receptor (Rahman et al., 2005). Secreted axon guidance cues have also been demonstrated to bind ECM proteins suggesting that immobilized guidance factors serve as adhesive ligands or provide mechanical support in association with ECM. For example, the repellant Slit must bind collagen for proper lamination of the zebrafish optic tectum (Xiao et al., 2011). Other secreted axon guidance cues such as netrins, BMPs and Sema3s bind the ECM and induce mechanical signals (Hu, 2001; Manitt and Kennedy, 2002; De Wit et al., 2005; Moore et al., 2012). To provide an additional level of control, local proteolysis of ECM may serve to release growth factors in a spatially and temporally controlled manner. Growth cones have recently been shown to target matrix metalloproteases using invadosomes (Santiago-Medina et al., 2015). Therefore, while bath application or local gradients of soluble guidance cues has been the prevailing method for studying axon guidance behaviors *in vitro*, the role of mechanical signaling by immobilized ligands in three dimensional environments is an important and often overlooked consideration for our full understanding of the mechanisms of neural network formation.

Growth cones *in vitro* have been shown to generate tension on neighboring cells and the underlying matrix (Lamoureux et al., 1989; Balgude et al., 2001; Moore et al., 2010; Moore and Sheetz, 2011). Many axon guidance cues are immobilized in the extracellular environment to some extent (as described above), therefore mechanical tensile forces likely contribute to many attractive and repulsive (release of adhesion) guidance behaviors. Recent evidence suggest that even under classic chemical gradient turning assays, mechanotransduction is necessary for chemoattraction. For example, chemical gradients of netrin-1 generated *in vitro* only promote growth cone turning when netrin can bind to the substratum (Moore et al., 2009). Here growth cones utilize netrin as an adhesive ligand that supports traction forces that exceed 60 pN (Moore et al., 2009). Inhibition of netrin substrata adsorption, via co-treatment with heparin, inhibited axon outgrowth (Moore et al., 2012). Interestingly, commissural interneurons *in vivo* will turn towards ectopically secreted full length netrin, but are not guided towards truncated netrin lacking the domains required for substratum adsorption (Moore et al., 2012). Further, guidance toward Netrin depends upon FAK activity, a MS kinase, and myosin-II motor-induced traction forces. Other "soluble" axon guidance cues may require immobilization to elicit their guidance effects on extending axons. For example, ephrinA5 appears to produce repulsive turning or collapse in both border turning assays or as a soluble ligand, but the ability of "soluble" ephrinA5 to bind was not tested in this study (Weinl et al., 2003). EphrinA repellants may disrupt growth cone adhesion to the ECM or to neighboring cells by preventing point contact formation (Woo et al., 2009), or by activating metalloprotease-mediated cleavage of cell surface ephrinA ligands (Hattori et al., 2000), respectively.

While immobilized ligands clearly support traction forces generated by cells and growth cones, many recent studies show that substratum elasticity, or stiffness, also influences the development of neurons (Tyler, 2012; Franze, 2013). Cells and neurons have a remarkable ability to adapt to their mechanical environment. While most cells minimally require anchorage to a solid substratum and do not fully differentiate in liquid suspension, the elasticity of the supporting adhesive substratum can vary over a wide range. Neurons are particularly adaptable cells, as they will morphologically differentiate on extremely soft substrata and tissues, such as brain [Young's modulus = ∼100–1000 Pascal (Pa)], as well as on extremely rigid environments, such as ECM-coated glass and bone (>10 gPa, 20 mPa, respectively), covering an impressive >10, 000 fold range of elasticities (Kruse et al., 2008; Tyler, 2012). Importantly, the elastic modulus (rigidity) of the cell substratum can strongly influence cell differentiation, morphology, motility, and survival (Geiger et al., 2001, 2009; Moore and Sheetz, 2011; Musah et al., 2014). Understanding the roles of substratum elasticity on neuronal development is critical since developing axons and dendrites will encounter widely varying elastic environments during pathfinding to their targets.

Numerous studies over the past decade have shown that growth cone motility depends on the compliance of the cell substratum (Tyler, 2012; Franze, 2013). This is a cell migration process known as *durotaxis*. Previous studies used a variety of materials to generate variable elastic cell culture conditions to study neuronal durotaxis, including polyacrylamide (PAA; Flanagan et al., 2002; Georges et al., 2006; Kostic et al., 2007; Jiang et al., 2008; Koch et al., 2012) and polydimethylsiloxane (PDMS) in 2D (von Philipsborn et al., 2006; Cheng et al., 2011; Kerstein et al., 2013), as well as collagen I gels (Willits and Skornia, 2004; Sundararaghavan et al., 2009) and agarose hydrogels for 3D conditions (Hammarback and Letourneau, 1986; Balgude et al., 2001; Mai et al., 2009). Here we compare results across these conditions (**Table 2**), but it is important to note that many variables beyond substratum compliance may contribute to observed differences. For example, non-biological materials typically must be conditioned with a biological ligand to support axon extension. A range of ECM proteins at varying concentrations or serum have been used to promote axon outgrowth. In addition to the variable biological conditions tested, the methods used to measure the elastic moduli of the cell substrata also varies. Therefore, Young's modulus values determined by atomic force microscopy (AFM) may differ from those measured by sheer stress rheometry or micro-position displacement devices. These caveats should be considered whenever comparing between different studies.

One of the first studies to examine neurite outgrowth under different elastic conditions cultured dorsal root ganglia (DRG) neurons within varying concentrations of agarose gels in the presence of 10% fetal bovine serum (FBS). This study found that axons extend more rapidly within softer gels (<20 Pa) and that the rate of outgrowth plateaus above 60 Pa (Balgude et al., 2001). More recently, PAA gels were used to test the effects of substratum elasticity on DRG axon outgrowth. By examining neurite lengths from fixed DRG neurons plated on PAA coated with laminin, Jeff Urbach and colleagues found that axon outgrowth peaks on 1000 Pa gels and decreases on PAA gels below and above this optimal elasticity (Koch et al., 2012). Interestingly, under the same conditions, this group found that hippocampal neurons exhibit no preference for soft substrata, suggesting this behavior may be selective for peripheral neurons. However, this result is contradictory to a previous report that found that hippocampal axons preferred soft conditions (500 Pa) over more rigid (4 KPa; Kostic et al., 2007). It is important to note that the latter study differed from the former as they used PAA gels coated with fibronectin rather than laminin. Other studies using different types of neurons and culture conditions, including within collagen gels, have found preferential outgrowth on softer substrata (**Table 2**, Balgude et al., 2001; Flanagan et al., 2002; Willits and Skornia, 2004; Georges et al., 2006; Jiang et al., 2008; Kerstein et al., 2013), but it will be important to standardize experimental conditions and elastic modulus measurements to make general statements regarding the effects of the mechanical environment on outgrowth. In addition to effects on axon outgrowth, other studies have shown that softer substrata promote neurite branching of several neuronal types (Wang et al., 2001; Flanagan et al., 2002; Georges et al., 2006; von Philipsborn et al., 2006).

TABLE 1 | Mechanosensitive (MS) proteins in growth cones.

Gene name	Mechanical activation	Downstream signaling	Growth cone mechanism	Key references (Bold—Mechano. *Italics—Growth cone*)
Adhesion proteins				
FAK	Increased kinase activity	• Tyrosine phosphorylation • Regulation of adhesion dynamics	• Required for attractive axon turning • Promotes axon outgrowth	*Robles and Gomez (2006)* *Myers et al. (2011)* ***Moore et al. (2012)***
RPTP-α	Increased phosphataseactivity	• Fyn recruitment to integrins • p130Cas phosphorylation	• Phosphatase activity inhibits axon outgrowth.	***Kostic et al. (2007)***
p130Cas	Increased availability of tyrosine residues	• Phosphorylated by Src and Abl kinases	• Required for *in vivo* and *in vitro* axon pathfinding and dendritic patterning.	**Sawada et al. (2006)** *Huang et al., 2007* *Riccomagno et al. (2014)*
Talin	Increased availability of vinculin binding sites	• Vinculin binding • Reinforcement of integrin -actin linkages	• Required for filopodia and growth cone motility.	**del Rio et al. (2009)** **Margadant et al. (2011)** ***Kerstein et al. (2013)*** *Sydor et al. (1996)*
Filamin	Increased availability of protein binding sites.	• Recruitment of Rho, ROCK, PAK, and PKC to actin cytoskeleton and adhesions.	• Required for *in vivo* axon pathfinding.	**Furuike et al. (2001)** **Razinia et al. (2012)** *Zheng et al. (2011)* *Nakamura et al. (2014)*
Ion channels				
TRPC1	Channel opening (membrane-stretch/ integrin transduction)	• Ca^{2+} influx • Activation of calpain • Activation of calcineurin	• Inhibition of axon outgrowth • Required for attractive/ repulsive axon turning	**Maroto et al. (2005)** *Wang and Poo (2005)* *Shim et al. (2005)* *Wen et al. (2007)* ***Kerstein et al. (2013)***
TRPC5	Channel opening (membrane-stretch)	• Ca^{2+} influx	• Inhibits axon outgrowth	*Greka et al. (2003)* **Gomis et al. (2008)**
TRPC6	Channel opening (membrane-stretch)	• Ca^{2+} influx	• Promotes axon outgrowth • Attractive axon turning	*Li et al. (2005)* **Spassova et al. (2006)**
TRPM7	Channel opening (membrane-stretch/ shear stress)	• Ca^{2+} influx • Kinase activity(?)	• Inhibits axon outgrowth	**Oancea et al. (2006)** **Wei et al. (2009)** *Turlova et al. (2014)*
TRPV2	Channel opening (membrane stretch)	• Ca^{2+} influx	• Promotes axon outgrowth	***Shibasaki et al. (2010)***
TRPV4	Channel opening (membrane-stretch/ integrin transduction)	• Ca^{2+} influx • Activation of calpain (suggested)	• Inhibits of axon outgrowth	**Matthews et al. (2010)** *Goswami et al. (2010)* ***Kerstein et al. (2013)***
Piezo2	Channel opening (membrane-stretch)	• Ca^{2+} influx	• Unknown	***Coste et al. (2010)***

Mechanical Environment Influences Cell Migration and Axon Growth *In vivo*

Growth cone navigation may be influenced by surrounding physical barriers causing them to grow around or in between different tissue structures. For example, when a severed motor neuron axon begins to regenerate it typically will extend, branch, and synapse in the same location as the pioneer axon. Regenerating axons are physically constrained to the tubes that Schwann cells formed around the original axon (Nguyen et al., 2002). Interestingly, peripheral axon regeneration declines with age, not because the axons lose their intrinsic outgrowth capabilities, but due to the lack of clearance of glial and nerve debris that impose physical barriers to the regenerating axons (Kang and Lichtman, 2013). In the central nervous system (CNS), similar regeneration limitations have been observed when immature neurons were transplanted into rats with striatal lesions (Isacson et al., 1995). In addition to regenerating axons, physical interactions are important during development as well. For example, zebrafish lateral line axons extend with the collective migration of lateral line primordial cells through a physical, but not chemical, interaction. The authors described this as a "tugging" action on the axons by the migrating lateral line primordia (Gilmour et al., 2004). Furthermore, zebrafish Rohan-Beard peripheral axons normally project ventrally, however when the contractions of the underlying muscle tissue are prevented, genetically or pharmacologically, these axons project more longitudinally (Paulus et al., 2009). In Zebrafish *diwanka* mutants, MN growth cones fail to exit the spinal cord into the periphery (Granato et al., 1996; Zeller and Granato,

TABLE 2 | The effects of substrate rigidity on neurite outgrowth and morphology.

Neuron type	Substrate (ECM)	Elasticity range (Modulus)	Neurite phenotype	Reference
E9 Chick DRG	3D Agarose (None)	0.003–0.130 kPa* (Shear)	Increased length on soft substrates	Balgude et al. (2001)
E9 Chick DRG	3D Collagen I Gel (varied collegan conc.)	0.002–0.017 kPa (Shear)	Increased length on soft substrates	Willits and Skornia (2004)
E8 Chick DRG	3D Collagen I Gel (varied genipin crosslinking)	0.05–0.80 kPa (Shear)	Increased length on soft substrates	Sundararaghavan et al. (2009)
E13.5 Mouse Spinal Cord	PAA (Matrigel)	0.050–0.550 kPa* (Shear)	Increased branching on soft substrates	Flanagan et al. (2002)
P0 Mouse Hippocampal	PAA (Fibronectin or Laminin)	0.5–7.5 kPa (Young's)	Increased length on soft substrates	Kostic et al. (2007)
P0 Rat DRG	PAA (Laminin)	0.150–5.0 kPa (Young's)	Maximum length on 1.0 kPa substratum.	Koch et al. (2012)
E18 Rat Hippocampal	PAA (Laminin)	0.150–5.0 kPa (Young's)	No affect on length	Koch et al. (2012)
E16 Rat Spinal Cord	PAA (PDL or Collagen I) (DNA oligonucleotide pairs used to vary crosslinking)	6.6–30 kPa (Young's)	Increased length on soft substrates.	Jiang et al. (2008)
Adult Mouse DRG	PDMS (Poly-L-Lysine)	18–1882 kPa (Young's)	Maximum length on 88 kPa substratum	Cheng et al. (2011)
Stage 22 Xenopus spinal cord	PDMS (Fibronectin)	950–1800 kPa (Young's)	Increased outgrowth on soft substrates	Kerstein et al. (2013)
E8–9 Chick DRG	Silk Fibroin Hydrogel (Fibronectin or Laminin)	4–33 kPa (Young's)	Maximum length on 7–22 kPa substrates	Hopkins et al. (2013)

*Abbreviations: kPa, kiloPascals; PAA, polyacrylamide; PDMS, Polydimethylsiloxane. *kPa were converted from kdynes/cm^2.*

1999; Schneider and Granato, 2006). *diwanka* mutations were found to be in a lysyl hydroxylase protein (LH3), an enzyme with glycosyltransferase activity that modifies type XVIII collagen. Interestingly, the glycosyltransferase activity of LH3 functions within adaxial cells to chemically modify collagen XVIII that is deposited on the surface of the developing myotome. In this model, collagen XVIII is glycosylated by LH3 and secreted into the ECM where it becomes a suitable substratum to promote the exit of motor axons into the periphery. While it is unclear what the precise roles of collagen glycosylation are toward developing axons, there is evidence it can regulate fibrillogenesis, crosslinking, remodeling and collagen–cell interactions, all of which likely influence mechanical signaling (Yamauchi and Sricholpech, 2012). Glycosylation of dystroglycan also regulates axon guidance at the floor plate of the developing mouse spinal cord and is required for binding and localizing Slit to the floor plate (Wright et al., 2012). However, it is unknown whether the immobilization of Slit is required full receptor activation, as it is for the ligand Netrin (described above). It will be important in the future to determine which immobilized axon guidance cues, such as ECM, cell adhesion molecules and growth factors, use mechanical signaling to elicit their effects on growth cones.

Axons Extend Through a Mechanically Diverse Environments *In vivo*

The elasticity of the extracellular environment *in vivo* varies across tissues, with age and under pathological conditions. For example, in breast cancer tissues, mammary carcinoma cell migration is influenced by the physical properties of the collagen matrix, such as fiber alignment, density, and stiffness (reviewed in Schedin and Keely, 2011). Interestingly, increases in density and stiffness of the ECM within breast tissue and mammary gland tumors are the key risk factors for the development of breast cancer and the metastatic potential of cancer cells (Boyd et al., 1998; Paszek et al., 2005; Provenzano et al., 2009). These findings under pathological conditions suggest that normal cell migration and the extension of neuronal processes, may also be influenced by local differences in the mechanical environment *in vivo*. The environment of elongating axons and dendrites, which can traverse great distances, varies widely in substratum elasticity (Young's Modulus) from flexible neural tissues to highly rigid skin, muscle and bone suggesting a role for growth cone durotaxis *in vivo*. (Discher et al., 2005, 2009). Furthermore, local variations in substratum elasticity have been observed within the CNS. AFM measurements made from dissociated hippocampal and retinal neurons found that individual neurons were more rigid than glial cells (Lu et al., 2006). Therefore, the extension of axons and dendrites along different cell types may be influenced by the intrinsic mechanical properties of the cells. In addition, regional differences in tissue elasticities have been observed across specific regions of the CNS. Scanning force micrographs of rat cerebellar slices showed that gray matter is more elastic than white matter (Christ et al., 2010). In addition, slices from developing mouse cerebral cortex show variations in tissue elasticity in both a spatial and temporal manner, suggesting a mechanical niche may influence cellular differentiation, migration, and morphology *in vivo* (Iwashita et al., 2014).

Substratum elasticity *in vivo* is determined by composition, density and orientation of different ECM components. For example, recent work has shown that cross-linking of collagen fibers by lysyl oxidase (Lox) in the drosophila eye disc controls the stiffness of the tissue. Further, disruption of Lox leads to ectopic migration of glial cells suggesting tissue stiffness defines specific migration patterns (Kim et al., 2014). In addition, Lox knockdown or overexpression in the mouse cerebellum modulates Purkinje neuron dendritic development, where increased Lox activity may inhibit outgrowth through increasing collagen cross-linking and substratum stiffness (Li et al., 2010). Recent studies have provided evidence to support a role for substratum stiffness in guiding developing axons *in vivo*, but future studies will need to clarify how and when axon growth is specifically modulated by substratum elasticity. In addition, the study of mechanosignaling during axon guidance requires the development of a robust and reliable *in vivo* model of growth cone durotaxis.

Future Prospectives and Challenges to the Field

There are many outstanding questions regarding the roles of mechanical forces in the regulation of growth cone motility and axon guidance. Within cells and growth cones, it is unclear which proteins function as mechanosensors and how molecular forces are transferred onto target proteins. In particular, it is not clear how MS ion channels are gated at the plasma membrane and the molecular targets of calcium signals. Ion channel gating may occur at point contact adhesions, where myosin II contractile forces are focused at integrin-ECM contacts (Gomez et al., 2001; Hayakawa et al., 2008; Matthews et al., 2010). Importantly, it is likely that specific calcium influx and release pathways control distinct downstream targets that can have opposing effects on motility (Gomez and Zheng, 2006). However, since many MS ion channels are activated by multiple stimuli, manipulating mechanically activated currents specifically is challenging. For example, TRPC1 subunits are known to assemble into channels that are activated by both mechanical and chemical signals (Wu et al., 2010). Another major challenge to our understanding of mechanical signaling, is the composition and regulation of ECM adhesions. This is particularly difficult in growth cones, as point contact adhesions are smaller and more dynamic than focal adhesions found in non-neuronal cells. Proteomic based approaches are being attempted for focal adhesions, but are hampered by sample heterogeneity (Kuo et al., 2012; Humphries et al., 2015). Point contact adhesions will certainly also be highly heterogenous within growth cones and their composition is regulated by cross talk from guidance cue receptors to control mechanical forces (Myers et al., 2011; Gomez and Letourneau, 2014). In addition, point contact adhesions have not been observed *in vivo*, where they will clearly differ depending on substratum association. During axon pathfinding to distal targets, growth cones will bind many different adhesive substrata, ranging from ECM proteins to cell adhesion molecules on neighboring neurons and glia. It is important to both visualize and manipulate point contact adhesions *in vivo* to test their roles in axon guidance.

Determining the roles of tissue elasticity and mechanical signaling is particularly difficult *in vivo*. While it is clear that growth cones must migrate across widely varying elastic microenvironments en route to their proper synaptic targets, it is not known whether changes in tissue elasticity influences growth cone morphology or motility. For example, motoneuron axons begin in the soft CNS, but exit by penetrating the surrounding basal lamina (Santiago-Medina et al., 2015) to enter the sclerotome, which they preferentially cross within the rostral half (Keynes and Stern, 1984). After entering the periphery, MN axons are sorted toward targets in the body wall and limb muscles (Bonanomi and Pfaff, 2010), which are significantly more rigid tissues(Engler et al., 2004; Discher et al., 2009). Distinguishing specific effects of the mechanical environment vs. chemical signals is difficult *in vivo*. However, progress has been made by examining the effects of mutations in ECM cross linking enzymes that regulate the mechanical, but not the chemical composition of the environment (Kim et al., 2014). Additional functional studies should test the effects on axon guidance of manipulations that both increase and decrease tissue elasticity. Moreover, these functional studies can be coupled with direction measurements of elastic modulus within tissues *in vivo* using AFM (Franze, 2011).

Acknowledgments

The authors would like to thank the members of the Gomez lab for helpful comments on this manuscript. This work was supported by NIH R56NS041564 and R21NS088477 to TMG, NIH F31NS074732 to PCK and NIH T32GM007507 to the Neuroscience Training Program.

References

Alessandri-Haber, N., Dina, O. A., Joseph, E. K., Reichling, D. B., and Levine, J. D. (2008). Interaction of transient receptor potential vanilloid 4, integrin and SRC tyrosine kinase in mechanical hyperalgesia. *J. Neurosci.* 28, 1046–1057. doi: 10.1523/JNEUROSCI.4497-07.2008

Anishkin, A., Loukin, S. H., Teng, J., and Kung, C. (2014). Feeling the hidden mechanical forces in lipid bilayer is an original sense. *Proc. Natl. Acad. Sci. U S A* 111, 7898–7905. doi: 10.1073/pnas.1313364111

Balgude, A. P., Yu, X., Szymanski, A., and Bellamkonda, R. V. (2001). Agarose gel stiffness determines rate of DRG neurite extension in 3D cultures. *Biomaterials* 22, 1077–1084. doi: 10.1016/s0142-9612(00)00350-1

Bamburg, J. R. (1999). Proteins of the ADF/cofilin family: essential regulators of actin dynamics. *Annu. Rev. Cell Dev. Biol.* 15, 185–230. doi: 10.1146/annurev.cellbio.15.1.185

Bard, L., Boscher, C., Lambert, M., Mège, R. M., Choquet, D., and Thoumine, O. (2008). A molecular clutch between the actin flow and N-cadherin adhesions drives growth cone migration. *J. Neurosci.* 28, 5879–5890. doi: 10.1523/JNEUROSCI.5331-07.2008

Bechara, A., Nawabi, H., Moret, F., Yaron, A., Weaver, E., Bozon, M., et al. (2008). FAK-MAPK-dependent adhesion disassembly downstream of L1 contributes to semaphorin3A-induced collapse. *EMBO J.* 27, 1549–1562. doi: 10.1038/emboj.2008.86

Berg, J. S., and Cheney, R. E. (2002). Myosin-X is an unconventional myosin that undergoes intrafilopodial motility. *Nat. Cell Biol.* 4, 246–250. doi: 10.1038/ncb762

Bonanomi, D., and Pfaff, S. L. (2010). Motor axon pathfinding. *Cold Spring Harb. Perspect. Biol.* 2:a001735. doi: 10.1101/cshperspect.a001735

Bornschlögl, T. (2013). How filopodia pull: what we know about the mechanics and dynamics of filopodia. *Cytoskeleton (Hoboken)* 70, 590–603. doi: 10.1002/cm.21130

Boyd, N. F., Lockwood, G. A., Byng, J. W., Tritchler, D. L., and Yaffe, M. J. (1998). Mammographic densities and breast cancer risk. *Cancer Epidemiol. Biomarkers Prev.* 7, 1133–1144.

Brown, M. E., and Bridgman, P. C. (2003). Retrograde flow rate is increased in growth cones from myosin IIB knockout mice. *J. Cell Sci.* 116, 1087–1094. doi: 10.1242/jcs.00335

Carlier, M. F., and Pantaloni, D. (2007). Control of actin assembly dynamics in cell motility. *J. Biol. Chem.* 282, 23005–23009. doi: 10.1074/jbc.r700020200

Caudy, M., and Bentley, D. (1986a). Pioneer growth cone morphologies reveal proximal increases in substrate affinity within leg segments of grasshopper embryos. *J. Neurosci.* 6, 364–379.

Caudy, M., and Bentley, D. (1986b). Pioneer growth cone steering along a series of neuronal and non-neuronal cues of different affinities. *J. Neurosci.* 6, 1781–1795.

Chan, K. T., Bennin, D. A., and Huttenlocher, A. (2010). Regulation of adhesion dynamics by calpain-mediated proteolysis of focal adhesion kinase (FAK). *J. Biol. Chem.* 285, 11418–11426. doi: 10.1074/jbc.M109.090746

Chan, C. E., and Odde, D. J. (2008). Traction dynamics of filopodia on compliant substrates. *Science* 322, 1687–1691. doi: 10.1126/science.1163595

Chèdotal, A., and Richards, L. J. (2010). Wiring the brain: the biology of neuronal guidance. *Cold Spring Harb. Perspect. Biol.* 2:a001917. doi: 10.1101/cshperspect.a001917

Cheng, C. M., LeDuc, P. R., and Lin, Y. W. (2011). Localized bimodal response of neurite extensions and structural proteins in dorsal-root ganglion neurons with controlled polydimethylsiloxane substrate stiffness. *J. Biomech.* 44, 856–862. doi: 10.1016/j.jbiomech.2010.12.006

Christ, A. F., Franze, K., Gautier, H., Moshayedi, P., Fawcett, J., Franklin, R. J., et al. (2010). Mechanical difference between white and gray matter in the rat cerebellum measured by scanning force microscopy. *J. Biomech.* 43, 2986–2992. doi: 10.1016/j.jbiomech.2010.07.002

Clark, K., Langeslag, M., Figdor, C. G., and van Leeuwen, F. N. (2007). Myosin II and mechanotransduction: a balancing act. *Trends Cell Biol.* 17, 178–186. doi: 10.1016/j.tcb.2007.02.002

Cluzel, C., Saltel, F., Lussi, J., Paulhe, F., Imhof, B. A., and Wehrle-Haller, B. (2005). The mechanisms and dynamics of (alpha)v(beta)3 integrin clustering in living cells. *J. Cell Biol.* 171, 383–392. doi: 10.1083/jcb.200503017

Cortesio, C. L., Boateng, L. R., Piazza, T. M., Bennin, D. A., and Huttenlocher, A. (2011). Calpain-mediated proteolysis of paxillin negatively regulates focal adhesion dynamics and cell migration. *J. Biol. Chem.* 286, 9998–10006. doi: 10.1074/jbc.M110.187294

Coste, B., Mathur, J., Schmidt, M., Earley, T. J., Ranade, S., Petrus, M. J., et al. (2010). Piezo1 and Piezo2 are essential components of distinct mechanically activated cation channels. *Science* 330, 55–60. doi: 10.1126/science.1193270

Davare, M. A., Fortin, D. A., Saneyoshi, T., Nygaard, S., Kaech, S., Banker, G., et al. (2009). Transient receptor potential canonical 5 channels activate Ca2+/calmodulin kinase Igamma to promote axon formation in hippocampal neurons. *J. Neurosci.* 29, 9794–9808. doi: 10.1523/JNEUROSCI.1544-09.2009

De Wit, J., De Winter, F., Klooster, J., and Verhaagen, J. (2005). Semaphorin 3A displays a punctate distribution on the surface of neuronal cells and interacts with proteoglycans in the extracellular matrix. *Mol. Cell. Neurosci.* 29, 40–55. doi: 10.1016/j.mcn.2004.12.009

Dent, E. W., Gupton, S. L., and Gertler, F. B. (2011). The growth cone cytoskeleton in axon outgrowth and guidance. *Cold Spring Harb. Perspect. Biol.* 3:a001800. doi: 10.1101/cshperspect.a001800

del Rio, A., Perez-Jimenez, R., Liu, R., Roca-Cusachs, P., Fernandez, J. M., and Sheetz, M. P. (2009). Stretching single talin rod molecules activates vinculin binding. *Science* 323, 638–641. doi: 10.1126/science.1162912

Discher, D. E., Janmey, P., and Wang, Y. L. (2005). Tissue cells feel and respond to the stiffness of their substrate. *Science* 310, 1139–1143. doi: 10.1126/science.1116995

Discher, D. E., Mooney, D. J., and Zandstra, P. W. (2009). Growth factors, matrices and forces combine and control stem cells. *Science* 324, 1673–1677. doi: 10.1126/science.1171643

Doyle, A., Marganski, W., and Lee, J. (2004). Calcium transients induce spatially coordinated increases in traction force during the movement of fish keratocytes. *J. Cell Sci.* 117, 2203–2214. doi: 10.1242/jcs.01087

Du, X., Gu, M., Weisel, J. W., Nagaswami, C., Bennett, J. S., Bowditch, R., et al. (1993). Long range propagation of conformational changes in integrin alpha IIb beta 3. *J. Biol. Chem.* 268, 23087–23092.

Dudanova, I., and Klein, R. (2013). Integration of guidance cues: parallel signaling and crosstalk. *Trends Neurosci.* 36, 295–304. doi: 10.1016/j.tins.2013.01.007

Eisenhoffer, G. T., and Rosenblatt, J. (2013). Bringing balance by force: live cell extrusion controls epithelial cell numbers. *Trends Cell Biol.* 23, 185–192. doi: 10.1016/j.tcb.2012.11.006

Engler, A. J., Griffin, M. A., Sen, S., Bönnemann, C. G., Sweeney, H. L., and Discher, D. E. (2004). Myotubes differentiate optimally on substrates with tissue-like stiffness: pathological implications for soft or stiff microenvironments. *J. Cell Biol.* 166, 877–887. doi: 10.1083/jcb.200405004

Faucherre, A., Nargeot, J., Mangoni, M. E., and Jopling, C. (2013). piezo2b regulates vertebrate light touch response. *J. Neurosci.* 33, 17089–17094. doi: 10.1523/JNEUROSCI.0522-13.2013

Flanagan, L. A., Ju, Y. E., Marg, B., Osterfield, M., and Janmey, P. A. (2002). Neurite branching on deformable substrates. *Neuroreport* 13, 2411–2415. doi: 10.1097/00001756-200212200-00007

Forscher, P., and Smith, S. J. (1988). Actions of cytochalasins on the organization of actin filaments and microtubules in a neuronal growth cone. *J. Cell Biol.* 107, 1505–1516. doi: 10.1083/jcb.107.4.1505

Franco, S. J., and Huttenlocher, A. (2005). Regulating cell migration: calpains make the cut. *J. Cell Sci.* 118, 3829–3838. doi: 10.1242/jcs.02562

Franze, K. (2011). Atomic force microscopy and its contribution to understanding the development of the nervous system. *Curr. Opin. Genet. Dev.* 21, 530–537. doi: 10.1016/j.gde.2011.07.001

Franze, K. (2013). The mechanical control of nervous system development. *Development* 140, 3069–3077. doi: 10.1242/dev.079145

Franze, K., Gerdelmann, J., Weick, M., Betz, T., Pawlizak, S., Lakadamyali, M., et al. (2009). Neurite branch retraction is caused by a threshold-dependent mechanical impact. *Biophys. J.* 97, 1883–1890. doi: 10.1016/j.bpj.2009.07.033

Friedland, J. C., Lee, M. H., and Boettiger, D. (2009). Mechanically activated integrin switch controls alpha5beta1 function. *Science* 323, 642–644. doi: 10.1126/science.1168441

Furuike, S., Ito, T., and Yamazaki, M. (2001). Mechanical unfolding of single filamin A (ABP-280) molecules detected by atomic force microscopy. *FEBS Lett.* 498, 72–75. doi: 10.1016/s0014-5793(01)02497-8

Gardel, M. L., Sabass, B., Ji, L., Danuser, G., Schwarz, U. S., and Waterman, C. M. (2008). Traction stress in focal adhesions correlates biphasically with actin retrograde flow speed. *J. Cell Biol.* 183, 999–1005. doi: 10.1083/jcb.200810060

Gauthier, N. C., Fardin, M. A., Roca-Cusachs, P., and Sheetz, M. P. (2011). Temporary increase in plasma membrane tension coordinates the activation of exocytosis and contraction during cell spreading. *Proc. Natl. Acad. Sci. U S A* 108, 14467–14472. doi: 10.1073/pnas.1105845108

Geffeney, S. L., and Goodman, M. B. (2012). How we feel: ion channel partnerships that detect mechanical inputs and give rise to touch and pain perception. *Neuron* 74, 609–619. doi: 10.1016/j.neuron.2012.04.023

Geiger, B., Bershadsky, A., Pankov, R., and Yamada, K. M. (2001). Transmembrane crosstalk between the extracellular matrix–cytoskeleton crosstalk. *Nat. Rev. Mol. Cell Biol.* 2, 793–805. doi: 10.1038/35099066

Geiger, B., Spatz, J. P., and Bershadsky, A. D. (2009). Environmental sensing through focal adhesions. *Nat. Rev. Mol. Cell Biol.* 10, 21–33. doi: 10.1038/nrm2593

Georges, P. C., Miller, W. J., Meaney, D. F., Sawyer, E. S., and Janmey, P. A. (2006). Matrices with compliance comparable to that of brain tissue select neuronal over glial growth in mixed cortical cultures. *Biophys. J.* 90, 3012–3018. doi: 10.1529/biophysj.105.073114

Giannone, G., Mège, R. M., and Thoumine, O. (2009). Multi-level molecular clutches in motile cell processes. *Trends Cell Biol.* 19, 475–486. doi: 10.1016/j.tcb.2009.07.001

Gilmour, D., Knaut, H., Maischein, H. M., and Nusslein-Volhard, C. (2004). Towing of sensory axons by their migrating target cells in vivo. *Nat. Neurosci.* 7, 491–492. doi: 10.1038/nn1235

Gomez, T. M., and Letourneau, P. C. (1994). Filopodia initiate choices made by sensory neuron growth cones at laminin/fibronectin borders in vitro. *J. Neurosci.* 14, 5959–5972.

Gomez, T. M., and Letourneau, P. C. (2014). Actin dynamics in growth cone motility and navigation. *J. Neurochem.* 129, 221–234. doi: 10.1111/jnc.12506

Gomez, T. M., Robles, E., Poo, M., and Spitzer, N. C. (2001). Filopodial calcium transients promote substrate-dependent growth cone turning. *Science* 291, 1983–1987. doi: 10.1126/science.1056490

Gomez, T. M., Roche, F. K., and Letourneau, P. C. (1996). Chick sensory neuronal growth cones distinguish fibronectin from laminin by making substratum contacts that resemble focal contacts. *J. Neurobiol.* 29, 18–34. doi: 10.1002/(sici)1097-4695(199601)29:1<18::aid-neu2>3.0.co;2-a

Gomez, T. M., and Zheng, J. Q. (2006). The molecular basis for calcium-dependent axon pathfinding. *Nat. Rev. Neurosci.* 7, 115–125. doi: 10.1038/nrn1844

Gomis, A., Soriano, S., Belmonte, C., and Viana, F. (2008). Hypoosmotic- and pressure-induced membrane stretch activate TRPC5 channels. *J. Physiol.* 586, 5633–5649. doi: 10.1113/jphysiol.2008.161257

Goswami, C., Kuhn, J., Heppenstall, P. A., and Hucho, T. (2010). Importance of non-selective cation channel TRPV4 interaction with cytoskeleton and their reciprocal regulations in cultured cells. *PLoS One* 5:e11654. doi: 10.1371/journal.pone.0011654

Granato, M., van Eeden, F. J., Schach, U., Trowe, T., Brand, M., Furutani-Seiki, M., et al. (1996). Genes controlling and mediating locomotion behavior of the zebrafish embryo and larva. *Development* 123, 399–413.

Greka, A., Navarro, B., Oancea, E., Duggan, A., and Clapham, D. E. (2003). TRPC5 is a regulator of hippocampal neurite length and growth cone morphology. *Nat. Neurosci.* 6, 837–845. doi: 10.1038/nn1092

Hammarback, J. A., and Letourneau, P. C. (1986). Neurite extension across regions of low cell-substratum adhesivity: implications for the guidepost hypothesis of axonal pathfinding. *Dev. Biol.* 117, 655–662. doi: 10.1016/0012-1606(86)90334-9

Hammarback, J. A., Palm, S. L., Furcht, L. T., and Letourneau, P. C. (1985). Guidance of neurite outgrowth by pathways of substratum-adsorbed laminin. *J. Neurosci. Res.* 13, 213–220. doi: 10.1002/jnr.490130115

Hattori, M., Osterfield, M., and Flanagan, J. G. (2000). Regulated cleavage of a contact-mediated axon repellent. *Science* 289, 1360–1365. doi: 10.1126/science.289.5483.1360

Hayakawa, K., Tatsumi, H., and Sokabe, M. (2008). Actin stress fibers transmit and focus force to activate mechanosensitive channels. *J. Cell Sci.* 121, 496–503. doi: 10.1242/jcs.022053

Heidemann, S. R., Lamoureux, P., and Buxbaum, R. E. (1990). Growth cone behavior and production of traction force. *J. Cell Biol.* 111, 1949–1957. doi: 10.1083/jcb.111.5.1949

Hines, J. H., Abu-Rub, M., and Henley, J. R. (2010). Asymmetric endocytosis and remodeling of beta1-integrin adhesions during growth cone chemorepulsion by MAG. *Nat. Neurosci.* 13, 829–837. doi: 10.1038/nn.2554

Hopkins, A. M., De Laporte, L., Tortelli, F., Spedden, E., Staii, C., Atherton, T. J., et al. (2013). Silk hydrogels as soft substrates for neural tissue engineering. *Adv. Funct. Mater.* 23, 5140–5149. doi: 10.1002/adfm.201300435

Houk, A. R., Jilkine, A., Mejean, C. O., Boltyanskiy, R., Dufresne, E. R., Angenent, S. B., et al. (2012). Membrane tension maintains cell polarity by confining signals to the leading edge during neutrophil migration. *Cell* 148, 175–188. doi: 10.1016/j.cell.2011.10.050

Hu, H. (2001). Cell-surface heparan sulfate is involved in the repulsive guidance activities of Slit2 protein. *Nat. Neurosci.* 4, 695–701. doi: 10.1038/89482

Huang, Z., Yazdani, U., Thompson-Peer, K. L., Kolodkin, A. L., and Terman, J. R. (2007). Crk-associated substrate (Cas) signaling protein functions with integrins to specify axon guidance during development. *Development* 134, 2337–2347. doi: 10.1242/dev.004242

Hui, H., McHugh, D., Hannan, M., Zeng, F., Xu, S. Z., Khan, S. U., et al. (2006). Calcium-sensing mechanism in TRPC5 channels contributing to retardation of neurite outgrowth. *J. Physiol.* 572, 165–172. doi: 10.1113/jphysiol.2005.102889

Humphries, J. D., Paul, N. R., Humphries, M. J., and Morgan, M. R. (2015). Emerging properties of adhesion complexes: what are they and what do they do? *Trends Cell Biol.* doi: 10.1016/j.tcb.2015.02.008 [Epub ahead of print].

Hyland, C., Mertz, A. F., Forscher, P., and Dufresne, E. (2014). Dynamic peripheral traction forces balance stable neurite tension in regenerating Aplysia bag cell neurons. *Sci. Rep.* 4:4961. doi: 10.1038/srep04961

Hynes, R. O. (2002). Integrins: bidirectional, allosteric signaling machines. *Cell* 110, 673–687. doi: 10.1016/S0092-8674(02)00971-6

Hynes, R. O. (2009). The extracellular matrix: not just pretty fibrils. *Science* 326, 1216–1219. doi: 10.1126/science.1176009

Hynes, R. O., and Naba, A. (2012). Overview of the matrisome–an inventory of extracellular matrix constituents and functions. *Cold Spring Harb. Perspect. Biol.* 4:a004903. doi: 10.1101/cshperspect.a004903

Isacson, O., Deacon, T. W., Pakzaban, P., Galpern, W. R., Dinsmore, J., and Burns, L. H. (1995). Transplanted xenogeneic neural cells in neurodegenerative disease models exhibit remarkable axonal target specificity and distinct growth patterns of glial and axonal fibres. *Nat. Med.* 1, 1189–1194. doi: 10.1038/nm1195-1189

Iwashita, M., Kataoka, N., Toida, K., and Kosodo, Y. (2014). Systematic profiling of spatiotemporal tissue and cellular stiffness in the developing brain. *Development* 141, 3793–3798. doi: 10.1242/dev.109637

Jacques-Fricke, B. T., Seow, Y., Gottlieb, P. A., Sachs, F., and Gomez, T. M. (2006). Ca2+ influx through mechanosensitive channels inhibits neurite outgrowth in opposition to other influx pathways and release from intracellular stores. *J. Neurosci.* 26, 5656–5664. doi: 10.1523/jneurosci.0675-06.2006

Jiang, F. X., Yurke, B., Firestein, B. L., and Langrana, N. A. (2008). Neurite outgrowth on a DNA crosslinked hydrogel with tunable stiffnesses. *Ann. Biomed. Eng.* 36, 1565–1579. doi: 10.1007/s10439-008-9530-z

Kang, H., and Lichtman, J. W. (2013). Motor axon regeneration and muscle reinnervation in young adult and aged animals. *J. Neurosci.* 33, 19480–19491. doi: 10.1523/JNEUROSCI.4067-13.2013

Kazmierczak, P., and Müller, U. (2012). Sensing sound: molecules that orchestrate mechanotransduction by hair cells. *Trends Neurosci.* 35, 220–229. doi: 10.1016/j.tins.2011.10.007

Kerstein, P. C., Jacques-Fricke, B. T., Rengifo, J., Mogen, B. J., Williams, J. C., Gottlieb, P. A., et al. (2013). Mechanosensitive TRPC1 channels promote calpain proteolysis of talin to regulate spinal axon outgrowth. *J. Neurosci.* 33, 273–285. doi: 10.1523/JNEUROSCI.2142-12.2013

Keynes, R. J., and Stern, C. D. (1984). Segmentation in the vertebrate nervous system. *Nature* 310, 786–789. doi: 10.1038/310786a0

Kim, S. N., Jeibmann, A., Halama, K., Witte, H. T., Wälte, M., Matzat, T., et al. (2014). ECM stiffness regulates glial migration in Drosophila and mammalian glioma models. *Development* 141, 3233–3242. doi: 10.1242/dev.106039

Kim, T. J., Seong, J., Ouyang, M., Sun, J., Lu, S., Hong, J. P., et al. (2009). Substrate rigidity regulates Ca2+ oscillation via RhoA pathway in stem cells. *J. Cell Physiol.* 218, 285–293. doi: 10.1002/jcp.21598

Kobayashi, T., and Sokabe, M. (2010). Sensing substrate rigidity by mechanosensitive ion channels with stress fibers and focal adhesions. *Curr. Opin. Cell Biol.* 22, 669–676. doi: 10.1016/j.ceb.2010.08.023

Koch, D., Rosoff, W. J., Jiang, J., Geller, H. M., and Urbach, J. S. (2012). Strength in the periphery: growth cone biomechanics and substrate rigidity response in peripheral and central nervous system neurons. *Biophys. J.* 102, 452–460. doi: 10.1016/j.bpj.2011.12.025

Kolodkin, A. L., and Tessier-Lavigne, M. (2011). Mechanisms and molecules of neuronal wiring: a primer. *Cold Spring Harb. Perspect. Biol.* 3:a001727. doi: 10.1101/cshperspect.a001727

Kostic, A., Sap, J., and Sheetz, M. P. (2007). RPTPalpha is required for rigidity-dependent inhibition of extension and differentiation of hippocampal neurons. *J. Cell Sci.* 120, 3895–3904. doi: 10.1242/jcs.009852

Kruse, S. A., Rose, G. H., Glaser, K. J., Manduca, A., Felmlee, J. P., Jack, C. R. Jr., et al. (2008). Magnetic resonance elastography of the brain. *Neuroimage* 39, 231–237. doi: 10.1016/j.neuroimage.2007.08.030

Kubota, H., Ishikawa, R., Ohki, T., Ishizuka, J., Mikhailenko, S. V., and Ishiwata, S. (2010). Modulation of the mechano-chemical properties of myosin V by drebrin-E. *Biochem. Biophys. Res. Commun.* 400, 643–648. doi: 10.1016/j.bbrc.2010.08.120

Kuo, J. C., Han, X., Yates, J. R., III, and Waterman, C. M. (2012). Isolation of focal adhesion proteins for biochemical and proteomic analysis. *Methods Mol. Biol.* 757, 297–323. doi: 10.1007/978-1-61779-166-6_19

Lagenaur, C., and Lemmon, V. (1987). An L1-like molecule, the 8D9 antigen, is a potent substrate for neurite extension. *Proc. Natl. Acad. Sci. U S A* 84, 7753–7757. doi: 10.1073/pnas.84.21.7753

Lamoureux, P., Buxbaum, R. E., and Heidemann, S. R. (1989). Direct evidence that growth cones pull. *Nature* 340, 159–162. doi: 10.1038/340159a0

Lee, J., Ishihara, A., Oxford, G., Johnson, B., and Jacobson, K. (1999). Regulation of cell movement is mediated by stretch-activated calcium channels. *Nature* 400, 382–386. doi: 10.1038/22578

Letourneau, P. C., Shattuck, T. A., and Ressler, A. H. (1987). "Pull" and "push" in neurite elongation: observations on the effects of different concentrations of cytochalasin B and taxol. *Cell Motil. Cytoskeleton* 8, 193–209. doi: 10.1002/cm.970080302

Li, J., Gu, X., Ma, Y., Calicchio, M. L., Kong, D., Teng, Y. D., et al. (2010). Nna1 mediates Purkinje cell dendritic development via lysyl oxidase propeptide and NF-kappaB signaling. *Neuron* 68, 45–60. doi: 10.1016/j.neuron.2010.08.013

Li, Y., Jia, Y. C., Cui, K., Li, N., Zheng, Z. Y., Wang, Y. Z., et al. (2005). Essential role of TRPC channels in the guidance of nerve growth cones by brain-derived neurotrophic factor. *Nature* 434, 894–898. doi: 10.1038/nature03477

Lin, C. H., and Forscher, P. (1995). Growth cone advance is inversely proportional to retrograde F-actin flow. *Neuron* 14, 763–771. doi: 10.1016/0896-6273(95)90220-1

Lin, C. H., Espreafico, E. M., Mooseker, M. S., and Forscher, P. (1996). Myosin drives retrograde F-actin flow in neuronal growth cones. *Neuron* 16, 769–782. doi: 10.1016/s0896-6273(00)80097-5

Liu, C., and Montell, C. (2015). Forcing open TRP channels: Mechanical gating as a unifying activation mechanism. *Biochem. Biophys. Res. Commun.* 460, 22–25. doi: 10.1016/j.bbrc.2015.02.067

Lo, C. M., Wang, H. B., Dembo, M., and Wang, Y. L. (2000). Cell movement is guided by the rigidity of the substrate. *Biophys. J.* 79, 144–152. doi: 10.1016/s0006-3495(00)76279-5

Lowery, L. A., and van Vactor, D. (2009). The trip of the tip: understanding the growth cone machinery. *Nat. Rev. Mol. Cell Biol.* 10, 332–343. doi: 10.1038/nrm2679

Lu, Y. B., Franze, K., Seifert, G., Steinhäuser, C., Kirchhoff, F., Wolburg, H., et al. (2006). Viscoelastic properties of individual glial cells and neurons in the CNS. *Proc. Natl. Acad. Sci. U S A* 103, 17759–17764. doi: 10.1073/pnas.0606150103

Mai, J., Fok, L., Gao, H., Zhang, X., and Poo, M. M. (2009). Axon initiation and growth cone turning on bound protein gradients. *J. Neurosci.* 29, 7450–7458. doi: 10.1523/JNEUROSCI.1121-09.2009

Manitt, C., and Kennedy, T. E. (2002). Where the rubber meets the road: netrin expression and function in developing and adult nervous systems. *Prog. Brain Res.* 137, 425–442. doi: 10.1016/s0079-6123(02)37034-1

Margadant, F., Chew, L. L., Hu, X., Yu, H., Bate, N., Zhang, X., et al. (2011). Mechanotransduction in vivo by repeated talin stretch-relaxation events depends upon vinculin. *PLoS Biol.* 9:e1001223. doi: 10.1371/journal.pbio.1001223

Maroto, R., Raso, A., Wood, T. G., Kurosky, A., Martinac, B., and Hamill, O. P. (2005). TRPC1 forms the stretch-activated cation channel in vertebrate cells. *Nat. Cell Biol.* 7, 179–185. doi: 10.1038/ncb1218

Marsick, B. M., Flynn, K. C., Santiago-Medina, M., Bamburg, J. R., and Letourneau, P. C. (2010). Activation of ADF/cofilin mediates attractive growth cone turning toward nerve growth factor and netrin-1. *Dev. Neurobiol.* 70, 565–588. doi: 10.1002/dneu.20800

Matthews, B. D., Thodeti, C. K., Tytell, J. D., Mammoto, A., Overby, D. R., and Ingber, D. E. (2010). Ultra-rapid activation of TRPV4 ion channels by mechanical forces applied to cell surface beta1 integrins. *Integr. Biol. (Camb)* 2, 435–442. doi: 10.1039/c0ib00034e

McHugh, B. J., Buttery, R., Lad, Y., Banks, S., Haslett, C., and Sethi, T. (2010). Integrin activation by Fam38A uses a novel mechanism of R-Ras targeting to the endoplasmic reticulum. *J. Cell Sci.* 123, 51–61. doi: 10.1242/jcs.056424

McHugh, B. J., Murdoch, A., Haslett, C., and Sethi, T. (2012). Loss of the integrin-activating transmembrane protein Fam38A (Piezo1) promotes a switch to a reduced integrin-dependent mode of cell migration. *PLoS One* 7:e40346. doi: 10.1371/journal.pone.0040346

Medeiros, N. A., Burnette, D. T., and Forscher, P. (2006). Myosin II functions in actin-bundle turnover in neuronal growth cones. *Nat. Cell Biol.* 8, 215–226. doi: 10.1038/ncb1367

Mingorance-Le Meur, A., and O'connor, T. P. (2009). Neurite consolidation is an active process requiring constant repression of protrusive activity. *EMBO J.* 28, 248–260. doi: 10.1038/emboj.2008.265

Mogilner, A., and Oster, G. (2003). Polymer motors: pushing out the front and pulling up the back. *Curr. Biol.* 13, R721–R733. doi: 10.1016/j.cub.2003.08.050

Moore, S. W., Biais, N., and Sheetz, M. P. (2009). Traction on immobilized netrin-1 is sufficient to reorient axons. *Science* 325:166. doi: 10.1126/science.1173851

Moore, S. W., Roca-Cusachs, P., and Sheetz, M. P. (2010). Stretchy proteins on stretchy substrates: the important elements of integrin-mediated rigidity sensing. *Dev. Cell* 19, 194–206. doi: 10.1016/j.devcel.2010.07.018

Moore, S. W., and Sheetz, M. P. (2011). Biophysics of substrate interaction: influence on neural motility, differentiation and repair. *Dev. Neurobiol.* 71, 1090–1101. doi: 10.1002/dneu.20947

Moore, S. W., Zhang, X., Lynch, C. D., and Sheetz, M. P. (2012). Netrin-1 attracts axons through FAK-dependent mechanotransduction. *J. Neurosci.* 32, 11574–11585. doi: 10.1523/JNEUROSCI.0999-12.2012

Munevar, S., Wang, Y. L., and Dembo, M. (2004). Regulation of mechanical interactions between fibroblasts and the substratum by stretch-activated Ca2+ entry. *J. Cell Sci.* 117, 85–92. doi: 10.1242/jcs.00795

Musah, S., Wrighton, P. J., Zaltsman, Y., Zhong, X., Zorn, S., Parlato, M. B., et al. (2014). Substratum-induced differentiation of human pluripotent stem cells reveals the coactivator YAP is a potent regulator of neuronal specification. *Proc. Natl. Acad. Sci. U S A* 111, 13805–13810. doi: 10.1073/pnas.1415330111

Myers, J. P., and Gomez, T. M. (2011). Focal adhesion kinase promotes integrin adhesion dynamics necessary for chemotropic turning of nerve growth cones. *J. Neurosci.* 31, 13585–13595. doi: 10.1523/JNEUROSCI.2381-11.2011

Myers, J. P., Robles, E., Ducharme-Smith, A., and Gomez, T. M. (2012). Focal adhesion kinase modulates Cdc42 activity downstream of positive and negative axon guidance cues. *J. Cell Sci.* 125(Pt. 12), 2918–2929. doi: 10.1242/jcs.100107

Myers, J. P., Santiago-Medina, M., and Gomez, T. M. (2011). Regulation of axonal outgrowth and pathfinding by integrin-ECM interactions. *Dev. Neurobiol.* 71, 901–923. doi: 10.1002/dneu.20931

Nakamura, F., Kumeta, K., Hida, T., Isono, T., Nakayama, Y., Kuramata-Matsuoka, E., et al. (2014). Amino- and carboxyl-terminal domains of Filamin-A interact with CRMP1 to mediate Sema3A signalling. *Nat. Commun.* 5:5325. doi: 10.1038/ncomms6325

Nguyen, Q. T., Sanes, J. R., and Lichtman, J. W. (2002). Pre-existing pathways promote precise projection patterns. *Nat. Neurosci.* 5, 861–867. doi: 10.1038/nn905

O'Connor, T. P., Duerr, J. S., and Bentley, D. (1990). Pioneer growth cone steering decisions mediated by single filopodial contacts in situ. *J. Neurosci.* 10, 3935–3946.

Oancea, E., Wolfe, J. T., and Clapham, D. E. (2006). Functional TRPM7 channels accumulate at the plasma membrane in response to fluid flow. *Circ. Res.* 98, 245–253. doi: 10.1161/01.res.0000200179.29375.cc

Paszek, M. J., Zahir, N., Johnson, K. R., Lakins, J. N., Rozenberg, G. I., Gefen, A., et al. (2005). Tensional homeostasis and the malignant phenotype. *Cancer Cell* 8, 241–254. doi: 10.1016/j.ccr.2005.08.010

Paulus, J. D., Willer, G. B., Willer, J. R., Gregg, R. G., and Halloran, M. C. (2009). Muscle contractions guide rohon-beard peripheral sensory axons. *J. Neurosci.* 29, 13190–13201. doi: 10.1523/JNEUROSCI.2179-09.2009

Pelham, R. J. Jr., and Wang, Y. I. (1997). Cell locomotion and focal adhesions are regulated by substrate flexibility. *Proc. Natl. Acad. Sci. U S A* 94, 13661–13665. doi: 10.1073/pnas.94.25.13661

Plotnikov, S. V., Pasapera, A. M., Sabass, B., and Waterman, C. M. (2012). Force fluctuations within focal adhesions mediate ECM-rigidity sensing to guide directed cell migration. *Cell* 151, 1513–1527. doi: 10.1016/j.cell.2012.11.034

Provenzano, P. P., Inman, D. R., Eliceiri, K. W., and Keely, P. J. (2009). Matrix density-induced mechanoregulation of breast cell phenotype, signaling and gene expression through a FAK-ERK linkage. *Oncogene* 28, 4326–4343. doi: 10.1038/onc.2009.299

Rahman, S., Patel, Y., Murray, J., Patel, K. V., Sumathipala, R., Sobel, M., et al. (2005). Novel hepatocyte growth factor (HGF) binding domains on fibronectin and vitronectin coordinate a distinct and amplified Met-integrin induced signalling pathway in endothelial cells. *BMC Cell Biol.* 6:8. doi: 10.1186/1471-2121-6-8

Ranade, S. S., Woo, S. H., Dubin, A. E., Moshourab, R. A., Wetzel, C., Petrus, M., et al. (2014). Piezo2 is the major transducer of mechanical forces for touch sensation in mice. *Nature* 516, 121–125. doi: 10.1038/nature13980

Razinia, Z., Mäkelä, T., Ylänne, J., and Calderwood, D. A. (2012). Filamins in mechanosensing and signaling. *Annu. Rev. Biophys.* 41, 227–246. doi: 10.1146/annurev-biophys-050511-102252

Riccio, A., Medhurst, A. D., Mattei, C., Kelsell, R. E., Calver, A. R., Randall, A. D., et al. (2002). mRNA distribution analysis of human TRPC family in CNS and peripheral tissues. *Brain Res. Mol. Brain Res.* 109, 95–104. doi: 10.1016/s0169-328x(02)00527-2

Riccomagno, M. M., Sun, L. O., Brady, C. M., Alexandropoulos, K., Seo, S., Kurokawa, M., et al. (2014). Cas adaptor proteins organize the retinal ganglion cell layer downstream of integrin signaling. *Neuron* 81, 779–786. doi: 10.1016/j.neuron.2014.01.036

Robles, E., and Gomez, T. M. (2006). Focal adhesion kinase signaling at sites of integrin-mediated adhesion controls axon pathfinding. *Nat. Neurosci.* 9, 1274–1283. doi: 10.1038/nn1762

Robles, E., Huttenlocher, A., and Gomez, T. M. (2003). Filopodial calcium transients regulate growth cone motility and guidance through local activation of calpain. *Neuron* 38, 597–609. doi: 10.1016/s0896-6273(03)00260-5

Rutishauser, U. (1985). Influences of the neural cell adhesion molecule on axon growth and guidance. *J. Neurosci. Res.* 13, 123–131. doi: 10.1002/jnr.490130109

Santiago-Medina, M., Gregus, K. A., and Gomez, T. M. (2013). PAK-PIX interactions regulate adhesion dynamics and membrane protrusion to control neurite outgrowth. *J. Cell Sci.* 126, 1122–1133. doi: 10.1242/jcs.112607

Santiago-Medina, M., Gregus, K. A., Nichol, R. H., O'Toole, S. M., and Gomez, T. M. (2015). Regulation of ECM degradation and axon guidance by growth cone invadosomes. *Development* 142, 486–496. doi: 10.1242/dev.108266

Sawada, Y., Tamada, M., Dubin-Thaler, B. J., Cherniavskaya, O., Sakai, R., Tanaka, S., et al. (2006). Force sensing by mechanical extension of the Src family kinase substrate p130Cas. *Cell* 127, 1015–1026. doi: 10.1016/j.cell.2006.09.044

Schedin, P., and Keely, P. J. (2011). Mammary gland ECM remodeling, stiffness and mechanosignaling in normal development and tumor progression. *Cold Spring Harb. Perspect. Biol.* 3:a003228. doi: 10.1101/cshperspect.a003228

Schmidt, C. E., Dai, J., Lauffenburger, D. A., Sheetz, M. P., and Horwitz, A. F. (1995). Integrin-cytoskeletal interactions in neuronal growth cones. *J. Neurosci.* 15, 3400–3407.

Schneider, V. A., and Granato, M. (2006). The myotomal diwanka (lh3) glycosyltransferase and type XVIII collagen are critical for motor growth cone migration. *Neuron* 50, 683–695. doi: 10.1016/j.neuron.2006.04.024

Shibasaki, K., Murayama, N., Ono, K., Ishizaki, Y., and Tominaga, M. (2010). TRPV2 enhances axon outgrowth through its activation by membrane stretch in developing sensory and motor neurons. *J. Neurosci.* 30, 4601–4612. doi: 10.1523/JNEUROSCI.5830-09.2010

Shigeoka, T., Lu, B., and Holt, C. E. (2013). Cell biology in neuroscience: RNA-based mechanisms underlying axon guidance. *J. Cell Biol.* 202, 991–999. doi: 10.1083/jcb.201305139

Shim, S., Goh, E. L., Ge, S. Y., Sailor, K., Yuan, J. P., Roderick, H. L., et al. (2005). XTRPC1-dependent chemotropic guidance of neuronal growth cones. *Nat. Neurosci.* 8, 730–735. doi: 10.1038/nn1459

Shimada, T., Toriyama, M., Uemura, K., Kamiguchi, H., Sugiura, T., Watanabe, N., et al. (2008). Shootin1 interacts with actin retrograde flow and L1-CAM to promote axon outgrowth. *J. Cell Biol.* 181, 817–829. doi: 10.1083/jcb.200712138

Shin, E. Y., Lee, C. S., Yun, C. Y., Won, S. Y., Kim, H. K., Lee, Y. H., et al. (2014). Non-muscle myosin II regulates neuronal actin dynamics by interacting with guanine nucleotide exchange factors. *PLoS One* 9:e95212. doi: 10.1371/journal.pone.0095212

Smilenov, L. B., Mikhailov, A., Pelham, R. J., Marcantonio, E. E., and Gundersen, G. G. (1999). Focal adhesion motility revealed in stationary fibroblasts. *Science* 286, 1172–1174. doi: 10.1126/science.286.5442.1172

Spassova, M. A., Hewavitharana, T., Xu, W., Soboloff, J., and Gill, D. L. (2006). A common mechanism underlies stretch activation and receptor activation of TRPC6 channels. *Proc. Natl. Acad. Sci. U S A* 103, 16586–16591. doi: 10.1073/pnas.0606894103

Strübing, C., Krapivinsky, G., Krapivinsky, L., and Clapham, D. E. (2003). Formation of novel TRPC channels by complex subunit interactions in embryonic brain. *J. Biol. Chem.* 278, 39014–39019. doi: 10.1074/jbc.m306705200

Sundararaghavan, H. G., Monteiro, G. A., Firestein, B. L., and Shreiber, D. I. (2009). Neurite growth in 3D collagen gels with gradients of mechanical properties. *Biotechnol. Bioeng.* 102, 632–643. doi: 10.1002/bit.22074

Suter, D. M., Errante, L. D., Belotserkovsky, V., and Forscher, P. (1998). The Ig superfamily cell adhesion molecule, apCAM, mediates growth cone steering by substrate-cytoskeletal coupling. *J. Cell Biol.* 141, 227–240. doi: 10.1083/jcb.141.1.227

Suter, D. M., Espindola, F. S., Lin, C. H., Forscher, P., and Mooseker, M. S. (2000). Localization of unconventional myosins V and VI in neuronal growth cones. *J. Neurobiol.* 42, 370–382. doi: 10.1002/(sici)1097-4695(20000215)42:3<370::aid-neu8>3.3.co;2-m

Sydor, A. M., Su, A. L., Wang, F. S., Xu, A., and Jay, D. G. (1996). Talin and vinculin play distinct roles in filopodial motility in the neuronal growth cone. *J. Cell Biol.* 134, 1197–1207. doi: 10.1083/jcb.134.5.1197

Symons, M. H., and Mitchison, T. J. (1991). Control of actin polymerization in live and permeabilized fibroblasts. *J. Cell Biol.* 114, 503–513. doi: 10.1083/jcb.114.3.503

Thievessen, I., Thompson, P. M., Berlemont, S., Plevock, K. M., Plotnikov, S. V., Zemljic-Harpf, A., et al. (2013). Vinculin-actin interaction couples actin retrograde flow to focal adhesions, but is dispensable for focal adhesion growth. *J. Cell Biol.* 202, 163–177. doi: 10.1083/jcb.201303129

Tojima, T., Akiyama, H., Itofusa, R., Li, Y., Katayama, H., Miyawaki, A., et al. (2007). Attractive axon guidance involves asymmetric membrane transport and exocytosis in the growth cone. *Nat. Neurosci.* 10, 58–66. doi: 10.1038/nn1814

Tojima, T., Itofusa, R., and Kamiguchi, H. (2010). Asymmetric clathrin-mediated endocytosis drives repulsive growth cone guidance. *Neuron* 66, 370–377. doi: 10.1016/j.neuron.2010.04.007

Tojima, T., Itofusa, R., and Kamiguchi, H. (2014). Steering neuronal growth cones by shifting the imbalance between exocytosis and endocytosis. *J. Neurosci.* 34, 7165–7178. doi: 10.1523/JNEUROSCI.5261-13.2014

Toriyama, M., Kozawa, S., Sakumura, Y., and Inagaki, N. (2013). Conversion of a signal into forces for axon outgrowth through Pak1-mediated shootin1 phosphorylation. *Curr. Biol.* 23, 529–534. doi: 10.1016/j.cub.2013.02.017

Turlova, E., Bae, C. Y., Deurloo, M., Chen, W., Barszczyk, A., Horgen, F. D., et al. (2014). TRPM7 Regulates Axonal Outgrowth and Maturation of Primary Hippocampal Neurons. *Mol. Neurobiol.* doi: 10.1007/s12035-014-9032-y [Epub ahead of print].

Turney, S. G., and Bridgman, P. C. (2005). Laminin stimulates and guides axonal outgrowth via growth cone myosin II activity. *Nat. Neurosci.* 8, 717–719. doi: 10.1038/nn1466

Tyler, W. J. (2012). The mechanobiology of brain function. *Nat. Rev. Neurosci.* 13, 867–878. doi: 10.1038/nrn3383

Vitriol, E. A., and Zheng, J. Q. (2012). Growth cone travel in space and time: the cellular ensemble of cytoskeleton, adhesion and membrane. *Neuron* 73, 1068–1081. doi: 10.1016/j.neuron.2012.03.005

Von Niederhäusern, V., Kastenhuber, E., Stäuble, A., Gesemann, M., and Neuhauss, S. C. (2013). Phylogeny and expression of canonical transient receptor potential (TRPC) genes in developing zebrafish. *Dev. Dyn.* 242, 1427–1441. doi: 10.1002/dvdy.24041

von Philipsborn, A. C., Lang, S., Bernard, A., Loeschinger, J., David, C., Lehnert, D., et al. (2006). Microcontact printing of axon guidance molecules for generation of graded patterns. *Nat. Protoc.* 1, 1322–1328. doi: 10.1038/nprot.2006.251

Vriens, J., Watanabe, H., Janssens, A., Droogmans, G., Voets, T., and Nilius, B. (2004). Cell swelling, heat and chemical agonists use distinct pathways for the activation of the cation channel TRPV4. *Proc. Natl. Acad. Sci. U S A* 101, 396–401. doi: 10.1073/pnas.0303329101

Wang, H. B., Dembo, M., Hanks, S. K., and Wang, Y. (2001). Focal adhesion kinase is involved in mechanosensing during fibroblast migration. *Proc. Natl. Acad. Sci. U S A* 98, 11295–11300. doi: 10.1073/pnas.201201198

Wang, F. S., Liu, C. W., Diefenbach, T. J., and Jay, D. G. (2003). Modeling the role of myosin 1c in neuronal growth cone turning. *Biophys. J.* 85, 3319–3328. doi: 10.1016/s0006-3495(03)74751-1

Wang, G. X., and Poo, M. M. (2005). Requirement of TRPC channels in netrin-1-induced chemotropic turning of nerve growth cones. *Nature* 434, 898–904. doi: 10.1038/nature03478

Wei, C., Wang, X., Chen, M., Ouyang, K., Song, L. S., and Cheng, H. (2009). Calcium flickers steer cell migration. *Nature* 457, 901–905. doi: 10.1038/nature07577

Weinl, C., Drescher, U., Lang, S., Bonhoeffer, F., and Löschinger, J. (2003). On the turning of Xenopus retinal axons induced by ephrin-A5. *Development* 130, 1635–1643. doi: 10.1242/dev.00386

Wen, Z., Guirland, C., Ming, G. L., and Zheng, J. Q. (2004). A CaMKII/calcineurin switch controls the direction of Ca(2+)-dependent growth cone guidance. *Neuron* 43, 835–846. doi: 10.1016/j.neuron.2004.08.037

Wen, Z., Han, L., Bamburg, J. R., Shim, S., Ming, G. L., and Zheng, J. Q. (2007). BMP gradients steer nerve growth cones by a balancing act of LIM kinase and Slingshot phosphatase on ADF/cofilin. *J. Cell Biol.* 178, 107–119. doi: 10.1083/jcb.200703055

Willits, R. K., and Skornia, S. L. (2004). Effect of collagen gel stiffness on neurite extension. *J. Biomater. Sci. Polym. Ed.* 15, 1521–1531. doi: 10.1163/1568562042459698

Winkle, C. C., McClain, L. M., Valtschanoff, J. G., Park, C. S., Maglione, C., and Gupton, S. L. (2014). A novel Netrin-1-sensitive mechanism promotes local SNARE-mediated exocytosis during axon branching. *J. Cell Biol.* 205, 217–232. doi: 10.1083/jcb.201311003

Woo, S., and Gomez, T. M. (2006). Rac1 and RhoA promote neurite outgrowth through formation and stabilization of growth cone point contacts. *J. Neurosci.* 26, 1418–1428. doi: 10.1523/jneurosci.4209-05.2006

Woo, S., Rowan, D. J., and Gomez, T. M. (2009). Retinotopic mapping requires focal adhesion kinase-mediated regulation of growth cone adhesion. *J. Neurosci.* 29, 13981–13991. doi: 10.1523/JNEUROSCI.4028-09.2009

Woo, S. H., Ranade, S., Weyer, A. D., Dubin, A. E., Baba, Y., Qiu, Z., et al. (2014). Piezo2 is required for Merkel-cell mechanotransduction. *Nature* 509, 622–626. doi: 10.1038/nature13251

Wright, K. M., Lyon, K. A., Leung, H., Leahy, D. J., Ma, L., and Ginty, D. D. (2012). Dystroglycan organizes axon guidance cue localization and axonal pathfinding. *Neuron* 76, 931–944. doi: 10.1016/j.neuron.2012.10.009

Wu, G., Lu, Z. H., Obukhov, A. G., Nowycky, M. C., and Ledeen, R. W. (2007). Induction of calcium influx through TRPC5 channels by cross-linking of GM1 ganglioside associated with alpha5beta1 integrin initiates neurite outgrowth. *J. Neurosci.* 27, 7447–7458. doi: 10.1523/jneurosci.4266-06.2007

Wu, L. J., Sweet, T. B., and Clapham, D. E. (2010). International union of basic and clinical pharmacology. LXXVI. Current progress in the mammalian TRP ion channel family. *Pharmacol. Rev.* 62, 381–404. doi: 10.1124/pr.110.002725

Xiao, T., Staub, W., Robles, E., Gosse, N. J., Cole, G. J., and Baier, H. (2011). Assembly of lamina-specific neuronal connections by slit bound to type IV collagen. *Cell* 146, 164–176. doi: 10.1016/j.cell.2011.06.016

Yamauchi, M., and Sricholpech, M. (2012). Lysine post-translational modifications of collagen. *Essays Biochem.* 52, 113–133. doi: 10.1042/bse0520113

Yang, Q., Zhang, X. F., Van Goor, D., Dunn, A. P., Hyland, C., Medeiros, N., et al. (2013). Protein kinase C activation decreases peripheral actin network density and increases central nonmuscle myosin II contractility in neuronal growth cones. *Mol. Biol. Cell* 24, 3097–3114. doi: 10.1091/mbc.e13-05-0289

Zeller, J., and Granato, M. (1999). The zebrafish diwanka gene controls an early step of motor growth cone migration. *Development* 126, 3461–3472.

Zhang, X. F., Hyland, C., Van Goor, D., and Forscher, P. (2012). Calcineurin-dependent cofilin activation and increased retrograde actin flow drive 5-HT-dependent neurite outgrowth in Aplysia bag cell neurons. *Mol. Biol. Cell* 23, 4833–4848. doi: 10.1091/mbc.e12-10-0715

Zheng, L., Michelson, Y., Freger, V., Avraham, Z., Venken, K. J., Bellen, H. J., et al. (2011). Drosophila Ten-m and filamin affect motor neuron growth cone guidance. *PLoS One* 6:e22956. doi: 10.1371/journal.pone.0022956

Conflict of Interest Statement: The authors declare that the research was conducted in the absence of any commercial or financial relationships that could be construed as a potential conflict of interest.

frontiers
in Cellular Neuroscience

MINI REVIEW
published: 27 July 2015
doi: 10.3389/fncel.2015.00282

Microtechnologies for studying the role of mechanics in axon growth and guidance

Devrim Kilinc, Agata Blasiak and Gil U. Lee**

Bionanosciences Group, School of Chemisty and Chemical Biology, University College Dublin, Belfield, Dublin, Ireland

The guidance of axons to their proper targets is not only a crucial event in neurodevelopment, but also a potential therapeutic target for neural repair. Axon guidance is mediated by various chemo- and haptotactic cues, as well as the mechanical interactions between the cytoskeleton and the extracellular matrix (ECM). Axonal growth cones, dynamic ends of growing axons, convert external stimuli to biochemical signals, which, in turn, are translated into behavior, *e.g.*, turning or retraction, *via* cytoskeleton–matrix linkages. Despite the inherent mechanical nature of the problem, the role of mechanics in axon guidance is poorly understood. Recent years has witnessed the application of a range of microtechnologies in neurobiology, from microfluidic circuits to single molecule force spectroscopy. In this mini-review, we describe microtechnologies geared towards dissecting the mechanical aspects of axon guidance, divided into three categories: controlling the growth cone microenvironment, stimulating growth cones with externally applied forces, and measuring forces exerted by the growth cones. A particular emphasis is given to those studies that combine multiple techniques, as dictated by the complexity of the problem.

Keywords: growth cones, cytoskeleton, mechanotransduction, microenvironment, axon towing

Edited by:
Daniel Marcel Suter,
Purdue University, USA

Reviewed by:
Stefania Ceruti,
Università degli Studi di Milano, Italy
Claudia Lodovichi,
Venetian Institute of Molecular Medicine, Italy
Naoyuki Inagaki,
Nara Institute of Science and Technology, Japan

****Correspondence:***
Devrim Kilinc and Gil U. Lee,
Bionanosciences Group, School of Chemistry and Chemical Biology,
O'Brien Centre for Science,
University College Dublin, Belfield,
Dublin 4, Ireland
devrim.kilinc@ucd.ie;
gil.lee@ucd.ie

Received: *01 June 2015*
Accepted: *10 July 2015*
Published: *27 July 2015*

Citation:
Kilinc D, Blasiak A and Lee GU (2015) Microtechnologies for studying the role of mechanics in axon growth and guidance.
Front. Cell. Neurosci. 9:282.
doi: 10.3389/fncel.2015.00282

Introduction

The guidance of axons to their proper targets is not only a fundamental event in the development of the nervous system, but also a potential therapeutic target for repairing the injured nervous system. A better understanding of axon guidance mechanisms may lead to novel therapies for neurological diseases, such as spinal cord injury or peripheral neuropathy. Axon guidance during development is orchestrated by numerous chemo- and haptotactic cues, and the timely expression of their appropriate receptors. Growth cones, the dynamic ends of growing axons, perceive attractive and repulsive cues and translate them into behavior, such as elongation, retraction, or turning (Kalil and Dent, 2005). The complexity of this chemotropic response becomes exhausting considering that growth cones also respond to various growth factors, developmental morphogens, neuromodulators, and extracellular matrix (ECM) proteins. Despite being tightly regulated by biochemical signals, axonal growth is essentially a series of mechanical processes that eventually drive the growth cone forward or cause its collapse. These processes involve the continuous rearrangement of cytoskeleton, actin filaments (F-actin) and microtubules, in particular (Lowery and Van Vactor, 2009). Force is generated through directed polymerization of cytoskeletal filaments, a process regulated by a range of associated proteins (Dent and Gertler, 2003), or by molecular motors operating on multiple filaments (Geraldo and Gordon-Weeks, 2009).

Internally generated forces may simply push the cell membrane forward or pull on transmembrane adhesion molecules, which form focal adhesion complexes and link the cytoskeleton to the ECM or to other cells. These mechanical linkages are believed to be where mechanotransduction, *i.e.*, the conversion of mechanical stimuli into biochemical signals, and *vice versa*, takes place.

Although the important role mechanics plays in axon guidance is more and more widely accepted, a thorough understanding of underlying mechanisms is lacking (Franze et al., 2013). We argue that this is largely due to the low accessibility of the experimental methods that permit mechanical probing of growth cones. Progress is being made in three distinct, yet overlapping aspects of the problem: controlling the growth cone microenvironment; applying forces to growth cones; and measuring forces generated in and/or exerted by growth cones. Since growth cones actively generate forces and are highly sensitive to the mechanical and other properties of their substrates, an ideal experimental model would integrate all three aspects of the problem in conjunction with biochemical stimulation. This way, mechanochemical inputs can be directly linked with mechanochemical outputs, and a comprehensive map of interactions can be laid out. In this mini-review we discuss novel microtechnologies that permit such integrative approach: engineered culture systems with controlled stiffness, topography, confinement, or protein patterning, and biophysical tools for applying or quantifying forces. We conclude by highlighting recent technologies that are yet to be translated into the axon guidance field.

Controlling the Growth Cone Microenvironment

The complexity of axon growth and guidance phenomena led to the development of minimalistic *in vitro* models, where the neuronal microenvironment is tightly controlled. The substrate stiffness is typically controlled by adjusting the cross-linker concentration in a polymer, *e.g.*, polyacrylamide, whose surface can be bio-functionalized to promote adhesion. Central (CNS) and peripheral (PNS) nervous system neurons exhibited different behavior on softer polyacrylamide compared to harder: PNS axons elongated less (Koch et al., 2012), whereas CNS axons formed more branches (Flanagan et al., 2002). The growth behavior also depended on the polymer material and whether neurons were cultured on 2D layers or within 3D matrices (Balgude et al., 2001; Blewitt and Willits, 2007). 3D collagen gels with varying stiffness can be created by imposing a crosslinker concentration gradient. When cultured in this gel, PNS axons grew longer down the gradient, *i.e.*, towards softer regions (Sundararaghavan et al., 2009). Examples of biomimetic 3D matrices include silk nanofiber (Dinis et al., 2014) and salmon fibrin (Ju et al., 2007) gels. Despite the tremendous effort put into developing 3D porous hydrogels as conduits for spinal cord repair, the effects of gel mechanical properties on axon growth remain largely unknown. This is due to the difficulty of isolating stiffness from other parameters, such as porosity and degradation rate (Macaya and Spector, 2012). A promising new material is the self-assembling peptide nanofiber gels, which promote neural growth when embellished with laminin-like sequences (Sur et al., 2012). The stiffness of these gels can be tuned by simply changing the sequence of the β-sheet-forming peptide, *i.e.*, independent of polymer density or cross-linker ratio (Sur et al., 2013).

While stiffness has an immediate effect on the growth cone–substrate mechanical coupling, geometrically restraining focal adhesions offers alternative means of control. Substrates decorated with patterns of adhesive regions (Hardelauf et al., 2014) or with microtopographical features (Hoffman-Kim et al., 2010) modulate neuronal polarity and guide axons. Patterns of adhesive regions can be created *via* microcontact printing, where molecules of interest are transferred to the substrate using an elastomeric stamp (Vogt et al., 2004). Alternative approaches include reactive plasma etching, where the stamp is used to protect a pattern from being etched away due to oxygen plasma (Kim et al., 2012), electron-beam lithography using adhesive and non-adhesive self-assembled monolayers (Yamamoto et al., 2012), and the "lift-off" method, where a patterned sacrificial layer is used to remove parts of coating. The latter was used to generate intricate patterns of polylysine (**Figure 1A**) to the study cytoskeletal organization in axon collateral branching (Withers et al., 2006). Multi-step patterning can be used to create complex patterns of multiple cell adhesion molecules (CAMs), which selectively promote axonal or dendritic growth (Shi et al., 2007). Alternatively, microdroplet printing can be used to pattern multiple ECM proteins to study the cooperation between ligands of different affinity (Féréol et al., 2011). Submicron feature sizes can be achieved *via* photopatterning, crosslinking of functional groups on a non-adhesive monolayer using a focused femtosecond laser. On photopatterned triangular isles of polylysine, axons preferentially grew in the "fast-forward" direction (**Figure 1B**; Scott et al., 2012). Finally, micropatterning is not limited to adhesive molecules: axonal guidance cues (von Philipsborn et al., 2006) and membrane-permeant analogs of second messengers that are downstream of these cues (Shelly et al., 2010) have been successfully patterned.

2D microtopography is typically created *via* photolithography, where large features, *e.g.*, corridors and chambers, act as geometric constraints that guide axons (Francisco et al., 2007), whereas small features may act as structural handles. Anisotropic features, *e.g.*, linear or circular grooves, promote unidirectional growth; whereas isotropic features, *e.g.*, uniform micropillar arrays, result in higher elongation rates (Li et al., 2015). Forming contact with a structural handle is sufficient for an early stage neuron to polarize, as evidenced by N-cadherin clustering at the contact site, where an axon is subsequently initiated (Micholt et al., 2013). Contact-mediated signaling was also observed at isolated anchorages, *e.g.*, carbon nanotube isles, where increased axonal tension resulted in synaptophysin-rich axon terminals. (Anava et al., 2009). Topography is suggested to modulate growth cone-substrate mechanical interactions at the molecular level (Moore and Sheetz, 2011). Accordingly, interaction with nanoscale anchorages increased focal adhesion density

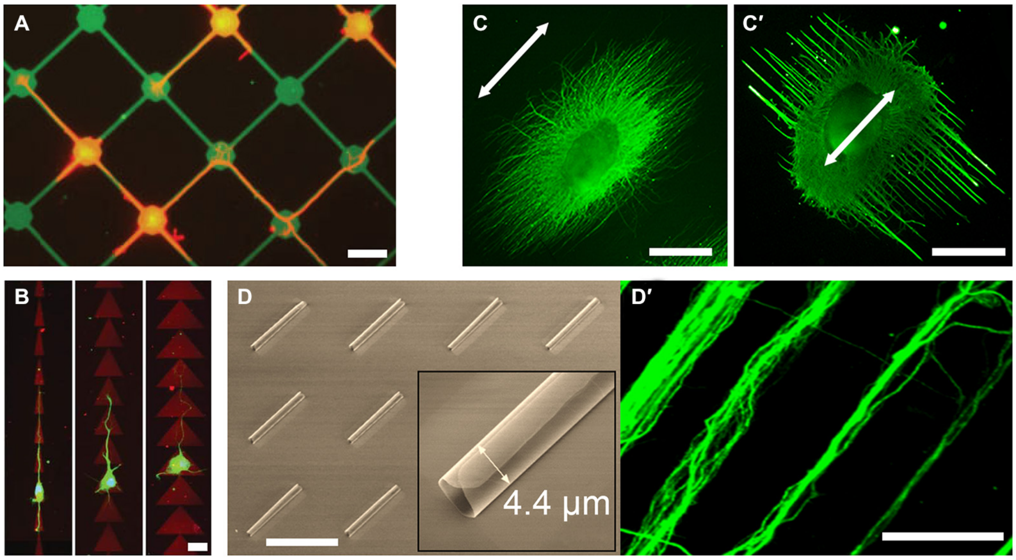

FIGURE 1 | Examples of novel growth cone microenvironments. **(A)** Rat hippocampal neurons (stained for tubulin; red) adhere preferentially to 15 μm nodes and 2 μm wide stripes of fluorescein isothiocyanate-conjugated poly-l-lysine (FITC-PLL; green), pattered *via* direct photolithography and lift-off method. Adapted with permission from Withers et al. (2006). **(B)** Rat hippocampal neurons (stained for tubulin; green) grown on "fast-forward" patterns of polylysine (red) on a polyethyleneglycol monolayer, prepared *via* laser micropatterning. Adapted from Scott et al. (2012) with permission from The Royal Society of Chemistry. **(C,C′)** Chick dorsal root ganglia (DRG; stained for neurofilaments; green) cultured on electrospun poly-(ε-caprolactone) nanofiber gels with different fiber collection times and support substrates, but with the same fiber alignment (arrow). Adapted with permission from Xie et al. (2014). **(D)** Scanning electron micrograph of the self-rolled-up silicon nitride microtubes array and **(D′)** aligned bundles of mouse cortical axons (stained for tubulin; green). Adapted with permission from Froeter et al. (2014). Copyright 2014 American Chemical Society. Scale bars = 20 μm **(A,B)**, 1 mm **(C)**, 50 μm **(D)**.

(thus traction force) in growth cone filopodia, suggesting a curvature-sensing mechanism based on asymmetric torque generation across the growth cone (Spedden et al., 2014). In 3D, nanotopography is readily introduced in electrospun nanofiber gels. Offering a variety of polymer formulations and biofunctionalization, these uniaxial scaffolds promote axon alignment and elongation (Schnell et al., 2007; Jin et al., 2011; Dinis et al., 2014). Interestingly, adjusting gel parameters, such as nanofiber density, induced axon alignment perpendicular (and not parallel) to the nanofiber orientation (**Figures 1C,C′**; Xie et al., 2014). Perpendicular (ladder) but not parallel (rope) growth was myosin-2-dependent, suggesting that nanoscale features are more than structural handles for growth cones.

Microfluidic devices provide additional means of microenvironmental control, such as imposing chemical gradients or fluidically isolating subcellular structures. These are important aspects of axon guidance *in vivo*, where growth cones experience different chemical environments than their somata and are typically exposed to chemotactic gradients. Gradients of substrate-bound cues can be imposed using flow-based devices (Dertinger et al., 2002); whereas gradients of freely-diffusing cues can be imposed using flow-based (Taylor et al., 2015) or diffusion-based (Dupin et al., 2015) devices. The latter can be achieved by flanking a culture chamber with source and sink channels and connecting them with narrow microchannels. Importantly, if the microchannels are narrow enough to permit the crossing of axons but not somata, axons can be fluidically isolated (Taylor et al., 2005). Bicompartmental devices thus allow probing growth cone-substrate interactions independent of other factors (Hur et al., 2011). Furthermore, physiologically-relevant neural networks can be constructed *in vitro* using narrowing microchannels ("axon diodes") that permit unidirectional crossing (Peyrin et al., 2011). Axons growing along the wall of the receiving chamber did not enter the diodes, suggesting that "axonal stiffness" is a limiting factor in turning behavior. Indeed, axon turning frequency decreases with increasing turning angles (Francisco et al., 2007). Accordingly, axons accelerate in narrow channels (funneling effect) where only U-turn is possible: axons grew 20× faster within silicon nitride nanomembrane tubes, 2.7–4.4 μm in diameter (**Figures 1D,D′**; Froeter et al., 2014).

Applying Forces to Growth Cones

Unlike passively modulating growth cone behavior through changing its microenvironment, external force application actively stimulates mechanosensitive pathways. Collagen-coated glass microelectrodes were the first tools to pull axons, where chick sensory neurites were towed at 40 μm/h and reached up to 1 mm length (Bray, 1984). Subsequent studies showed that the towing rate was proportional to tension (~1 μm/h per 10 pN) above a force threshold, which depended on the neuron type and the target CAM (Chada et al., 1997). Interestingly, over long timescales, central and peripheral neurons exhibited drastically different (fluid-like vs. solid-like, respectively) responses.

The last decade witnessed the development of microtechnologies for growth cone force application. Force can be applied indirectly through simply counteracting the force exerted by the growth cone cytoskeleton. This involves targeting a CAM with a microbead that is either restrained with a microneedle (**Figures 2A,A′**; Decourt et al., 2009), or trapped in a laser beam (Bard et al., 2008). Here, the targeted CAM is coupled to the actin retrograde flow, the constant inward movement of F-actin as it polymerizes at the leading edge and depolymerizes at the inner regions of the growth cone. Restraining the bead interrupts the retrograde flow and diverts the growth cone through locally reorganizing its actin cytoskeleton, followed by the advance of microtubules towards the bead (Schaefer et al., 2008). A bead restrained with a microneedle can exert practically unlimited (yet typically unknown) amounts of force, whereas laser traps operate in a narrow force range (<10 pN). One promising alternative is magnetic tweezers (MTW), where time-modulated forces >1 nN can be applied directly (Kilinc and Lee, 2014).

Classical MTW involves plasma membrane-bound targets. 450 pN acting on integrins (*via* Ø4.5 μm bead) was sufficient to initiate and tow chick forebrain axons (Fass and Odde, 2003), whereas 10–100 pN (Ø40 nm beads) stretched individual filopodia but failed to promote growth cone advance (Pita-Thomas et al., 2015). In contrast, ∼10 pN (Ø1.4 μm beads) acting on neural CAM was sufficient to tow mechanically-compromised axons (Kilinc et al., 2014). Recently, researchers started using internalized nanoparticles as MTW handles: upon exposure

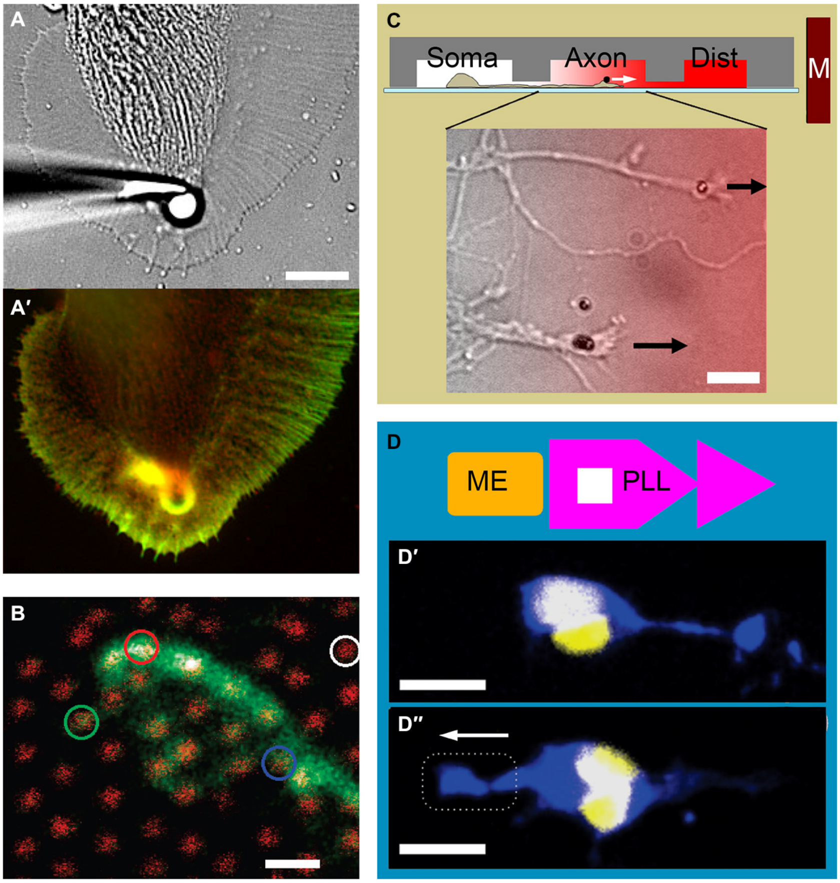

FIGURE 2 | Examples of growth cone force application and measurement. (A) Force application via a 5 μm polystyrene bead coated with apCAM, restrained using a glass pipette. **(A′)** Actin (green) and cortactin (red) distribution in an *Aplysia* growth cone is visualized after 7 min of force application. Note the cytoskeletal alignment and the actin-rich arc around the bead. Adapted with permission from Decourt et al. (2009). **(B)** The growth cone of a mouse dorsal root ganglion neuron expressing green fluorescent protein cultured on an array of 40 nm diameter, 4 μm high gallium phosphide nanowires with 1 μm spacing (red). Adapted with permission from Hällström et al. (2010). Copyright 2010 American Chemical Society. **(C)** Three-compartmental microfluidic device for isolating axons and exposing them to linear concentration gradients. Soma, somatic; Axon, axonal; Dist, distal. Growth cones of mouse cortical neurons targeted with neural cell adhesion molecule (NCAM)-functionalized 1.4 μm superparamagnetic beads. Arrows indicate force direction. Overlay color indicates Semaphorin 3A gradient. Adapted from Kilinc et al. (2014). **(D)** Combination of adhesive patterning and force application. The substrate consists of an array of "modified fast-forward" poly-l-lysine patterns (PLL; purple) and embedded ferromagnetic elements (ME; gold). **(D′)** Rat cortical neurons with internalized magnetic nanoparticles polarize in the forward direction in the absence of force. **(D″)** Neuronal polarization is reverted in the presence of magnetic force. Neurons are stained against Tau protein (blue) and 4′,6-diamidino-2-phenylindole (DAPI; yellow). Broken line indicates magnet position. Arrow indicates force direction. Adapted with permission from Kunze et al. (2015). Copyright 2015 American Chemical Society. Scale bars = 10 μm **(A)**, 1 μm **(B)**, 20 μm **(C)**, 16 μm **(D)**.

to magnetic field, nerve growth factor (NGF)-functionalized nanoparticles accumulated in the growing tips of PC12 neurites and affected their orientation (Riggio et al., 2014). Nanoparticles have also been functionalized with agonists of signaling pathways to control axon growth. Localizing Tropomyosin receptor kinase B (TrkB) pathway agonists to growth cone periphery *via* MTW forces interfered with the local F-actin remodeling and affected growth cone advance (Steketee et al., 2011). Finally, axons with internalized nanoparticles can be stimulated in parallel, using micromagnet arrays embedded in the substrate (Kunze et al., 2015). In summary, bead-based microtechnologies, MTW in particular, now offer a wide range of forces to be exerted on growth cones, externally or from within. MTW is becoming more and more accessible to neurobiologists, thanks to the recent progress in particle technology and the emergence of patterned micromagnets.

Measuring Forces in Growth Cones

A complete understanding of growth cone mechanics requires the characterization of mechanical properties of growth cones and the forces they generate. The stiffness of live *Aplysia* growth cones was mapped out using the atomic force microscope, where the thicker central domain was determined to be 3× and 5× softer than lamellipodia and filopodia, respectively (Xiong et al., 2009). Due to their smaller size, the (visco)elastic properties of mammalian growth cones cannot be characterized with this technique. Instead, local stresses can be estimated from the actin retrograde flow while the growth cone is being compressed (Betz et al., 2011). Once the local stress distribution is known, the internal force field can be calculated. We mentioned that force can be exerted by restraining a microbead bound to a CAM that is coupled to the underlying cytoskeleton. If the bead is restrained using a calibrated optical trap, the exerted force can be determined (Cojoc et al., 2007). Although this measurement can be made at multiple spots by employing optical holograms (Mejean et al., 2009), optical tweezers cannot map out growth cone forces. It is, however, possible to map out traction forces, which the growth cones exert to the substrate *via* focal adhesions. Through time-lapse imaging of fluorescent markers embedded in a soft gel, the strain field (thus the force field) can be measured (Koch et al., 2012; Toriyama et al., 2013; Hyland et al., 2014). Alternatively, neurons can be cultured on micropillar arrays. Force acting on each micropillar can be calculated from its bending, which is a function of its stiffness, height and diameter. Despite being available for over a decade (Tan et al., 2003), this technology could not be applied in neurobiology, due to the high spacing between polymeric pillars. This problem has recently been overcome using arrays of gallium phosphide nanowires (Ø40 nm; 1 μm spacing), which permit force detection at 15 pN resolution (**Figure 2B**; Hällström et al., 2010).

Combining Mechanical and Biochemical Stimuli

As growth cones harness mechanical and biochemical stimuli alike, experimental models that separately control the two types of stimuli are sought-after. "Designer" growth cone environments can be created by combining chemical gradients, topographic features, adhesive patterns, and stiffness modulation. For example, growth behavior has been investigated in 2D by presenting neurons with competing topographical (parallel grooves) and chemotactic (immobilized NGF) cues, where the former dominated axon polarization (Gomez et al., 2007a). Interestingly, topographical cues exhibited a strong effect on axon initiation, but a weaker effect on axon elongation after initiation (Gomez et al., 2007b). 3D culture inherently combines the effects of matrix stiffness and nanotopography. As mentioned earlier, self-assembling peptide nanofiber gels now provide independent control on the matrix stiffness (Sur et al., 2013). Effects of topography (maybe also matrix stiffness) and of haptotactic cues can also be compared in 3D by culturing cells on an electrospun nanofiber gel with a gradient of surface-bound laminin (Zander and Beebe, 2014). When the gradient was parallel to the nanofibers, PC12 neurites grew preferentially up the laminin gradient; however, when the gradient was imposed in the perpendicular direction, they were unaffected. These examples show that combinatorial approaches can be very effective in designing growth cone microenvironments.

Direct force application has recently been combined with topographical, chemotactic, and adhesive cues to study neuron polarization and axon growth. Neural stem cells have been cultured on an elastic substrate with microgrooves to compare stretch-induced and microtopography-induced axon orientation and growth (Chang et al., 2013). Neurites stretched parallel to the microchannel geometry grew longer and displayed higher neuronal gene expression, compared to those stretched in the perpendicular direction. We have recently presented a microfluidic device that not only (fluidically) isolates axons from somata, but also exposes them to chemotactic gradients parallel to their elongation direction (Kilinc et al., 2014). Exclusive access to the "axon chamber" facilitated the targeting of growth cones with magnetic beads, leading to parallel MTW force application (**Figure 2C**). By subjecting axons (and not somata) to a panel of inhibitory molecules, we demonstrated that low pN forces can steer CNS axons towards potent axon repellents, when their molecular motors are locally inhibited. Finally, the competition between force application and substrate patterning has been studied using a microfabricated substrate containing arrays of "fast-forward" adhesive patterns and embedded magnetic elements (Kunze et al., 2015). Low pN forces delivered *via* internalized magnetic nanoparticles reverted the neuron polarization induced by the micropattern (**Figures 2D,D′,D″**).

New Tools and Future Outlook

A number of techniques for measuring and applying forces have emerged that can be implemented to study the mechanics of axon growth in the coming years. For example, the stress inside living cells or at the cell-substrate interface can be measured using Förster resonance energy transfer (FRET)-based molecular tension sensors. These sensors have already been incorporated into several focal adhesion proteins, including integrin (Morimatsu et al., 2013), vinculin (Grashoff et al., 2010), and spectrin (Meng and Sachs, 2012), and can report the stress distribution within growth cones in real-time. In addition, nanoparticle tension probes, based on distance-dependent fluorescent quenching of substrate-bound gold nanoparticles, can report tension across individual integrins with submicron resolution (Liu et al., 2014). An emerging technology for massively parallel force application is acoustic tweezers, the manipulation of microparticles using standing acoustic waves (Ding et al., 2012). Similarly, standing magnetic field waves can be generated using a micromagnet array to control the motion of individual magnetic beads in parallel (Li et al., 2013).

Our understanding of the mechanics of axon guidance is in its infancy compared to its biochemistry. Recent and emerging microtechnologies now provide us with a range of tools that can be integrated into sophisticated experimental platforms for closing this gap. The ideal experimental platform will allow us to manipulate and precisely measure the mechanical interactions in and around a growth cone, in a tightly controlled microenvironment. Such a high level of control will help us dissect the mechanotransduction mechanisms in growth cones downstream of other, *e.g.*, biochemical, stimuli, in order to reach a more complete understanding of the growth cone behavior.

Acknowledgments

The authors acknowledge the support from Science Foundation Ireland (08/RP1/B1376 and 08/IN1/B2072; GUL), and the Nanoremedies Programme funded under the Programme for Research in Third-Level Institutions and co-funded under the European Regional Development Fund, AXA Doctoral Fellowship (AB), and Marie Curie Intra-European Fellowship (DK).

References

Anava, S., Greenbaum, A., Ben Jacob, E., Hanein, Y., and Ayali, A. (2009). The regulative role of neurite mechanical tension in network development. *Biophys. J.* 96, 1661–1670. doi: 10.1016/j.bpj.2008.10.058

Balgude, A. P., Yu, X., Szymanski, A., and Bellamkonda, R. V. (2001). Agarose gel stiffness determines rate of DRG neurite extension in 3D cultures. *Biomaterials* 22, 1077–1084. doi: 10.1016/s0142-9612(00)00350-1

Bard, L., Boscher, C., Lambert, M., Mège, R. M., Choquet, D., and Thoumine, O. (2008). A molecular clutch between the actin flow and N-cadherin adhesions drives growth cone migration. *J. Neurosci.* 28, 5879–5890. doi: 10.1523/JNEUROSCI.5331-07.2008

Betz, T., Koch, D., Lu, Y. B., Franze, K., and Käs, J. A. (2011). Growth cones as soft and weak force generators. *Proc. Natl. Acad. Sci. U S A* 108, 13420–13425. doi: 10.1073/pnas.1106145108

Blewitt, M. J., and Willits, R. K. (2007). The effect of soluble peptide sequences on neurite extension on 2D collagen substrates and within 3D collagen gels. *Ann. Biomed. Eng.* 35, 2159–2167. doi: 10.1007/s10439-007-9389-4

Bray, D. (1984). Axonal growth in response to experimentally applied mechanical tension. *Dev. Biol.* 102, 379–389. doi: 10.1016/0012-1606(84)90202-1

Chada, S., Lamoureux, P., Buxbaum, R. E., and Heidemann, S. R. (1997). Cytomechanics of neurite outgrowth from chick brain neurons. *J. Cell Sci.* 110, 1179–1186.

Chang, Y. J., Tsai, C. J., Tseng, F. G., Chen, T. J., and Wang, T. W. (2013). Micropatterned stretching system for the investigation of mechanical tension on neural stem cells behavior. *Nanomedicine* 9, 345–355. doi: 10.1016/j.nano.2012.07.008

Cojoc, D., Difato, F., Ferrari, E., Shahapure, R. B., Laishram, J., Righi, M., et al. (2007). Properties of the force exerted by filopodia and lamellipodia and the involvement of cytoskeletal components. *PLoS One* 2:e1072. doi: 10.1371/journal.pone.0001072

Decourt, B., Munnamalai, V., Lee, A. C., Sanchez, L., and Suter, D. M. (2009). Cortactin colocalizes with filopodial actin and accumulates at IgCAM adhesion sites in aplysia growth cones. *J. Neurosci. Res.* 87, 1057–1068. doi: 10.1002/jnr.21937

Dent, E. W., and Gertler, F. B. (2003). Cytoskeletal dynamics and transport in growth cone motility and axon guidance. *Neuron* 40, 209–227. doi: 10.1016/s0896-6273(03)00633-0

Dertinger, S. K., Jiang, X., Li, Z., Murthy, V. N., and Whitesides, G. M. (2002). Gradients of substrate-bound laminin orient axonal specification of neurons. *Proc. Natl. Acad. Sci. U S A* 99, 12542–12547. doi: 10.1073/pnas.192457199

Ding, X., Lin, S. C., Kiraly, B., Yue, H., Li, S., Chiang, I. K., et al. (2012). On-chip manipulation of single microparticles, cells and organisms using surface acoustic waves. *Proc. Natl. Acad. Sci. U S A* 109, 11105–11109. doi: 10.1073/pnas.1209288109

Dinis, T. M., Vidal, G., Jose, R. R., Vigneron, P., Bresson, D., Fitzpatrick, V., et al. (2014). Complementary effects of two growth factors in multifunctionalized silk nanofibers for nerve reconstruction. *PLoS One* 9:e109770. doi: 10.1371/journal.pone.0109770

Dupin, I., Lokmane, L., Dahan, M., Garel, S., and Studer, V. (2015). Subrepellent doses of slit1 promote netrin-1 chemotactic responses in subsets of axons. *Neural Dev.* 10:5. doi: 10.1186/s13064-015-0036-8

Fass, J. N., and Odde, D. J. (2003). Tensile force-dependent neurite elicitation via anti-beta1 integrin antibody-coated magnetic beads. *Biophys. J.* 85, 623–636. doi: 10.1016/s0006-3495(03)74506-8

Féréol, S., Fodil, R., Barnat, M., Georget, V., Milbreta, U., and Nothias, F. (2011). Micropatterned ECM substrates reveal complementary contribution of low and high affinity ligands to neurite outgrowth. *Cytoskeleton (Hoboken)* 68, 373–388. doi: 10.1002/cm.20518

Flanagan, L. A., Ju, Y. E., Marg, B., Osterfield, M., and Janmey, P. A. (2002). Neurite branching on deformable substrates. *Neuroreport* 13, 2411–2415. doi: 10.1097/00001756-200212200-00007

Francisco, H., Yellen, B. B., Halverson, D. S., Friedman, G., and Gallo, G. (2007). Regulation of axon guidance and extension by three-dimensional constraints. *Biomaterials* 28, 3398–3407. doi: 10.1016/j.biomaterials.2007.04.015

Franze, K., Janmey, P. A., and Guck, J. (2013). Mechanics in neuronal development and repair. *Annu. Rev. Biomed. Eng.* 15, 227–251. doi: 10.1146/annurev-bioeng-071811-150045

Froeter, P., Huang, Y., Cangellaris, O. V., Huang, W., Dent, E. W., Gillette, M. U., et al. (2014). Toward intelligent synthetic neural circuits: directing and accelerating neuron cell growth by self-rolled-up silicon nitride microtube array. *ACS Nano* 8, 11108–11117. doi: 10.1021/nn504876y

Geraldo, S., and Gordon-Weeks, P. R. (2009). Cytoskeletal dynamics in growth-cone steering. *J. Cell Sci.* 122, 3595–3604. doi: 10.1242/jcs.042309

Gomez, N., Chen, S., and Schmidt, C. E. (2007a). Polarization of hippocampal neurons with competitive surface stimuli: contact guidance cues are preferred over chemical ligands. *J. R. Soc. Interface* 4, 223–233. doi: 10.1098/rsif.2006.0171

Gomez, N., Lu, Y., Chen, S., and Schmidt, C. E. (2007b). Immobilized nerve growth factor and microtopography have distinct effects on polarization versus axon elongation in hippocampal cells in culture. *Biomaterials* 28, 271–284. doi: 10.1016/j.biomaterials.2006.07.043

Grashoff, C., Hoffman, B. D., Brenner, M. D., Zhou, R., Parsons, M., Yang, M. T., et al. (2010). Measuring mechanical tension across vinculin reveals regulation of focal adhesion dynamics. *Nature* 466, 263–266. doi: 10.1038/nature09198

Hällström, W., Lexholm, M., Suyatin, D. B., Hammarin, G., Hessman, D., Samuelson, L., et al. (2010). Fifteen-piconewton force detection from neural growth cones using nanowire arrays. *Nano Lett.* 10, 782–787. doi: 10.1021/nl902675h

Hardelauf, H., Waide, S., Sisnaiske, J., Jacob, P., Hausherr, V., Schöbel, N., et al. (2014). Micropatterning neuronal networks. *Analyst* 139, 3256–3264. doi: 10.1039/c4an00608a

Hoffman-Kim, D., Mitchel, J. A., and Bellamkonda, R. V. (2010). Topography, cell response and nerve regeneration. *Annu. Rev. Biomed. Eng.* 12, 203–231. doi: 10.1146/annurev-bioeng-070909-105351

Hur, E. M., Yang, I. H., Kim, D. H., Byun, J., Saijilafu, W.-L., Xu, W. L., et al. (2011). Engineering neuronal growth cones to promote axon regeneration over inhibitory molecules. *Proc. Natl. Acad. Sci. U S A* 108, 5057–5062. doi: 10.1073/pnas.1011258108

Hyland, C., Mertz, A. F., Forscher, P., and Dufresne, E. (2014). Dynamic peripheral traction forces balance stable neurite tension in regenerating aplysia bag cell neurons. *Sci. Rep.* 4:4961. doi: 10.1038/srep04961

Jin, G. Z., Kim, M., Shin, U. S., and Kim, H. W. (2011). Neurite outgrowth of dorsal root ganglia neurons is enhanced on aligned nanofibrous biopolymer scaffold with carbon nanotube coating. *Neurosci. Lett.* 501, 10–14. doi: 10.1016/j.neulet.2011.06.023

Ju, Y. E., Janmey, P. A., McCormick, M. E., Sawyer, E. S., and Flanagan, L. A. (2007). Enhanced neurite growth from mammalian neurons in three-dimensional salmon fibrin gels. *Biomaterials* 28, 2097–2108. doi: 10.1016/j.biomaterials.2007.01.008

Kalil, K., and Dent, E. W. (2005). Touch and go: guidance cues signal to the growth cone cytoskeleton. *Curr. Opin. Neurobiol.* 15, 521–526. doi: 10.1016/j.conb.2005.08.005

Kilinc, D., Blasiak, A., O'mahony, J. J., and Lee, G. U. (2014). Low piconewton towing of CNS axons against diffusing and surface-bound repellents requires the inhibition of motor protein-associated pathways. *Sci. Rep.* 4:7128. doi: 10.1038/srep07128

Kilinc, D., and Lee, G. U. (2014). Advances in magnetic tweezers for single molecule and cell biophysics. *Integr. Biol. (Camb)* 6, 27–34. doi: 10.1039/c3ib40185e

Kim, H. J., Park, J. W., Byun, J. H., Poon, W. W., Cotman, C. W., Fowlkes, C. C., et al. (2012). Quantitative analysis of axonal transport by using compartmentalized and surface micropatterned culture of neurons. *ACS Chem. Neurosci.* 3, 433–438. doi: 10.1021/cn3000026

Koch, D., Rosoff, W. J., Jiang, J., Geller, H. M., and Urbach, J. S. (2012). Strength in the periphery: growth cone biomechanics and substrate rigidity response in peripheral and central nervous system neurons. *Biophys. J.* 102, 452–460. doi: 10.1016/j.bpj.2011.12.025

Kunze, A., Tseng, P., Godzich, C., Murray, C., Caputo, A., Schweizer, F. E., et al. (2015). Engineering cortical neuron polarity with nanomagnets on a chip. *ACS Nano* 9, 3664–3676. doi: 10.1021/nn505330w

Li, P., Kilinc, D., Ran, Y. F., and Lee, G. U. (2013). Flow enhanced non-linear magnetophoretic separation of beads based on magnetic susceptibility. *Lab Chip* 13, 4400–4408. doi: 10.1039/c3lc50816a

Li, W., Tang, Q. Y., Jadhav, A. D., Narang, A., Qian, W. X., Shi, P., et al. (2015). Large-scale topographical screen for investigation of physical neural-guidance cues. *Sci. Rep.* 5:8644. doi: 10.1038/srep08644

Liu, Y., Medda, R., Liu, Z., Galior, K., Yehl, K., Spatz, J. P., et al. (2014). Nanoparticle tension probes patterned at the nanoscale: impact of integrin clustering on force transmission. *Nano Lett.* 14, 5539–5546. doi: 10.1021/nl501912g

Lowery, L. A., and Van Vactor, D. (2009). The trip of the tip: understanding the growth cone machinery. *Nat. Rev. Mol. Cell Biol.* 10, 332–343. doi: 10.1038/nrm2679

Macaya, D., and Spector, M. (2012). Injectable hydrogel materials for spinal cord regeneration: a review. *Biomed. Mater.* 7:012001. doi: 10.1088/1748-6041/7/1/012001

Mejean, C. O., Schaefer, A. W., Millman, E. A., Forscher, P., and Dufresne, E. R. (2009). Multiplexed force measurements on live cells with holographic optical tweezers. *Opt. Express* 17, 6209–6217. doi: 10.1364/oe.17.006209

Meng, F., and Sachs, F. (2012). Orientation-based FRET sensor for real-time imaging of cellular forces. *J. Cell Sci.* 125, 743–750. doi: 10.1242/jcs.093104

Micholt, L., Gärtner, A., Prodanov, D., Braeken, D., Dotti, C. G., and Bartic, C. (2013). Substrate topography determines neuronal polarization and growth in vitro. *PLoS One* 8:e66170. doi: 10.1371/journal.pone.0066170

Moore, S. W., and Sheetz, M. P. (2011). Biophysics of substrate interaction: influence on neural motility, differentiation and repair. *Dev. Neurobiol.* 71, 1090–1101. doi: 10.1002/dneu.20947

Morimatsu, M., Mekhdjian, A. H., Adhikari, A. S., and Dunn, A. R. (2013). Molecular tension sensors report forces generated by single integrin molecules in living cells. *Nano Lett.* 13, 3985–3989. doi: 10.1021/nl4005145

Peyrin, J. M., Deleglise, B., Saias, L., Vignes, M., Gougis, P., Magnifico, S., et al. (2011). Axon diodes for the reconstruction of oriented neuronal networks in microfluidic chambers. *Lab Chip* 11, 3663–3673. doi: 10.1039/c1lc20014c

Pita-Thomas, W., Steketee, M. B., Moysidis, S. N., Thakor, K., Hampton, B., and Goldberg, J. L. (2015). Promoting filopodial elongation in neurons by membrane-bound magnetic nanoparticles. *Nanomedicine* 11, 559–567. doi: 10.1016/j.nano.2014.11.011

Riggio, C., Calatayud, M. P., Giannaccini, M., Sanz, B., Torres, T. E., Fernandez-Pacheco, R., et al. (2014). The orientation of the neuronal growth process can be directed via magnetic nanoparticles under an applied magnetic field. *Nanomedicine* 10, 1549–1558. doi: 10.1016/j.nano.2013.12.008

Schaefer, A. W., Schoonderwoert, V. T., Ji, L., Mederios, N., Danuser, G., and Forscher, P. (2008). Coordination of actin filament and microtubule dynamics during neurite outgrowth. *Dev. Cell* 15, 146–162. doi: 10.1016/j.devcel.2008.05.003

Schnell, E., Klinkhammer, K., Balzer, S., Brook, G., Klee, D., Dalton, P., et al. (2007). Guidance of glial cell migration and axonal growth on electrospun nanofibers of poly-epsilon-caprolactone and a collagen/poly-epsilon-caprolactone blend. *Biomaterials* 28, 3012–3025. doi: 10.1016/j.biomaterials.2007.03.009

Scott, M. A., Wissner-Gross, Z. D., and Yanik, M. F. (2012). Ultra-rapid laser protein micropatterning: screening for directed polarization of single neurons. *Lab Chip* 12, 2265–2276. doi: 10.1039/c2lc21105j

Shelly, M., Lim, B. K., Cancedda, L., Heilshorn, S. C., Gao, H., and Poo, M. M. (2010). Local and long-range reciprocal regulation of cAMP and cGMP in axon/dendrite formation. *Science* 327, 547–552. doi: 10.1126/science.1179735

Shi, P., Shen, K., and Kam, L. C. (2007). Local presentation of L1 and N-cadherin in multicomponent, microscale patterns differentially direct neuron function in vitro. *Dev. Neurobiol.* 67, 1765–1776. doi: 10.1002/dneu.20553

Spedden, E., Wiens, M. R., Demirel, M. C., and Staii, C. (2014). Effects of surface asymmetry on neuronal growth. *PLoS One* 9:e106709. doi: 10.1371/journal.pone.0106709

Steketee, M. B., Moysidis, S. N., Jin, X. L., Weinstein, J. E., Pita-Thomas, W., Raju, H. B., et al. (2011). Nanoparticle-mediated signaling endosome localization regulates growth cone motility and neurite growth. *Proc. Natl. Acad. Sci. U S A* 108, 19042–19047. doi: 10.1073/pnas.1019624108

Sundararaghavan, H. G., Monteiro, G. A., Firestein, B. L., and Shreiber, D. I. (2009). Neurite growth in 3D collagen gels with gradients of mechanical properties. *Biotechnol. Bioeng.* 102, 632–643. doi: 10.1002/bit.22074

Sur, S., Newcomb, C. J., Webber, M. J., and Stupp, S. I. (2013). Tuning supramolecular mechanics to guide neuron development. *Biomaterials* 34, 4749–4757. doi: 10.1016/j.biomaterials.2013.03.025

Sur, S., Pashuck, E. T., Guler, M. O., Ito, M., Stupp, S. I., and Launey, T. (2012). A hybrid nanofiber matrix to control the survival and maturation of brain neurons. *Biomaterials* 33, 545–555. doi: 10.1016/j.biomaterials.2011.09.093

Tan, J. L., Tien, J., Pirone, D. M., Gray, D. S., Bhadriraju, K., and Chen, C. S. (2003). Cells lying on a bed of microneedles: an approach to isolate mechanical force. *Proc. Natl. Acad. Sci. U S A* 100, 1484–1489. doi: 10.1073/pnas.0235407100

Taylor, A. M., Blurton-Jones, M., Rhee, S. W., Cribbs, D. H., Cotman, C. W., and Jeon, N. L. (2005). A microfluidic culture platform for CNS axonal injury, regeneration and transport. *Nat. Methods* 2, 599–605. doi: 10.1038/nmeth777

Taylor, A. M., Menon, S., and Gupton, S. L. (2015). Passive microfluidic chamber for long-term imaging of axon guidance in response to soluble gradients. *Lab Chip* 15, 2781–2789. doi: 10.1039/c5lc00503e

Toriyama, M., Kozawa, S., Sakumura, Y., and Inagaki, N. (2013). Conversion of a signal into forces for axon outgrowth through Pak1-mediated shootin1 phosphorylation. *Curr. Biol.* 23, 529–534. doi: 10.1016/j.cub.2013.02.017

Vogt, A. K., Stefani, F. D., Best, A., Nelles, G., Yasuda, A., Knoll, W., et al. (2004). Impact of micropatterned surfaces on neuronal polarity. *J. Neurosci. Methods* 134, 191–198. doi: 10.1016/j.jneumeth.2003.11.004

von Philipsborn, A. C., Lang, S., Loeschinger, J., Bernard, A., David, C., Lehnert, D., et al. (2006). Growth cone navigation in substrate-bound ephrin gradients. *Development* 133, 2487–2495. doi: 10.1242/dev.02412

Withers, G. S., James, C. D., Kingman, C. E., Craighead, H. G., and Banker, G. A. (2006). Effects of substrate geometry on growth cone behavior and axon branching. *J. Neurobiol.* 66, 1183–1194. doi: 10.1002/neu.20298

Xie, J., Liu, W., MacEwan, M. R., Bridgman, P. C., and Xia, Y. (2014). Neurite outgrowth on electrospun nanofibers with uniaxial alignment: the effects of fiber density, surface coating and supporting substrate. *ACS Nano* 8, 1878–1885. doi: 10.1021/nn406363j

Xiong, Y., Lee, A. C., Suter, D. M., and Lee, G. U. (2009). Topography and nanomechanics of live neuronal growth cones analyzed by atomic force microscopy. *Biophys. J.* 96, 5060–5072. doi: 10.1016/j.bpj.2009.03.032

Yamamoto, H., Demura, T., Morita, M., Banker, G. A., Tanii, T., and Nakamura, S. (2012). Differential neurite outgrowth is required for axon specification by cultured hippocampal neurons. *J. Neurochem.* 123, 904–910. doi: 10.1111/jnc.12001

Zander, N. E., and Beebe, T. P. Jr. (2014). Immobilized laminin concentration gradients on electrospun fiber scaffolds for controlled neurite outgrowth. *Biointerphases* 9:011003. doi: 10.1116/1.4857295

Conflict of Interest Statement: The authors declare that the research was conducted in the absence of any commercial or financial relationships that could be construed as a potential conflict of interest.

frontiers
in Cellular Neuroscience

ORIGINAL RESEARCH
published: 29 October 2015
doi: 10.3389/fncel.2015.00417

Traction force and tension fluctuations in growing axons

Robert J. Polackwich[1]*, **Daniel Koch**[1], **Ryan McAllister**[1], **Herbert M. Geller**[2] and **Jeffrey S. Urbach**[1]

[1] Department of Physics and The Institute for Soft Matter Synthesis and Metrology, Georgetown University, Washington, DC, USA, [2] Developmental Neurobiology Section, Cell Biology and Physiology Center, National Heart, Lung, and Blood Institute, National Institutes of Health, Bethesda, MD, USA

Actively generated mechanical forces play a central role in axon growth and guidance, but the mechanisms that underly force generation and regulation in growing axons remain poorly understood. We report measurements of the dynamics of traction stresses from growth cones of actively advancing axons from postnatal rat DRG neurons. By tracking the movement of the growth cone and analyzing the traction stress field from a reference frame that moves with it, we are able to show that there is a clear and consistent average stress field that underlies the complex spatial stresses present at any one time. The average stress field has strong maxima on the sides of the growth cone, directed inward toward the growth cone neck. This pattern represents a contractile stress contained within the growth cone, and a net force that is balanced by the axon tension. Using high time-resolution measurements of the growth cone traction stresses, we show that the stress field is composed of fluctuating local stress peaks, with a large number peaks that live for a short time, a population of peaks whose lifetime distribution follows an exponential decay, and a small number of very long-lived peaks. We show that the high time-resolution data also reveal that the tension appears to vary randomly over short time scales, roughly consistent with the lifetime of the stress peaks, suggesting that the tension fluctuations originate from stochastic adhesion dynamics.

Keywords: growth cone, stress, mechanical, traction force, axon outgrowth, DRG neurons

Edited by:
Kyle Miller,
Michigan State University, USA

Reviewed by:
Tiago Ferreira,
McGill University, Canada
Timothy Gomez,
University of Wisconsin, USA
Kristian Franze,
University of Cambridge, UK

***Correspondence:**
Robert J. Polackwich
rjp73@georgetown.edu

Received: 10 July 2015
Accepted: 02 October 2015
Published: 29 October 2015

Citation:
Polackwich RJ, Koch D, McAllister R, Geller HM and Urbach JS (2015) Traction force and tension fluctuations in growing axons. Front. Cell. Neurosci. 9:417. doi: 10.3389/fncel.2015.00417

1. INTRODUCTION

Cell growth and movement is an inherently mechanical process, involving modulation of intracellular and extracellular forces, but surprisingly little is known about the role of dynamic forces in axon growth and guidance (Franze et al., 2013). Axons are under tension during growth and tension is actively regulated *in vivo* (Rajagopalan et al., 2010), and growth rates can be modulated by externally applied forces (reviewed in Suter and Miller, 2011). Changes in tension have also been shown to affect vesicle transport and synapse formation (Ahmed and Saif, 2014). During outgrowth, the tension is related to traction stresses generated by force-bearing adhesion sites between the growth cone and the extracellular matrix (ECM). We have recently shown that mapping of those stresses provides a dynamic readout of neurite tension, as well as a detailed picture of the complex pattern of stresses generated during growth (Koch et al., 2012). Similar results were obtained in studies of *aplysia* bag cell neurons (Hyland et al., 2014).

As summarized below in the Background section, the fluctuating forces in the axon and growth cone involve the orchestrated activity of a diverse array of cytoskeletal components and motor proteins. The assembly and disassembly of structures linking the cytoskeleton to the substrate and the generation of active forces is an inherently stochastic process. The cell must manage these random fluctuations to produce sustained growth, and adjust those same processes as needed to produce changes such as growth cone turning in response to guidance cues. The fluctuations themselves may provide clues to the mechanism of orchestration. In this manuscript, we investigate several interrelated aspects of force fluctuations revealed by traction force microscopy: the persistent stress patterns that underlie the complex traction stresses generated by the growth cone, the lifetime distribution of local stress peaks, and the dynamics of fluctuations in axon tension. Taken together, these results support a model of force dynamics where motor activity in the axon and growth cone is continually generating contractile stress, and the observed fluctuations originate primarily from the stochastic assembly and disassembly of adhesions in the growth cone.

2. BACKGROUND

Axon growth and guidance is controlled by the complex interplay of actin polymerization, actin retrograde flow, and microtubule polymerization (reviewed in Dent et al., 2011; Gomez and Letourneau, 2013; Liu and Dwyer, 2014). Actin polymerization generates lamellipodial protrusions and filopodial growth at the leading edge of the growth cone, and adhesion sites link the actin cytoskeletal to the ECM. This process is catalyzed by guidance cues and growth-promoting ligands that trigger signaling that locally modulates actin polymerization (reviewed in Suter and Miller, 2011; Gomez and Letourneau, 2013). Adhesions, also called focal or point contacts, act as a "clutch" which, when engaged, produce a reduction in myosin-II powered retrograde flow that can facilitate membrane protrusion and microtubule invasion into the peripheral zone of the growth cone (Chan and Odde, 2008; Gomez and Letourneau, 2013). The local stresses generated by the growth cone thus provide a direct dynamic readout of clutch engagement (Chan and Odde, 2008; Koch et al., 2012; Toriyama et al., 2013; Hyland et al., 2014).

By generating stresses through ECM linkages, cells can sense the stiffness of their environment, and there is now extensive evidence that the mechanics of the cellular environment plays a critical role in a wide range of normal and pathological biological processes, and that neuronal response to rigidity plays a role in both normal development (Tyler, 2012; Franze, 2013) and the effectiveness of implants intended to promote recovery from nervous system injury (Minev et al., 2015). The brain and spinal cord are extremely soft (Franze et al., 2013), so the rigid glass substrates used in most *in vitro* studies provide a particularly poor representation of the *in vivo* environment. Neuronal growth and dendrite branching are modulated by substrate stiffness (reviewed in Franze et al., 2013), and some of the mechanosensing pathways have been identified (Previtera et al., 2010; Kilinc et al., 2014), but the picture remains mostly incomplete.

We have shown that DRG neurite outgrowth is optimal on substrates of intermediate stiffness while hippocampal neuron outgrowth appears insensitive to stiffness, and that this difference in sensitivity is correlated with differences in adhesion-generated traction forces (Koch et al., 2012). Stress-generating adhesions provide the critical mechanical link between the growth cone and the ECM, and thus are central players in rigidity sensing, tension generation and the modulation of cytoskeletal dynamics during neurite outgrowth and guidance. The production of traction stresses represent one central target of the richly complex biochemical signaling pathways associated with motility and guidance (Dent et al., 2011), and conversely the stress generation produces distinct signaling from adhesion proteins (Kuo, 2013). Stress fluctuations therefore represent an invaluable readout of the growth cone's rigidity sensing and motility machinery.

3. MATERIALS AND METHODS

3.1. Cell Culture

All animal experiments in this study were conducted in accordance with the recommendations of the Institutional Animal Care and Use Committee (IACUC) of Georgetown University, using a protocol approved by the IACUC. Dorsal Root Ganglia (DRG) were obtained from the lumbar region of P0-P1 rat pups, trimmed, washed in Dulbecco's modified Eagle's medium (DMEM), and enzymatically digested for 20 min in 3 ml 0.25% trypsin/10 μg/ml DNase/Ca^{2+} and Mg^{2+}-free Hanks balanced salt solution (HBSS). The reaction was stopped by an addition of an equal volume of fetal bovine serum (FBS), followed by an addition of DMEM to a final volume of 15 ml. Ganglia were then dissociated by titration with a fire-polished Pasteur pipette. Cells were then pelleted, resuspended in 5 ml DMEM, and passed through a 100 μm cell strainer. The cell strainer was rinsed twice with 5 ml DMEM and the cell suspension was pooled, pelleted, twice washed in DMEM, and resuspended in Neurobasal media (Life Technologies, Grand Island, NY). Cells were cultured in Neurobasal medium with 2% B27, 5% horse serum, 100 units/ml penicillin, 100 mg/ml streptomycin, 0.5 μg/ml Fungizone, and 10 mM HEPES along with an addition of 2 nM nerve growth factor. Cells were plated at relatively low densities of 1×10^4 cells/dish and incubated at 37° and 5% CO^2 atmosphere. Glia cell numbers were kept very low by careful trimming during the dissection process and plating at low density. Furthermore, single neurons/growth cones were selected for observations to avoid interference from glial cells or other neurons. Cell viability on the microscope stage was ensured by means of a live cell chamber (Tokai Hit, Shizuoka-Ken, Japan) equipped with an objective heater that controlled temperature and pH.

3.2. Polyacrylamide Hydrogel Substrates

Polyacrylamide (PAA) hydrogels were prepared according to published procedures (Pelham and Wang, 1997; Sabass et al., 2008), with some modifications. Briefly, 20 mm glass-bottomed dishes (MatTek, Ashland, MA) were wiped with 0.1 N NaOH and silanized with 3-aminopropyl-trimethoxysilane (Sigma-Aldrich, St. Louis, MO). The dishes were washed extensively and the glass surface was treated for 30 min with 0.5% glutaraldehyde followed by a final wash. Afterwards, 18-mm coverglasses were coated with Sigmacote (Sigma-Aldrich) to make non-adhesive top coverslips. Acrylamide and bis-acrylamide (Bio-Rad Laboratories, Richmond, CA) were mixed in PBS solution to a final volume of 1 ml at appropriate concentrations to achieve the desired gel stiffness. For traction force measurements, FluoSphere bead solution (0.2 μm, 660 nm; Invitrogen) was added at 5% volume. The final solution was degassed for 15 min and put on ice for 5 min. Polymerization was initiated by addition of 10 μl freshly prepared ammonium persulfate (10% w/v solution; Sigma-Aldrich) and 3 μl of *N,N,N,N*-tetramethylethylenediamine (TEMED; AcorsOrganics, Morris Plains, NJ). Immediately after initiation, 5 μl of PAA solution was pipetted onto the MatTek dish coverglass and the non-adhesive top coverslip was quickly placed onto the gel droplet and gently pressed down. The dish was inverted to facilitate settling of fluorescent beads at the upper gel surface. After 30 min, the gel was immersed in water for 10 min, and then the top coverslips were gently removed under water. The gels were allowed to swell in dH^2O for 1–2 h before the surface coating treatment. The gels were coated with 2 $\mu g/cm^2$ [5 μl of 1 mg/ml CellTak (BD BioSciences) in 200 μl dH^2O] in a 20 min incubation at room temperature followed by $\mu g/cm^2$ (5 μl of 1 mg/ml laminin in 200 μl PBS) laminin incubation for 2 h at 37° C. Before seeding with cells, the gels were incubated in cell culture media for a minimum of 2 h at 37° C. Previous studies showed no significant difference in laminin adsorption onto gels of different stiffness (Georges et al., 2006; Kostic et al., 2007). Stiffness was characterized during polymerization by rheology measurements performed on a stress-controlled bulk rheometer (Anton Paar KG, Graz, Austria) with 1 Hz oscillatory shear at 1% strain for 30 min. The Young's modulus used in the traction stress calculation was determined from the measure storage modulus G' as $E = 2G'(1 + \nu)$ using a Poisson ratio ν of 0.45 (Frey et al., 2007).

3.3. Image Processing and Traction Force Microscopy

PAA hydrogels were prepared as described above, and the displacements of the fluorescent beads on the gel surface were tracked in order to determine the traction stresses generated by the growth cones. (See Style et al., 2014, for an overview of this technique). Specifically, fluorescence images of beads and bright-field transmission images of cells were recorded as 3D stack time series for 1–2 h with 1–5 min time resolution on a Leica TCS SP5 confocal laser scanning microscope (Leica, Deerfield, IL) equipped with a 63x water immersion objective at z steps of 0.3–0.5 μm. Image slices of each stack were median filtered to reduce noise, and afterwards each stack was reduced to a 2D image via maximum intensity projection. The resulting images were drift-corrected by detecting the shift of each image with respect to the first image. The shift was calculated in each corner region (1/5 × 1/5 of the image) from the peak of the cross-correlation, and the median of the four values was used for the drift correction. The reference image representing the zero-stress configuration was calculated from the median of the intensity time course at each pixel. Bead displacements between images and the reference image were detected on a 0.75 μm 2D grid using cross-correlation. The corresponding deformation field was obtained by 2D Gaussian interpolation. We calculated the traction stress field from the deformation field for each image in a time series by implementing a Fourier transform-based algorithm using the Boussinesq Green's function as presented by Sabass et al. (2008).

In order to minimize Z-drift, high time-resolution data was taken as 2D images only after a minimum system equilibration time of 1 h with the sample dish on the microscope stage. The data was recorded with time intervals of 1 or 2 s with manual correction of Z-focus every few minutes when necessary to correct for any residual Z-drift.

3.4. Growth Cone Traction Force Analysis

Each dataset considered consisted of a set of N observations, or images, separated by time Δt. For each image in a dataset, we calculated a relative stress threshold $S_{threshold}$

$$S_{threshold}(n) = 3S_{noise}(n), \tag{1}$$

where we defined the stress noise, S_{noise}, as the median value of the maximum stresses extracted from the four corner regions of the traction stress map associated with observation n. We imposed the threshold $S_{threshold}(n)$ on each corresponding traction stress map, resulting in at least one surviving region of stress. We then drew the convex hull defined by the stress peaks of the thresholded traction stress map, which can generally be understood as the polygon determined by the smallest perimeter totally enclosing all remaining stress regions. We defined an approximate "location" of the growth cone by calculating the centroid (geometric center) of the resulting convex hull (**Figure 1**). The resulting set of position vectors $R = \{\vec{r}_1, \vec{r}_2, ...\vec{r}_n, ...\vec{r}_{N-1}, \vec{r}_N\}$ described the trajectory of the growth cone over the timespan of the dataset (**Figure 2**). We defined the vector $\vec{v}_n$

$$\vec{v}_n = \frac{\vec{r}_{n+1} - \vec{r}_n}{\Delta t}, \tag{2}$$

as the growth cone velocity, giving the instantaneous direction of travel of the growth cone at the time of observation n.

To investigate the nature of traction force generation from the "perspective" of the growth cone, we independently rotated each image's traction force map around the convex hull centroid so as to orient the growth cone velocity along the negative x-axis (**Figure 3**). This involved rotating each traction force map by the positive angle separating the velocity vector and the negative x-axis, which we chose as the positive direction of travel for any arbitrary growth cone. After rotation, traction force maps were cropped and resampled appropriately to preserve the original scale and resolution of the pre-rotated image. After rotation, the resulting traction force maps for each dataset were added together to create an average picture of the spatial distribution of tractions forces generated in the inertial reference frame of the growth cone over the timespan of the dataset (**Figure 4**).

The nature and morphology of the growth cones were often highly dynamic. Specifically, the position and direction of movement as obtained from a function of the spatial distribution of traction forces (described above) could vary greatly on small

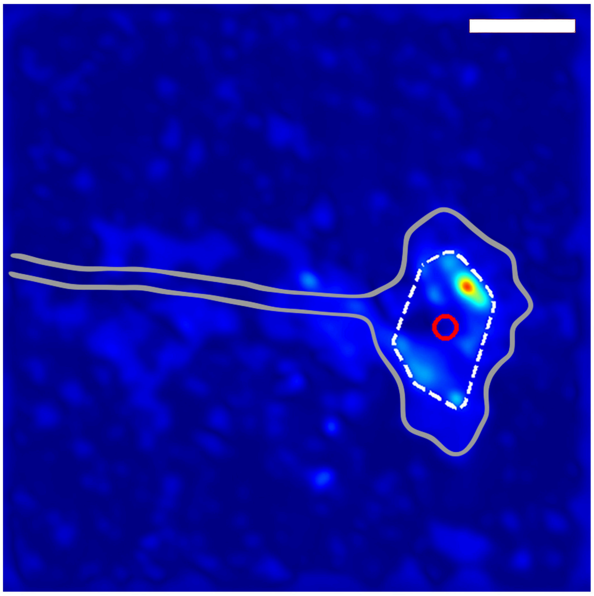

FIGURE 1 | Method for determining growth cone position. The gray outline shows the general shape of the growth cone. The dashed while line indicates the convex hull of the thresholded traction force map, and the red circle shows the location of the centroid of the convex hull used to define the location of the growth cone. The scale bar represents 10 μm.

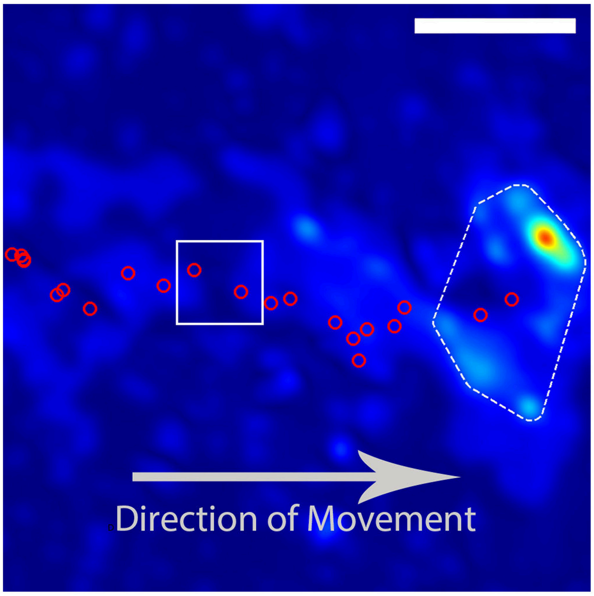

FIGURE 2 | Example trajectory of a DRG growth cone. The red circles indicate the calculated positions of the growth cone based on images taken at intervals of 180 s. The growth cone is moving from the left to the right of the image. The DRG final position and traction stress field as depicted in **Figure 1**. The red circles inside the white box indicate the growth-cone positions used in **Figure 3**. The scale bar represents 10 μm.

timescales compared to the the directional variation of the axon trajectory characterized over larger time frames. Thus, on short timescales, instantaneous displacement produced large variations relative to the long-term behavior of the growth cone, so we imposed a discrete moving-window smoothing function on R for each dataset. The size of the window was determined as a function of Δt to account for the variation in observation time resolutions across the datasets considered for this analysis. A further measure was taken to account for periods where the growth cone "stalled" or ceased forward movement. If the dot product of the velocity vector and its successor was less than zero, those time points were removed from consideration due to the fact that our analyses focused only on the general forward movement of the axon and growth cone. Explicitly, if for any consecutive time points n, $n+1$,

$$\vec{v}_n \cdot \vec{v}_{n+1} < 0, \tag{3}$$

the traction force maps associated with those time points were not included in our analysis for that particular dataset.

Stress peak tracking was done using Imaris (Bitplane, Zurich) particle tracking software. Stress peaks were initially detected and tracked automatically using a region-growing detection algorithm, where a peak A in one frame was associated with a peak B in the next frame if both the distance between A and B was small enough and if B was the closest to A of all peaks detected in the second frame. Tracks were then manually hand checked and edited for each dataset to account for errors due to algorithmic limitations (**Supplementary Video 1**).

We calculated the autocorrelation,

$$R(\tau) = \frac{< [(F(t) - \mu)(F(t+\tau) - \mu)] >}{\sigma^2},$$

for the net force time series for each high-time resolution dataset, where τ was the time separation, σ is the standard deviation of the time series, μ is the average of the time series, and each sum is over all time t. We considered lag times, or time separation, τ up to 480 s, and normalized the result for each dataset by its mean (**Figure 7**).

We also calculated the mean squared displacement of the net force,

$$MSD(\tau) =< [F(t+\tau) - F(t)]^2 >,$$

for each high-time resolution dataset, where τ was the time separation, and each sum is over all time t. We considered values of τ to 900 (s), half the duration of the capture lengths of the datasets, and normalized the result for each dataset by its mean (**Figure 8**).

The traction force calculation and analysis code used in the methods described above may be found at https://github.com/rjpolackwich/gctf.

4. RESULTS

4.1. Determination of Average Growth Cone Stress Field

We have previously reported that growth cone traction stresses for developing rat DRG neurites display complex spatiotemporal patterns, with maximum stresses typically appearing in the peripheral region between the central zone close to the axon neck

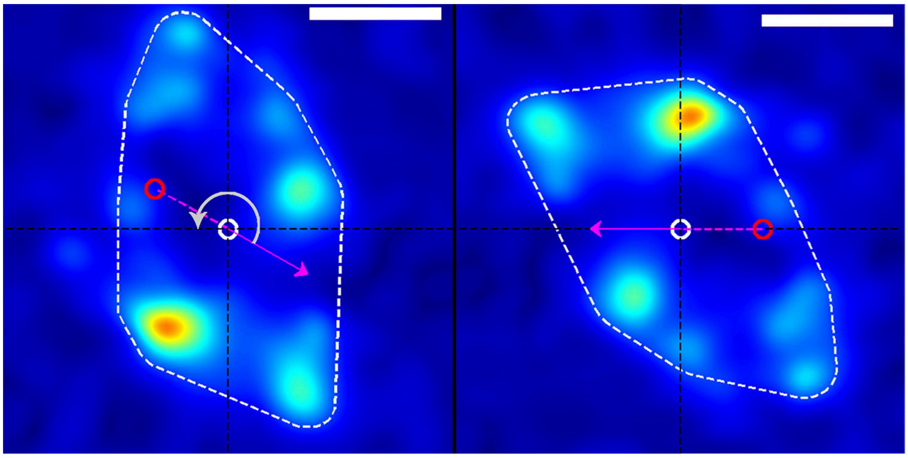

FIGURE 3 | Rotation of stress field coordinate system (left) into the frame of reference of the growth cone (right). The dashed white border shows the convex hull of the thresholded traction stress map from which the growth-cone position was calculated. The red and white circles represent the growth-cone positions at the previous and current time points, respectively (in this example, from the white box in **Figure 1**). The magenta arrow indicates the direction of movement of the growth-cone between these time points. The panel on the right is produced by rotating the stress field on the left through an angle (gray arrow) around the current centroid (white circle) such that the direction of motion is placed along the negative x-axis. This procedure transforms from the reference frame of the laboratory to the frame of reference or perspective of the growth cone. The scale bar represents 5 μm.

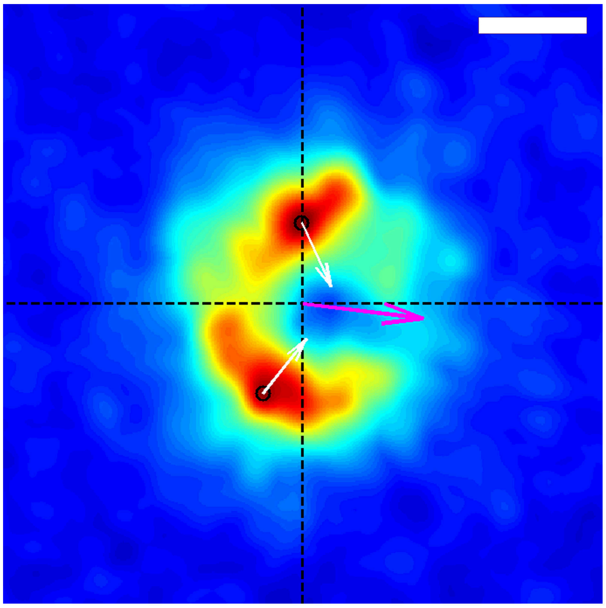

FIGURE 4 | Average spatial distribution of traction forces exerted by the growth-cone shown in Figure 1 over the time span of the entire data capture, in the frame of reference of the growth-cone. The growth-cone is moving to the left along the horizontal axis shown. The purple arrow situated at the origin indicates the direction of the net force. The black circles indicate the locations of the stress peaks in the positive and negative y-planes, and the white arrows depict the corresponding direction and relative magnitude of those stresses. The scale bar represents 5 μm.

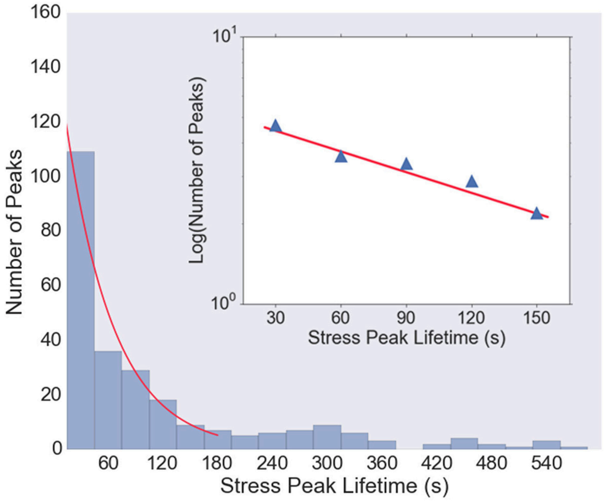

FIGURE 5 | Histogram of lifetimes of stress peaks. Most stress peaks are of short duration, with some longer, and peak lifetimes of about 30–150 s are well-fit with an exponential distribution (red curve). Very short (<15 s) and very long (>600 s) lived stress peaks are not shown in the histogram. Inset: Log-linear plot of histogram values from $t = 30$ to $t = 150$ s, with a least-square fit (red line) with slope 1/38 s, indicating that the majority of the stress peak lifetimes follow a Poisson distribution with a decay time of about 38 s.

and the filopdia at the distal end of the axon (Koch et al., 2012). At any particular instant, a snapshot of that stress field appears quite disordered, although the peak stresses are usually directed toward the central zone, and the integrated net force was found to be parallel with the axon, as required by force balance.

In order to determine the average behavior produced by the fluctuating stress field, we developed an algorithm for determining growth cone positions directly from the stress field. We observed that, since the traction stresses are consistently distributed around the DRG growth cone, they provide a "footprint" that reliably encompasses the center of the growth cone. As described in Section 3 and shown in **Figure 1**, we used the center of the convex hull of this footprint to algorithmically extract growth cone positions from each stress map. Comparisons with cell outlines from images taken concurrently with traction force microscopy confirmed that the position determined by this method provided a reasonable estimate for the middle of the growth cone (**Supplementary Video 2**).

Using the resulting series of growth cone positions (**Figure 2**), we transformed each stress field to a coordinate system fixed on the advancing growth cone (**Figure 3**), as described in Section 3. Averaging the stress fields from the entire time series for the advancing growth cone produced a remarkably clear and consistent symmetric pattern, one example of which is shown in **Figure 4**. The average stress field has strong maxima on the sides of the growth cone, directed inward toward the growth cone neck. This pattern is reminiscent of the "force dipoles" observed in isolated cells (Mandal et al., 2014; Tanimoto and Sano, 2014), but with a residual unbalanced net force, indicative of the axonal tension. We performed this analysis on 10 datasets of DRG trajectories across a range of relatively soft (150–400 Pa) polyacrylamide substrates, captured at time intervals ranging between 120 and 180 s. We found that the average traction force pictures were similar across all substrate stiffness studied (**Supplementary Figure 1**).

4.2. Localized Stress Peak Lifetimes

The traction stresses arise from dynamic stress-bearing adhesions that form and dissipate on timescales too short to be measured with the low temporal resolution of the data described above and reported in Koch et al. (2012). Therefore, we performed a series of traction force measurements with much higher time resolution, with an image every 2 s. This procedure required subjecting the cells to nearly continuous illumination, and many neurites retracted in response, but we were able to record 5 data sets from steadily advancing growth cones. For these data sets, the rise and fall of localized traction stress maxima could be clearly resolved (See Section 3 and **Supplementary Video 1**).

Figure 5 shows the histogram of stress peak lifetimes extracted from all five data sets. There are a large number of very short-lived peaks, followed by an intermediate regime that is well-described by a Poisson distribution (an exponential decay) characterized by a decay time of 38 s (**Figure 5**, inset), followed by a long tail of very long-lived peaks. The length of the trajectories (1800 s) is sufficiently long that the statistics in the exponentially decaying region are be significantly affected by the finite observation time.

4.3. Neurite Tension Fluctuations

The traction stress maps provide a direct, dynamic readout of neurite tension. As reported in Koch et al. (2012), the tension in DRG neurites varies over a modest range, and is independent of substrate stiffness over the accessible range (see Supplementary Figure S6B in Koch et al., 2012). The high time resolution of the data analyzed here provides a much more detailed picture of the tension dynamics. The time series for all 5 cells are shown in **Figure 6**. The tension appears to vary randomly over short time scales, although the change from one image to the next is usually small, indicated that measurement noise does not contribute significantly to the fluctuations (each stress map is computed independently).

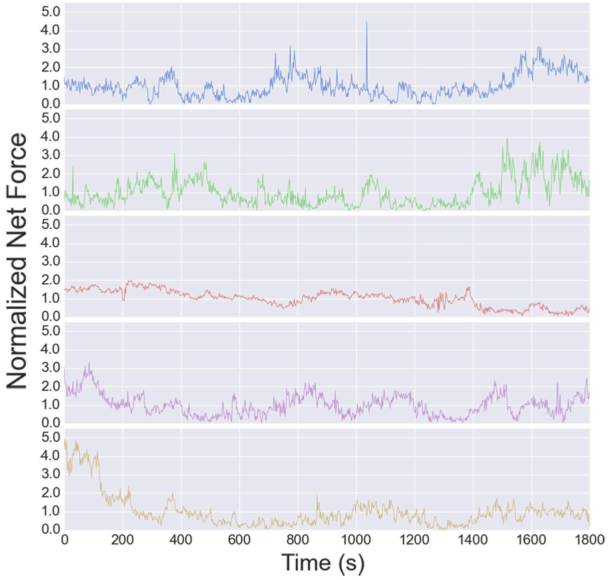

FIGURE 6 | Net tension vs. time for each growth cone used for the fluctuation analysis. The fluctuation size is larger than the mean, resulting in a negative autocorrelation at long times (**Figure 7**).

The timescale for the tension fluctuations can be quantitatively determined through the calculation of the autocorrelation function, shown in **Figure 7**. This standard analysis for stochastic signals shows the extent to which the variations in the tension at one time are correlated with those at a later time. The correlation at very short times is near unity, indicating the fluctuations from one image to the next are small, as stated above. The correlations decay relatively quickly, however, with an initial rapid drop followed by a region from 10 to 80 s that is well-described by an exponential decay with a decay time of 95 s, indicating that tension fluctuations over times much larger than this are mostly uncorrelated. This decay time is a little more than twice that of decay time for the exponential region of the stress peak lifetime distribution (**Figure 5**).

While the short time dynamics of the tension fluctuations appears stochastic, the tension cannot grow without bound. The total traction stress generated across the growth cone is nearly constant (Koch et al., 2012), which may be related to the relatively constant overall growth cone size. The effect of this constraint on the tension fluctuations can be seen in the growth of the mean squared displacement (MSD) over time, show in **Figure 8**. This analysis, often used for trajectories of diffusing particles, describes the average difference between tension values separated by a time τ. The MSD grows rapidly at short times, as expected by the stochastic fluctuations evidenced in the autocorrelation function. However, the MSD saturates after ∼400 s, indicating that the range of fluctuations is constrained. The MSD curves

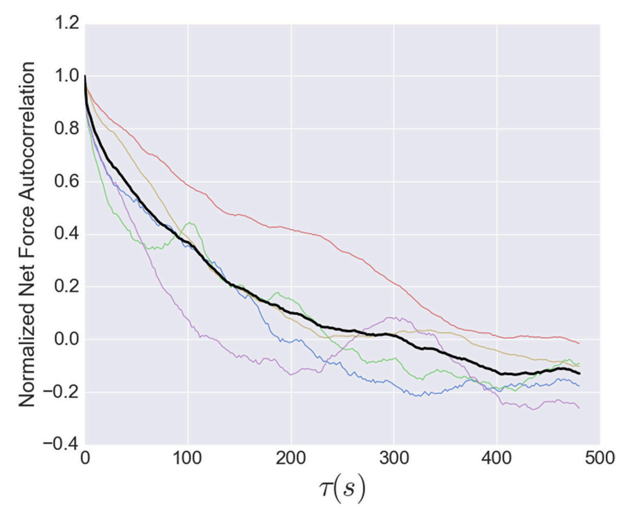

FIGURE 7 | Normalized net force autocorrelation. The fluctuations in the tension (net force) are shown for each dataset (colored lines) up to lag times of 500 s. The black line represents the ensemble average. Fluctuations from one image to the next are small, however, the correlations decay relatively quickly, with an initial rapid drop followed by a roughly exponential decay from 10 to 80 s with a decay time of 95 s, indicating that tension fluctuations at larger times are mostly uncorrelated. This decay time is a little more than twice that of decay time for the exponential region of the stress peak lifetime distribution (**Figure 5**).

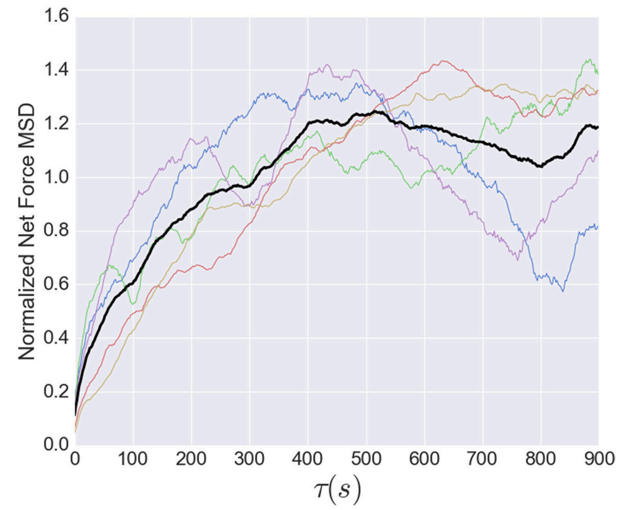

FIGURE 8 | Normalized mean squared displacement of net force fluctuations. The colored lines represent the individual MSD's, while the black line shows the average of all five. Each dataset was normalized by its average. The MSD is bounded (as expected because the growth cone's net force is limited) and grows sub-diffusively, with an apparent exponent of approximately 3/7.

in **Figure 8** are normalized to the average tension, and the fact that the saturation occurs at a value greater than unity is a consequence of the large fluctuations in tension relative to the average (**Figure 6**). The overall shape of the MSD curve is thus consistent with diffusive motion within a bounded region, but the curvature is much stronger than for normal diffusion. In fact, from 2 to 200 s the MSD grows roughly as $\tau^{3/7}$, compared to an exponent of one for normal diffusion. However, given the substantial cell-to-cell variability observed, significantly more data will be required before strong quantitative conclusions can be drawn about the average population statistics.

5. DISCUSSION

We have shown that there is a clear, robust pattern underlying the complex spatio-temporal dynamics of traction stresses generated by the growth cones of advancing rat DRG axons. The pattern is reminiscent of the force dipoles observed in isolated motile cells, which typically arise from the effects of myosin motors generating tension in actin stress fibers anchored at adhesion sites at opposite sides of a cell (Mandal et al., 2014; Tanimoto and Sano, 2014). Unlike isolated cells, however, traction stresses within the growth cone are not balanced, and instead have a net force that is equal to the tension in the axon. A similar situation is observed in the much larger growth cones of *aplysia* bag cell neurons, but with significantly reduced temporal variation (Hyland et al., 2014). On the other hand, the much smaller growth cones of rat hippocampal axons produce intermittent, localized traction stresses that are always parallel with the axon. One straightforward explanation for this range of behaviors is that the size of the growth cone determines the number of independently fluctuating adhesion sites that are present in the growth cone at any instant. If there is only one, tension can only be generated between that site and the axon. When there are multiple sites, tension can be generated both between adhesion sites and between the adhesions and the axon. For large growth cones, the number of adhesion sites may be large enough that the fractional fluctuations are relatively small, and the stress pattern is directly related to the relatively constant distribution of adhesion sites.

Using traction stress measurements with very high time resolution, we were able to characterize the lifetimes of individual sites of traction stress. We find that there are a large number of very short-lived sites, and a roughly equal number that are distributed in a Poisson distribution, with a characteristic decay time of 38 s. This is roughly consistent with the timescale reported for traction stress peaks in *aplysia* growth cones (Hyland et al., 2014) and for growth cone adhesion sites (Woo and Gomez, 2006), although significantly longer than the timescale of ∼10 s reported for fluctuations in protrusive activity at the leading edge of the growth cone (Betz et al., 2007). In addition, some growth cones also display very long-lived adhesion sites that translate as they advance, producing large axon tension.

The high time-resolution measurements show remarkable fluctuations in the net force, representing the axon tension. To our knowledge, this is the first report of this phenomenon. The autocorrelation of the fluctuations suggests an underlying stochastic component that varies on a timescale of tens of seconds, but that the tension does not fluctuate too far from its long-time average. The most likely source of the tension fluctuations is the formation and disassembly of adhesions, as discussed above. The similarity in timescales between local stress maxima lifetimes and overall tension fluctuations supports this simple picture. However, fluctuations in active tension generation in the axon may play a role as well.

Mature axons, where the growth cone is no longer present, exhibit a resting tension, and their response to perturbations can be modeled by active contraction and viscoelastic relaxation (Bernal et al., 2010). Recent results from force measurements on towed axons are consistent with contractile forces originating both from the rear of the growth cone and the axon itself, as well as viscous dissipation from the flow of cytoskeletal components (O'Toole et al., 2015). Thus, a reasonable minimal model combining these results would include active force generation in the axon and the base of the growth cone, as well as in the growth cone itself (to generate the force-dipole component, as well as a component parallel to the axon), with fluctuations arising solely from the adhesion dynamics. In this picture, the myosin-dependent contractility that is necessary for traction stress generation (Koch et al., 2012) produces an essentially constant contractile stress (and a roughly constant rate of actin retrograde flow in the growth cone), and the crucial dynamics are those of the adhesions and their connection to the growth cone cytoskelton. The stochastic adhesion dynamics may provide a mechanism for probing substrate stiffness and thus enable mechanical guidance (durotaxis), and can be sensitively modulated during chemical guidance (chemotaxis).

The work presented here is limited to a small number of growth cones, and restricted to those that are steadily advancing. Future studies should include a wider range of behaviors, in particular pausing, turning, and branching, as these are essential for understanding axon guidance and neuronal maturation. In addition, high time-resolution traction force measurements on other neuronal cell types are necessary to determine if the picture presented can be applied to neurons with small growth cones showing highly intermittent tension, as seen in rat hippocampal neurons (Koch et al., 2012), and those with large growth cones showing nearly constant tension, as observed in *aplysia* growth cones (Hyland et al., 2014). Finally, experimental manipulations of cytoskeletal components are required to illuminate the underlying mechanisms of force generation within the growth cone and its role in axon growth and guidance.

AUTHOR CONTRIBUTIONS

JP performed the data analysis presented in the manuscript, DK performed all experiments and initial analyses, RM assisted with all phases of the project, and HG and JU supervised the work. JP, RM, and JU generated the manuscript, with input from DK and HG.

ACKNOWLEDGMENTS

This work was supported by National Institute of Neurological Disorders and Stroke grant 1R01NS064250-01 (JU) and the National Heart, Lung, and Blood Institute Intramural Research Program (HG).

SUPPLEMENTARY MATERIAL

The Supplementary Material for this article can be found online at: http://journal.frontiersin.org/article/10.3389/fncel.2015.00417

Supplementary Figure 1 | Average spatial traction force distributions exerted by 9 different growth-cones, as described by Figure 4. We observed a consistent "force dipole" pattern across a range of substrate stiffnesses. Each label refers to the value of the Young's modulus of the substrate (in Pascal). Scale bars represent 5 microns.

Supplementary Video 1 | Example automatic peak tracking results. The location of identified stress peaks are marked with red spheres. Obvious gaps in stress peak trajectories were manually corrected after automatic tracking to account for algorithmic errors.

Supplementary Video 2 | Tracking of a growth cone over time. A growth cone is tracked using the traction stress convex hill centroid method as described in Methods for a fluorescently labeled axon (actin-GFP transfection as described in Koch et al., 2012).

REFERENCES

Ahmed, W. W., and Saif, T. A. (2014). Active transport of vesicles in neurons is modulated by mechanical tension. *Sci. Rep.* 4:4481. doi: 10.1038/srep04481

Bernal, R., Melo, F., and Pullarkat, P. (2010). Drag force as a tool to test the active mechanical response of PC12 neurites. *Biophys. J.* 98, 515–523. doi: 10.1016/j.bpj.2009.10.024

Betz, T., Koch, D., Stuhrmann, B., Ehrlicher, A., and Käs, J. (2007). Statistical analysis of neuronal growth: edge dynamics and the effect of a focused laser on growth cone motility. *New J. Phys.* 9, 426–426. doi: 10.1088/1367-2630/9/11/426

Chan, C. E., and Odde, D. J. (2008). Traction dynamics of filopodia on compliant substrates. *Science* 322, 1687–1691. doi: 10.1126/science.1163595

Dent, E. W., Gupton, S. L., and Gertler, F. B. (2011). The Growth Cone Cytoskeleton in Axon Outgrowth and Guidance. *Cold Spring Harb. Perspect. Biol.* 3:a001800. doi: 10.1101/cshperspect.a001800

Franze, K. (2013). The mechanical control of nervous system development. *Development* 140, 3069–3077. doi: 10.1242/dev.079145

Franze, K., Janmey, P. A., and Guck, J. (2013). Mechanics in neuronal development and repair. *Annu. Rev. Biomed. Eng.* 15, 227–251. doi: 10.1146/annurev-bioeng-071811-150045

Frey, M., Engler, A., Discher, D., Lee, J., and Wang, Y. (2007). Microscopic methods for measuring the elasticity of gel substrates for cell culture: microspheres, microindenters, and atomic force microscopy. *Methods Cell Biol.* 83, 47–65. doi: 10.1016/S0091-679X(07)83003-2

Georges, P., Miller, W., Meaney, D., Sawyer, E., and Janmey, P. (2006). Matrices with compliance comparable to that of brain tissue select neuronal over glial growth in mixed cortical cultures. *Biophys. J.* 90, 3012–3018. doi: 10.1529/biophysj.105.073114

Gomez, T. M., and Letourneau, P. C. (2013). Actin dynamics in growth cone motility and navigation. *J. Neurochem.* 129, 221–234. doi: 10.1111/jnc.12506

Hyland, C., Mertz, A. F., Forscher, P., and Dufresne, E. (2014). Dynamic peripheral traction forces balance stable neurite tension in regenerating Aplysia bag cell neurons. *Sci. Rep.* 4:4961. doi: 10.1038/srep04961

Kilinc, D., Blasiak, A., O'Mahony, J. J., and Lee, G. U. (2014). Low piconewton towing of CNS axons against diffusing and surface-bound repellents requires the inhibition of motor protein-associated pathways. *Sci. Rep.* 4:7128. doi: 10.1038/srep07128

Koch, D., Rosoff, W. J., Jiang, J., Geller, H. M., and Urbach, J. S. (2012). Strength in the periphery: growth cone biomechanics and substrate rigidity response in peripheral and central nervous system neurons. *Biophys. J.* 102, 452–460. doi: 10.1016/j.bpj.2011.12.025

Kostic, A., Sap, J., and Sheetz, M. (2007). RPTPalpha is required for rigidity-dependent inhibition of extension and differentiation of hippocampal neurons. *J. Cell Sci.* 120, 3895–904. doi: 10.1242/jcs.009852

Kuo, J.-C. (2013). Mechanotransduction at focal adhesions: integrating cytoskeletal mechanics in migrating cells. *J. Cell. Mol. Med.* 17, 704–712. doi: 10.1111/jcmm.12054

Liu, G., and Dwyer, T. (2014). Microtubule dynamics in axon guidance. *Neurosci. Bull.* 30, 569–583. doi: 10.1007/s12264-014-1444-6

Mandal, K., Wang, I., Vitiello, E., Orellana, L. A. C., and Balland, M. (2014). Cell dipole behaviour revealed by ECM sub-cellular geometry. *Nat. Commun.* 5:5749. doi: 10.1038/ncomms6749

Minev, I. R., Musienko, P., Hirsch, A., Barraud, Q., Wenger, N., Moraud, E. M., et al. (2015). Electronic dura mater for long-term multimodal neural interfaces -SM. *Science* 347, 159–163. doi: 10.1126/science.1260318

O'Toole, M., Lamoureux, P., and Miller, K. (2015). Measurement of subcellular force generation in neurons. *Biophys. J.* 108, 1027–1037. doi: 10.1016/j.bpj.2015.01.021

Pelham, R. J., and Wang, Y. (1997). Cell locomotion and focal adhesions are regulated by substrate flexibility. *Proc. Natl. Acad. Sci. U.S.A.* 94, 13661–13665. doi: 10.1073/pnas.94.25.13661

Previtera, M. L., Langhammer, C. G., Langrana, N. A., and Firestein, B. L. (2010). Regulation of dendrite arborization by substrate stiffness is mediated by glutamate receptors. *Ann. Biomed. Eng.* 38, 3733–3743. doi: 10.1007/s10439-010-0112-5

Rajagopalan, J., Tofangchi, A., and Saif, M. T. A. (2010). Drosophila neurons actively regulate axonal tension *in vivo*. *Biophys. J.* 99, 3208–3215. doi: 10.1016/j.bpj.2010.09.029

Sabass, B., Gardel, M., Waterman, C., and Schwarz, U. (2008). High resolution traction force microscopy based on experimental and computational advances. *Biophys. J.* 94, 207–220. doi: 10.1529/biophysj.107.113670

Style, R. W., Boltyanskiy, R., German, G. K., Hyland, C., MacMinn, C. W., Mertz, A. F., et al. (2014). Traction force microscopy in physics and biology. *Soft Matter* 10, 4047. doi: 10.1039/c4sm00264d

Suter, D. M., and Miller, K. E. (2011). The emerging role of forces in axonal elongation. *Prog. Neurobiol.* 94, 91–101. doi: 10.1016/j.pneurobio.2011.04.002

Tanimoto, H., and Sano, M. (2014). A simple force-motion relation for migrating cells revealed by multipole analysis of traction stress. *Biophys. J.* 106, 16–25. doi: 10.1016/j.bpj.2013.10.041

Toriyama, M., Kozawa, S., Sakumura, Y., and Inagaki, N. (2013). Conversion of a signal into forcesfor axon outgrowth through Pak1-mediated Shootin1 phosphorylation. *Curr. Biol.* 23, 529–534. doi: 10.1016/j.cub.2013.02.017

Tyler, W. J. (2012). The mechanobiology of brain function. *Nat. Rev. Neurosci.* 13, 867–878. doi: 10.1038/nrn3383

Woo, S., and Gomez, T. (2006). Rac1 and RhoA promote neurite outgrowth through formation and stabilization of growth cone point contacts. *J. Neurosci.* 26, 1418–1428. doi: 10.1523/JNEUROSCI.4209-05.2006

Conflict of Interest Statement: The authors declare that the research was conducted in the absence of any commercial or financial relationships that could be construed as a potential conflict of interest.

frontiers in Cellular Neuroscience

REVIEW
published: 06 July 2015
doi: 10.3389/fncel.2015.00252

Ciliobrevins as tools for studying dynein motor function

Douglas H. Roossien[1], **Kyle E. Miller**[2]* **and Gianluca Gallo**[3]*

[1] Department of Cell and Developmental Biology, University of Michigan, Ann Arbor, MI, USA, [2] Department of Integrative Biology, Michigan State University, East Lansing, MI, USA, [3] Department of Anatomy and Cell Biology, Shriners Hospitals Pediatric Research Center, Temple University School of Medicine, Philadelphia, PA, USA

Dyneins are a small class of molecular motors that bind to microtubules and walk toward their minus ends. They are essential for the transport and distribution of organelles, signaling complexes and cytoskeletal elements. In addition dyneins generate forces on microtubule arrays that power the beating of cilia and flagella, cell division, migration and growth cone motility. Classical approaches to the study of dynein function in axons involve the depletion of dynein, expression of mutant/truncated forms of the motor, or interference with accessory subunits. By necessity, these approaches require prolonged time periods for the expression or manipulation of cellular dynein levels. With the discovery of the ciliobrevins, a class of cell permeable small molecule inhibitors of dynein, it is now possible to acutely disrupt dynein both globally and locally. In this review, we briefly summarize recent work using ciliobrevins to inhibit dynein and discuss the insights ciliobrevins have provided about dynein function in various cell types with a focus on neurons. We temper this with a discussion of the need for studies that will elucidate the mechanism of action of ciliobrevin and as well as the need for experiments to further analyze the specificity of ciliobreviens for dynein. Although much remains to be learned about ciliobrevins, these small molecules are proving themselves to be valuable novel tools to assess the cellular functions of dynein.

Keywords: axon, growth cone, tension, microtubule, transport

Edited by:
Dieter Wicher,
Max Planck Institute for Chemical Ecology, Germany

Reviewed by:
Simone di Giovanni,
Imperial College London, UK
Anthony Brown,
Ohio State University, USA

***Correspondence:**
Kyle E. Miller,
Department of Integrative Biology, Michigan State University, 288 Farm Lane, Room 336, East Lansing, MI 48824, USA
kmiller@msu.edu
Gianluca Gallo,
Department of Anatomy and Cell Biology, Shriners Hospitals Pediatric Research Center, Temple University School of Medicine, 3500 North Broad Street, Philadelphia, PA 19140, USA
tue86088@temple.edu

Received: 29 April 2015
Accepted: 22 June 2015
Published: 06 July 2015

Citation:
Roossien DH, Miller KE and Gallo G (2015) Ciliobrevins as tools for studying dynein motor function. Front. Cell. Neurosci. 9:252. doi: 10.3389/fncel.2015.00252

Introduction

Motor proteins are a class of specialized enzymes that transform the chemical energy stored in ATP molecules to mechanical energy. There are three superfamilies of motor proteins (kinesins, myosins, and dyneins), which together total over 100 different motor proteins in humans (Vale, 2003). Though they vary in function, they are all closely associated with cytoskeletal filaments. Dyneins are ATPases which bind microtubules and walk toward the minus end (Sale and Satir, 1977; Paschal and Vallee, 1987; Paschal et al., 1987). Dyneins are divided into three classes. Axonemal dynein is found between microtubule doublets in cilia and flagella and powers microtubule sliding during motility. Cytoplasmic dynein contains two classes, one of which drives transport along microtubules in cilia and flagella (referred to as class 2 or IFT dynein) and another found throughout the remainder of the cell with a variety of functions (class 1) (Vale, 2003). Unless otherwise specified cytoplasmic dynein 1 will herein be referred to as dynein.

Research on the structure and mechanism of dynein function has lagged behind that of the kinesin and myosin motor superfamilies because of its large size and the large number of closely associated regulatory proteins. Recent advances in solving dynein crystal structures have begun to reveal the mechanochemical mechanism beyond what was previously inferred from functional studies. The motor head of dynein is made up of six ATPase domains arranged in a ring (Neuwald et al., 1999). Across this lies a linker domain that changes shape based on the status of ATP binding (Burgess et al., 2003; Kon et al., 2005, 2012; Imamula et al., 2007; Roberts et al., 2009). This linker domain is contiguous with a tail domain, which interacts with a wide variety of regulatory proteins and cargo (**Figure 1**). A coiled-coil stalk domain emanates from out of the motor head ring and contains a microtubule binding domain (MTBD) at its tip (Gee et al., 1997). When ATP binds to the motor head, the linker domain rotates like a hinge (Roberts et al., 2012) and the MTBD detaches from the microtubule (Porter and Johnson, 1983). ATP hydrolysis then occurs causing the MTBD to bind in a new position further along the microtubule toward the minus end (Carter et al., 2008), which in turn induces ADP + P_i release (Holzbaur and Johnson, 1989). This last step in the cycle causes the linker domain to straighten and pull its attached cargo forward as the "power stroke" step (Kon et al., 2005; Kikkawa, 2013) and the mechanochemical cycle can begin again (**Figure 2**).

How dynein achieves long distance processivity is still unclear, though several lines of evidence suggest dimerization of two heavy chains is responsible for ensuring the motors do not dissociate from the microtubule (Reck-Peterson et al., 2006). The proposed mechanism for dimer function is that stepping of the two dynein heavy chains is uncoordinated and that the presence of the linker between the two increases the probability each will take forward steps as opposed to backward, such that the net result is forward movement of the dimer in 8 nm increments (Reck-Peterson et al., 2006; Dewitt et al., 2012; Qiu et al., 2012). This does not, however, account for the observation that individual heavy chains can processively take 8 nm steps under high load (Mallik et al., 2004), the mechanism of which remains controversial.

Unlike the kinesin and myosin superfamilies, each of which have evolved a large number of subfamilies and isoforms designed to perform specific functions in the cell, the dynein superfamily contains relatively few types (Vale, 2003). Instead, the cell utilizes accessory proteins to adapt the dynein motor complex to numerous cellular functions (**Figure 1**) (Vallee et al., 2012; Pfister, 2015). These include non-catalytic subunits of the dynein holoenzyme itself; two dynein light chains, a light intermediate chain, and an intermediate chain (DIC). These non-catalytic subunits mostly regulate binding to additional regulatory proteins and cargo (Roberts et al., 2013). Dynactin is a regulatory protein required for long distance dynein-driven transport of materials in living cells (Gill et al., 1991; Schroer and Sheetz, 1991). It is the most commonly studied dynein regulator and is required for almost all known functions of dynein *in vivo* (Schroer, 2004).

Dynactin itself is a large multi-protein complex. The major subunit, $p150^{Glued}$, binds to DIC to maintain an intact dynein-dynactin complex (Karki and Holzbaur, 1995; Vaughan and Vallee, 1995). It can also bind microtubules at its N-terminus (Waterman-Storer et al., 1995; Vaughan et al., 2002). This interaction may keep dynein tethered to the microtubule to increase processivity (King and Schroer, 2000). In addition to direct microtubule binding, $p150^{Glued}$ can interact with the microtubule +TIP proteins EB1 and CLIP-170 (Valetti et al., 1999; Vaughan et al., 1999, 2002). Though the precise mechanism is not yet understood, the interactions between dynactin and CLIP-170 target dynein specifically to the plus ends of microtubules, where it can remain in position until cargo binds for transport toward the minus end (Vaughan et al., 2002). Alternatively, the plus end complex can be targeted to the cell cortex along with dynein via Num1 (Markus et al., 2009) or IQGAP1 (Fukata et al., 2002). Lastly, dynactin directly binds the actin related proteins Arp1 and Arp11 (Karki et al., 2000; Eckley and Schroer, 2003), which target the dynein complex to the pointed ends of actin filaments (Eckley et al., 1999; Eckley and Schroer, 2003). Dynactin thus augments dynein function by both increasing the processivity of the motor and regulating its localization.

In addition to localization and cargo binding, dynein regulators can also directly affect motor function. BicD, for example, can increase the velocity of minus-end directed movement of vesicles, though the mechanism is still unknown (Schlager et al., 2014). Originally identified as genes causing brain developmental disorders such as lissencephaly when mutated, Lis1 and NudE have since been shown to have roles in central

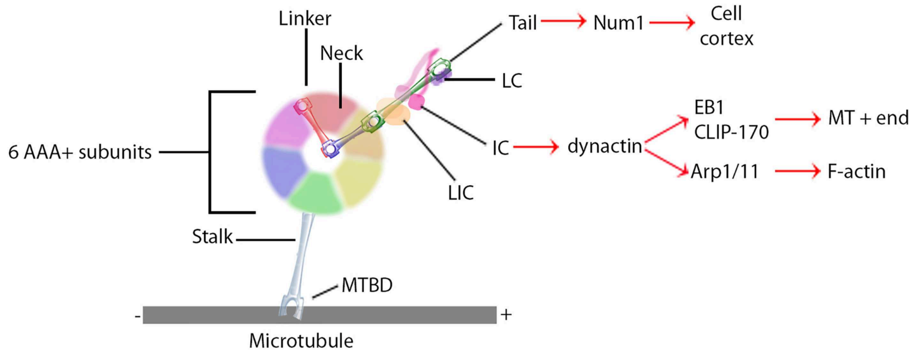

FIGURE 1 | General dynein complex structure and binding interactions. Black lines identify components of the core dynein complex whereas red arrows signify binding proteins or localizations. MTBD, microtubule binding domain; LIC, light intermediate chain; IC, intermediate chain; LC, light chain.

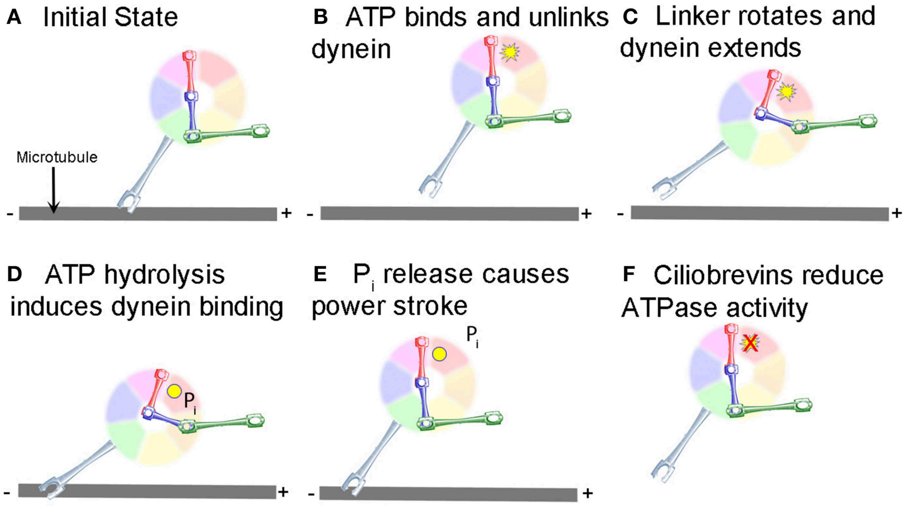

FIGURE 2 | Mechanochemical cycle of dynein. (A) Dynein is bound to the microtubule in the initial state. **(B)** ATP, represented by the yellow starburst, binds to the AAA+ ATPase domain, causing the MTBD to release from the MT. **(C)** Unlinking of the stalk from the MT causes a conformational change in the linker, which rotates and extends the stalk closer to the minus end of the MT. **(D)** Hydrolysis of ATP to ADP.P_i induces binding of the MTBD to the new location on the MT (ADP shown as a yellow circle). **(E)** Release of P_i from the motor causes the "powerstroke" and pulls the tail and any attached cargo closer to the minus end of the MT. **(F)** Ciliobrevins, as indicated by the red X, inhibit dynein ATPase activity blocking the step shown in panels **(C,D)**. While this is known to inhibit the motor cycle, how this occurs remains unclear.

cell biological processes involving the microtubule cytoskeleton through their interactions with dynein. Lis1 is unique in its ability to bind directly to the motor domain (**Figure 1**), where it is recruited by NudE to produce a slow yet persistent microtubule-bound force generating dynein state (Yamada et al., 2008; McKenney et al., 2010; Torisawa et al., 2011). Another recent advance in solving three-dimensional crystal structure has shown that Lis1 binds to the AAA+ ring and sterically prevents the linker from completing its conformational change (Toropova et al., 2014). Lis1 has thus been described as a "clutch" (Huang et al., 2012) that keeps the motor coupled to the microtubule yet still able to generate force. In a sense, Lis1 can convert dynein from a mobile cargo transporter to a stable force-producing machine.

Dynein Function in Cells

The best characterized function of dynein is for cellular transport. *In vitro*, purified dynein bound to coverslips can move microtubules and dynein in solution can transport plastic beads across stationary microtubules (Lye et al., 1987; Paschal et al., 1987; Euteneuer et al., 1988). In living cells and axons dynein moves membranous vesicles toward microtubule minus ends (Schnapp and Reese, 1989; Schroer et al., 1989). Dynein mediates the transport and cellular distribution of various membranous organelles, such as mitochondria (Pilling et al., 2006), endosomes (Aniento et al., 1993; Driskell et al., 2007), and Golgi (Corthesy-Theulaz et al., 1992). Because most microtubules in the axon are oriented with their minus ends directed toward the cell body, dynein drives axonal transport of membranous organelles in the retrograde direction (Schnapp and Reese, 1989; Pilling et al., 2006; Yi et al., 2011). Dynein also transports short microtubules in the axon via Stop-and-Go transport, though in the anterograde direction (Ahmad et al., 1998, 2006). This is proposed to occur because the dynein motor domain is bound to a short microtubule while the cargo-binding domain is anchored to a structure with more resistance, such as the cross-linked bundle of microtubules or, alternatively, the cortical actin meshwork (Pfister, 1999; Baas et al., 2006). The latter presumably occurs through the interaction between dynactin and Arp1/11. Thus, dynein plays a critical role in the transport of a variety of different types of cargo in the axon and in non-neuronal cells. In all of these cases, the mechanochemical cycle brings the motor head closer to the minus end of the microtubule regardless of whether the microtubule or motor head is stationary.

Other cellular functions have recently been ascribed to dynein in addition to cellular transport, all of which rely on dynein force generation. During mitosis, dynein is required for proper mitotic spindle assembly and alignment (O'connell and Wang, 2000; Rusan et al., 2002; Goshima et al., 2005; Nguyen-Ngoc et al., 2007), capture and alignment of chromosomes (Schmidt et al., 2005), and separation of the centrosomes (Gonczy et al., 1999). Dynein at the actin-rich cortex is presumed to drive a majority of these mitotic functions. By using cortical actin as an anchor, the tendency of the motor to walk toward the minus end moves the microtubule in the plus end direction (Hendricks et al., 2012; Mazel et al., 2013). There is also a growing body of evidence in large cells, such as Zebrafish and *Xenopus* zygotes, that dynein is anchored in the cytoplasm to exert forces on large microtubule arrays (Kimura and Onami, 2005; Wuhr et al., 2010).

Most studies on dynein function in axons have focused on transport, be it Stop-and-Go transport of microtubules or retrograde transport of organelles. There have been, however, a few notable observations made of dynein function in the context of axonal elongation. Overexpression or injection of the dynactin subunit dynamitin disrupts dynein function by dissociating the dynein-dynactin complex (Echeverri et al., 1996; Wittmann and Hyman, 1999). When injected into weakly adhered neurons, the axons lose their ability to resist forces generated by non-muscle myosin II and undergo retraction (Ahmad et al., 2000). Depletion of dynein heavy chain by siRNA makes axons more sensitive to retraction induced by nitric oxide and disrupts growth cone turning (Myers et al., 2006). The rate of axon elongation is drastically reduced with both of these means of dynein disruption as well (Ahmad et al., 2000; Myers et al., 2006). In neurons grown on poly-amine substrates and then treated with soluble laminin, which increases the rate of axon elongation (Lein et al., 1992), there is a dramatic relocalization of dynein to the leading edge of the growth cone that correlates with increases in the rate of elongation (Grabham et al., 2007). These studies indicate that dynein contributes to axonal elongation, in addition to driving retrograde axonal transport. While the importance of dynein to the process of axonal elongation is well-accepted, a difficult issue has been to determine if the primary importance of dynein lies in the sustained delivery of components or if it plays additional roles in axon elongation at the growth cone or along the axon shaft. The primary obstacle to resolving this has been a lack of tools whereby dynein motor function can be acutely and locally disrupted.

Ciliobrevins Inhibit the Motor Activity of Cytoplasmic Dynein

Ciliobrevins are a group of small molecules recently determined to be inhibitors of the motor activity of dynein 1 and 2 (Firestone et al., 2012). The discovery of ciliobrevins begun with the identification of a benzoyl dihydroquinazolinone (HPI-4) in a screen of compounds with the ability to impair cellular effects downstream of smoothened signaling in the hedgehog signaling pathway (Hyman et al., 2009). Interestingly, prolonged treatment with HPI-4 was also observed to decrease the number and length of cilia. To follow up on this observation, Firestone et al. (2012) synthesized analogs of HPI-4 and found a group that inhibited hedgehog signaling but did not affect cilia, and one group which affected both. The latter group was termed the ciliobrevins (A-D). The hedgehog pathway drives the accumulation of a signaling component termed Gli2 at the tip of cilia. Ciliobrevin A and D were found to mimic the effects of the N-terminal domain of hedgehog on the targeting of Gli2 to the tips of cilia. This observation suggested to Firestone et al. (2012) that ciliobrevins may be affecting aspects of the intra-flagellar/cilial transport of Gli2. Kinesins and dynein are respectively considered to mediate the anterograde and retrograde transport of flagellar/cilia components. Loss of dynein 2 had been previously reported to result in increased levels of Gli2 in cilia, as observed with ciliobrevins, suggesting ciliobrevins may be interfering with dynein function. Using *in vitro* reconstituted systems for tracking the motor activity of dynein, as reported by the motor protein's ability to move assembled microtubules, ciliobrevin A and D were found to block dynein activity. In contrast, ciliobrevins had no effect on kinesin-1 mediated microtubule movements. Analysis of the ATPase activity of dynein and kinesin 1 and 5 revealed that ciliobrevin D affects dynein ATPase function, but not the tested kinesins. Hanes-Woolf analysis indicates that ciliobrevins may act as ATP competitors for the dynein ATPase (**Figure 2F**). Ciliobrevins did not affect the binding of dynein to microtubules in the ADP-loaded state. Ciliobrevins were also shown to be effective in living cells, and blocked a variety of phenomena considered to be dependent on dynein 1 or 2. Ciliobrevins inhibited melanosome aggregation in Xenopus melanophores, peroxisome movement in insect cells, and disrupted spindle pole assembly and kinetochore microtubule attachment in NIH-3T3 and HeLa cells. Collectively, the work by Firestone et al. (2012) provides compelling evidence that ciliobrevins A and D are effective inhibitors of dynein activity and can be used to assay dynein functions in living cells.

Utilization of Ciliobrevins to Probe the Functions of Dynein in Non-neuronal Cells

Since their initial discovery and characterization, ciliobrevins have been used by multiple groups to probe the functions of dynein in living non-neuronal cells. Kim et al. (2014) used ciliobrevin A to determine the role of dynein in the targeting of smoothened into cilia. Consistent with the work of Firestone et al. (2012), ciliobrevin initially decreased the efflux of smoothened from cilia, while longer term treatments also impaired to targeting of smoothened into cilia. Cao et al. (2015) used ciliobrevin D to investigate the role of dynein in the targeting of the membrane protein SAG1-C65 to the periciliar domain of *Chlamydomona.* Sikirzhytski et al. (2014) used ciliobrevin D at sub-maximal doses to decrease, but not completely inhibit, dynein activity during mitosis. This resulted in normal bipolar spindles and chromosome congression into the metaphase plate, but increased the width of the spindle pole. Fu et al. (2014) used ciliobrevin D to inhibit cilia formation and concluded that cilia are necessary for the differentiation of muscle cells. Eyre et al. (2014) used ciliobrevin D to investigate the role of dynein in the control of the subcellular distribution of the hepatitis C viral protein NS5A, which is required for efficient viral RNA replication and infectious viron assembly. This study revealed that dynein is required for the intracellular traffic of NS5A and efficient viral RNA replication. Yi et al. (2013) used ciliobrevin D to determine that the reorientation of the centrosome toward the immunological synapse in T cells depends on a microtubule dependent and dynein driven mechanism. In contrast, Liu et al. (2013) found that while inhibition of dynein or myosin II alone, using both pharmacological (ciliobrevin D and blebbistatin, respectively) and molecular approaches, generated only mild effects on centrosome positioning toward the immunological synapse, inhibition of both motors caused much more pronounced effects.

Recent evidence indicates that dynein also has roles in the orchestration of active signaling mechanisms in cells. Clippinger and Alwine (2012) used ciliobrevin to determine that dynein transports mTOR to the perinuclear domain. The lack of mTOR transport results in impairment of mTOR activity due to the failure to localize it in the proximity of the upstream activator RheB. Using lymphocytes, Wang et al. (2015) investigated the role of dynein in the internalization and centripetal transport of CD40 following binding to its ligand CD154. Ciliobrevin D treatment impaired the internalization and transport of CD40, as well as the activation of the downstream MAPK pathway by CD154-CD40.

Investigations with ciliobrevins are contributing to the growing literature indicating an interdependence between anterograde and retrograde transport mechanisms. Blasius et al. (2013) addressed the role of retrograde transport mechanisms in the regulation of the accumulation of kinesin-1 motors in the distal processes of differentiated CAD cells. Acute treatment with ciliobrevin A or D decreased the levels of kinesin-1 at the distal tips of processes. This observation is counter to the expectation of increased levels of distal kinesin-1 if retrograde transport mediated the evacuation of kinesin-1 from the tips of processes, indicating that retrograde transport does not have a major role in maintaining the distal accumulation of kinesin-1. However, the observation indicates a possible impairment of the anterograde transport and delivery of kinesin-1, which was further suggested by additional considerations in Blasius et al. (2013). Similarly, Ye et al. (2013) found that ciliobrevin treatment rapidly (2–3 min) inhibited the intraflagellar retrograde transport of the intraflagellar transport component IFT88, but at longer times following treatment (30 min) also inhibited its anterograde transport. In a study of the role of intraflagellar transport mechanisms in cilia-mediated *Chlamydomonas* gliding motility, Shih et al. (2013) also observed that ciliobrevin D treatment affected both retrograde and anterograde intra-flagellar transport. The bidirectional effects of inhibiting dynein and treatment with ciliobrevin D on microtubule based transport mechanisms are further considered in the next section. Collectively, these studies emphasize the usefulness of ciliobrevins as tools for addressing the cellular functions of dynein in a variety of cellular model systems.

Use of Ciliobrevins to Address the Role of Dynein in Primary Neurons

The dynein-dependent retrograde transport of organelles and proteins from the distal axon to the cell body is a fundamental aspect of neurobiology, and the malfunction of transport mechanisms is considered to underlie aspects of neurodegenerative conditions (Ikenaka et al., 2012; Kanaan et al., 2013). Two studies on the intra-axonal translation of proteins with functions in the cell body have used ciliobrevins to block their subsequent retrograde transport. Melemedjian et al. (2014) provided evidence that IL-6 treatment of the distal axons of sensory peripheral nerves *in vivo* induces the intra-axonal synthesis of the transcription factor CREB, which subsequently undergoes retrograde axonal transport along the nerves and contributes to the development of pain sensitivity. In this study, ciliobrevin D was locally delivered along peripheral nerves, proximal to the site of IL-6 treatment, and found to block the IL-6 induced pain sensitivity. Similarly, local delivery of microtubule depolymerizing drugs, which also perturb transport, blocked the development of pain sensitivity. Control experiments indicated that the effects of ciliobrevin D and microtubule depolymerizing drugs were indeed local. Similarly, Baleriola et al. (2014) report that Amyloid β-peptide 1-42, considered to contribute to the development of Alzheimer's disease, induced the intra-axonal synthesis of the transcription factor ATF4 which in turn is a component of the ensuing cell death mechanism within the neuronal cell body. Treatment with ciliobrevin A specifically to axons using microfluidic chambers prevented the retrograde transport of axonally synthesized ATF4 and decreased Amyloid β-peptide 1-42 induced cell death. These studies provide evidence that ciliobrevins provide a new venue for investigating the role of retrograde axonal transport in experimental paradigms involving acute and localized treatments.

Two studies using cultured embryonic sensory neurons report that treatment with ciliobrevin D causes the rapid, and reversible, cessation of axon extension (Roossien et al., 2014; Sainath and Gallo, 2014). Local application of ciliobrevin D to the growth cone, using microperfusion, was sufficient to stall the extension of the axon, indicating a role for dynein at the growth cone during axon extension (Roossien et al., 2014). The main axon also generates collateral branches which assist in the formation of complex circuitry. Ciliobrevin D inhibited the formation of axon branches in response to the branch inducing signal nerve growth factor (NGF; Sainath and Gallo, 2014). Roossien et al. (2014) also noted that, similar to inhibition of dynein activity through the intracellular injection of function blocking antibodies, ciliobrevin D treatment inhibited the en bloc translocation of the axonal microtubule array, as deduced from the motion of docked mitochondria. In the same study, treatment with ciliobrevin D also increased axon tension, providing insights into the effects of dynein inhibition on axon extension. The effects of the local and acute inhibition of dynein function, achieved through treatment with ciliobrevin in these studies, further agues for a role of dynein in regulating axon extension through mechanisms operative within the axon itself.

Interestingly, ciliobrevin D treatment impaired both the retrograde and anterograde transport of mitochondria (Roossien et al., 2014; Sainath and Gallo, 2014) and lysosomes and Golgi-derived vesicles along axons (Sainath and Gallo, 2014). The bidirectional effects of altering dynein function on transport are not novel, and interested readers are directed to the discussion in both publications. The novelty of the observations using ciliobrevin D in the context of the role of dynein in bidirectional transport is that they indicate that inhibition of the ATPase activity of dynein alone may translate into bidirectional effects on transport. In contrast, a study of the *initial* emergence of neurites from the cell bodies of cultured *Drosophila* neurons failed to note effects of ciliobrevin D treatment on neurite formation (Lu et al., 2013). The initial formation of neurites from the cell bodies of these neurons was found to depend on kinesin-1 driven microtubule gliding into the nascent processes. In this study ciliobrevin D impaired the kinesin-1 dependent motility of mitochondria as noted in the studies by Roossien et al. (2014) and Sainath and Gallo (2014), but did not affect kinesin-1 mediated microtubule sliding. The observation that ciliobrevin D affects one form of kinesin-1 driven motility, but not another, is interesting and indicates that the bidirectional effects of inhibiting dynein may not translate to all cargoes. One possibility that may explain these differences is that in some cases kinesin and dynein activity are regulated cooperatively; such that when one motor is active the other is inhibited (Miller et al., 2005; Fu and Holzbaur, 2014; Hancock, 2014). Taking this idea to its logical conclusion raises the possibility that when ciliobrevin binds to dynein it causes it to assume a physical confirmation that mimics an "active" motor and thus suppresses kinesin. Yet in other cases, there is a "tug-of-war" between kinesin and dynein where the activity of the motors is not coordinated and thus disruption of dynein allows kinesin to win. Another possibility is that when kinesin and dynein work cooperatively, there is a checkpoint mechanism in place that ensures that functional kinesin and dynein are both bound to the cargo. Thus, if either kinesin or dynein are absent or dysfunctional, the checkpoint is flagged and the cargo is motionless. If this occurred ciliobrevin may inhibit bi-directional transport by either causing the disassociation of dynein from the motor complex or by causing dynein to assume a confirmation that is "non-functional." Finally, it is possible that ciliobrevin locks dynein in a confirmation where it is stably associated with microtubules but is unable to generate forces. If this occurred, the drag associated with dynein microtubule binding could decrease kinesin-based transport. These highly speculative possibilities highlight the importance of understanding the molecular mechanism of action of ciliobrevin.

The studies by Roossien et al. (2014) and Sainath and Gallo (2014) both noted that treatment with ciliobrevin D alone induces some degree of retraction of the distal axon in established axons that were actively extending. Ciliobrevin D was also found to decrease the microtubule content of distal axons (Sainath and Gallo, 2014) and mitochondria exhibited net retrograde displacements in the distal-most segment of the axon (Roossien et al., 2014). When myosin II activity was inhibited using blebbistatin (Roossien et al., 2014), or actin filaments depolymerized using latrunculin-A (Sainath and Gallo, 2014), growth cones advanced faster and underwent collapse and exhibited retrograde cytoplasmic evacuation, respectively. Interestingly, treatment with ciliobrevin D partially countered both of these effects. These observations are generally consistent with the notion of antagonistic relationships between the actomyosin system and dynein (Ahmad et al., 2000; Myers et al., 2006). Further suggestions that dynein may be involved in the regulation of the axonal actin cytoskeleton arise from the investigation of the reorganization of actin filaments in axons undergoing Wallerian degeneration following severing from the cell body (Sainath and Gallo, 2014). During degeneration the actin filament content of axons was found to increase, and treatment with ciliobrevin D prevented the increase in axonal actin filaments while promoting the morphological degeneration of axons. These observations suggest an antagonistic role for dynein in axon degeneration, possibly through the regulation of the actin cytoskeleton which may have a protective modulatory role in the timing of the ensuing degeneration.

Firestone et al. (2012) found that ciliobrevin treatment resulted in the loss of pre-existing microtubules in mitotic spindles, but did not affect microtubules in non-mitotic NIH-3T3 cells. As noted above, Sainath and Gallo (2014) observed that ciliobrevin D treatment resulted in decreased levels of microtubules in the distal axon, and also altered the relative levels of tubulin post-translational modifications. While at first glance it may be surprising that the microtubules of a post-mitotic neuron would behave similarly to those of a mitotic cell in response to ciliobrevin treatment, this observation is consistent with the notion that neurons utilize aspects of the mitotic microtubule apparatus to extend their axons (Ferhat et al., 1998a,b; Buster et al., 2003; Nadar et al., 2008; Falnikar et al., 2011; Lin et al., 2012). However, Firestone et al. (2012) did not observe abnormal subcellular targeting of the p150^{Glued} dynactin subunit following treatment with ciliobrevins. In contrast, ciliobrevin D treatment resulted in the redistribution of p150^{Glued} to linear structures in axons (Sainath and Gallo, 2014), presumably mitochondria, indicating differences in the effects of ciliobrevin treatment on the distribution of p150^{Glued} in sensory neurons relative to NIH-3T3 cells.

Concluding Remarks

The multifaceted functionality of dynein in neurons (**Figure 3**) makes it difficult to interpret the results of experiments involving the manipulation of dynein levels and function. Further complicating this problem has been the lack of reagents that are capable of acutely and locally disrupting dynein. For example, knocking down or overexpressing dynein affects the extension of axons, but because these approaches are chronic and global it has been difficult to resolve if dynein is playing a direct role in elongation at the growth cone, along the axon shaft or as the result of disrupting the trafficking of materials to and from the cell body. The strength of ciliobrevins is that they allow for acute and localized inhibition of dynein function. Nonetheless, while ciliobrevins are an attractive tool, cautionary notes ought to be taken into consideration. Dynein belongs to the AAA+ ATPase family of proteins, which mediate a variety of cellular processes. Firestone et al. (2012) did not detect effects on ciliobrevins on two other AAA+ ATPase proteins (p97 and Mcm2-7). However, given the diversity of this molecular family, further scrutiny will be required to rule out potential off target effects. Similarly, continued screening for possible effects of ciliobrevins on additional motor proteins is warranted. The bidirectional effects of ciliobrevins on the axonal transport of organelles may be due to the previously noted inter-dependence of antero and retrograde mechanisms, but may also reflect off target effects. The importance of this particular question in the field underscores the need for a tool that more confidently separates the action of individual motor subtypes in an acute and local fashion. Whether the ciliobrevins accomplish this degree of specificity is still unclear and will remain a limitation of their use until further insight into their action is gained. The bidirectional effects of inhibiting dynein

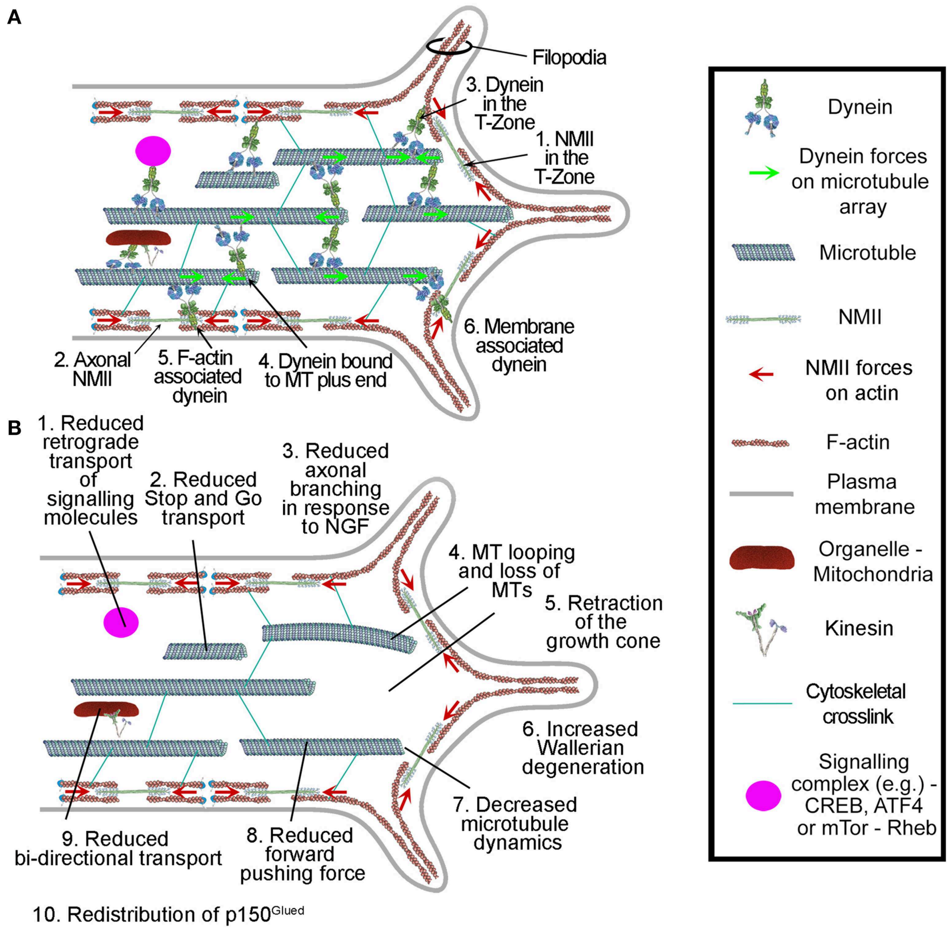

FIGURE 3 | Summary of the roles of dynein in axons and growth cones. (A) Dynein localization and interactions in axons and growth cones. **(B)** Reported effects of dynein depletion/inhibition on axons and growth cones. All but items 2 and 7 were observed through chronic manipulation of dynein and also using ciliobrevins. The effects of ciliobrevins on stop-and-go transport and microtubule plus tip dynamics, items 2 and 7, remain to be directly determined. The role for dynein in axon degeneration, item 6, is based solely on the use of ciliobrevin D and requires confirmation though additional approaches.

function on transport mechanisms thus ought to be considered in the interpretation of experimental results which may be an indirect consequence of altered anterograde transport and not directly attributable to dynein *per se*. Alternatively, dynein can also serve to organize aspects of signal transduction mechanisms (Clippinger and Alwine, 2012; Kim et al., 2014; Wang et al., 2015). Thus, the effects of inhibiting dynein, even if acutely, may ultimately be due to its contribution to signaling mechanisms independent of its direct roles in the regulation of microtubules, an interpretational aspect that ought to be considered. For example, the inhibition of axon branching in response to NGF by ciliobrevin D (Sainath and Gallo, 2014) may in part be due to a role for dynein in organizing mTOR-Rheb signaling (Clippinger and Alwine, 2012), which is required for NGF-induced branching (Spillane et al., 2012). Continued analysis of the cellular effects of ciliobrevins will provide further insights into the degree of specificity of action of these compounds, and provide a richer landscape for the interpretation of results addressing the cellular functions of dynein. Specific important questions to answer going forward are as follows: Does ciliobrevin block the ability of ATP to bind dynein and thus leaves dynein in a nucleotide free conformation where it is bound tightly to the microtubule? Does it bind to dynein and locks it into an inactive conformation that mimics the ADP bound state, which again would cause it to associate tightly with microtubules? Does it bind to dynein and induces it to assume a transition state that mimics the active conformation, where dynein is weakly attached to the microtubule? Or does it does it bind to dynein and cause it to disassociate from the cargo? While some of these possibilities seem more plausible than others, clear answers to these questions will help in the interpretation of studies that use ciliobrevin, though it is likely that caution will continue to be needed in the interpretation of future studies. In sum, ciliobrevins are an important new tool as they now allow tight spatial and temporal manipulation of dynein. Nonetheless, ciliobrevins come with their own interpretational issues; they still remain to be fully characterized and off target effects remain a concern.

Author Contributions

DR, KM, and GG all continued equally to the writing of this manuscript. KM and GG share senior authorship.

Acknowledgments

This work was supported by awards NIH NS078030 (GG) and NSF IOS_0951019 (KM). NIH 1R01MH094607-01A1 (KM).

References

Ahmad, F. J., Echeverri, C. J., Vallee, R. B., and Baas, P. W. (1998). Cytoplasmic dynein and dynactin are required for the transport of microtubules into the axon. *J. Cell Biol.* 140, 391–401. doi: 10.1083/jcb.140.2.391

Ahmad, F. J., He, Y., Myers, K. A., Hasaka, T. P., Francis, F., Black, M. M., et al. (2006). Effects of dynactin disruption and dynein depletion on axonal microtubules. *Traffic* 7, 524–537. doi: 10.1111/j.1600-0854.2006.00403.x

Ahmad, F. J., Hughey, J., Wittmann, T., Hyman, A., Greaser, M., and Baas, P. W. (2000). Motor proteins regulate force interactions between microtubules and microfilaments in the axon. *Nat. Cell Biol.* 2, 276–280. doi: 10.1038/35010544

Aniento, F., Emans, N., Griffiths, G., and Gruenberg, J. (1993). Cytoplasmic dynein-dependent vesicular transport from early to late endosomes. *J. Cell Biol.* 123, 1373–1387. doi: 10.1083/jcb.123.6.1373.

Baas, P. W., Vidya Nadar, C., and Myers, K. A. (2006). Axonal transport of microtubules: the long and short of it. *Traffic* 7, 490–498. doi: 10.1111/j.1600-0854.2006.00392.x

Baleriola, J., Walker, C. A., Jean, Y. Y., Crary, J. F., Troy, C. M., Nagy, P. L., et al. (2014). Axonally synthesized ATF4 transmits a neurodegenerative signal across brain regions. *Cell* 158, 1159–1172. doi: 10.1016/j.cell.2014.07.001

Blasius, T. L., Reed, N., Slepchenko, B. M., and Verhey, K. J. (2013). Recycling of kinesin-1 motors by diffusion after transport. *PLoS ONE* 8:e76081. doi: 10.1371/journal.pone.0076081

Burgess, S. A., Walker, M. L., Sakakibara, H., Knight, P. J., and Oiwa, K. (2003). Dynein structure and power stroke. *Nature* 421, 715–718. doi: 10.1038/nature01377

Buster, D. W., Baird, D. H., Yu, W., Solowska, J. M., Chauviere, M., Mazurek, A., et al. (2003). Expression of the mitotic kinesin Kif15 in postmitotic neurons: implications for neuronal migration and development. *J. Neurocytol.* 32, 79–96. doi: 10.1023/A:1027332432740

Cao, M., Ning, J., Hernandez-Lara, C. I., Belzile, O., Wang, Q., Dutcher, S. K., et al. (2015). Uni-directional ciliary membrane protein trafficking by a cytoplasmic retrograde IFT motor and ciliary ectosome shedding. *Elife* 4:e05242. doi: 10.7554/eLife.05242

Carter, A. P., Garbarino, J. E., Wilson-Kubalek, E. M., Shipley, W. E., Cho, C., Milligan, R. A., et al. (2008). Structure and functional role of dynein's microtubule-binding domain. *Science* 322, 1691–1695. doi: 10.1126/science.1164424

Clippinger, A. J., and Alwine, J. C. (2012). Dynein mediates the localization and activation of mTOR in normal and human cytomegalovirus-infected cells. *Genes Dev.* 26, 2015–2026. doi: 10.1101/gad.196147.112

Corthesy-Theulaz, I., Pauloin, A., and Pfeffer, S. R. (1992). Cytoplasmic dynein participates in the centrosomal localization of the Golgi complex. *J. Cell Biol.* 118, 1333–1345. doi: 10.1083/jcb.118.6.1333

Dewitt, M. A., Chang, A. Y., Combs, P. A., and Yildiz, A. (2012). Cytoplasmic dynein moves through uncoordinated stepping of the AAA+ ring domains. *Science* 335, 221–225. doi: 10.1126/science.1215804

Driskell, O. J., Mironov, A., Allan, V. J., and Woodman, P. G. (2007). Dynein is required for receptor sorting and the morphogenesis of early endosomes. *Nat. Cell Biol.* 9, 113–120. doi: 10.1038/ncb1525

Echeverri, C. J., Paschal, B. M., Vaughan, K. T., and Vallee, R. B. (1996). Molecular characterization of the 50-kD subunit of dynactin reveals function for the complex in chromosome alignment and spindle organization during mitosis. *J. Cell Biol.* 132, 617–633. doi: 10.1083/jcb.132.4.617

Eckley, D. M., Gill, S. R., Melkonian, K. A., Bingham, J. B., Goodson, H. V., Heuser, J. E., et al. (1999). Analysis of dynactin subcomplexes reveals a novel actin-related protein associated with the arp1 minifilament pointed end. *J. Cell Biol.* 147, 307–320. doi: 10.1083/jcb.147.2.307

Eckley, D. M., and Schroer, T. A. (2003). Interactions between the evolutionarily conserved, actin-related protein, Arp11, actin, and Arp1. *Mol. Biol. Cell* 14, 2645–2654. doi: 10.1091/mbc.E03-01-0049

Euteneuer, U., Koonce, M. P., Pfister, K. K., and Schliwa, M. (1988). An ATPase with properties expected for the organelle motor of the giant amoeba, *Reticulomyxa*. *Nature* 332, 176–178. doi: 10.1038/332176a0

Eyre, N. S., Fiches, G. N., Aloia, A. L., Helbig, K. J., McCartney, E. M., McErlean, C. S., et al. (2014). Dynamic imaging of the hepatitis C virus NS5A protein during a productive infection. *J. Virol.* 88, 3636–3652. doi: 10.1128/JVI.02490-13

Falnikar, A., Tole, S., and Baas, P. W. (2011). Kinesin-5, a mitotic microtubule-associated motor protein, modulates neuronal migration. *Mol. Biol. Cell* 22, 1561–1574. doi: 10.1091/mbc.E10-11-0905

Ferhat, L., Cook, C., Chauviere, M., Harper, M., Kress, M., Lyons, G. E., et al. (1998a). Expression of the mitotic motor protein Eg5 in postmitotic neurons: implications for neuronal development. *J. Neurosci.* 18, 7822–7835

Ferhat, L., Kuriyama, R., Lyons, G. E., Micales, B., and Baas, P. W. (1998b). Expression of the mitotic motor protein CHO1/MKLP1 in postmitotic neurons. *Eur. J. Neurosci.* 10, 1383–1393. doi: 10.1046/j.1460-9568.1998.00159.x

Firestone, A. J., Weinger, J. S., Maldonado, M., Barlan, K., Langston, L. D., O'donnell, M., et al. (2012). Small-molecule inhibitors of the AAA+ ATPase motor cytoplasmic dynein. *Nature* 484, 125–129. doi: 10.1038/nature10936

Fu, M. M., and Holzbaur, E. L. (2014a). Integrated regulation of motor-driven organelle transport by scaffolding proteins. *Trends Cell Biol.* 24, 564–574. doi: 10.1016/j.tcb.2014.05.002

Fu, W., Asp, P., Canter, B., and Dynlacht, B. D. (2014b). Primary cilia control hedgehog signaling during muscle differentiation and are deregulated in rhabdomyosarcoma. *Proc. Natl. Acad. Sci. U.S.A.* 111, 9151–9156. doi: 10.1073/pnas.1323265111

Fukata, M., Watanabe, T., Noritake, J., Nakagawa, M., Yamaga, M., Kuroda, S., et al. (2002). Rac1 and Cdc42 capture microtubules through IQGAP1 and CLIP-170. *Cell* 109, 873–885. doi: 10.1016/S0092-8674(02)00800-0

Gee, M. A., Heuser, J. E., and Vallee, R. B. (1997). An extended microtubule-binding structure within the dynein motor domain. *Nature* 390, 636–639. doi: 10.1038/37663

Gill, S. R., Schroer, T. A., Szilak, I., Steuer, E. R., Sheetz, M. P., and Cleveland, D. W. (1991). Dynactin, a conserved, ubiquitously expressed component of an activator of vesicle motility mediated by cytoplasmic dynein. *J. Cell Biol.* 115, 1639–1650. doi: 10.1083/jcb.115.6.1639

Gonczy, P., Pichler, S., Kirkham, M., and Hyman, A. A. (1999). Cytoplasmic dynein is required for distinct aspects of MTOC positioning, including centrosome separation, in the one cell stage Caenorhabditis elegans embryo. *J. Cell Biol.* 147, 135–150. doi: 10.1083/jcb.147.1.135

Goshima, G., Nedelec, F., and Vale, R. D. (2005). Mechanisms for focusing mitotic spindle poles by minus end-directed motor proteins. *J. Cell Biol.* 171, 229–240. doi: 10.1083/jcb.200505107

Grabham, P. W., Seale, G. E., Bennecib, M., Goldberg, D. J., and Vallee, R. B. (2007). Cytoplasmic dynein and LIS1 are required for microtubule advance during growth cone remodeling and fast axonal outgrowth. *J. Neurosci.* 27, 5823–5834. doi: 10.1523/JNEUROSCI.1135-07.2007

Hancock, W. O. (2014). Bidirectional cargo transport: moving beyond tug of war. *Nat. Rev. Mol. Cell Biol.* 15, 615–628. doi: 10.1038/nrm3853

Hendricks, A. G., Lazarus, J. E., Perlson, E., Gardner, M. K., Odde, D. J., Goldman, Y. E., et al. (2012). Dynein tethers and stabilizes dynamic microtubule plus ends. *Curr. Biol.* 22, 632–637. doi: 10.1016/j.cub.2012.02.023

Holzbaur, E. L., and Johnson, K. A. (1989). Microtubules accelerate ADP release by dynein. *Biochemistry* 28, 7010–7016. doi: 10.1021/bi00443a034

Huang, J., Roberts, A. J., Leschziner, A. E., and Reck-Peterson, S. L. (2012). Lis1 acts as a "clutch" between the ATPase and microtubule-binding domains of the dynein motor. *Cell* 150, 975–986. doi: 10.1016/j.cell.2012.07.022

Hyman, J. M., Firestone, A. J., Heine, V. M., Zhao, Y., Ocasio, C. A., Han, K., et al. (2009). Small-molecule inhibitors reveal multiple strategies for Hedgehog pathway blockade. *Proc. Natl. Acad. Sci. U.S.A.* 106, 14132–14137. doi: 10.1073/pnas.0907134106

Ikenaka, K., Katsuno, M., Kawai, K., Ishigaki, S., Tanaka, F., and Sobue, G. (2012). Disruption of axonal transport in motor neuron diseases. *Int. J. Mol. Sci.* 13, 1225–1238. doi: 10.3390/ijms13011225

Imamula, K., Kon, T., Ohkura, R., and Sutoh, K. (2007). The coordination of cyclic microtubule association/dissociation and tail swing of cytoplasmic dynein. *Proc. Natl. Acad. Sci. U.S.A.* 104, 16134–16139. doi: 10.1073/pnas.0702370104

Kanaan, N. M., Pigino, G. F., Brady, S. T., Lazarov, O., Binder, L. I., and Morfini, G. A. (2013). Axonal degeneration in Alzheimer's disease: when signaling abnormalities meet the axonal transport system. *Exp. Neurol.* 246, 44–53. doi: 10.1016/j.expneurol.2012.06.003

Karki, S., and Holzbaur, E. L. (1995). Affinity chromatography demonstrates a direct binding between cytoplasmic dynein and the dynactin complex. *J. Biol. Chem.* 270, 28806–28811. doi: 10.1074/jbc.270.48.28806

Karki, S., Tokito, M. K., and Holzbaur, E. L. (2000). A dynactin subunit with a highly conserved cysteine-rich motif interacts directly with Arp1. *J. Biol. Chem.* 275, 4834–4839. doi: 10.1074/jbc.275.7.4834

Kikkawa, M. (2013). Big steps toward understanding dynein. *J. Cell Biol.* 202, 15–23. doi: 10.1083/jcb.201304099

Kim, J., Hsia, E. Y., Sever, N., Beachy, P. A., and Zheng, X. (2014). Simultaneous measurement of smoothened entry into and exit from the primary cilium. *PLoS ONE* 9:e104070. doi: 10.1371/journal.pone.0104070

Kimura, A., and Onami, S. (2005). Computer simulations and image processing reveal length-dependent pulling force as the primary mechanism for C. elegans male pronuclear migration. *Dev. Cell* 8, 765–775. doi: 10.1016/j.devcel.2005.03.007

King, S. J., and Schroer, T. A. (2000). Dynactin increases the processivity of the cytoplasmic dynein motor. *Nat. Cell Biol.* 2, 20–24. doi: 10.1038/71338

Kon, T., Mogami, T., Ohkura, R., Nishiura, M., and Sutoh, K. (2005). ATP hydrolysis cycle-dependent tail motions in cytoplasmic dynein. *Nat. Struct. Mol. Biol.* 12, 513–519. doi: 10.1038/nsmb930

Kon, T., Oyama, T., Shimo-Kon, R., Imamula, K., Shima, T., Sutoh, K., et al. (2012). The 2.8 A crystal structure of the dynein motor domain. *Nature* 484, 345–350. doi: 10.1038/nature10955

Lein, P. J., Banker, G. A., and Higgins, D. (1992). Laminin selectively enhances axonal growth and accelerates the development of polarity by hippocampal neurons in culture. *Brain Res. Dev. Brain Res.* 69, 191–197. doi: 10.1016/0165-3806(92)90159-T

Lin, S., Liu, M., Mozgova, O. I., Yu, W., and Baas, P. W. (2012). Mitotic motors coregulate microtubule patterns in axons and dendrites. *J. Neurosci.* 32, 14033–14049. doi: 10.1523/JNEUROSCI.3070-12.2012

Liu, X., Kapoor, T. M., Chen, J. K., and Huse, M. (2013). Diacylglycerol promotes centrosome polarization in T cells via reciprocal localization of dynein and myosin II. *Proc. Natl. Acad. Sci. U.S.A.* 110, 11976–11981. doi: 10.1073/pnas.1306180110

Lu, W., Fox, P., Lakonishok, M., Davidson, M. W., and Gelfand, V. I. (2013). Initial neurite outgrowth in Drosophila neurons is driven by kinesin-powered microtubule sliding. *Curr. Biol.* 23, 1018–1023. doi: 10.1016/j.cub.2013.04.050

Lye, R. J., Porter, M. E., Scholey, J. M., and McIntosh, J. R. (1987). Identification of a microtubule-based cytoplasmic motor in the nematode C. elegans. *Cell* 51, 309–318. doi: 10.1016/0092-8674(87)90157-7

Mallik, R., Carter, B. C., Lex, S. A., King, S. J., and Gross, S. P. (2004). Cytoplasmic dynein functions as a gear in response to load. *Nature* 427, 649–652. doi: 10.1038/nature02293

Markus, S. M., Punch, J. J., and Lee, W. L. (2009). Motor- and tail-dependent targeting of dynein to microtubule plus ends and the cell cortex. *Curr. Biol.* 19, 196–205. doi: 10.1016/j.cub.2008.12.047

Mazel, T., Biesemann, A., Krejczy, M., Nowald, J., Muller, O., and Dehmelt, L. (2013). Direct observation of microtubule pushing by cortical dynein in living cells. *Mol. Biol. Cell.* 25, 95–106. doi: 10.1091/mbc.E13-07-0376

McKenney, R. J., Vershinin, M., Kunwar, A., Vallee, R. B., and Gross, S. P. (2010). LIS1 and NudE induce a persistent dynein force-producing state. *Cell* 141, 304–314. doi: 10.1016/j.cell.2010.02.035

Melemedjian, O. K., Tillu, D. V., Moy, J. K., Asiedu, M. N., Mandell, E. K., Ghosh, S., et al. (2014). Local translation and retrograde axonal transport of CREB regulates IL-6-induced nociceptive plasticity. *Mol. Pain* 10:45. doi: 10.1186/1744-8069-10-45

Miller, K. E., DeProto, J., Kaufmann, N., Patel, B. N., Duckworth, A., and van Vactor, D. (2005). Direct observation demonstrates that Liprin-α is required for trafficking of synaptic vesicles. *Curr. Biol.* 15, 684–689. doi: 10.1016/j.cub.2005.02.061

Myers, K. A., Tint, I., Nadar, C. V., He, Y., Black, M. M., and Baas, P. W. (2006). Antagonistic forces generated by cytoplasmic dynein and myosin-II during growth cone turning and axonal retraction. *Traffic* 7, 1333–1351. doi: 10.1111/j.1600-0854.2006.00476.x

Nadar, V. C., Ketschek, A., Myers, K. A., Gallo, G., and Baas, P. W. (2008). Kinesin-5 is essential for growth-cone turning. *Curr. Biol.* 18, 1972–1977. doi: 10.1016/j.cub.2008.11.021

Neuwald, A. F., Aravind, L., Spouge, J. L., and Koonin, E. V. (1999). AAA+: a class of chaperone-like ATPases associated with the assembly, operation, and disassembly of protein complexes. *Genome Res.* 9, 27–43. doi: 10.1101/gr.9.1.27

Nguyen-Ngoc, T., Afshar, K., and Gonczy, P. (2007). Coupling of cortical dynein and G alpha proteins mediates spindle positioning in Caenorhabditis elegans. *Nat. Cell Biol.* 9, 1294–1302. doi: 10.1038/ncb1649

O'connell, C. B., and Wang, Y. L. (2000). Mammalian spindle orientation and position respond to changes in cell shape in a dynein-dependent fashion. *Mol. Biol. Cell* 11, 1765–1774. doi: 10.1091/mbc.11.5.1765

Paschal, B. M., Shpetner, H. S., and Vallee, R. B. (1987). MAP 1C is a microtubule-activated ATPase which translocates microtubules *in vitro* and has dynein-like properties. *J. Cell Biol.* 105, 1273–1282. doi: 10.1083/jcb.105.3.1273

Paschal, B. M., and Vallee, R. B. (1987). Retrograde transport by the microtubule-associated protein MAP 1C. *Nature* 330, 181–183. doi: 10.1038/330181a0

Pfister, K. K. (1999). Cytoplasmic dynein and microtubule transport in the axon: the action connection. *Mol. Neurobiol.* 20, 81–91. doi: 10.1007/BF02742435

Pfister, K. K. (2015). Distinct functional roles of cytoplasmic dynein defined by the intermediate chain isoforms. *Exp. Cell Res.* 334, 54–60. doi: 10.1016/j.yexcr.2014.12.013

Pilling, A. D., Horiuchi, D., Lively, C. M., and Saxton, W. M. (2006). Kinesin-1 and Dynein are the primary motors for fast transport of mitochondria in *Drosophila* motor axons. *Mol. Biol. Cell* 17, 2057–2068. doi: 10.1091/mbc.E05-06-0526

Porter, M. E., and Johnson, K. A. (1983). Transient state kinetic analysis of the ATP-induced dissociation of the dynein-microtubule complex. *J. Biol. Chem.* 258, 6582–6587.

Qiu, W., Derr, N. D., Goodman, B. S., Villa, E., Wu, D., Shih, W., et al. (2012). Dynein achieves processive motion using both stochastic and coordinated stepping. *Nat. Struct. Mol. Biol.* 19, 193–200. doi: 10.1038/nsmb.2205

Reck-Peterson, S. L., Yildiz, A., Carter, A. P., Gennerich, A., Zhang, N., and Vale, R. D. (2006). Single-molecule analysis of dynein processivity and stepping behavior. *Cell* 126, 335–348. doi: 10.1016/j.cell.2006.05.046

Roberts, A. J., Kon, T., Knight, P. J., Sutoh, K., and Burgess, S. A. (2013). Functions and mechanics of dynein motor proteins. *Nat. Rev. Mol. Cell Biol.* 14, 713–726. doi: 10.1038/nrm3667

Roberts, A. J., Malkova, B., Walker, M. L., Sakakibara, H., Numata, N., Kon, T., et al. (2012). ATP-driven remodeling of the linker domain in the dynein motor. *Structure* 20, 1670–1680. doi: 10.1016/j.str.2012.07.003

Roberts, A. J., Numata, N., Walker, M. L., Kato, Y. S., Malkova, B., Kon, T., et al. (2009). AAA+ Ring and linker swing mechanism in the dynein motor. *Cell* 136, 485–495. doi: 10.1016/j.cell.2008.11.049

Roossien, D. H., Lamoureux, P., and Miller, K. E. (2014). Cytoplasmic dynein pushes the cytoskeletal meshwork forward during axonal elongation. *J. Cell Sci.* 127, 3593–3602. doi: 10.1242/jcs.152611

Rusan, N. M., Tulu, U. S., Fagerstrom, C., and Wadsworth, P. (2002). Reorganization of the microtubule array in prophase/prometaphase requires cytoplasmic dynein-dependent microtubule transport. *J. Cell Biol.* 158, 997–1003. doi: 10.1083/jcb.200204109

Sainath, R., and Gallo, G. (2014). The dynein inhibitor Ciliobrevin D inhibits the bidirectional transport of organelles along sensory axons and impairs NGF-mediated regulation of growth cones and axon branches. *Dev. Neurobiol.* 75, 757–777. doi: 10.1002/dneu.22246

Sale, W. S., and Satir, P. (1977). Direction of active sliding of microtubules in Tetrahymena cilia. *Proc. Natl. Acad. Sci. U.S.A.* 74, 2045–2049.

Schlager, M. A., Serra-Marques, A., Grigoriev, I., Gumy, G. F., Esteves da Silva, M., Wulf, P. S., et al. (2014). Bicaudal d family adaptor proteins control the velocity of Dynein-based movements. *Cell Rep.* 8, 1248–1256. doi: 10.1016/j.celrep.2014.07.052

Schmidt, D. J., Rose, D. J., Saxton, W. M., and Strome, S. (2005). Functional analysis of cytoplasmic dynein heavy chain in Caenorhabditis elegans with fast-acting temperature-sensitive mutations. *Mol. Biol. Cell* 16, 1200–1212. doi: 10.1091/mbc.E04-06-0523

Schnapp, B. J., and Reese, T. S. (1989). Dynein is the motor for retrograde axonal transport of organelles. *Proc. Natl. Acad. Sci. U.S.A.* 86, 1548–1552.

Schroer, T. A. (2004). Dynactin. *Annu. Rev. Cell Dev. Biol.* 20, 759–779. doi: 10.1146/annurev.cellbio.20.012103.094623

Schroer, T. A., and Sheetz, M. P. (1991). Two activators of microtubule-based vesicle transport. *J. Cell Biol.* 115, 1309–1318. doi: 10.1083/jcb.115.5.1309

Schroer, T. A., Steuer, E. R., and Sheetz, M. P. (1989). Cytoplasmic dynein is a minus end-directed motor for membranous organelles. *Cell* 56, 937–946. doi: 10.1016/0092-8674(89)90627-2

Shih, S. M., Engel, B. D., Kocabas, F., Bilyard, T., Gennerich, A., Marshall, W. F., et al. (2013). Intraflagellar transport drives flagellar surface motility. *Elife* 2:e00744. doi: 10.7554/eLife.00744

Sikirzhytski, V., Magidson, V., Steinman, J. B., He, J., Le Berre, M., Tikhonenko, I., et al. (2014). Direct kinetochore-spindle pole connections are not required for chromosome segregation. *J. Cell Biol.* 206, 231–243. doi: 10.1083/jcb.201401090

Spillane, M., Ketschek, A., Donnelly, C. J., Pacheco, A., Twiss, J. L., and Gallo, G. (2012). Nerve growth factor-induced formation of axonal filopodia and collateral branches involves the intra-axonal synthesis of regulators of the actin-nucleating Arp2/3 complex. *J. Neurosci.* 32, 17671–17689. doi: 10.1523/JNEUROSCI.1079-12.2012

Torisawa, T., Nakayama, A., Furuta, K., Yamada, M., Hirotsune, S., and Toyoshima, Y. Y. (2011). Functional dissection of LIS1 and NDEL1 towards understanding the molecular mechanisms of cytoplasmic dynein regulation. *J. Biol. Chem.* 286, 1959–1965. doi: 10.1074/jbc.M1110.169847

Toropova, K., Zou, S., Roberts, A. J., Redwine, W. B., Goodman, B. S., Reck-Peterson, S. L., et al. (2014). Lis1 regulates dynein by sterically blocking its mechanochemical cycle. *Elife* 3:e03372. doi: 10.7554/eLife.03372

Vale, R. D. (2003). The molecular motor toolbox for intracellular transport. *Cell* 112, 467–480. doi: 10.1016/S0092-8674(03)00111-9

Valetti, C., Wetzel, D. M., Schrader, M., Hasbani, M. J., Gill, S. R., Kreis, T. E., et al. (1999). Role of dynactin in endocytic traffic: effects of dynamitin overexpression and colocalization with CLIP-170. *Mol. Biol. Cell* 10, 4107–4120. doi: 10.1091/mbc.10.12.4107

Vallee, R. B., McKenney, R. J., and Ori-McKenney, K. M. (2012). Multiple modes of cytoplasmic dynein regulation. *Nat. Cell Biol.* 14, 224–230. doi: 10.1038/ncb2420

Vaughan, K. T., Tynan, S. H., Faulkner, N. E., Echeverri, C. J., and Vallee, R. B. (1999). Colocalization of cytoplasmic dynein with dynactin and CLIP-170 at microtubule distal ends. *J. Cell Sci.* 112(Pt 10), 1437–1447.

Vaughan, K. T., and Vallee, R. B. (1995). Cytoplasmic dynein binds dynactin through a direct interaction between the intermediate chains and p150Glued. *J. Cell Biol.* 131, 1507–1516. doi: 10.1083/jcb.131.6.1507

Vaughan, P. S., Miura, P., Henderson, M., Byrne, B., and Vaughan, K. T. (2002). A role for regulated binding of p150(Glued) to microtubule plus ends in organelle transport. *J. Cell Biol.* 158, 305–319. doi: 10.1083/jcb.200201029

Wang, H. M., Yan, Q., Yang, T., Cheng, H., Du, J., Yoshioka, K., et al. (2015). Scaffold protein JLP is critical for CD40 signaling in B lymphocytes. *J. Biol. Chem.* 290, 5256–5266. doi: 10.1074/jbc.M114.618496

Waterman-Storer, C. M., Karki, S., and Holzbaur, E. L. (1995). The p150Glued component of the dynactin complex binds to both microtubules and the actin-related protein centractin (Arp-1). *Proc. Natl. Acad. Sci. U.S.A.* 92, 1634–1638.

Wittmann, T., and Hyman, T. (1999). Recombinant p50/dynamitin as a tool to examine the role of dynactin in intracellular processes. *Methods Cell Biol.* 61, 137–143.

Wuhr, M., Tan, E. S., Parker, S. K., Detrich, H. W. III, and Mitchison, T. J. (2010). A model for cleavage plane determination in early amphibian and fish embryos. *Curr. Biol.* 20, 2040–2045. doi: 10.1016/j.cub.2010.10.024

Yamada, M., Toba, S., Yoshida, Y., Haratani, K., Mori, D., Yano, Y., et al. (2008). LIS1 and NDEL1 coordinate the plus-end-directed transport of cytoplasmic dynein. *EMBO J.* 19, 2471–2483. doi: 10.1038/emboj.2008.182

Ye, F., Breslow, D. K., Koslover, E. F., Spakowitz, A. J., Nelson, W. J., and Nachury, M. V. (2013). Single molecule imaging reveals a major role for diffusion in the exploration of ciliary space by signaling receptors. *Elife* 2:e00654. doi: 10.7554/eLife.00654

Yi, J., Wu, X., Chung, A. H., Chen, J. K., Kapoor, T. M., and Hammer, J. A. (2013). Centrosome repositioning in T cells is biphasic and driven by microtubule end-on capture-shrinkage. *J. Cell Biol.* 202, 779–792. doi: 10.1083/jcb.201301004

Yi, J. Y., Ori-McKenney, K. M., Mckenney, R. J., Vershinin, M., Gross, S. P., and Vallee, R. B. (2011). High-resolution imaging reveals indirect coordination of opposite motors and a role for LIS1 in high-load axonal transport. *J. Cell Biol.* 195, 193–201. doi: 10.1083/jcb.201104076

Conflict of Interest Statement: The authors declare that the research was conducted in the absence of any commercial or financial relationships that could be construed as a potential conflict of interest.

frontiers
in Cellular Neuroscience

ORIGINAL RESEARCH
published: 10 November 2015
doi: 10.3389/fncel.2015.00441

Force Generation by Molecular-Motor-Powered Microtubule Bundles; Implications for Neuronal Polarization and Growth

Maximilian Jakobs[1, 2], *Kristian Franze*[1] *and Assaf Zemel*[3]*

[1] Department of Physiology, Development and Neuroscience, University of Cambridge, Cambridge, UK, [2] Bonn Cologne Graduate School of Physics and Astronomy, University of Cologne, Cologne, Germany, [3] Institute of Dental Sciences and Fritz Haber Research Center for Molecular Dynamics, Hebrew University of Jerusalem, Jerusalem, Israel

The heavily cross-linked microtubule (MT) bundles found in neuronal processes play a central role in the initiation, growth and maturation of axons and dendrites; however, a quantitative understanding of their mechanical function is still lacking. We here developed computer simulations to investigate the dynamics of force generation in 1D bundles of MTs that are cross-linked and powered by molecular motors. The motion of filaments and the forces they exert are investigated as a function of the motor type (unipolar or bipolar), MT density and length, applied load, and motor connectivity. We demonstrate that only unipolar motors (e.g., kinesin-1) can provide the driving force for bundle expansion, while bipolar motors (e.g., kinesin-5) oppose it. The force generation capacity of the bundles is shown to depend sharply on the fraction of unipolar motors due to a percolation transition that must occur in the bundle. Scaling laws between bundle length, force, MT length and motor fraction are presented. In addition, we investigate the dynamics of growth in the presence of a constant influx of MTs. Beyond a short equilibration period, the bundles grow linearly in time. In this growth regime, the bundle extends as one mass forward with most filaments sliding with the growth velocity. The growth velocity is shown to be dictated by the inward flux of MTs, to inversely scale with the load and to be independent of the free velocity of the motors. These findings provide important molecular-level insights into the mechanical function of the MT cytoskeleton in normal axon growth and regeneration after injury.

Keywords: axon outgrowth, microtubules, molecular motors, force generation, neuronal polarization

Edited by:
Daniel Marcel Suter,
Purdue University, USA

Reviewed by:
David Odde,
University of Minnesota, USA
Matthew Ryan O'Toole,
Kettering University, USA
Peter Jung,
Ohio University, USA

Correspondence:
Assaf Zemel
assaf.zemel@ekmd.huji.ac.il

Received: *24 June 2015*
Accepted: *26 October 2015*
Published: *10 November 2015*

Citation:
Jakobs M, Franze K and Zemel A (2015) Force Generation by Molecular-Motor-Powered Microtubule Bundles; Implications for Neuronal Polarization and Growth. Front. Cell. Neurosci. 9:441. doi: 10.3389/fncel.2015.00441

1. INTRODUCTION

During development, neurons assume highly complex morphologies. After migration to their target location, neurons extend several short processes (neurites). One of these neurites eventually becomes an axon, the dominating cell process that can extend over considerable distances. The remaining neurites typically remain shorter and become highly branched dendrites. This change in cell morphology, so-called neuronal polarization, is critical for network formation and functioning. While many chemical signals controlling neurite growth and axon specification have been identified, the intracellular mechanisms driving outgrowth are still poorly understood (Suter and Miller, 2011).

A long-standing question pertains to the mechanism by which MTs and the actomyosin network, along the neurite and within the growth cone (GC), regulate axonal growth (Heidemann and Buxbaum, 1993; Suter and Miller, 2011; Dehmelt, 2014). The GC is the highly motile structure at the neurite tip which navigates the neurite to its target. Forces generated at the GC leading edge via actin polymerization and actomyosin contraction result in a (tensile) pulling stress on the emerging neurite (Lamoureux et al., 1989; Franze et al., 2009; Betz et al., 2011; Koch et al., 2012; Toriyama et al., 2013; Hyland et al., 2014). It has nevertheless been shown that neurites can grow and assume correct axonal morphologies even without a GC (Marsh and Letourneau, 1984; Letourneau et al., 1987; Ruthel and Hollenbeck, 2000). MTs accumulating next to the plasma membrane and later on pushed into the neurite shaft are believed to provide the complementary force needed for neurite initiation and growth (Ahmad and Baas, 1995; Dehmelt et al., 2006; Dehmelt, 2014). Within an emerging neurite as well as along the shaft of mature axons and dendrites, MTs are organized in thick and dense bundles comprising tens of filaments per cross-section, 1–100 μm in length, that are cross-linked by a variety of microtubule associated proteins (MAPs) including passive cross-linkers and molecular motors (Kapitein and Hoogenraad, 2015). A growing body of evidence indicates that the dynein and kinesin molecular motors residing in these bundles exert sliding forces between the MTs, which push against the actomyosin cortex that surrounds those bundles (Ahmad et al., 2000; Dehmelt et al., 2006; Jolly et al., 2010; Lu et al., 2013, 2015; Roossien et al., 2014). Although MTs eventually undergo 'catastrophe' and depolymerize under load, experiments show that they could still bear significant compressional forces before they do so and thus contribute to the outward pushing of obstacles (Janson et al., 2003). A well known example is their role in the assembly and dynamics of the mitotic spindle during cell division (Civelekoglu-Scholey and Scholey, 2010; Mogilner and Craig, 2010). There is also ample of evidences that MT pushing forces are involved in axon initiation and growth. Both the depletion of MTs from the core of axons and the inhibition of cytoplasmic dynein or kinesin-1 motors result in axon retraction and impaired growth, while dismantling of actin filaments or inhibition of myosin II molecular motors facilitates growth (Bradke and Dotti, 1999; Ahmad et al., 2000; Dehmelt et al., 2006; Jolly et al., 2010; Lu et al., 2013, 2015; Roossien et al., 2014).

Additionally, the tension along neurites was shown to increase with MT depolymerization and decrease with actin disruption (Dennerll et al., 1988). Forces on the order of 10^2–10^3 pN have been reported to be essential for mechanically initiating axon growth by external loading (Bray, 1984; Dennerll et al., 1989; Zheng et al., 1991; Chada et al., 1997; Fass and Odde, 2003). These experiments provide estimates of the restoring forces that may be acting on the MT bundles in developing axons and dendrites. This range of forces is approximately 10–100-fold higher than the force needed to pull a tether from a (bare) lipid bilayer (Dai and Sheetz, 1995; Hochmuth et al., 1996; Atilgan et al., 2006). The larger range of resisting forces is believed to arise from the cytoskeletal cortex underlying the lipid bilayer and the contractile actomyosin forces generated therein (Ahmad et al., 2000; Xu et al., 2013).

These observations highlight the role of molecular motor activity in the regulation of axon initiation and growth. There is nevertheless poor understanding of how molecular motors cooperatively function in the dense MT bundles of axons and dendrites. While some processes, such as filament sorting and bundle expansion, have been investigated (Kapitein et al., 2005, 2008; Kerssemakers et al., 2006; Braun et al., 2009), experimentally monitoring the molecular organization and motion of single filaments within neurites remains challenging. Computer simulations provide an invaluable complementary tool to gain molecular-level insight into the internal organization, dynamics and function of these cellular structures. They also provide the opportunity to dissect the contribution of individual molecular constituents to the overall macroscopic behavior of the system and determine the most crucial parameters for force generation. Models of both actomyosin and MT bundles have been reported and studied in different contexts such as stress fiber formation and cytokinesis (Nédélec, 2002; Mogilner et al., 2006; Paul et al., 2009; Lenz et al., 2012; Kim, 2014; Bidone et al., 2015; Ward et al., 2015).

In this manuscript, we present a computational investigation of the dynamics and force generation properties of 1D bundles of MTs that are cross-linked and powered by molecular motors. The dynamics of bundle expansion are analyzed as a function of the motor type, bundle polarity, filament length, filament-motor connectivity, and strength of the applied load. We demonstrate that both unipolar and bipolar motor types (e.g., kinesin-1 and kinesin-5, respectively) efficiently sort oppositely oriented filaments. However, only unipolar motors are found to provide the driving force for bundle expansion, while bipolar motors hinder this motion. The capacity of MT bundles to exert a force is shown to depend sharply on the fraction of cross-links formed by unipolar motors; only if a threshold fraction is surpassed can the bundle become percolated and exert a force on the boundaries. The dependence of this percolation threshold on the MT density and length is presented. We also investigated the growth of MT bundles in the presence of a constant influx of MTs. Beyond a short equilibration period the bundles grow linearly in time. In this (steady-state) growth regime, the growth velocity is found to be dictated by the inward flux of MTs and the magnitude of the opposing load, but interestingly, to be independent of the free velocity of the motors. This is because at this stage of growth most filaments slide with the growth velocity while the relative velocity between filaments is small and the force exerted by the motors approaches the maximal stall force of the motors; similar behavior has been observed experimentally (Suter and Miller, 2011; Roossien et al., 2014). The bundle width and growth velocity adjust spontaneously to the load. We discuss these findings in the context of neurite initiation and growth and their implications for axon specification.

2. MODEL

2.1. Bundle Structure

We consider a cylindrical bundle of MTs, cross-linked by ensembles of molecular motors and oriented along the *x*-axis of a Cartesian coordinate system (**Figure 1**). The bundle comprises a total of $N = N_R + N_L$ filaments of which N_R point with their + end to the right (assigned as the GC direction) and N_L point with their + end to the left (cell body direction). For simplicity we assume that all filaments in a bundle have an equal length, l. The filaments are arranged on a hexagonal lattice in the $y - z$ plane and along the bundle axis. We set the initial bundle length to L_0, and sequentially position the N filaments along the x-axis with their centers randomly chosen between $x = 0$ to $x = L_0$ and their y, z coordinates increasing gradually from the bundle center outward to obtain a hexagonally packed cylindrical bundle (**Figure 1B**). The inter-filament spacing in the $y - z$ plane (∼50 nm) is assumed to allow individual molecular motors to intervene between the filaments and cross-link them with their respective "cargo" or "walking" domains. This architecture allows the motors to slide the filaments past each other and to collectively induce global changes in bundle length and force (Chen et al., 1992; Kapitein et al., 2005, 2008; Kerssemakers et al., 2006; Braun et al., 2009).

Axons and dendrites comprise different types of motor proteins that may generally be classified as unipolar or bipolar motors (Zemel and Mogilner, 2009). Unipolar motors, such as cytoplasmic dynein or kinesin-1, possess one "walking" domain with which it preforms a power-stroke and moves along a filament, and one "cargo" domain, with which it binds a cargo or another filament. Bipolar motors, such as kinesin-5, have walking domains on both ends.

Only very little is known on how these motors organize between adjacent MTs in dense bundles such as those of axons and dendrites. It is generally expected that some degree of cooperativity exists in the binding of the motors to the filaments and that this will render the motors to locally segregate between the filaments. As a working hypothesis, we thus assume that each overlapping region between filaments is occupied by one type of motor only, or is otherwise devoid of motors. This approximates the more complex situation that may exist where different motors occupy the same region between filaments and one motor type dominates due to inter-motor binding correlations. We distinguish two generic binding arrangements of unipolar motors to neighboring filaments (left panels **Figure 1C**). In one scenario, the motors bind the filaments in an uncorrelated fashion with their cargo or walking domains oriented randomly between the filaments; in a second scenario, they bind the filaments in a correlated fashion having their cargo and walking domains oriented toward the same MT.

During bundle configuration, all possible overlap regions between filaments are identified and their probability of being cross-linked by unipolar or bipolar motors is determined by a control parameter, χ_i, which dictates the fraction of MT overlaps that are cross-linked by the given motor type $i = \{up, bp\}$. The total fraction of overlaps that are populated by motors is given by $\chi_{up} + \chi_{bp} = \chi$. In the calculations presented below we typically assumed that $\chi = 1$, indicating that all overlapping regions between filaments are cross-linked by motors; as would

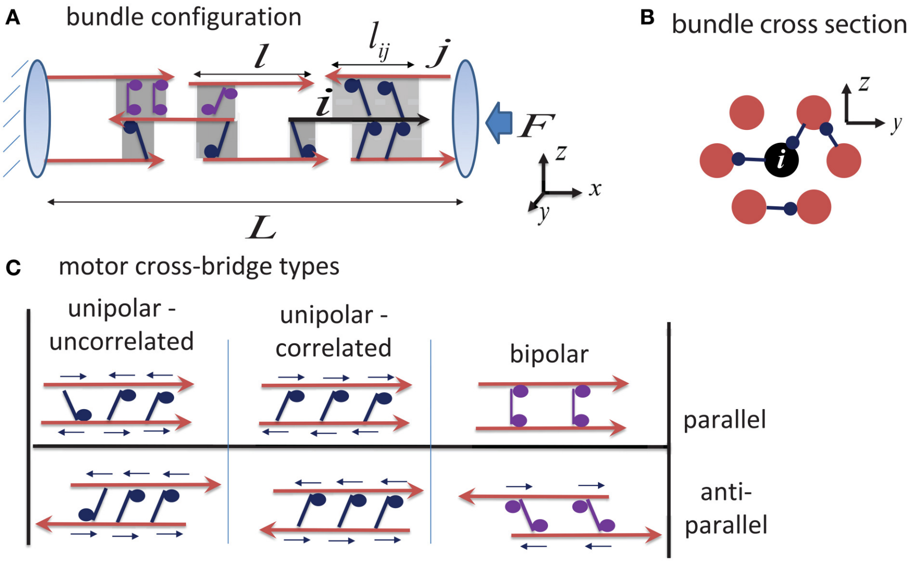

FIGURE 1 | Schematic illustration of bundle structure. (A) Shows a side view of the bundle connectivity. MT filaments are shown as red arrows (indicating the MT polarity), and shaded regions mark the overlap regions between them which may either be cross-linked by motors, or be unoccupied. Highlighted in black is a "central filament," i, interacting with its neighboring filaments. The force on any filament i is calculated by summing the contributions from all motors that interact with it (see Equation 1); the calculation uses the overlap length between the filaments, l_{ij}, that is assumed to be proportional to the number of motors cross-linking the filaments. The left boundary is held fixed (mimicking the dense cytoskeleton at the neurite entry), and expansion occurs to the right against an opposing load, F, arising from the contractile actomyosin cytoskeleton in the neurite cortex. **(B)** Shows the hexagonal packing of filaments in a bundle cross-section (Chen et al., 1992). Each filament potentially has six nearest neighbors in a cross section, but it may interact with more than six filaments along its length. **(C)** Illustrates three distinct motor-filament configurations; see Section 2.2 for the consequences of these interaction types. Small arrows above each motor indicate the direction of the force that the motor exerts on the filaments. Note how bipolar motors fail to exert forces between parallel filaments.

be the case for sufficiently high density of motors in the bulk. We nevertheless devote a whole Section (3.2) to demonstrate the interesting role that χ may have in dilute motor systems.

During the simulation, filaments are sled by the motors they connect to according to force-velocity relations which we detail below. It is assumed that the motors maintain their interaction to the filaments as long as the overlap between them exists. Once an overlap is broken, the motors are assumed to bind elsewhere in the bundle such that the proportion between motor types χ_i remains fixed. The use of χ_i, although simplifies the much more complicated thermodynamic problem of considering the energetic tendency of the motors to populate the overlap regions between filaments, allows us to draw important conclusions on how a mixture of motors may affect the forces that such bundles may exert.

2.2. Model Equations

We here derive the equations used in our simulations to calculate the motion of filaments in the bundle. Because the motion of MTs in the dense bundles we discuss is essentially one-dimensional we only consider filament movements along the x-axis and neglect transverse (radial) forces that may arise due to interactions with the lipid membrane or membrane-associated proteins. In addition, in the low Reynolds number environment of the cell the velocity of each filament is proportional to the total force exerted on it (Howard, 2001). We thus write the following equation for the velocity of each filament, i, in the bundle :

$$\xi\, v_i = f_i = \sum_j f_{i,j}^m + f_i^{ex} \tag{1}$$

The first term on the right hand side (rhs), $f_i^m = \sum_j f_{i,j}^m$, is the force exerted on filament i due to its motor-driven interaction with all nearby filaments j (see **Figure 1A**). Each contribution, $f_{i,j}^m = f_{i,j}^m(v_j - v_i)$, depends on the relative velocity of the two interacting filaments; the specific form of this force-velocity relation is dictated by the type of motors and their organization in between the filaments, as discussed below. For simplicity, linear force-velocity relationships have been assumed; this is consistent with experiments (Mallik et al., 2004; Valentine et al., 2006), and generalization of this approach to more complex force-velocity relationships is numerically straightforward. The second term is the contribution of external forces; in our simulations it is applicable only to filaments in contact with the boundaries. On the left, ξ, is the drag coefficient representing the viscous environment of filaments in the bundle. We anticipate that ξ is significantly higher than the drag coefficient in aqueous solution due to weak binding interactions of the filaments with other proteins in their neighborhood; we used the value $\xi = 0.023\,\text{pN s}/\mu\text{m}$ per 1 μm filament based on diffusion constant measurements reported in Tawada and Sekimoto (1991).

2.2.1. Motor Cross-bridging Types and Corresponding Force-velocity Relations

We assume that the motors occupy the overlapping regions between neighboring filaments with a uniform and constant density, λ, and that the force they exert is additive and proportional to the total overlap length l_{ij} of neighboring filaments, see **Figure 1A**. Consequently, $\lambda\, l_{ij}$, is the mean number of motors within this overlap. For simplicity, we assume that motors along l_{ij} share the load equally and omit the complex non-linear effect of indirect non-linear inter-motor interactions (Klumpp and Lipowsky, 2005; Kunwar et al., 2008). The forces generated by the motors are characterized by force-velocity relationships which we specify below for the different possible cross-bridging types.

2.2.1.1. Orientationally correlated unipolar motors

In an overlap region between filaments, unipolar motors may be correlated, or randomly oriented as illustrated **Figure 1C**. In the former case, all motors in a given overlap bind their walking domains to one filament and their cargo domains to the other filament. While not much is known about the orientation of motors in the crowded environment of dense MT bundles, some indirect evidence for such arrangement of motors exists (Haimo and Rosenbaum, 1981; Haimo and Fenton, 1984; Vilfan et al., 2001; Sciambi et al., 2005). In a dense interconnected bundle, each MT filament may interact with multiple MTs at the same time (**Figures 1A,B**) and the motors within each overlap region can exert a different net force on the given filament. When expressing the force acting on a given filament, i, it is essential to know if the motors in an overlapping region with a filament j are bound with their walking domains to filament i or to filament j. The following force-velocity relationship holds when motors bind their walking domains to filament i and cargo domains to filament j:

$$f_{i,j}^m = -\lambda l_{ij} f_s \left[n_i - \frac{v_j - v_i}{v_0} \right]; \tag{2}$$

when the motors' walking domains are bound to filament j one has:

$$f_{i,j}^m = \lambda\, f_s\, l_{ij} \left[n_j - \frac{v_i - v_j}{v_0} \right] \tag{3}$$

The factors f_s and v_0 are the stall force and free velocity of the motors, respectively. $n_i\hat{x}$ is the walking direction of the molecular motor on the filament, e.g., a value of $n_i = -1$ represents a motor that walks in the negative direction of the x-axis (for instance when a minus-end directed motor moves on a filament that points with its minus-end toward the negative direction of the x-axis).

2.2.1.2. Orientationally uncorrelated unipolar motors

When the binding of unipolar motor proteins to a pair of neighboring filaments is orientationally uncorrelated, we sum the contributions of the two populations of motors in that overlap region; this leads to the following force-velocity relationship in the limit of large numbers of motors:

$$f_{i,j}^m = \frac{1}{2}\,\lambda\, f_s\, l_{ij} \left[(n_j - n_i) + \frac{2(v_j - v_i)}{v_0} \right] \tag{4}$$

The factor 1/2 reflects the equal probability of individual motors to bind the filaments in a given overlap with either their walking or cargo domains. Note that for an isolated parallel pair (i.e., $n_j = n_i$ and no other cross-links), Equations (4) and (1) yield $v_i = v_j = 0$, as expected, because the motor forces on each filament cancel each other. This is in contrast to the correlated motor binding case, in which the motors can exert significant sliding forces on a pair of parallel filaments. For an antiparallel pair, Equations (4) and (2) are equivalent.

2.2.1.3. Bipolar motors

The situation in this case is similar to that of uncorrelated unipolar motors, if we assume that the two walking domains of each motor are independent of one another. Unlike unipolar motors, a bipolar motor can glide between the filaments with a finite velocity, $\vec{v}_m = v_m\hat{x}$, relative to a stationary frame of reference. If this motor is connected to a pair of filaments $\{i,j\}$, it exerts equal and opposite forces $f_i = -f_j$. Implementing a linear force-velocity relationship for each of the walking domains independently yields: $f_i = -f_s[n_i - (v_m - v_i)/v_0]$ and $f_j = -f_s[n_j - (v_m - v_j)/v_0]$. We thus find a limiting equation for the motor velocity in a pair of sliding filaments: $v_m = \frac{1}{2}[v_i + v_j + v_0(n_i + n_j)]$. Substituting this in the expression for f_i we find:

$$f^m_{i,j} = \frac{1}{2}\lambda f_s l_{ij}\left[(n_j - n_i) + \frac{v_j - v_i}{v_0}\right] \tag{5}$$

Note that the only apparent difference between this case and Equation (4) above is that bipolar motors slide the filaments with free velocity that is twice as large as that driven by orientationally uncorrelated unipolar motors. In addition, bipolar motors that distribute uniformly between two *parallel* filaments do not exert a net force on the filaments but merely bundle them together or act as viscous elements that slow down their relative motion. This applies to motors that persistently move across the filaments with constant speed, as observed for instance for the bipolar motor kinesin-5 (Cheerambathur et al., 2008; Kapitein et al., 2008). Because orientationally uncorrelated unipolar motors behave similarly to bipolar motors we discuss them interchangeably in what follows and draw the comparison between correlated-unipolar motors and bipolar motors.

Within an interconnected bundle each filament, i, may have multiple cross-links with other filaments and the cross-bridges may be of the different types discussed above; the overall motor-generated force is calculated as a sum: $f^m_i = \sum_j f^m_{i,j}$. This, together with the boundary conditions discussed below, constitute an algebraic set of linear equations for the velocities of all the filaments in the bundle. Once the velocities have been determined, all filaments are propagated by a small distance, $v_i\, dt$, where $dt \sim 0.2$ s is a sufficiently small time step to avoid numerical error. This results in a "trajectory" of the filaments in the bundle that can be averaged over an ensemble of starting configurations. Between 50 and 1000 trajectories have been averaged to characterize the mean behavior of the bundles. For simplicity, all bundles studied comprised either plus-end or minus-end-directed motors but not their mixtures.

2.2.2. Boundary Conditions

In all simulations an opposing force, F^{ex}, was assumed to act on the right boundary to resist the motor-driven motion of the filaments. The left boundary was assumed to be supported by a stiff spring that sustains the same load but in the opposite direction. We considered two types of external load: (i) a fixed load, $F^{ex} = \text{const}$, (ii) an elastic load, $F^{ex}(t) = -k[L(t) - L_0]$, where k is the spring constant of the compliant right boundary. In either case, the total force F^{ex} distributes among all filaments touching the right boundary, and $-F^{ex}$ distributes over the filaments touching the left boundary. The distribution of F^{ex} and $-F^{ex}$ amongst the different filaments on the right and left boundaries, respectively, is not necessarily even. Rather, we assumed that all the right boundary filaments, whose tips exceed the boundary $x = L(t)$, displace with equal speed, v_R; and all filaments exceeding the left boundary, $x = 0$, (principally) move with equal speed v_L. These conditions are formulated as follows: For the right boundary filaments:

$$\sum_{i=1}^{n_R} f^{ex}_i = F^{ex} \tag{6}$$

$$v_1 = v_2 = \cdots = v_R \tag{7}$$

For the left boundary filaments:

$$\sum_{i=1}^{n_L} f^{ex}_i = -F^{ex} \tag{8}$$

$$v_1 = v_2 = \cdots = v_L \tag{9}$$

In our simulations, we used a stiff spring on the left boundary to prevent motion of that boundary; hence, $v_L \approx 0$, and the speed of bundle expansion is given by $dL/dt = v_R$. These conditions supplement the set of equations, Equation (1), for the velocities of the filaments, with $n_R + 1$ new equations to solve for the $n_R + 1$ unknowns, $\{f^{ex}_i\}$ and v_R, on the right boundary, and $n_L + 1$ new equations for the $n_L + 1$ unknowns, $\{f^{ex}_i\}$ and v_L on the left boundary. For all other filaments f^{ex}_i is identically zero. For N filaments one diagonalizes an $N \times N$ matrix at each iteration in time to solve for the velocities of all filaments in the bundle.

3. RESULTS

3.1. Unipolar Motors Provide the Driving Force for Bundle Expansion and Bipolar Motors Hinder it

Bundles comprising a total of $N \sim 100$ MTs (of which N_R and N_L point with their plus-ends to the right and left, respectively), closely packed in a hexagonal array within a cylinder of axial length $L_0 = 50\,\mu$m, were simulated subject to an opposing spring on the right boundary and a fixed boundary on the left; the total force generated by the bundle is $F(t) = k[L(t) - L_0]$, where $L(t)$ is the evolving bundle length and k is the external spring constant.

Figure 2A illustrates the calculated evolution of $L(t)$ and $F(t)$ in mixed bundles of filaments that are cross-linked by different ensembles of motors. Blue curves correspond to bundles with unipolar cross-bridges only, purple curves to bundles with bipolar cross-bridges only, and black curves to bundles with a 50% mixture of unipolar and bipolar cross-bridges; solid, dashed and dotted curves respectively represent different polarity ratios, $N_R/N = 1, 0.2, 0.5$, of filaments in the bundle. Bundles comprising unipolar cross-bridges only (blue curves) are shown to exert the strongest steady state forces, and the addition of bipolar motors hinders force generation. Between parallel filaments, bipolar motors behave as transient cross-linkers and thereby hinder movement and force generation. Bundles cross-linked by these motors only, may only expand for a limited time until the bundles get sorted apart and motion stops (purple curves).

When interacting with anti-parallel filaments, both unipolar and bipolar motors have a tendency to sort the filaments apart (Zemel and Mogilner, 2009). The filaments are eventually sorted into two separate domains of parallel filaments, one comprising only right-oriented filaments, and the other only left-oriented filaments, with a transition zone between them. The inset in **Figure 2A** provides a quantification of the dynamics of sorting. An order parameter, $S(t) = (N\,L(t))^{-1}\int_0^{L(t)} |n_R(x,t) - n_L(x,t)|dx$, has been defined to average the local polarity of the bundle (namely, the local difference between the number of right- and left-oriented filaments, $|n_R(x,t) - n_L(x,t)|/N$) over the bundle length at any given time; $S = 1$ corresponds to a bundle that is locally parallel across its length, and $S = 0$ to a bundle that is locally mixed everywhere. The panel shows that sorting occurs on a time scale of ~10 s and that bipolar motors sort the filaments faster. Consequently, only the initial expansion dynamics depend on the bundle polarity, N_R/N, while the steady-state force and length are polarity-ratio independent (compare dotted, dashed and solid curves in **Figure 2A**). We find that the time to reach the stationary state for the (50%) orientationally-mixed bundles (dotted curves) is longer than for the more polar ones. In the mixed bundles, the initial sorting of filaments reduces the force that can be generated against the boundary. This is because filaments that undergo sorting move faster and contribute less to force generation; as a consequence the bundle expands more slowly[1].

Figure 2B shows the calculated steady-state force, F_{ss}, for bundles with varying fractions of bipolar cross-bridges. We find that the exerted steady-state force is a monotonically decreasing function of the fraction of bipolar cross-bridges. Interestingly, as soon as the fraction of bipolar cross-bridges surpasses a critical value, the force exerted by the bundle sharply decreases to zero (this is more clearly seen with the dashed-blue curve plotted for bundles with 5 μm long filaments in which the sharp change occurs at a smaller value of $\chi_{bp} \approx 0.8$). The sharpness of this transition and the critical value of χ_{bp} increase with the number of filaments and their length. The sharp transition and

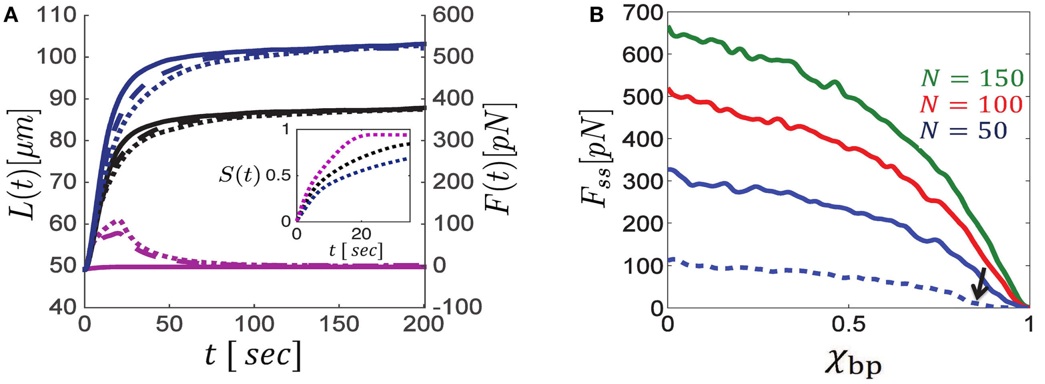

FIGURE 2 | Dynamics of bundle expansion and force generation, shown for varying polarity ratios of filaments and fraction of bipolar cross-bridges. **(A)** Shows the evolution of bundle length (left y-axis) and force (right y-axis) for different fractions of bipolar cross-bridges, χ_{bp}, and different polarity ratios, N_R/N; the number of filaments is $N = 100$. Blue curves correspond to bundles comprising unipolar cross-bridges only ($\chi_{bp} = 0$), black curves are for a 50:50 mixture of bipolar and unipolar cross-bridges ($\chi_{bp} = 0.5$), and purple curves are for bundles with bipolar cross-bridges only ($\chi_{bp} = 1$). Solid, dashed and dotted curves correspond to polarity ratios: $N_R/N = 1, 0.2, 0.5$, respectively. Bundle polarity is found to have a minor effect on the expansion dynamics and no effect on the steady state force. The inset shows the dynamics of filament sorting in mixed bundles ($N_R/N = 0.5$) as quantified by the order parameter $S(t)$ (defined in the text); $S = 0$ is found for a bundle that is locally mixed across its length, and $S = 1$ is found for a bundle that is locally parallel all along. $S(t)$ evolves to ~1 on a time scale of ~10 s, with bipolar motors being more efficient. Consequently the steady-state force, F_{SS}, is determined by forces exerted in parallel bundles and is independent of the bundle polarity. **(B)** Shows F_{SS} as a function of the fraction of bipolar cross-bridges for varying numbers of MTs. The same stall force is used for both unipolar and bipolar motors and F_{SS} is found to be proportional to $\lambda\, f_s$ (see Section 3.3). The MT length in all curves of **(A,B)** is 10 μm, except for the dashed blue curve in **(B)** which is for l = 5 μm. Note the sharp drop in bundle force as the bipolar motor fraction surpasses the value $\chi_{bp} \approx 0.8$ (indicated by a black arrow). Other parameters used in these calculations are: $v_0 = 1$ μm/s, $L_0 = 50$ μm, $k = 10$ pN μm, $\chi = 1$.

---

[1] Calculations are presented for equal stall force for the bipolar and unipolar motors. When the bipolar-motor stall force is increased, only the dynamics of bundle expansion is affected but there is no effect on the steady-state force; F_{ss} is dictated by the stall force of unipolar motors (see Section 3.3). Because bipolar motors sort the filaments faster, sorting occurs more quickly when their stall force exceeds that of the unipolar motors, but the time to reach the steady-state is prolonged due to the increase in the viscosity of the bundle.

the dependence on system size are reminiscent of a percolation transition occurring in the bundle. Since bipolar motors do not exert sliding forces between parallel filaments (Equation 5), but rather behave as passive frictional elements between them, they are unable to sustain long-term stresses in the bundle. Thus, a system with a high fraction of bipolar cross-bridges and low fraction of (orientationally correlated) unipolar cross-bridges may become disconnected from one side to the other and long-term forces cannot be generated in such bundles. For a sufficiently large number of filaments, this so-called percolation transition occurs at a critical fraction of active overlaps in the bundle that depends on the density of filaments and their length, as discussed next.

3.2. Percolation Transition Dictates a Motor-density Threshold for Force Generation

To demonstrate that the sharp changes in force generation indeed result from a percolation transition we have directly calculated the percolation probability, p, in bundles containing unipolar motors only and systematically varied the connectivity parameter, χ (see **Figure 3**). p is defined as the probability for the bundle to be percolated, namely, that at least one route of interconnected MTs transverses the bundle from left to right and allows the transmission of force to the boundaries. To calculate this probability numerous bundle configurations were generated with fixed numbers of MTs of same length, l, and fixed connectivity fraction, χ (the number of overlaps cross-linked by motors divided by the total number of overlaps between neighboring filaments); we also used a relatively stiff spring to prevent significant bundle expansion and thereby kept the density of filaments, N/L, fairly constant. For each configuration we determined whether the bundle was percolated or not. p was then determined as the number of percolated bundles divided by the total number of configurations generated, and we investigated it as a function of N/L, l, and χ.

Figure 3A shows the percolation probability, p, as function of the connectivity fraction, χ, for varying MT densities N/L. **Figure 3B** shows the calculated force exerted by the bundle. Since expansion was minor, the calculated force was also the steady-state force. As expected, the point at which the force increases sharply with χ is the point where the percolation probability increases sharply to 1. We denote this percolation threshold by χ^c. The inset figure in **Figure 3A** shows that χ^c is a decreasing function of the MT density and MT length. This result is expected since the longer the filaments, or the higher their density, the more likely it is to find an interconnected route of filaments that transverses the bundle. Another expected behavior is that the percolation transition becomes sharper and resembles a phase transition as the system size (number of filaments) increases (Stauffer and Aharony, 1992). The percolation threshold is a structural property of the bundle reflecting the hexagonal organization of the filaments in the $y-z$ plane and their axial spread along the x-axis. We find that χ^c varies from ~0.08 for 50 filaments to ~0.04 for 150 filaments in case that $l = 10\,\mu m$, and correspondingly between 0.1 and 0.2 when $l = 5\,\mu m$. For comparison, the bond-percolation threshold is 0.34 for a two-dimensional triangular lattice and 0.25 for a three-dimensional cubic lattice (Stauffer and Aharony, 1992).

Interestingly, the percolation thresholds calculated in **Figure 3A** are consistent with those found in the previous section when the fraction of bipolar cross-bridges was varied systematically, indicating that the sharp decrease in force with $\chi_{bp} = 1 - \chi_{up}$ resulted from a percolation transition. Another consequence of the percolation transition has been reported in our previous investigation of circularly-closed ringed bundles. It has been demonstrated that beyond a threshold level of bundle connectivity the induced velocity of the filaments sharply drops

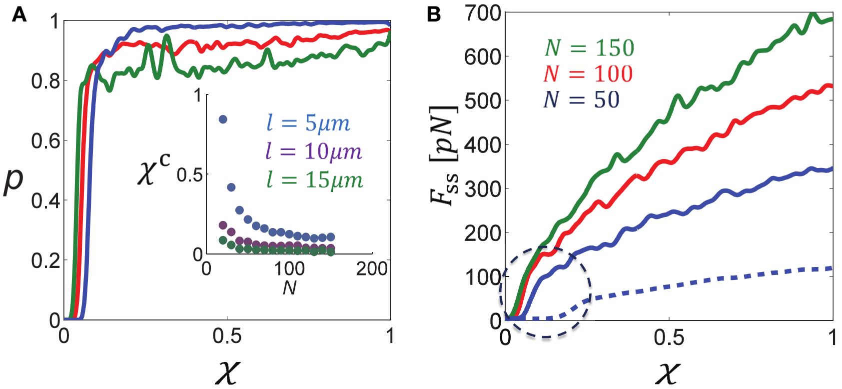

FIGURE 3 | Percolation transition in cross-linked bundles of filaments. (A) Shows the percolation probability, p (of a bundle of fixed length $L \approx L_0$ to be interconnected from left to right), as a function of the fraction of active cross-links, χ, for different numbers of MTs (color coding is indicated in **B**). The percolation probability is seen to sharply increase to ~1 when a critical fraction χ^c is surpassed. The inset figure shows that χ^c is a decreasing function of the filament density, N/L and length, l. **(B)** Shows the steady-state force, F_{ss}, as a function of χ for different N. Solid curves correspond to $l = 10\,\mu m$ and the dashed blue curve to $l = 5\,\mu m$. Note the sharp increase in F_{ss} when χ surpasses the percolation threshold, χ^c, that is found in **(A)**. Parameters used in these calculations: $L_0 = 50\,\mu m$, $\lambda f_s = 10$ pN/μm, $k = 10$ pN/μm.

down due to interference of motor activity (Zemel and Mogilner, 2009).

The demonstration that interconnected bundles of MTs may undergo a sharp transition in their capacity to generate a force with variations of unipolar motor density may have important implications for neurite initiation and growth. During neuronal development force thresholds must be met to permit initial neurite extension and axon specification (Heidemann and Buxbaum, 1993; Chada et al., 1997; Fass and Odde, 2003). Following initiation, neurites undergo rapid growth and retraction cycles. Subsequently, one neurite starts rapid growth and becomes the axon. We suggest here that availability of unipolar motors at the cell periphery might be one of those limiting factors; once it surpasses a critical threshold, MT bundles in that region can become percolated and neurite initiation may proceed.

3.3. Scaling Laws of Force Generation in Bundles with a Fixed Number of Filaments

Another important characterization of cytoskeleton-motor bundles is the relation between the bundle geometric characteristics, diameter and length, and the force that it generates. We concentrate here on forces generated in bundles with a fixed number of filaments; growth arising from an influx of filaments will be discussed in the next section. Because the MTs overlap, the generated force not only depends on the number of filaments in a cross section, but also on the mean overlap length between them. We shall therefore also reveal how the force/length relation depends on the MT length, l, and the motor connectivity factor, χ. The relationships discussed here pertain to the steady-state where bundle length and force are stationary. For clarity, we omit the subscript indication of the steady-state and denote the steady-state force and length by F and L, respectively. The following simulations have been carried out: (i) Bundles with a fixed number of MTs, N, were allowed to expand against an opposing spring with varying degrees of stiffness and the resulting steady state length and force were measured. We performed these calculations in bundles comprising MTs of different lengths and with variable degrees of the motor connectivity parameter χ (**Figure 4A**). (ii) We used a stiff spring to prevent changes of bundle length and carried out simulations with varied N (**Figure 4B**) or l (**Figure 4C**). In a given simulation all MTs had the same length. Since bundle polarity showed only little effect on the dynamics of bundle expansion and had no effect on the steady-state force, all simulations were carried out with polar bundles. Our results can be summarized via the following scaling relation:

$$F(L,N)/(\lambda f_s) \sim \sqrt{\chi}\, l^2 N/L^2 \tag{10}$$

with the geometric relation:

$$L\, d^2 \sim N\, l \tag{11}$$

where d is the bundle diameter. The scaling expressed in Equation (10) is demonstrated in **Figure 4**, showing F separately as function of L, N, and l. The scaling of F with $\sqrt{\chi}$ is seen in **Figure 3B** for $\chi > \chi^c$. To explain these dependencies we first note that for any given cross-section in the bundle the force scales as, $F \sim \lambda\, \bar{l}_{ov}\, \bar{m}$, where $\bar{m}$ is the mean number of MTs in a cross section, $\lambda \bar{l}_{ov}$ is the mean number of motors interacting with a given filament and $\bar{l}_{ov}$ is the total average length of overlap per filament. We find in our simulations that $\bar{l}_{ov} \sim l/L$. The inverse dependence on bundle length reflects the increase in number of interactions per filament with bundle compression; the square root dependence on χ follows because for a given cross section with m filaments around a given filament, $\sim m^2$ is the total number of pair interactions and χm^2 is the fraction of those occupied by motors; hence only $\sqrt{\chi} m$ interact with one given filament in that cross section. Combining these relations, using Equation (11) and noting that $\bar{m} \sim d^2$ one arrives at the scaling in Equation (10).

3.4. Inward Microtubule Flux and Bundle Growth Against a Load

We now consider the growth of MT bundles in the presence of a constant influx of filaments. This is relevant for growing neurites that extend over considerable distances and thus require a constant supply of new MTs. Experiments have demonstrated that the application of a pulling load on the cell membrane of

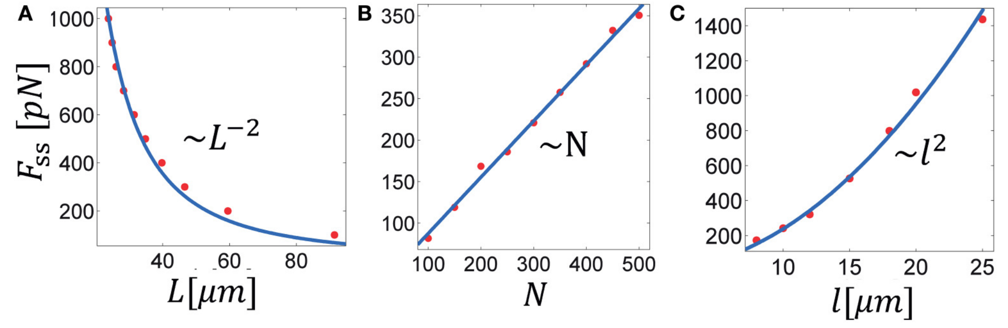

FIGURE 4 | Scaling laws in MT bundle force generation. The three panels show the steady-state force as function of: **(A)** the steady-state bundle length, **(B)** the number of MTs, and **(C)** the MT length. Solid lines represent best fits of the denoted scaling law to the calculated data. These results are summarized in Equation (10), see text. Parameters used in the calculation: $\lambda f_S = 10$ pN/μm, $\chi_{up} = 1$; in **(A,C)**: $N = 300$; in **(A,B)**: $l = 10$ μm.

neurons may initiate axon growth if a threshold level of force is applied. Moreover, this growth rate has been shown to linearly increase with the applied load (Zheng et al., 1991; Chada et al., 1997; Fass and Odde, 2003). Motivated by these results we have carried out the following simulations to investigate the properties of bundle growth under varying levels of *opposing* load when a constant supply of filaments is added per unit time. MT bundles were prepared with a starting number of $N_0 = 100$ filaments and initial length L_0 and new filaments of length l were added at a constant frequency, ω, on the left hand side of the bundle; the bundles were allowed to expand against a fixed load, F on the right boundary and a stiff spring on the left boundary. The simulations were carried out with varying levels of F (**Figure 5B**), and ω (**Figure 5C**); we also investigated the effects of the MT length, l (**Figure 5D**), and the fraction of bipolar cross-bridges in the bundle χ_{bp} (**Figure 5E**), assuming that all MT overlaps are occupied, either by unipolar motors or by bipolar motors $\chi_{bp} = 1 - \chi_{up}$.

The growth dynamics for varying load levels are shown in **Figure 5A**. After a short period during which the filaments adjust the overlap between them against the load, growth continues linearly in time at a constant speed, $v_g = (dL/dt)_{ss}$. At this state, both the mean number of filaments in a cross-section, $\bar{m}$, and the mean overlap length between filaments remain fixed. **Figures 5B–E**, respectively show how v_g depends on the applied load, F, the inward flux rate, ω, the microtubule length l and the fraction of bipolar cross-bridges in the bundle, χ_{bp}. We find that the growth rate scales as: $v_g \sim \omega\sqrt{\chi_{up}}\, l^{\alpha}/F$, where α varies from $\alpha = 1.8$ for short MTs to $\alpha = 0.8$ for long MTs at some intermediate MT length (here, $l \approx 25\,\mu\text{m}$) that decreases/increases with decreasing/increasing stall force of the motors.

These dependencies can be explained based on the geometric relation, $L = N\, l/\bar{m}$, expressed in Equation (11), where $\bar{m} \sim d^2$. Taking the time derivative of the equation above while keeping $\bar{m}$ fixed results in the following intuitive expression for the steady-state bundle growth rate v_g:

$$v_g = \frac{\omega\, l}{\bar{m}} \tag{12}$$

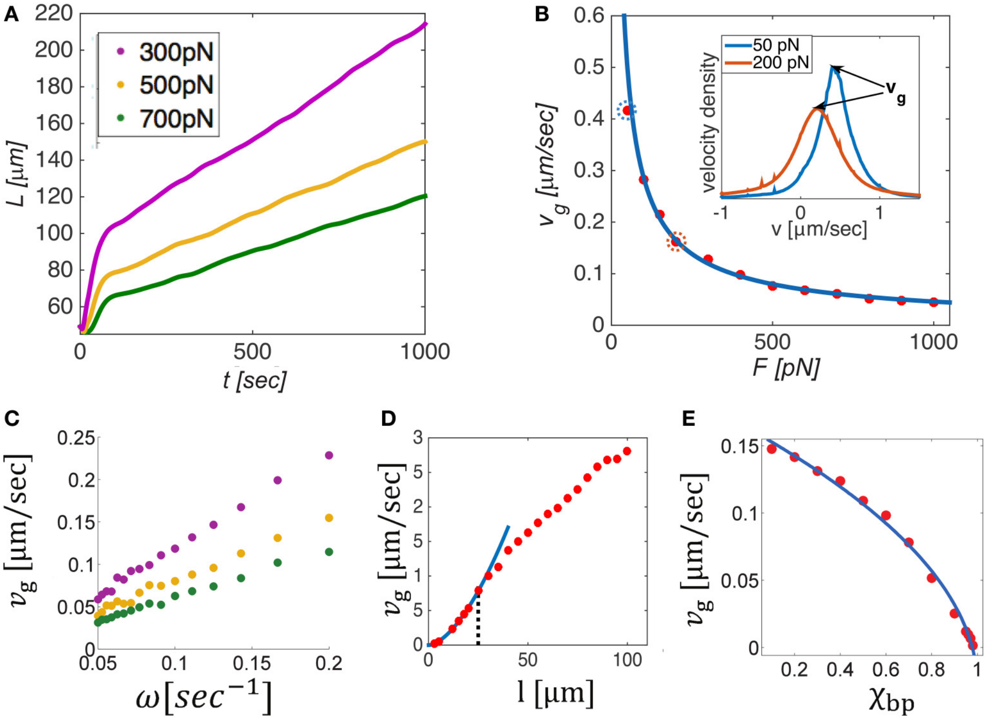

FIGURE 5 | Dynamics and mechanics of bundle growth against a constant opposing load when a constant supply of MTs is added on the left boundary at a fixed frequency, ω. (A) Shows the evolution of bundle length, $L(t)$, for different levels of opposing load. Beyond a short equilibration period, the bundles grow linearly in time and a constant velocity v_g can be defined. The steady state growth rate, v_g, is shown in **(B–E)** as a function of the opposing load, F, the influx frequency ω, the MT length, l, and the bipolar cross-bridge fraction χ_{bp}. Solid lines in panels B and E provide best fits to the simulation data. v_g is found to decrease with the load as $F^{-0.8}$ **(B)**, and to linearly scale with ω **(C)**. The inset in **(B)** shows velocity distributions of the filaments for $F = 50$ pN and $F = 200$ pN (circled dots in the main panel). The peak velocity equals v_g, implying that most filaments move as one mass with the growth velocity. The dependence of v_g on filament length **(D)** is biphasic: changing from $v_g \sim l^{1.8}$ for short MTs ($l < 25\,\mu$m, blue curve) to $v_g \sim l^{0.8}$ for longer MTs; the transition point (dotted black line) depends on the stall force of the motors, see text. Interestingly, v_g is seen to rise above the motor free velocity, $v_0 = 1\,\mu$m/s, illustrating that the bundle can grow much faster than individual motors are able to move. Increasing the amount of bipolar motors in the system decreases the growth velocity severely and finally halts growth for $\chi_{bp} = 1$. Unless otherwise mentioned we used $N = 100$, $L_0 = 50\,\mu$m, $\omega = 0.1$ s^{-1}, $l = 10\,\mu$m, $\chi_{up} = 1$, $v_0 = 1\,\mu$m/s, and $\lambda f_s = 10$ pN/μm. In **(D)**, $L_0 = 120\,\mu$m to allow longer filaments to be explored. In **(D,E)**, we used $F = 200$ pN.

where $\omega = dN/dt$. The added MT mass per unit time, $\omega\, l$, distributes over the bundle cross section $\bar{m}$, to produce a unit change in bundle length. Interestingly, $\bar{m}$ turns out to be proportional to F, which means that during growth the bundle adjusts its cross-section to match the number of filaments that share the load. Moreover, we find that the proportionality factor, $F/\bar{m}$, scales linearly with the motor density (per unit filament length, λ) and stall force of the motors, and as the square root of the unipolar cross-bridge fraction: $F/\bar{m} \sim \lambda\, f_s \sqrt{\chi_{up}}$. The $F/\bar{m}$ ratio reflects the number of motors that share the load per filament in a cross section. The square root dependence on χ_{up} arises because the number of *active overlaps* driving a given filament scales in this way, as previously explained in Section 3.3.

The proportionality factor between F and $\bar{m}$ depends in a non-trivial way on the MT length. For short MTs, $\bar{m}/F$ decreases with l and for long MTs it increases smoothly with l (not shown). This reflects the manner by which the filaments in the bundle adjust their interactions in response to the load. There are principally two ways in which they can do so: (i) by increasing the average overlap between pairs of filaments, and (ii) by increasing the number of filaments in a cross-section, $\bar{m}$. For short enough MTs, only the latter choice is possible, hence $\bar{m}$ decreases with l. For long MTs, (i) and (ii) provide two degrees of freedom for achieving force balance, hence $\bar{m}$ depends weakly on l. This behavior predicts an interesting dependence of bundle width on the MT length. In addition, it provides an explanation for the sigmoidal dependence of the growth rate, v_g, on l, which shows an approximately quadratic dependence for short MTs, followed by a (nearly) linear dependence for long MTs, as shown in **Figure 5D**. The transition between these two scaling regimes depends on the stall force of the motors. The larger the stall force the better the filaments can sustain the load without increasing the number of filaments in a cross section, $\bar{m}$. Consequently, the transition point shifts to lower values of l when λf_s is increased.

Summarizing these considerations we conclude:

$$v_g \sim \frac{\lambda f_s \sqrt{\chi_{up}}\, \omega l^{\alpha}}{F} \tag{13}$$

where $\alpha \approx 1.8$ for short MTs and $\alpha \approx 0.8$ for longer MTs and the transition occurs at some intermediate MT length that decreases with the stall force of the motors.

The inset of **Figure 5B** show the velocity distribution of filaments in the bundle for two cases of opposing force (50 and 200 pN). Notably, most filaments are found to move with the growth velocity, v_g. This implies that during steady-state growth the relative velocity between most filaments is zero. Although some filaments do continue to perform back and forth movements along the bundle length, the majority of them remain stationary with respect to each other and are collectively pushed as one mass at a constant velocity v_g. In this situation, most motors are stationary, exerting their maximal stall-force f_s. A remarkable consequence of this behavior is that the growth velocity of the bundle is independent of the free velocity of the motors, despite the fact that the entire motion is driven by motor activity only. Another important prediction is that the velocity distribution of filaments becomes wider when the opposing force is increased. The reason is that under conditions of larger force, the number of filaments in a cross-section is larger and this increases the diversity of possible interactions between filaments. As a consequence a wider range of filament velocities is found.

These results are consistent with experimental observations on neural growth. It is frequently reported that MT filaments in axons and dendrites are mostly stationary and that growth is in the range of 1 μm/min, an order of magnitude slower than the free velocity of typical motor proteins (Howard, 2001; Suter and Miller, 2011). According to our calculations the growth velocity is primarily dictated by the inward flux of filaments and the load acting on the bundle. This is consistent with the experimentally determined linear dependence of the growth rate on an external pulling load. This is because external pulling of the neurite tip relieves the opposing force acting on the growing MT bundle (see **Figure 6**). In a restricted range of loads, the scaling of v_g with F appears linear (see **Figure 5B** for $F \gtrsim 200$ pN) which might explain the reported experimental observations (Zheng et al., 1991; Chada et al., 1997; Fass and Odde, 2003). The threshold level of force (not to confuse with the percolation transition in Section 3.2) for axon initiation may relate to a number of factors, e.g., to the densities of MTs and/or the unipolar motors at the cell periphery, which limit the force that emerging bundles can spontaneously exert against the restoring forces in the plasma membrane and the underlying actin cytoskeleton.

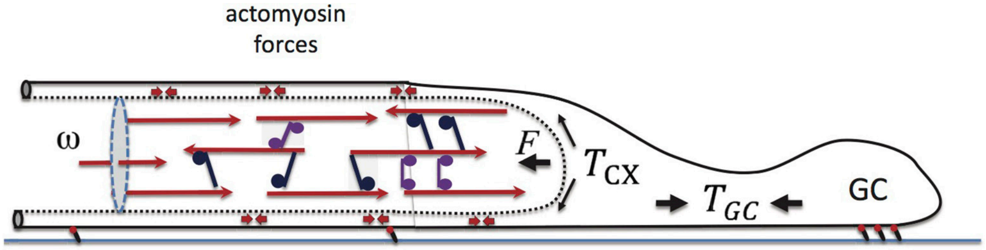

FIGURE 6 | Elements of force balance during neurite growth. Our major focus is on the motor-cross-linked MT bundle at the neurite core. The opposing force on the neurite, F, arises from actively generated actomyosin tension, T_{CX}, in the neurite cortex, and is biased by the GC-generated tension, T_{GC}. Actomyosin, force dipoles embedded in the cortex are illustrated with small double headed arrows. Also shown is the inward flux, ω, which is found to play a primary role in determining the neurite growth rate, v_g.

4. DISCUSSION

In this manuscript we focused on a major cytoskeleton structure contributing to the force balance of emerging neuronal processes—the heavily cross-linked MT bundle(s) in the neurite core. While there is ample evidence that both the MT filaments and the motor proteins associated with them are essential for axon elongation (Suter and Miller, 2011; Dehmelt, 2014), there is limited understanding of how these 1D molecular assemblies function. The major limitation in investigating these structures is their small size and their highly dense and compact architecture, which impedes quantitative imaging and analysis of their structure. Furthermore, there is also limited theoretical understanding of how assemblies of molecular motors and cytoskeletal filaments function collectively. We here used coarse-grained computer simulations to investigate the dynamics and force generation properties of such bundles. Our work, although presented in the context of axon initiation and growth, is relevant also for many other cellular processes in which such bundles play a key role, such as mitosis, blood platelet formation, and apoptosis (Scholey et al., 2003; Patel et al., 2005). The approach we took is intermediate between detailed computer simulations (Nédélec, 2002; Mogilner et al., 2006; Paul et al., 2009; Kim, 2014; Bidone et al., 2015; Ward et al., 2015), in which the motion and power-stroke dynamics of all individual motors are accounted for explicitly, and continuum approaches (Kruse and Julicher, 2000; Kruse et al., 2003; Liverpool and Marchetti, 2003; Ziebert and Zimmermann, 2005), which account for the motor-induced fluxes of filaments in an average manner, and in which only pairs of interacting filaments are taken into consideration. Our approach enabled us to investigate the dynamics exhibited by heavily cross-linked bundles of filaments. Rather than representing the motors individually, we used the force-velocity relationships that characterize their motion, and we did so simultaneously for all overlapping regions between filaments that are cross-linked by motors. This approach allows to simulate the dynamics of such bundles on an hours time scale (which is relevant for neurite growth) and to average over ensembles of trajectories in order to reveal some of their generic properties.

We first used our simulations to investigate how the motor type, unipolar or bipolar, the polarity ratio of the filaments, and the bundle connectivity affect the capacity of these bundles to exert a force. We found that both types of motors efficiently sort out oppositely-oriented filaments. Within seconds to minutes, the bundles get sorted and the dynamics become dominated by interactions between parallel filaments. Thus, the polarity ratio of the bundle has only a marginal effect on the dynamics of bundle expansion and no effect on its force generation capacity in the steady-state. Furthermore, our simulations robustly showed that only unipolar motors can provide the driving force for bundle expansion while the presence of bipolar motors impedes it. This result is expected since bipolar motors are unable to exert a force between parallel filaments, see Equation (5) and (Kapitein et al., 2005). In addition, the presence of bipolar motors in the bundle competes with the binding of unipolar motors to the filaments, and due to the reduced occupancy of the latter they slow down bundle expansion and weaken overall force generation. This is shown in **Figure 2B**, where the effect of χ_{bp} is demonstrated.

Importantly, we conclude that unipolar motors can drive bundle expansion only if the motors bind the filaments in an orientationally coordinated fashion (**Figure 2B**). If these motors randomly bind the filaments they exert a similar inhibitory effect on bundle expansion as bipolar motors do (cf. Equations 4 and 5). Our calculations may thus provide insight into the orientational organization and type of motors responsible for force generation in the dense MT bundles of neurites. Such information on the binding of dynein and kinesin-1 motors in the MT bundles of neurites or other cellular structures is, however, still lacking. Evidence for correlated binding of dynein to MTs has been reported in some *in vitro* studies (Haimo and Rosenbaum, 1981; Haimo and Fenton, 1984). Orientational correlation in unipolar motor binding to filaments may arise from steric or specific interactions between the motors and between the motors and the filaments. We hypothesize that it may also arise from a force-dependent binding rate of the motors. Because oppositely oriented motors between parallel filaments hinder each others' motion, the forces exerted by the motors are enhanced; this may cause the motors to detach from the filaments and to rebind with higher affinity in a correlated fashion. To test this hypothesis, we carried out preliminary calculations using the Cytosim simulation package [46], which allows to track the dynamics of individual molecular motors in small clusters of filaments. Our calculations indicate that force-dependent detachment rates of motors indeed lead to their spontaneous organization in a correlated fashion between the filaments.

Our conclusions are consistent with experiments highlighting the role of the unipolar motors, cytoplasmic dynein (Ahmad et al., 2000; Roossien et al., 2014) and kinesin-1 (Lu et al., 2013, 2015) in neurite initiation and growth, as well as with studies on kinesin-5, a bipolar motor, that has been shown to have inhibitory effects on neurite growth (Haque et al., 2004; Myers and Baas, 2007; Falnikar et al., 2011). Kinesin-5 has been suggested to play an important role in steering the motion of the GC. In that region, kinesin-5, has been shown to prevent MTs from entering filopodia and impede the movement of the filaments they connect to, thus causing other MT bundles to forcefully orient the GC (Nadar et al., 2008).

We have furthermore demonstrated a sharp dependence of bundle force generation on the motor connectivity parameter, χ (**Figure 3A**), and equivalently, on the fraction of unipolar cross-bridges, χ_{up}, in a mixture of unipolar and bipolar motors. Below a critical value, χ^c, the fraction of overlapping MTs that are cross-linked by motors is not sufficient to form a percolated bundle; hence forces cannot be transmitted across the bundle to extend it forward. The likelihood of the bundle to be percolated drops sharply below χ^c (**Figure 3B**). This behavior, known as a percolation transition (Stauffer and Aharony, 1994), may play an important role in neurite initiation and axon specification. It has been shown that prior to axon specification, kinesin-1 (a unipolar motor) accumulates at the tip of the emerging neurite that eventually becomes the axon, Jacobson et al. (2006); it is absent in the tips of the other neurites that grow slower and later turn into dendrites. It is tempting to speculate that the sudden rise in kinesin-1 concentration at the tip of the future axon enables the MT-connectivity to surpass the percolation threshold necessary for the neurite to expand against the mechanical barrier of the actomyosin cortex, and thereby trigger a rapid growth phase that eventually leads to axon specification.

Variations in χ_{up} may arise due to the presence of bipolar motors and other MT-associated proteins (MAPs) which may compete with unipolar motor binding. In addition, variations in χ_{up} may arise due to the effects of MT binding proteins on the inter-filament spacing. MAPs vary in size, ranging from 80kDa (tau protein) to 200kDa (MAP2). Larger MAPs have been shown to increase the spacing between MT filaments in neurites (Chen et al., 1992; Mukhopadhyay and Hoh, 2001). Tau is enriched in axons, while MAP2 is mostly expressed in dendrites (Bernhardt and Matus, 1984; Kosik and Finch, 1987). Thus, axons have much shorter inter-filament spacing (∼25 nm) than dendrites (∼60 nm) (Chen et al., 1992). Small spacing between filaments, through enrichment of tau over MAP2, can thus facilitate the cross-linking of MTs by motors and cause χ to surpass the percolation threshold χ^c and thereby facilitate axon elongation. This might also explain how Tau contributes to inducing axon-like structures in Sf9 cells (Baas et al., 1991).

Our simulations allowed us to reveal generic scaling laws for the dependence of MT bundle force on the bundle length. One of the factors that strongly influences this dependence is the MT length, l. We find that for bundles that expand with a fixed number of filaments, $F \sim l^2$. This dependency may be of importance during axon initiation and regeneration. Stabilization of MTs in neurites of primary cultures is known to precede cell polarization and axon growth. Furthermore, fast MT polymerization correlates with faster outgrowth (Baas and Ahmad, 1993; Witte et al., 2008; Lu et al., 2013). According to our predictions, the force exerted by bundles with long and stable MTs increases quadratically with the MT length, thus selective stabilization in one neurite could lead to enhanced neurite outgrowth and axon formation. These results may shed light on the striking recent demonstrations that the MT stabilizing drugs Taxol (Hellal et al., 2011) and epothilone B (Ruschel et al., 2015) may promote axon regeneration after spinal cord injury.

Finally, in the last RESULTS section, we considered the growth of MT bundles when a constant supply of MTs is added to the bundle per unit time; this is relevant for neurites in their growth phase (after initiation). The quantity $\omega\, l$ in Equation (12) dictates the rate of (net) MT mass addition into the bundle. During growth, this mass can either distribute across the bundle cross-section or contribute to elongation. We found that the bundles maintain a uniform number of filaments per cross-section, $\langle m(x)\rangle \equiv \bar{m}$, along their length (with slight variations near the fixed left boundary). This number, which reflects the width of the bundle, is determined by the load acting on the bundle. We find that $\bar{m}$ does not alter during steady-state growth and that it scales linearly with the opposing force on the bundle, $\bar{m} \sim F$. Thus, a load acting on the bundle determines its width during steady-state growth. This is consistent with experiments that have shown that the number of MTs per cross-section in developing axons remains constant during different growth stages (Baas et al., 1989). Hence, the overall caliber of the MT bundle remains unchanged in pre-synaptic axons.

In **Figure 6** we have schematically illustrated a few elements that are believed to play a major role in the force balance of growing neurites (Suter and Miller, 2011). The cross-linked MT bundles found in the neurite core act against an actomyosin-filled cortex, that in turn connects to the "towing" machinery of the GC. Within the cortex, myosin II motors generate a tensile load, T_{CX}, whose contribution along the x-axis is F. GC motility and actomyosin forces in this cellular domain produce elastic tension, T_{GC}, at the cell front. The larger T_{GC}, the weaker is the load F on the bundle, and consequently the neurite can grow faster. Additionally, F can be reduced experimentally by external pulling. In that case, T_{GC} is replaced by the applied force and consequently v_g increases as observed experimentally (Zheng et al., 1991; Chada et al., 1997; Fass and Odde, 2003).

These conclusions may provide important insight into the different functions of the MT machinery in axons and dendrites. Our predictions may also be applicable to other systems in which MT bundles play a key role, such as in the mitotic spindle of dividing cells, or within the pro-platelet shafts emanating from megakaryocytes during platelet formation (Patel et al., 2005). *In vitro* studies, which allow control of the MT density, bundle size, MT length distribution, and motor type, will be invaluable to test the scaling laws described in this manuscript.

AUTHOR CONTRIBUTIONS

AZ and MJ wrote the simulation code, MJ ran the calculations, MJ, KF, AZ designed the work and wrote the paper.

ACKNOWLEDGMENTS

We thank François Nédélec for his help with the Cytosim software and to Sarah Foster and Thomas Martin for proofreading. We are grateful to the UK Medical Research Council (Career Development Award to KF), the Israel Science Foundation (grant no. 1396/09 to AZ) and the Bonn Cologne Graduate School as well as Erasmus+ (MJ) for financial support.

REFERENCES

Ahmad, F. J., and Baas, P. W. (1995). Microtubules released from the neuronal centrosome are transported into the axon. *J. Cell Sci.* 108, 2761–2769.

Ahmad, F. J., Hughey, J., Wittmann, T., Hyman, A., Greaser, M., and Baas, P. W. (2000). Motor proteins regulate force interactions between microtubules and microfilaments in the axon. *Nat. Cell Biol.* 2, 276–280. doi: 10.1038/35010544

Atilgan, E., Wirtz, D., and Sun, S. X. (2006). Mechanics and dynamics of actin-driven thin membrane protrusions. *Biophys. J.* 90, 65–76. doi: 10.1529/biophysj.105.071480

Baas, P. W., and Ahmad, F. J. (1993). The transport properties of axonal microtubules establish their polarity orientation. *J. Cell Biol.* 120, 1427–1437. doi: 10.1083/jcb.120.6.1427

Baas, P. W., Black, M. M., and Banker, G. A. (1989). Changes in microtubule polarity orientation during the development of hippocampal neurons in culture. *J. Cell Biol.* 109, 3085–3094. doi: 10.1083/jcb.109.6.3085

Baas, P. W., Pienkowski, T. P., and Kosik, K. S. (1991). Processes induced by tau expression in sf9 cells have an axon-like microtubule organization. *J. Cell Biol.* 115, 1333–1344. doi: 10.1083/jcb.115.5.1333

Bernhardt, R., and Matus, A. (1984). Light and electron microscopic studies of the distribution of microtubule-associated protein 2 in rat brain: a difference between dendritic and axonal cytoskeletons. *J. Comp. Neurol.* 226, 203–221. doi: 10.1002/cne.902260205

Betz, T., Koch, D., Lu, Y.-B., Franze, K., and Käs, J. A. (2011). Growth cones as soft and weak force generators. *Proc. Natl. Acad. Sci. U.S.A.* 108, 13420–13425. doi: 10.1073/pnas.1106145108

Bidone, T. C., Tang, H., and Vavylonis, D. (2015). Dynamic actomyosin network morphology in 3d model of cytokinetic ring assembly. *Biophys. J.* 108, 300a. doi: 10.1016/j.bpj.2014.11.1632

Bradke, F., and Dotti, C. (1999). The role of local actin instability in axon formation. *Science* 283, 1931–1934. doi: 10.1126/science.283.5409.1931

Braun, M., Drummond, D. R., Cross, R. A., and McAinsh, A. D. (2009). The kinesin-14 klp2 organizes microtubules into parallel bundles by an atp-dependent sorting mechanism. *Nat. Cell Biol.* 11, 724–730. doi: 10.1038/ncb1878

Bray, D. (1984). Axonal growth in response to experimentally applied mechanical tension. *Dev. Biol.* 102, 379–389. doi: 10.1016/0012-1606(84)90202-1

Chada, S., Lamoureux, P., Buxbaum, R. E., and Heidemann, S. R. (1997). Cytomechanics of neurite outgrowth from chick brain neurons. *J. Cell Sci.* 110, 1179–1186.

Cheerambathur, D. K., Brust-Mascher, I., Civelekoglu-Scholey, G., and Scholey, J. M. (2008). Dynamic partitioning of mitotic kinesin-5 cross-linkers between microtubule-bound and freely diffusing states. *J. Cell Biol.* 182, 429–436. doi: 10.1083/jcb.200804100

Chen, J., Kanai, Y., Cowan, N. J., and Hirokawa, N. (1992). Projection domains of map2 and tau determine spacings between microtubules in dendrites and axons. *Nature* 360, 674–677. doi: 10.1038/360674a0

Civelekoglu-Scholey, G., and Scholey, J. M. (2010). Mitotic force generators and chromosome segregation. *Cell. Mol. Life Sci.* 67, 2231–2250. doi: 10.1007/s00018-010-0326-6

Dai, J., and Sheetz, M. P. (1995). Mechanical properties of neuronal growth cone membranes studied by tether formation with laser optical tweezers. *Biophys. J.* 68, 988. doi: 10.1016/S0006-3495(95)80274-2

Dehmelt, L. (2014). Cytoskeletal self-organization in neuromorphogenesis. *Bioarchitecture* 4, 75–80. doi: 10.4161/bioa.29070

Dehmelt, L., Nalbant, P., Steffen, W., and Halpain, S. (2006). A microtubule-based, dynein-dependent force induces local cell protrusions: implications for neurite initiation. *Brain Cell Biol.* 35, 39–56. doi: 10.1007/s11068-006-9001-0

Dennerll, T. J., Joshi, H. C., Steel, V. L., Buxbaum, R. E., and Heidemann, S. R. (1988). Tension and compression in the cytoskeleton of pc-12 neurites. ii: quantitative measurements. *J. Cell Biol.* 107, 665–674. doi: 10.1083/jcb.107.2.665

Dennerll, T. J., Lamoureux, P., Buxbaum, R. E., and Heidemann, S. R. (1989). The cytomechanics of axonal elongation and retraction. *J. Cell Biol.* 109, 3073–3083. doi: 10.1083/jcb.109.6.3073

Falnikar, A., Tole, S., and Baas, P. W. (2011). Kinesin-5, a mitotic microtubule-associated motor protein, modulates neuronal migration. *Mol. Biol. Cell* 22, 1561–1574. doi: 10.1091/mbc.E10-11-0905

Fass, J. N., and Odde, D. J. (2003). Tensile force-dependent neurite elicitation via anti-β1 integrin antibody-coated magnetic beads. *Biophys. J.* 85, 623–636. doi: 10.1016/S0006-3495(03)74506-8

Franze, K., Gerdelmann, J., Weick, M., Betz, T., Pawlizak, S., Lakadamyali, M., et al. (2009). Neurite branch retraction is caused by a threshold-dependent mechanical impact. *Biophys. J.* 97, 1883–1890. doi: 10.1016/j.bpj.2009.07.033

Haimo, L. T., and Fenton, R. D. (1984). Microtubule crossbridging by chlamydomonas dynein. *Cell Motil.* 4, 371–385. doi: 10.1002/cm.970040506

Haimo, L. T., and Rosenbaum, J. L. (1981). Dynein binding to microtubules containing microtubule-associated proteins. *Cell Motil.* 1, 499–515. doi: 10.1002/cm.970010409

Haque, S. A., Hasaka, T. P., Brooks, A. D., Lobanov, P. V., and Baas, P. W. (2004). Monastrol, a prototype anti-cancer drug that inhibits a mitotic kinesin, induces rapid bursts of axonal outgrowth from cultured postmitotic neurons. *Cell Motil. Cytoskeleton* 58, 10–16. doi: 10.1002/cm.10176

Heidemann, S. R., and Buxbaum, R. E. (1993). Mechanical tension as a regulator of axonal development. *Neurotoxicology* 15, 95–107.

Hellal, F., Hurtado, A., Ruschel, J., Flynn, K. C., Laskowski, C. J., Umlauf, M., et al. (2011). Microtubule stabilization reduces scarring and causes axon regeneration after spinal cord injury. *Science* 331, 928–931. doi: 10.1126/science.1201148

Hochmuth, F. M., Shao, J. Y., Dai, J., and Sheetz, M. P. (1996). Deformation and flow of membrane into tethers extracted from neuronal growth cones. *Biophys. J.* 70, 358. doi: 10.1016/S0006-3495(96)79577-2

Howard, J. (2001). *Mechanics of Motor Proteins and the Cytoskeleton*. Sunderland, MA: Sinauer Associates.

Hyland, C., Mertz, A. F., Forscher, P., and Dufresne, E. (2014). Dynamic peripheral traction forces balance stable neurite tension in regenerating *Aplysia* bag cell neurons. *Sci. Rep.* 4:4961. doi: 10.1038/srep04961

Jacobson, C., Schnapp, B., and Banker, G. A. (2006). A change in the selective translocation of the kinesin-1 motor domain marks the initial specification of the axon. *Neuron* 49, 797–804. doi: 10.1016/j.neuron.2006.02.005

Janson, M. E., de Dood M. E., and Dogterom, M. (2003). Dynamic instability of microtubules is regulated by force. *J. Cell Biol.* 161, 1029–1034. doi: 10.1083/jcb.200301147

Jolly, A. L., Kim, H., Srinivasan, D., Lakonishok, M., Larson, A. G., and Gelfand, V. I. (2010). Kinesin-1 heavy chain mediates microtubule sliding to drive changes in cell shape. *Proc. Natl. Acad. Sci. U.S.A.* 107, 12151–12156. doi: 10.1073/pnas.1004736107

Kapitein, L. C., Peterman, E. J., Kwok, B. H., Kim, J. H., Kapoor, T. M., and Schmidt, C. F. (2005). The bipolar mitotic kinesin eg5 moves on both microtubules that it crosslinks. *Nature* 435, 114–118. doi: 10.1038/nature03503

Kapitein, L. C., and Hoogenraad, C. C. (2015). Building the neuronal microtubule cytoskeleton. *Neuron* 87, 492–506. doi: 10.1016/j.neuron.2015.05.046

Kapitein, L. C., Kwok, B. H., Weinger, J. S., Schmidt, C. F., Kapoor, T. M., and Peterman, E. J. G. (2008). Microtubule cross-linking triggers the directional motility of kinesin-5. *J. Cell Biol.* 182, 421–428. doi: 10.1083/jcb.200801145

Kerssemakers, J., Howard, J., Hess, H., and Diez, S. (2006). The distance that kinesin-1 holds its cargo from the microtubule surface measured by fluorescence interference contrast microscopy. *Proc. Natl. Acad. Sci. U.S.A.* 103, 15812–15817. doi: 10.1073/pnas.0510400103

Kim, T. (2014). Determinants of contractile forces generated in disorganized actomyosin bundles. *Biomech. Model. Mechanobiol.* 14, 345–355. doi: 10.1007/s10237-014-0608-2

Klumpp, S., and Lipowsky, R. (2005). Cooperative cargo transport by several molecular motors. *Proc. Natl. Acad. Sci. U.S.A.* 102, 17284–17289. doi: 10.1073/pnas.0507363102

Koch, D., Rosoff, W. J., Jiang, J., Geller, H. M., and Urbach, J. S. (2012). Strength in the periphery: growth cone biomechanics and substrate rigidity response in peripheral and central nervous system neurons. *Biophys. J.* 102, 452–460. doi: 10.1016/j.bpj.2011.12.025

Kosik, K. S., and Finch, E. A. (1987). Map2 and tau segregate into dendritic and axonal domains after the elaboration of morphologically distinct neurites: an immunocytochemical study of cultured rat cerebrum. *J. Neurosci.* 7, 3142–3153.

Kruse, K., and Jülicher, F. (2000). Actively contracting bundles of polar filaments. *Phys. Rev. Lett.* 85, 1778–1781. doi: 10.1103/PhysRevLett.85.1778

Kruse, K., Zumdieck, A., and Julicher, F. (2003). Continuum theory of contractile fibres. *Eur. Lett.* 64, 716–722. doi: 10.1209/epl/i2003-00618-2

Kunwar, A., Vershinin, M., Xu, J., and Gross, S. P. (2008). Stepping, strain gating, and an unexpected force-velocity curve for multiple-motor-based transport. *Curr. Biol.* 18, 1173–1183. doi: 10.1016/j.cub.2008.07.027

Lamoureux, P., Buxbaum, R. E., and Heidemann, S. R. (1989). Direct evidence that growth cones pull. *Nature* 340, 159–162. doi: 10.1038/340159a0

Lenz, M., Gardel, M. L., and Dinner, A. R. (2012). Requirements for contractility in disordered cytoskeletal bundles. *New J. Phys.* 14:033037. doi: 10.1088/1367-2630/14/3/033037

Letourneau, P. C., Shattuck, T. A., and Ressler, A. H. (1987). "pull" and "push" in neurite elongation: observations on the effects of different concentrations of cytochalasin b and taxol. *Cell Motil. Cytoskeleton* 8, 193–209. doi: 10.1002/cm.970080302

Liverpool, T. B., and Marchetti, M. C. (2003). Instabilities of isotropic solutions of active polar filaments. *Phys. Rev. Let.* 90:138102. doi: 10.1103/PhysRevLett.90.138102

Lu, W., Fox, P., Lakonishok, M., Davidson, M. W., and Gelfand, V. I. (2013). Initial neurite outgrowth in drosophila neurons is driven by kinesin-powered microtubule sliding. *Curr. Biol.* 23, 1018–1023. doi: 10.1016/j.cub.2013.04.050

Lu, W., Lakonishok, M., and Gelfand, V. I. (2015). Kinesin-1–powered microtubule sliding initiates axonal regeneration in drosophila cultured neurons. *Mol. Biol. Cell* 26, 1296–1307. doi: 10.1091/mbc.E14-10-1423

Mallik, R., Carter, B. C., Lex, S. A., King, S. J., and Gross, S. P. (2004). Cytoplasmic dynein functions as a gear in response to load. *Nature* 427, 649–652. doi: 10.1038/nature02293

Marsh, L., and Letourneau, P. C. (1984). Growth of neurites without filopodial or lamellipodial activity in the presence of cytochalasin b. *J. Cell Biol.* 99, 2041–2047. doi: 10.1083/jcb.99.6.2041

Mogilner, A., and Craig, E. (2010). Towards a quantitative understanding of mitotic spindle assembly and mechanics. *J. Cell Sci.* 123, 3435–3445. doi: 10.1242/jcs.062208

Mogilner, A., Wollman, R., Civelekoglu-Scholey, G., and Scholey, J. (2006). Modeling mitosis. *Trends Cell Biol.* 16, 88–96. doi: 10.1016/j.tcb.2005.12.007

Mukhopadhyay, R., and Hoh, J. H. (2001). Afm force measurements on microtubule-associated proteins: the projection domain exerts a long-range repulsive force. *FEBS Lett.* 505, 374–378. doi: 10.1016/S0014-5793(01)02844-7

Myers, K. A., and Baas, P. W. (2007). Kinesin-5 regulates the growth of the axon by acting as a brake on its microtubule array. *J. Cell Biol.* 178, 1081–1091. doi: 10.1083/jcb.200702074

Nadar, V. C., Ketschek, A., Myers, K. A., Gallo, G., and Baas, P. W. (2008). Kinesin-5 is essential for growth-cone turning. *Curr. Biol.* 18, 1972–1977. doi: 10.1016/j.cub.2008.11.021

Nédélec, F. (2002). Computer simulations reveal motor properties generating stable antiparallel microtubule interactions. *J. Cell Biol.* 158, 1005–1015. doi: 10.1083/jcb.200202051

Patel, S. R., Richardson, J. L., Schulze, H., Kahle, E., Galjart, N., Drabek, K., et al. (2005). Differential roles of microtubule assembly and sliding in proplatelet formation by megakaryocytes. *Blood* 106, 4076–4085. doi: 10.1182/blood-2005-06-2204

Paul, R., Wollman, R., Silkworth, W. T., Nardi, I. K., Cimini, D., and Mogilner, A. (2009). Computer simulations predict that chromosome movements and rotations accelerate mitotic spindle assembly without compromising accuracy. *Proc. Natl. Acad. Sci. U.S.A.* 106, 15708–15713. doi: 10.1073/pnas.0908261106

Roossien, D. H., Lamoureux, P., and Miller, K. E. (2014). Cytoplasmic dynein pushes the cytoskeletal meshwork forward during axonal elongation. *J. Cell Sci.* 127, 3593–3602. doi: 10.1242/jcs.152611

Ruschel, J., Hellal, F., Flynn, K. C., Dupraz, S., Elliott, D. A., Tedeschi, A., et al. (2015). Systemic administration of epothilone b promotes axon regeneration after spinal cord injury. *Science* 348, 347–352. doi: 10.1126/science.aaa2958

Ruthel, G., and Hollenbeck, P. J. (2000). Growth cones are not required for initial establishment of polarity or differential axon branch growth in cultured hippocampal neurons. *J. Neurosci.* 20, 2266–2274.

Scholey, J. M., Brust-Mascher, I., and Mogilner, A. (2003). Cell division. *Nature* 422, 746–752. doi: 10.1038/nature01599

Sciambi, C. J., Komma, D. J., Sköld, H. N., Hirose, K., and Endow, S. A. (2005). A bidirectional kinesin motor in live drosophila embryos. *Traffic* 6, 1036–1046. doi: 10.1111/j.1600-0854.2005.00343.x

Stauffer, D., and Aharony, A. (1992). *Introduction to Percolation Theory, 2nd Edn.* London: Taylor and Francis.

Stauffer, D., and Aharony, A. (1994). *Introduction to Percolation Theory*. Boca Raton, FL; London; New York, NY; Washington, DC: CRC Press.

Suter, D. M., and Miller, K. E. (2011). The emerging role of forces in axonal elongation. *Prog. Neurobiol.* 94, 91–101. doi: 10.1016/j.pneurobio.2011.04.002

Tawada, K., and Sekimoto, K. (1991). Potein fiction exerted by motor enzymes through a weak-binding interaction. *J. Theor. Biol.* 150, 193–200. doi: 10.1016/S0022-5193(05)80331-5

Toriyama, M., Kozawa, S., Sakumura, Y., and Inagaki, N. (2013). Conversion of a signal into forces for axon outgrowth through pak1-mediated shootin1 phosphorylation. *Curr. Biol.* 23, 529–534. doi: 10.1016/j.cub.2013.02.017

Valentine, M. T., Fordyce, P. M., Krzysiak, T. C., Gilbert, S. P., and Block, S. M. (2006). Individual dimers of the mitotic kinesin motor eg5 step processively and support substantial loads *in vitro*. *Nat. Cell Biol.* 8, 470–476. doi: 10.1038/ncb1394

Vilfan, A., Frey, E., Schwabl, F., Thormählen, M., Song, Y. H., and Mandelkow, E. (2001). Dynamics and cooperativity of microtubule decoration by the motor protein kinesin. *J. Mol. Biol.* 312, 1011–1026. doi: 10.1006/jmbi.2001.5020

Ward, J. J., Roque, H., Antony, C., and Nédélec, F. (2015). Mechanical design principles of a mitotic spindle. *eLife* 3:e03398. doi: 10.7554/eLife.03398

Witte, H., Neukirchen, D., and Bradke, F. (2008). Microtubule stabilization specifies initial neuronal polarization. *J. Cell Biol.* 180, 619–632. doi: 10.1083/jcb.200707042

Xu, K., Zhong, G., and Zhuang, X. (2013). Actin, spectrin, and associated proteins form a periodic cytoskeletal structure in axons. *Science* 339, 452–456. doi: 10.1126/science.1232251

Zemel, A., and Mogilner, A. (2009). Motor-induced sliding of microtubule and actin bundles. *Phys. Chem. Chem. Phys.* 11, 4821–4833. doi: 10.1039/b818482h

Zheng, J., Lamoureux, P., Santiago, V., Dennerll, T., Buxbaum, R. E., and Heidemann, S. R. (1991). Tensile regulation of axonal elongation and initiation. *J. Neurosci.* 11, 1117–1125.

Ziebert, F., and Zimmermann, W. (2005). Nonlinear competition between asters and stripes in filament-motor systems. *Eur. Phys. J. E* 18, 41–54. doi: 10.1140/epje/i2005-10029-3

Conflict of Interest Statement: The authors declare that the research was conducted in the absence of any commercial or financial relationships that could be construed as a potential conflict of interest.

frontiers
in Cellular Neuroscience

REVIEW
published: 16 September 2015
doi: 10.3389/fncel.2015.00359

Quantifying mechanical force in axonal growth and guidance

Ahmad I. M. Athamneh* and *Daniel M. Suter*

Bindley Bioscience Center, Birck Nanotechnology Center, Department of Biological Sciences, Purdue University, West Lafayette, IN, USA

Mechanical force plays a fundamental role in neuronal development, physiology, and regeneration. In particular, research has shown that force is involved in growth cone-mediated axonal growth and guidance as well as stretch-induced elongation when an organism increases in size after forming initial synaptic connections. However, much of the details about the exact role of force in these fundamental processes remain unknown. In this review, we highlight: (1) standing questions concerning the role of mechanical force in axonal growth and guidance; and (2) different experimental techniques used to quantify forces in axons and growth cones. We believe that satisfying answers to these questions will require quantitative information about the relationship between elongation, forces, cytoskeletal dynamics, axonal transport, signaling, substrate adhesion, and stiffness contributing to directional growth advance. Furthermore, we address why a wide range of force values have been reported in the literature, and what these values mean in the context of neuronal mechanics. We hope that this review will provide a guide for those interested in studying the role of force in development and regeneration of neuronal networks.

Keywords: growth cone biomechanics, axon elongation, mechanotransduction, cytoskeleton, biophysics, traction force

Edited by:
Dieter Wicher,
Max Planck Institute for Chemical Ecology, Germany

Reviewed by:
Kristian Franze,
University of Cambridge, UK
Dennis Bray,
Universty of Cambridge, UK

***Correspondence:**
Daniel M. Suter,
Bindley Bioscience Center, Birck Nanotechnology Center, Department of Biological Sciences, Purdue University, 915 West State Street, West Lafayette, IN 47907-2054, USA
dsuter@purdue.edu

Received: *21 May 2015*
Accepted: *27 August 2015*
Published: *16 September 2015*

Citation:
Athamneh AIM and Suter DM (2015) Quantifying mechanical force in axonal growth and guidance. Front. Cell. Neurosci. 9:359. doi: 10.3389/fncel.2015.00359

Introduction

The role mechanical forces play in the development and maintenance of neuronal networks has been increasingly recognized and addressed (Bray, 1979; Lamoureux et al., 1989; Suter and Miller, 2011; Franze et al., 2013). Many aspects of axonal growth and development have been examined in the context of mechanical force including cytoskeletal dynamics (Lee and Suter, 2008; Schaefer et al., 2008), axonal transport (Loverde et al., 2011; O'Toole and Miller, 2011; Ahmed and Saif, 2014), growth cone guidance (Suter et al., 1998; Suter and Forscher, 2001; Moore et al., 2009), and molecular motor activity (Bridgman et al., 2001). It has been shown that growth cones generate traction force (Lamoureux et al., 1989; Heidemann et al., 1990) and respond to mechanical stress (Franze et al., 2009) or change in substrate rigidity (Chan and Odde, 2008; Koch et al., 2012). Furthermore, it has been found that mechanical tension induces axonal growth (Bray, 1984; Zheng et al., 1991; Pfister et al., 2004) and that axonal tension is tightly regulated (Lamoureux et al., 1989; Rajagopalan et al., 2010; Hyland et al., 2014). Despite significant advances, many aspects of the mechanical control of axonal growth and guidance as well as maintenance of axons after synapse formation remain unclear.

Standing Questions Pertaining to the Role of Force in Neuronal Processes

There is ample evidence that axonal elongation is influenced by both biochemical and biomechanical factors. The neuronal growth cone controls the direction and rate of axonal growth by navigating the surrounding environment searching for molecular, mechanical, and topographical cues. The machinery responsible for sensing stiffness of the extracellular matrix (ECM) as well as of neighboring cellular surfaces is primarily powered by the actin cytoskeleton, which is highly dynamic and is constantly turning over in the peripheral (P) domain and transition (T) zone (**Figure 1**). Actin polymerizes at the leading edge and is pulled backward by myosin motors, resulting in retrograde F-actin flow (Lin et al., 1996; Medeiros et al., 2006). Traction force is generated as a result of coupling of the F-actin flow to cellular and ECM substrates through adhesion receptors, such as immunoglobulin superfamily cell adhesion molecules, N-cadherin, and integrins (Suter et al., 1998; Bard et al., 2008; Shimada et al., 2008). Several reviews have discussed this substrate-cytoskeletal coupling model including what is known about the role of the cytoskeleton, molecular motors as well as signaling pathways involved (Suter and Forscher, 2000; Suter and Miller, 2011; Gomez and Letourneau, 2014).

How Does Substrate Stiffness Affect Axonal Growth?

While it has been shown that the neuronal growth cone controls the advance of axons in part by sensing and responding to the substrate stiffness, little is known about the physical parameters governing these mechanisms. According to the prevailing model, the level of traction force is determined by the abundance and strength of coupling between F-actin flow and cellular surfaces or ECM. Coupling is influenced by the presence of adhesion substrates as well as the stiffness of the environment. The substrate must be compliant enough to allow adhesion to mature and form strong coupling capable of bearing increasing tension. If the substrate is too stiff, newly formed adhesions abruptly break as lack of compliance in the substrate results in rapid building of tension. This "motor-clutch" model provides a mechanism that inherently senses and responds to substrate stiffness (Chan and Odde, 2008). Consistent with this model, experiments have demonstrated the effect of substrate stiffness on coupling and traction force development in growth cones, but the consequences on neurite outgrowth are not fully clear yet. Furthermore, different types of neuron responded differently to substrate stiffness. For example, softer substrates were shown to promote better neurite growth and branching in spinal cord (Flanagan et al., 2002; Jiang et al., 2008) and hippocampal neurons (Kostic et al., 2007), but not cortical neurons (Norman and Aranda-Espinoza, 2010). Another study found that stiffer substrates significantly increased neurite outgrowth in cortical neurons (Stabenfeldt and LaPlaca, 2011). In a later study, neurite outgrowth of dorsal root ganglion neurons from the peripheral nervous system (PNS) were sensitive to changes in substrate stiffness unlike hippocampal neurons from the central nervous system (CNS; Koch et al., 2012), which seems to contradict earlier observations (Franze et al., 2013). It is important to note that the range of substrate stiffness employed in these studies are not all the same, which makes a direct comparison of the results more challenging, even for the same type of neuron. The apparent discrepancies in the literature, which indicate that different neurons may exhibit different mechanosensitivity, have if anything kept alive the debate about the effect of substrate stiffness on axonal growth, and certainly challenged our understanding of the mechanisms underlying mechanotransduction in neuronal growth cones.

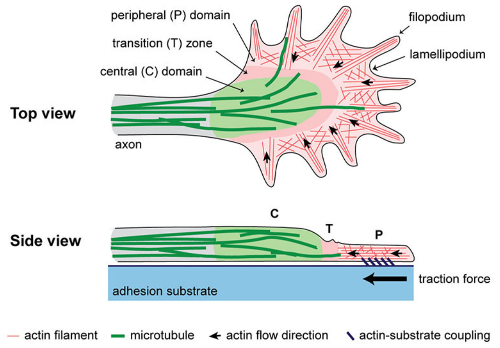

FIGURE 1 | A simplified schematic of the cytoplasmic domains and cytoskeletal structures in the growth cone. Traction force is generated as a result of coupling of F-actin flow in the P domain to an extracellular adhesion substrate.

Recently, it has been shown that compliance, necessary to allow time for coupling to mature, is provided by elastic micron-scale deformations in the actomyosin network and the nascent adhesions themselves (Mejean et al., 2013). Adding to the complexity is the observed biphasic dependence of traction force on the substrate stiffness; i.e., traction force generated by nonneuronal and neuronal cell has been shown to increase linearly with the substrate stiffness but then plateau at sufficiently higher substrate stiffness (Saez et al., 2005; Ghibaudo et al., 2008; Koch et al., 2012; Trichet et al., 2012; Yip et al., 2013). This biphasic behavior complicates comparative analysis amongst studies using different experimental techniques or substrates of different stiffness.

Do Growth Cones Respond to Mechanical Force or Deformation?

The lack of understanding of the mechanisms underlying mechanotransduction is manifested in the ongoing debate whether cell respond to force (stress) or deformation (strain) (Saez et al., 2005; Yip et al., 2013). In our lab, we have shown that the absolute level of substrate deformation appears to be a better predictor of adhesion-mediated growth cone advance when compared to the level of traction force (Athamneh et al., in press). We probed *Aplysia* growth cones with microneedles (MNs) having stiffness ranging from 0.003 to 0.1 N/m, and found that the threshold deformation for a positive growth cone response was about 1 μm of MN deflection regardless of how much force was exerted by the growth cone (Athamneh et al., in press). Therefore, our data highlight the fundamental role of strain vs. stress in controlling the mechanical response during cell migration. Other studies on mechanosensing have also shown evidence of micron-scale deformations involved in sensing and responding to substrate stiffness. For example, rat embryo fibroblasts cultured on a micropillar array caused a constant deformation of 0.84 μm regardless of micropillar stiffness (Trichet et al., 2012). Furthermore, it was found that the mechanical properties of substrate-cytoskeleton linkages in *Aplysia* growth cones were dominated by elastic structures that undergo micron-sized reversible deformations (Mejean et al., 2013). It is not entirely clear at this time what is the physiological significance of the micron-scale deformation, or how can it be reconciled with our understanding of mechanotransduction. However, these micron-scale deformations imply that mechanotransduction not only involves cell adhesion receptors and coupling proteins (Suter et al., 1998; Bard et al., 2008; Shimada et al., 2008), stretch-induced phosphorylation (Suter and Forscher, 2001; Kostic et al., 2007) and activation of ionic channels (Rajnicek and McCaig, 1997; Gomez et al., 2001; Franze et al., 2009; Kerstein et al., 2013), but also involves cytoskeletal reorganization spanning a significant micron-scale spatial range. Clearly, more work is needed to understand the relationship between events taking place at the nano-scale molecular level and cytoskeletal and cytoplasmic domain rearrangements at the micron-scale level in addition to the signaling/feedback mechanisms spanning the two length scales.

How Does the Growth Cone Build Up Traction Force in Substrate-Mediated Growth?

Related to feedback signaling transcending multiple length scales is the question: how does the growth cone build up traction force in substrate-mediated growth? We have shown that traction force increases gradually over time as the growth cone encounters a new adhesion substrate. The maximum level of the force generated depends on the stiffness of the new substrate, implying continuous strengthening of the clutch and/or active recruitment of molecular motors (Athamneh et al., in press). Similar results were reported for rat embryo fibroblasts cultured on a micropillar array (Trichet et al., 2012). We also know from previous studies that the growth cone response to a physically restrained adhesion substrate includes adhesion formation, Src tyrosine phosphorylation, slowing of retrograde F-actin flow, increased actin assembly, advancing of microtubules, and leading edge advance (Suter et al., 1998, 2004; Suter and Forscher, 2001; Lee and Suter, 2008; Schaefer et al., 2008). Despite all this knowledge, the details of how the different events are orchestrated to gradually build up traction force, up to 10^2 nN range (Athamneh et al., in press), and guide axonal growth in the direction of the adhesion site are not entirely clear.

What is the Actual Role of Molecular Motors in Growth Cone Steering?

Experimental evidence suggests that in addition to actin and microtubule assembly dynamics, a number of molecular motors are involved in adhesion-mediated growth cone steering. Myosin II is essential for generating retrograde actin flow (Lin et al., 1996; Bridgman et al., 2001), growth cone steering (Turney and Bridgman, 2005), and actin-filament recycling in the T zone (Medeiros et al., 2006). Dynein is important for microtubule forward movement during growth cone steering and axonal elongation (Myers et al., 2006; Grabham et al., 2007; Roossien et al., 2014). Additionally, it has been suggested that kinesin-5 is involved in growth cone steering by opposing the action of cytoplasmic dynein to affect selective polarization of microtubules in the P domain (Nadar et al., 2008). Furthermore, kinesin-1-driven microtubule sliding promotes initial axonal extension in developing *Drosophila* neurons (Lu et al., 2013). However, the details of motor activity during adhesion-mediated growth, including what structures support these motor activities in order to generate pushing/pulling forces, are not known. Also not clear is how motor activity in growth cones is influenced by different substrates (Lin et al., 1996; Turney and Bridgman, 2005; Medeiros et al., 2006; Ketschek et al., 2007; Rösner et al., 2007; Kollins et al., 2009).

What is the Role of Mechanical Force in Regulating Axonal Transport?

On the axon level, it has been show that tension is tightly regulated (Lamoureux et al., 1989; Rajagopalan et al., 2010; Hyland et al., 2014) and induces axonal growth (Bray, 1984; Zheng et al., 1991; Chada et al., 1997; Pfister et al., 2004), although the mechanism is not yet fully understood (Suter and Miller, 2011). For axons to grow, components must be transported. It follows that understanding the effect of tension on axonal transport is key to understanding the mechanisms of tension-induced growth, although very little is known in this area (O'Toole and Miller, 2011). Increased tension has been shown to decrease fast mitochondria transport in DRG neurons (Loverde et al., 2011), but increased fast vesicles transport in *Aplysia* neurons (Ahmed and Saif, 2014). It was suggested that tension also influences motor activity in the axon, although the details of what motors are affected by tension are not known (Ahmed and Saif, 2014).

In summary, many questions related to the role of force in axonal growth and guidance remain unanswered. We believe that satisfying answers to these questions will require quantitative information about the relationship between elongation, forces, cytoskeletal dynamics, axonal transport, signaling, substrate adhesion, and stiffness contributing to axonal growth and guidance. In the following section, we list experimental techniques used to quantify forces in axons and growth cones and discuss relevant findings.

Techniques for Quantitative Force Measurements in Axons and Growth Cones

Force-Calibrated Microneedles

Bray (1984) was the first to use MNs to demonstrate that neurites grow in response to mechanical tension. Earlier, Bray (1979) used vectorial analysis of the outlines of individually isolated sensory neurons to produce the first evidence that growth cones pull neurites by generating traction force. First quantitative force measurements in axons were performed using force-calibrated MNs by the Heidemann group (Dennerll et al., 1988). A permanent "rest tension" was identified in PC-12 neurites ranging over three orders of magnitude (10^{-2}–10^{0} nN) (Dennerll et al., 1988). In these experiments, the MN was attached to the neurite at a middle point between the soma and the growth cone, and then moved rapidly perpendicular to the neurite's long axis causing tension in the neurite and needle deflection. The same group later attached a MN to the soma of a cultured chick sensory neuron and raised it so that the cell became attached to the substrate at the growth cone only. Neurite tension was found to be in the 10^{0} nN range and strongly correlated with growth cone advance (Lamoureux et al., 1989). Later, the same group showed that axonal elongation correlated with applied tension using a MN (Zheng et al., 1991). Recently, O'Toole et al. (2015) developed a mathematical model to discern individual subcellular forces within the axon and growth cone by relating theses forces to the net axonal tension measured with a MN. Determination of subcellular forces was enabled by labeling of docked mitochondria to monitor subcellular strain. The mean force generated by the rear of the growth cone and axon was 2.0 and 0.6 nN, respectively, suggesting that contractile forces are generated in microtubule-rich regions at the rear of the growth cone and along the axon. We have used MNs in our laboratory to measure traction force in *Aplysia* growth cones as they respond to an adhesion substrate (Athamneh et al., in press).

MNs provide a simple, direct, and effective method for applying and measuring forces in neurons with sensitivity in the 10^{-3} nN range, although the technique can be time-consuming. It does not require specialized instruments or sophisticated analysis procedures. However, the technique is very sensitive to vibration and care must be taken not to cause damage to the cell. Additionally, whereas MNs were effective in measuring traction force in large *Aplysia* growth cones, they can be too large for measurements in other cell types with smaller growth cones. When cultured on poly-L-lysine, *Aplysia* growth cones on average cover an area of approximately 1.25×10^{3} μm^{2} (Wu et al., 2008), which is 5–10 times larger than growth cones from other species.

Traction Force Microscopy

In traction force microscopy (TFM), cells are cultured on a deformable substrate, which can be a hydrogel or a nanowire array. Fluorescent beads are embedded as markers within the substrate to facilitate optical detection of the deformation caused by the cell. Force exerted by the cell is calculated using measured deformations and the stiffness of the substrate. Due to the popularity of TFM in the field of cell biomechanics, numerous reviews and method articles have been published describing the theory behind the techniques as well as methods for substrate preparation and fabrication (Sabass et al., 2008; Plotnikov et al., 2014; Style et al., 2014; Schwarz and Soiné, 2015). Bridgman et al. (2001) used the technique to study the role of Myosin IIB in generation of filopodia-mediated traction force in growth cones from mouse superior cervical ganglion neurons. The traction force generated by a single filopodium was found to be in the 10^{0} nN range and partially reduced in Myosin IIB knock-out neurons, suggesting that Myosin IIB was acting in combination with other myosins (Bridgman et al., 2001). Chan and Odde (2008) used TFM to validate their "motor-clutch" model. They identified a 1 kPa threshold for substrate stiffness below which a single filopodium of embryonic-chick—forebrain neurons exhibited oscillatory load-and-fail dynamics, with slower retrograde flow and higher traction forces. On substrates stiffer than 1 kPa, filopodia showed frictional slippage, with fast retrograde flow and low traction forces (Chan and Odde, 2008). Koch et al. (2012) compared traction forces generated by growth cones of rat dorsal root ganglion and hippocampal neurons and found that the growth cones of PNS neurons produce higher traction forces compared to CNS neurons (10^{0} vs. 10^{-1} nN range). For both neuron types, traction forced increased with increasing stiffness, which is consistent with other studies. Toriyama et al. (2013) observed that netrin-1 positively regulates traction force in the growth cone of rat hippocampal neurons through Pak1-mediated shootin1 phosphorylation, which enhances F-actin-substrate coupling leading to higher force generation. Traction force was found to be highest in the actin-rich P domain of *Aplysia* growth cones, and although traction force redistributes continuously, the net resulting neurite tension was tightly regulated around 3.1 nN (Hyland et al., 2014). In NG108-15 neuroblastoma cells neurite tension was measured as 0.6 nN (Betz et al., 2011), which is consistent with earlier neurite tension measurements in PC-12 cells using MNs (Dennerll et al., 1988). Finally, using a microfabricated nanowire array TFM revealed a wide range of traction forces (10^{-2}–10^{1} nN) in the growth cones of rat dorsal root ganglion neurons depending on nanowire stiffness (Hällström et al., 2010).

While TFM provides high-resolution force measurements at the growth cone and single filopodia levels, the uniformity of the substrate stiffness does not mimic the complex environment *in vivo* particularly well. The introduction of a stiffness gradient or a defined stiffness micropattern for neurons to interact with remains a technical challenge. Accordingly, force values reported using conventional TFM on a uniform substrate may represent a "quasi" steady state condition and not traction force generation in response to a change in adhesion substrate.

Optical Tweezers

The optical tweezer (OT; or optical trap) setup consists of a highly focused infrared laser beam that can physically hold (i.e., trap) a microbead. The tweezers can be calibrated to know how much force (typically in 10^{-3}–10^{0} nN range) is required to remove the trapped bead from its focal center. Because of its high force sensitivity, this technique has been extensively used to measure molecular forces produced by proteins, especially molecular motors (Elting and Spudich, 2012). Using OTs, it was shown that the forces generated by the filopodia in the growth cones of CNS (hippocampal) neurons were larger when compared with PNS (Dorsal Root Ganglia) neurons (5×10^{-3} vs. $1–2 \times 10^{-3}$ nN) (Amin et al., 2013). The lamellipodia of both CNS and PNS neurons generated similar lateral forces level up to 20×10^{-3} nN, but exerted larger vertical force in PNS neurons (4×10^{-3} vs. $1–5 \times 10^{-3}$ nN) (Amin et al., 2013). Mejean et al. (2013) used an optical trap to characterize the mechanics of apCAM-mediated nascent adhesions in *Aplysia* growth cones and found that for forces in the 10^{-3} nN scale, nascent adhesions were dominated by an elastic structure, which can be reversibly deformed by up to 1 μm (Mejean et al., 2013). These results suggested a substrate-cytoskeleton interface dominated by a compliant cross-linked network and not a number of stiff molecular springs in parallel. The compliance of the network may provide more time for nascent adhesions to strengthen before larger forces develop. Also using an optical trap, Bard et al. (2008) studied N-cadherin-mediated substrate-cytoskeletal coupling and found that at low forces ($<16 \times 10^{-3}$ nN) slippage of cadherin-cytoskeleton bonds occurred, while at high forces actin accumulated strengthening nascent N-cadherin coupling. Moore et al. (2009) showed that the advancing growth cones of spinal commissural neurons generated traction force greater than 63×10^{-3} nN when confronted with a restrained netrin-1 bead (Moore et al., 2009). Without the bead, the same growth cone generated 9×10^{-3} nN local traction force as determined by TFM.

Using OTs for force measurements can be technically involved. However, once established, the technique can provide superb resolution and spatial selectivity. It also overcomes the issue of substrate uniformity suffered by TFM. A major limitation of OTs is that the level of force that can be applied without causing damage to the cells is in the 10^{-3} nN range. Thus, OTs typically cannot sustain enough force to induce adhesion-mediated growth cone advance or steering responses (Bard et al., 2008; Shahapure et al., 2010; Amin et al., 2013; Mejean et al., 2013), especially in neurons with large growth cones such as *Aplysia*.

Atomic Force Microscopy

Atomic force microscopy (AFM) can be used both for applying and measuring forces in neurons (Franze et al., 2009), although it has been mostly used for imaging and measuring cell topography and elasticity (McNally and Borgens, 2004; Grzywa et al., 2006; Xiong et al., 2009; Spedden et al., 2012). Using AFM in the lateral force measurements mode, Fuhs et al. (2013) measured the forward pushing forces of mouse retinal ganglion cell and NG108-15 growth cones and found them to be on the order of 10^{-1} nN. In the same paper, the authors reported that the total traction force generated by the NG108-15 growth cones as measured by TFM was two orders of magnitude higher. While AFM lateral force measurements may appear to be an ideal solution for measuring traction force in growth cones, significant technical difficulties exist particularly related to calibrating the torsional response of the AFM cantilever (Karhu et al., 2009). Karhu et al. (2009) showed that frictional-force measurement using AFM was possible in longitudinal imaging mode and provided several advantages over lateral imaging mode. In our lab, we have developed a new AFM-based method for measuring retrograde traction force in growth cones that does not require lateral force calibration by following the approach developed by Karhu et al. (2009). We used the new method with an apCAM-coated colloidal cantilever to measure the temporal traction force profile in *Aplysia* growth cones as they encounter a physically-restrained adhesion substrate (Athamneh et al., in press). In summary, commercially available AFM systems provide high-resolution data over a large force range from 10^{-3} to 10^{2} nN. However, calibration and data analysis require significant involvement. Additionally, care must be taken to account for noise and instrumental drift, especially in temporal measurements for an extended period of time.

MEMS Force Sensors

Microelectromechanical system (MEMS)-based force sensors are microfabricated from a single silicon crystal and can provide high-resolution quantitative measurements over a large dynamic range (Rajagopalan and Saif, 2011). Using a MEMS sensor, it was found that axons of embryonic *Drosophila* neurons that have formed neuromuscular junctions maintain a rest tension of 1–13 nN (Siechen et al., 2009; Rajagopalan et al., 2010), which is in good agreement with the *in vitro* studies determining neurite rest tension with either TFM (Betz et al., 2011; Hyland et al., 2014) or MNs (Dennerll et al., 1988). Axons responded to perturbation of the rest tension by either relaxing or contracting to restore original rest tension (Rajagopalan et al., 2010). The advantages and limitations of MEMS-based force sensors for the

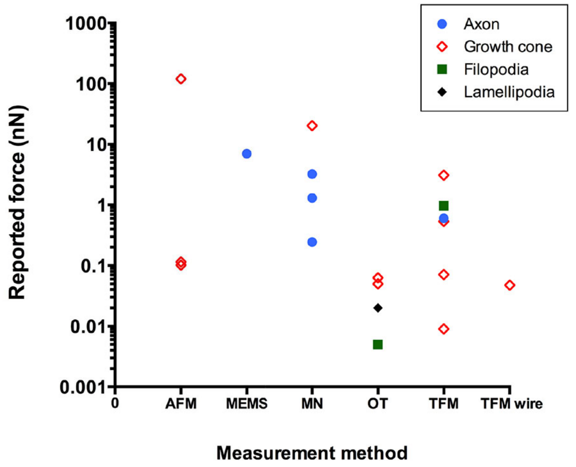

FIGURE 2 | Reported literature values of force in neurons using different experimental techniques (AFM, atomic force microscopy; MEMS, microelectromechanical system-based force sensors; MN, microneedle; OT, optical tweezers; TFM, traction force microscopy).

TABLE 1 | Force measurements reported in the literature for different cell types and experimental techniques.

Cell type	Part of the cell probed	Reported force value (nN)			Method	Reference
		Lowest	Highest	Mean		
PC-12	Axon	0	10	0.244	MN	Dennerll et al. (1988)
Embryonic chick sensory neurons	Axon	0.46	6		MN	Lamoureux et al. (1989)
Superior cervical ganglion neurons	Filopodia		1.6	0.97	TFM	Bridgman et al. (2001)
Aplysia Californica bag cell neurons	Growth cones	0.5	8.5	3.1	TFM	Hyland et al. (2014)
Rat dorsal root ganglion	Growth cones		1.179	0.537	TFM	Koch et al. (2012)
Rat central nervous systems neurons	Growth cones		0.247	0.071	TFM	Koch et al. (2012)
Rat dorsal root ganglion neurons	Growth cones	0.015	0.08		TFM wire	Hällström et al. (2010)
Rat hippocampal and dorsal root ganglia	Filopodia	0.001	0.005	0.005	OT	Amin et al. (2013)
Rat hippocampal and dorsal root ganglia	Lamellipodia	0.001	0.02	0.02	OT	Amin et al. (2013)
Aplysia Californica bag cell neurons	Lamellipodia	0.0001	0.1		OT	Mejean et al. (2013)
Spinal commissural neuron	Growth cone		0.063		OT	Moore et al. (2009)
Spinal commissural neuron	Growth cone	0.002	0.037	0.009	TFM	Moore et al. (2009)
NG108-15	Axon			0.602	TFM	Betz et al. (2011)
Chick sensory neurons	Axon	0.4	4.8	1.3	MN	O'Toole et al. (2015)
Drosophila motor neurons *in vivo*	Axon	1	13	7	MEMS	Rajagopalan et al. (2010)
NG108-15	Growth cone		0.15	0.102	AFM	Fuhs et al. (2013)
Mouse retinal ganglion cell	Growth cone		0.17	0.115	AFM	Fuhs et al. (2013)
Aplysia Californica bag cell neurons	Growth cone	82	158	120	AFM	Athamneh et al. (in press)
Aplysia Californica bag cell neurons	Growth cone	2.5	92.2	20.3	MN	Athamneh et al. (in press)

AFM, atomic force microscopy; MEMS, microelectromechanical system-based force sensors; MN, microneedle; OT, optical tweezers; TFM, traction force microscopy.

study of cell biomechanics have been reviewed by Rajagopalan and Saif (2011).

Summary and Conclusions

Figure 2 and **Table 1** show force values reported in the literature for different parts of the neuron using different experimental techniques. The graph illustrates the wide range of force values even for the same experimental technique or the same part of the neuron. For example, values reported for traction force generated by the growth cone ranged over five orders of magnitude. Indeed, different force values can be expected for different types of neurons and different sizes of neuronal areas probed, which will result in different amounts of cytoskeletal structures and motors that are engaged in the process. Furthermore, different experimental techniques may provide slightly different values for the same neuron and area. However, it is possible that some of the variations in force values could be due to calibration problems. If anything, the discrepancy illustrated in **Figure 2** suggests that extreme caution must be taken when comparing force values reported in different studies. Setting up standardized calibration methods for each force measurement method might be an approach to reduce some of the variations currently found in the literature.

Quantitative studies of mechanical forces in axons and growth cones have yielded significant findings about the critical role of force in growth cone dynamics and axonal elongation. However, many important questions remain unanswered, and apparent discrepancies in the literature, particularly related to the effect of substrate stiffness on neurite outgrowth, need to be addressed. Although the details of the mechanism by which growth cones sense and responds to substrate stiffness are still unclear, it appears to be a highly coordinated mechanism involving a combination of biochemical and biomechanical processes spanning multiple length scales. Understanding the details of this mechanism will undoubtedly require and stimulate more research involving quantitative force measurements.

Acknowledgments

The authors are grateful to the National Science Foundation for support of this work under Grant No. 1146944-IOS.

References

Ahmed, W. W., and Saif, T. A. (2014). Active transport of vesicles in neurons is modulated by mechanical tension. *Sci. Rep.* 4:4481. doi: 10.1038/srep04481

Amin, L., Ercolini, E., Ban, J., and Torre, V. (2013). Comparison of the force exerted by hippocampal and DRG growth cones. *PLoS One* 8:e73025. doi: 10.1371/journal.pone.0073025

Athamneh, A. I. M., Cartagena-Rivera, A. X., Raman, A., and Suter, D. M. (in press). Substrate deformation predicts neuronal growth cone advance. *Biophys. J.* (in press).

Bard, L., Boscher, C., Lambert, M., Mège, R.-M., Choquet, D., and Thoumine, O. (2008). A molecular clutch between the actin flow and N-cadherin adhesions drives growth cone migration. *J. Neurosci.* 28, 5879–5890. doi: 10.1523/JNEUROSCI.5331-07.2008

Betz, T., Koch, D., Lu, Y.-B., Franze, K., and Käs, J. A. (2011). Growth cones as soft and weak force generators. *Proc. Natl. Acad. Sci. U S A* 108, 13420–13425. doi: 10.1073/pnas.1106145108

Bray, D. (1979). Mechanical tension produced by nerve cells in tissue culture. *J. Cell Sci.* 37, 391–410.

Bray, D. (1984). Axonal growth in response to experimentally applied mechanical tension. *Dev. Biol.* 102, 379–389. doi: 10.1016/0012-1606(84)90202-1

Bridgman, P. C., Dave, S., Asnes, C. F., Tullio, A. N., and Adelstein, R. S. (2001). Myosin IIB is required for growth cone motility. *J. Neurosci.* 21, 6159–6169.

Chada, S., Lamoureux, P., Buxbaum, R. E., and Heidemann, S. R. (1997). Cytomechanics of neurite outgrowth from chick brain neurons. *J. Cell Sci.* 110, 1179–1186.

Chan, C. E., and Odde, D. J. (2008). Traction dynamics of filopodia on compliant substrates. *Science* 322, 1687–1691. doi: 10.1126/science.1163595

Dennerll, T. J., Joshi, H. C., Steel, V. L., Buxbaum, R. E., and Heidemann, S. R. (1988). Tension and compression in the cytoskeleton of PC-12 neurites. II: quantitative measurements. *J. Cell Biol.* 107, 665–674. doi: 10.1083/jcb.107.2.665

Elting, M. W., and Spudich, J. A. (2012). Future challenges in single-molecule fluorescence and laser trap approaches to studies of molecular motors. *Dev. Cell* 23, 1084–1091. doi: 10.1016/j.devcel.2012.10.002

Flanagan, L. A., Ju, Y. E., Marg, B., Osterfield, M., and Janmey, P. A. (2002). Neurite branching on deformable substrates. *Neuroreport* 13, 2411–2415. doi: 10.1097/00001756-200212200-00007

Franze, K., Gerdelmann, J., Weick, M., Betz, T., Pawlizak, S., Lakadamyali, M., et al. (2009). Neurite branch retraction is caused by a threshold-dependent mechanical impact. *Biophys. J.* 97, 1883–1890. doi: 10.1016/j.bpj.2009.07.033

Franze, K., Janmey, P. A., and Guck, J. (2013). Mechanics in neuronal development and repair. *Annu. Rev. Biomed. Eng.* 15, 227–251. doi: 10.1146/annurev-bioeng-071811-150045

Fuhs, T., Reuter, L., Vonderhaid, I., Claudepierre, T., and Käs, J. A. (2013). Inherently slow and weak forward forces of neuronal growth cones measured by a drift-stabilized atomic force microscope. *Cytoskeleton (Hoboken)* 70, 44–53. doi: 10.1002/cm.21080

Ghibaudo, M., Saez, A., Trichet, L., Xayaphoummine, A., Browaeys, J., Silberzan, P., et al. (2008). Traction forces and rigidity sensing regulate cell functions. *Soft Matter* 4, 1836–1843. doi: 10.1039/b804103b

Gomez, T. M., and Letourneau, P. C. (2014). Actin dynamics in growth cone motility and navigation. *J. Neurochem.* 129, 221–234. doi: 10.1111/jnc.12506

Gomez, T. M., Robles, E., Poo, M.-M., and Spitzer, N. C. (2001). Filopodial calcium transients promote substrate-dependent growth cone turning. *Science* 291, 1983–1987. doi: 10.1126/science.1056490

Grabham, P. W., Seale, G. E., Bennecib, M., Goldberg, D. J., and Vallee, R. B. (2007). Cytoplasmic dynein and LIS1 are required for microtubule advance during growth cone remodeling and fast axonal outgrowth. *J. Neurosci.* 27, 5823–5834. doi: 10.1523/jneurosci.1135-07.2007

Grzywa, E. L., Lee, A. C., Lee, G. U., and Suter, D. M. (2006). High-resolution analysis of neuronal growth cone morphology by comparative atomic force and optical microscopy. *J. Neurobiol.* 66, 1529–1543. doi: 10.1002/neu.20318

Hällström, W., Lexholm, M., Suyatin, D. B., Hammarin, G., Hessman, D., Samuelson, L., et al. (2010). Fifteen-piconewton force detection from neural growth cones using nanowire arrays. *Nano Lett.* 10, 782–787. doi: 10.1021/nl902675h

Heidemann, S. R., Lamoureux, P., and Buxbaum, R. E. (1990). Growth cone behavior and production of traction force. *J. Cell Biol.* 111, 1949–1957. doi: 10.1083/jcb.111.5.1949

Hyland, C., Mertz, A. F., Forscher, P., and Dufresne, E. (2014). Dynamic peripheral traction forces balance stable neurite tension in regenerating *aplysia* bag cell neurons. *Sci. Rep.* 4:4961. doi: 10.1038/srep04961

Jiang, F. X., Yurke, B., Firestein, B. L., and Langrana, N. A. (2008). Neurite outgrowth on a DNA crosslinked hydrogel with tunable stiffnesses. *Ann. Biomed. Eng.* 36, 1565–1579. doi: 10.1007/s10439-008-9530-z

Karhu, E., Gooyers, M., and Hutter, J. L. (2009). Quantitative friction-force measurements by longitudinal atomic force microscope imaging. *Langmuir* 25, 6203–6213. doi: 10.1021/la900005z

Kerstein, P. C., Jacques-Fricke, B. T., Rengifo, J., Mogen, B. J., Williams, J. C., Gottlieb, P. A., et al. (2013). Mechanosensitive TRPC1 channels promote calpain proteolysis of talin to regulate spinal axon outgrowth. *J. Neurosci.* 33, 273–285. doi: 10.1523/JNEUROSCI.2142-12.2013

Ketschek, A. R., Jones, S. L., and Gallo, G. (2007). Axon extension in the fast and slow lanes: substratum-dependent engagement of myosin II functions. *Dev. Neurobiol.* 67, 1305–1320. doi: 10.1002/dneu.20455

Koch, D., Rosoff, W. J., Jiang, J., Geller, H. M., and Urbach, J. S. (2012). Strength in the periphery: growth cone biomechanics and substrate rigidity response in peripheral and central nervous system neurons. *Biophys. J.* 102, 452–460. doi: 10.1016/j.bpj.2011.12.025

Kollins, K. M., Hu, J., Bridgman, P. C., Huang, Y. Q., and Gallo, G. (2009). Myosin-II negatively regulates minor process extension and the temporal development of neuronal polarity. *Dev. Neurobiol.* 69, 279–298. doi: 10.1002/dneu.20704

Kostic, A., Sap, J., and Sheetz, M. P. (2007). RPTPα is required for rigidity-dependent inhibition of extension and differentiation of hippocampal neurons. *J. Cell Sci.* 120, 3895–3904. doi: 10.1242/jcs.009852

Lamoureux, P., Buxbaum, R. E., and Heidemann, S. R. (1989). Direct evidence that growth cones pull. *Nature* 340, 159–162. doi: 10.1038/340159a0

Lee, A. C., and Suter, D. M. (2008). Quantitative analysis of microtubule dynamics during adhesion-mediated growth cone guidance. *Dev. Neurobiol.* 68, 1363–1377. doi: 10.1002/dneu.20662

Lin, C. H., Espreafico, E. M., Mooseker, M. S., and Forscher, P. (1996). Myosin drives retrograde F-Actin flow in neuronal growth cones. *Neuron* 16, 769–782. doi: 10.1016/s0896-6273(00)80097-5

Loverde, J. R., Ozoka, V. C., Aquino, R., Lin, L., and Pfister, B. J. (2011). Live imaging of axon stretch growth in embryonic and adult neurons. *J. Neurotrauma* 28, 2389–2403. doi: 10.1089/neu.2010.1598

Lu, W., Fox, P., Lakonishok, M., Davidson, M. W., and Gelfand, V. I. (2013). Initial neurite outgrowth in *drosophila* neurons is driven by kinesin-powered microtubule sliding. *Curr. Biol.* 23, 1018–1023. doi: 10.1016/j.cub.2013.04.050

McNally, H. A., and Borgens, R. B. (2004). Three-dimensional imaging of living and dying neurons with atomic force microscopy. *J. Neurocytol.* 33, 251–258. doi: 10.1023/b:neur.0000030700.48612.0b

Medeiros, N. A., Burnette, D. T., and Forscher, P. (2006). Myosin II functions in actin-bundle turnover in neuronal growth cones. *Nat. Cell Biol.* 8, 216–226. doi: 10.1038/ncb1367

Mejean, C. O., Schaefer, A. W., Buck, K. B., Kress, H., Shundrovsky, A., Merrill, J. W., et al. (2013). Elastic coupling of nascent apCAM adhesions to flowing actin networks. *PLoS One* 8:e73389. doi: 10.1371/journal.pone.0073389

Moore, S. W., Biais, N., and Sheetz, M. P. (2009). Traction on immobilized netrin-1 is sufficient to reorient axons. *Science* 325:166. doi: 10.1126/science.1173851

Myers, K. A., Tint, I., Nadar, C. V., He, Y., Black, M. M., and Baas, P. W. (2006). Antagonistic forces generated by cytoplasmic dynein and myosin-II during growth cone turning and axonal retraction. *Traffic* 7, 1333–1351. doi: 10.1111/j.1600-0854.2006.00476.x

Nadar, V. C., Ketschek, A., Myers, K. A., Gallo, G., and Baas, P. W. (2008). Kinesin-5 is essential for growth cone turning. *Curr. Biol.* 18, 1972–1977. doi: 10.1016/j.cub.2008.11.021

Norman, L., and Aranda-Espinoza, H. (2010). Cortical neuron outgrowth is insensitive to substrate stiffness. *Cell. Mol. Bioeng.* 3, 398–414. doi: 10.1007/s12195-010-0137-8

O'Toole, M., Lamoureux, P., and Miller, K. E. (2015). Measurement of subcellular force generation in neurons. *Biophys. J.* 108, 1027–1037. doi: 10.1016/j.bpj.2015.01.021

O'Toole, M., and Miller, K. E. (2011). The role of stretching in slow axonal transport. *Biophys. J.* 100, 351–360. doi: 10.1016/j.bpj.2010.12.3695

Pfister, B. J., Iwata, A., Meaney, D. F., and Smith, D. H. (2004). Extreme stretch growth of integrated axons. *J. Neurosci.* 24, 7978–7983. doi: 10.1523/jneurosci.1974-04.2004

Plotnikov, S. V., Sabass, B., Schwarz, U. S., and Waterman, C. M. (2014). "Chapter 20 – high-resolution traction force microscopy," in *Methods in Cell Biology*, Vol. 123, eds J. C. Waters and T. Wittman (Atlanta, GA: Elsevier), 367–394. doi: 10.1016/B978-0-12-420138-5.00020-3

Rajagopalan, J., and Saif, M. T. A. (2011). MEMS Sensors and Microsystems for Cell Mechanobiology. *J. Micromech. Microeng.* 21, 054002–054012. doi: 10.1088/0960-1317/21/5/054002

Rajagopalan, J., Tofangchi, A., and A. Saif, M. T. (2010). *Drosophila* neurons actively regulate axonal tension *in vivo*. *Biophys. J.* 99, 3208–3215. doi: 10.1016/j.bpj.2010.09.029

Rajnicek, A., and McCaig, C. (1997). Guidance of CNS growth cones by substratum grooves and ridges: effects of inhibitors of the cytoskeleton, calcium channels and signal transduction pathways. *J. Cell Sci.* 110, 2915–2924.

Rösner, H., Möller, W., Wassermann, T., Mihatsch, J., and Blum, M. (2007). Attenuation of actinomyosinII contractile activity in growth cones accelerates filopodia-guided and microtubule-based neurite elongation. *Brain Res.* 1176, 1–10. doi: 10.1016/j.brainres.2007.07.081

Roossien, D. H., Lamoureux, P., and Miller, K. E. (2014). Cytoplasmic dynein pushes the cytoskeletal meshwork forward during axonal elongation. *J. Cell Sci.* 127, 3593–3602. doi: 10.1242/jcs.152611

Sabass, B., Gardel, M. L., Waterman, C. M., and Schwarz, U. S. (2008). High resolution traction force microscopy based on experimental and computational advances. *Biophys. J.* 94, 207–220. doi: 10.1529/biophysj.107.113670

Saez, A., Buguin, A., Silberzan, P., and Ladoux, B. (2005). Is the mechanical activity of epithelial cells controlled by deformations or forces? *Biophys. J.* 89, L52–L54. doi: 10.1529/biophysj.105.071217

Schaefer, A. W., Schoonderwoert, V. T., Ji, L., Mederios, N., Danuser, G., and Forscher, P. (2008). Cytoskeletal dynamics underlying neurite outgrowth. *Dev. Cell* 15, 146–162. doi: 10.1016/j.devcel.2008.05.003

Schwarz, U. S., and Soiné, J. R. D. (2015). Traction force microscopy on soft elastic substrates: a guide to recent computational advances. *Biochim. Biophys. Acta* doi: 10.1016/j.bbamcr.2015.05.028 [Epub ahead of print].

Shahapure, R., Difato, F., Laio, A., Bisson, G., Ercolini, E., Amin, L., et al. (2010). Force generation in lamellipodia is a probabilistic process with fast growth and retraction events. *Biophys. J.* 98, 979–988. doi: 10.1016/j.bpj.2009.11.041

Shimada, T., Toriyama, M., Uemura, K., Kamiguchi, H., Sugiura, T., Watanabe, N., et al. (2008). Shootin1 interacts with actin retrograde flow and L1-CAM to promote axon outgrowth. *J. Cell Biol.* 181, 817–829. doi: 10.1083/jcb.200712138

Siechen, S., Yang, S., Chiba, A., and Saif, T. (2009). Mechanical tension contributes to clustering of neurotransmitter vesicles at presynaptic terminals. *Proc. Natl. Acad. Sci. U S A* 106, 12611–12616. doi: 10.1073/pnas.0901867106

Spedden, E., White, J. D., Naumova, E. N., Kaplan, D. L., and Staii, C. (2012). Elasticity maps of living neurons measured by combined fluorescence and atomic force microscopy. *Biophys. J.* 103, 868–877. doi: 10.1016/j.bpj.2012.08.005

Stabenfeldt, S. E., and LaPlaca, M. C. (2011). Variations in rigidity and ligand density influence neuronal response in methylcellulose-laminin hydrogels. *Acta Biomater.* 7, 4102–4108. doi: 10.1016/j.actbio.2011.07.026

Style, R. W., Boltyanskiy, R., German, G. K., Hyland, C., MacMinn, C. W., Mertz, A. F., et al. (2014). Traction force microscopy in physics and biology. *Soft Matter* 10, 4047–4055. doi: 10.1039/c4sm00264d

Suter, D. M., Errante, L. D., Belotserkovsky, V., and Forscher, P. (1998). The ig superfamily cell adhesion molecule, apCAM, mediates growth cone steering by substrate–cytoskeletal coupling. *J. Cell Biol.* 141, 227–240. doi: 10.1083/jcb.141.1.227

Suter, D. M., and Forscher, P. (2000). Substrate–cytoskeletal coupling as a mechanism for the regulation of growth cone motility and guidance. *J. Neurobiol.* 44, 97–113. doi: 10.1002/1097-4695(200008)44:2<97::aid-neu2>3.0.co;2-u

Suter, D. M., and Forscher, P. (2001). Transmission of growth cone traction force through apCAM–cytoskeletal linkages is regulated by Src family tyrosine kinase activity. *J. Cell Biol.* 155, 427–438. doi: 10.1083/jcb.200107063

Suter, D. M., and Miller, K. E. (2011). The emerging role of forces in axonal elongation. *Prog. Neurobiol.* 94, 91–101. doi: 10.1016/j.pneurobio.2011.04.002

Suter, D. M., Schaefer, A. W., and Forscher, P. (2004). Microtubule dynamics are necessary for Src family kinase-dependent growth cone steering. *Curr. Biol.* 14, 1194–1199. doi: 10.1016/j.cub.2004.06.049

Toriyama, M., Kozawa, S., Sakumura, Y., and Inagaki, N. (2013). Conversion of a signal into forces for axon outgrowth through pak1-mediated shootin1 phosphorylation. *Curr. Biol.* 23, 529–534. doi: 10.1016/j.cub.2013.02.017

Trichet, L., Le Digabel, J., Hawkins, R. J., Vedula, S. R. K., Gupta, M., Ribrault, C., et al. (2012). Evidence of a large-scale mechanosensing mechanism for cellular adaptation to substrate stiffness. *Proc. Natl. Acad. Sci. U S A* 109, 6933–6938. doi: 10.1073/pnas.1117810109

Turney, S. G., and Bridgman, P. C. (2005). Laminin stimulates and guides axonal outgrowth via growth cone myosin II activity. *Nat. Neurosci.* 8, 717–719. doi: 10.1038/nn1466

Wu, B., Decourt, B., Zabidi, M. A., Wuethrich, L. T., Kim, W. H., Zhou, Z., et al. (2008). Microtubule-mediated Src tyrosine kinase trafficking in neuronal growth cones. *Mol. Biol. Cell* 19, 4611–4627. doi: 10.1091/mbc.e08-06-0603

Xiong, Y., Lee, A. C., Suter, D. M., and Lee, G. U. (2009). Topography and nanomechanics of live neuronal growth cones analyzed by atomic force microscopy. *Biophys. J.* 96, 5060–5072. doi: 10.1016/j.bpj.2009.03.032

Yip, A. K., Iwasaki, K., Ursekar, C., Machiyama, H., Saxena, M., Chen, H., et al. (2013). Cellular response to substrate rigidity is governed by either stress or strain. *Biophys. J.* 104, 19–29. doi: 10.1016/j.bpj.2012.11.3805

Zheng, J., Lamoureux, P., Santiago, V., Dennerll, T., Buxbaum, R. E., and Heidemann, S. R. (1991). Tensile regulation of axonal elongation and initiation. *J. Neurosci.* 11, 1117–1125.

Conflict of Interest Statement: The authors declare that the research was conducted in the absence of any commercial or financial relationships that could be construed as a potential conflict of interest.

Advantages of publishing in Frontiers

OPEN ACCESS
Articles are free to read, for greatest visibility

COLLABORATIVE PEER-REVIEW
Designed to be rigorous – yet also collaborative, fair and constructive

FAST PUBLICATION
Average 85 days from submission to publication (across all journals)

COPYRIGHT TO AUTHORS
No limit to article distribution and re-use

TRANSPARENT
Editors and reviewers acknowledged by name on published articles

SUPPORT
By our Swiss-based editorial team

IMPACT METRICS
Advanced metrics track your article's impact

GLOBAL SPREAD
5'100'000+ monthly article views and downloads

LOOP RESEARCH NETWORK
Our network increases readership for your article

Frontiers
EPFL Innovation Park, Building I • 1015 Lausanne • Switzerland
Tel +41 21 510 17 00 • Fax +41 21 510 17 01 • info@frontiersin.org
www.frontiersin.org

Find us on